Durham University

Durham E-Theses

STUDY OF PHARMACEUTICAL CRYSTAL HYDRATES AND THEIR PREDICTION BASED ON PRE-NUCLEATION AGGREGATION

MOHD NADZRI BIN-MOHD-NAJIB

How to cite:

BIN-MOHD-NAJIB, MOHD NADZRI (2019) STUDY OF PHARMACEUTICAL CRYSTAL HYDRATES AND THEIR PREDICTION BASED ON PRE-NUCLEATION AGGREGATION. Doctoral thesis, Durham University.

Use policy

The full-text may be used and/or reproduced, and given to third parties in any format or medium, without prior permission or charge, for personal research or study, educational, or not-for-profit purposes provided that:

- a full bibliographic reference is made to the original source
- a https://etheses.durham.ac.uk/id/eprint/13279/ is made to the metadata record in Durham E-Theses
- the full-text is not changed in any way

The full-text must not be sold in any format or medium without the formal permission of the copyright holders.

Please consult the full Durham E-Theses policy for further details.

Academic Support Office, The Palatine Centre, Durham University, Stockton Road, Durham, DH1 3LE
e-mail: e-theses.admin@durham.ac.uk Tel: +44 0191 334 6107
https://etheses.durham.ac.uk

Study of pharmaceutical crystal hydrates and their prediction based on pre-nucleation aggregation

Mohd Nadzri Bin Mohd Najib

PhD. Pharmaceutical Chemistry

School of Medicine, Pharmacy and Health
Durham University
and
School of Pharmacy
Queen's University Belfast

2019

DECLARATION

The findings from Chapter 3 research has been published as a journal article in Chemistry - A European Journal, with the same title (DOI:10.1002/chem.201703658).

STATEMENT OF COPYRIGHT

The copyright of this thesis rests with the author. No quotation from it should be published without the author's prior written consent and information derived from it should be acknowledged.

ABSTRACT

STUDY OF PHARMACEUTICAL CRYSTAL HYDRATES AND THEIR PREDICTION BASED ON PRE-NUCLEATION AGGREGATION

It is well documented that hydrate formation is a constant problem in the pharmaceutical industry as its formation can reduce the drug's aqueous solubility and may impact the overall stability and safety. Furthermore, the current technology used in the prediction and screening process demands time, money, effort, as well as some elements of serendipity, leaving hydrate formation largely unpredictable and a challenge. This study probes hydrate formation passively and actively. Passive investigation demands the crystalline hydrate form to be present *prior* to analysis, while the active probe does not. The use of common solid-state characterisation techniques in the passive analysis shows the complexity in the solid-state landscape of crystalline hydrate forms. Two different systems in the form of charged and neutral pharmaceutical compounds, namely sodium diatrizoate and tranilast (Chapter 3 and 4) best highlight the passive approach. The focus of the research then shifts to the development of an active hydrate prediction technology (Chapter 5) exploiting the principles of host-guest chemistry, titration techniques and binding constants to show the affinity of solute molecules to water in the pre-nucleation state for compounds forming stable hydrates. The novel active approach is further scrutinised in Chapter 6 with the analysis of metastable and non-hydrate forming compounds, followed by a blind study to predict the hydrate-forming ability of several other compounds. In the final chapter, the potential usage of the developed prediction method is expanded to stable solvated crystal forms and protein binding affinity prediction. The usefulness of the developed method will grow with more compounds and systems analysed. In addition, analysis of more hydrate-forming compounds with different hydrate-forming

ability will further clarify, update and expand the current database. **KEYWORDS:** hydrate; prediction; binding constant; pre-nucleation state.

ACKNOWLEDGMENTS

All praises to Allah for the strengths He has given me and His blessing in completing this thesis.

First and foremost, I would like to express my utmost gratitude to my supervisor, Dr. Katharina Edkins whose invaluable help in the form of impromptu and planned discussions, meetings, constructive comments and suggestions throughout the experimental and the write-up of this thesis, which are immensely important to the success of this research. Also, my appreciation goes to my Durham University supervisor, Prof. Colin Bain whose early input and comments set us on our way. Not forgotten, Dr. Alan Kenwright, my co-supervisor from Durham University who helped in the initial exploration of NMR methodology.

I would also like to thank Dr. James McCabe of AstraZeneca who welcomed me, and took me under his wings in during my short stint at AstraZeneca Macclesfield facility. would like to extend my acknowledgement to Dr. Kevin Back of Pfizer, Dr. Antonella Ciancetta of Queen University and Dr. Dmitri Yufit of Durham University, who have graciously assisted us in our analysis. Sincere thanks to the members of the Edkin's group, past and present especially to the post-docs, Dr. Christopher Jones and Dr. Abdessamad Kaasis

Last and certainly not the least, my deepest gratitude goes to my beloved parents, Mohd Najib Zakaria and Safiah Abdullah, my wife Mardiana, and the children Irfan, Nafees and Zara. Your endless love, prayers and encouragement is the fuel that keeps me going. To my sponsors, UiTM and the Ministry of Higher Education as well as friends and those who indirectly contributed in this research, your attention, help and consideration is highly appreciated. Thank you all so very much!

DEDICATION

To my wife Diana, my two boys, Irfan and Nafees, and the little princess, Zara.

You are my strength.

TABLE OF CONTENTS

Title Page i

Declaration ii

Statement of Copyright ii

Abstract iii

Acknowledgements v

Dedication vi

Table of contents vii

List of Tables ……..xiv

List of Figures xvi

CHAPTER 1: GENERAL INTRODUCTION, THEORY, AND BACKGROUND 1

1.1 Introduction 1

1.1.1 Background, significance and problem with hydrate in pharmaceuticals 1

1.1.2 Hydrate classification 5

1.1.3 Water of crystalline hydrate interaction preference 9

1.2 A view on Crystal Structure Prediction (CSP) 10

1.3 Hydrates and crystallisation theory 12

1.3.1 Classic nucleation theory (CNT) vs non-classical theory 14

1.4 The relationship between solid and solution-state analysis 15

1.5 Noncovalent interactions 17

1.5.1 Water interaction in solution 19

1.6 Host-guest chemistry 21

1.6.1 Binding constant 22

1.6.2 Thermodynamics of molecular interactions and relation to binding constant 29

1.6.3 Job's plot 30

1.7 Ideal and non-ideal aqueous mixing and the importance of water activity 31

1.8 Hypothesis and aim 36

1.9 References 38

CHAPTER 2: MATERIALS, METHODOLOGIES AND THEIR PRINCIPLES 50

2.1 Materials 50

2.1.1 Analysed compounds 50

2.2 Analytical methods 51

2.2.1 Crystallisation screening 51

2.2.2 Karl Fischer titration 53

2.2.3 Thermal analysis 55

2.2.4 Gravimetric moisture sorption analysis 62

2.2.5 Fourier transform infrared spectroscopy 63

2.2.6 X-ray diffraction 67

2.2.7 Calculations and stock solution preparation. 72

2.2.8 Proton nuclear magnetic resonance (^{1}H-NMR) spectroscopy .. 75

2.2.9 Continuous variation method (Job's plot) 79

2.2.10 ^{1}H-NMR dilution experiment 80

2.2.11 ^{1}H-NMR titration experiment 80

2.3 Binding constant determination using open source fitting tool: Supremolecular.org 81

2.4 Molecular dynamics (MD) simulations: Tetrazole/DMF system 83

2.5 References 86

CHAPTER 3: THE COMPLEX SOLID-STATE LANDSCAPE OF SODIUM DIATRIZOATE HYDRATES 91

3.1 Chapter overview 91

3.2 Introduction 92

3.2.1 Background 92

3.2.2 Challenges due to sodium salt hydrates formation 93

3.3 Aims 97

3.3.1 The model compound: Sodium diatrizoate 97

3.4 Results and Discussion 99

3.4.1 The octahydrate 99

3.4.2 The 0.3-1 hydrate 108

3.4.3 Crystal form from direct crystallisation: The monohydrate 111

3.4.4 The 0.5-3.5 hydrate 119

3.4.5 The solvates 124

3.5 Chapter summary and conclusion 129

3.6 References 132

CHAPTER 4: EXTENSIVE HYDRATE AND SOLVATE FORMATION OF THE ANTIALLERGIC COMPOUND TRANILAST 137

4.1 Chapter overview 137

4.2 Introduction 138

4.2.1 Background and significance 138

4.3 Results and discussion 140

4.3.1 Initial screen and the resultant forms 140

4.4 Highlight on the TRN hydrate forms 142

4.5 Hydrate forms from direct re-crystallisation of TRN and pathways to forms derived from them 144

4.5.1 Hydrate I (monohydrate I) 144

4.5.2 Hydrate II (2.3 hydrate) polymorph III and hydrate III (0.8 hydrate) 146

4.5.3 Hydrate IV (1.5-1.8 hydrate) 154

4.6 Methanol/water solvate (solvate I) and pathways to forms derived from solvate I 155

4.6.1 Solvate I (methanol/water solvate) and hydrate V (0.70-0.80 hydrate) 155

4.6.2 Hydrate VI (monohydrate), VII (0.60-0.70 hydrate) and VIII (0.40 hydrate) 159

4.6.3 Hydrate IX (trihydrate) 162

4.7 Other solvate forms from direct re-crystallisation of TRN and forms derived from them 166

4.7.1 Solvate II (2-propanol monosolvate) 166

4.7.2 Solvate III (chloroform monosolvate), hydrate X (monohydrate) and hydrate XI (hemihydrate) 169

4.7.3 Solvate IV (DCM ¾ solvate) 173

4.7.4 Solvate V, VI and VII 177

4.8 Chapter summary and conclusion 177

4.9 References 180

CHAPTER 5: INFLUENCE OF WATER TOWARDS PRE-NUCLEATION AGGREGATES LEADING TO THE FORMATION OF STABLE CRYSTALLINE HYDRATES 184

5.1 Chapter overview 184

5.2 Introduction 185

5.2.1 Background 185

5.2.2 The new approach towards understanding the role of water in hydrate-forming drug compounds 186

5.2.3 The model/the host: diatrizoic acid (DTA), cimetidine (CIM), tranilast (TRN), and piroxicam (PXM) 187

5.3 Results and Discussion 191

5.3.1 DTA solid-state preliminary analysis 191

5.3.2 FTIR: DTA solution-state titration and kinetic study 195

5.3.3 ^{1}H NMR: DTA-water titration 206

5.3.4 CIM solid-state preliminary analysis 220

5.3.5 FTIR: CIM solution-state titration 222

5.3.6 ^{1}H NMR: CIM-water titration 224

5.3.7 TRN-water preliminary data and FTIR titration 236

5.3.8 ^{1}H NMR: TRN-water titration 237

5.3.9 Preliminary FTIR solid and solution-state analysis of PXM .. 248

5.3.10 ^{1}H NMR PXM-water titration 253

5.4 Conclusion 263

5.5 References 266

CHAPTER 6: THE AFFINITY AND SELECTIVITY OF METASTABLE, ELUSIVE, AND NON-HYDRATE FORMING COMPOUNDS TOWARDS WATER AND PRE-NUCLEATION AGGREGATE FORMATION 274

6.1 Introduction 274

6.2 The tested compounds and results 275

6.2.1 The elusive or non-hydrate forming drug: Naproxen 275

6.2.2 The metastable or weak hydrate forming drugs: Paracetamol 282

6.2.3 The blind test 290

6.3 Conclusion 325

6.4 References 330

CHAPTER 7: EXTENDED USE OF THE TITRATION TECHNOLOGY: PROBING DIMETHYLFORMAMIDE SOLVATE FORMATION AND PROSPECTIVE SCREENING TOOL FOR PROTEIN BINDING FRAGMENTS 334

7.1 Introduction 334

7.2 Results for the model compound: 4-(1H-Tetrazol-5-yl) phenol 335

7.2.1 TTZ ^{1}H-NMR dilution experiment 336

7.2.2 TTZ-water ^{1}H-NMR titration in DMSO-d_6 337

7.2.3 TTZ-DMF ^{1}H-NMR titration in DMSO-d_6..... 340

7.2.4 TTZ ^{1}H-NMR cross-titration with water and DMF: Part I 342

7.2.5 TTZ ^{1}H-NMR cross-titration with water and DMF: Part II.... 346

7.2.6 ^{1}H-NMR TTZ-DMF titration in an acetone-d_6 environment... 349

7.2.7 TTZ-DMF ^{1}H-NMR titration in water environment MD simulation..... 352

7.3 DMF as a prospective proteomimetic agent..... 356

7.3.1 2-Chloro-4-hydroxybenzoic acid (2C4HBA) 357

7.3.2 4-Hydroxybenzoic acid (PHBA)..... 364

7.3.3 5-Phenyl-1H-tetrazole (5PHT)..... 369

7.3.4 5-(4-Pyridyl)-1H-Tetrazole (54PYT)..... 373

7.4 Chapter conclusion..... 376

7.5 References..... 379

LIST OF TABLES

Table 2.1. Example of water-compound titration setup 74

Table 2.2. Job's plot setup for 0.1 M host and 0.1 M guest compounds. 10 sets of tubes were used, each containing different volume which corresponded to the different intended host or guest fractions 79

Table 2.3. Details of the simulated TTZ/DMF systems 85

Table 3.1. Summary of slow cooling, fast cooling, precipitation, and evaporation experiments 112

Table 3.3: Crystallographic data of the crystal forms of DTS 117

Table 5.1. Calculated ΔG of DTA-water binding based on 2:1 binding model 219

Table 5.2. ^{1}H NMR chemical shift (ppm) of free cimetidine and complexed with water in deuterated DMSO at titration endpoint. 226

Table 5.3. ^{1}H-NMR chemical shift (ppm) of free cimetidine and complexed with water in deuterated acetone. 231

Table 5.4. Calculated ΔG of TRN-water binding based on three (3) different binding models. 246

Table 5.5. Vibration assignments for PXM anhydrous Form I and the monohydrate 250

Table 5.6. Calculated ΔG of PXM-water binding based on three (3) different binding models 262

Table 5.7. Calculated ΔG of all compound-water binding based on 2:1 binding model. 265

Table 6.1. Peak shift difference between the start, and the last titration point of 450:1 G:H molar ratio. 279

Table 6.2. K values based on the fitting to all available binding model, the 1:1, 2:1 and 1:2, H:G ratios 281

Table 6.3. Resonance structures of a paracetamol molecule. Figure was adapted from Bernal et al.[7] 283

Table 6.4. K values based on the fitting of NH proton (Proton 3) to all available binding model, the 1:1, 2:1 and 1:2 H:G ratios. * Generated K values based on the fitting of non-labile protons (Proton 2, 4, and 5) 289

Table 6.5. K values based on the fitting to all available binding model, the 1:1, 2:1 and 1:2, H:G ratios 294

Table 6.6. K values based on the fitting to all available binding model, the 1:1, 2:1 and 1:2, H:G ratios 301

Table 6.7. K values based on the fitting to all available binding model, the 1:1, 2:1 and 1:2, H:G ratios 307

Table 6.8. K values based on the fitting to all available binding model, the 1:1, 2:1 and 1:2, H:G ratios 314

Table 6.9. K values based on the fitting to all available binding model, the 1:1, 2:1 and 1:2, H:G ratios 322

Table 6.10. All K_{21} and ΔG for all the probed compounds. 329

Table 7.1. Dilution effect of TTZ with 450 molar equivalents of anhydrous DMSO 337

Table 7.2. Calculated ΔG of TTZ-water binding in DMSO-d_6 environment based on three (3) different binding models. 340

Table 7.3. Comparison between the peak shift magnitude in water and DMF titration in DMSO environment 341

Table 7.4. Calculated ΔG of TTZ-water binding in the DMF-d_7 environment based on three (3) different binding models. 346

Table 7.5. Calculated ΔG of TTZ-DMF-d_7 binding in D_2O environment based on three (3) different binding models. 349

Table 7.6. Calculated ΔG of TTZ- protiated* and DMF-d_7 binding in an acetone-d_6 environment based on proton 2 fitting to three (3) different binding models. 351

Table 7.7. Calculated ΔG of 2C4HBA-DMF binding in D_2O environment based on three (3) different binding models. 361

Table 7.8. Calculated ΔG of 2C4HBA-DMF binding in an acetone-d_6 environment based on three (3) different binding models. 363

Table 7.9. Calculated ΔG of PHBA-DMF binding in D_2O environment based on three (3) different binding models. 366

Table 7.10. Calculated ΔG of PHBA-DMF binding in acetone-d_6 environment based on three (3) different binding models. 368

Table 7.11. Calculated ΔG of 5PHT-DMF binding in acetone-d_6 environment based on three (3) different binding models. 372

Table 7.12. Calculated ΔG of 54PYT-DMF binding in D_2O environment based on three (3) different binding models. 375

Table 7.13. All K_{21} or K_{12} and ΔG for all the probed compounds. 378

LIST OF FIGURES

Figure 1.1 Solid as one of the three classical classifications for states of matter, along with its sub-classification. Crystalline form and its division is also highlighted. 2

Figure 1.2. Typical DVS sorption and desorption curve cycles for hypothetical compound A (A) and B (B) 6

Figure 1.3. a) Paroxetine hydrochloride form II packing showing void (brown) occupied by water;[35] b) DB7 HyA packing showing void (yellow) occupied by water.[33] 7

Figure 1.4. Packing motif of SLT phase 4 showing channel feature with water's oxygen atoms represented in space-fill style. Figure adapted from Tieger et al.[36] 7

Figure 1.5. a) DA monosodium tetrahydrate showing sodium coordinated water molecule,[40] while b) shows DA disodium salt, with water molecule coordinated to three different sodium cations.[41] 8

Figure 1.6 (a) Distribution of the total number of hydrogen bonds per water molecule and (b)Patterns of hydrogen bonds around water molecules as a frequency (%) for each observed environment[44] 10

Figure 1.7 Solubility curve and metastable zone plotted against temperature and concentration. The figure is adapted from Panagiotou and Fisher.[65] 12

Figure 1.8. The Gibbs free energy in relation to the radius of nuclei. The figure was adapted from three sources.[67–69] 13

Figure 1.9.Crystallisation theories. a) Representation of CNT and non-classical theory[85,86] b) Schematic showing the free energy variation for a variety of possible pathways for crystallisation from ions in solution *DOLLOP = Dynamically Ordered Liquid-Like Oxyanion Polymer *ACC = aggregating clusters amorphous/crystalline [82] 15

Figure 1.10. Comparison of non-covalent interactions and their typical range of binding strength, in comparison to covalent bonds. The figure is adapted from Steed and Atwood.[94] 18

Figure 1.11. Selected illustration of noncovalent bond interactions, (a) ionic bond, (b) van der Walls, (c) hydrogen bond, (d) polar–π interaction, (e) CH–π interaction, (f) cation–π interaction, (g) aromatic CH–π, (h) π–π stacking interaction 18

Figure 1.12. Maps of two (2) water molecules (dimer), representing a donor (left) and acceptor (right), showing the regions of increased and decreased electron densities.

Red indicates the loss of electron density while blue represent regions of electron density build-up. This figure was obtained from Scheiner and Kar.[96] 19

Figure 1.13. Tetrahedral structure of water (downloaded from google free media repository) 20

Figure 1.14. a) Lewis acid-base depiction b) Example of water as Lewis acid and base (downloaded from google free media repository) 20

Figure 1.15. Typical interactions in a host-guest interaction in solution. H is the host, and G represent the G. 21

Figure 1.16. Correlation of thermodynamic parameters, K and temperature according to van't Hoff equation. Figure adapted from Hirose.[105] 30

Figure 1.17. Typical Job plot showing the change physical property (P) with the change in the mole fraction of compound A (X_A). The Y_{max} at $X_A = 0.5$, indicating a 1:1 (host to guest) stoichiometry. Left skew would be associated to 1:2, while the opposite, 2:1 respectively. 31

Figure 1.18. The enthalpy of mixing of DMSO and acetonitrile to water as functions of mole fraction of water, adapted from Shin et al.[111] Wakisaka et al.[109] and Lai et al.[110]. The dashed line corresponds to the ideal binary mixture whose excess enthalpy of mixing is zero. 33

Figure 1.20. Raoult's Law ideal total partial pressure line (P_{tot}, red line) generated form the pure partial pressure of each component respectively (solid black line). 34

Figure 1.21. The vapour pressure of pure components (solid black lines), the ideal vapour pressure of the binary mixture (solid red line) and the total vapour pressure of DMSO and water binary system (± 3kPa, black dashed line)[112] at 25℃ showing negative deviation. 35

Figure 2.1 Illustration of the different crystallisation experiments used and their impcat to the solubility curve, adapted from Giulietti et al.[1] 52

Figure 2.2. Schematic on the cross polariser setup in a polarised microscope, showing the effects upon observation of different samples 56

Figure 2.3. Example of thermal microscopy observation of a sample in a paraffin oil preparation under polarised light. A) Depicts typical desolvation process with bubbles formation. B) Depicts melting C) and D) shows the lost of birefringent 57

Figure 2.4. Thermogravimetric thermograms of hypothetical materials I-V, showing different TGA curves corresponding to various events that could be observed following heating/analysis. 59

Figure 2.5. Endothermic and exothermic events typically observed in a DSC thermogram curve (A), while (B) depict the onset and offset of the curve with their cross-point which is the peak. 61

Figure 2.6. The ball-and-spring model for the gas phase of a CO_2 molecule, and its vibration mode, adapted from Burghaus [11] 64

Figure 2.7. Schematics for FT-IR Spectroscopy ATR adapted from Perkin-Elmer technical note.[12] 65

Figure 2.8. FTIR liquid holder setup. Image obtained from google free image repository. 66

Figure 2.9. Schematics of a typical X-ray diffraction setup. 67

Figure 2.10. Bragg diffraction depicting two in-phase X-ray beams with wavelength λ. The beams are reflected from two different atoms in a crystal. The lower beam covers an extra distance of 2d sinθ, and will produce constructive inteference with the upper beam, leading to a peak pattern at the angle θ. Image adapted form google free media repository. 68

Figure 2.11. Schematics of a synchrotron facility[21] 1) electron gun – ganerate the electron via thermionic emission, 2) linac – short for linear accelerator, where electrons are accelerated to close to the speed of light 3) booster ring – ramp or boost the enegy of the circulating electron, typically from 100-200 mega electron volts to 3-6 giga electron volts 4) storage ring – an injection system transfers electrons with enough energy to produce light from the booster ring, 5) beamline and 6) end station.– comprises of the optics cabin, the experimental cabin, and the control cabin.which allow radiation tailoring, house the support mechanism, and the environment for the sample study and cotain the detector to control the experiments and collect the data. Image adapted from google free image repsitory and labelled acccordingly. 71

Figure 2.12. The effect of external magnetic spin on the 1/2 nuclear spin of some nuclei. 76

Figure 2.13. Fitting of a hypothetical resonance peak shift against G:H molar ratio to a theoretical binding isotherm represented by the red line. 82

Figure 3.1. Sodium diatrizoate (DTS) structure. 98

Figure 3.2. Sorption/desorption isotherms of the commercial sample of DTS. The starting point is at 40% RH following a sorption step, then desorption to 0% RH, and finally sorption up to 90% RH again. 99

Figure 3.3. Thermal microscopy (TM) photomicrograph of Hy8 at different temperature points. Top set (a to c) is dry powdered sample while bottom set (d to f) is in the mother liquor. 100

Figure 3.4. Humidity controlled PXRD patterns starting from a) amorphous product at 30% RH forming Hy8 at 90% RH b) Hy8 at 90% RH and passing through the transition to Hy4 towards 35% RH c) continuation from 35% RH to 5% RH showing sample losing crystallinity (amorphisation). 102

Figure 3.5. The octahydrate (Hy8) PXRD trace comparison to the calculated powder pattern (black) of the tetrahydrate (Hy4). 103

Figure 3.6. TGA thermograms of tetra- vs octa- hydrate forms of DTS 104

Figure 3.7. TGA (top) and corresponding DSC (bottom) thermograms of both recorded at 10 °C min^{-1}. The measurement was conducted on the wet sample to ensure full hydration 104

Figure 3.8. Hy4 PXRD comparison to the calculated powder pattern (black) and Hy8. 105

Figure 3.9. Photomicrograph of Hy8 and Hy4 habit. 105

Figure 3.10. High-resolution dynamic vapour sorption (DVS) isotherm of the transition between Hy8 and Hy4. The grey line represents desorption curve, the black line sorption. 106

Figure 3.11. High-resolution DVS of the dehydration of Hy4. Insert represents the mass change (*dm*), respective RH levels and mass change rate (*dm/dt*) of the steps below 5% RH. 107

Figure 3.12. PXRD patterns of nitrogen dried vs heated sample of Hy8..... 109

Figure 3.13. Hydrate Hy0.3-1.0 (heated sample) PXRD comparison to Hy4 and Hy8 110

Figure 3.14. TGA thermogram of Hy0.3-1.0 recorded at 10 °C min^{-1} 110

Figure 3.15. DVS isotherm of Hy0.3-1.0 showing slow conversion to Hy8 at higher humidities. Identical Hy8 desorption curve observed afterwards. 110

Figure 3.16. Photomicrograph showcasing the unique needle habit, only observe in Hy1 form. 111

Figure 3.17. Monohydrate (Hy1) PXRD along with the calculated pattern (black) in comparison to Hy4, Hy8, and Hy0.3-1.0. 113

Figure 3.18. TGA thermogram of Hy1 recorded at 10 °C min^{-1}..... 114

Figure 3.19. DVS isotherm of Hy1 starting from room conditions down. Isotherm is normalised to the lowest point of the measurement. 114

Figure 3.20. DTS Hy1 molecule showing water coordination towards the sodium cation (far left: blue arrow); sodium-acid (middle: yellow arrow) coordination observed towards a second DTA as the catameric strand grows; acid-sodium coordination (far right: green arrow) towards a third DTA. The colour code is carbon grey, nitrogen blue, oxygen red, iodine purple, sodium cyan and hydrogen light grey and this colour coding will be adapted for all following figures. 117

Figure 3.21. Packing representation of the single crystal structure of Hy1. For this and all following structural representations, anisotropic displacement parameters are drawn at 50% probability. 119

Figure 3.22. Photomicrograph of the platy second hydrate grows concomitantly with the needle habit of Hy1 form. 120

Figure 3.23. Hydrate 0.5-3.5 PXRD comparison to Hy1, Hy4, Hy8, and Hy0.3-1.0. 120

Figure 3.24. TGA thermogram of Hy0.5-3.5 recorded at 10 °C min^{-1}. 121

Figure 3.25. DVS isotherm of Hy0.5-3.5 starts from room condition, with initial desorption down the humidity range. Isotherm is normalised to the lowest point of the measurement. 121

Figure 3.26. A cluster of sodium cations, carboxylate moieties and water molecules of the Hy0.5-3.5 structure. 123

Figure 3.27. Packing of the crystal structure of Hy0.5-3.5 along the crystallographic a axis with clearly visible pores. 124

Figure 3.28. PXRD patterns of the solvates of DTS with the calculated patterns of the crystal structures (grey). 125

Figure 3.29. Photomicrograph of the methanol trisolvates habit. 125

Figure 3.30. TGA thermograms of the methanol and 1:1 DMSO/H_2O solvates of DTS. 126

Figure 3.31:1D coordination polymers of the (a) methanol and (b) DMSO/H_2O solvates of DTS. 126

Figure 3.32: Packing of the crystal structure of DTS (a) methanol and (b) DMSO/H_2O with the DMSO channels running along c. 127

Figure 3.33: Photomicrograph of the DMSO/water solvate habit. 128

Figure 3.34: Schematic representation of the crystal forms and transformation pathways of DTS 129

Figure 4.1. TGA (top) and corresponding DSC (bottom) thermograms of TRN polymorph I both recorded at 10 °C min^{-1}. 142

Figure 4.2. TG (top) and corresponding DSC (bottom) thermograms of TRN polymorph II both recorded at 10 °C min^{-1}.....142

Figure 4.3. PXRD of TRN polymorph I, II and hydrate I. Grey coloured trace is the calculated powder pattern of polymorph I (α Form,[20] Form I[22]) 144

Figure 4.4. TG (top) and corresponding DSC (bottom) thermograms of TRN hydrate I both recorded at 10 °C min^{-1}.....145

Figure 4.5. TRN hydrate I DVS cycle (a) with PXRD the sample from before and after DVS analysis (b) 146

Figure 4.6. TGA of TRN hydrate II before and after DVS run (0% RH) both recorded at 10 °C min^{-1} 147

Figure 4.7. (a) Water molecules are acting as DDA, bridging three TRN molecule. (b) The two molecules of water which are in the channels are highlighted in by the black circle. (c) Black arrow is highlighting the channels. The colour code is carbon grey, oxygen red, and hydrogen light grey.....148

Figure 4.8. DVS isotherm of TRN hydrate II (2.3 hydrate).....149

Figure 4.9. FTIR of dehydrated hydrate II, via heat and 0% RH.....150

Figure 4.10. PXRD of TRN polymorph I, II and III. Grey coloured trace is the calculated powder pattern of polymorph I 150

Figure 4.11. Hydrate II desorption to 0% RH followed by prolonged isotherm at 90% RH. 151

Figure 4.12. FTIR of polymorph III exposed to 98% RH for 36 hours showed similar spectra to hydrate II.....152

Figure 4.13. Predicted (GREY) and experimental PXRD (BLACK) of TRN hydrate II, polymorph III and hydrate III. Humidity controlled PXRD sample was taken at 40% RH before being exposed to 3% RH and subsequently exposed to 90% RH for four (4) hours at each step respectively.....153

Figure 4.14. TGA of hydrate IV recorded at 10 °C $min^{-1.}$ 155

Figure 4.15. FTIR of hydrate I-IV, highlighting the vibration at 3413 cm^{-1} of hydrate IV 155

Figure 4.16. NMR spectra of the fresh solvate I sample..... 156

Figure 4.17. TGA of the freshly prepared TRN solvate I and solvate I isotherm for 10 minutes. 157

Figure 4.18. DVS isotherm (initially to higher humidities) of hydrate V (formed from methanol desolvation of solvate I) The sample contain between 0.84-0.81moles of water upon exposure to RH between 40-80% going up the humidity range. Meanwhile (b) DVS isotherm (initially to lower humidities) of hydrate V. The sample is shown to contain between 0.72-0.70 moles of water upon exposure to RH between 40-10% up the humidity range..... 159

Figure 4.19. Humidity controlled PXRD of hydrate V (formed from methanol desolvation of solvate I) BLACK traces corresponds to the first sorption-desorption cycle, GREY traces corresponds to the second sorption-desorption cycle. Each step is left at isotherm for one hour before pattern is obtained 160

Figure 4.20. FTIR spectra of hydrate V at the end of DVS runs, initially going up vs. initially going down 162

Figure 4.21. TGA of TRN solvate I vs. the same form exposed to 98% RH chamber forming the trihydrate (hydrate IX)) 163

Figure 4.22. NMR of fresh TRN solvate I sample vs. sample exposed to 98% RH chamber or the trihydrate /hydrate IX)..... 164

Figure 4.23. PXRD comparison of hydrate IX to other hydrate form derived from solvate I. Unique feature of this form is highlighted with (+) symbol..... 165

Figure 4.24. PXRD solvate II alongside the from which it transform to at higher RH, hydrate I. 167

Figure 4.25. TGA of solvate II, showing the mass loss recorded before, and after DVS analysis (0% RH) 167

Figure 4.26. DVS isotherm of solvate II 168

Figure 4.27. FTIR spectra of solvate II after DVS cycle, showing similarities to hydrate I spectra 169

Figure 4.28. TGA of Solvate III before and after DVS analysis (weight loss as 0% RH) 170

Figure 4.29. DVS isotherm of solvate III 170

Figure 4.30. Crystal packing of solvate III, showing channel of chloroform molecule (GREEN)[8] 171

Figure 4.31. Humidity controlled PXRD of Solvate III (TRN chloroform monosolvate), matching to the calculated powder pattern (GREY). Each scan interval is two (2) hours. 172

Figure 4.32. TGA and DSC analysis of Solvate IV 174

Figure 4.33. Desolvation of solvate IV (DCM ¾ solvate) at isotherm. 174

Figure 4.34. PXRD of Solvate IV (TRN DCM ¾ solvate), the pattern did not match to the calculated powder pattern (GREY)[22] 175

Figure 4.35. FTIR spectra of desolvated solvate IV without heat (0% RH) and at different heating interval. Heating to 150 °C yeilded polymorph IV while >170°C forms polymorph I. 176

Figure 4.36. PXRD spectra of solvate IV ad different heating interval. Heating to 150 °C yeilded polymorph IV while >170°C forms polymorph I 176

Figure 5.1. Chemical structure of DTA 188

Figure 5.2. Chemical structure of CIM 189

Figure 5.3. Chemical structure of TRN 189

Figure 5.4. General chemical structure of PXM (a) and the different ionisation states modifications of PXM under various conditions (b)-(e). 190

Figure 5.5. PXRD of DTA dihydrate and the anhydrous form II. The small differences between the measured and predicted DTA dihydrate patterns are due to the platy habit of this crystalline form, hence highly preferred oriented. Also, the two measurements were taken at two different temperatures, i.e. ambient and 120 K.[22] 191

Figure 5.6. TGA (a) and DSC (b) of DTA dihydrate and anhydrous forms. Also, additional follow-up TGA of the anhydrous form, after ambient environment exposure for 30 minutes. 192

Figure 5.7. DVS isotherm of the DTA dihydrate. 193

Figure 5.8. DTA dihydrate and anhydrous form FTIR spectra 194

Figure 5.9. DTA 1.54 M in DMSO solution FTIR spectrum with vibration range of interest are highlighted in the inserts. 196

Figure 5.10. a) DMSO-DTA solution mix vs b): DMSO-only, exposed to ambient conditions for 150 minutes. 197

Figure 5.11. The FTIR spectra highlighting on the NH and OH stretching region of DTA in DMSO-DTA solution mixture following exposure to ambient conditions for 150 minutes. 198

Figure 5.12. The FTIR spectra highlighting on the C=O stretching region of DTA in DMSO-DTA solution mixture following exposure to ambient conditions for 150 minutes. 200

Figure 5.13. DMSO-DTA mixture vapour-sorption gravimetric experiment, where mixture sample was exposed to isotherm at 40% RH for 120 minutes 200

Figure 5.14. High concentration DTA-water FTIR spectra for the titration experiment with controlled water content in an open system 201

Figure 5.15. The FTIR spectra highlighting on the C=O stretching region of DTA in DMSO-DTA solution mixture with high vs. low DTA concentration 203

Figure 5.16. Low concentration DTA-water titration experiment with pre-determined water content in a closed system 205

Figure 5.17. DTA ^{1}H NMR spectrum in DMSO-d_6 environment..... 207

Figure 5.18. DMSO-DTA dilution experiment..... 208

Figure 5.19. a) High vs. b) low DTA concentration of ^{1}HNMR DTA-water titration experiment..... 210

Figure 5.20. a) Shows HC_2O_4 dimer where yellow-coloured isosurface represents electron loss and the blue colour suggests electron increase.[57,58] b). Shows F_2CCFH-water complexation resulting in shifts or rearrangement of electron density throughout the compound. Blue regions corresponds to electron density gain, and red regions represent loss.[56] 212

Figure 5.21. Job plot showing the 2:1 stoichiometry of the complexation between DTA and water in DMSO-d_6 using ^{1}H NMR. ([DTA] + [H2O] = 0.1 M)..... 214

Figure 5.22. a) Scatter plot of the amide proton peaks, NH-A =10 ppm, NH-B = 9.9 ppm, from 0-7:1 G:H molar ratio of high DTA concentration ^{1}HNMR titration experiments, fitted to the 2:1 binding model, and b) shows the host, H guest G, speciation plot. 215

Figure 5.23. a) Scatter plot of the amide proton peaks, NH-A =10 ppm, NH-B = 9.9 ppm, from 0-1087:1 G:H molar ratio of low DTA concentration ^{1}HNMR titration experiments, fitted to the 2:1 binding model. The inset in a) shows the fitting overlooking the upfield points b) shows the host-guest, speciation plot. 216

Figure 5.24 a) Scatter plot of the amide proton NH-A =10 ppm, NH-B = 9.9 ppm, at 25-1087:1 G:H molar ratio of low DTA concentration ^{1}HNMR titration experiments, fitted to the 2:1 binding model, and b) shows the host, H guest G, speciation plot. 217

Figure 5.25. FTIR spectra (LEFT)and PXRD traces of CIM anhydrous Form A and monohydrate M1 220

Figure 5.26. TGA (a) and DSC (b) traces of CIM Form A and monohydrate M1 .. 221

Figure 5.27. DVS of the anhydrous Form A and the monohydrate M1 221

Figure 5.28. 0.05 M CIM in DMSO solution (a) showing unobstructed view of the vibration of interest. (b) shows the solution-state FTIR titration of CIM from 0-600 G:H ratios. 223

Figure 5.29. CIM proton 1-8 assignment form higher to lower ppm as they appear in the spectra along with their respective symbols. a) shows CIM spectrum in DMSO-d_6 environment, and b) in acetone-d_6 respectively. 224

Figure 5.30. Peak shift in CIM dilution experiment. a) in DMSO-d_6 environment, while b) in acetone-d_6 environment 225

Figure 5.31. TOP form LEFT to RIGHT: Proton 1-4 peak shifts, while BOTTOM, from LEFT to RIGHT: Proton 5-8 peak shift in DMSO environment 226

Figure 5.32. Point of reference, the structure of CIM, with their corresponding symbols and numbering scheme. 229

Figure 5.33. TOP form LEFT to RIGHT: Proton 1-4 peak shifts, while BOTTOM, from LEFT to RIGHT: Proton 5-8 peak shift in acetone-d_6 environment 231

Figure 5.34. CIM Job plot experiment.in a) DMSO-d_6 environment, b) acetone-d_6 environment Job plot showing the 1:1 stoichiometry of the complexation between CIM and water in DMSO-d_6 while a 2:1 stoichiometry of the complexation in acetone using ^{1}H NMR. ([CIM] + [H_2O] = 0.1 M) 232

Figure 5.35. Proton 1-8 peak shift scatter plot form 0-35 G:H molar ratio in DMSO 233

Figure 5.36. Proton 1-8 peak shift scatter plot form 0-450:1 G:H molar ratio in acetone environment. 234

Figure 5.37. Example of fitting for binding constant determination to 2:1 model for proton 2 (a), and proton 3 (b). 234

Figure 5.38. CIM speciation plot following 2:1 binding stoichiometry 235

Figure 5.39. The solved structure of TRN 2.3 hydrate. Water molecules are acting as DDA, bridging three TRN molecule. The colour code is carbon grey, oxygen red, and hydrogen light grey. 236

Figure 5.40. Peak assignment, a) the OH of the acid group, the NH, and the two methoxy groups identified as Proton 1, 2, 12 and 13, with their respective symbols. b) Proton 3-11 and their respective symbols. 238

Figure 5.41. Proton 2 (NH) of TRN in a dilution experiment with anhydrous DMSO up to 500 molar ratios 238

Figure 5.42. The spectra of proton 1 from zero to five molar ratios of water..... 238

Figure 5.43. a) Shows the spectra of NH proton (proton 2) from 0-400 G:H molar ratios. b) shows the scatter plot of the peak position chemical shift. 239

Figure 5.44. Spectra and chemical shift of TRN proton 3 to 11 from 0-400 G:H molar ratios. 240

Figure 5.45. Scatter plot of proton 3 showing a linear upfield shift. 241

Figure 5.46. Scatter plot of proton 4 (a) showing a linear downfield shift and proton 5 (b) with the initial upfield, followed by a downfield shift. 242

Figure 5.47. Scatter plot of proton 6 (a) and proton 7 (b), both showing upfield shifts. 242

Figure 5.48. Scatter plot of proton 8 showing initial upfield, followed by a plateau curve, and subsequent downfield shift. 243

Figure 5.49. Scatter plot of proton 9 (a) and proton 10 (b), both showing downfield shifts 244

Figure 5.50. Scatter plot of proton 11 showing an upfield shift. 244

Figure 5.51. a) shows chemical shifts of proton 12 and 13, showing a non significant peak shift with water titration. b) shows the scatter plot of the peaks positions. 245

Figure 5.52. Job plot showing unclear complexation between TRN and water in DMSO-d_6 using ^{1}H-NMR. ([TRN] + [H_2O] = 0.1 M) 245

Figure 5.53. Example of fitting for binding constant determination for proton 2. .. 247

Figure 5.54. TRN speciation plot following 2:1 binding stoichiometry 247

Figure 5.55. FTIR spectra of PXM anhydrous and monohydrate form with labelling of relevant peaks. 249

Figure 5.56. Solution-state FTIR titration analysis of PXM focusing on the region from 1350 to 1100 cm^{-1}. 252

Figure 5.57. Peak assignment, a) the N^+H, the NH, and the methyl group identified as Proton 1, 2 and 11, with their respective symbols. b) shows proton 3-10 and their respective symbols. 253

Figure 5.58. PXM dilution experiment with anhydrous acetonitrile from 0-40:1 G:H molar ratios with five molar ratios gap. a) highlight proton 2, while b) shows proton 3-10 chemical shift regions. 254

Figure 5.59. Spectra of proton 1 from zero to 617 molar ratios of water 255

Figure 5.60.a) Spectra of proton 2 (NH), showing a downfield shift with water titration. b) scatter plot of the peaks positions. 256

Figure 5.61. a) The spectra of proton 3, showing an upfield shift with water titration. b) shows scatter plot of the peaks positions. 257

Figure 5.62. Spectra of proton 4-9, showing complex spectra shift and peak profile changes with water titration 257

Figure 5.63. Scatter plot of the peaks positions of proton 4 or 5 (the initial split peak) showing a downfield shift. 258

Figure 5.64.a) Spectra of proton 10, showing a downfield shift with water titration. b) shows the scatter plot of the peaks positions. 259

Figure 5.65. a) Spectra of proton 11, showing initial downfield followed by a subsequent upfield shift with water titration. b): scatter plot of the peaks positions. 260

Figure 5.66. Job plot showing the 1:1 stoichiometry of the complexation between PXM and water in acetonitrile$_{d3}$ using ^{1}H NMR. ([PXM] + [H_2O] = 0.1 M)..... 261

Figure 5.67.a) Example of fitting of proton 2 for binding constant determination fitted to 1:1 binding model. b) PXM speciation plot following 1:1 binding stoichiometry..... 262

Figure 6.1. Two-dimensional chemical structure (A) and three-dimensional arrangement (B) of Naproxen. The colour code is carbon grey, oxygen red, and hydrogen light grey. 275

Figure 6.2. ^{1}H-NMR spectrum of NAP in acetonitrile-d_3 environment. Specific chemical shift regions on the spectra which are identified as proton 1-10 are highlighted with the respective symbols and correspond to inset chemical structure. Figure 3 A highlights proton 1, 8-10 and B highlights proton 2-7. 277

Figure 6.3. Dilution of 0.02 M NAP with non-deuterated acetonitrile. Dilution is done in a single tube, with the highest dilution factor used is 450 molar ratios. 278

Figure 6.4. ^{1}H-NMR chemical shift region for proton 1, showing the broad nature of the peak, and its disappearance once water is introduced into the system..... 279

Figure 6.5. A showing ^{1}H-NMR chemical shift region for Proton 2-7 and their respective peak shifts. B shows the scatter plot to the respective peaks. 280

Figure 6.6. A shows ^{1}H-NMR chemical shift region for proton 8 and 9, with their respective peak shifts. B shows the scatter plot to the respective peaks. 280

Figure 6.7. A showing ^{1}H-NMR chemical shift region for Proton 10 and their respective peak shifts. B shows the scatter plot to the respective peaks..... 281

Figure 6.8. Job plot of NAP showing the stoichiometry of interaction as 1:1, with X_{max}= 0.5. 281

Figure 6.9. Proposed ΔG values for the hydrate prediction gauge 282

Figure 6.10. Two-dimensional chemical structure (A) and three-dimensional arrangement (B) of Paracetamol. The colour code is carbon grey, oxygen red, nitrogen blue, and hydrogen light grey. 283

Figure 6.11. ^{1}H-NMR spectra of PCM in acetonitrile-d_3 environment. Specific chemical shift regions on the spectra which are identified as proton 1-5 are highlighted with the respective symbols and corresponds to inset chemical structure. 285

Figure 6.12. ^{1}H-NMR spectra of the dilution experiment of 0.02 M PCM with non-deuterated acetonitrile up to 10:1 G:H ratio. 286

Figure 6.13. A ^{1}H-NMR chemical shift for PCM proton 1-4 showing peak shift, while B shows the scatter plot of the peak shift for respective protons. 287

Figure 6.14. A showing the final ^{1}H-NMR peak shift for PCM, which is proton 5-corresponding to the CH_3, with B showing the scatter plot of the peak shift. 288

Figure 6.15. The job plot of PCM revealed that the stoichiometry of interaction is favouring the 2:1 binding with Xmax=0.6. 288

Figure 6.16. PCM ΔG position on the hydrate prediction gauge favouring hydrate formation 290

Figure 6.17. Chemical structure of Pyrazine 290

Figure 6.18. ^{1}H-NMR spectrum of PYZ in acetonitrile-d_3 environment. Specific chemical shift region on the spectra appears as a single peak corresponding to the four protons in the inset chemical structure. 291

Figure 6.19. Dilution of 0.02 M PYZ with non-deuterated acetonitrile. Dilution is done in a single tube, with the highest dilution factor used is 500:1 G:H molar ratios. ... 292

Figure 6.20. A shows the ^{1}H-NMR peak shift for PYZ, showing the initial delayed shift from 0-10, G:H ratio, while B. shows the scatter plot, with a larger shift is observed once more water is introduced into the system. 293

Figure 6.21. Job plot of PYZ showing the stoichiometry of interaction as 1:1, with X_{max}= 0.5. 294

Figure 6.22. ΔG position of PYZ on the hydrate prediction gauge does not favour hydrate formation 295

Figure 6.23. Chemical structure of Acetazolamide 296

Figure 6.24. ^{1}H-NMR spectrum of ACT in DMSO-d_6 environment. Specific chemical shift regions on the spectra which are identified as proton 1 (■), 2 (▫) and 3 (▲) are highlighted with the respective symbols and corresponds to inset chemical structure. 296

Figure 6.25. Dilution of 0.02 M ACT with non-deuterated anhydrous DMSO. Dilution is done in a single tube, with the highest dilution factor used is 500:1 G:H molar ratios. 297

Figure 6.26. ^{1}H-NMR chemical shift region for proton 1, showing the broad nature of the peak, and its broadening and eventual disappearance once 20 molar ratios of water are introduced into the system..... 298

Figure 6.27. A depicts the ^{1}H-NMR peak shift for ACT proton 2, showing the initial delayed shift from 0-10, G:H ratio. B shows the scatter plot showing a larger shift observed once more water is introduced into the system as compared to data points at the lower water content (inset, 0-10 G:H ratio). 299

Figure 6.28. A shows ^{1}H-NMR peak shift for ACT proton 3, showing the initial delayed shift from 0-10, G:H ratio. Scatter plot showed a larger shift is observed once more water is introduced into the system as compared to data points at the lower water content (inset, 0-10 G:H ratio). 300

Figure 6.29. Job plot of ACT showing the stoichiometry of interaction as 1:1, with Xmax= 0.5..... 301

Figure 6.30. ΔG position of ACT on the hydrate prediction gauge which is in the NO hydrate zone. 302

Figure 6.31. Chemical structure of Dapsone..... 303

Figure 6.32. ^{1}H-NMR spectrum of DAP in acetonitrile-d_3 environment. Specific chemical shift regions on the spectra which are identified as proton 1 (■), 2 (▫) and 3 (▲) are highlighted with the respective symbols and corresponds to inset chemical structure..... 303

Figure 6.33. Dilution of 0.02 M DAP with non-deuterated acetonitrile. Dilution is done in a single tube, with the highest dilution factor used is 500:1 G:H molar ratios.... 304

Figure 6.34. A ^{1}H-NMR peak shift for DAP proton 1, showing shift from 0-994, G:H ratio. While B shows scatter plot, with a linear shaped shift observed for the peak of proton 1 as more water is introduced into the system..... 305

Figure 6.35. A ^{1}H-NMR peak shift for DAP proton 2, showing shift from 0-994, G:H ratio. While B shows scatter plot, with a linear shaped shift observed for the peak of proton 2 as more water is introduced into the system..... 305

Figure 6.36. A shows the ^{1}H-NMR peak shift for DAP proton 3, showing an immediate shift from 0-4, G:H ratio. Meanwhile B depicts the scatter plot shows a non-linear shape shift observed as more water is introduced into the system..... 306

Figure 6.37. The Job plot of DAP revealed that the stoichiometry of interaction is favouring the 2:1 binding with X_{max}=0.6. 307

Figure 6.38. Placement of DAP on the hydrate prediction gauge in the grey zone between the respective areas. 308

Figure 6.39. Chemical structure of 4,4'-Dipyridyl 309

Figure 6.40. ^{1}H-NMR spectrum of DPY in acetonitrile-d_3 environment. Specific chemical shift regions on the spectra which are identified as proton 1 and 2 are highlighted with the respective symbols and corresponds to inset chemical structure. 310

Figure 6.41. Dilution of 0.02 M DPY with non-deuterated acetonitrile. Dilution was performed in a single tube, with the highest dilution factor used was 500:1 G:H molar ratios. 311

Figure 6.42. ^{1}H-NMR peak shift for DPY proton 1 and 2 showing peak shift in opposite direction, upfield for proton 1 and downfield for proton 2. 312

Figure 6.43. Scatter plot of proton 1 and proton 2. A showed proton 1 upfield shift to lower ppm with increasing water:DPY ratio. B showed proton 2 downfield shift to higher ppm with increasing water:DPY ratio..... 313

Figure 6.44. The Job's plot of DPY revealed that the stoichiometry of interaction is favouring the 2:1 binding with X_{max}=0.6. 313

Figure 6.45. DPY placement on the hydrate-forming area on the gauge..... 314

Figure 6.46. Chemical structure of Flurbiprofen 315

Figure 6.47.^{1}H-NMR spectra of FBN in acetonitrile-d_3 environment. Specific chemical shift regions on the spectra which are identified as proton 1-9 are highlighted with the respective symbols and corresponds to inset chemical structure. A highlights proton 1, 8 and 9, while B highlights proton 2-7. 316

Figure 6.48. Dilution of 0.02 M FBN with non-deuterated anhydrous DMSO. Dilution is done in a single tube, with the highest dilution factor used is 500:1 G:H molar ratios. 317

Figure 6.49. ^{1}H-NMR chemical shift region for proton 1 of FBN, showing the broad nature of the peak, and its broadening and eventual disappearance once 20 molar ratios of water are introduced into the system 318

Figure 6.50. A ^{1}H-NMR peak shift for FBN proton 2-5 showing peak shift, while B shows the scatter plot of the peak shift for respective protons. 318

Figure 6.51. A ^{1}H-NMR peak shift for FBN proton 6 (♦, ◇ representing the slip peaks) and 7 showing peak shift, while B shows the scatter plot of the peak shift for respective protons.....319

Figure 6.52. A ^{1}H-NMR peak shift for FBN proton 8 showing peak shift, while B shows the scatter plot of the peak shift for respective protons. Massive peaks at higher G:H ratios corresponds to the water peaks which is moving across the chemical region at its concentration increases.....320

Figure 6.53. A ^{1}H-NMR peak shift for FBN proton 9 showing peak shift, while B shows the scatter plot of the peak shift for respective protons. 321

Figure 6.54. The Job's plot of FBN revealed that the stoichiometry of interaction is favouring the 1:2 binding with X_{max}=0.4. 321

Figure 6.55. ΔG placement of FBN on our hydrate gauge. TRN and DPY marker on the gauge are opted out for clarity.....322

Figure 6.56. FBN 3/2 hydrate structure showing the channel formed by six FBN molecules, where water molecules are located.[38] The colour code is carbon grey, oxygen red, fluorine green and hydrogen light grey 323

Figure 6.57. Overall placement of all analysed compounds which is based on the respective ΔG, on our generated hydrate gauge.....327

Figure 7.1. Chemical structure of DMF 334

Figure 7.2. Chemical structure of 4-(1H-Tetrazol-5-yl) phenol 335

Figure 7.3. ^{1}H-NMR spectrum of TTZ in DMSO-d_6 environment. Specific chemical shift regions on the spectrum which are identified as proton 1 (▲), 2 (■) and 3 (○) are highlighted with the respective symbols and corresponding inset of the chemical structure.....336

Figure 7.4. ^{1}H-NMR chemical shift region for proton 1, 2 and 3 and their respective peak shifts following water titration at 50 molar ratio gaps.....338

Figure 7.5. The scatter plot corresponding to the peak shift of proton 1 following water titration up to 450 molar ratios.....338

Figure 7.6. The scatter plot corresponding to the peak shift of proton 2 (A) and 3 (B) following water titration up to 450 molar ratios. 339

Figure 7.7. Job plot of TTZ-water interaction suggesting the stoichiometry of interaction as 1:2, with X_{max}= 0.3 339

Figure 7.8. The peaks of TTZ in DMF environment for water titration (A). The peaks of TTZ in D_2O environment for DMF titration (B). The calibration standard used in A is TMS while in B DSS, both showing peak at 0.00 ppm. 343

Figure 7.9. 0.02 M TTZ-H_2O titration in a deuterated DMF-d_7 environment up to 400:1 G:H ratio. 344

Figure 7.10. A shows the scatter plot for peak shift of proton at the ortho position, while B shows the scatter plot for peak shift of proton at meta position on TTZ benzene ring for TTZ-water titration in DMF-d_7 environment. 345

Figure 7.11. 0.02 M TTZ-DMF-d_7 titration in a deuterated water environment up to 400:1 G:H ratio. Note that the chemical shift scale is similar to that of Figure 9.... 347

Figure 7.12. A shows the scatter plot for peak shift of proton at the ortho position, while B shows the scatter plot for peak shift of proton at meta position on TTZ benzene ring for TTZ-DMF titration in D_2O environment. 348

Figure 7.13. Job plot of TTZ-DMF-d_7 interaction suggesting the stoichiometry of interaction as 1:2, with X_{max}= 0.4 348

Figure 7.14. 0.02 M TTZ-DMF titration (A) protiated DMF and (B) DMF-d_7 in acetone-d_6 environment, up to 100:1 G:H ratio. 350

Figure 7.15. The scatter plot for peak shift of proton at meta position (proton 2) on TTZ benzene ring for TTZ-DMF titration (protiated and deuterated) in the acetone-d_6 environment..... 351

Figure 7.16. TTZ in aqueous solution TTZ in vdW representation (cyan carbon atoms). Water on the left displayed as a blue continuous surface. Right: detail of TTZ molecule placement in the periodic cell (water molecules are not displayed). 353

Figure 7.17. TTZ/DMF (5 eq.) system in water. TTZ (cyan carbon atoms) and DMF (all atom in orange) in vdW representation. Water in CPK representation (oxygen atoms only, in red). Right: TTZ/DMF molecules placement in the periodic cell (water molecules are not displayed). 354

Figure 7.18. TTZ/DMF (15 eq.) system in water. TTZ (cyan carbon atoms) and DMF (all atom in orange) in vdW representation. Water in CPK representation (oxygen atoms only, in red). Right: TTZ/DMF molecules placement in the periodic cell (water molecules are not displayed). 354

Figure 7.19. TTZ/DMF (25 eq.) system in water. TTZ (cyan carbon atoms) and DMF (all atom in orange) in vdW representation. Water in CPK representation (oxygen atoms only, in red). Right: TTZ/DMF molecules placement in the periodic cell (water molecules are not displayed). 355

Figure 7.20. TTZ/DMF (50 eq.) system in water. TTZ (cyan carbon atoms) and DMF (all atom in orange) in vdW representation. Water in CPK representation (oxygen atoms only, in red). Right: TTZ/DMF molecules placement in the periodic cell (water molecules are not displayed). 355

Figure 7.21. ^{1}H-NMR spectrum of 2C4HBA in D_2O (A) and acetone-d_6 (B) environments. Specific chemical shift regions on the spectrum which are identified as proton 1 (▪), 2 (∘) and 3 (▲) are highlighted with the respective symbols and corresponding inset of the chemical structure. 358

Figure 7.22. 0.02 M 2C4HBA-DMF titration in D_2O environment, up to 150:1 G:H ratio. Note that the growing small peak at 7.7 ppm is one of the satellite peaks of the guest, DMF. 359

Figure 7.23. The scatter plot for peak shift of proton 1 in 2C4BHA-DMF titration in D_2O environment. 359

Figure 7.24. The scatter plot for peak shift of proton 2 in 2C4BHA-DMF titration in D_2O environment. 360

Figure 7.25.The scatter plot for peak shift of proton 3 in 2C4BHA-DMF titration in D_2O environment. 360

Figure 7.26. 0.02 M 2C4HBA-DMF titration in acetone-d_6 environment, up to 150:1 G:H ratio 362

Figure 7.27. The scatter plot for peak shift of proton 1 (▪) in 2C4BHA-DMF titration in acetone-d_6 environment 362

Figure 7.28. The scatter plot for peak shift of proton 2 (∘) and 3(▲) in 2C4BHA-DMF titration in acetone-d_6 environment. 363

Figure 7.29. ^{1}H-NMR spctrum of PHBA in D_2O environment. Specific chemical shift regions on the spectrum which are identified as proton 1 (▪) and 2 (∘) are highlighted with the respective symbols and corresponding inset of the chemical structure. 364

Figure 7.30. 0.02 M PHBA-DMF titration in D_2O environment, up to 400:1 G:H ratio 365

Figure 7.31. The scatter plot for peak shift of proton 2 (∘) in PBHA-DMF titration up to 100, and up to 400:1 G:H ratio (inset) in D_2O environment. 366

Figure 7.32. 0.02 M PHBA-DMF titration in acetone-d_6 environment, up to 250:1 G:H ratio 368

Figure 7.33. The scatter plot for peak shift of proton 1 (A, ▪) and 2 (B,∘) PBHA-DMF titration up to 250:1 G:H ratio in acetone-d_6 environment. 368

Figure 7.34. ^{1}H-NMR spectrum of 5PHT in acetone-d_6 environment. Specific chemical shift regions on the spectrum which are identified as proton 1 ( ), 2 ( ) and 3 ( ) are highlighted with the respective symbols and corresponding inset of the chemical structure. 370

Figure 7.35. 0.02 M 5PHT-DMF titration in acetone-d_6 environment, up to 500:1 G:H ratio 370

Figure 7.36. The scatter plot for peak shift of proton 1 up to 500 guest molar ratio in D_2O environment. 371

Figure 7.37. The scatter plot for peak shift of proton 2 (A) and 3 (B) up to 100 guest molar ratio, and 500 (inset) guest molar ratio in D_2O environment..... 372

Figure 7.38. ^{1}H-NMR spectrum of 54PYT in D_2O environment. Specific chemical shift regions on the spectrum which are identified as proton 1 (▪) and 2 (∘) are highlighted with the respective symbols and corresponding inset of the chemical structure. 374

Figure 7.39. 0.02 M 54PYT-DMF titration in D_2O environment, up to 200:1 G:H ratio 374

Figure 7.40.The scatter plot for peak shift of proton 1 (A) and 2 (B) up to 200 guest molar ratio in D2O environment. 375

Figure 7.41. ΔG of TTZ and its placement on our hydrate gauge with respect to previously analysed compound using our titration method 376

CHAPTER 1

GENERAL INTRODUCTION, THEORY, AND BACKGROUND

1.1 Introduction

1.1.1 Background, significance and problem with hydrate in pharmaceuticals

Polymorphism is a phenomenon in which the same chemical compound exhibits different crystal structures,[1] and the occurrence affects numerous fields especially the pharmaceutical industry. Initial interest towards polymorphism in pharmaceutical industry was low. Nevertheless, high profile litigation cases in the 90's propelled the interest and since then, the phenomenon has been vastly studied.[2] With a multibillion-pound industry at stake, pharmaceutical companies are doing as much as they can to unravel, control, and in some cases, take advantage of the seemingly unpredictable phenomenon.[3] Thus, the problem is investigated from different angles in order to understand the forces at work. The pharmaceutical industry is heavily affected due to the definite use of solids in the production of pharmaceuticals.

Solids can be classified into two major categories based on molecular packing which can be either amorphous or crystalline. According to IUCr, crystalline solid is any solid having three-dimensional lattice periodicity and essentially discrete diffraction pattern.[4] In contrast, amorphous solids' structural regularity is limited to the immediate neighbours of any particular molecule within the solid.[5]

While both solid forms are pharmaceutically relevant, the latter is more widely used in most active pharmaceutical ingredients (APIs) as well as excipients as they provide stability, ease of processing and handling, compared to other physical forms.[6] There are many areas of the unit operation in the pharmaceutical industry such as grinding, milling, heating, and compressing, or manufacturing conditions that include a solvent, like crystallisation, lyophilisation, wet granulation, coating process, or spray-drying,[7] that provide environments or conditions that may contribute to the emergence of multiple forms of the crystalline solids like polymorphs, solvates or hydrates (Figure 1.1).

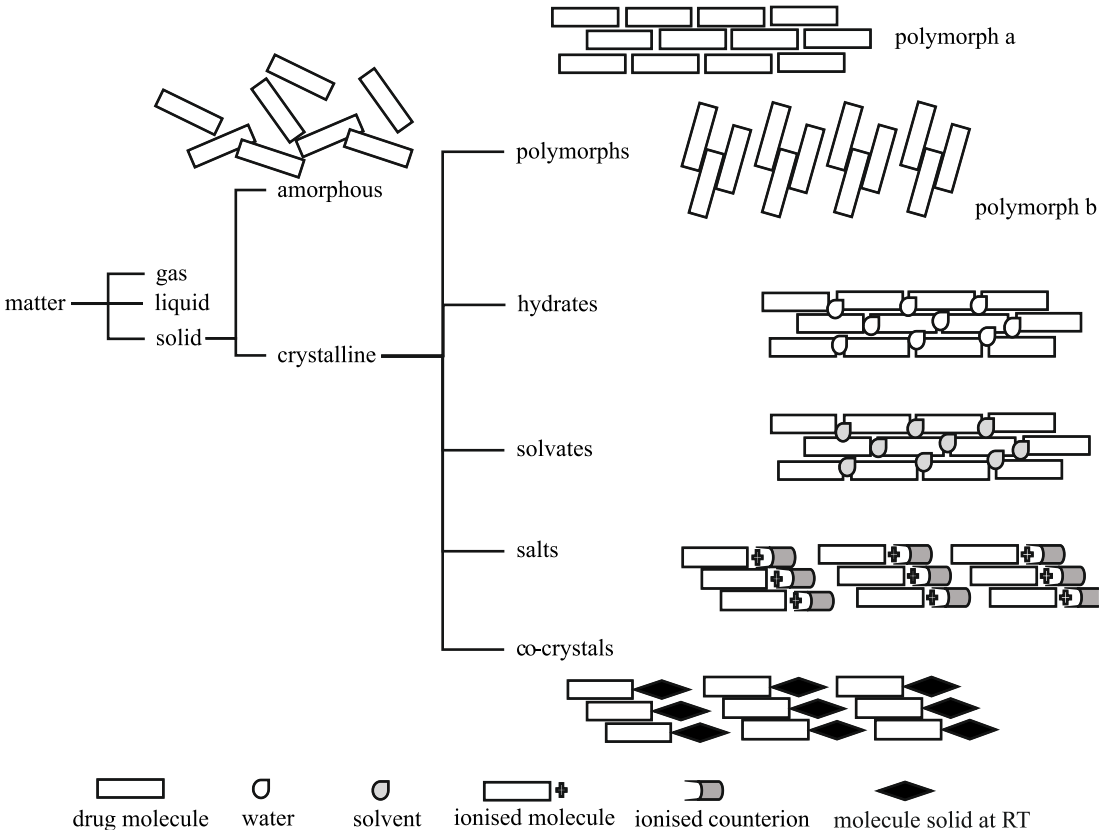


Figure 1.1 Solid as one of the three classical classifications for states of matter, along with its sub-classification. Crystalline form and its division is also highlighted.

The vast arrays of crystalline forms can be a double-edged sword. Sudden emergence of an unexpected crystalline form is a massive problem to a pharmaceutical

company, *e.g.* in the case of antiretroviral drug ritonavir, which led to the removal and subsequent relaunch of the drug.[8,9] On the positive side, the multitude option of crystalline forms allows drug developers and manufacturers advantage over patent length. In addition, modifications to crystalline form, *e.g.* solvent inclusion, salt formation, co-crystal formation which also allow tailoring of desired physical and chemical properties of a compound.

Amongst all of the mentioned crystalline modifications (Figure 1.1), hydrate formation is deemed most problematic in the pharmaceutical industry primarily due to the crystalline form's improved stability which led to it having lower solubility in water compared to its anhydrous form.[10] The term hydrate is generally applied to crystals that have water as an integral part of the crystal lattice which is incorporated into the structure.[11] It is the most frequently identified solvate within small organic drug molecules, with approximately a third of drug compound can form a hydrate.[12] The fact that water is ubiquitous means that pharmaceutical solids are inevitably exposed to water, intentionally or unintentionally, whether during processing, storage or even after production or sale, all of which could lead to hydrate formation.[13,14] Consistent and good aqueous solubility is crucial for pharmaceutical processing. During manufacturing, solubility differences between the anhydrate and hydrate forms can affect handling and processability of the compound. In addition, a sudden reduction in aqueous solubility due to hydrate formation will force modification to the processing of the compound, *e.g.* additional solvent usage or unit process, and can eventually lead to increase in manufacturing costs. Hydration of a drug compound is unavoidable as contact to water during the manufacturing process of a drug is extensive, due to the direct use or indirect exposure. For instance, in processes like lyophilisation,[15] and wet granulation, the use of water and water containing materials,

e.g. excipients, that are capable of transferring water to the drug molecule could cause a hydrate to form.[16] Furthermore, the potentially different habits between the anhydrate and hydrate form may impede the flowability, as well as affecting the particulate level properties.

Moreover, crystalline hydrate formation may lead to increased rate of chemical degradation.[17] This is because, bound water molecules can be mobile and migrate within the crystal lattice, or along the solid surface,[18] resulting to water absorption.The presence of water enhances the drug molecular mobility, enhancing the chemical reactivity,[19] and consequently leading to drug degradation. However, this is not true for all cases as the apparent chemical incompatibility between water and β-lactams drugs, which are notoriously known to be suseptible to hydrolysis of the lactam ring by water,[20,21] is reduced through crystallisation or hydrate formation.[22]

Hydrate formation can also occur after leaving the production facility. Hydration due to high relative humidity (RH) or direct contact with water, may occur during storage, in a retail setting, *e.g.* on shelves, or even after sales during application of the formulation by the patient, being swallowed with a glass of water or improper container closure. One such case of hydrate formation due to exposure to high RH conditions during storage is for the drug berberine chloride dihydrate, transforming into a tetrahydrate during storage at 75% RH.[23] Similar cases were also reported for the drug dexmedetomidine hydrochloride [24] and droloxifene citrate [25] which exhibited similar conversion into their respective hydrate forms at high RH. The conditions in the gastrointestinal tract are more complicated and would present a bigger risk if a drug forms a hydrate in the biological environment. The bioavailability of the final drug product can be affected by the reduced solubility and dissolution rate. An example

where product changes after consumption is the conversion of carbamazepine anhydrate to hydrate as simulated in intestinal fluids.[26]

All in all, unintentional hydrate formation at any point, represents a major problem and will cause poor repercussion towards the overall safety, manufacturing, performance and effectively hamper the final medicinal product's full potential. Therefore, it is very important to identify any possible hydrate form(s) in the early phases of the drug development process.

1.1.2 Hydrate classification

Hydrate is generally classified based on the manner and amount (in moles) of water is released upon disassociating with the crystal, *i.e.* stoichiometric or non-stoichiometric.[6,10,27,28] A stoichiometric hydrate has well-defined water content and the incorporated water interact strongly with the host compound and each other. Upon dehydration, the absence of water molecule causes instability to the crystal network, which would collapse forming a new reduced water content crystal form or an amorphous state.[29] The resultant anhydrous crystal form would also have a distinctly different crystal structure and pattern to that of the hydrate form. Also, the sorption isotherm (Figure 1.2 A) would show a step-shaped phase change which is measured by the mass change, following hydration/dehydration due to variation in relative humidity or water vapour pressure,[28] as reported for nedocromil sodium hydrates, transitioning under isotherm from hemiheptahydrate to trihydrate to monohydrate with reducing RH, and to anhydrous form with subsequent heating.[30]

In contrast, non-stoichiometric hydrates have a weak binding of water in crystal lattice channels.[27] When exposed to high or low humidity; the crystal lattice may

undergo expansion or contraction resulting from changes in the dimensions of unit cells,[6,28] which would translate into continuous sorption-desorption isotherm curve, with no step-like feature (Figure 1.2 B). Non-stoichiometric hydrates pose additional problems in dosage form development due to the unpredictability of water content.[6] One such case is the continuous changes in the crystal lattice of cromolyn sodium. Cromolyn sodium forms non-stoichiometric hydrates as the compound continuously liberates and absorbs water. The incessant variations of the lattice made cromolyn sodium physically variable, which complicates formulation and processing.[31] A single compound may exist as both stoichiometric and non-stoichiometric hydrates as shown in the case of brucine, where the HyA is non-stoichiometric, while HyB and C are stoichiometric hydrates.[32] Similar feature is observed in 3-(4-dibenzo[b,f][1,4]oxepin-11-yl-piperazin-1-yl)-2,2 dimethylpropanoic acid (DB7), where Hy 2 is a stoichiometric hydrate and Hy A is non-stoichiometric.[33]

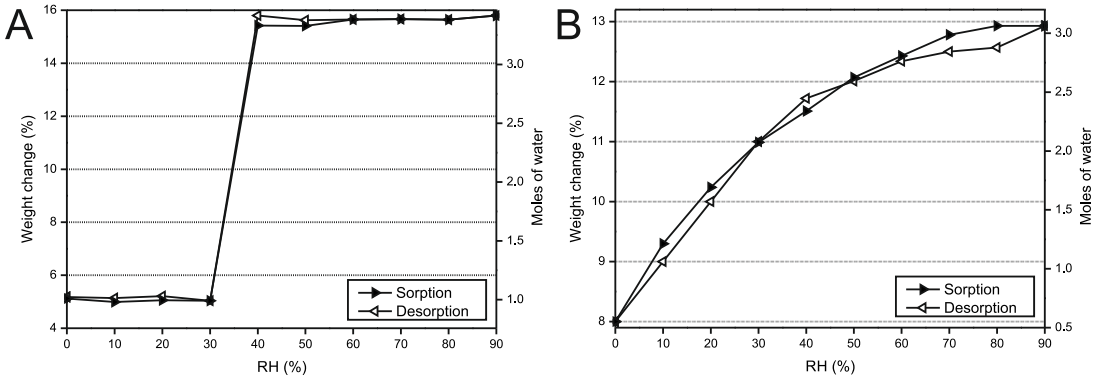


Figure 1.2. Typical DVS sorption and desorption curve cycles for hypothetical compound A (A) and B (B)

Hydrate can also be classified based on the structural aspects of the water positions in the crystal lattice.[34] Water can be incorporated into the lattice via three methods: firstly, water molecules can be isolated from one another by parts of the host molecule (in cavities or chambers) within the crystal. [34] One such example is reported

on paroxetine hydrochloride as illustrated in Figure 1.3 (a).[35] Another example of isolated hydrate form is Hy A of DB7 shown in Figure 1.3 (b).[33]

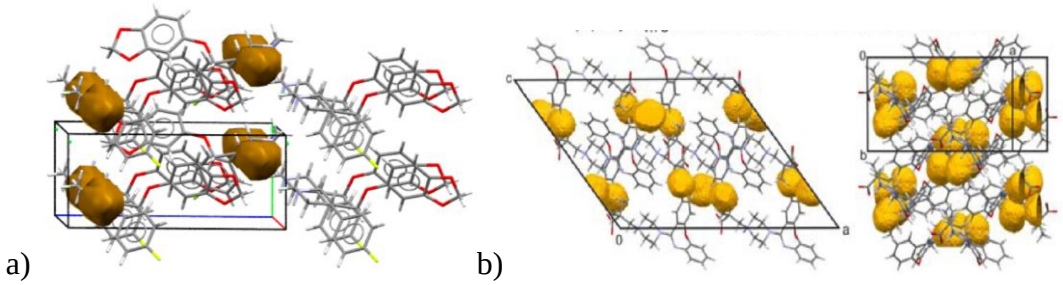


Figure 1.3. a) Paroxetine hydrochloride form II packing showing void (brown) occupied by water;[35] b) DB7 HyA packing showing void (yellow) occupied by water.[33]

The second way of incorporation involves the interaction of water molecules with each other and their located in channels within the crystal, as in the case of sitagliptin L-tartrate hydrates (SLT).[36] SLT was reported to exist as five hydrate forms, which include a tetrahydrate, and four other phases having 0.5 moles of water per molecule of SLT located. The channel feature is reported in Phase 1, 2, and 4 of the SLT hemihydrate forms (Figure 1.4).

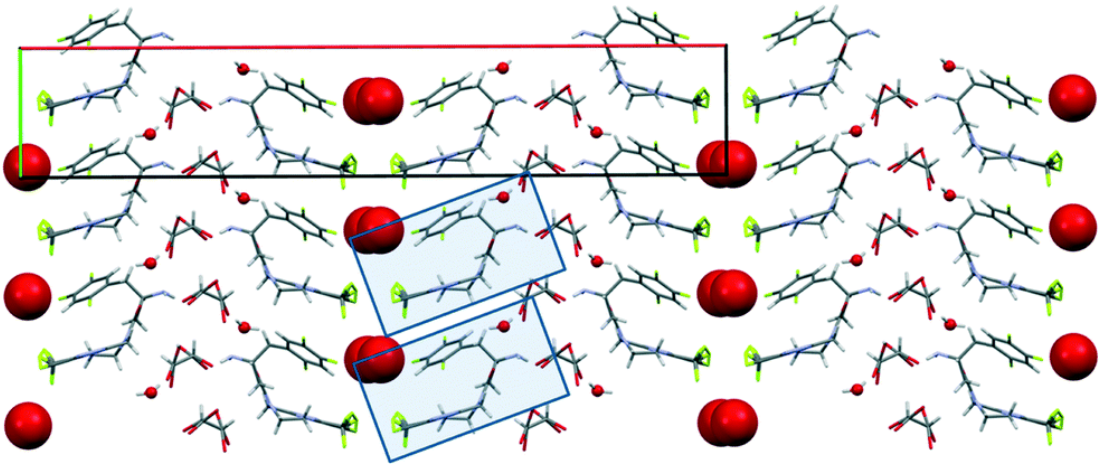
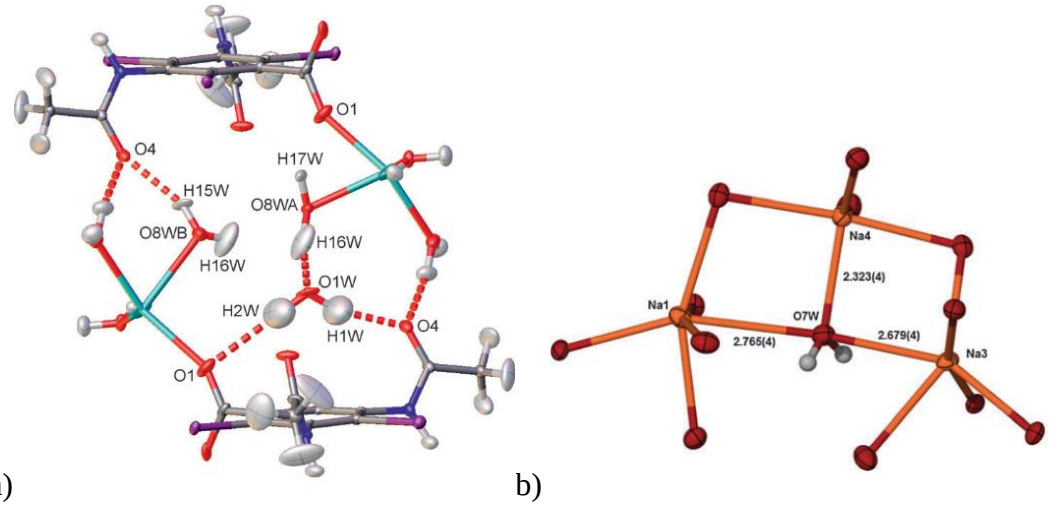


Figure 1.4. Packing motif of SLT phase 4 showing channel feature with water's oxygen atoms represented in space-fill style. Figure adapted from Tieger et al.[36]

Other examples of channel hydrate includes sitafloxacin hydrate,[37] norfloxacin hydrate,[38] Hy2 of DB7,[33] as well as AMG 222 tosylate.[39] Similar to the SLT hydrate behaviour, AMG 222 tosylate showed whereupon dehydration an isostructural dehydrate is formed, and the channels remain void and accessible to water for rehydration.

Finally, oxygen atoms (in water molecules) can be attracted towards specific positive sites in the crystal such as cations (*e.g.* sodium or calcium) as in the case of diatrizoic acid (DA) monosodium[40] and disodium salt.[41] The DA monosodium hydrate form is the tetrahydrate, which showed four molecules of water coordinated to the sodium cation, two of which is shared with a second sodium cation form a second molecule. In the other hand, DA disodium is mixed a solvate with 8.5 molecules of water and one molecule of ethanol per molecule of salt, showing one water molecule coordinated to three sodium cations (Figure 1.5).



a) b)

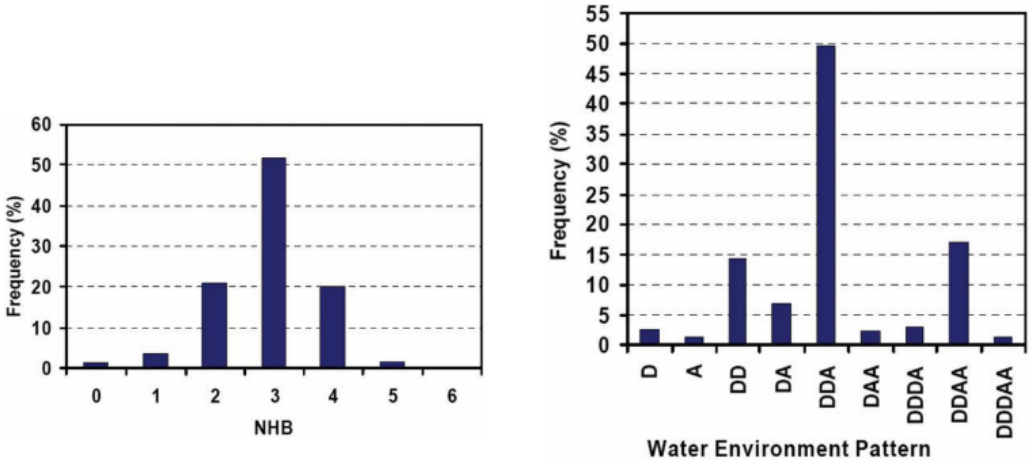
Figure 1.5. a) DA monosodium tetrahydrate showing sodium coordinated water molecule,[40] while b) shows DA disodium salt, with water molecule coordinated to three different sodium cations.[41]

There is also report of two types of water interaction in a single unit cell as in the case sulfadiazine calcium (hydrate I) where both channel-type and ion-coordinated

water present.[42] The ratio of water molecules with to host molecules for hydrate are commonly denoted as numerical prefix of mainly Greek origin: Hemi – ½, Mono – 1, Sesqui - 1½, Di – 2, Tri – 3, Tetra – 4, Penta – 5, Hexa – 6, Hepta – 7, Octa – 8, Nona – 9, Deca – 10, Undeca – 11 and Dodeca – 12.[43]

1.1.3 Water of crystalline hydrate interaction preference

A recent study suggests that there is a preference towards the hydrogen bond patterns for the water molecules in organic crystalline hydrates.[44] Report from crystal structure database (CSD) data analysis on the distribution pattern of the hydrogen-bonded environment of the water molecules in hydrates reveals that, three (3) number of hydrogen bonds (NHB) per water molecule coordination is the most frequent motif with 2390 observations (accounting for 52%), out of 4616 molecules. Only about 1% of water molecules do not show any hydrogen bonds, signifying true 'inclusion compounds', filling in space between molecules. The report also identifies donor bonds OH···X as (D), while acceptor bonds O···HX as (A), and subsequently determine the most common environment based on these identifications. The two (2) donor-bonds and one (1) acceptor-bond, DDA 50%, is the most common configuration, followed by DDAA at 17%, DD at 14%, and DA at 7% (Figure 1.6). Although these observations account for water motif and orientation in the solid-state, any connection towards this preference in the solution-state would be interesting, hinting that the common feature/ prominent role of water feature exists earlier, as early as the pre-nucleation stage.



(a) (b)

Figure 1.6 (a) Distribution of the total number of hydrogen bonds per water molecule and (b)Patterns of hydrogen bonds around water molecules as a frequency (%) for each observed environment[44]

1.2 A view on Crystal Structure Prediction (CSP)

The interest and technological advancement geared towards finding and predicting all possible form for a crystalline compound, especially hydrate is ever present and growing. The current experimental approach includes screening using solution crystallisation,[45–47] liquid-assisted grinding (LAG)[48], water slurry experiment,[49–51] and etc., all of which require time, money and effort, as well as an element of serendipity. Therefore, the move towards hastening and automating the process is very tempting. Recently, the *in-silico* approach is slowly being extended to predict hydrate formation *e.g. via* computational and statistical models.[52–57]

One such method is using crystal structure prediction (CSP), which works by simulating trial crystal structures of solids, which are then assessed based on their calculated energies. The computed crystal energy landscapes are now being used to aid polymorph screening of small molecule pharmaceuticals.[55] A different

computational approach which uses of electrostatic potential as a reliable indicator to predict hydrogen bond formation, and potentially hydrate formation propensity, also faces problem as the approach is limited to specific compound only.[58] Another computational method also aimed towards hydrate prediction is using conductor-like screening model for real solvents (COSMO-RS). COSMO-RS has been used for virtual screening of solvents for solid desolvation and co-formers for co-crystallisation, but recently the use is extended towards virtual hydrate screening of organic molecules.[59] The outcome however is not so positive as the chosen parameters provide a poor prediction of hydration propensities of pharmaceutical organic molecules.

Most of the *in-silico* approaches faces a few hurdles, *e.g.* generalisations of hydrate formation remains implausible as each solid compound responds uniquely to the possible formation of hydrate,[6] the inconsistent modelling of water,[60] huge computing power and time consuming as calculation is limited to one stoichiometry of variable at a time in the asymmetric unit of the theoretical structure (*e.g.* co-crystals, salts or solvates/hydrates),[55] and finally the computational approach also does not inform the crystallisation technique to obtain the calculated or predicted stable hydrate form. With regards to water models, though advances have been made,[61] there is yet to exists a system that can accurately and adequately model all of water abnormalities.[60] As it is, the perfect theoretical approach to lattice energy calculations still does not exist.[62] In the end, the *in silico* approach still demands time, money, and effort, leaving hydrates formation largely unpredictable and remains a challenge in crystal engineering. [63]

1.3 Hydrates and crystallisation theory

The simplest way to prepare a hydrate is through re-crystallisation with water or from solvent mixture that contain water. Stable hydrates can also be formed by suspending the anhydrous form in water. From a purely thermodynamic point of view, crystallisation occurs when super-saturation, under-cooling or pressure causes the crystalline phase to be more stable than the corresponding solution or melt (Figure 1.7).[64]

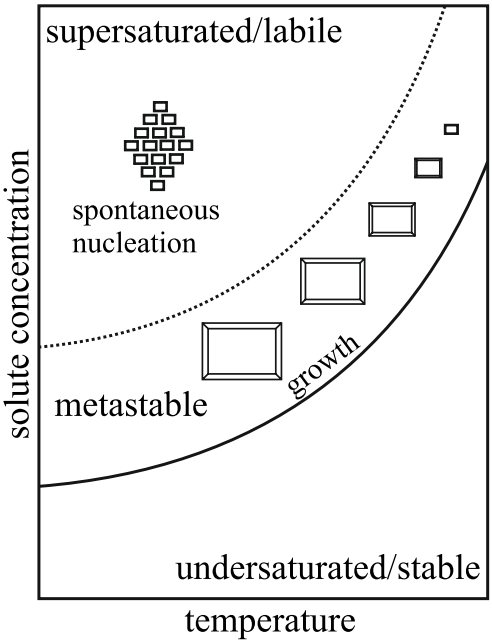


Figure 1.7 Solubility curve and metastable zone plotted against temperature and concentration. The figure is adapted from Panagiotou and Fisher.[65]

Fundamentally, there are two main processes in crystallisation, namely nucleation and growth.[66] Nucleation is a first-order phase transition, during which particles are made from their constituents, ions, atoms, or molecules. The growth of these nuclei occurs because the flux of molecules attaching to the crystal surface exceeds the flux of molecules detaching from the surface which is true for crystallisation from the melt, solution or gas phase.[66] Based on Gibbs free energy

change (Equation 1.1), spontaneous crystallisation must have a negative ΔG value. The ΔH is the enthalpy change, in joule, ΔS is the entropy change, in joule per kelvin, T is Temperature in kelvin.

(Equation 1.1)

$$\Delta G = \Delta H - T\Delta S$$

The crystalline phase presents less entropy or disorder than an amorphous solid which is unstructured or chaotic, so ΔS is negative. That means that the crystallisation process is enthalpy driven. Therefore, ΔH has to be negative and large enough to make up for the loss of entropy, in order to make the process spontaneous.

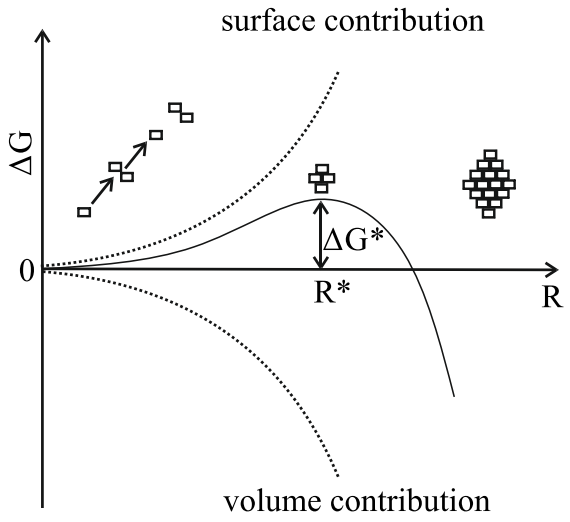


Figure 1.8. The Gibbs free energy in relation to the radius of nuclei. The figure was adapted from three sources.[67–69]

Figure 1.8 illustrates the Gibbs free energy for crystallisation (ΔG) as a function of the radius of the nucleus or aggregate size (R), shown as a solid line. Dotted lines represent contributions of surface formation and bulk incorporation. R* and ΔG* represent the size of the critical nucleus and the activation free energy, *i.e.* the energy barrier for nucleation, respectively. At R < R*, only transient aggregates form and re-dissolve. Since the energy barrier has yet been overcome, nucleation does not occur.

Upon exceeding the critical radius, crystal–liquid interfacial energy is lower than the activation energy, prompting the nucleus to grow in size spontaneously and become a crystal.[68,70] Scientists have long referred to the classical nucleation theory framework to explain the nucleation kinetics of the transition from liquid to solid, or crystallisation and from gas to liquid, or condensation.[71–74] Recently, the non-classical theory has been proposed for crystal formation.[42–50]

1.3.1 Classic nucleation theory (CNT) vs non-classical theory

Developed by Volmer, CNT is a model of first-order phase transition involving crystal nucleation from a supersaturated phase.[71] With the continual refinement of the original idea over the decades, CNT has been widely referred to with regards to nucleation from aqueous solution. It assumes that the molecular structure of a nucleus is similar to that of the final crystal form,[71–73] hence the crystals forms from solution in a single step transitioning from solution to solid with the initial formation of a crystal nucleus. CNT also assumes that the surface free energy of the nuclei according to this model will equal one of the crystal interfaces and that the size of the nuclei, *i.e*. radius for spherical nuclei, or the side length for cubic clusters, decreases smoothly as supersaturation increases.[75] Nevertheless, some might argue that CNT cannot explain some phenomena like dense liquid phases [76,77] or (meta)stable clusters [78] associated with pre-nucleation intermediates and thus making CNT appear too simplified.[79] Therefore, all of the recent reports of the emergence of pre-nucleation aggregates as well as recent crystallisation kinetic studies have opened the possible alternative to the CNT dubbed the non-classical theory. Reports of stable solute species in a

homogeneous solution; like the pre-nucleation ion clusters forming in an undersaturated solution of dissolved biominerals seen in calcium carbonate, phosphate and oxalate,[78] or the metastable (pseudo-)phases in protein crystallisation,[80,81] suggest a two-step mechanism in crystallisation process contradicting the CNT. A recent report even proposes a variety of pathways with more than two steps proposed to crystal formation (Figure 1.9 (b)).[82] One common theme is that a distinct separation between clusters is proposed; first being the stable dense phase, followed by the crystalline order. [83] The stable dense phase is simply identified as the pre-nucleation cluster (PNC).[84]

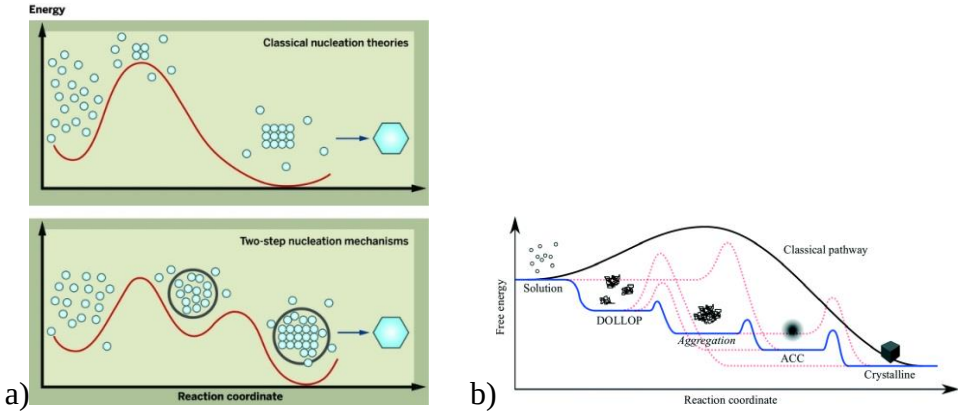


Figure 1.9.Crystallisation theories. a) Representation of CNT and non-classical theory[85,86] b) Schematic showing the free energy variation for a variety of possible pathways for crystallisation from ions in solution *DOLLOP = Dynamically Ordered Liquid-Like Oxyanion Polymer *ACC = aggregating clusters amorphous/crystalline [82]

1.4 The relationship between solid and solution-state analysis

Solution state analysis has been used to succesfully show intermolecular interaction reflective to the solid-state successfully. In 2004, Christopher Hunter and his team used proton (^{1}H) NMR to probe crystal nucleation. They found that the structures of the aggregates formed by the two (2) compounds tested in solution are

similar to the structures of dimer motifs found in the crystalline material. The finding supports the notion that solution NMR experiments can be an experimental tool for probing the organisation of molecules in the solid state.[87] In another recent report, the formation of mesostructure (structure or superstructure of intermediate size or complexity) during crystallisation of DL-valine was observed using Dynamic Light Scattering and Brownian microscopy. The mesostructure was found to be present in both undersaturated and supersaturated solutions below the temperature of 35 °C. Here, the authors showed the relationship between mesostructure size and the rate of nucleation, measured in the solution state.[88]

More interestingly, in another report, also linking the use of solution state analysis to crystal nucleation, whereby here, a direct relationship between molecular self-association in solution and hydrogen bonded motifs in the subsequently crystallised tetrolic acid was reported. Although the actual process of molecular clustering is still unknown, the authors note that IR spectroscopy is an efficient tool to be used in indicating the formation of the fundamental growth units in the crystallisation event.[89] In the experimental framework, they identified two major IR absorption bands corresponding to different hydrogen bonded motifs which are the –C=O anti-symmetric stretch (1740–1660 cm^{-1}) and the –OH···O– (960–875 cm^{-1}) which characterises the carboxylic acid dimer. The author then emphasised the persistence or absence of the hydrogen-bonded motifs in the solutions. They also associate an unusually high peak –C=O at 1710 cm^{-1} in saturated and diluted dioxane to a major weakening of intermolecular hydrogen bonds, or the existence of monomeric solute species.

Another example of solution state analysis association to the solid state is through the report on ortho-methyl carbazolone (OCB).[90] OCB has four polymorphs, with only form I showing catemer motif, while the dimer was observed in remaining three forms. The authors use FTIR titration to prove the existance of OCB dimers in solution through the observation of N–H vibration in solution. When the solution IR spectra were compared to the solid-state spectra of forms I–IV, they found comparable N–H vibration at 3300 cm^{-1} in solution to that of the three-dimer crystal forms, forms II, III, and IV showing N-H vibration at 3369 to 3366 cm^{-1}, which corresponds to the said motif. The result again shows close relationship between the solution and solid-state, which was observable *via* FTIR.

1.5 Noncovalent interactions

Noncovalent interactions play vital roles in chemical system, *e.g.* crystallisation, self-assembly[91] as well as biological system, *e.g.* DNA, RNA, and proteins synthesis.[92,93] Noncovalent bond does not involve the sharing of electrons, but rather involves more dispersed variations of weak, reversible, inter- and intramolecular attractive forces which "holds" molecule together. Possible noncovalent interaction that could form in solution include van der Waals, dipole-dipole, hydrophobic bonds, hydrogen bonds and ionic bonds. The binding strength of these noncovalent interaction is illustrated in Figure 1.10, which typically lower compared to the energy for covalent, *e.g.* C– C or C–H bond. Variation of the mentioned noncovalent interactions involving molecules having benzene ring in their make-up is also possible which include π–π stacking interaction, polar–π interaction, CH–π interaction, cation–π interaction, aromatic CH–π, or T-shaped stacking interaction and π–π stacking interaction (Figure 1.11).

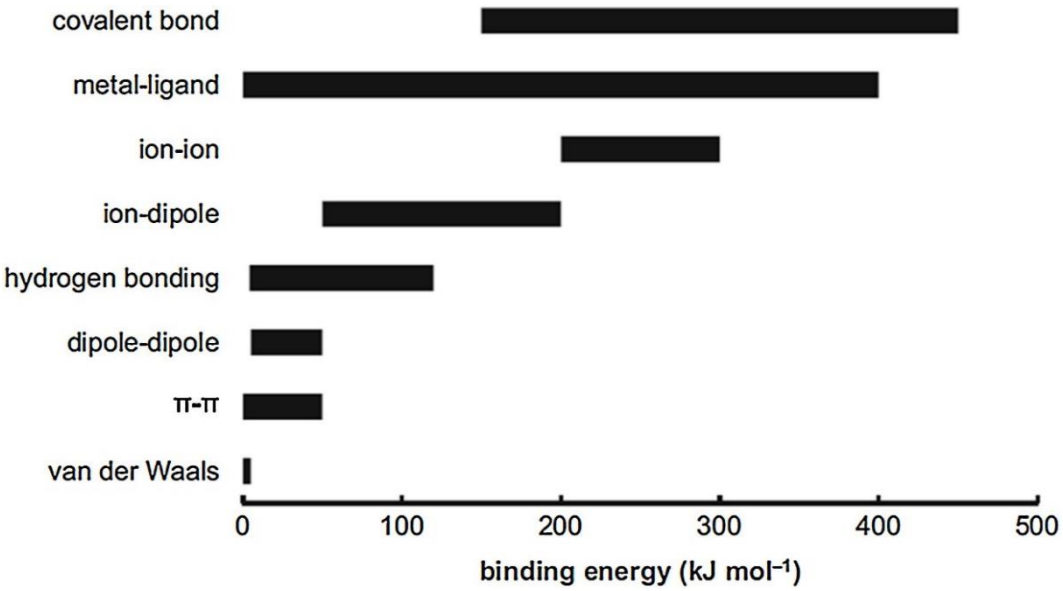


Figure 1.10. Comparison of non-covalent interactions and their typical range of binding strength, in comparison to covalent bonds. The figure is adapted from Steed and Atwood.[94]

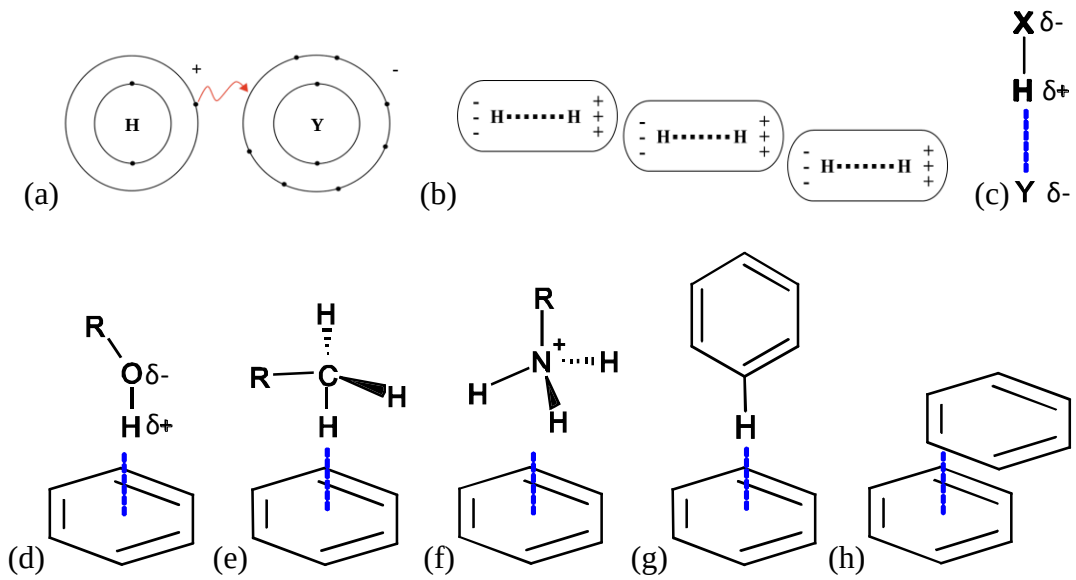


Figure 1.11. Selected illustration of noncovalent bond interactions, (a) ionic bond, (b) van der Walls, (c) hydrogen bond, (d) polar–π interaction, (e) CH–π interaction, (f) cation–π interaction, (g) aromatic CH–π, (h) π–π stacking interaction

Among all the mentioned noncovalent interaction, hydrogen bonding is one of the stronger interaction (compared to van der Walls), and the most common ones.

Hydrogen bonds ranges widely in strength from very strong (gas phase enthalpies of ~40 kcal/mol, *e.g.* [F ⋯ HF]-) to weak (gas phase enthalpies of 1 – 5 kcal/mol, *e.g.* [HOH⋯OH_2]), the latter (weak) are most prevalent in chemistry and biology. From an electronic standpoint, a "classic" hydrogen bond is simply an interaction between a partially positively charged hydrogen atom (denote as $H^{\delta+}$, usually identified as proton donor), and a partially negatively charged atom in the acceptor molecule, (denote as $Y^{\delta-}$, in Figure 1.11 (c)), which have a lone pair in the vicinity of the H atom.[95]

However, it must be stressed that the effect of hydrogen bond formation to the electron density takes place not only in the immediate locality of the H and Y atoms but within entire molecules.[96] Following a hydrogen bond, all atoms and bonds of the whole complex take part in the interactions as illustrated below Figure 1.12.

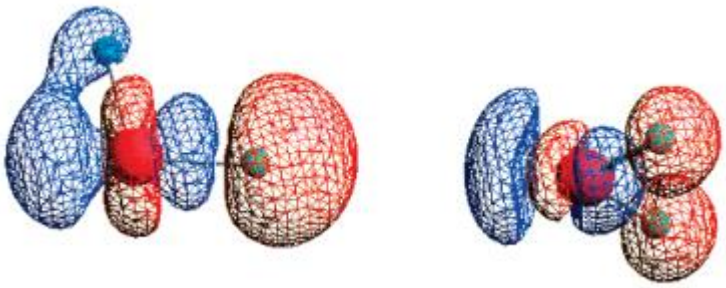


Figure 1.12. Maps of two (2) water molecules (dimer), representing a donor (left) and acceptor (right), showing the regions of increased and decreased electron densities. Red indicates the loss of electron density while blue represent regions of electron density build-up. This figure was obtained from Scheiner and Kar.[96]

1.5.1 Water interaction in solution

Structurally, the water molecule has a tetrahedral distribution of two positively and two negatively charged regions as indicated in Figure 1.13. Therefore, we anticipate the following water-solute interactions.

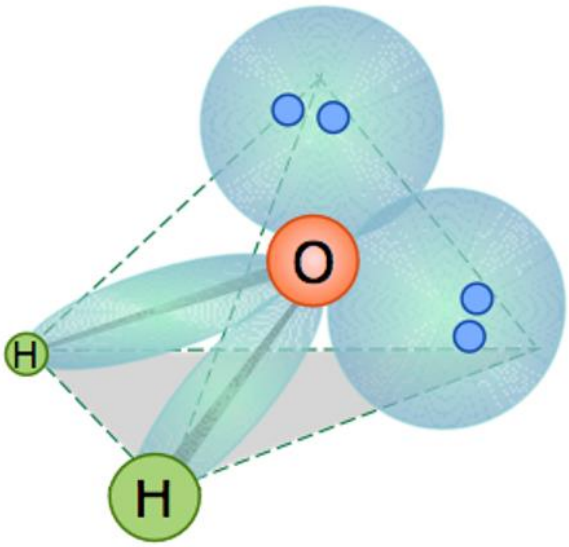


Figure 1.13. Tetrahedral structure of water (downloaded from google free media repository)

Firstly, on each negatively charged region, the water molecule interacts with its neighbours via a coordinate covalent (dative) bond, where one atom, *e.g.* the oxygen of water, contributes both of the electrons in the shared pair. Once formed, a coordinate covalent bond behaves in the same as any other covalent bond. The oxygen of the water molecule can also act as a proton acceptor and forms hydrogen bond with neighbours which are electron acceptor groups (or proton donors, *i.e.* Lewis acid). Meanwhile, on each of the positively charged regions, the water molecule interacts with its neighbours which are electron donor groups (or proton acceptors, *i.e.* Lewis base) by donating proton to hydrogen bond. The interaction is indicated in Figure 1.14 a) and b).

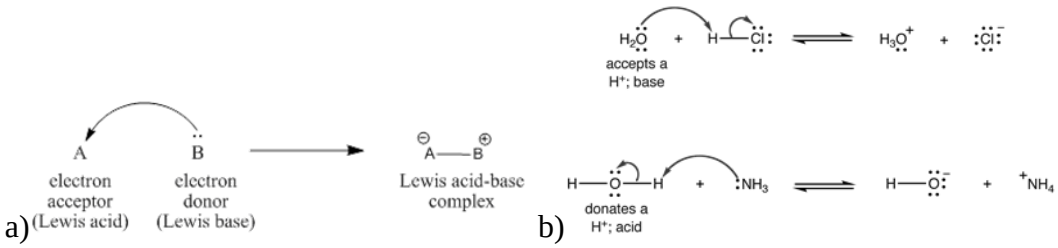


Figure 1.14. a) Lewis acid-base depiction b) Example of water as Lewis acid and base (downloaded from google free media repository)

1.6 Host-guest chemistry

In our effort to investigate the role of water in hydrate formation, host-guest chemistry is utilise to probe possible water-compound complex formation, which are potentially driven and held together by the mentioned noncovalent bonds (1.3) and forming distinctive structural relationships in solution.

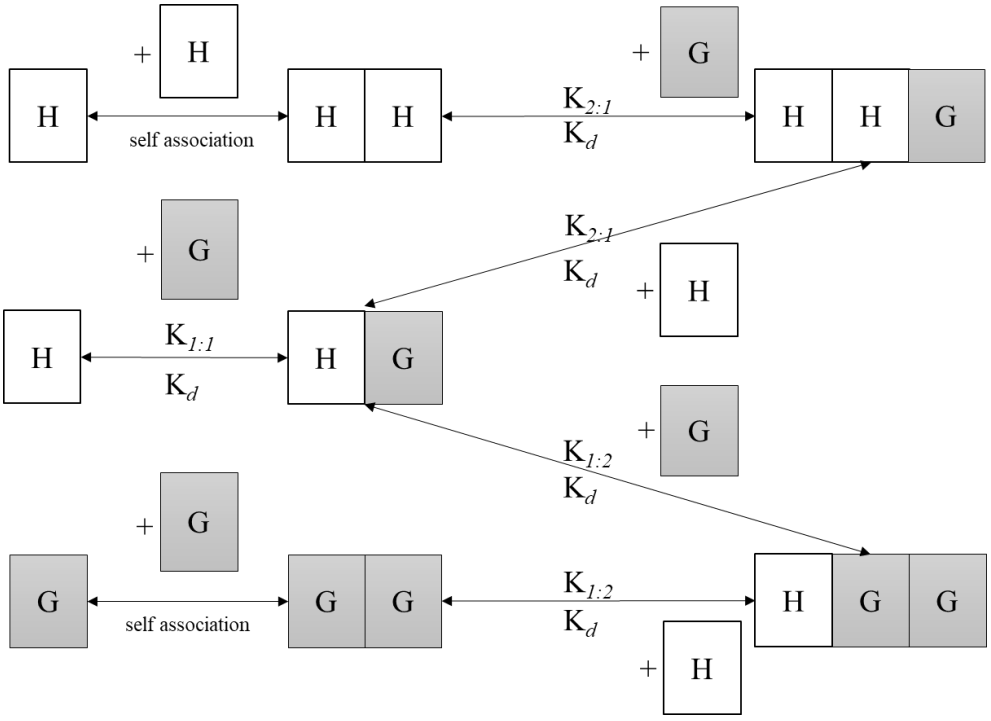


Figure 1.15. Typical interactions in a host-guest interaction in solution. H is the host, and G represent the G.

Host-guest chemistry is a branch of supramolecular chemistry, typically utilised to probe the extend, structure and binding affinity in molecular complexes (Figure 1.15).[97] Our solution-state analysis is based on a modified host-guest chemistry titration, where water will be the guest and added in small aliquots with respect to a constant host, which method is discussed in detail in Chapter 2. The solvent is chosen based on two main criteria; adequate host and host:guest complex solubility, and the guest-solvent miscibility. The measures taken ensures that the change later observed is not due to host concentration variations or solvent separation. Essentially, the

titration method used allows for determination of binding constant (K_a or K) between the water (guest, G) and a tested compound (host, H), based on the physical change (ΔY), *e.g.* NMR peak shifts, and the two known parameters, of host initial host ($[H]_0$) and guest ($[G]_0$) concentration using an open source software, Bindfit obtained from http://supramolecular.org/. The software uses algorithm and some initial guesses for K and calculate ΔY, and compare it to the measured ΔY and then vary K and ΔY until a good fit is obtained. Once K is obtained, it is easy to calculate the Gibbs free energy (ΔG), form the formula, $\Delta G = -RT \ln (K)$, which would indicate the strength of interaction between the reactants.

1.6.1 Binding constant

A chemical equilibrium is the state in which the forward reaction rate, which is the binding constant (K_a or K) and the reverse reaction rate, which is the disassociation constant (K_d) are equal (Equation 1.2, where host = H, guest = G and a, b are stoichiometry of the reactants). Binding constant value would represent the foward relationship favouring the formation of the products in relation to reactants present at equilibrium in a reversible chemical reaction at a given temperature. Meanwhile, the K_d can be obtained from the inverse of K_a value ($K_a=1/K_d$). Binding constant would also reflect the binding affinity of a host toward particular guest under equilibrium conditions. The unit for K_a is in $Molar^{-1}$ (M^{-1}) while for K_d is in Molar (M). The affinity of a H toward a G in the case of 1:1 stoichiometry is defined by Equation 1.3, which results from the rearrangement of Equation 1.2 to express binding constant K or K_a in relation to host, guest, and product or complex concentration, when a and b values in Equation 1.2 are one (1).

(Equation 1.2)

$$a[H]+b[G] \rightleftharpoons H_aG_b$$

(Equation 1.3)

$$K \text{ or } K_a = \frac{[HG]}{[H][G]}$$

If the concentration of the complex [HG] is known, the remaining concentrations can be determined by the mass balance equation for total or initial host (Equation 1.4) or guest (Equation 1.5) concentration

(Equation 1.4)

$$[H]_0 = [H] + [HG]$$

(Equation 1.5)

$$[G]_0 = [G] + [HG]$$

In Equation 1.4 and 1.5, the total concentrations of the host and the guest are represented by $[H]_0$ and $[G]_0$. Meanwhile, [G] and [H] here is the free host and guest respectively. Once [H], [G], and [HG] are all known, then K_a is easily calculated. Regrettably, direct measurement of [HG] (or [H] and [G]) is not possible. Therefore, the next best approach is to measure the concentration of the complex [HG] indirectly through titration experiments. The only experimentally determined values are the concentrations of the H and G, and the physical property (Y), which is changing (ΔY) which are then fitted to the theoretical binding isotherm. The basis for this indirect assumption is that the ΔY, *e.g.* NMR resonance peak shift or $\Delta\delta$, observed during the course of a titration, is correlated to the concentration of the complex [HG] ($Y_{\Delta HG}$). ΔY in the system are monitored and then plotted as a function of guest added to host (equivalent guests, [G]/[H]). The K_a mathematical model is developed by realising that

the mentioned correlation (ΔY or $\Delta\delta$ correlates directly to the concentration of the complex [HG]).

Historically, the linear approach *e.g.* Benesi-Hildebrand plot,[98,99] Lineweaver-Burke plots,[100] Scatchard plots[101,102] were used to determine *K*, which frequently involves shortcuts *e.g.* assuming that initial guest concentration is much larger or that complex formed completely at the end of titration. The later assumption, would incline that the reaction is indeed linear and thus misrepresent the result.[99,103] The older references also overly simplify the equations by transforming the HG relationship to linear equations ($y = mx + c$), which could then be plotted by hand to obtain the K_a and other parameters of interest, by going-over the slope and intercepts. In fact, a non-linear regression approach with exact solutions of the quadratic equation would produce the most accurate result.

K_a experimental measurement method also often depend on the analysis of a binding isotherm. A binding isotherm is not experimentally measured, but rather generated by using mathematical model, *i.e.* Nelder-Mead algorithm[104] which is based on solving a quadratic line. The binding isotherm would simulate theoretical change in the concentration of one component as a function of the concentration of another component at a constant temperature.

In term of the formed species, is unlikely that only a singular species is formed from the interacting reactants, especially in a dilute solution as shown in Figure 1.15. Several species can co-exist in the same equilibria. Fast analytical tool, *e.g.* infra-red analysis, could observe these overlapping species in solution, however, a slower timescale instrument, *i.e.* nuclear magnetic resonance (NMR) would only detect the average change of species. Key association aside from 1:1 are, 1:2 and 2:1 in

stoichiometry. Limited binding and a mathematical model to that of the mentioned stoichiometries means that only these species are analysed, although in reality a variety of species can be present especially in a dilute solution environment. For a 2:1 or 1:2 complex to form from a direct simultaneous collision of one host with two guests, is rather implausible. Therefore, a stepwise process following modified Equation 1.2 when *a* and *b* values are one (1) and two (2) respectively resulting in Equation 1.6 and Equation 1.7 is more plausible. For a 2:1 interaction, the modification in the stoichiometry value is reversed, where *a* is two (2) and *b* is one (1). In a 1:2 complexations, the initial step K_1 is expressed in Equation 1.6, while the second step, K_{12} (OR K_{21}) is expressed in Equation 1.7, in relation to host, guest, and product or complex concentration.

(Equation 1.6)

$$K_1 = \frac{[HG]}{[H][G]}$$

(Equation 1.7)

$$K_{12} = \frac{[HG_2]}{[H][G]}$$

OR

$$K_{21} = \frac{[H_2G]}{[H][G]}$$

As mentioned, direct measurement of [HG] (or [H] and [G]) is not possible, however, by modifying Equation 1.3, it is possible to determine free [G], by combining it with Equation 1.4, as shown below.

i. $K_a = \frac{[HG]}{[H][G]}$

ii. $K_a = \frac{[HG]}{([H]_0-[HG])([G])}$

Firstly, Equation 1.4 is rearranged and expressed as $[H] = [H]_0-[HG]$, and subsequently used to replace the [H] in Equation 1.3 (i-ii).

iii. $K_a ([H]_0-[HG])([G]) = [HG]$

iv. $K_a [H]_0[G] - K_a [HG][G] - [HG] = 0$

Next, the formula is rearranged and expressed as [HG] (iii), and solved to 0 (iv).

v. $K_a [H]_0[G] - [HG] (K_a [G] +1) = 0$

The expression (v) is simplified by factoring [HG].

vi. $K_a [H]0[G] = [HG] (K_a [G] +1)$

vii. $$\frac{K_a [H]_0[G]}{(K_a [G] +1)} = [HG]$$

The formula is rearranged (vi) and expressed as [HG] (vii).

viii. $$\frac{K_a [H]_0[G]}{(K_a [G] +1)} = [G]_0 - [G]$$

Value for [HG] in (viii) is replaced with the rearranged Equation 1.5 which is expressed as [HG].

ix. $$\frac{K_a [H]_0[G]}{(K_a [G] +1)} + [G] = [G]_0$$

The whole formula is rearranged again in (ix), this time expressed as $[G]_0$

x. $K_a [H]_0[G] + [G] (K_a [G] +1) = [G]_0 (K_a [G] +1)$

The whole equation in (x) is multipled by $(K_a [G] +1)$ to remove the denominator.

xi. $K_a [H]_0[G] + K_a [G]^2 + [G] = K_a [G][G]_0 + [G]_0$

xii. $$[H]_0[G] + [G]^2 + \frac{[G]}{K_a} = [G][G]_0 + \frac{[G]_0}{K_a}$$

The expression in (xi) is divided by K_a and subsequently rearranged (xii).

xiii. $[H]_0[G] - [G][G]_0 + [G]^2 + \frac{[G]}{K_a} - \frac{[G]_0}{K_a} = 0$

The expression in (xiii) is rearranged and solved to zero.

xiv. $[G]^2 + [G]\left([H]_0 - [G]_0 + \frac{1}{K_a}\right) - \frac{[G]_0}{K_a} = 0$

Factoring [G] in formula (xiv) yeilded a quaratic equation of $ax^2 - bx - c = 0$, where 'a' equals to 1, x is [G], 'b' is $[H]_0 - [G]_0 - 1/K_a$ and 'c' equals to $[G]_0/K_a$

The quadratic equation (xiv) is solve using quadratic formula for x, resulting in the final Equation 1.8, which is the expression for free guest [G] concentration as a function of the total host (H_0), total guest (G_0), and K_a. [103]

$$x = \frac{-b \pm \sqrt{b^2 - 4ac}}{2a}$$

(Equation 1.8)

$$[G] = \frac{1}{2}\left(G_0 - H_0 - \frac{1}{K_a}\right) - \sqrt{\left(G_0 - H_0 - \frac{1}{K_a}\right)^2 + 4\frac{G_0}{K_a}}$$

By modifying Equation 1.3, it is possible to determine free [HG], by combining it with Equation 1.4 and Equation 1.5 as shown below.

xv. $K_a = \frac{[HG]}{[H][G]}$

xvi. $K_a = \frac{[HG]}{([H]_0 - [HG])([G]_0 - [HG])}$

Firstly, Equation 1.4 and Equation 1.5 are rearranged and expressed as $[H] = [H]_0 - [HG]$ and $[G] = [G]_0 - [HG]$ respectively, and subsequently used to replace the [H] in Equation 1.3 (xv and xvi).

xvii. $K_a = \dfrac{[HG]}{[H]_0[G]_0-([H]_0[HG])-([G]_0[HG])+ [HG]^2)}$

Next, the denominator are expanded resulting in (xvii).

xviii. $K_a ([H]_0[G]_0-([H]_0[HG])-([G]_0[HG])+ [HG]^2)) = [HG]$

The formula (xviii) is rearranged and expressed as [HG].

xix. $K_a [H]_0[G]_0- K_a [H]_0[HG]- K_a [G]_0[HG]+ K_a [HG]^2- [HG] = 0$

xx. $K_a [HG]^2 – [HG] (K_a [H]_0+ K_a [G]_0+1) + K_a [H]_0[G]_0 = 0$

Formula in (xix) is solved to 0 and rearranged to get (xx).

xxi. $\dfrac{K_a [HG]^2 – [HG] (K_a [H]_0+K_a[G]_0+1) -K_a[H]_0[G]_0}{K_a} = 0$

xxii. $[HG]^2 – [HG] ([H]_0+[G]_0+\underline{1}) + [H]_0[G]_0 = 0$
K_a

Formula in (xx) is divided with K_a as in (xxi), resulting in the quadratic equation (xxii). The quadratic equation (xxii) is solve using quadratic formula for x, $ax^2 + bx + c = 0$, where ‘a' equals to 1, ‘x’ is [HG], ‘b’ equals to $–([H]_0+[G]_0+\underline{1}/K_a)$ and ‘c’ is $-([H]_0[G]_0)$. Solving using quadratic formula for x below results in the final Equation 1.9, which is the expression for host-guest [HG] concentration as a function of the total host (H_0), total guest (G_0), and K_a.[103]

$$x = \frac{b \pm \sqrt{b^2 \mp 4ac}}{2a}$$

(Equation 1.9)

$$[HG]=\frac{1}{2}\left(G_0+H_0+\frac{1}{K_a}\right)-\sqrt{\left(G_0+H_0+\frac{1}{K_a}\right)^2+4[H_0][G_0]}$$

Equation 1.9 is very important, as based on this, we can now use the already available total or initial concentrations of the host ($[H]_0$) and guest ($[G]_0$) to quantify the free host [H] and guest [G] in Equation 1.4 and 1.5. Using the K_a measured from the titration experiment, substituted into this equation, all of the components are now measurable, and would provide insight into the speciation at play in solution. For a 2:1 or 1:2 complexation, similar rearrangement of Equation 1.7 once K_{12} OR K_{21} is obtained would allow measurement to similar equations and values as described in (i-xxii).

1.6.2 Thermodynamics of molecular interactions and relation to binding constant

According to Hirose, whilst binding constant is measured to quantify the host-guest complexation process, thermodynamic parameters *e.g.* enthalpy, entropy and Gibbs free energy are more suitable criteria to represent the strength of the interaction.[105]

Substituting Equation 1.1, ($\Delta G = \Delta H - T\Delta S$) into Equation 1.10, yielded the van't Hoff equation, Equation 1.11. Based on the van't Hoff equation, the thermodynamic parameters mentioned are now interrelated to each other.

Equation 1.10 Gibbs free energy for a system at chemical equilibrium

$$\Delta G = - R\,T \ln K$$

Equation 1.11. The van't Hoff equation

$$\ln K = - \frac{\Delta H}{R} + \frac{1}{T} + \frac{\Delta S}{R}$$

In principle, if more than one binding constants are obtained at different temperatures, van't Hoff equation (Equation 1.11) can be utilised to solve the

remaining thermodynamic parameters, from the slope and intercept of the line in Figure 1.16.

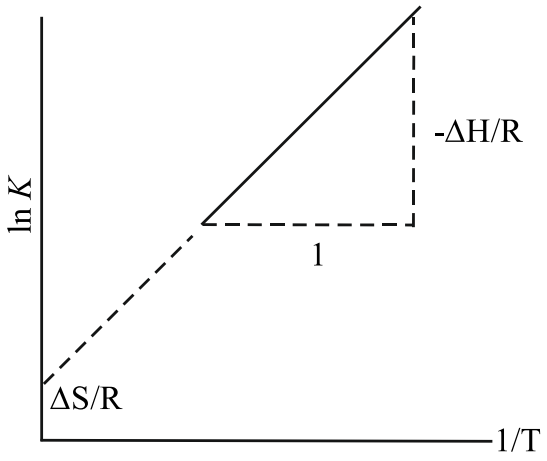


Figure 1.16. Correlation of thermodynamic parameters, K and temperature according to van't Hoff equation. Figure adapted from Hirose.[105]

1.6.3 Job's plot

The continuous variation method, or Job's plot,[106] has always been the most popular method for determining stoichiometry in host-guest chemistry. The method requires the total molar concentration of the tested two binding components, *e.g.* the host and the guest to be kept constant, but their mole respective fractions are varied. The physical change (Y) *e.g.* NMR peak shifts from the opposing mole fraction variation are plotted against the mole fractions of either of the two components, typicially the host. The maximum value on the plot would then correspond to the stoichiometry of the chosen component of the two species. Essentially, Job plot considers only one complex in solution which predominates over all others species under the conditions of the experiment (Figure 1.17). This requirement means that only systems with high association constants, or systems in which only one stoichiometry

can form. However, this requirement is also the biggest limitations,[107] as in solution; there are potentially more than one complex could be present.

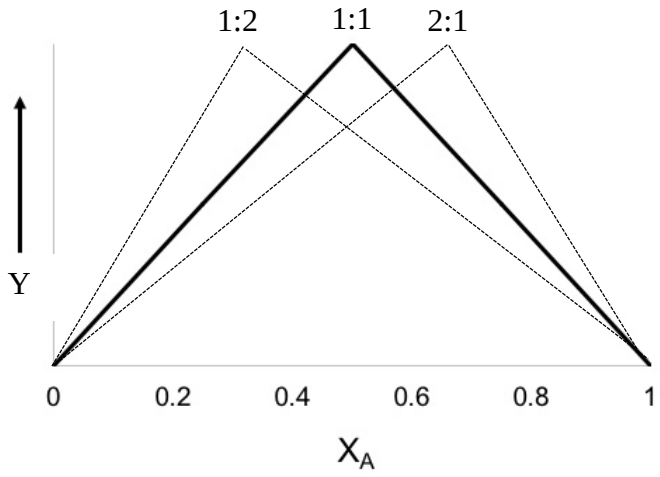


Figure 1.17. Typical Job plot showing the change physical property (P) with the change in the mole fraction of compound A (X_A). The Y_{max} at $X_A = 0.5$, indicating a 1:1 (host to guest) stoichiometry. Left skew would be associated to 1:2, while the opposite, 2:1 respectively.

In addition, a recent report shows that the observed maxima in the Job's plot can be misleading, showing clear sensitive to the binding ratio and host concentration than to the real stoichiometry.[108] In short, the method is not working in the supramolecular system, misleading about stoichiometry assembly and finally, can lead to incorrect K_a determination.[108] Job plot can, however, be an educated gauge to the possible interaction, and the result from the analysis is considered with caution.

1.7 Ideal and non-ideal aqueous mixing and the importance of water activity

Ideal mixture in general is a mixture of two very closely similar substances, which would result in a very small overall energy (enthalpy) change when the two substances are mixed. The more chemically identical the two mixing compounds are, the closer their mixing will be to an ideal mixture, however, the more dissimilar their

nature are, the more strongly the solution is expected to differ from ideality. Therefore, by this definition, all our solution state analysis involving organic solvent-water mixture would be in a non-ideal binary solvent mixture, as none of the solvent used is analogous in chemical structure to water. For example, DMSO and acetonitrile both miscible with water at any mixing ratio, however, the thermodynamic properties of mixing for the different solvents with water are completely different from one another and suggests non-ideal mixture with water as the enthalpy of mixing $\neq 0$: which is endothermic for acetonitrile-water[109] and exothermic for DMSO-water (Figure 1.18).[110]

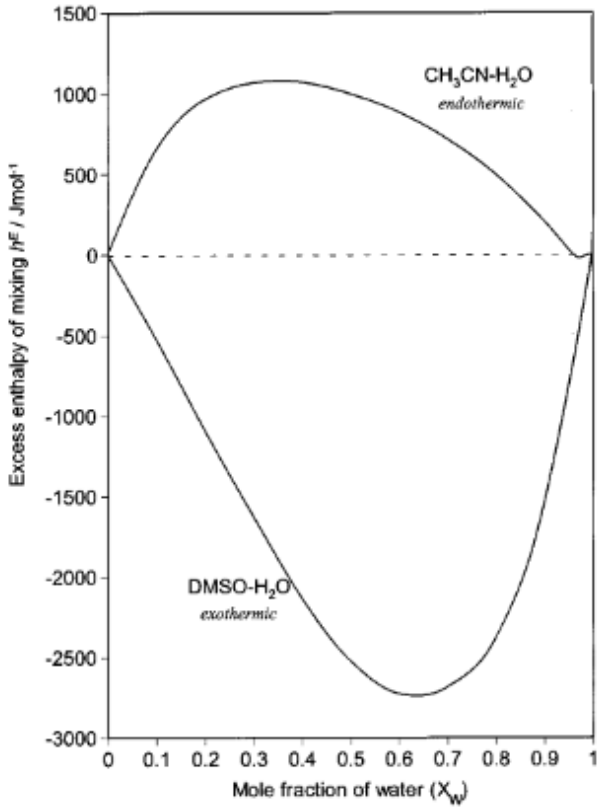


Figure 1.18. The enthalpy of mixing of DMSO and acetonitrile to water as functions of mole fraction of water, adapted from Shin et al.[111] Wakisaka et al.[109] and Lai et al.[110]. The dashed line corresponds to the ideal binary mixture whose excess enthalpy of mixing is zero

However, two different solvents can still achieve ideal mixing property based on the amount *e.g.* mole fraction and partial pressure of each component present in the mixture, as indicated by Raoult's Law for ideal mixture (Equation 1.12). Ideal mixture follows Raoult's Law, and the law states that the partial vapour pressure of a component in a mixture is equal to the vapour pressure of the pure component at that temperature multiplied by its mole fraction in the mixture. The total vapour pressure of the mixture is then equal to the sum of the individual partial pressures

(Equation 1.12)

i. $P_a = X_a \times P_a^\circ$

ii. $P_b = X_b \times P_b^\circ$

iii. $P_a + P_b = P_{tot}$

X_a and X_b are the mole fractions of components *a* and *b* respectively, while P_a° and P_b° are the partial pressure of the respective pure liquids. The ideal mixture total partial pressure line can be generated by the sum of P_a and P_b.or P_{tot} (Figure 1.20). For a nearly ideal mixture, experimental or measured partial pressure of the mixture is near enough to generated straight line. On the other hand, the less ideal the mixture is, the more curved the lines become.

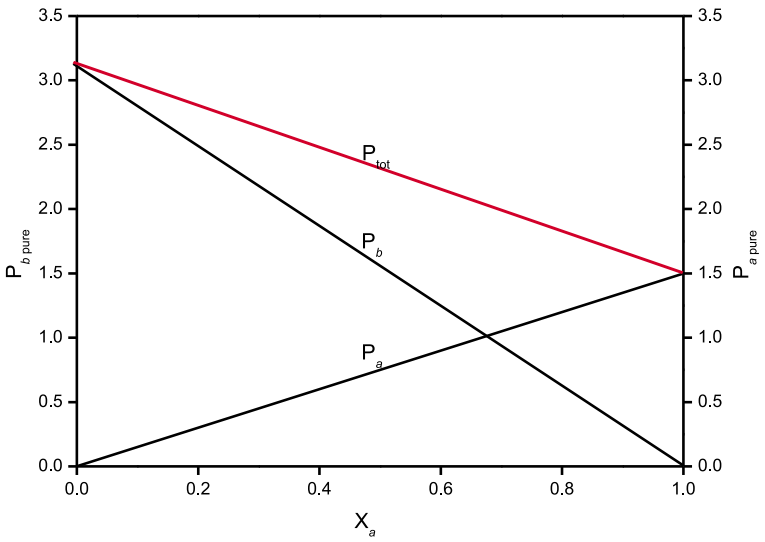


Figure 1.20. Raoult's Law ideal total partial pressure line (P_{tot}, red line) generated form the pure partial pressure of each component respectively (solid black line).

For example, considering DMSO-water mixture; pure DMSO have a vapour pressure of 0.075 kPa while the partial pressure of liquid water is 3.124 kPa at 25℃, Qian et al.[112] has measure the total vapour pressure of DMSO and water binary system, and reconstruction of their data (Figure 1.21) and compared to the P_{tot} line for ideal mixture reveals that the experimental line[112] close to generated straight line for an ideal mixture with negative deviation observed.

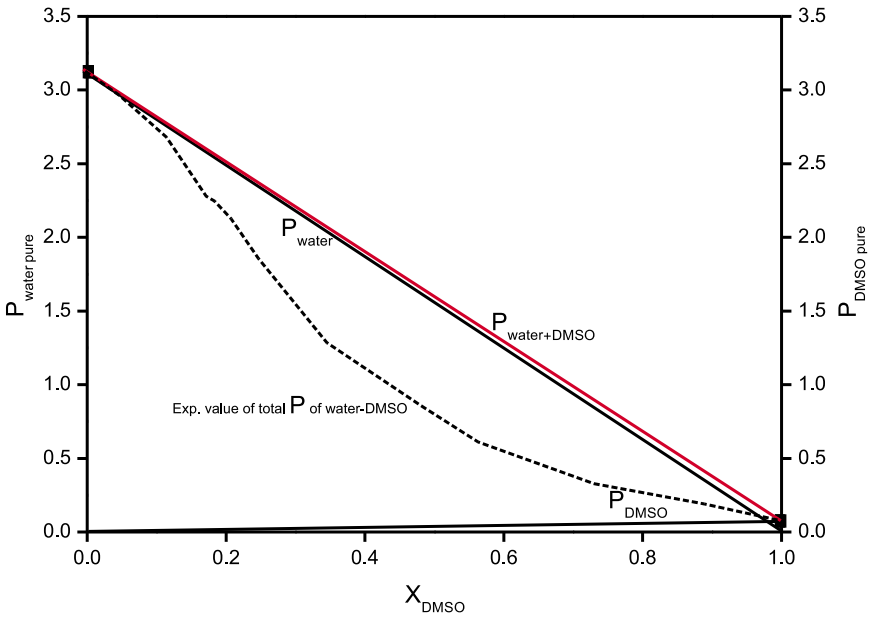


Figure 1.21. The vapour pressure of pure components (solid black lines), the ideal vapour pressure of the binary mixture (solid red line) and the total vapour pressure of DMSO and water binary system (± 3kPa, black dashed line)[112] at 25°C showing negative deviation.

The negative deviation of the experimental data suggests that the forces between the DMSO and water in the mixture are stronger than the mean of the forces between the particles in the pure liquids, most likely due to hydrogen bonding as reported in other binary mixture.[113] The hydrogen bonding interaction proposed is in line with the observed exothermic reaction (typically correlate bond formation)[114] of the mixture[111] and echoed in a molecular dynamics (MD) simulation study which reported that in an aqueous solution containing low DMSO concentrations, the DMSO molecule is likely to bound to water in a 1:2 ratios,[115] while in another MD simulation study, in a mixture of above 50% DMSO content, the stoichiometry changes, favouring the 2 DMSO:1 water complexes.[116] Also, in a water-rich DMSO mixtures, tetrahedral ordering of water molecules is observed,[117] suggesting that the water clusters were observed only at much higher water mole fractions: $X_w > 0.93$.[111] However, in another recent finding, DMSO is said to exhibit either ideal-solution-like between 30–90 mole % or self-interaction, or aggregation, regime above 90 mole %.[118] The report suggests that, > 30% DMSO-water mixture, DMSO is more likely to self interact hence DMSO-water mixture and would show good homogeneity, which in line with the mentioned law. Therefore, throughout our experiments amount (mole fraction) of guest *e.g.* water added is monitored with respect to the main solvent, *e.g.* DMSO, acetonitrile, or acetone, as to ensure that the overall mixture is close to being ideal.

1.8 Hypothesis and aim

Crystallographic analysis has always been the approach to investigate hydrate formation, behaviour and phase-transition. The search for the most suitable crystal form at the early stages of drug development usually involves screening and identifying any, if not all possible hydrate form(s) as a part of the overall intellectual property protection strategy for a given compound. However, due to the unpredictability surrounding hydrate formation, as well as the tremendous amount of time, money, and effort required for crystal forms screening, and subsequent characterisation for a single compound, a faster and more efficient prediction approach for hydrates is warranted.

It has been highlighted in 1.3 that solution-state analysis can provide positive evidence reflective to the solid state, and similar approach with hydrate if successful would open a new door towards understanding hydrate formation. We stipulate that there is some degree of molecular recognition between a hydrate-forming compound and water which would lead to formation of pre-nucleation complexes in solution. The said interaction would yield a significant structural "value" rather than a random interaction, especially for a compound that can form a stable hydrate. This project thus will focus on probing the role of water in hydrate formation by analysing not only the solid-state but also the solution state. We are interested in taking this approach because a successful connection of the solution and the solid state would allow the possibility of an early prediction of hydrate formation. Successful application of the approach would ultimately lead to a faster and more focused screening process.

The various solid-state analytical methods will be use to dissect any, if not all the hydrate form obtained. The information gained should provide insight towards the

prominent interactions present and aid the understanding of the subsequent solution-state analysis. We hypothesise, in the solution-state, that there will be significant interactions between the active compound and water, showing a stronger interaction in solution for a more stable hydrate. We will hence test this hypothesis initially on the class of stable hydrates, and moving on to lower stability ones from there. We will only use water-organic solvent mixture at different mole fractions. Doing so would allow us to control the water content and activity. The focus will be on the molecular interactions crucial for hydrate formation, namely the hydrogen bond interactions.

All in all, this investigation is an attempt to understand the influence and early role and influence of water on hydrate formation. The focus is on understanding this phenomenon by studying the ability of water and drug molecule to interact, in both the solid hydrate crystalline (crystallographic) state, as well as the earlier stages of the pre-nucleation state (in solution). Thus, the efforts towards understanding the forces at play - prior, throughout and after the crystallisation process is ever-relevant and utmost importance. While active, pre-nucleation (in solution) analysis utilised to probe events leading towards crystallisation of a specific crystal form (hydrate) is an exciting approach, our effort also covers a thorough investigation on crystals in their solid-state, of which the fundamentals and the method are discussed in the chapter 2.

1.9 References

1. IUCr. Polymorphism - Online Dictionary of Crystallography. Available at: http://reference.iucr.org/dictionary/Polymorphism. (Accessed: 4th May 2016)

2. Cruz-Cabeza, A. J., Reutzel-Edens, S. M. & Bernstein, J. Facts and fictions about polymorphism. *Chem. Soc. Rev.* **44**, 8619–8635 (2015).

3. Cabri, W., Ghetti, P., Pozzi, G. & Alpegiani, M. Polymorphisms and patent, market, and legal battles: Cefdinir case study. *Org. Process Res. Dev.* **11**, 64–72 (2007).

4. IUCr. Report of the Executive Committee for 1991. *Acta Crystallogr. Sect. A Found. Crystallogr.* **48**, 922–946 (1992).

5. Florence, A. T. & Attwood, D. Properties of the Solid State. in *Physicochemical Principles of Pharmacy* 5–35 (Macmillan Education UK, 1998). doi:10.1007/978-1-349-14416-7_2

6. Vippagunta, S. R., Brittain, H. G. & Grant, D. J. W. Crystalline solids. *Adv. Drug Deliv. Rev.* **48**, 3–26 (2001).

7. Bauer, J. Polymorphism—A Critical Consideration in Pharmaceutical Development, Manufacturing, and Stability. *J. Valid. Technol.* **5**, 15–23 (2008).

8. Bauer, J. *et al.* Ritonavir: An extraordinary example of conformational polymorphism. *Pharm. Res.* **18**, 859–866 (2001).

9. Chemburkar, S. R. *et al.* Dealing with the impact of ritonavir polymorphs on the late stages of bulk drug process development. *Org. Process Res. Dev.* **4**, 413–417 (2000).

10. Khankari, R. & Grant, D. J. W. Pharmaceutical hydrates. *Thermochim. Acta* **248**, 61–79 (1995).

11. Bauer, J. F. Drying Pharmaceutical Solids— Hydrates and Enantiotropic Polymorphs. *J. Valid. Technol.* **15**, 49–56 (2009).

12. Brittain, H. G. *Polymorphism in pharmaceutical solids*. *Journal of Controlled Release* **192**, (Informa Healthcare USA, 2009).

13. Airaksinen, S. *et al.* Role of water in the physical stability of solid dosage formulations. *J. Pharm. Sci.* **94**, 2147–2165 (2005).

14. Szakonyi, G. & Zelkó, R. The effect of water on the solid state characteristics of pharmaceutical excipients: Molecular mechanisms, measurement techniques, and quality aspects of final dosage form. *Int. J. Pharm. Investig.* **2**, 18–25 (2012).

15. Yu, L., Milton, N., Groleau, E. G., Mishra, D. S. & Vansickle, R. E. Existence of a mannitol hydrate during freeze-drying and practical implications. *J. Pharm. Sci.* **88**, 196–195 (1999).

16. Airaksinen, S. *et al.* Excipient selection can significantly affect solid-state phase transformation in formulation during wet granulation. *AAPS PharmSciTech* **6**, E311–E322 (2005).

17. Ohtake, S. & Shalaev, E. Effect of Water on the Chemical Stability of Amorphous Pharmaceuticals: I. Small Molecules. *J. Pharm. Sci.* **102**, 1139–1154 (2013).

18. Jelinski, L. W., Dumais, J. J., Stark, R. E., Ellis, T. S. & Karasz, F. E. Interaction of Epoxy Resins with Water. A Quadrupole Echo Deuterium NMR Study. *Macromolecules* **16**, 1019–1021 (1983).

19. Ahlneck, C. & Zografi, G. The molecular basis of moisture effects on the physical and chemical stability of drugs in the solid state. *Int. J. Pharm.* **62**, 87–95 (1990).

20. Proctor, P., Gensmantel, N. P. & Page, M. I. The chemical reactivity of penicillins and other β-lactam antibiotics. *J. Chem. Soc., Perkin Trans. 2* **0**, 1185–1192 (2004).

21. Dorman, D. E. *et al.* Isolation and Structure Elucidation of the Major Degradation Products of Cefaclor in the Solid State. *J. Pharm. Sci.* **86**, 540–549

(1997).

22. Hickey, M. B. *et al.* Hydrates and solid-state reactivity: a survey of beta-lactam antibiotics. *J. Pharm. Sci.* **96**, 1090–1099 (2007).

23. Nakagawa, H., Miyata, T. & Sugimoto, I. The Effect of Water of Crystallization of Berberine Chloride on Disintegration and Dissolution Behaviors of the Tablet. *YAKUGAKU ZASSHI Pharm. Soc. Japan* **98**, 1305–1310 (1978).

24. Rajala, R., Laine, E. & Örn, G. Characterization and hygroscopic properties of dexmedetomidine hydrochloride, a new drug substance. *Eur. J. Pharm. Sci.* **1**, 219–225 (1994).

25. Burger, A. & Lettenbichler, A. Preformulation studies on droloxifene citrate: pseudopolymorphism and hygroscopicity. *Eur. J. Pharm. Biopharm.* **39**, 64–69 (1993).

26. Letho, P. *et al.* In vivo study of a polymeric glucose-sensitive insulin delivery system using a rat model. *J. Pharm. Sci.* **98**, 985–996 (2009).

27. Byard, S., Abraham, A., Paul, P. J., Harris, R. K. & Hodgkinson, P. A multi-technique approach to the study of structural stability and desolvation of two unusual channel hydrate solvates of finasteride. *J. Pharm. Sci.* **101**, 176–186 (2012).

28. Authelin, J. R. Thermodynamics of non-stoichiometric pharmaceutical hydrates. *Int. J. Pharm.* **303**, 37–53 (2005).

29. Byrn, S. R., Pfeiffer, R. R. & Stowell, J. G. *Solid-state chemistry of drugs*. (SSCI, Inc, 1999).

30. Khankari, R., Chen, L. & Grant, D. J. Physical characterization of nedocromil sodium hydrates. *J. Pharm. Sci.* **87**, 1052–61 (1998).

31. Chen, L. R., Young Jr., V. G., Lechuga-Ballesteros, D. & Grant, D. J. W. Solid-state behavior of cromolyn sodium hydrates. *J. Pharm. Sci.* **88**, 1191–1200 (1999).

32. Braun, D. E. & Griesser, U. J. Stoichiometric and Nonstoichiometric Hydrates of Brucine. *Cryst. Growth Des.* **16**, 6111–6121 (2016).

33. Braun, D. E., Koztecki, L. H., McMahon, J. A., Price, S. L. & Reutzel-Edens, S. M. Navigating the Waters of Unconventional Crystalline Hydrates. *Mol. Pharm.* **12**, 3069–88 (2015).

34. Morris, K. R. Structural Aspects of Hydrates and Solvates. in *Polymorphism in Pharmaceutical Solids* (ed. Brittain, H. G.) 125–181 (1999).

35. Pina, M. F. *et al.* Identification and characterization of stoichiometric and nonstoichiometric hydrate forms of paroxetine HCl: Reversible changes in crystal dimensions as a function of water absorption. *Mol. Pharm.* **9**, 3515–3525 (2012).

36. Tieger, E. *et al.* Studies on the crystal structure and arrangement of water in sitagliptin L-tartrate hydrates. *CrystEngComm* **18**, 3819–3831 (2016).

37. Suzuki, T., Araki, T., Kitaoka, H. & Terada, K. Characterization of non-stoichiometric hydration and the dehydration behavior of sitafloxacin hydrate. *Chem. Pharm. Bull. (Tokyo).* **60**, 45–55 (2012).

38. Roy, S. *et al.* Crystal Structures of Norfloxacin Hydrates. *Cryst. Growth Des.* **8**, 4343–4346 (2008).

39. Kiang, Y.-H., Cheung, E., Stephens, P. W. & Nagapudi, K. Structural studies of a non-stoichiometric channel hydrate using high resolution X-ray powder diffraction, solid-state nuclear magnetic resonance, and moisture sorption methods. *J. Pharm. Sci.* **103**, 2809–18 (2014).

40. Fucke, K. *et al.* Insights into the Crystallisation Process from Anhydrous, Hydrated and Solvated Crystal Forms of Diatrizoic Acid. *Chem. - A Eur. J.* **21**, 1036–1047 (2015).

41. Fucke, K., Peach, M. J. G., Howard, J. A. K. & Steed, J. W. A new water···Na+ coordination motif in an unexpected diatrizoic acid disodium salt crystal form. *Chem. Commun.* **48**, 9822 (2012).

42. Sun, J. *et al.* Preparation and Dehydration Kinetics of Complex Sulfadiazine Calcium Hydrate with Both Channel-Type and Coordinated Water. *Org. Process Res. Dev.* **20**, 780–785 (2016).

43. IUPAC. *Nomenclature of Inorganic Chemistry: IUPAC Recomendations 2005*. *Pure and Applied Chemistry* (2005). doi:10.1515/ci.2005.27.6.25

44. Infantes, L., Fábián, L. & Motherwell, W. D. S. Organic crystal hydrates: what are the important factors for formation. *CrystEngComm* **9**, 65 (2007).

45. Blagden, N. *et al.* A novel batch cooling crystallizer for in situ monitoring of solution crystallization using energy dispersive X-ray diffraction. *Cryst. Growth Des.* **3**, 197–201 (2003).

46. Feth, M. P. *et al.* Challenges in the development of hydrate phases as active pharmaceutical ingredients - An example. *Eur. J. Pharm. Sci.* **42**, 116–129 (2011).

47. Liu, G. *et al.* Crystallization of Piroxicam Solid Forms and the Effects of Additives. *Chem. Eng. Technol.* **37**, 1297–1304 (2014).

48. Friščić, T., Trask, A. V., Jones, W. & Motherwell, W. D. S. Screening for Inclusion Compounds and Systematic Construction of Three-Component Solids by Liquid-Assisted Grinding. *Angew. Chemie Int. Ed.* **45**, 7546–7550 (2006).

49. Morissette, S. L. *et al.* High-throughput crystallization: polymorphs, salts, co-crystals and solvates of pharmaceutical solids. *Adv. Drug Deliv. Rev.* **56**, 275–300 (2004).

50. Lee, A. Y., Erdemir, D. & Myerson, A. S. Crystal Polymorphism in Chemical Process Development. *Annu. Rev. Chem. Biomol. Eng* **2**, 259–80 (2011).

51. Li, Y., Chow, P. S., Tan, R. B. H. & Black, S. N. Effect of Water Activity on the Transformation between Hydrate and Anhydrate of Carbamazepine. *Org. Process Res. Dev.* **12**, 264–270 (2008).

52. Braun, D. E., Gelbrich, T., Kahlenberg, V. & Griesser, U. J. Insights into hydrate formation and stability of morphinanes from a combination of

experimental and computational approaches. *Mol. Pharm.* **11**, 3145–3163 (2014).

53. Braun, D. E., Kahlenberg, V. & Griesser, U. J. Experimental and Computational Hydrate Screening: Cytosine, 5-Flucytosine, and Their Solid Solution. *Cryst. Growth Des.* **17**, 4347–4364 (2017).

54. Braun, D. E., Karamertzanis, P. G. & Price, S. L. Which, if any, hydrates will crystallise? Predicting hydrate formation of two dihydroxybenzoic acids. *Chem. Commun. (Camb).* **47**, 5443–5 (2011).

55. Price, S. L., Braun, D. E. & Reutzel-Edens, S. M. Can computed crystal energy landscapes help understand pharmaceutical solids? *Chem. Commun.* **52**, 7065–7077 (2016).

56. Takieddin, K., Khimyak, Y. Z. & Fábián, L. Prediction of Hydrate and Solvate Formation Using Statistical Models. *Cryst. Growth Des.* **16**, 70–81 (2016).

57. Hulme, A. T. & Price, S. L. Toward the Prediction of Organic Hydrate Crystal Structures. *J. Chem. Theory Comput.* **3**, 1597–1608 (2007).

58. Galabov, B., Bobadova-Parvanova, P., Ilieva, S. & Dimitrova, V. The electrostatic potential at atomic sites as a reactivity index in the hydrogen bond formation. *J. Mol. Struct. THEOCHEM* **630**, 101–112 (2003).

59. Abramov, Y. A. Virtual hydrate screening and coformer selection for improved relative humidity stability. *CrystEngComm* **17**, 5216–5224 (2015).

60. Braun, D. E. & Griesser, U. J. Supramolecular Organization of Nonstoichiometric Drug Hydrates: Dapsone. *Front. Chem.* **6**, 31 (2018).

61. Guillot, B. A reappraisal of what we have learnt during three decades of computer simulations on water. *J. Mol. Liq.* **101**, 219–260 (2002).

62. Day, G. M. & Görbitz, C. H. Introduction to the special issue on crystal structure prediction. *Acta Crystallogr. Sect. B Struct. Sci. Cryst. Eng. Mater.* **72**, 435–436 (2016).

63. Clarke, H. D. *et al.* Structure-stability relationships in cocrystal hydrates: Does the promiscuity of water make crystalline hydrates the nemesis of crystal engineering? *Cryst. Growth Des.* **10**, 2152–2167 (2010).

64. Zahn, D. Thermodynamics and Kinetics of Prenucleation Clusters, Classical and Non-Classical Nucleation. *ChemPhysChem* **16**, 2069–2075 (2015).

65. Panagiotou, T. & Fisher, R. J. Enhanced Transport Capabilities via Nanotechnologies: Impacting Bioefficacy, Controlled Release Strategies, and Novel Chaperones. *J. Drug Deliv.* **2011**, 1–14 (2011).

66. DeYoreo, J. J. & Vekilov, P. G. Principles of Crystal Nucleation and Growth. *Rev. Mineral. Geochemistry* **54**, 57–93 (2003).

67. Boistelle, R. & Astier, J. P. Crystallization mechanisms in solution. *J. Cryst. Growth* **90**, 14–30 (1988).

68. Garcia-Ruiz, J. M. Nucleation of protein crystals. *J. Struct. Biol.* **142**, 22–31 (2003).

69. Saridakis, E. & Chayen, N. E. Towards a 'universal' nucleant for protein crystallization. *Trends Biotechnol.* **27**, 99–106 (2009).

70. Saridakis, E. & Chayen, N. E. Imprinted polymers assisting protein crystallization. *Trends Biotechnol.* **31**, 515–520 (2013).

71. Volmer, M. & Weber, A. Keimbildung in übersättigten Gebilden. *Zeitschrift für Phys. Chemie* **119U**, 277–301 (1926).

72. Mattei, A. & Li, T. Polymorph formation and nucleation mechanism of tolfenamic acid in solution: An investigation of pre-nucleation solute association. *Pharm. Res.* **29**, 460–470 (2012).

73. De Yoreo, J. Crystal nucleation: More than one pathway. *Nat. Mater.* **12**, 284–285 (2013).

74. Lutsko, J. F. Systematically extending classical nucleation theory. *New J. Phys.* **20**, 103015 (2018).

75. Vekilov, P. G. Dense liquid precursor for the nucleation of ordered solid phases from solution. *Cryst. Growth Des.* **4**, 671–685 (2004).

76. Wolf, S. E., Leiterer, J., Kappl, M., Emmerling, F. & Tremel, W. Early homogenous amorphous precursor stages of calcium carbonate and subsequent crystal growth in levitated droplets. *J. Am. Chem. Soc.* **130**, 12342–12347 (2008).

77. Bewernitz, M. a., Gebauer, D., Long, J., Cölfen, H. & Gower, L. B. A Metastable Liquid Precursor Phase of Calcium Carbonate and its Interactions with Polyaspartate. *Faraday Discuss.* **159**, 291 (2012).

78. Gebauer, D., Völkel, A. & Cölfen, H. Stable Prenucleation Calcium Carbonate Clusters. *Science* **322**, 1819–1823 (2008).

79. Gebauer, D. & Cölfen, H. Prenucleation clusters and non-classical nucleation. *Nano Today* **6**, 564–584 (2011).

80. Vekilov, P. G. The two-step mechanism of nucleation of crystals in solution. *Nanoscale* **2**, 2346–57 (2010).

81. Vorontsova, M., Maes, D. & Vekilov, P. G. Recent advances in the understanding of two-step nucleation of protein crystals. *Faraday Discuss.* **4**, 1166–1169 (2015).

82. Harding, J. H., Freeman, C. L. & Duffy, D. M. Oriented crystal growth on organic monolayers. *CrystEngComm* **16**, 1430 (2014).

83. Davey, R. J., Schroeder, S. L. M. & ter Horst, J. H. Nucleation of organic crystals--a molecular perspective. *Angew. Chem. Int. Ed. Engl.* **52**, 2166–79 (2013).

84. Gebauer, D., Kellermeier, M., Gale, J. D., Bergström, L. & Cölfen, H. Pre-nucleation clusters as solute precursors in crystallisation. *Chemical Society Reviews* **43**, 2348–2371 (2014).

85. Kemsley, J. *Illuminating Crystal Nucleation*. *Chemical & Engineering News* **93**, (2015).

86. Nielsen, M. H., Aloni, S. & Yoreo, J. J. De. In situ TEM imaging of CaCO 3 nucleation reveals coexistence of direct and indirect pathways. *Science (80-.).* **345**, 1158–1162 (2014).

87. Spitaleri, A., Hunter, C. A., Mccabe, J. F., Packer, M. J. & Cockroft, S. L. A 1 H NMR study of crystal nucleation in solution. *CrystEngComm* **6**, 489–493 (2004).

88. Jawor-Baczynska, A., Moore, B. D. & Sefcik, J. Effect of mixing, concentration and temperature on the formation of mesostructured solutions and their role in the nucleation of dl-valine crystals. *Faraday Discuss.* **179**, 141–54 (2015).

89. Parveen, S., Davey, R. J., Dent, G. & Pritchard, R. G. Linking solution chemistry to crystal nucleation: The case of tetrolic acid. *Chem. Commun.* **0**, 1531–1533 (2005).

90. Edkins, R. M., Hayden, E., Steed, J. W. & Fucke, K. Conserved hydrogen bonding in tetrahydrocarbazolone derivatives: influence of solution-state assembly on crystal form nucleation. *Chem. Commun.* **51**, 5314–5317 (2015).

91. Saleh , G., Gatti , C., Lo Presti, L. & Contreras-García, J. Revealing Non-covalent Interactions in Molecular Crystals through Their Experimental Electron Densities. *Chem. - A Eur. J.* **18**, 15523–15536 (2012).

92. Riley, K. E. & Hobza, P. Noncovalent interactions in biochemistry. *Ltd. WIREs Comput Mol Sci* **1**, 3–17 (2011).

93. Lodish, H. *et al. Molecular Cell Biology*. *W. H. Freeman* (W. H. Freeman, 2003).

94. Steed, J. W. & Atwood, J. L. *Supramolecular Chemistry*. (Wiley, 2009).

95. Poater, J., Fradera, X., Solà, M., Duran, M. & Simon, S. On the electron-pair nature of the hydrogen bond in the framework of the atoms in molecules theory. *Chem. Phys. Lett.* **369**, 248–255 (2003).

96. Scheiner, S. & Kar, T. Red- versus blue-shifting hydrogen bonds: Are there fundamental distinctions? *J. Phys. Chem. A* **106**, 1784–1789 (2002).

97. Cram, D. J. & Cram, J. M. Host-Guest Chemistry. *Science* **183**, 803–809

98. Benesi, B. A. & Hildebrand, J. H. Spectrophotometry of Iodine with Aromatic Hydrocarbons A Spectrophotometric Investigation of the Interaction of Iodine with Aromatic Hydrocarbons. *J. Am. Chem. Soc.* **71**, 2703–2707 (1949).

99. Yang, C., Liu, L., Mu, T.-W. & Guo, Q.-X. The Performance of the Benesi-Hildebrand Method in Measuring the Binding Constants of the Cyclodextrin Complexation. *Anal. Sci.* **16**, 537–539 (2000).

100. Woosley, J. T. & Muldoon, T. G. Use of the direct linear plot to estimate binding constants for protein-ligand interactions. *Biochem. Biophys. Res. Commun.* **71**, 155–160 (1976).

101. Schwarz, G. On the analysis of linear binding effects associated with curved scatchard plots. *Biophys. Chem.* **6**, 65–76 (1976).

102. Feldman, H. A. Mathematical theory of complex ligand-binding systems at equilibrium: Some methods for parameter fitting. *Anal. Biochem.* **48**, 317–338 (1972).

103. Thordarson, P. Determining association constants from titration experiments in supramolecular chemistry. *Chem. Soc. Rev.* **40**, 1305–1323 (2011).

104. Wright, M. H. Nelder, Mead, and the Other Simplex Method. *Doc. Math.* (2010).

105. Hirose, K. A Practical Guide for the Determination of Binding Constants. *J. Incl. Phenom. Macrocycl. Chem.* **39**, 193–209 (2001).

106. Job, P. Formation and stability of inorganic complexes in solution. *Ann. di Chim. Appl.* **9**, 113–203 (1928).

107. Hibbert, D. B. & Thordarson, P. The death of the Job plot, transparency, open science and online tools, uncertainty estimation methods and other developments in supramolecular chemistry data analysis. *Chem. Commun.* **52**, 12792–12805 (2016).

108. Ulatowski, F., Dąbrowa, K., Bałakier, T. & Jurczak, J. Recognizing the Limited Applicability of Job Plots in Studying Host–Guest Interactions in Supramolecular Chemistry. *J. Org. Chem.* **81**, 1746–1756 (2016).

109. Wakisaka, A., Abdoul-Carime, H., Yamamoto, Y. & Kiyozumi, Y. Non-ideality of binary mixtures: Water-methanol and water-acetonitrile from the viewpoint of clustering structure. *J. Chem. Soc. - Faraday Trans.* **94**, 369–374 (1998).

110. Lai, J. T. W. *et al.* Excess partial molar enthalpies, entropies, Gibbs energies, and volumes in aqueous dimethylsulfoxide. *J. Solution Chem.* **24**, 89–102 (1995).

111. Shin, D. N., Wijnen, J. W., Engberts, J. B. F. N. & Wakisaka, A. On the origin of microheterogeneity: Mass spectrometric studies of acetonitrile-water and dimethyl sulfoxide-water binary mixtures (part 2). *J. Phys. Chem. B* **106**, 6014–6020 (2002).

112. Qian, X., Han, B., Liu, Y., Yan, H. & Liu, R. Vapor pressure of dimethyl sulfoxide and water binary system. *J. Solution Chem.* **24**, 1183–1189 (1995).

113. Kwak, K., Rosenfeld, D. E., Chung, J. K. & Fayer, M. D. Solute−Solvent Complex Switching Dynamics of Chloroform between Acetone and Dimethylsulfoxide−Two-Dimensional IR Chemical Exchange Spectroscopy. *J. Phys. Chem. B* **112**, 13906–13915 (2008).

114. Brown, T. L. *et al. Chemistry : The central science*. (Pearson Australia, 2014).

115. Vaisman, I. I. & Berkowitz, M. L. Local structural order and molecular associations in water-DMSO mixtures. Molecular dynamics study. *J. Am. Chem. Soc.* **114**, 7889–7896 (1992).

116. Borin, I. A. & Skaf, M. S. Molecular association between water and dimethyl sulfoxide in solution: A molecular dynamics simulation study. *J. Chem. Phys.* **110**, 6412 (1999).

117. Luzar, A. & Chandler, D. Structure and hydrogen bond dynamics of water–dimethyl sulfoxide mixtures by computer simulations. *J. Chem. Phys.* **98**, 8160–

8173 (1993).

118. Oh, K.-I., Rajesh, K., Stanton, J. F. & Baiz, C. R. Quantifying Hydrogen-Bond Populations in Dimethyl Sulfoxide/Water Mixtures. *Angew. Chemie - Int. Ed.* **56**, 11375–11379 (2017).

CHAPTER 2

MATERIALS, METHODOLOGIES AND THEIR PRINCIPLES

2.1 Materials

2.1.1 Analysed compounds

Sodium diatrizoate (DTS), diatrizoic acid (DTA), cimetidine (CIM), piroxicam (PXM), naproxen (NAP), paracetamol (PCM), flurbiprofen (FBN), 4,4-dipyridyl (DPY), pyrazine (PYZ) and 4-hydroxybenzoic acid (PHBA) were purchased from Sigma-Aldrich having ≥98.0% purity. Acetazolamide (ACT), 5-Phenyl-1H-tetrazole (5PHT) and 5-(4-pyridyl)-1H-tetrazole (54PYT) were purchased from Alfa Aesar with 99% purity. Dapsone (DAP, ≥97.0%) and 2-chloro-4-hydroxybenzoic acid (2C4HBA, ≥98.0%) were purchased from Tokyo Chemical Industry Co. Ltd. (TCI). Tranilast (TRN, ≥98.0%) was purchased from Flurochem Ltd. All compounds were used unrefined in all experiments. The 4-(1H-tetrazol-5-yl) phenol (TTZ) was synthesised by Dr. Clinton Veale's group at the University of KwaZulu Natal in South Africa.

Acetonitrile (≥99.9%), *n*-amyl alcohol (1-pentanol, ≥99.0%), 1-butanol (≥99.4%), 2-butanol (≥99.5%), dimethyl sulfoxide (DMSO, ≥99.9%), 1,4-dioxane (≥99.0%), N,N-dimethyl formamide (DMF, anhydrous 99.8%), dichloromethane (DCM,≥99.8%), ethyl acetate (anhydrous ≥99.8%), 2-butanone (ethyl methyl ketone, ≥99.0%), hexane (anhydrous 95.0%), 1-propanol (anhydrous 99.5%), 2-propanol (anhydrous 99.5%), nitromethane (96.0%), were purchased from Sigma-Aldrich. Diethyl ether (99.99%), chloroform (99.98%) acetone (≥99.8%), ethanol (≥99.8%),

and methanol (≥99.6%) were purchased from VWR International. Tetrahydrofuran (THF, anhydrous 99.9%) was purchased from Acros Organics. All solvents were used without further purification.

Heavy water (D_2O), DMSO-d_6 and acetonitrile-d_3 were purchased from Sigma-Aldrich, while acetone-d_6 and DMF-d_7 were purchased from Apollo Scientific Ltd. All deuterated solvents were ≥99.8% pure and used without further purification.

Tetramethylsilane (TMS) and 4,4-dimethyl-4-silapentane-1-sulfonic acid (DSS) were purchased from Sigma-Aldrich and used as standard for all NMR analysis.

The Karl Fisher titration reagents used were HYDRANAL^{TM} Coulomat A, Coulomat CG and Water Standard 1.0 which were purchased from Honeywell.

2.2 Analytical methods

2.2.1 Crystallisation screening

Polymorph screen is done with the aim to find most of the crystal forms from a selected compound. Thermodynamically controlled experiments *i.e.* slow cooling, and kinetically controlled experiments *i.e.* fast cooling, evaporation, and precipitation crystallisation are used in our screening (Figure 2.1). Approximately 20 mg of the selected compound is used in each of the crystallisation experiments. For the cooling experiments, each of the tested compounds is dissolved in sufficient solvent (*i.e.* acetonitrile, *n*-amyl alcohol 1-butanol, 2-butanol, DMSO, 1,4-dioxane, DMF, DCM, ethyl acetate, 2-butanone, hexane, 1-propanol, 2-propanol, nitromethane, diethyl ether, chloroform, acetone, ethanol, methanol, and THF), to produce a hot saturated solution.

The hot mixture is then cooled at different cooling rates. There different rates are generated by either placing the hot sample in an insulating wooden block which is left then to cool to 25 °C or immidiately quenching the hot sample in an ice and water bath at 0 °C. For evaporation, the material is dissolved in sufficient solvent to produce an undersaturated solution at room temperature and left to evaporate at ambient conditions. Precipitation is conducted by producing a saturated solution at 25 °C and adding a second solvent which the compound is not soluble in or anti-solvents, that is miscible with the first solvent. In the case of the fast cooling and precipitation experiments, the crystals were immediately removed from solution once they formed, whereas evaporation and slow cooling experiments were left for 24 hours before analysis.

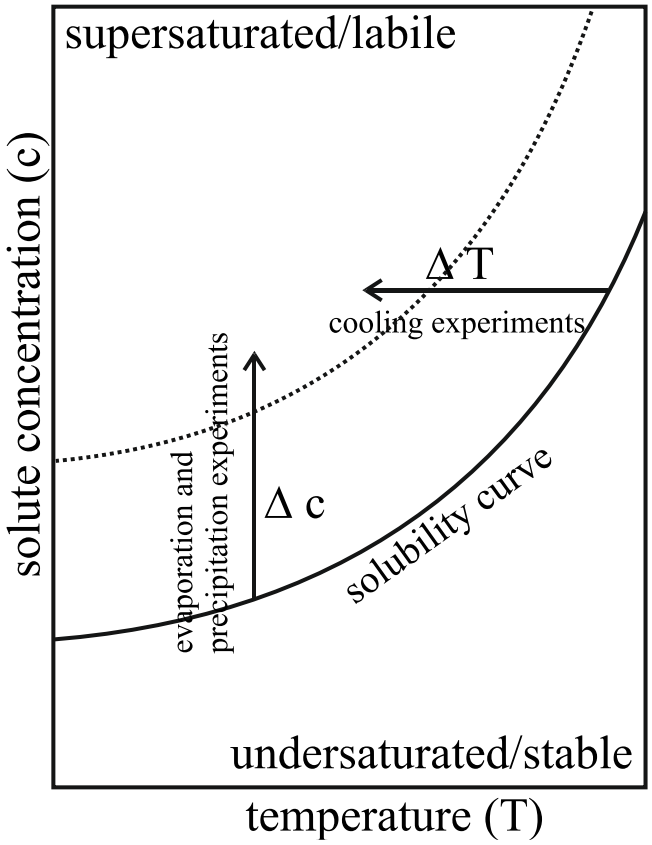


Figure 2.1 Illustration of the different crystallisation experiments used and their impcat to the solubility curve, adapted from Giulietti et al.[1]

2.2.2 Karl Fischer titration

Karl Fischer (KF) titration remains among the most common water quantification method for most compounds or products, and the method is based on the Bunsen reaction between iodine and sulphur dioxide in an aqueous medium (Equation 2.1).[2] In 1935, Karl Fischer published a paper in Angewandte Chemie in Germany which entitled (translated), "New method for the dimensional analysis of the water content of liquids and solid bodies".[3] In the paper, he reported that the Bunsen reaction could be modified and used for water determination in a non-aqueous system containing an excess of sulphur dioxide.[3] In the early iteration of the method, a primary alcohol (e.g. methanol) was used as the solvent, and a pyridine base as the buffering agent (note that reagents used nowadays are pyridine-free and contain imidazole or primary amines instead).[4]

(Equation 2.1)

$$2H_2O + SO_2 + I_2 \rightarrow H_2SO_4 + 2HI$$

(Equation *2.2)* shows the corrected KF equation,[5] with a subsequent two-step process suggested by Scholz.[4] The equation indicates that the alcohol reacts with sulphur dioxide (SO_2) and base to form an intermediate alkyl sulphite salt (A), which is then oxidized by iodine to an alkyl sulphate salt (B).[6,7]

(Equation 2.2)

A. $ROH + SO_2 + R'N \rightarrow [R'NH]SO_3R$

B. $[R'NH]SO_3R + H_2O + I_2 + 2R'N \rightarrow 2[R'NH]I + [R'NH]SO_4R$

The ROH in the equation 2.2 corresponds to any primary? alcohol. SO_2 is sulphur dioxide and R'N is the pyridine base. The $[R'NH]SO_3R$ corresponds to the formed

alkyl sulphite salt. The 2[R'NH]I and [R'NH]SO_4R in the equation represent the final products of hydroiodic acid salt and alkyl sulphate salt, respectively.

The oxidation reaction (Equation 2.2 B) consumes water and iodine in a 1:1 ratio and thus allows for the accurate determination of water contents. In our experiments, the KF titrations were performed using a Metrohm AG 899 coulometer titrator (Metrohm Ltd., Herisau, Switzerland) as the method allows for the measurement of small water contents (10 µg to 200 mg water).[8] In coulometric KF, iodine is generated electrochemically in situ during the titration, and the amount of water determination is based on the current required for the generation of iodine, according to Equation 2.3. Water content quantification is based on the total charge passed (Q) to generate the corresponding iodine, as measured by Equation 2.3, where Q = charge in coulombs, C, I = current in amperes, Aand t= time in seconds, s. C corresponds to Coulomb, a unit of electric charge. Note that one (1) mg of H_2O = 10.72 C.[7]

Equation 2.3

$$Q = It$$

The KF medium was calibrated using Water Standard 1.0 and titrated to dryness before each analysis. Between 5 and 10 mg of sample was weighed (±0.1 mg) using a Kern ABJ 200-4NM analytical balance (Kern & Sohn GmbH, Balingen, Germany) for each analysis.

The 860 KF Thermoprep oven setup (Metrohm Ltd., Herisau, Switzerland) was used alongside the coulometer titrator for compounds which could not be analysed by direct KF titration. This could be due to limited solubility in the reagents, reaction with the KF reagent under generation of water, very slow release of the incorporated water

only, or release not until heated to high temperatures. An initial blank vial which was exposed to ambient humidity was measured, followed by the measurement of the sample using tightly sealed sample vials with a nitrogen purge over the sample, which washes any emission from the oven-heated sample into the coulometric KF titrator and subsequently analysed.

2.2.3 Thermal analysis

The thermal analysis measures the specific property of a sample upon change in temperature. Three methods were used in our experiments, which were hot-stage microscopy, thermogravimetric analysis and differential scanning calorimetry. All three methods provide complementary information towards the characterisation of a sample.

2.2.3.1 Hot-stage microscopy

Hot-stage microscopy provides optical observations of the sample during temperature change. Events such as crystallisation, melting, decomposition, phase transition and desolvation can be visually monitored through the normal or polarised light microscope. Polarised light has waves that vibrate only in one direction. The used of polarising microscope with crossed polarisers setup allows for contrast generation of an anisotropic sample against the background, therefore the sample would "light up" in the dark surrounding. Crossed polarisers (Figure *2.2*, usually consist of an analyser, attached on the eye-piece, and the polariser above the light source), would generate a dark field if their transmission directions are aligned at the right angles. Typically, polarised microscope is particularly useful when examining birefringent effect, which is an effect that occur when a ray of light is split or double refracted by

polarisation into two rays of different paths upon incident with anisotropic crystal which selectively absorb the polarised light (Figure *2.2*). Polarised microscope also helps in identification of single crystal as the sample is rotated, a single crystal would appear as a uniformed coloured image, instead of multi-coloured.

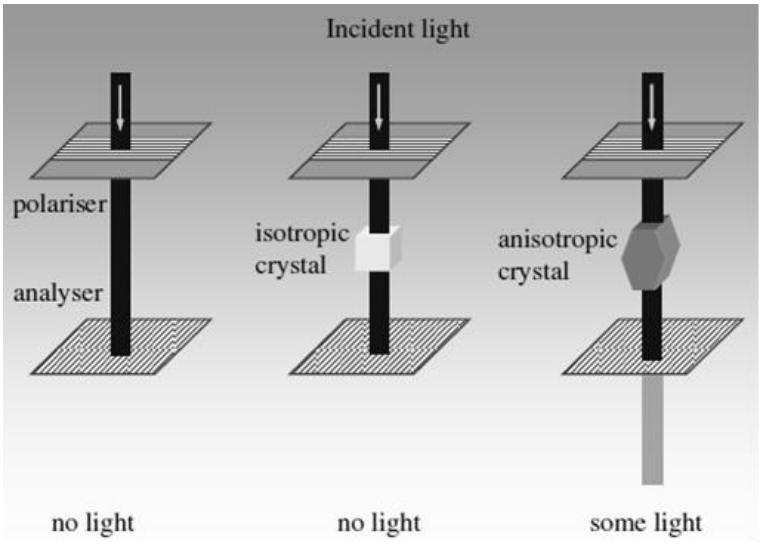


Figure 2.2. Schematic on the cross polariser setup in a polarised microscope, showing the effects upon observation of different samples.

The sample for thermal microscopy is mounted as either dry or in paraffin oil embedded preparation, allowing observation of the different thermal events. A dry preparation allows for observation of phase transition, melting, decomposition and the loss of birefringence. An oil embedded preparation can also observe similar events, in addition to events which involves liberation of volatile inclusion *e.g.* dehydration or desolvation. For example, in a paraffin oil embedded preparation, a desolvation event would typically be accompanied by bubble formation (Figure 2.3 A). Following melting, the observed solid may appear as a droplet and loses the ability to diffract light (Figure 2.3 B). In addition, as the crystalline form desolvates a sample may will lose some birefringent, meaning the sample is less able to diffract light hence

appearing darker (Figure 2.3 D). Though the observations are subjective and qualitative, the method does provide quick, easy, and visually stimulating data.

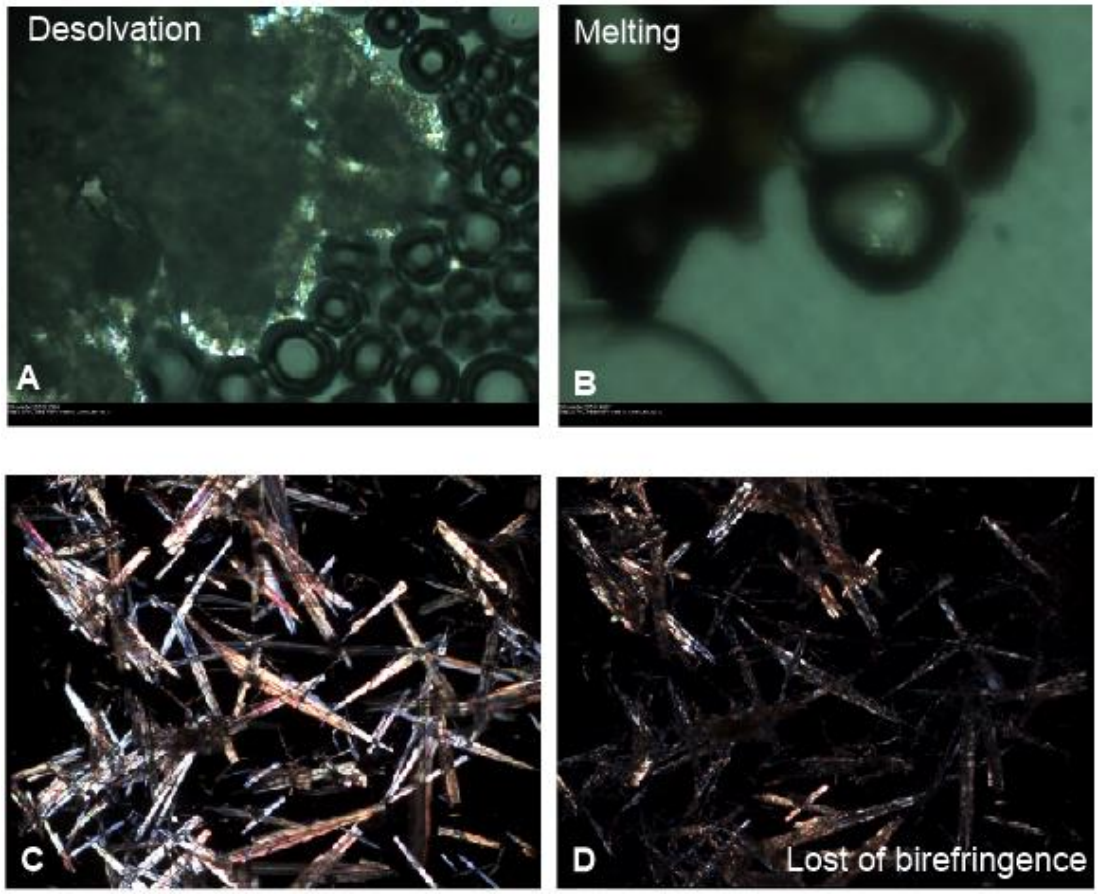


Figure 2.3. Example of thermal microscopy observation of a sample in a paraffin oil preparation under polarised light. A) Depicts typical desolvation process with bubbles formation. B) Depicts melting C) and D) shows the lost of birefringent

Hot-stage microscopic observations were carried out using a Leica DM 2700P polarising microscope (Leica Microsystems GmbH, Wetzlar, Germany) equipped with THMS600 heating and freezing microscope stage and controller (Linkam Scientific Instruments, Tadworth, U.K.). The setup was completed with QICAM Fast1394 (Qimaging, British Colombia, Canada) colour video camera attachment, supported by Linksys32 version 2.4.3.

2.2.3.2 Thermogravimetric analysis

The second thermal analysis method used is the thermogravimetric analysis (TGA). TGA measures the changes in weight of the sample over time or a temperature range (Figure 2.4).TGA is a common technique used to characterise materials in various fields, including pharmaceuticals. A TGA instrument consists of a sample pan that is supported by a precision balance. Following initial weight measurement, the pan is loaded into in a furnace which is then heated or cooled. A sample purge gas, which may be inert or a reactive gas, flows over the sample and exits through an exhaust, controls the sample environment. Several events can be discovered through the observations of a TGA curve, *e.g.* showing the anhydrous state of a compound when no weight change is observed over the different temperature range (Figure 2.4, hypothetical compound I), accurate determination of the amount of volatile inclusion released from the sample (Figure 2.4, hypothetical compound II), rapid desolvation curve characteristics of surface solvent or non-stoichiometric hydrate (Figure 2.4, hypothetical compound III), multi-stage desolvation, with relatively stable intermediate, *e.g.* solvate-hydrate transitioning to a stable hydrate, before complete desolvation into the anhydrous form (Figure 2.4, hypothetical compound IV), and multi-stage desolvation, with no stable intermediate (Figure 2.4, hypothetical compound V). The measured weight change also aids in the identification of the volatile components, especially for water when compared to the value obtained from KF titration. Our TGA scans were carried out with either Q 500 or Q 50 (TA Instruments, New Castle, DE, U.S.A). Nitrogen served as the purge gas at a flow rate of 60 mL min^{-1}. Samples of 1 to 5 mg were accurately weighed (±0.1 mg) into 50 μL platinum pans. A heating rate of 10 °C min^{-1} was used and each sample was heated from 25 °C to 300 °C.

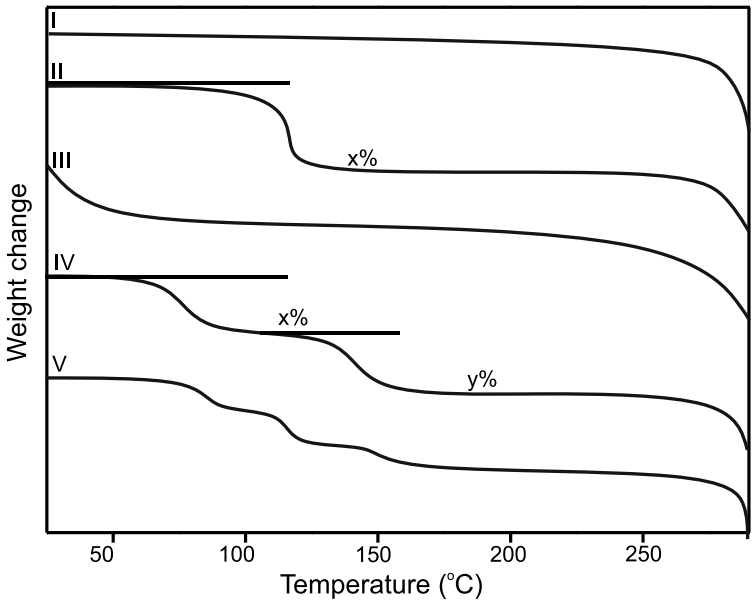


Figure 2.4. Thermogravimetric thermograms of hypothetical materials I-V, showing different TGA curves corresponding to various events that could be observed following heating/analysis.

2.2.3.3 Differential scanning calorimetry

Finally, differential scanning calorimetry (DSC) measures the amount of energy or energy flow required to minimise the temperature difference between a sample and a reference as function of temperature. Both the sample and reference are heated or cooled to a specific temperature *e.g.* 300 °C at similar rate in each experiment, hence any physical transition to the sample, *e.g.* phase transition, desolvation, melting would result in heat being absorbed or released from the sample in comparison to the reference. Endothermic events *e.g.* desolvation, melting, glass transition, polymorphic transition in enantiotropic system which require heat uptake by the sample in comparison to the reference, hence would typically result in an upwards plot on the DSC thermogram (Figure 2.5). The reverse could be said to exothermic events, *e.g.* polymorphic transition in a monotropic system, crystallisation, oxidation and cross-linking, where the sample releases energy from the system to its surrounding, resulting in a downward plot on the DSC thermogram (Figure *2.5* A).

Note that the up/down plot is software and user preference dependent. There is no fixed convention on the upward/downward direction of the respective thermal event. Other information that could be extracted from a DSC thermogram would be from the integration of its peak (Figure 2.5 B). The peak, is characterised by the onset, the peak and the offset temperature. The onset is a thermodynamic event, while the peak is kinetically controlled, therefore in melting point determination, the onset will remain the same for the same compound, while the peak may differ due to different sample amount or prep. From the cross-point of the onset and offset temperatures defines the maximum or minimum point the peak temperature of the corresponding thermal event, *e.g.* melting point (Figure 2.5 B).The area under the curve of a thermal event gives its enthalpy.

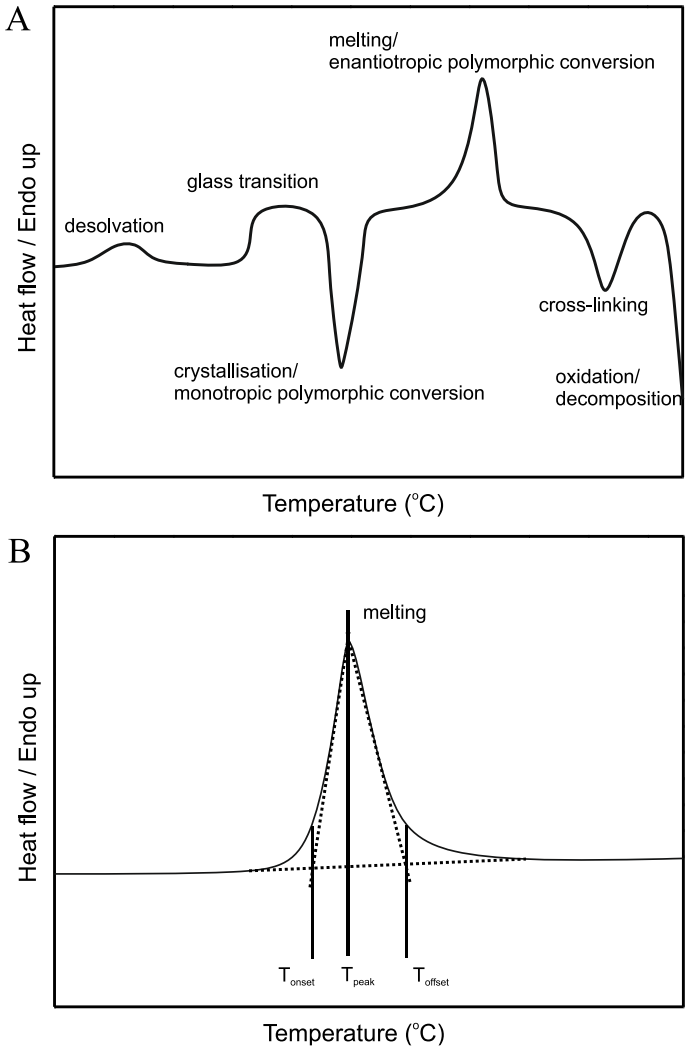


Figure 2.5. Endothermic and exothermic events typically observed in a DSC thermogram curve (A), while (B) depict the onset and offset of the curve with their cross-point which is the peak.

The DSC scans are carried out either on Q 2000 or Q 20 (TA Instruments, New Castle, DE, US). Nitrogen served as the purge gas at a flow rate of 60 mL min^{-1}. Approximately 1 to 5 mg of the different samples was accurately weighed (±0.1 mg) using a microbalance (Sartorius, Göttingen, Germany), loaded into aluminium standard pans (TA Instruments, New Castle, DE, U.S.A) and sealed. A heating rate of 10 °C min^{-1} was used and each sample was heated from 25 °C to 300 °C or up until decomposition, whichever is earlier.

2.2.4 Gravimetric moisture sorption analysis

The influence of water vapour towards phase transition cannot be overstated, and stability tests at elevated relative humidity is a requirement in the American and European Pharmacopoeia.[9,10] Storing the test sample in a closed desiccator over a saturated salt solution having a specific relative humidity (RH) would achieve the goal for testing the stability at that particular humidity, however the method is laborious due to the static system, as well as the numerous saturated-salt-solution desiccators are required to achieve a complete RH range. Gravimetric moisture sorption analysis provides a faster, systematic, and more comprehensive alternative. The technique measures the change in mass of a sample upon exposure to various RH.

The measurement is done by exposing the selected sample to a series of RH and monitoring the mass change over the RH variation, at constant temperature of 25 °C. The constant temperature ensures that humidity remains constant at equilibrium as both are interconnected. The sample mass was allowed to reach a gravimetric equilibrium of ±0.01% *w*/*w* at a specific humidity level, before progressing to the next. Then, the equilibrium mass values at each RH step were used to generate the isotherm. The calculated isotherms are typically divided into two components: sorption for increasing humidity steps and desorption for decreasing humidity steps (chapter 1, Figure 1.2).

Gravimetric moisture sorption analysis was carried out using a humidity and temperature controlled dynamic vapour sorption (DVS) apparatus, (Surface Measurement Systems, Boro Labs Ltd. Aldermaston, Berks, U.K.) equipped with a Cahn D200 digital recording ultra-microbalance with a mass resolution of ±0.01 μg. Initially, samples between 10 to 15 mg were pre-weighed (±0.1 mg) using a Kern ABJ

200-4NM analytical balance (Kern & Sohn GmbH, Balingen, Germany) and then loaded in TA Tzero pans (TA Instruments, Switzerland). Moisture uptake and release cycles (reported relative to the dry weight) were monitored over a sorption/desorption range of 0 to 90% RH with increments of 10% RH at a constant temperature of 25 °C. Higher resolution runs with 1% RH steps were performed if deemed necessary, e.g. over phase transitions ranges.

2.2.5 Fourier transform infrared spectroscopy

Molecules have bonds that are continually vibrating and upon exposure to infrared (IR) radiation, different molecules would absorb the energy differently and reach the excited vibrational state at a different and specific frequency. The energy difference between ground and the excited states must be the exact same frequency to the radiation and causes a change in dipole moment for the vibration to be IR-active. For example, the symmetric stretch of a CO_2 molecule does not result in a change to the initially zero dipole moment, so this vibration is IR-inactive. On the other hand, the asymmetric stretch and bending of the CO_2 molecule do result in a change in dipole moment so these are IR-active. The resulting signal at the detector undergoes Fourier Transform, resulting in a spectrum representing a molecular 'ID' of the sample, which again corresponds to different vibrations of the different chemical bonds present.

With regards to vibrating bonds, these bonds can vibrate with stretch motions or bending motions. The concept for the bond vibrations is best represented by the 'ball-and-spring theory', as in Figure 2.6, showing three balls attached by a spring.

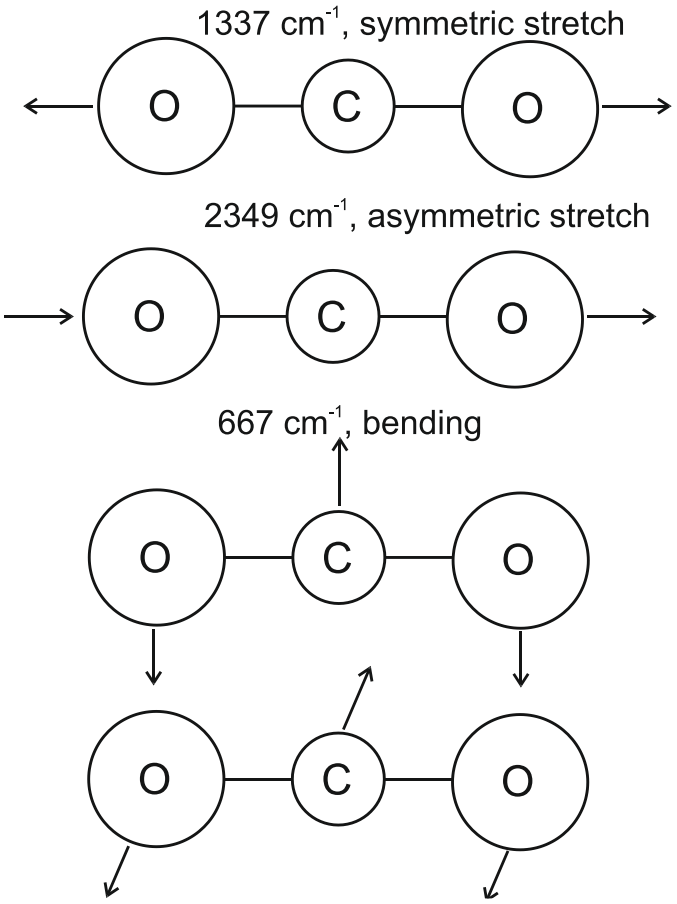


Figure 2.6. The ball-and-spring model for the gas phase of a CO_2 molecule, and its vibration mode, adapted from Burghaus [11]

Based on the observation of CO_2 molecule (Figure 2.6), the movement of oxygen and carbon balls or molecules toward, or away from the one another, along the line of the spring represents a stretching vibration, which can either be symmetric or asymmetric (1337 and 2349 cm^{-1}stretch vibration, Figure 2.6). A bending vibration at 667 cm^{-1} in Figure 2.6 occurs when the angle between atoms change.

The spectra are generated as a function of transmittance, % transmittance, or absorbance, over frequency in wavenumber, which is the number of waves in one centimetre (cm^{-1}). For historical reason, the unit for frequency in the *x*-axis is wavenumber (instead of wavelength) following general consensus in the scientific community. The wavenumber is the inverse of the wavelength in cm and the range

typically used is between 4000 to 400 cm^{-1}, which corresponds to 2.5 to 25 µm in wavelength.

The Fourier Transform infrared (FTIR) spectra of solid and solution phases were collected on a Spectrum Two IR Spectrometers (Perkin-Elmer, Massachusetts, U.S.A). For the solid-state analysis, samples were placed on a diamond Attenuated Total Reflectance (ATR) accessory. ATR measures the internally reflected infrared beam which creates an evanescent wave, which protrudes between 0.5 µ - 5 µ beyond the crystal surface and into the sample. Therefore, good contact between the sample and the crystal surface is crucial. In IR-active regions, the evanescent wave will be attenuated or altered, and passed to the detector in the IR spectrometer.[12]

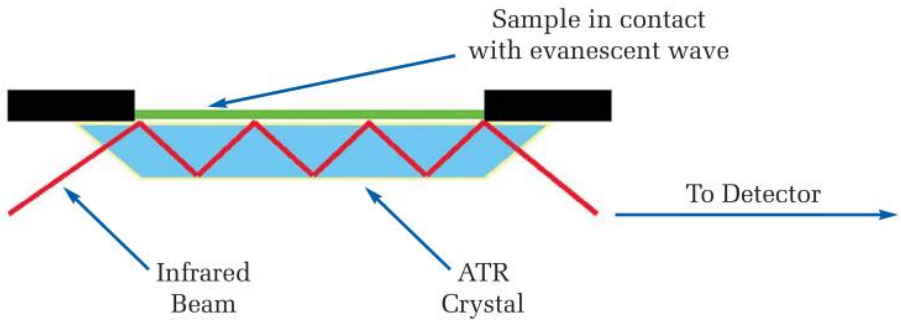


Figure 2.7. Schematics for FT-IR Spectroscopy ATR adapted from Perkin-Elmer technical note.[12].

Meanwhile, in FTIR solution-state analysis, both ATR and liquid transmission cell were used for measurement. Approximately 100 µL of the prepared solution was placed either directly on the ATR with hollow steel attachment placed around the diamond to help contain the test solution, or in the liquid cell sample holder through the filling port, where the sample solution was sandwiched between two zinc selenide salt plates (Perkin Elmer) of equal thickness (4 mm), with no spacer separating them. According to Kameya and Hanamura,[13] using a liquid cell with no spacer is useful to evaluate compound with extremely strong absorption band. A constant path length is

necessary upon performing quantitative analyses, and thus we are discussing the obtained data only qualitatively. Two neoprene gaskets placed in front and the back of the salt plates helps seal the setup (Figure 2.8).

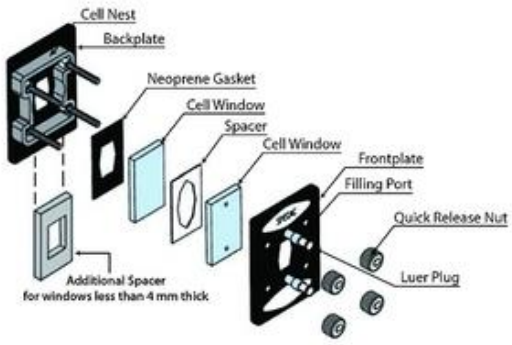


Figure 2.8. FTIR liquid holder setup. Image obtained from google free image repository.

In all IR experiments, four scans were collected for each sample over a wavenumber region of 4000 cm^{-1} to 400 cm^{-1}, and the measure of significance for the FTIR experiments is a change in four (4) wavenumber. The resolution set was 4 cm^{-1}, which means that the degree of fineness of the data obtained by measurement (i.e., the minimum peak interval that can be distinguished) is 2 cm^{-1}. Therefore an unchanged peak can appear at different positions or 'wiggle' within ± 2 cm^{-1}. A four wavenumber difference cut-off ensures that true peak shift change was observed if any does occur.

The peak shift change may occur due to various reasons, *e.g.* hydrogen bond formation or breaking. The effect of the hydrogen bond formation is observed on the donor and acceptor side. For example on the donor side, the formation of hydrogen bond between an NH to a carbonyl in OCB,[14] the N–H stretch of the monomer (3350 cm^{-1}) appears 181 cm^{-1} wavenumber higher than that of the hydrogen-bonded dimer. On the acceptor side, the hydrogen bond formed would stretches the carbonyl bond, effectively 'pulling' the C=O away from one another leading to the weakening of O=C

bond, shifting the peak to a lower stretching vibration frequency.[15] These observations again follow the 'ball and spring theory', where weakening a bond (lengthening of the bond) will decrease the vibrational frequency (and *vice versa*).[16,17]

2.2.6 X-ray diffraction

X-ray diffraction (XRD) analysis is based on the scattering of X-rays by a crystalline sample, which then undergoes constructive and destructive interference, generating a distinct pattern. X-rays are generated through the collision of high-velocity electrons produced by an anode filament (usually tungsten), with a metal target, usually copper (Cu) or molybdenum (Mo), in a cathode ray tube. The X-rays are then filtered using a graphite crystal or double mirror optic to produce monochromatic radiation, collimated to concentrate, and directed toward the sample as illustrated in Figure 2.9.

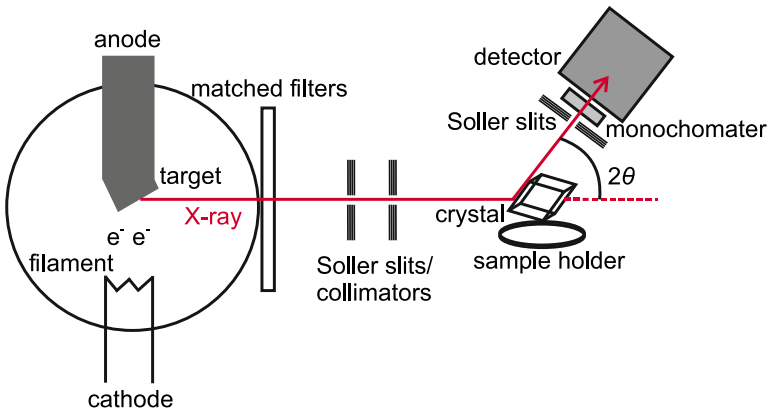


Figure 2.9. Schematics of a typical X-ray diffraction setup.

The interaction of the incident X-rays with the sample produces constructive interference (and a diffracted ray) when the conditions satisfy Bragg's Law ($n\lambda=2d \sin\theta$,[18] Figure 2.9) where θ is the scattering angle, n is a positive integer and λ is the wavelength of the incident wave, the mentioned pattern would be produced, which is

unique to the tested compound. Bragg's law states that as the X-ray of wavelength λ is incident onto the surface of a crystal, at an angle of incidence, θ, the beam will be reflected back with a same angle of scattering, θ.[18] Therefore, when the interplanar distance d, is equal to a whole number, n, of wavelength, a constructive interference will occur (Figure 2.10) leading to a peak formation on the detector, at the angle θ.[18]

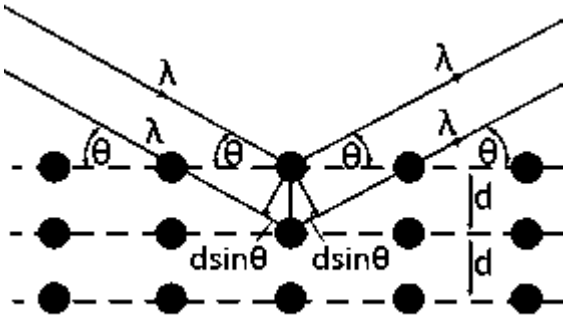


Figure 2.10. Bragg diffraction depicting two in-phase X-ray beams with wavelength λ. The beams are reflected from two different atoms in a crystal. The lower beam covers an extra distance of $2d \sin\theta$, and will produce constructive inteference with the upper beam, leading to a peak pattern at the angle θ. Image adapted form google free media repository.

2.2.6.1 Powder X-ray diffraction (PXRD)

Powder X-ray diffraction (PXRD) data were obtained using an Empyrean powder diffractometer (PANalytical, Almelo, Netherlands) equipped with Cu-Kα radiation (wavelength of 1.5418 Å), graphite monochromator, 0.2 mm fixed Soller slits and PIXcel detector. In addition, a PANalytical X-Pert PRO (PANalytical Ltd, UK) equipped with Cu-Kα radiation (λ = 1.5418 Å) was also used. The operating tube voltage of 40 kV and tube current of 40 mA were used. For each sample, a scan was conducted in the Bragg-Brentano (θ-2θ) geometry between 2 to 40° 2θ, at a rate of 0.5° 2θ per minute. The samples were prepared as a dry powder and placed on a zero-background sample holder.

2.2.6.2 Humidity-controlled powder X-ray diffraction

This experiment was performed with the help of Dr. Kevin Back of Pfizer and Dr. James McCabe of AstraZeneca.

Humidity-controlled PXRD data were obtained using a D8 Discover powder diffractometer (Bruker, Coventry, UK) equipped with a Cu-Kα source (wavelength of 1.5406 Å), primary motorised slits set at 10 mm fixed sample size, Soller slits, secondary motorised slits set at 48 opening angle and a LynxEye detector. The operating tube voltage of 40 kV and tube current of 40 mA was used, and the diffractometer was equipped with a CHCplus+ humidity chamber. The samples were mounted on a silicon wafer (zero background) mount and all scans were conducted in the Bragg–Brentano (θ-2θ) geometry from 2 to 40° 2θ, with a step size of 0.018° 2θ and a time per step of 0.2 seconds. The sample was held at 25 °C and the humidity varied in steps, with the sample allowed to equilibrate for 2 hours at each step. Analysis software used in AstraZeneca was DIFFRAC.EVA version 4.1.1.5.

2.2.6.3 Single crystal X-ray diffraction

This experiment was performed with the help of Dr. Christopher Jones and Dr. Katharina Edkins.

Data were obtained on single crystals coated in perfluoropolyether oil and mounted on MiTeGen sample holders. The samples were placed directly into the pre-cooled cryostream and kept at 120 K. Datasets of DTS Hy1 and the DMSO H_2O solvate were collected on a D8 diffractometer (Bruker, Coventry, UK) operated with Mo-Kα radiation, double mirror monochromator and a photon detector. The DTS methanol solvate was measured on an Xcalibur diffractometer (Oxford Diffraction, Oxford, UK) operated with graphite-monochromated Mo-Kα radiation. The data were

reduced using the APEX2 software package (Bruker, Coventry, UK), solved with olex.solve and refined with olex.refine as included in the Olex2 software package.[19]

Meanwhile, the single crystal data for TRN 2.3 hydrate, the ethanol and 2-propanol solvates were obtained using SuperNova, Dual source EosS2 diffractometer (Rigaku) operated with Cu-Kα radiation. The operating tube voltage of 40 kV and tube current of 1.5 mA was used along with Atlas CCD detector and 4-axis KAPPA goniometer (Rigaku). The crystal was kept at 120 K during data collection. Data reduction by Crysalis (Rigaku). All non-hydrogen atoms were identified from electron density maps and refined anisotropically, whilst hydrogen atoms were modelled in geometrically ideal positions and refined as a riding model.

The synchrotron radiation X-ray diffraction is used to analysed single crystal of very small size. This experiment was performed with the help of Dr. Dmitry S. Yufit and Dr. Katharina Edkins.

Synchrotron X-rays are produced by high energy electrons as they circulate around the synchrotron, a particle accelerator, which is a machine that accelerates the said electrons to extremely high energy and then make them change direction periodically.[20] The schematics of a synchrotron machine, or facility to be exact, is as in (Figure 2.11) along with their respective sections' function. The electrons are generated by electron gun labelled as (1) in Figure 2.11. The electrons are then accelerated to close to the speed of light in linac (2). Booster ring (3) increases the energy of the circulating electron while storage ring (4) stores the high energy electrons which are kept on circular path through magnet. The constantly accelerated motion of the electrons leads to the emission of radiation in the form of X-rays.

Additional magnets (wigglers and undulators) typically located in the storage ring, change the electrons' acceleration which produce different synchrotron spectrum.

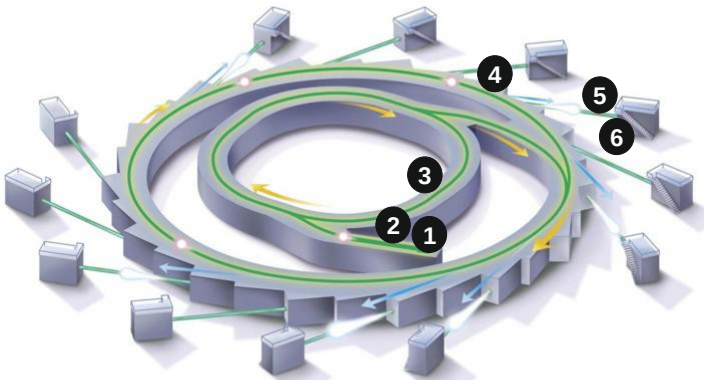


Figure 2.11. Schematics of a synchrotron facility[21] 1) electron gun – ganerate the electron *via* thermionic emission, 2) linac – short for linear accelerator, where electrons are accelerated to close to the speed of light 3) booster ring – ramp or boost the enegy of the circulating electron, typically from 100-200 mega electron volts to 3-6 giga electron volts 4) storage ring – an injection system transfers electrons with enough energy to produce light from the booster ring, 5) beamline and 6) end station.– comprises of the optics cabin, the experimental cabin, and the control cabin.which allow radiation tailoring, house the support mechanism, and the environment for the sample study and cotain the detector to control the experiments and collect the data. Image adapted from google free image repsitory and labelled acccordingly.

The resulting X-rays are emitted as bright white light, *i.e.* they contain a wide range of wavelengths, and are guided towards a beamline and instrument next to the accelerator. If monochromatic X-rays are needed, a crystal with the appropriate lattice spacing is used to diffract that wavelength out of the white beam. This monochromatic beam is significantly less intense in terms of number of photons per time, however, since the overall intensity of the synchrotron beam is high, the lower intensity is not an issue. Synchrotron X-rays are leaps and bounds better than laboratory X-ray in terms of brightness and the angular spread of the beam. The high energy beams provide deeper penetration. Also, the small wavelengths allow the probing of smaller features, *e.g.* bonds in molecules at a shorter timescale.[20]

The dataset for $DTS_{0.5\text{-}0.35}$ were collected on instrument I19 at the Diamond Light Source, Didcot, UK at 120 K. The data were reduced using an APEX2 software package (Bruker, Coventry, UK), solved with olex.solve and refined with olex.refine as included in the Olex2 software package.[19] All non-hydrogen atoms were identified from electron density maps and refined anisotropically, whilst hydrogen atoms were modelled in geometrically ideal positions and refined as a riding model.

2.2.7 Calculations and stock solution preparation.

In our titration analysis, G:H molar ratio is used in order to generate the required data point for the binding constant measurement. The measurement requires that the host concentration to remained constant, while the guest concentrations are varied. Molar concentration calculations and values guide the actual molar ratio used in all titration analysis. For all experiments, a host concentration of either 0.02, 0.05 or 1.0 M was used. A stock solution of the host was made by weighing the solid in a vial and adding a weighed amount of solvent necessary to produce the required concentration. Throughout the experiments, various calibrated Hamilton precision glass syringes with maximum volume capacity from 10 to 1000 µL were used, with the weight of the added solvent additionally recorded using Ohaus Adventurer Pro balance (New Jersey, USA) to maximise accuracy. An adequate volume of the stock was prepared so that it was sufficient to prepare the subsequent guest stocks.

For the titration and dilution experiments (FTIR or NMR), it is equally important to determine the guest concentration needed throughout the experiment. For water as the guest, several problems occur: the very low molecular weight of 18.015 g mol^{-1} compared to the host molar mass limits the measurable amount which can be

prepared. The fact that water is ubiquitous and will be absorbed into any solvent when exposed to the environment makes the lower G:H ratios very difficult to obtain, especially when a lower host concentration (0.02 M) is used. Therefore, one molar ratio gaps were used in our titrations at low guest concentrations, followed by 10 and then 50:1 G:H ratio gaps at higher guest concentrations.

To ensure small aliquots of water could be incorporated into the solvent mixture for the titration experiments, several guest stocks were prepared at a specified guest concentration, *i.e*. 0.5, 5.0 and 20.0 M (named STOCK 1, 2, and 3 respectively). The mentioned guest stock concentrations are used as they allowed for the syringe-able amount (more than 20 μL each time), especially at lower guest concentration ratio, and that the total solution volumes were less than 1.1 mL.

To prepare the guest stock solutions, the guest was weighed accurately into a vial and host stock solution (STOCK 0) was carefully added to obtain the correct concentration. This was to ensure that the host concentration remained constant throughout the titration and that resulting changes were due to guest addition and not host dilution.

To estimate the volume (V_B) from STOCK 1, 2, and 3, that were needed to obtain the required concentration of G:H ratio for all the mentioned data points, the following modifed molar concentration (Figure 2.6) was used. Note that the concentration mentioned is referring to guest or water concentration as the host was kept constant.

(Equation 2.4)

$$M_A V_A + M_B V_B = M_C V_C$$

M_A is the initial molar concentration while V_A is the initial volume. M_B corresponds to the molar concentration of stock used. V_B is the volume of stock needed. M_C is targeted concentration corresponding to Vc, the total volume of A nd B. The volume that an NMR tube could accommodate also limits the sum of V_B that was added. The tube was emptied between stock change intervals, with overlapping measurement done on the re-tubing point to ensure accuracy. Ideally, the peak position of the overlapping run would be the same, however, if a volatile solvent was used, small differences were expected due to evaporation of the solvent. The average between the two overlapping peaks was used as it would better represent the data point.

Table 2.1. Example of water-compound titration setup

[Host] M	[Guest] M M_A or M_C	G:H	Initial vol. V_A	add (μL) V_B	from STOCK # M_B
0.02	0	0	600.00	Initial	STOCK 0 (0 M)
0.02	0.02	1	625.00	25.0	STOCK 1 (0.5 M)
0.02	0.04	2	652.17	27.2	STOCK 1 (0.5 M)
0.02	0.06	3	681.82	29.6	STOCK 1 (0.5 M)
0.02	0.08	4	714.29	32.5	STOCK 1 (0.5 M)
0.02	0.1	5	750.00	35.7	STOCK 1 (0.5 M)
0.02	0.12	6	789.47	39.5	STOCK 1 (0.5 M)
0.02	0.14	7	833.33	43.9	STOCK 1 (0.5 M)
0.02	0.16	8	882.35	49.0	STOCK 1 (0.5 M)
0.02	0.18	9	937.50	55.1	STOCK 1 (0.5 M)
0.02	0.2	10	1000.00	62.5	STOCK 1 (0.5 M)
0.02	0.2	10	600.00	Initial	Re-tube
0.02	0.4	20	626.09	26.1	STOCK 2 (5.0 M)
0.02	0.6	30	654.55	28.5	STOCK 2 (5.0 M)
0.02	0.8	40	685.71	31.2	STOCK 2 (5.0 M)
0.02	1	50	720.00	34.3	STOCK 2 (5.0 M)
0.02	1.2	60	757.89	37.9	STOCK 2 (5.0 M)

0.02	1.4	70	800.00	42.1	STOCK 2 (5.0 M)
0.02	1.6	80	847.06	47.1	STOCK 2 (5.0 M)
0.02	1.8	90	900.00	52.9	STOCK 2 (5.0 M)
0.02	2	100	960.00	60.0	STOCK 2 (5.0 M)
0.02	2	100	600.00	Initial	Re-tube
0.02	3	150	635.29	35.3	STOCK 3 (20.0 M)
0.02	4	200	675.00	39.7	STOCK 3 (20.0 M)
0.02	5	250	720.00	45.0	STOCK 3 (20.0 M)
0.02	6	300	771.43	51.4	STOCK 3 (20.0 M)
0.02	7	350	830.77	59.3	STOCK 3 (20.0 M)
0.02	8	400	900.00	69.2	STOCK 3 (20.0 M)
0.02	9	450	981.82	81.8	STOCK 3 (20.0 M)
0.02	10	500	1080.00	98.2	STOCK 3 (20.0 M)

The mixed solutions were made homogeneous by inverting the tube at least three times. It must be stressed that although volume measurements were used to guide our titration, actual weights of all compounds and solvents added to or removed from the tube (*e.g*. to avoid overfilling) were determined to ensure accuracy. The G:H ratios were then re-calculated for the final presented data to ensure that correct values were used in the subsequent binding constant determination. Resultant peak shifts are plotted following requirements of the binding constant determination software, discussed in subsection 2.4.

2.2.8 Proton nuclear magnetic resonance (^{1}H-NMR) spectroscopy

Nuclear magnetic resonance (NMR) spectroscopy is a technique used to observe the local magnetic fields around atomic nuclei, and plays a significant role in various fields including solving organic and biomolecular (*e.g*. DNA or protein) structural problems, obtaining three-dimensional structure of a specific protein, host-

ligand interaction.[22–24] The magnetic property of the atomic nuclei is fundamental to the technique. The technique relies on the fact that nuclei with odd mass and/or odd atomic number (e.g. ^{1}H, ^{13}C, ^{15}N, ^{31}P) have a spinning property. With respect to ^{1}H, a spinning proton with nuclear spins of 1/2 generates a magnetic field, similar to a small magnet. In the absence of an external influence, the directions are randomly orientated, however, exposure to an external magnetic field, B_0, causes the nuclei to either following the external magnetic field (spin aligned) or against it (spin opposed). The direction aligned with the external magnetic field is the lower energy spin state hence will be the more populated state (Figure 2.12).

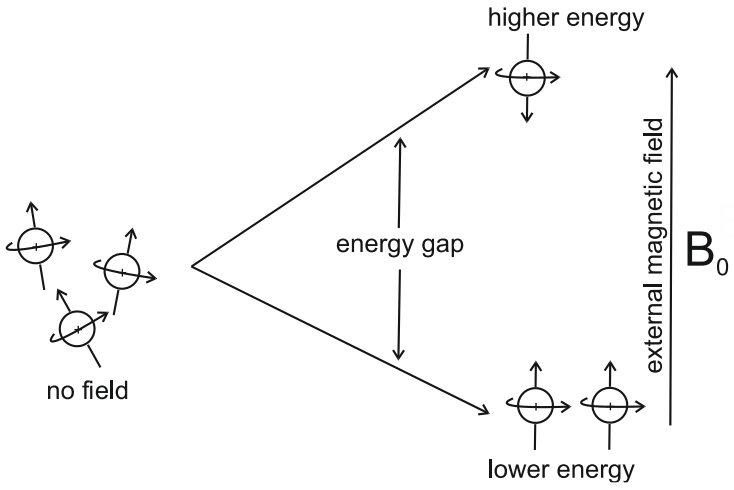


Figure 2.12. The effect of external magnetic spin on the 1/2 nuclear spin of some nuclei.

A subsequent exposure to a radio frequency (RF, energy) radiation, leads to the nuclei absorbing the energy, which in turn affects the nuclear magnetic spin by changing or "flipping" the direction of the nuclear magnetic spin. The energy required to flip the direction depends on the strength of the used external magnetic field. The energy transfers between the low base energy state to a higher energy state take place at a wavelength that correspond to a specific radio frequency of about 60 - 100 MHz. As the spin returns to its base level, the absorbed energy is emitted at the same

frequency. The radio frequency signal emitted by the sample decays exponentially, generating a free induction decay signal (FID). The FID contains all of the information in the NMR that matches the transfer or gap, however it is difficult to acquire information in this format. Fourier transformation of the FID, a time domain signal, produces the frequency domain NMR spectrum which corresponds to the nucleus of interest.[25] Flipping of the proton from one magnetic alignment to the other by radio waves is known as resonance condition. The resonance condition relies on the exact combination of external magnetic field and radio frequency. For a specific radio frequency *e.g.* 100 MHz, and depending on the neighbouring or attached atom, each hydrogen atom will need a slightly different applied magnetic field in order to bring it into the resonance condition. Therefore, the required magnetic field is a useful indication to the hydrogen atom's environment in the molecule.

Our experiments are focused primarily on proton NMR (^{1}H-NMR). The deuterated solvents were used to ensure that the solvent protons do not overpower the spectrum and hinders detection of the tested compounds. ^{1}H-NMR data were acquired in commercially available deuterated solvents, *i.e*. DMSO-d_6, acetonitrile-d_6, acetone-d_3 or DMF-d_7 on a Varian Inova-500 spectrometer (^{1}H at 499.77 MHz) and on Bruker Ultrashield 400 Plus (^{1}H at 400 MHz). In general, an NMR spectrum can either be acquired by varying or sweeping the magnetic field over a small range while observing the radio frequency signal from the sample, or by varying the radio frequency radiation while holding the external field constant.[26] For both instruments, the latter concept was used. The data from Varian Inova-500 spectrometer were analysed on MestRe nova (Mnova) software (Mestrelab Research). Meanwhile, the data obtained from Bruker Ultrashield 400 Plus were analysed using Topspin-NMR software (Bruker). The chemical shifts were measured in the range of +16 to -4 ppm.

For all the ^{1}H-NMR experiment, the peak shift is only considered as significant when the value exceeds ±0.002 ppm. The Varian Inova-500 and the Bruker Ultrashield 400 Plus spectrometer are highly sensitive NMR instruments, capable of measuring changes to the resonance peak, *i.e*. peak shifts, up to the fourth decimal place ppm. However, along with the sensitivity comes measurement error due to various reasons *e.g.* different NMR tubes use, sample exposure to sunlight, the presence of metal object close to the NMR instrument, concentration variation etc. For example, different tube may have different concentricity and camber. Concentricity is the difference between two radial centres obtained by using the outer and inner tube's circumference as reference points, in short the thickness variation. Meanwhile, camber is a measurement of the degree of curvature of the tube with respect to the tube's radial axis, in short the straightness of the tube.[27] If the used tubes have high concentricity and camber values which vary significantly from one tube to another, it would lead to magnetic field non-homogeneity and poor NMR spectra.[27] Exposure to sunlight may increase the temperature of the sample prior to analysis. However, according to Loening and Keeler,[28] in most cases minor temperature differences to the sample do not lead to much inaccuracies in the resultant spectrum, as long as the system temperature or the temperature reported by the spectrometer is constant. Since our measurements deal with very small shifts, however, these inaccuracies have an impact on the resulting data. Meanwhile, the presence of metal object close to the NMR instrument can disrupt the field around the superconducting coil and in consequence interfere with the super-conducting magnet unit. A magnetically attached metal object to the NMR unit would disrupt the shimming and therefore resonance peak shape.[29]

To minimise these errors, all experiments are done using a single tube, and started at approximately the same time of the day and room conditions (window blind

closed to avoid sunlight exposure) at relatively the same concentration and temperature. Zero-point standards were also used so that all generated chemical shifts can be calibrated internally. In the majority of our experiments, TMS was used as the standard, while in the D_2O environment DSS was used due to limited solubility of TMS in water. These zero-point standards are susceptible to influence by temperature, as it has been reported that TMS varies slightly with temperature with -0.0004 ppm $°C^{-1}$.[30] However, since our measurements are at a constant temperature of 25 °C with air conditioning in the room and temperature control within the magnet, this effect can be neglected. The temperature shift of the standard is also negligibly small when compared to the ±0.002 ppm resolution of the instrument.

2.2.9 Continuous variation method (Job's plot)

The fundamental of Job's plot has been mentioned in Chapter 1. In principle, Job's plot considers only one complex in solution which predominates over all other species under the conditions of the experiment. Job's plot analysis requires that the sum of the host and guest concentrations is kept constant throughout the experiment whilst varying each component of the mixture. Using the stock solution as described in 2.3.1, the used mixtures are illustrated in Table 2.2.

Table 2.2. Job's plot setup for 0.1 M host and 0.1 M guest compounds. 10 sets of tubes were used, each containing different volume which corresponded to the different intended host or guest fractions.

[H]	[G]	Host fraction	Vol. stock Host	Vol. stock guest
0.00	0.10	0.0	0	500
0.01	0.09	0.1	50	450
0.02	0.08	0.2	100	400
0.03	0.07	0.3	150	350
0.04	0.06	0.4	200	300

0.05	0.05	0.5	250	250
0.06	0.04	0.6	300	200
0.07	0.03	0.7	350	150
0.08	0.02	0.8	400	100
0.09	0.01	0.9	450	50
0.10	0.00	1.0	500	0

All spectra were calibrated by fixing the shift to a TMS standard. The Job's plot curve was generated by multiplying the change in the resonance peak shift by the host fraction. Plotting resultant peak shift against the host fraction or concentration would, in most cases, produce a quadratic curve, with a maximum at the host fraction (*x*-axis) equalling the stoichiometry of the host-guest complex.

2.2.10 ^{1}H-NMR dilution experiment

^{1}H-NMR dilution experiments were performed to ensure that the subsequent peak shift observed is a result of the titration experiment due to interaction with guest *e.g.* water, and not the effect of dilution of the tested compound. ^{1}H-NMR dilution experiments were carried out by preparing sufficient amount stock solutions of the selected compound in the respective deuterated solvent, as indicated in 2.3.1, and diluting the main stock with molar ratio aliquots of the main solvent comparable to the guest ratio added.

2.2.11 ^{1}H-NMR titration experiment

The titration experiment was done to probe the initial effect of water interaction with the tested compound. Sample preparation is as mentioned 2.3.1 and as indicated in Table 2.1. Selection of a suitable solvent system for the whole titration experiment is very important. Since the guest is water or DMF, two main criteria should be

fulfilled; adequate host and host:guest complex solubility, and the guest-solvent miscibility. The initial water content of the solvent was determined either through KF titration or by integrating the NMR water peak and comparing it to a known (host or TMS) concentration or mass. A high or lower host concentration can be used depending on required analysis, however, for most of our titration, a lower, NMR-visible concentration was selected as it can avoid the precipitation of the resultant host-guest complex. Although heating the solution can remove the precipitate, the heat introduced would affect the solution concentration (due to solvent evaporating) as the host concentration must be kept constant throughout the experiment using the measures mentioned in 2.3.1.

The maximum guest concentration used was limited by the solubility of the host and/or the host-guest complex. Precipitation or peak shift plateau signalled the endpoint to the titration. Although reliable binding constants may be obtained from ten data points with equal spacing (c.f. Job's plots), it is customary to obtain 15-20 data points with more values at lower guest concentrations (Table 2.1, setup for 27 data points).[31] The higher number of data points at lower guest concentration is crucial as they provide early indication towards the trajectory of the subsequently fitted curve. The resultant resonance peak shifts were then recorded and plotted for binding constant measurement in following subsection (2.4).

2.3 Binding constant determination using open source fitting tool: Supremolecular.org

A web-based open-source freeware, BindFit from http://supramolecular.org was used to calculate the binding constants (K_a).[31–33] The binding constant

determination is based on the fitting of the observed peak shift data points to a simulated isotherm line (Figure 2.13).

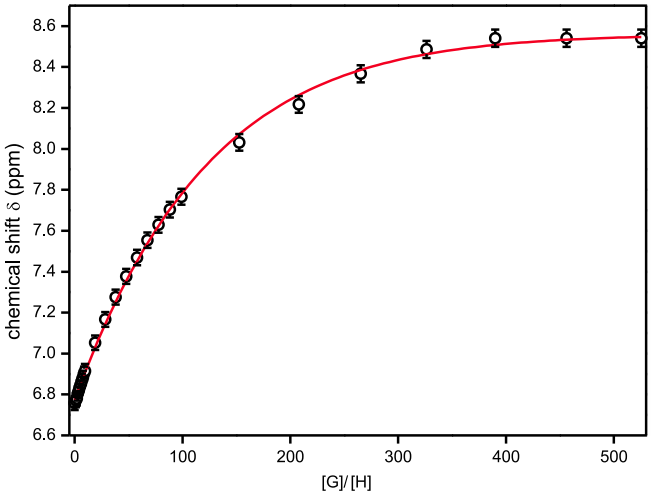


Figure 2.13. Fitting of a hypothetical resonance peak shift against G:H molar ratio to a theoretical binding isotherm represented by the red line.

However, unlike commercial software packages like GraphPad[34] or modified fitting programs running on generic mathematical programming software like Origin, Excel, Matlabs or Mathematicas, BindFit fits all the observable peak changes, hence K_a determination is based on more than one set of data. For example, following a ^{1}H-NMR titration, more than one proton resonance is visible and will show noticeable shifts upon complexation of the host, therefore, all the visible protons have to be considered in the fitting. According to Thordarson,[31] fitting more data of the same titration (named global analysis) will reduce error compared to single-experiment or local fitting.

Once the peak shift data are obtained and the binding constant (K_a) determined, the free energy (ΔG) changes can be calculated and used as a measure of affinity (along with the obtained K_a values) between the components, according to (Equation *2.5*. Herein, ΔG refers to the Gibb's free energy, R corresponds to the universal gas

constant, 8.3147 J K^{-1} mol^{-1}, *T* is the temperature in kelvin and *K* is the binding constant.

(Equation 2.5)

$$\Delta G = -R\ T\ \ln(K_a)$$

The stoichiometry selection for the binding model is initially based on Job's plot measurements. At the same time, all the data points are also fitted to all the available models (1:1, 2:1 and 1:2) in the BindFit software as the programme also gives an indication towards the best fitting interaction stoichiometry (fit which generated the least % error). Having a Job's plot to support the selected fitting is always the best route, however, if multiple species are present in the test solution, Job's plot result will not be reliable as the plot only considers one dominant species in its measurement.[35]

2.4 Molecular dynamics (MD) simulations: Tetrazole/DMF system

This simulation was performed by Dr. Antonella Ciancetta, a collaborator at QUB. MD simulation is a computer simulation of atoms and/or molecules interacting using basic laws of physics, *e.g.* Newton's law of motion.[36] MD allows for investigation into the kinetic and thermodynamic property of a system including macromolecular stability,[37]molecular recognition and the properties of complexes[38,39] as well as many others. MD is widely used in molecular design (*e.g.* drug and protein design[40,41]) and structure determination and refinement (*e.g.* X-ray and NMR).[42,43]

The three basic steps are followed in any MD simulation, which is simplified as firstly setting up the initial state (system setup). In MD, atoms are typically represented as hard spheres which interact according to a van der Waals (Lennard-Jones) potential.[44] Partial charges are calculated by quantum methods to represent the

distribution of electronic charge on those molecules.[45] Meanwhile, bonds and their respective angle of constraints are typically represented as *e.g.* Hooke's Law,[44] or harmonic and anharmonic oscillators.[46] The second step is the introduction of the interaction potential in the system (system equilibration). Prior to starting the simulation, a range of velocities is chosen that matches the Boltzmann distribution for a temperature, and then those velocities are assigned randomly to each atom. Similar methods are then used to put energy into the bond angles and dihedrals. The last step is to run the prediction on molecule movement, typically *via* Newton's equation of motion (system production) which allow structural fluctuations *e.g.* molecules transferring both energy and momentum to one another *via* electrostatics and van der Waals interactions, to be observed relative to time.[44] The details of Dr. Antonella Ciancetta simulation work is as follows:

System setup. Molecules were placed in a cubic box of 100 Å x 100 Å x 100 Å dimensions. The binary tetrazole/DMF mixture was set up by using packmol.[47] Five different systems were simulated with increasing DMF concentration, as shown in Table 2.3. Water molecules were added to the mixture by means of HTMD (Acellera, Barcelona Spain, version 1.9.10).[48] MD simulations with periodic boundary conditions were carried out with the ACEMD engine (Acellera, version 2017.11.30)[49] and CHARMM36[4]/CgenFF(3.0.1)[50,51] force field for water and solute molecules, respectively.

System equilibration. The systems were equilibrated by performing a 5000-step minimisation followed by 4 ns of MD simulation in the NPT ensemble by maintaining the temperature at 310 K using a Langevin thermostat with a low damping constant of 1 ps^{-1}, and the pressure at 1 atm using a Berendensen barostat. Bond lengths involving

hydrogen atoms were constrained using the M-SHAKE[52] algorithm with an integration time step of 2 fs.

System production. The equilibrated systems were subjected to 200 ns of unrestrained MD simulations (NVT ensemble, damping constant of 0.1 ps^{-1}, single run). Long-range Coulombic interactions were handled using the particle mesh Ewald summation method (PME)[53] with grid size rounded to the approximate integer value of cell wall dimensions. A non-bonded cut off distance of 9 Å with a switching distance of 7.5 Å was used. The simulations were run on one 1080 Ti NVIDIA GPUs (Nvidia, Santa Clara, CA).

Table 2.3. Details of the simulated TTZ/DMF systems

System Number	Tetrazole equivalents	DMF equivaents	Number of water molecules	Total number of atoms in the system
1	1	0	32013	96255
2	1	5	31375	95061
3	1	15	30193	92955
4	1	25	28872	90432
5	1	50	26083	85665

2.5 References

1. Giulietti, M., Seckler, M. M., Derenzo, S., Ré, M. I. & Cekinski, E. Industrial crystallization and precipitation from solutions: State of the technique. *Brazilian J. Chem. Eng.* **18**, 423–440 (2001).

2. Zhang, Y. *et al.* Experimental Investigation on Multiphase Bunsen Reaction in the Thermochemical Sulfur–Iodine Cycle. *Ind. Eng. Chem. Res.* **53**, 3021–3028 (2014).

3. Fischer, K. Neues Verfahren zur maßanalytischen Bestimmung des Wassergehaltes von Flüssigkeiten und festen Körpern. *Angew. Chemie* **48**, 394–396 (1935).

4. Scholz, E. Die Karl-Fischer-Reaktion. in 3–14 (Springer Berlin Heidelberg, 1984). doi:10.1007/978-3-642-69368-7_2

5. Smith, D. M., Bryant, W. M. . & Mitchell, J. *Analytical Procedures Employing Karl Fischer Reagent.1 IV. The Determination of Acid Anhydrides*. *This Journal* **62**, (1940).

6. *HYDRANAL™ Product Overview Guide*.

7. Tissue, B. M. *Basics of Analytical Chemistry and Chemical Equilibria*. *Basics of Analytical Chemistry and Chemical Equilibria* (John Wiley & Sons, Inc., 2013). doi:10.1002/9781118647042

8. Metrohm. *Coulometric water content determination according to Karl Fischer*.

9. *Pharmacopoeia Europaea 9.0*. (Deutscher Apotheker Verlag, 2016).

10. *United States Pharmacopoeia*. **40**, (The Stationary Office, 2017).

11. Burghaus, U. Surface chemistry of CO2 – Adsorption of carbon dioxide on clean surfaces at ultrahigh vacuum. *Prog. Surf. Sci.* **89**, 161–217 (2014).

12. Perkin Elmer. Principles of Attenuated Total Reflectance (ATR) FT-IR Spectroscopy.

13. Kameya, Y. & Hanamura, K. Enhancement of solar radiation absorption using nanoparticle suspension. *Sol. Energy* **85**, 299–307 (2011).

14. Edkins, R. M., Hayden, E., Steed, J. W. & Fucke, K. Conserved hydrogen bonding in tetrahydrocarbazolone derivatives: influence of solution-state assembly on crystal form nucleation. *Chem. Commun.* **51**, 5314–5317 (2015).

15. Steiner, T. The hydrogen bond in the solid state. *Angew. Chem. Int. Ed.* **41**, 49–76 (2002).

16. Colthup, N. B., Daly, L. H. & Wiberley, S. E. *Introduction to infrared and Raman spectroscopy*. (Academic Press, 1975).

17. Socrates, G. *Infrared and raman characteristic group frequencies : tables and charts.* (John Wiley & Sons, 2007).

18. Bragg, W. *The crystalline state*,. (Macmillan, 1934).

19. Dolomanov, O. V., Bourhis, L. J., Gildea, R. J., Howard, J. A. K. & Puschmann, H. OLEX2 : a complete structure solution, refinement and analysis program. *J. Appl. Crystallogr.* **42**, 339–341 (2009).

20. Balerna, A. & Mobilio, S. Introduction to synchrotron radiation. in *Synchrotron Radiation: Basics, Methods and Applications* 3–28 (Springer Berlin Heidelberg, 2015). doi:10.1007/978-3-642-55315-8_1

21. Aquilanti, G., Vaccari, L., Plaisier, J. R. & Goldoni, A. Instrumentation at synchrotron radiation beamlines. in *Synchrotron Radiation: Basics, Methods and Applications* 65–104 (Springer Berlin Heidelberg, 2015). doi:10.1007/978-3-642-55315-8_3

22. Abraham, R. J. & Mobli, M. An NMR, IR and theoretical investigation of 1 H Chemical Shifts and hydrogen bonding in phenols. *Magn. Reson. Chem* **45**, 865–877 (2007).

23. Berg, J. M. (Jeremy M., Tymoczko, J. L., Stryer, L. & Stryer, L. *Biochemistry*. (W.H. Freeman, 2002).

24. Skinner, A. L. & Laurence, J. S. High-field solution NMR spectroscopy as a tool for assessing protein interactions with small molecule ligands. *J. Pharm. Sci.* **97**, 4670–95 (2008).

25. Ionin, B. I. & Ershov, B. A. The Fundamentals of NMR Spectroscopy. in *NMR Spectroscopy in Organic Chemistry* 1–59 (Springer US, 1970). doi:10.1007/978-1-4684-1785-2_1

26. Becker, E. D. *High resolution NMR : theory and chemical applications*. (Academic Press, 2000).

27. Rahman, A.-, Choudhary, M. I., Wahab, A. & Elsevier. *Solving Problems with NMR Spectroscopy*. *Solving Problems with NMR Spectroscopy* (Elsevier/AP, 2016). doi:10.1016/b978-0-12-066320-0.x5000-9

28. Loening, N. M. & Keeler, J. Temperature accuracy and temperature gradients in solution-state NMR spectrometers. *J. Magn. Reson.* **159**, 55–61 (2002).

29. Fuks, L. F., Huang, F. S. C., Carter, C. M., Edelstein, W. A. & Roemer, P. B. Susceptibility, lineshape, and shimming in high-resolution NMR. *J. Magn. Reson.* **100**, 229–242 (1992).

30. Hoffman, R. E. Standardization of chemical shifts of TMS and solvent signals in NMR solvents. *Magn. Reson. Chem.* **44**, 606–616 (2006).

31. Thordarson, P. Determining association constants from titration experiments in supramolecular chemistry. *Chem. Soc. Rev.* **40**, 1305–1323 (2011).

32. BindFit v0.5 | Supramolecular. Available at: http://app.supramolecular.org/bindfit/. (Accessed: 10th August 2017)

33. Thordarson, P. Binding Constants and Their Measurement. in *Supramolecular Chemistry* (John Wiley & Sons, Ltd, 2012). doi:10.1002/9780470661345.smc018

34. Motulsky, H. & Christopoulos, A. Fitting curves with GraphPad Prism. in *Fitting Models to Biological Data Using Linear and Nonlinear Regression* 296–297 (2003). doi:10.1002/pst.167

35. Hibbert, D. B. & Thordarson, P. The death of the Job plot, transparency, open science and online tools, uncertainty estimation methods and other developments in supramolecular chemistry data analysis. *Chem. Commun.* **52**, 12792–12805 (2016).

36. Leach, A. R. *Molecular modelling : principles and applications*. (Prentice Hall, 2001).

37. Tiana, G., Simona, F., De Mori, G. M. S., Broglia, R. A. & Colombo, G. Understanding the determinants of stability and folding of small globular proteins from their energetics. *Protein Sci.* **13**, 113–124 (2004).

38. Wang, W., Donini, O., Reyes, C. M. & Kollman, P. A. Biomolecular Simulations: Recent Developments in Force Fields, Simulations of Enzyme Catalysis, Protein-Ligand, Protein-Protein, and Protein-Nucleic Acid Noncovalent Interactions. *Annu. Rev. Biophys. Biomol. Struct.* **30**, 211–243 (2002).

39. Brooijmans, N. & Kuntz, I. D. Molecular Recognition and Docking Algorithms. *Annu. Rev. Biophys. Biomol. Struct.* **32**, 335–373 (2003).

40. Wong, C. F. & McCammon, J. A. Protein Simulation and Drug Design. *Adv. Protein Chem.* **66**, 87–121 (2003).

41. Koehl, P. & Levitt, M. De novo protein design. I. In search of stability and specificity. *J. Mol. Biol.* **293**, 1161–1181 (1999).

42. Brunger, A. T. & Adams, P. D. Molecular Dynamics Applied to X-ray Structure Refinement. *Acc. Chem. Res.* **35**, 404–412 (2002).

43. Linge, J. P., Williams, M. A., Spronk, C. A. E. M., Bonvin, A. M. J. J. & Nilges, M. Refinement of protein structures in explicit solvent. *Proteins Struct. Funct. Bioinforma.* **50**, 496–506 (2003).

44. Adcock, S. A. & McCammon, J. A. Molecular Dynamics: Survey of Methods for Simulating the Activity of Proteins. *Chem. Rev.* **106**, 1589–1615 (2006).

45. Bleiziffer, P., Schaller, K. & Riniker, S. Machine Learning of Partial Charges

Derived from High-Quality Quantum-Mechanical Calculations. *J. Chem. Inf. Model.* **58**, 579–590 (2018).

46. König, G. & Brooks, B. R. Correcting for the free energy costs of bond or angle constraints in molecular dynamics simulations. *Biochim. Biophys. Acta* **1850**, 932–943 (2015).

47. Martínez, L., Andrade, R., Birgin, E. G. & Martínez, J. M. PACKMOL: A package for building initial configurations for molecular dynamics simulations. *J. Comput. Chem.* **30**, 2157–2164 (2009).

48. Doerr, S., Harvey, M. J., Noé, F. & De Fabritiis, G. HTMD: High-Throughput Molecular Dynamics for Molecular Discovery. *J. Chem. Theory Comput.* **12**, 1845–1852 (2016).

49. Harvey, M. J., Giupponi, G. & Fabritiis, G. De. ACEMD: Accelerating Biomolecular Dynamics in the Microsecond Time Scale. *J. Chem. Theory Comput.* **5**, 1632–1639 (2009).

50. Vanommeslaeghe, K. & MacKerell, A. D. Automation of the CHARMM General Force Field (CGenFF) I: Bond Perception and Atom Typing. *J. Chem. Inf. Model.* **52**, 3144–3154 (2012).

51. Vanommeslaeghe, K., Raman, E. P. & MacKerell, A. D. Automation of the CHARMM General Force Field (CGenFF) II: Assignment of Bonded Parameters and Partial Atomic Charges. *J. Chem. Inf. Model.* **52**, 3155–3168 (2012).

52. Krautler, V., van Gunsteren, W. F. & Hunenberger, P. H. A fast SHAKE algorithm to solve distance constraint equations for small molecules in molecular dynamics simulations. *J. Comput. Chem.* **22**, 501–508 (2001).

53. Essmann, U. *et al.* A smooth particle mesh Ewald method. *J. Chem. Phys.* **103**, 8577–8593 (1995).

CHAPTER 3

THE COMPLEX SOLID-STATE LANDSCAPE OF SODIUM DIATRIZOATE HYDRATES

3.1 Chapter overview

Pharmaceutical sodium salts are hygroscopic,[1] hence are prone to incorporate water into their crystal structures, forming hydrate.[2,3] The screen of the sodium salt model compound, diatrizoic acid monosodium salt, yielded five hydrates and two solvate forms. The water content of the hydrates varies from 0.3 to 8 molar equivalents of water, showing interconvertibility, stoichiometric and non-stoichiometric behaviour, and potential of amorphisation during release of water. One of the solvates was also found to be a water mixed solvate. The complex system observed highlights the importance of having a comprehensive data on any pharmaceutical sodium salts solid-state phase transition and hydration behaviour as it provides a guide for better formulation and manufacturing, as well as ensuring dose uniformity and stability of the final formulation. This chapter emphasises on the importance of thorough hydrate screening for pharmaceutical sodium salts, as the probability of water incorporation into their crystal structures is high. Also, this chapter showcases the complexity of the resultant crystalline hydrate system, which interconverts with the varying condition. Consequently, this chapter points to the need for early detection and characterisation of hydrates. The findings from this research has been published in Chemistry - A European Journal, with the same title (DOI:10.1002/chem.201703658).[4]

3.2 Introduction

3.2.1 Background

Optimisation of the physical and chemical properties of a new active pharmaceutical ingredient (API), such as flowability, hardness, stability, and solubility, is a routine challenge in the pharmaceutical industry. Many compounds are often synthesised having non-optimal properties, whether for manufacturing or patient safety, or even both. Thus further steps are taken, *e.g.* change of crystal form, co-crystallisation or salt formation, to improve the unwanted properties. Salt formation is common to improve the solubility for molecules showing low to very low solubility in water. However, the salt formation will undoubtedly affect other physicochemical properties of the compound such as melting point, chemical stability, hygroscopicity and *etc*.[5] Traditionally, the salt-forming agents are chosen based on trial and error,[6,7] and the salt form selected by pharmaceutical chemists is based on a practical basis addressing cost and ease of production. However, in recent times intelligent design for the salt selection process is more favourable,[5,8] with more than half of all drug molecules used in medicine marketed as salts.[9] Overall, sodium salts are amongst the most abundant salt forms, second only to hydrochloride salts of basic APIs.[10] The current European Pharmacopoeia 9.0[11] monographs 79 pharmaceutically active small organic compounds as their sodium salt, 13 of which is individually or solely monographed as the hydrate form due to the form's high stability and/or prevalence.

3.2.2 Challenges due to sodium salt hydrates formation

In general, water can interact with crystalline solids through surface moisture adsorption, deliquescence, capillary condensation, and crystal hydrate formation.[12] The latter is less apparent (hence more severe) as water is incorporated into the crystal lattice, making the physical state appearance similar to that of a dry powder. The likelihood of water inclusion increases with the presence of charged (*e.g.* sodium salt) or polar groups (*e.g.* carbonyl (C=O),[13] which is a common feature for pharmaceuticals. Though not definite, the possibility of crystalline hydrate formation especially in sodium salts could potentially counteract the benefits of the initial salt formation. Also, to avoid hydration of a salt is difficult as water is ubiquitous, for instance, atmospheric water cannot be avoided, and aqueous processing solutions are needed. Consequently, unexpected transformation spells numerous challenges. Humidity levels variations which lead to crystalline hydrates transformation can occur throughout the manufacturing process, for example, upon transitioning between high humidity (*e.g.* wet granulation) to low humidity (*e.g.* drying) processes.[14–16] Post-production, a crystalline compound can face humidity variations during storage, mainly due to an inconsistent temperature of the environment (*e.g.* storage condition or climate)[17,18] or upon consumption. Contact with body fluids or as the patient takes the medication with water, could initiate the salt-hydrate transformation.

A third of pharmaceutical compound can potentially form a hydrate,[19,20] hence the formation is particularly problematic for pharmaceuticals, as due to thermodynamic reasons, hydrates have the lowest solubility in water of all solid forms of a specific compound.[2] Lower solubility means lower bioavailability as a compound needs to be in solution to be absorbed. There are three general classes of crystalline

hydrate, firstly is the isolated site hydrates, where a single water molecule is individually incorporated or trapped in small clusters. Secondly is channel hydrates, where the structure features water-filled pores or sheets. The third class is metal-associated hydrates, which is particularly important for pharmaceutical sodium salts as the water molecules coordinate to metal centres in the crystal structure. On top of the reduced solubility, metal-associated hydrates can show high or very high stability against dehydration, which means that is harder to remove the bound water.

Bound water molecules can be mobile and migrate within the crystal lattice, or along the solid surface.[21] As a result, water absorption enhances the drug molecular mobility, which in turn enhances the chemical reactivity.[12] Several studies have confirmed the correlation between increased molecular mobility caused by the plasticising effect of water and drug degradation,[22] especially for amorphous material.[23,24] This translates into the reduced stability of the drug compound and may lead to recalls. One such example is in the case of levothyroxine sodium pentahydrate which has been recalled due to stability failures which lead reduced potency earlier than the expiration date.[25]

Sodium salts are hygroscopic and have an enhanced water interaction.[1] It is also not uncommon to see both interactions of ion coordination and hydrogen bonding in a single sodium salt crystalline hydrate.[26] Incorporation of the water molecules into the crystal lattice also produces a different unit cell than that of the anhydrate form, and along with the introduction of additional forces mentioned, alters the physical properties, including solubility and dissolution rate of the sodium salt. Such variation of interaction and hydrate formation capability from a singular sodium salt is shown here in the case of diclofenac sodium, which can exists in four hydrates forms namely a trihydrate, two tetrahydrate forms and a pentahydrate form.[27,28] Similar attribute can

also be observed in nedocromil sodium, which is reported to be present as a hemiheptahydrate, a trihydrate, and a monohydrate.[29] Sodium deoxycholate is another example, showing a variety of crystalline hydrate forms, ranging from dihydrate and a tetra- and even octahydrate,[30,31] with a recent study suggesting that hydrate interaction is non-stoichiometric.[32] Finally, in the report on naproxen sodium, this sodium salt has been characterised to exist as four hydrate forms; a monohydrate, two dihydrates and a tetrahydrate form.[33] The various hydrate forms possibilities translates into more uncertainty towards aqueous solubility and the chemical stability of the drug. The variance in solubility is very likely to have an impact on the bioavailability and toxicity profiles of the drug,[34,35] which would translate into content uniformity problems for patients and jeopardise their safety.

Chances of sodium salt and water interaction is high as water is everywhere. Sodium salt affinity towards water, coupled with the effect of hydration level variations can not only trigger the transformation of sodium salts to hydrates but also cause the formed hydrates to dehydrate or change their hydration level, especially if they are in a metastable state. Such metastable hydrate-hydrate transformation is reported in the case of pantoprazole sodium, reported to exists as four hydrates (i.e. hemihydrate, monohydrate, sesquihydrate and dihydrate)- in which the hemihydrate and monohydrate are metastable and readily transform to the dihydrate (stable form) at high relative humidity (RH).[36] In another case, anhydrate sodium naproxen (the metastable form), has been reported to change to the dihydrate form above 43% RH,[17] while a more recent publication highlights a more complex interchange between the hydrate forms of sodium naproxen.[37] Here, it is reported that both temperature and RH affect the resultant sodium naproxen hydrate form. At 25 °C and 50% RH, anhydrous sodium naproxen (AH) transforms directly to one dihydrate polymorph (DH-II), while

at 50 °C and similar RH, AH transforms stepwise to a monohydrate (MH) then to the other dihydrate polymorph (DH-I). DH-II transforms to a tetrahydrate (TH) more readily following sorption than DH-I at respective temperature and humidities. Both dihydrate polymorphs transform to the same MH following desorption at respective humidities.[37] In the case of amorphous sodium indomethacin, it is reported to be stable at 21% RH for two months, but, upon exposure to 56% RH and above, the amorphous form rapidly crystallises to the trihydrate.[38] This goes to show that variation in hydration level, *e.g.* RH instability, can affect the solid's profile significantly.

Hydrate formation can have a positive impact from a formulation point of view. As the most thermodynamically stable form, crystalline hydrate with good bioavailability is often pursued as the form of choice. Celecoxib sodium salt is such a case in which the mixed propylene glycol/hydrate form was found to be the most stable form at low and high humidities compared to the anhydrous solvate form.[39] In some cases, a hydrate form is pursued as it improves drug absorption, as demonstrated in the pentahydrate of the celecoxib sodium salt, which improves the oral drug absorption by breaking up the strong hydrogen bonding interactions present in crystals of the poorly soluble marketed anhydrous form of the drug.[39] Hydrated sodium salts can also offer an advantage from a manufacturing point of view, as shown in the case of diclofenac sodium tetrahydrate having improved flowability within the powder bed than its anhydrous counterpart, which eases industrial processes such as mixing, tabletting and capsule filling.[40]

3.3 Aims

Given the problems and challenges mentioned, it is astounding that much focus of the publications on the crystal structure of pharmaceutical sodium salt has been on the predominant phase of these compounds, crystallisation procedures in the case of patent literature, and solubility and dissolution rate.[41–43] As a result, many of the pharmaceutical sodium salts have not been fully characterised, and thus their phase transition behaviour cannot inform processing and manufacturing steps. Hence, this chapter aims to characterise a monographed sodium salt thoroughly, focusing on solid-state phase transition with regards to salt-hydrate transformation. Sodium diatrizoate is selected as the model compound as the solid-state landscape has not yet been investigated in depth with just a single hydrate form reported for this sodium salt.[44]

3.3.1 The model compound: Sodium diatrizoate

Sodium diatrizoate (DTS) is a radiocontrast agent containing iodine, and multiple proton donor and acceptor sites (Figure 3.1). The sodium salt along with the free acid form is monographed in the European, British as well as United States pharmacopoeias.[11,45,46] The sodium salt is the optimisation product of diatrizoic acid (DTA), which has low aqueous solubility; reported to exists in three anhydrous modifications, two hydrates and nine solvate forms.[47] The reported hydrate forms are the di- and tetarto (¼) hydrate. Meanwhile, a single tetrahydrate form is reported for DTS, with an earlier report suggesting that the form contains 4 moles of water (tetrahydrate).[44] Meanwhile, a recent report has found this form to incorporate 4.5 molar equivalents of water per salt unit instead.[47] The X-ray and neutron crystal structures show that, while most water is coordinated to the sodium cations, there are

channels in the structure through which the water can potentially freely diffuse in and out. Commercial preparations include the similarly monographed diatrizoate meglumine[45] and/or sodium salt at various concentration, 30, 50, 60, and 76 % (w/v) solution.[48] DTS salt has an advantage over the meglumine salts, as the later have a higher viscosity than the sodium salt. Higher viscosity formulation would require greater injection pressures to deliver the same amount of material, increasing the possibility of patient trauma and catheter damage. Moreover, meglumine salt usually has a lower iodine content as a result of the increased weight of the meglumine ion. Therefore, the amount of iodine delivered per second will be smaller.[49] Trade names include Hypaque, Gastrografin and Urografin, the latter being a combination of the sodium and meglumine salts. Although marketed as a solution, information on the solid state can inform the manufacturing, ensuring the correct form is manufactured and along with the humidity studies, help to identify optimal conditions to generate bulk phases safely. Also, in-depth investigation of sodium salts used pharmaceutically would guarantee dose uniformity and stability of the final formulation.

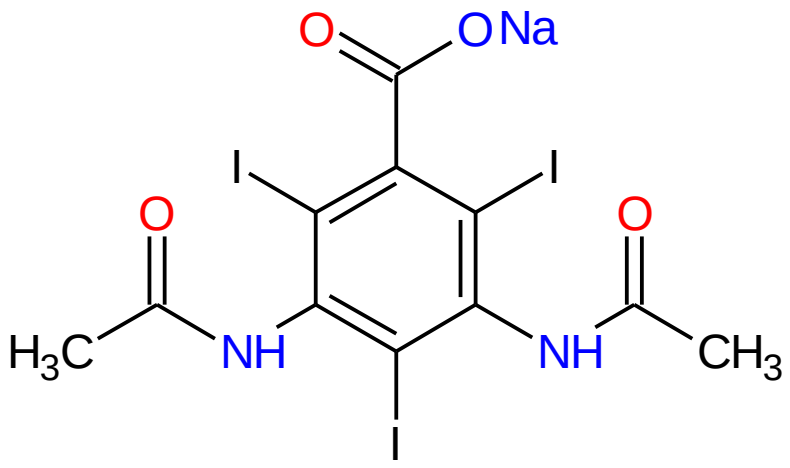


Figure 3.1. Sodium diatrizoate (DTS) structure.

3.4 Results and Discussion

The screen reveals DTS to exist in at least five different hydrated crystal forms. Powder X-ray diffraction shows all of them to be distinctly different, with three (Hy8, Hy1 and Hy0.5-3.5) crystallise directly from solution, while the other two result from the conversion of another form induced either by humidity or heating. Also, a methanol trisolvate and a mixed DMSO/H_2O monosolvate directly crystallise from the respective solvents. An unsolvated crystal form could not be identified.

3.4.1 The octahydrate

Initial dynamic vapour sorption (DVS) isotherm of the amorphous commercial sample shows that the sample takes up a maximum of 22.76% of its weight (Figure 3.2) at the highest measured humidity, 90% RH. This amount corresponds well to a calculated stoichiometry of 8 moles of water per DTS unit (calculated weight change 22.67%), and the crystal form present at high RH values will furtheron be called Hy8.

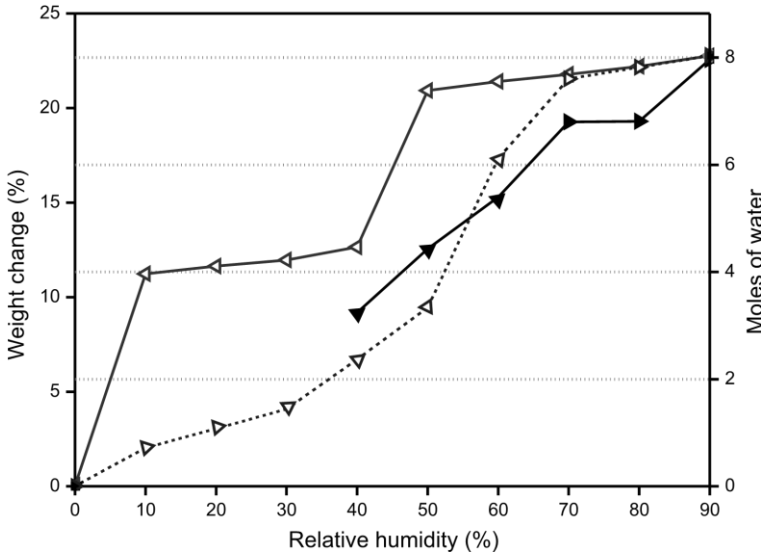


Figure 3.2. Sorption/desorption isotherms of the commercial sample of DTS. The starting point is at 40% RH following a sorption step, then desorption to 0% RH, and finally sorption up to 90% RH again.

Hy8 could also be obtained by storing the commercial product in a water slurry, resulting in a crystalline sample consisting of thin diamond shaped plates (Figure 3.3). The observed habit corresponds well to the previously reported crystallisation behaviour from water.[47] Heating up of the crystals using thermal microscopy (TM) revealed the low thermal stability of this crystal form. The dry powdered sample lost birefringence above 40 °C, while a sample containing mother liquor to avoid desolvation before heating, dissolved in the surplus solvent above 33 °C.

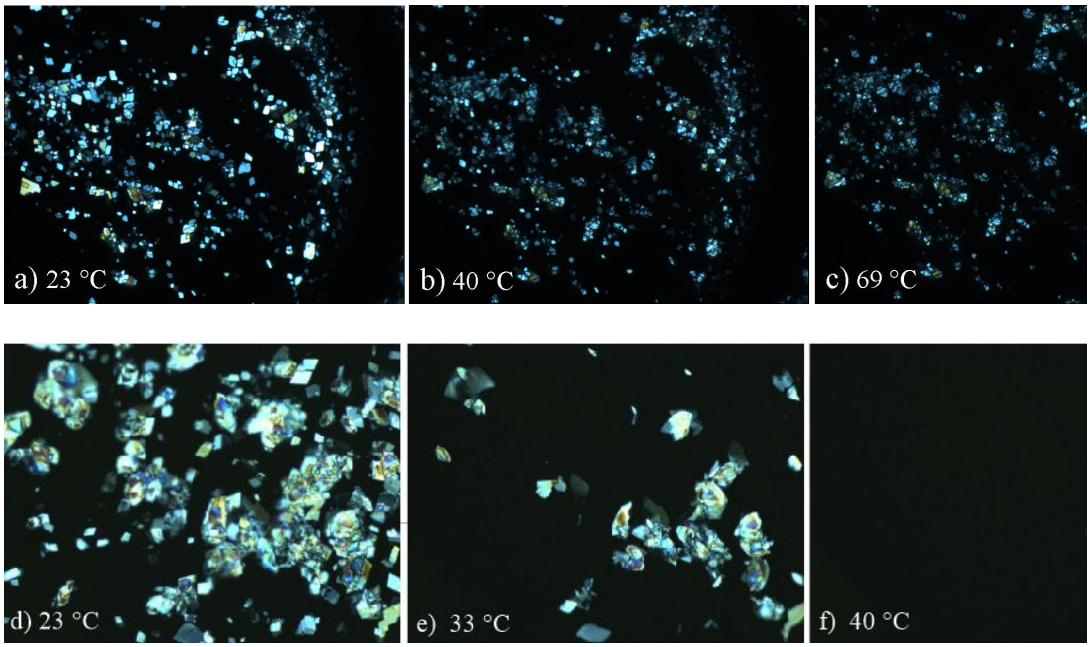


Figure 3.3. Thermal microscopy (TM) photomicrograph of Hy8 at different temperature points. Top set (a to c) is dry powdered sample while bottom set (d to f) is in the mother liquor.

The powder X-ray diffraction (PXRD) trace of these plates is different to the known tetrahydrate (Hy4), as compared to the calculated pattern of Hy4 which is based on the neutron structure.[47] Humidity controlled PXRD also confirmed the octahydrate formation (Figure 3.4 (a)) starting from the amorphous commercial product. Coming from a low (Figure 3.4 (a) bottom trace) to higher humidity (Figure 3.4 (a) top trace) shows clear crystallisation process indicated by the sharp peaks appearing at 80% RH

coming from the amorphous sample, which is represented by the typical broad hump PXRD trace at the lower humidities.

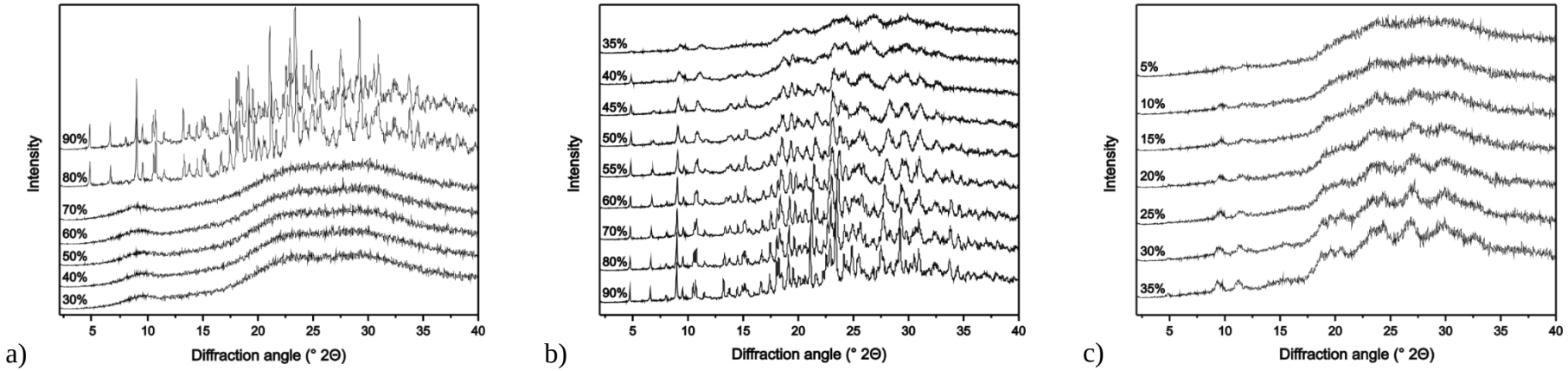


Figure 3.4. Humidity controlled PXRD patterns starting from a) amorphous product at 30% RH forming Hy8 at 90% RH b) Hy8 at 90% RH and passing through the transition to Hy4 towards 35% RH c) continuation from 35% RH to 5% RH showing sample losing crystallinity (amorphisation).

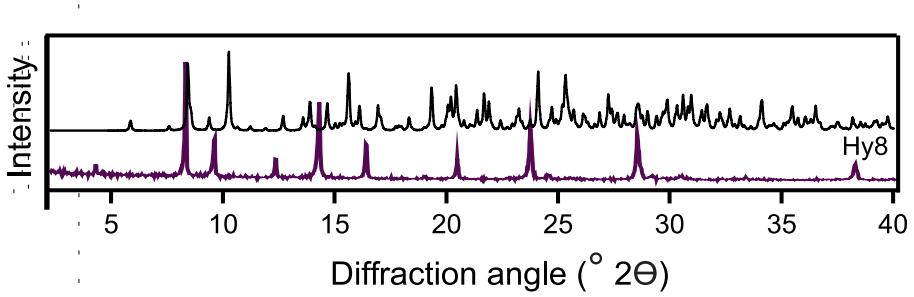


Figure 3.5. The octahydrate (Hy8) PXRD trace comparison to the calculated powder pattern (black) of the tetrahydrate (Hy4).

Thermogravimetric analysis (TGA) of Hy8 shows a dehydration step with the weight loss of 37.70% (Figure 3.6). Closer investigation of this dehydration up to 150 °C (Figure 7) reveals a two-step desolvation profile, even though no intermediate equilibrium is reached. Weight loss starts immediately with a slope of -0.3% weight change per °C in the range from 22.6 °C to 63.9 °C. The weight loss between these temperatures sums up to 12.81%. After this first weight loss region, the slope changes slightly and becomes steeper (-0.5% per °C) between 63.9 °C to 110.1 °C. The second weight loss recorded equals 22.56%, which corresponds to 7.963 moles of water. DSC analysis confirms this two-step profile which shows two overlapping endothermic events corresponding to the events observed in the TGA trace (Figure 3.7). This high total weight loss value of nearly 37% for the whole run was due to the wetness of the sample, which was analysed in slurry to compensate its instability. In the first weight loss step, the surface attached and interstitial water evaporates leading to the intact Hy8 crystal form. The second endothermic event seen in the DSC and weight loss value from TGA of that event corresponds well to the data expected for Hy8.

Desorption of Hy8 by reducing the humidity leads to the formation of the known tetrahydrate at RH values lower than 50% (Figure 3.2), as confirmed by PXRD (Figure 3.8). Hy4 could also be obtained by storing the commercial sample in an

aqueous slurry and drying the powder at room conditions. TGA analysis of the form from ambient temperature and humidity records 11.29% weight difference, which translates into 4.5 moles of water (Figure 3.6).

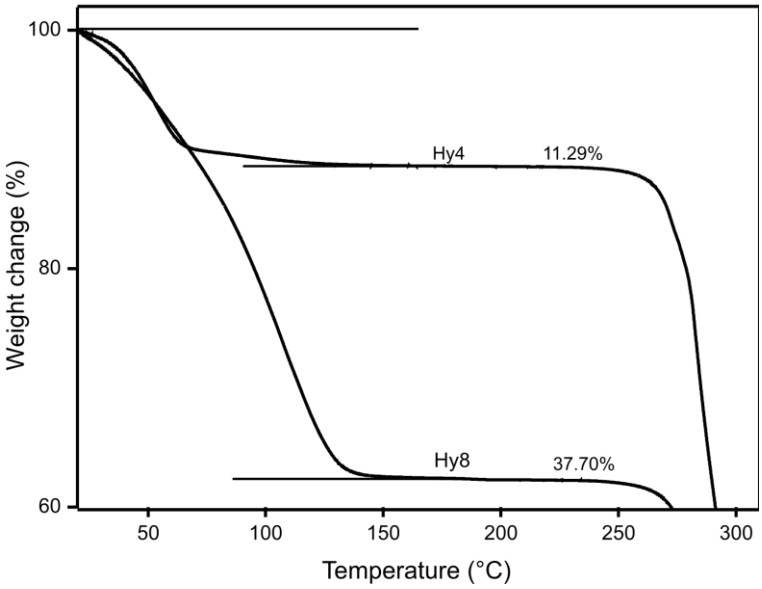


Figure 3.6. TGA thermograms of tetra- vs octa- hydrate forms of DTS

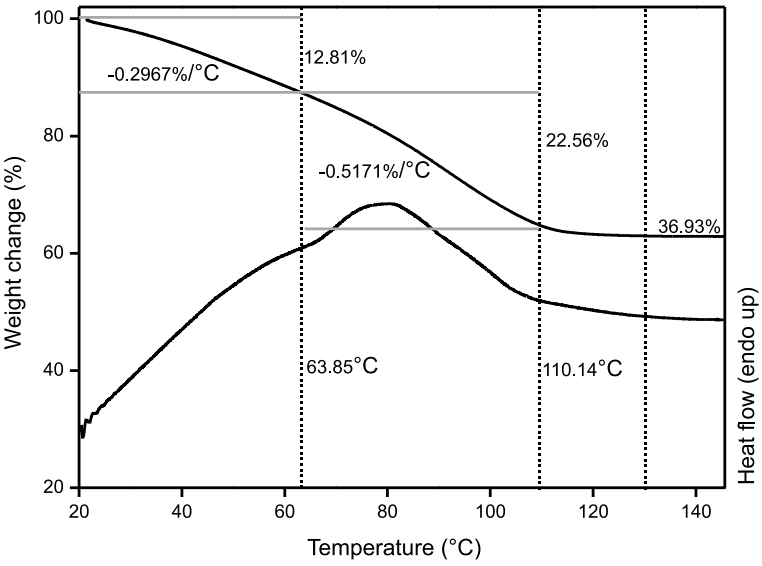


Figure 3.7. TGA (top) and corresponding DSC (bottom) thermograms of both recorded at 10 °C min^{-1}. The measurement was conducted on the wet sample to ensure full hydration

The curve from the desorption cycle of the humidity controlled PXRD compliments the data, showing Hy4 formation from desorption of Hy8 (Figure 3.4 (b)) as the humidity reduces from 90 to 35%. The experimental powder pattern of this form shows some resemblance to the pattern calculated from the single crystal structure published earlier.[47] However, due to the platy nature, this crystal form suffers from pronounced preferred orientation. The presence of a phase transition between the temperature of the powder and the single crystal measurements (300 vs 120 K) cannot be unambiguously ruled out.

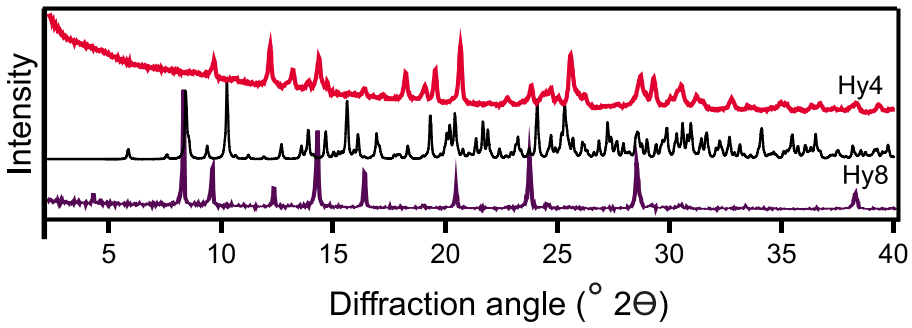


Figure 3.8. Hy4 PXRD comparison to the calculated powder pattern (black) and Hy8.

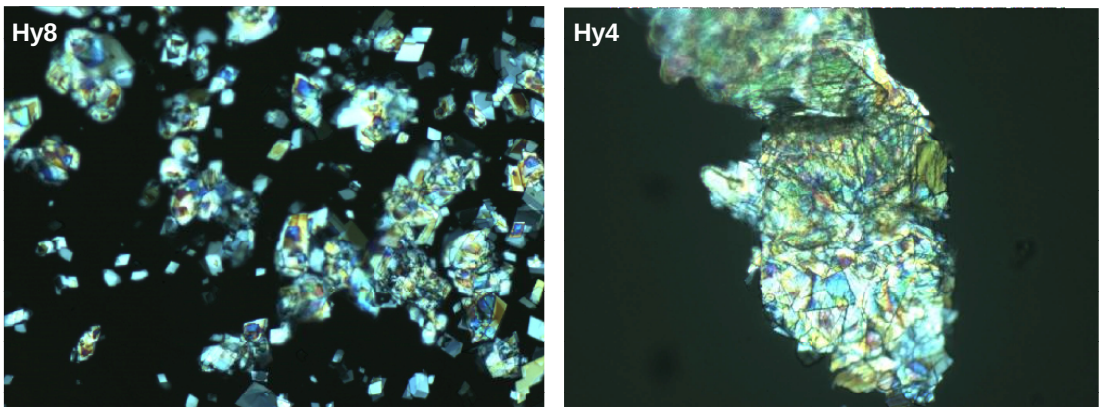


Figure 3.9. Photomicrograph of Hy8 and Hy4 habit.

Due to it originating from Hy8, which is the initial crystallisation product from water, the crystal habit of Hy4 resembles that of Hy8 (Figure 3.9). Surprisingly, the crystals of Hy4 are perfectly translucent and do not show any signs of blackening of the particles or any sign of a change from the bright single coloured interference (in dark-field) to a dim-grey interference colour or pseudomorphosis in short. Pseudomorphosis typically follows crystal form changes and solvent loss from the crystals; the lack of it points to the close structural relationship of these two highly hydrated crystal forms.

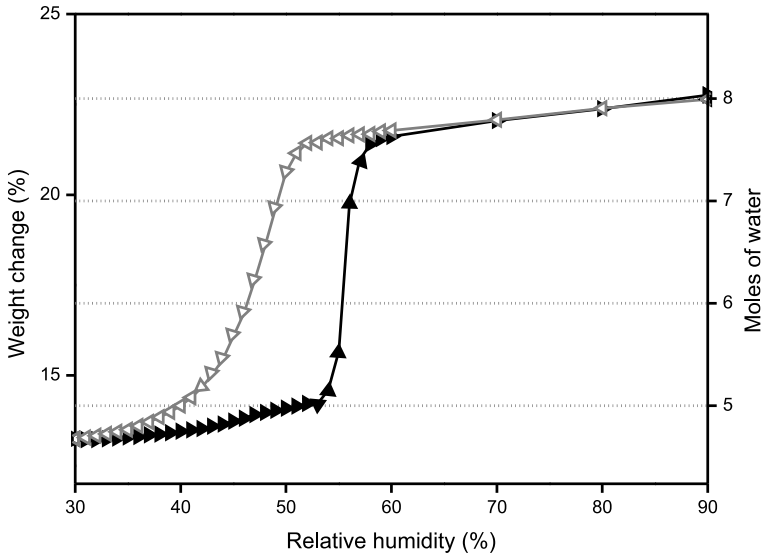


Figure 3.10. High-resolution dynamic vapour sorption (DVS) isotherm of the transition between Hy8 and Hy4. The grey line represents desorption curve, the black line sorption.

The high-resolution DVS shows the reversibility of the transition between Hy8 and Hy4 (Figure 3.10). Hy8 is stable with only minor weight change above 50% RH. The sample then continuously releases water beyond this point, which accumulates to 2.280 moles of water upon reaching 40% RH. Following sorption of Hy4, it is clear that the phase transition to Hy8 starts above 55% RH, which follows a different path

to that of the desorption, suggesting different kinetics between the two processes, with both having a single step transition.

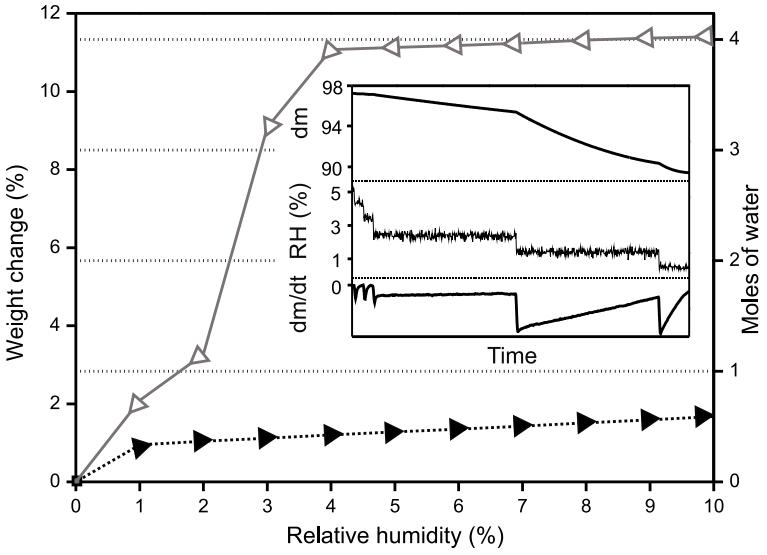


Figure 3.11. High-resolution DVS of the dehydration of Hy4. Insert represents the mass change (*dm*), respective RH levels and mass change rate (*dm/dt*) of the steps below 5% RH.

Hy4 is stable between 40 and 10% RH. (Figure 3.2). Storing Hy4 within this stability range shows a slight variation in water content of 0.5%, varying between 4.47 and 3.97 molar equivalents of water incorporated, which corroborates earlier report that full occupancy of all water positions for Hy4 would result in a stoichiometry of 4.5 water molecules per DTS unit.[47] This result suggests that the variation in water content is connected to partial occupancy of the distinct water positions within the crystal form. It is thus likely that the structure of Tønnesen *et al.* has been measured at the lower end of this humidity spectrum and therefore resulted in four water molecules being refined. The DVS also corroborates the TGA data mentioned earlier; as the TGA liberates all incorporated water from the fresh sample, with 4.5 molar equivalent form Hy4 being also recorded (Figure 3.6). Below 10% RH, the remaining water is released (Figure 3.2). High-resolution DVS of this transition (Figure 3.11) shows that step-like

dehydration takes place below 4% RH, in which the sample loses 7.8% of its weight (2.76 molar equivalents of water). This mass loss leads to an intermediate monohydrate, which is stable at 2% RH but undergoes a further mass loss below this humidity. As the humidity controlled PXRD can only detect down to 5% RH, the existence of the transient monohydrate cannot be confirmed via this method. Following desorption (Figure 3.4 (c)) from 35% RH and lower, the sample undergoes amorphisation (loses crystallinity), which is evident from the trace losing its peaks and becoming broader, thus making the comparison to previous traces more difficult. From the DVS data, however, it is conclusive that this intermediate is indeed a crystalline phase, as the mass of the sample is in equilibrium at 2% RH, while this is not reached at 1% RH (Figure 3.11 insert). At the lower humidity, the sample is in the process of releasing the remaining incorporated water; however, the mass step is not at its final value, as clearly shown by the remaining slope in the *dm*/*dt* curve. Even though only existing at an extremely narrow humidity range, the monohydrate does not represent a kinetic intermediate, as the crystal form is evidently stable over six hours (potentially longer) under these conditions, which is the time that this step has taken in the measurement.

3.4.2 The 0.3-1 hydrate

Tracking the DVS sorption curve of the completely dehydrated sample up from 0 to 1% RH, a weight gain of 0.95% (0.34 molar equivalence of water) is observed (Figure 3.11). The sample takes up another 0.72% in weight, (corresponding to 0.25 moles of water) in a linear manner over the following nine steps up to 10% RH, and the trend continues upwards to 40% RH (Figure 3.15), at which further 1.07% uptake (0.38 molar equivalent of water), adding up to a total of 0.97 molar equivalence of

water is incorporated; hence this form is identified as Hy0.3-1.0. PXRD of Hy0.3-1.0 is different from the previous traces (Figure 3.13). Two different experimental routes could reproduce this form; firstly, by mirroring the conditions of the DVS, through drying a sample of the Hy8 at 25 °C in dry nitrogen flow over ten hours using TGA. Secondly, the Hy8 was dehydrated by TGA at 150 °C for ten minutes. The resulting materials show similar PXRD patterns, and even though the peaks have low intensity, their positions are distinctly different to those of Hy8 and Hy4 (Figure 3.12 and Figure 3.13). In comparison, the peaks are broader and less intense, which is in agreement with the fact that the sample undergoes amorphisation at low humidity as discussed earlier.

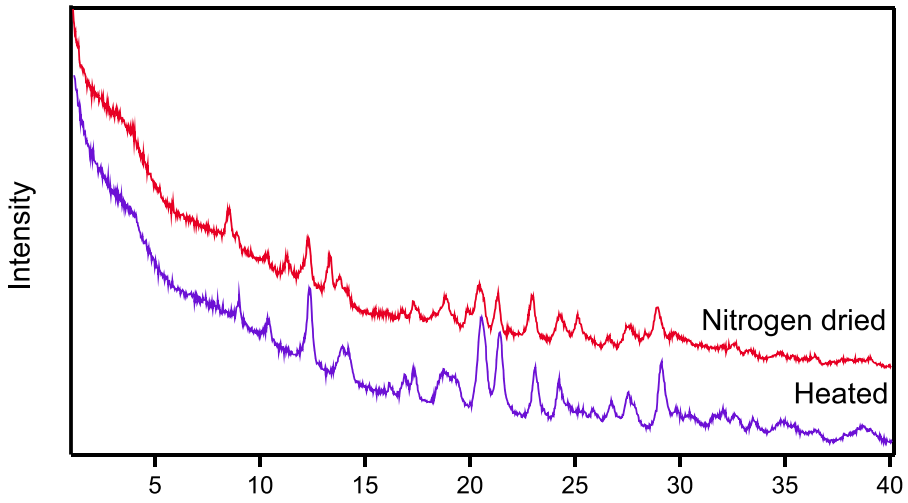


Figure 3.12. PXRD patterns of nitrogen dried vs heated sample of Hy8

TGA of both samples showed a comparable weight loss of approximately 1% corresponding to 0.4 molar equivalents of water after being exposed to environmental humidity (Figure 3.14).

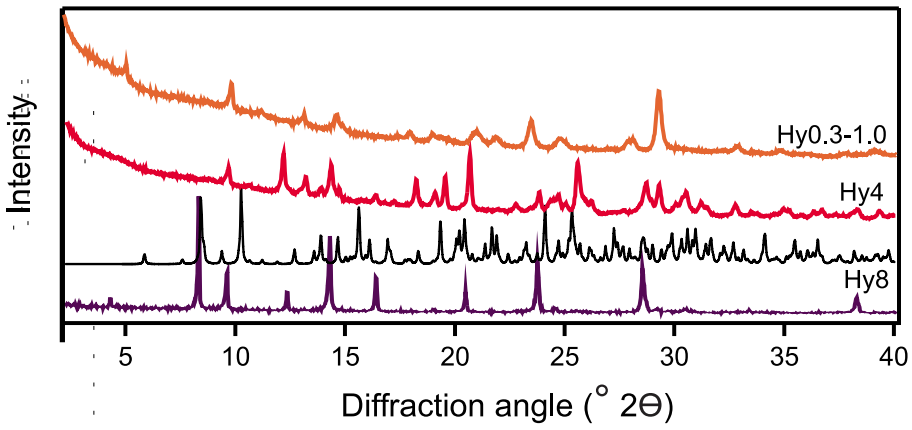


Figure 3.13. Hydrate Hy0.3-1.0 (heated sample) PXRD comparison to Hy4 and Hy8

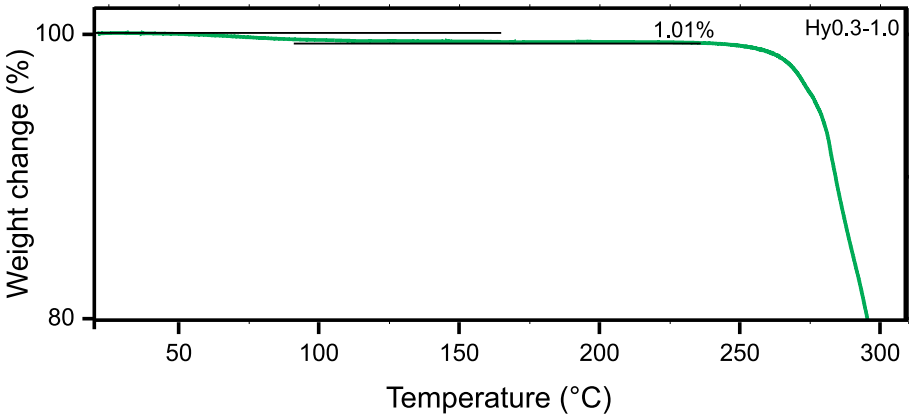


Figure 3.14. TGA thermogram of Hy0.3-1.0 recorded at 10 °C min^{-1}

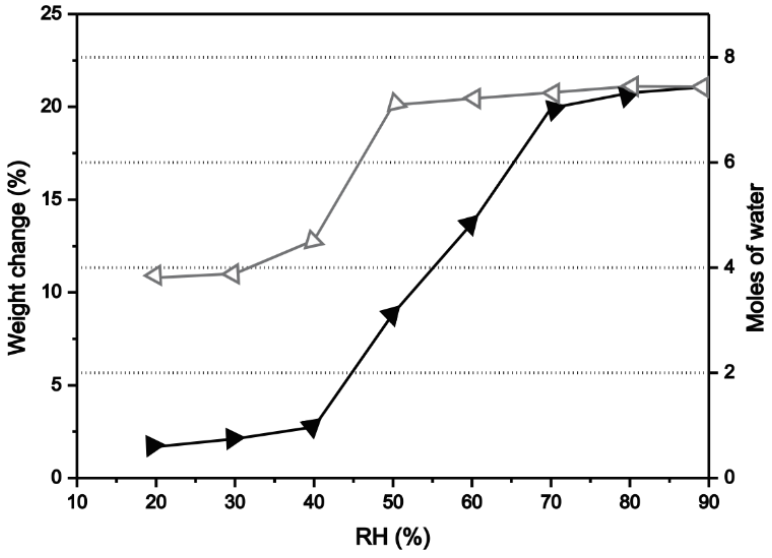


Figure 3.15. DVS isotherm of Hy0.3-1.0 showing slow conversion to Hy8 at higher humidities. Identical Hy8 desorption curve observed afterwards.

Upon sorption above 40% RH, the form takes up water at a higher rate, then transforms into Hy8 from 70% RH onwards. The curve records only a small increase from 70% RH (19.93%) onwards to the highest point of saturation of 90% RH, which is 21.09%, (7.44 moles of water); gaining just 1.38 moles of water from the 70% RH mark. The final figure is less than the expected value for Hy8, and the slow transition is reminiscent of the transition of Hy4 to Hy8 and presumably hampered by the low crystallinity of the sample as shown by the humidity-dependent PXRD data, and potential amorphous fraction (Figure 3.4) introducing a kinetic component to the event.

3.4.3 Crystal form from direct crystallisation: The monohydrate

A full crystallisation screening was performed to attain the intermediate hydrated forms (following desorption of Hy4 at 2% RH). The screen resulted in two more hydrate forms, which one form is showing unique needle-shaped crystals habit (Figure 3.16). Two solvate forms were also found from methanol and DMSO respectively. Table 3.1 lists a summary of the crystal forms obtained from the screening process.

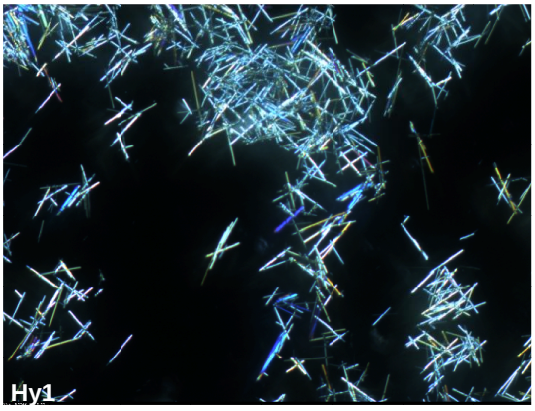


Figure 3.16. Photomicrograph showcasing the unique needle habit, only observe in Hy1 form.

The first of the two new hydrate forms is crystallised from evaporation and slow cooling experiments using acetone, acetonitrile, the higher alcohols, nitromethane, ethyl acetate, THF and 2-butanone under ambient conditions. As stated, microscopic observation revealed that this form appears to have needles habit in contrast to the previous platy forms. PXRD analysis of this needle form shows different peak positions compared to Hy0.3-1.0, Hy4 and Hy8 (Figure 3.17), confirming that it was indeed a new form.

Table 3.1. Summary of slow cooling, fast cooling, precipitation, and evaporation experiments

Solvents	Slow cooling	Evaporation	Fast cooling	Precipitation
Acetone	Hy1	Amorphous	x[a]	x
Acetonitrile	Hy1	x	Amorphous	x
Amylalcohol	Hy1	x	x	x
1-Butanol	Hy1	x	x	x
2-Butanol	Hy1	Hy1	x	x
Chloroform	Amorphous	Amorphous	x	x
Dichloromethane	Amorphous	x	x	x
Diethyl ether	Amorphous	x	x	x
Dimethylformamide	Amorphous	x	Amorphous	x
Dimethylsulfoxide	x	x	x	Solvate
Dioxane	Hy1	Amorphous	x	x
Ethyl acetate	Hy1	x	x	x
Ethyl-methyl-ketone	Hy1	x	x	x

Ethanol	Hy1	Hy1+Hy2	x	x
Hexane	Amorphous	x	x	x
Methanol	Solvate	Hy1	x	Amorphous
Nitromethane	Hy1	x	x	x
1-Propanol	Hy1	Hy1	Amorphous	x
2-Propanol	Hy1	Hy1	Amorphous	x
Tetrahydrofuran	Hy1	Amorphous	x	x
Water	Hy4/Hy8	x	Hy4/Hy8	Hy4/Hy8

[a]: indicating solvent did not evaporate/ crystal did not form/ experiment unable to be performed.

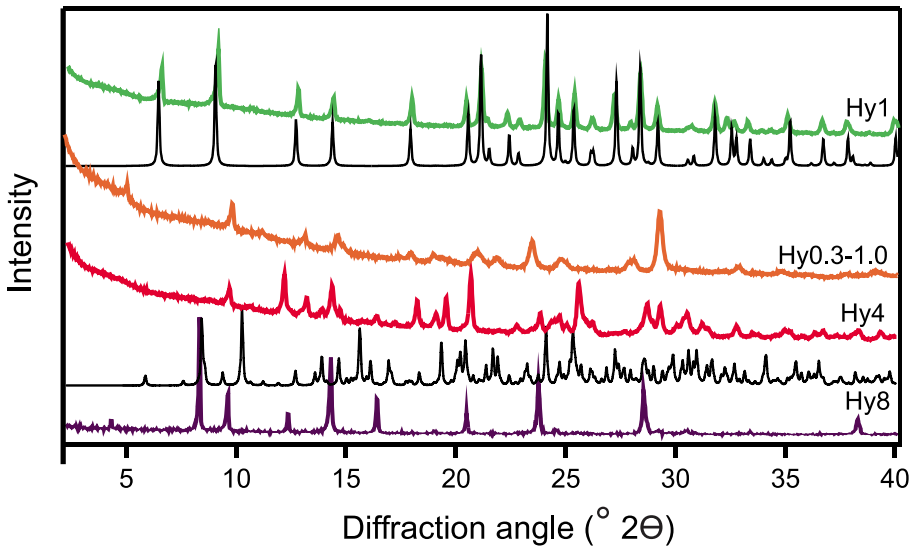


Figure 3.17. Monohydrate (Hy1) PXRD along with the calculated pattern (black) in comparison to Hy4, Hy8, and Hy0.3-1.0.

TGA analysis from ambient to 300 °C, shows 3.26% weight loss (Figure 3.18), which corresponds to 1.1 molar equivalents of water, hence this form in referred to as a monohydrate (Hy1). The TGA trace of Hy1 still share the continuous weight loss

feature when compared to the thermogram of Hy4 and Hy8 (Figure 3.6), with almost immediate, continuous weight loss observed even at lower temperature, however the dehydration slope of Hy 1 is less steep, with an apparent weight drop above 50 °C, hinting towards a more relatively stable hydrate compared to Hy4 and Hy8. A steeper slope would suggest that the volatile inclusion is not 'held' or bound as strong, hence liberated quicker at a similar heating rate.

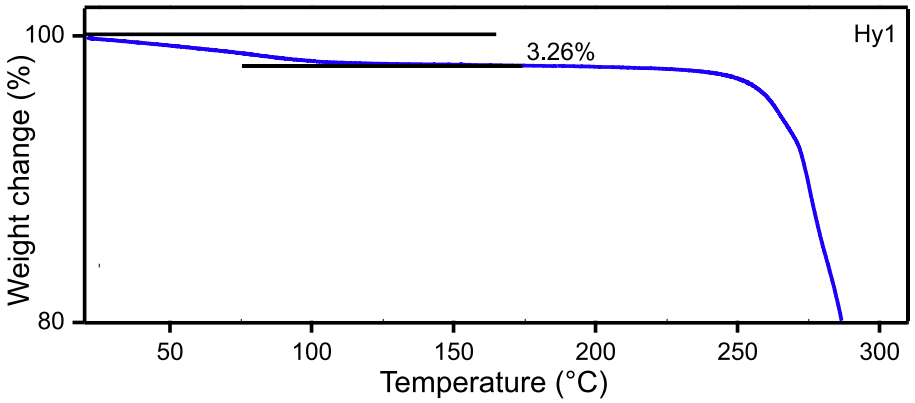


Figure 3.18. TGA thermogram of Hy1 recorded at 10 °C min^{-1}

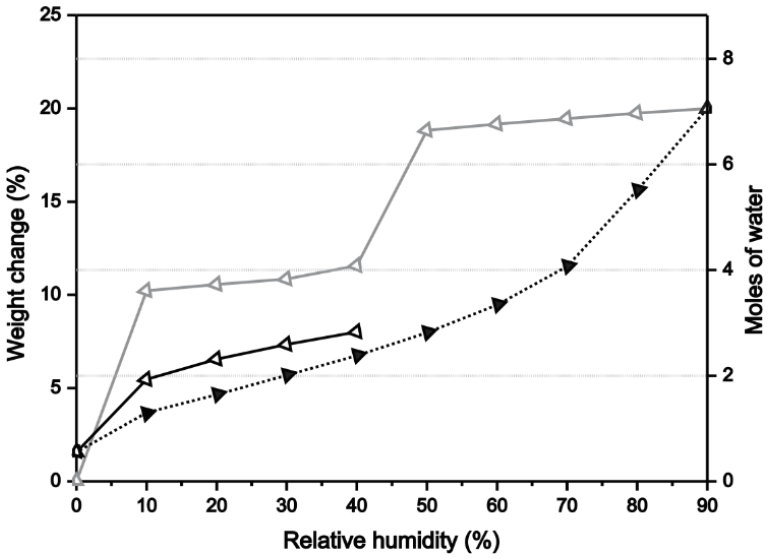


Figure 3.19. DVS isotherm of Hy1 starting from room conditions down. Isotherm is normalised to the lowest point of the measurement.

The DVS isotherm of Hy1 (Figure 3.19) shows that the initial DVS value reads 8% of volatile inclusion, a marked increase as compared to the water content of the same form (Hy1) as determined by Karl-Fischer titration which is just above 1 mole of water (3.75% corresponding to 1.375 molar equivalents of water. The reason for a higher DVS reading could be due to a low impurity of the material, potentially a higher hydrate, even though PXRD detected no impurities (Figure 3.17). Another possibility is that this hydrate shows non-stoichiometric characteristics, by having the ability to incorporate a higher amount of water at higher humidity. Desorption isotherm starting from 40% RH (room conditions) towards lower humidity shows a gradual release of the incorporated solvent with an increase in rate from 10% towards 0% RH. Following the sorption isotherm from 0 to 40% RH, the curve runs in parallel to the desorption, but at a lower weight. The increase in weight for the sorption run is due to the intake of water since the atmosphere in the instrument only contains water vapour. The difference in desorption and sorption curve would corroborate the assumption of a low fraction impurity containing either a considerable amount of water or a heavier solvent, e.g. ethanol from the solution crystallisation. Over the range from 10 to 60% RH, the sample shows an almost linear uptake of water, which agrees on the hypothesis of Hy1 being a non-stoichiometric hydrate. Unfortunately, the sample amount of Hy1 accessible by crystallisation is too low to perform humidity controlled PXRD measurements to prove this hypothesis. At humidity levels between 60 and 90% RH, the rate of weight gain increase as the sample converts to Hy8. A clear indication of Hy8 formation is that a similar curve to that of the octahydrate is observed following desorption.

Hy1 single crystals are grown in a slowly cooled ethanol solution and crystallise out in tetragonal space group *I*4*cm* with half a molecular unit in the

asymmetric unit (Table 3.2). As expected, water is coordinated to the sodium cation (Figure 3.20). The packing shows both linear coordination polymeric strands as well as hydrogen bonding motifs running on parallel along the *c* axis (Figure 3.21). Similar to Hy4, the sodium cations coordinate to the deprotonated acid, however, the coordination scheme between Hy1 and Hy4 forms is different. The previous report mentions that the carboxylate in Hy4 coordinates to the sodium ion through one oxygen atom, while the other oxygen atom accepts a hydrogen bond from a water molecule. While Hy1 also shows one carboxylic atom coordinating to one sodium cation, but the other oxygen atom coordinates to two more sodium cation in the subsequent layer, along the *c* axis. This coordination pattern results in a square of alternating sodium and oxygen atoms, in which each carboxylic acid bonds to three sodium cations and each sodium bonds to three carboxylates. The water molecule finally bonds to a sodium cation, creating a fourth coordination bond. Remarkably, the incorporated water molecule does not donate any hydrogen bonds to the surrounding molecules and only acts as a filler for the coordination shell and space filler for the structure. The diatrizoate anions show the cis conformation in which the amide carbonyl moieties point towards one side of the central ring and the amino moieties are directed to the opposite side.[47] The conformation allows chain-like or catemeric hydrogen bonding between the coordination polymeric strands along the *c* axis. Halogen bonds are not found in this structure. Overall, Hy1 packs more efficiently compared to Hy4 with a calculated density of 2.50 *vs.* 2.33 g cm^{-3} (Table 3.2). As most solution crystallisations resulted in Hy1 (Table 3.1), suggests that this form has lower energy, hence relatively more stable than the other forms. As mentioned earlier, TGA of the Hy1 also points to the form's higher relative stability compared to Hy4 and Hy8 due to a more gradual, less steep desolvation curve.

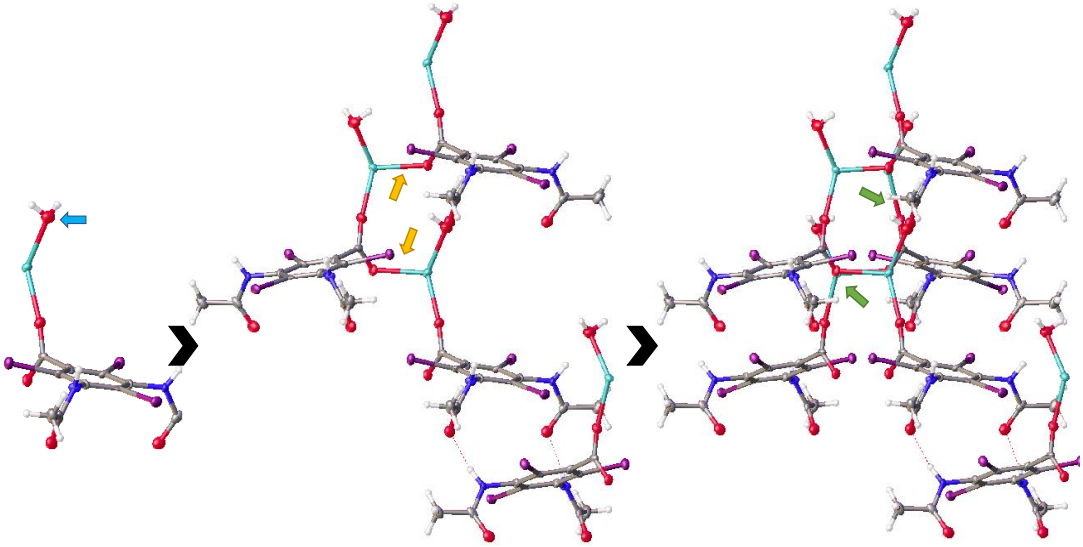


Figure 3.20. DTS Hy1 molecule showing water coordination towards the sodium cation (far left: blue arrow); sodium-acid (middle: yellow arrow) coordination observed towards a second DTA as the catameric strand grows; acid-sodium coordination (far right: green arrow) towards a third DTA. The colour code is carbon grey, nitrogen blue, oxygen red, iodine purple, sodium cyan and hydrogen light grey and this colour coding will be adapted for all following figures.

Table 3.2: Crystallographic data of the crystal forms of DTS

Crystal form	Hy1	Hy0.5-3.5	Methanol solvate	DMSO/H_2O 1:1 solvate
Formula	$C_{11}H_8N_2O_4I_3$ Na x H_2O	$C_{11}H_8N_2O_4I_3$ Na x 1.6 H_2O	$C_{11}H_8N_2O_4I_3$ Na x 3 CH_4O	$C_{11}H_8N_2O_4I_3$ Na x H_2O x C_2H_6SO
*M*r [g mol^{-1}]	653.92	660.90	732.01	732.05
Crystal system	Tetragonal	Tetragonal	Monoclinic	Orthorhombic
Space group	*I*4*cm*	*I*4$_1$/*a*	*P*2$_1$/*c*	*Pca*2$_1$
T [K]	120	100	120	120
a [Å]	19.965(1)	24.947(1)	7.9669(3)	16.9591(8)
b [Å]	19.965(1)	24.947(1)	11.2998(3)	12.9735(6)

c [Å]	8.7022(7)	12.7382(7)	24.4405(7)	9.6080(4)
α [°]	90	90	90	90
β [°]	90	90	90.753(3)	90
γ [°]	90	90	90	90
V [Å^3]	3468.5(4)	7927(8)	2200.1(1)	2113.9(2)
Z	8	16	4	4
ρ_{calcd} [g cm^{-3}]	2.5043	2.2147	2.210	2.300
λ [Å]	0.71073	0.68890	0.71073	0.71073
μ [mm^{-1}]	5.453	4.774	4.317	4.585
F(000)	2390	4823	1376	1364
θ range for data collection	2.04 – 26.00	1.80 – 25.99	2.455 – 26.000	2.40 – 26.00
Index ranges	-26 > h > 24	-40 > h > 40	-9 > h > 7	-21 > h > 21
	-25 > k > 25	-40 > k > 40	-13 > k > 13	-16 > k > 16
	-12 > l > 12	-20 > l > 20	-30 > l > 30	-12 > l > 12
Reflections collected	24882	88103	16707	30704
Independent reflections	1784	3894	4314	4131
Refinement method		Full-matrix least-squares on F^2		
Data/restraints/parameters	1784/9/112	3894/0/210	4314/9/258	4131/0/239
GOOF on F^2	0.9375	1.0255	1.044	1.0536
Final R indices (I>2σ(I))	R_1 = 2.83	R_1 = 7.32	R_1 = 3.54	R_1 = 1.69
	wR_2 = 8.22	wR_2 = 23.90	wR_2 = 7.09	wR_2 = 3.67
R indices (all data)	R_1 = 4.19	R_1 = 7.52	R_1 = 5.10	R_1 = 1.84
	wR_2 =8.89	wR_2 = 24.14	wR_2 = 7.82	wR_2 = 3.76
Largest difference peak and hole [e Å^{-3}]	1.1572 and -1.0746	-3.0348 and 3.8870	1.313 and -0.676	0.8993 and -0.9424

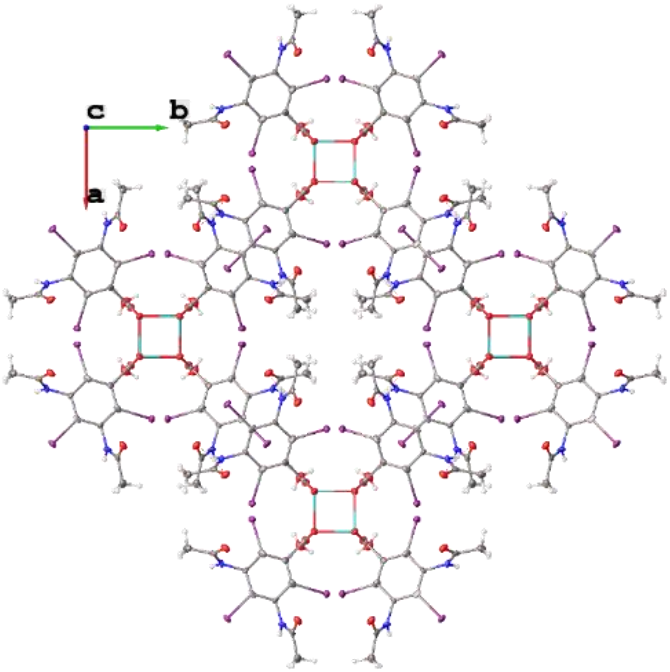


Figure 3.21. Packing representation of the single crystal structure of Hy1. For this and all following structural representations, anisotropic displacement parameters are drawn at 50% probability.

3.4.4 The 0.5-3.5 hydrate

Another hydrate form obtained from direct crystallisation is a platy form, which grows concomitantly with Hy1 from the evaporation of ethanol solution (Figure 3.22). The platy crystal has a distinctly different PXRD trace compared to the other previously discussed forms (Figure 3.23). The platy form is then isolated and seeded using slow-cool experiment with ethanol as the solvent for subsequent analysis. TGA measurements reveal a water content of 6.83%, which correlates with 2.6 molar equivalents of water (Figure 3.24).

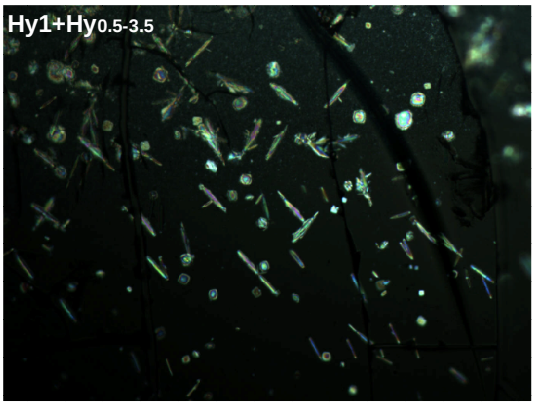


Figure 3.22. Photomicrograph of the platy second hydrate grows concomitantly with the needle habit of Hy1 form.

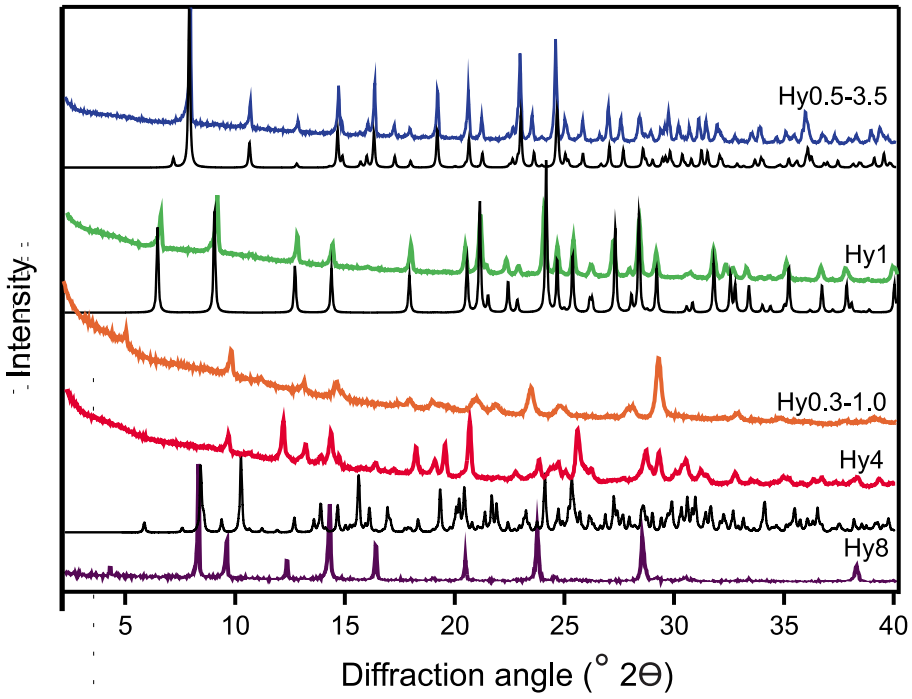


Figure 3.23. Hydrate 0.5-3.5 PXRD comparison to Hy1, Hy4, Hy8, and Hy0.3-1.0.

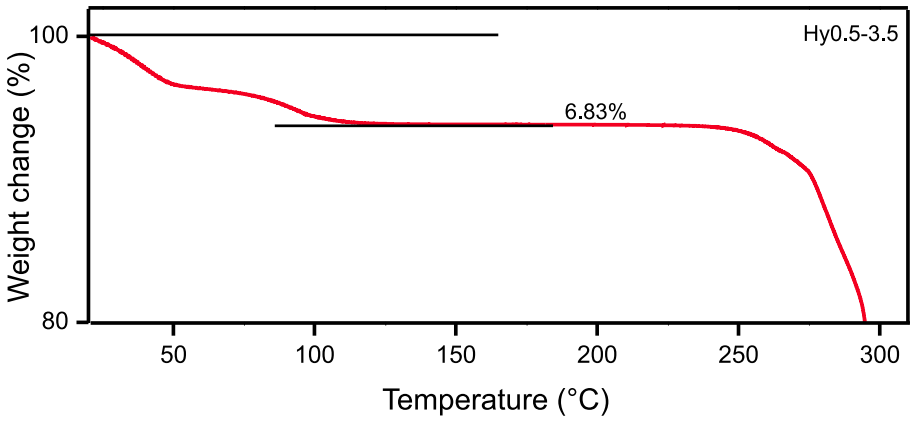


Figure 3.24. TGA thermogram of Hy0.5-3.5 recorded at 10 °C min^{-1}.

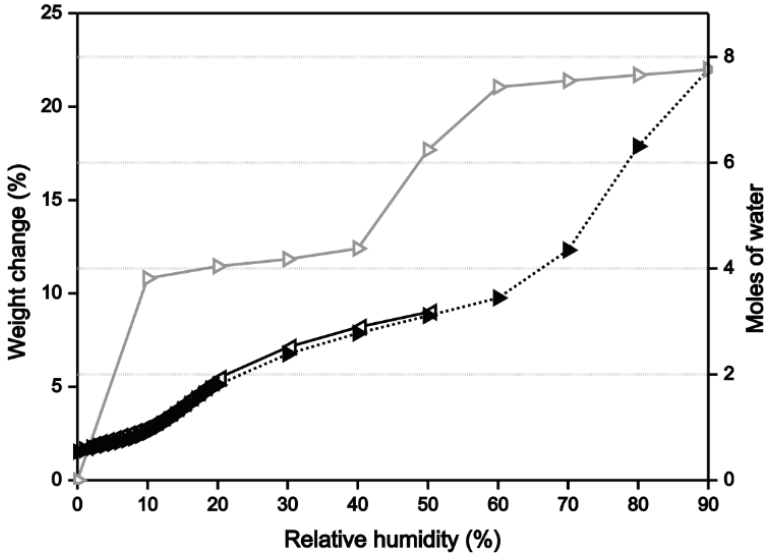


Figure 3.25. DVS isotherm of Hy0.5-3.5 starts from room condition, with initial desorption down the humidity range. Isotherm is normalised to the lowest point of the measurement.

The DVS isotherm of this hydrate reveals that the sample contains 8.99% volatile component (3.2 molar equivalents of water), which is slightly higher weight percentage compare to the weight loss from TGA measurement when normalised to the lowest isotherm point of zero (Figure 3.25). Upon lowering the humidity, the sample loses weight in a continuous manner, which speeds up between 20 and 10% RH while stabilising again between 10 and 0% RH. Following desorption, the lowest water content of this hydrate is 0.5 molar equivalents, recorded at 0% RH. The sorption

isotherm follows an almost identical path to the desorption proving the non-stoichiometric character of this hydrate. The highest water content of this form is 9.75% (3.44 molar equivalents of water), as the humidity reaches 60% RH. Thus the ranges of this hydrate are between 0.5 and 3.5 molar equivalents of water, hence it is identified as Hy0.5-3.5. Above 60% RH, the sample takes up water at a higher rate and transforms to the octahydrate. Almost full hydration of Hy8 is reached indicating only minor traces of impurities. The second desorption isotherm trace is the same as that of Hy8. Diffraction data of Hy0.5-3.5 were collected on the synchrotron beamline I19 at Diamond Light Source, Oxfordshire, UK, due to the small size of the individual crystals. The structure solution shows that this hydrate crystallises in the tetragonal space group $I4_1/a$ with one molecular unit in the asymmetric unit (Table 3.2). Surprisingly, only 1.6 molar equivalents of water can be refined, even though additional electron density points towards more disordered water in this structure. As in the other hydrates, the carboxylate moieties coordinate to the sodium cations; however, in Hy0.5-3.5 only one of the oxygen atoms is involved in the coordination. The resulting motif is a slightly twisted cube with alternating sodium and oxygen atoms at its corners (Figure 3.26). Each sodium cation furthermore coordinates to a water oxygen atom, whilst two half-occupied water positions bridge two faces of the cube. Comparable to Hy4, the second oxygen atom of the carboxylate moiety is involved in hydrogen bonding with a coordinate water molecule (donor-acceptor heavy atom distance: 2.74(2) Å). The hydrogen bonding motif found between the diatrizoate ions resembles that of Hy4: centrosymmetric dimers show hydrogen bonding between one amide N-H moiety to the non-coordinated oxygen atom of the carboxylate, whilst the N-H of the second amide hydrogen bonds to a third diatrizoate amide carbonyl. The latter hydrogen bond leads to spirals along the 41 axis. Halogen

bonds involving the iodine atoms are realised with both amide carbonyl oxygens as well as to the disordered water.

The structure contains a 2-dimensional network of solvent-accessible channels, which run along the crystallographic *a* and *b* axes (Figure 3.27). These channels are the reason for the non-stoichiometric behaviour observed by DVS, as water from the environment can diffuse in and out of the structure without changing the overall scaffold. This hypothesis is corroborated by the remaining electron density, which is located within the channels and points towards additional disordered water molecules. Compared to Hy4 and Hy1, Hy0.5-3.5 has with 2.14 g cm^{-3} the lowest density, which may be due to missing modelled water. However, the low density points towards the highest energy and thus the lowest stability of this crystal form. This is corroborated by the occurrence of Hy0.5-3.5 in only one crystallisation experiment and even then only concomitantly with the more stable Hy1.

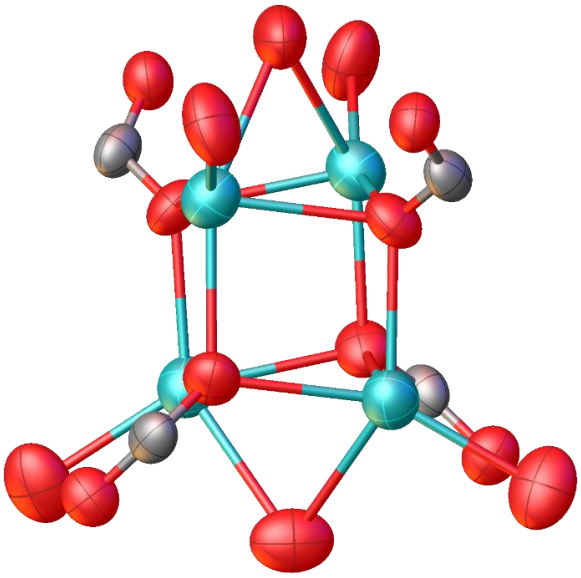


Figure 3.26. A cluster of sodium cations, carboxylate moieties and water molecules of the Hy0.5-3.5 structure.

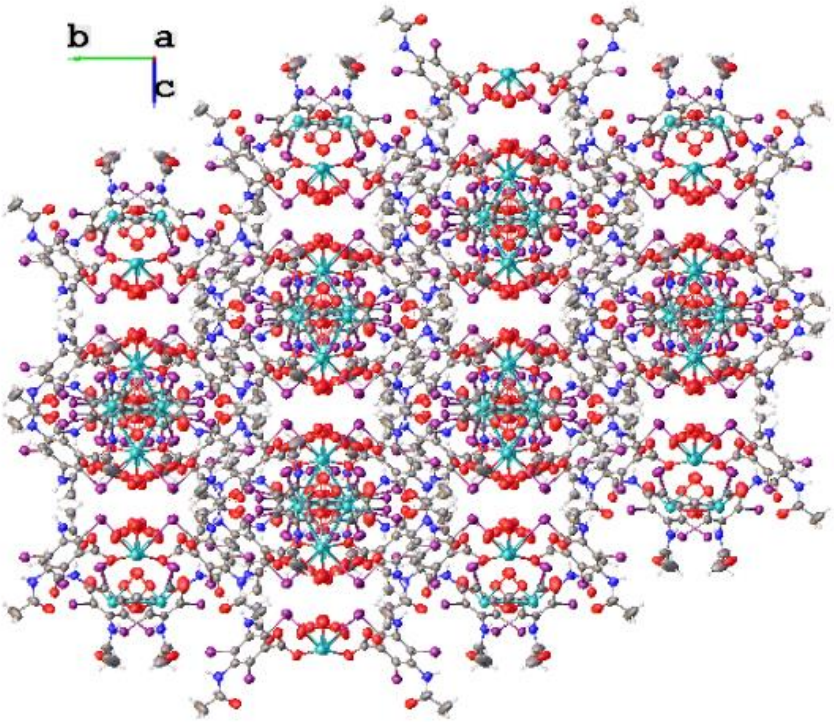


Figure 3.27. Packing of the crystal structure of Hy0.5-3.5 along the crystallographic a axis with clearly visible pores.

3.4.5 The solvates

In addition to the hydrated crystal forms, DTS was also found to exist as two solvates, of methanol and DMSO respectively, as confirmed by PXRD (Figure 3.28). The methanol solvate shows a weight loss of 13.03% by TGA, which corresponds to 3 molar equivalents of methanol (calculated weight loss 13.113%, Figure 3.30). The methanol trisolvate grows as large blocks from the slow cooling experiment of methanol. As methanol is only slightly bigger than water and can comparably coordinate to the sodium cation, it is not surprising DTS takes up such a high number of methanol molecules, considering the complex hydration behaviour as discussed above. TGA of the methanol solvate suggests the form's low stability as the weight

loss of starts at room temperature, and it is likely that desolvation occurs under dry conditions. The low stability is also apparent from the fact that Hy1 is crystallised from methanol by evaporation under ambient conditions (approximately 40% RH).

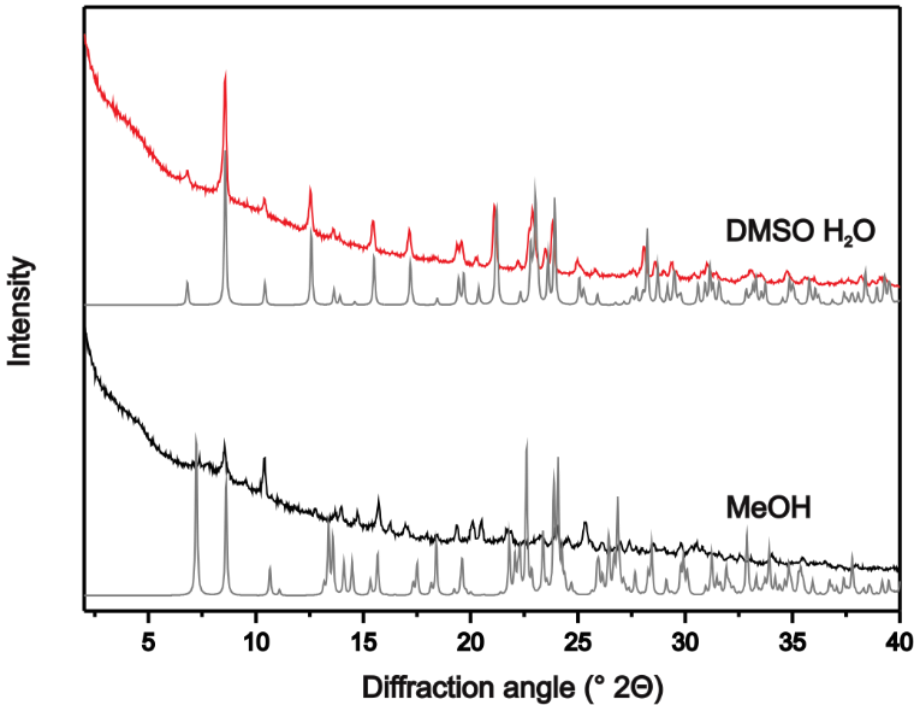


Figure 3.28. PXRD patterns of the solvates of DTS with the calculated patterns of the crystal structures (grey).

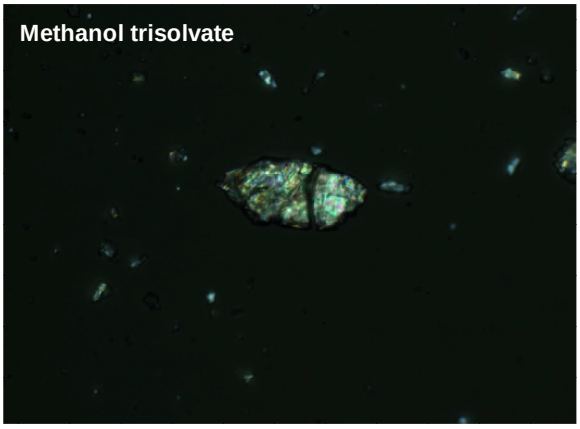


Figure 3.29. Photomicrograph of the methanol trisolvates habit.

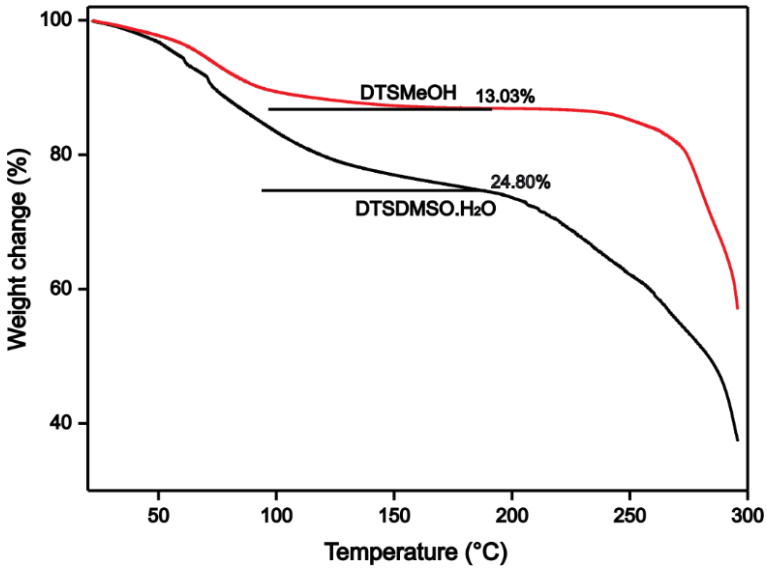


Figure 3.30. TGA thermograms of the methanol and 1:1 DMSO/H_2O solvates of DTS.

Methanol solvate single crystal is grown in a slowly cooled methanol solution to a size suitable for X-ray diffraction. The resultant structure revealed to be indeed a trisolvate, with three solvent molecules coordinating to the sodium cation; along with carboxylate group and one amide carbonyl.

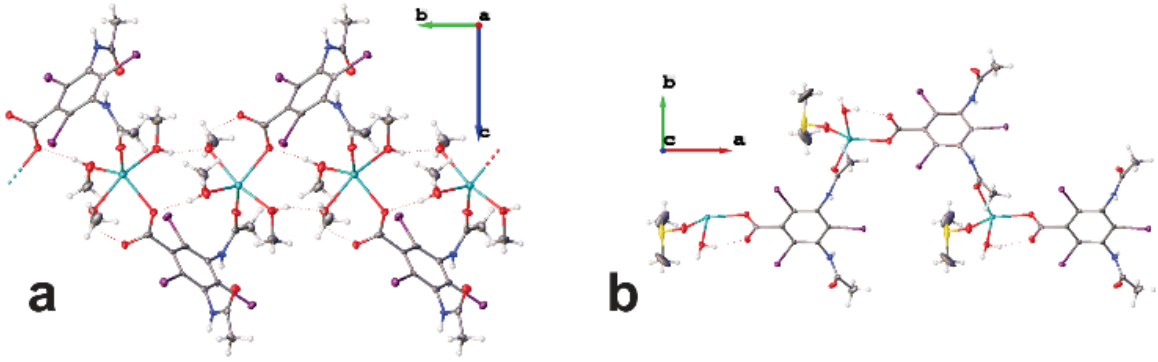


Figure 3.31:1D coordination polymers of the (a) methanol and (b) DMSO/H_2O solvates of DTS.

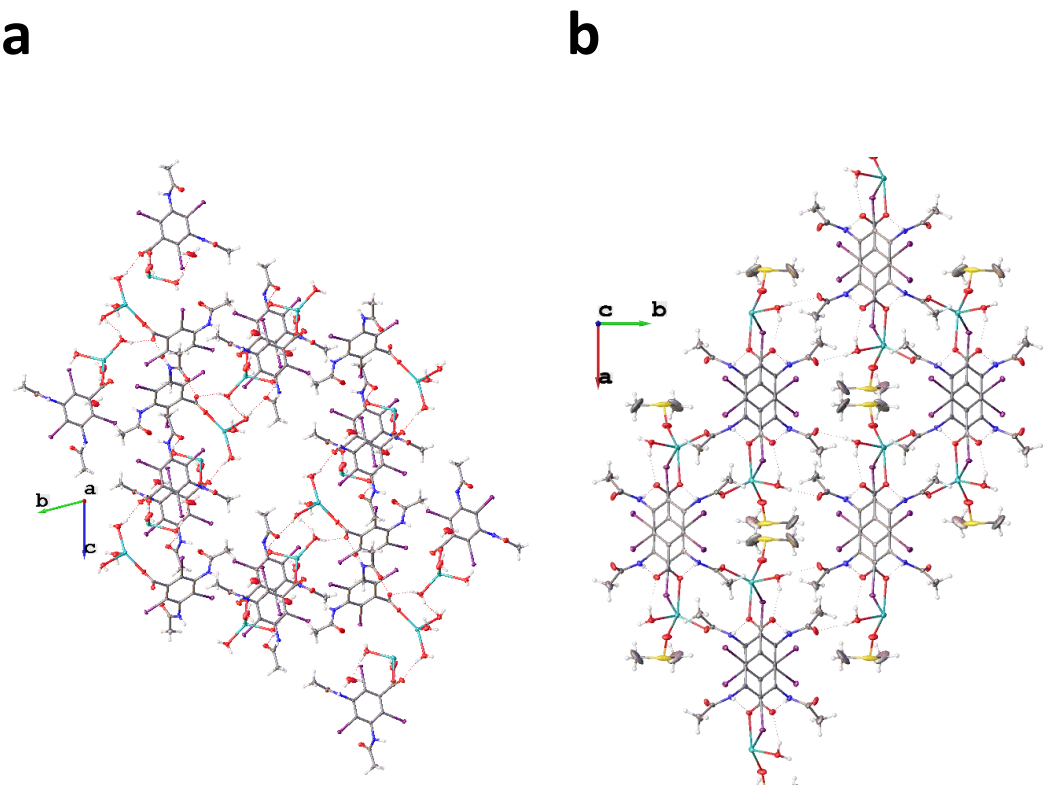


Figure 3.32: Packing of the crystal structure of DTS (a) methanol and (b) DMSO/H_2O with the DMSO channels running along c.

The structure crystallises in the monoclinic space group $P2_1/c$ with one molecular unit in the asymmetric unit. The latter interaction is not realised in any of the hydrate structures and leads to 1D coordination polymeric chains along the crystallographic *b* axis. The second amide group accepts a hydrogen-bond from the amide N-H moiety of a neighbouring anion, which connects the polymeric chains with each other. Two of the methanol molecules are hydrogen-bonding to the carboxylate moiety of the anion, whilst the third methanol donates a hydrogen bond to a neighbouring methanol molecule. The solvate has relatively low stability despite having no clear channels which stop the solvent from diffusing through, coupled with the fact that the incorporated methanol being hydrogen-bonded.

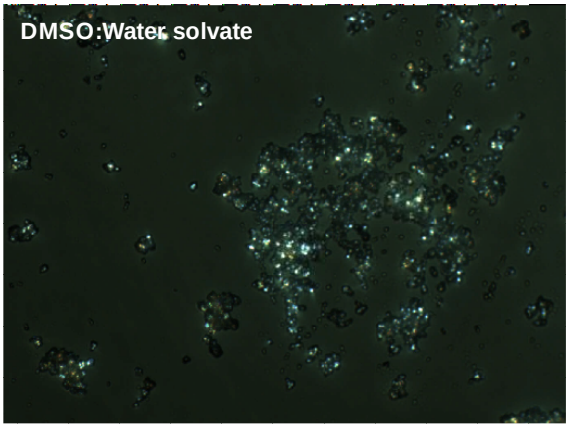


Figure 3.33: Photomicrograph of the DMSO/water solvate habit.

The second solvate is obtained from precipitation of DTS from DMSO solution with dichloromethane as the antisolvent. The small, irregularly shape (Figure 3.33), metastable solvate shows an experimental weight loss of by 24.8% TGA (Figure 3.30); which corresponds to one molecule of DMSO and water each per DTS. TGA observation also revealed although different, both solvent species are showing similar trace trend with immediate weight loss at a lower temperature. Both solvent species also release the incorporated solvents from the crystal lattice at about the same time, showing that the initial crystal structure is not stable without either of the guest components and collapses.

DMSO/water mixed solvate crystallises in the orthorhombic space group $Pca2_1$ with one molecular unit in the asymmetric unit. The sodium cation has the lowest coordination number with only four oxygen atoms (one from each solvent, two from diatrizoate) interacting with it. The coordination of two oxygen atoms of the anion through the carboxylate as well as one amide carbonyl leads to the presence of 1D coordination polymeric chains comparable to the methanol solvate. However, the geometry of the chain in this solvate is more open and linear due to the lack of hydrogen bonds, which in the case of the methanol solvate leads to a spiral with a short

pitch length. The open chains of the DMSO/H2O 1:1 solvate pack closely on top of each other leading to a herringbone packing. Whilst the incorporated water is donating hydrogen bonds to both the carboxylate and the amide moiety of the anion; the DMSO molecules are only coordinated to the sodium ion through their oxygen atoms and thus show higher motion around this hinge (detected as larger ADPs, Figure 3.32 (b)). Even though this mixed solvate is metastable, it gives another indication of the high attraction of DTS to water.

3.5 Chapter summary and conclusion

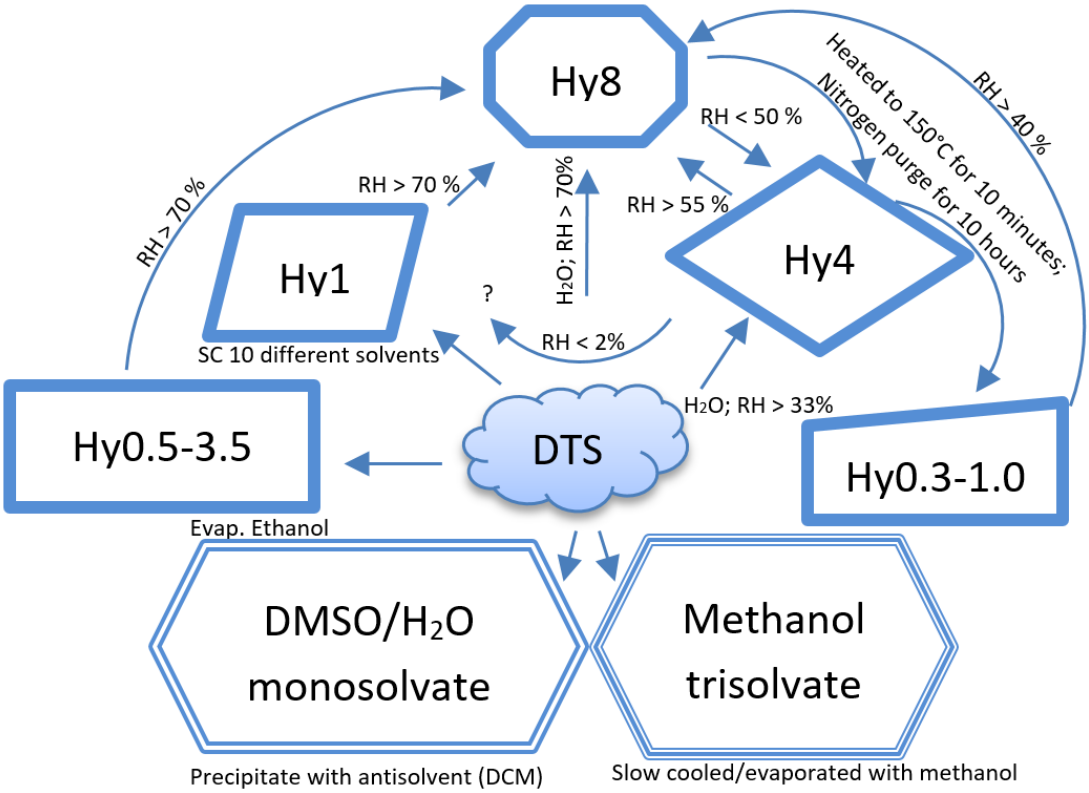


Figure 3.34: Schematic representation of the crystal forms and transformation pathways of DTS

In-depth solid-state workup reveals that diatrizoic acid monosodium salt to exists in at least five hydrated crystal forms and two solvates (Figure 3.34). Overall, a wide range of water incorporation is observed, with three of them (Hy8, Hy1 and

Hy0.5-3.5) crystallise directly from solution while dehydration of Hy8 yields the remaining hydrates (Hy4 and Hy0.3-1) along with one unconfirmed transient monohydrate. All the reported hydrate forms convert to Hy8 at high humidity levels. Meanwhile, the solvates contain three moles of methanol or one mole each of DMSO and water in a mixed solvate.

Strong involvement of the sodium cation along with additional stabilising hydrogen bonding is observed from structural analysis of three hydrates and both solvates. The monohydrate and both solvates show 1D coordination polymers through interaction between the organic anion and the sodium ion. Coordination of all incorporated water is directed towards the cation and hydrogen bonds to other moieties of the crystal structure. However, Hy4 is reported to have a second water coordination motif, where water molecule acts as a bridge between the two amide carbonyl groups of the same molecule.[47] No anhydrous crystal form of DTS could be identified. DTS complex solid-state behaviour highlights the importance of having a complete solid-state landscape for any sodium salt under variable humidity conditions. The connection, as well as interconversion between the DTS hydrates, showcases the importance of humidity-controlled experiments to fully understand any pharmaceutical sodium salts, before formulation and manufacturing.

As almost all of the structure of the crystalline form of DTS obtained contained water (except for the methanol solvate), it is a clear indication that water incorporation into the crystal lattice stabilises the structure. As the formed hydrates show a wide range of water content, consequently, such variety will be problematic in terms of measuring and maintaining dose, solubility and uniformity of any produced solid formulation. The instability and frequent phase changes with varying the humidity,

coupled with possible amorphisation upon dehydration or desolvation, presents an additional complication for manufacturing and stability of the final formulation. Even though DTS is not currently marketed as a solid, it is a good model compound to demonstrate the potential hazards of sodium salts in water-containing environments as well as highlighting the importance of a full and in-depth characterisation of other sodium salts used pharmaceutically. Furthermore, although it is common for most alkali and earth alkali salts to form hydrates by taking up water to complete their coordination shell, as well as for compound with charged or polar groups to incorporate water, in all cases, one cannot definitively say a hydrate has or will form.This uncertainty makes the screening for hydrates challenging and even more so when it comes to determining the stoichiometry (the compound: water ratio). Earlier prediction of hydrate formation would allow control over the emerging form; hence, investigating the interactions of drug and water in the solution-state is potentially useful as this allows observation to be done before the formation of the crystalline form.

3.6 References

1. Morris, K. R. *et al.* An integrated approach to the selection of optimal salt form for a new drug candidate. *Int. J. Pharm.* **105,** 209–217 (1994).

2. Khankari, R. & Grant, D. J. W. Pharmaceutical hydrates. *Thermochim. Acta* **248,** 61–79 (1995).

3. Paulekuhn, G. S., Dressman, J. B. & Saal, C. Trends in active pharmaceutical ingredient salt selection based on analysis of the Orange Book database. *J. Med. Chem.* **50,** 6665–72 (2007).

4. Najib, M. N. M., Back, K. & Edkins, K. The Complex Solid-State Landscape of Sodium Diatrizoate Hydrates. *Chem. - A Eur. J.* **23,** 17339–17347 (2017).

5. Bastin, R. J., Bowker, M. J. & Slater, B. J. Salt Selection and Optimisation Procedures for Pharmaceutical New Chemical Entities. *Org. Process Res. Dev.* **4,** 427–435 (2000).

6. Serajuddin, A. T. M. Salt formation to improve drug solubility. *Adv. Drug Deliv. Rev.* **59,** 603–616 (2007).

7. Berge, S. M. *et al.* Pharmaceutical salts. *J. Pharm. Sci.* **66,** 1–19 (1977).

8. Gould, P. L. Salt selection for basic drugs. *Int. J. Pharm.* **33,** 201–217 (1986).

9. Bansal, A. K., Kumar, L. & Amin, A. Salt Selection in Drug Development. *Pharm. Technol.* **32,** 128–146 (2008).

10. Paulekuhn, G. S., Dressman, J. B. & Saal, C. Trends in active pharmaceutical ingredient salt selection based on analysis of the orange book database. *J. Med. Chem.* **50,** 6665–6672 (2007).

11. *Pharmacopoeia Europaea 9.0*. (Deutscher Apotheker Verlag, 2016).

12. Ahlneck, C. & Zografi, G. The molecular basis of moisture effects on the physical and chemical stability of drugs in the solid state. *Int. J. Pharm.* **62,** 87–95 (1990).

13. Infantes, L., Chisholm, J. & Motherwell, S. Extended motifs from water and chemical functional groups in organic molecular crystals. *CrystEngComm* **5,** 480 (2003).

14. Debnath, S., Predecki, P. & Suryanarayanan, R. Use of Glancing Angle X-Ray Powder Diffractometry to Depth-Profile Phase Transformations during Dissolution of Indomethacin and Theophylline Tablets. *Pharm. Res.* **21,** 149–159 (2004).

15. Airaksinen, S. *et al.* Role of water in the physical stability of solid dosage formulations. *J. Pharm. Sci.* **94,** 2147–2165 (2005).

16. Szakonyi, G. & Zelkó, R. The effect of water on the solid state characteristics of pharmaceutical excipients: Molecular mechanisms, measurement techniques, and quality aspects of final dosage form. *Int. J. Pharm. Investig.* **2,** 18–25 (2012).

17. Di Martino, P., Barthélémy, C., Palmieri, G. F. & Martelli, S. Physical characterization of naproxen sodium hydrate and anhydrate forms. *Eur. J. Pharm. Sci.* **14,** 293–300 (2001).

18. Di Martino, P. *et al.* A new tetrahydrated form of sodium naproxen. *J. Pharm. Sci.* **96,** 156–67 (2007).

19. Qu, H. *et al.* Influence of Temperature on Solvent-Mediated Anhydrate-to-Hydrate Transformation Kinetics. *Pharm. Res.* **28,** 364–373 (2011).

20. Tian, F. *et al.* Factors affecting crystallization of hydrates. *J. Pharm. Pharmacol.* **62,** 1534–1546 (2010).

21. Jelinski, L. W., Dumais, J. J., Stark, R. E., Ellis, T. S. & Karasz, F. E. Interaction of Epoxy Resins with Water. A Quadrupole Echo Deuterium NMR Study. *Macromolecules* **16,** 1019–1021 (1983).

22. Byrn, S., Pfeiffer, R., Ganey, M., Hoiberg, C. & Poochikian, G. Pharmaceutical solids: a strategic approach to regulatory considerations. *Pharm. Res.* **12,** 945–954 (1995).

23. Shalaev, E. Y. & Zografi, G. How Does Residual Water Affect the Solid-state Degradation of Drugs in the Amorphous State? *J. Pharm. Sci.* **85,** 1137–1141 (1996).

24. Yoshioka, S. & Aso, Y. Correlations between Molecular Mobility and Chemical Stability During Storage of Amorphous Pharmaceuticals. *J. Pharm. Sci.* **96,** 960–981 (2007).

25. Collier, J. W. *et al.* Influence of formulation and processing factors on stability of levothyroxine sodium pentahydrate. *AAPS PharmSciTech* **11,** 818–825 (2010).

26. Stephenson, G. A. & Diseroad, B. A. Structural relationship and desolvation behavior of cromolyn, cefazolin and fenoprofen sodium hydrates. *Int. J. Pharm.* **198,** 167–177 (2000).

27. Bartolomei, M., Rodomonte, A., Antoniella, E., Minelli, G. & Bertocchi, P. Hydrate modifications of the non-steroidal anti-inflammatory drug diclofenac sodium: Solid-state characterisation of a trihydrate form. *J. Pharm. Biomed. Anal.* **45,** 443–449 (2007).

28. Jaiboon, N. *et al.* New orthorhombic form of 2-[(2,6-dichlorophenyl)amino]benzeneacetic acid (diclofenac acid). *Anal. Sci.* **17,** 1465–1466 (2001).

29. Khankari, R., Chen, L. & Grant, D. J. W. Physical characterization of nedocromil sodium hydrates. *J. Pharm. Sci.* **87,** 1052–1061 (1998).

30. Vold, R. D. & McBain, J. W. The Solubility Curve of Sodium Deoxycholate in Water. *J. Am. Chem. Soc.* **63,** 1296–1298 (1941).

31. Ono, M. *et al.* Water Vapor Adsorption Behavior of Sodium Deoxycholate Anhydrous Forms. *Chem. Pharm. Bull. (Tokyo).* **53,** 180–183 (2005).

32. Su, Z. *et al.* Crystalline, liquid crystalline, and isotropic phases of sodium deoxycholate in water. *J. Pharm. Sci.* **100,** 4836–4844 (2011).

33. Malaj, L., Censi, R. & Di Martino, P. Mechanisms for Dehydration of Three

Sodium Naproxen Hydrates. *Cryst. Growth Des.* **9,** 2128–2136 (2009).

34. Pouton, C. W. Formulation of poorly water-soluble drugs for oral administration: Physicochemical and physiological issues and the lipid formulation classification system. *Eur. J. Pharm. Sci.* **29,** 278–287 (2006).

35. Savjani, K. T., Gajjar, A. K. & Savjani, J. K. Drug Solubility: Importance and Enhancement Techniques. *ISRN Pharm.* **2012,** 1–10 (2012).

36. Zupančič, V., Ograjšek, N., Kotar-Jordan, B. & Vrečer, F. Physical characterization of pantoprazole sodium hydrates. *Int. J. Pharm.* **291,** 59–68 (2005).

37. Raijada, D. *et al.* Exploring the Solid-Form Landscape of Pharmaceutical Hydrates: Transformation Pathways of the Sodium Naproxen Anhydrate-Hydrate System. *Pharm. Res.* **30,** 280–289 (2013).

38. Tong, P. & Zografi, G. Effects of water vapor absorption on the physical and chemical stability of amorphous sodium indomethacin. *AAPS PharmSciTech* **5,** 9–16 (2004).

39. Remenar, J. F. *et al.* Celecoxib sodium salt: engineering crystal forms for performance. *CrystEngComm* **13,** 1081–1089 (2011).

40. Bartolomei, M., Bertocchi, P., Antoniella, E. & Rodomonte, A. Physico-chemical characterisation and intrinsic dissolution studies of a new hydrate form of diclofenac sodium: Comparison with anhydrous form. *J. Pharm. Biomed. Anal.* **40,** 1105–1113 (2006).

41. Yamaguchi, K., Tamura, Z. & Maeda, M. Disodium fluorescein octahydrate. *Acta Crystallogr. Sect. C Cryst. Struct. Commun.* **53,** 284–285 (1997).

42. Rochdaoui, R., Sylvestre, J. P., Quy Dao, N., Lee, M. R. & Neuman, A. Structure du trihydrogéno hydroxy-1 ethanedi(phosphonate)-1,1 de sodium monohydrate. *Acta Crystallogr. Sect. C Cryst. Struct. Commun.* **46,** 2083–2086 (1990).

43. Croci, M. & Maruzzelli, G. Manufacture of semi-synthetic penicillin

antibiotics. (1981).

44. Tønnesen, L. E., Pedersen, B. F. & Klaveness, J. Acta Chem. Scand. 603–608 (1996). doi:10.3891/acta.chem.scand.50-0603

45. *United States Pharmacopoeia*. **40,** (The Stationary Office, 2017).

46. Substances, U. K. medicinal. British Pharmacopoeia. *Vol. V* **I,** A634 (2012).

47. Fucke, K. *et al.* Insights into the Crystallisation Process from Anhydrous, Hydrated and Solvated Crystal Forms of Diatrizoic Acid. *Chem. - A Eur. J.* **21,** 1036–1047 (2015).

48. Dowsett, D. *Radiological Sciences Dictionary: Keywords, names and definitions*. (Hodder Arnold, 2009).

49. Snopek, A. M. *Fundamentals of Special Radiographic Procedures.* (Elsevier Health Sciences, 2013).

CHAPTER 4

EXTENSIVE HYDRATE AND SOLVATE FORMATION OF THE ANTIALLERGIC COMPOUND TRANILAST

4.1 Chapter overview

Hydrate formation is a major problem in the pharmaceutical industry as it can reduce aqueous solubility and may impact drug stability. As part of our project to understand hydrate formation as well as the role which water plays, we investigate tranilast, an orally administered drug with poor aqueous solubility, reported to exists as an amorphous, five polymorphic monohydrates, three polymorphs and two solvates. However, data on the hydration behaviour is limited, with the monohydrate structures remaining unknown. Hence, a thorough polymorphism screening and a systemic investigation into the hydration behaviour were performed. Overall, we have observed 22 forms, of which 18 are novel. In addition to six solvates and one solvent/water mixed solvate, we have found tranilast to exist as at least 11 hydrate forms: a trihydrate, a 2.3 hydrate, a 1.8 (transient) hydrate, three polymorphic monohydrates (one of which has been reported before), two 0.8 hydrates (exact water content are 0.8 and 0.7-0.8), a 0.6-0.7 hydrate, a hemihydrate and a 0.4 hydrate. Interestingly, gravimetric humidity variation analysis shows a stoichiometric hydrate to a non-stoichiometric interchange; also a complex hydrate interconversion coming from the methanol/water mixed solvate. Tranilast shows an unusually complex hydration behaviour for an uncharged drug molecule, highlighting the importance of a thorough understanding of the solid-state landscape to ensure patients' safety and efficient manufacturing process

4.2 Introduction

4.2.1 Background and significance

Hydrate formation is well-known issue in pharmaceuticals. It is estimated that one in three active pharmaceutical ingedients (APIs) can crystallise as the hydrate form.[1] Water inclusion generally changes the intermolecular interactions within a crystal lattice. As a result, the hydrate is more thermodynamically stable in aqueous environments, having a lower free Gibbs energy than the anhydrous form, effectively lowering its solubility.[2] A drug must be present in solution at the site of absorption to be absorbed. Unintentional hydrate formation which lead to the decrease in the aqueous solubility is problematic. Poor solubility is a longstanding and significant problem in pharmaceuticals, which is over-emphasised for oral solid dosage form. Considering that the oral route of drug administration is the most simple and convenient for patients,[3] and solid, *e.g.* tablets, is the most popular oral dosage form (not only to patient, but also to manufacturer for various reasons, ranging from the ease of ingestion and production, to versatility in accommodating drug candidate),[4] the problem will persist as the oral route and solid continues to be the route and dosage form of choice. To exacerbate, the number of new chemical entities in drug development having poor water solubility has significantly increased (to almost 90% in one report).[5,6] As highlighted in chapter 3, API modification to improve aqueous solubility, *e.g.* salts formation, can backfire and lead to the formation of complex hydrate landscapes instead. For example, sodium diatrizoate is found to exist as five hydrate forms, with water content ranging from 0.3 to 8 molar equivalents, and showing complex transition profile between the forms (chapter 3).[7] Another example is sodium naproxen which has been reported to exist as one monohydrate, two

polymorphic dihydrate and a tetrahydrate.[8] The report revealed that the interconversion between the different sodium naproxen hydrate forms are centred around the polymorphic dihydrate form. Another salt form drug reported to have a complex solid form landscape is sitagliptin L-tartrate, which exist as a tetrahydrate and four hemihydrate forms.[9] The controlling factor for the different hydrate formation is said to be the different solvent composition, making finding the relationship between the forms difficult. Other examples of salt drugs having complex hydrate landscape include pamidronate disodium (existing as mono-, tri-, tetra- and pentahydrate),[10,11] and pantoprazole sodium (existing as hemi-, mono, sesqui- and dihydrate).[12] In contrast, the complex hydrate landscape is less familiar for the neutral or uncharged molecule. For example, paracetamol[13–15] is reported to exist as three hydrate forms, cimetidine exist as three polymorphic monohydrates,[16] while gabapentin exists as two polymorphic monohydrate[17,18] and a heptahydrate.[19]

Interestingly, the simple hydrate landscape property is not echoed for an antiallergic drug, tranilast (TRN). TRN has been reported to exist as five polymorphic monohydrates, two solvates, three polymorphs, and one amorphous form.[20] However, the literature of the solid-state forms are ambiguous, with CCDC database search accounts for two dissimilar crystal structure of the anhydrous polymorph,[21,22] two different chloroform ($CHCl_3$) solvate structure,[22,23] and dichloromethane (DCM) solvate.[22] In general, TRN is poorly water-soluble hence has low bioavailability. Interestingly, the solubilities of the monohydrate forms (I and II) surpass the anhydrous forms (α and β)[20]. The monohydrate II solubility also reported matching that of the amorphous form. This unusual characteristic is also observed in erythromycin[24] and norfloxacin.[25] The reason for this unconventional behaviour is that both TRN and erythromycin hydrate forms have higher surface energy or lower

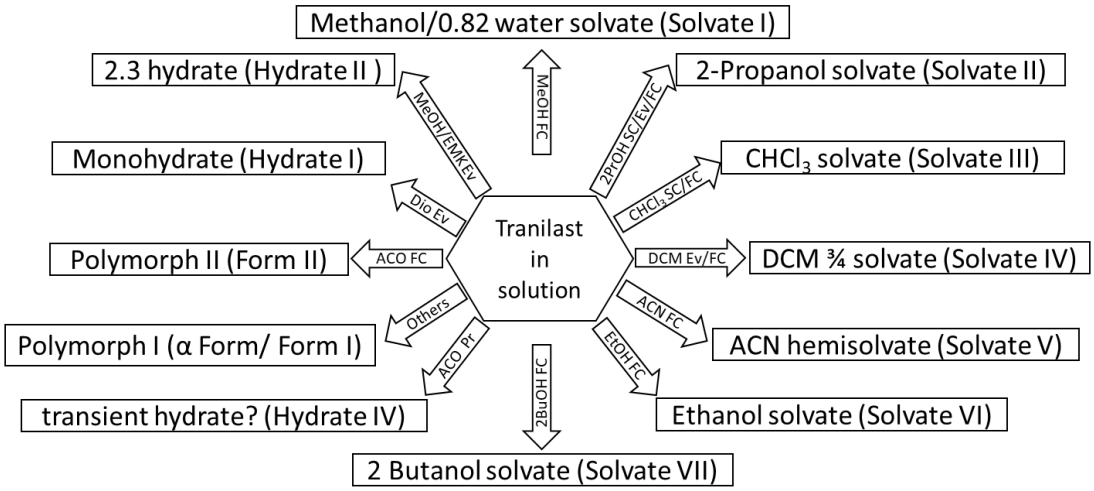
hydrophobicity; while the zwitterionic nature of norfloxacin, allows the hydrated form to generate more highly charged molecule and could be easily hydrated with water compared to the anhydrous form.

TRN was approved in Japan and South Korea for the treatment of bronchial asthma since 1982,[26,27] with indications for keloids and hypertrophic scar added in 1993.[28] A recent review on TRN therapeutic application summarises additional effectiveness in the management of a wide range of conditions, *e.g.*, diabetes, cardiovascular complications and various cancer.[29] Since the significance of TRN is increasing, the ambiguity surrounding the solid-state deserves clarification. A throrough understanding of the solid-state stability and phase transition of TRN can improve the chemical processes, suggest a more efficient formulation method, and lead to stronger patent for the compound.

4.3 Results and discussion

4.3.1 Initial screen and the resultant forms

Our initial polymorph screen of TRN with 20 different solvents (as detailed in chapter 2), using thermodynamically and kinetically controlled experiments reveal one novel hydrate form, five new solvates with one being water mixed and one anhydrous form. We also found the reported polymorph I (α Form,[20] Form I[22]), the monohydrate, and the two solvates. However, the DCM solvate from this study produces a different powder pattern compared to the previous report.[22] The following nomenclature used is based on our finding, with reference to the reported forms mentioned if needed (Scheme 4.1)



Scheme 4.1.Initial polymorph screen with 20 different solvents

KF of the anhydrous form I showed 1.4% of the analysed sample to be water. However, TG and DSC traces of form I in Figure 4.1 showed no dehydration curve confirming its respective anhydrous state. The dissimilar observation suggest that TRN reacts with KF reagent and generates the mentioned sum of water. Subsequent value from KF analysis is considered with caution. TG of polymorph II in Figure 4.2 shows minimal weight change of 1.30%, however due to the absent of a dehydration curve in both TG and DSC, the loss is potentially from the surface solvent as this form was crystallised from quench cooling of TRN from a hot acetone solution. Hence, it is most likely that traces of acetone still present on the surface, but not incorporated into the lattice. Also, an endothermic event was observed at 91 °C, indicative of a polymorphic transition in enantiotropic system.[30] The resultant crystal form above the transition temperature is polymorph I. Polymorph II is metastable as in the presence of the mother liquor, polymorph II transformed into polymorph I with simple agitation even at at ambient condition. The distinction between polymorph I and II is clear based on their respective PXRD patterns in Figure 4.3.

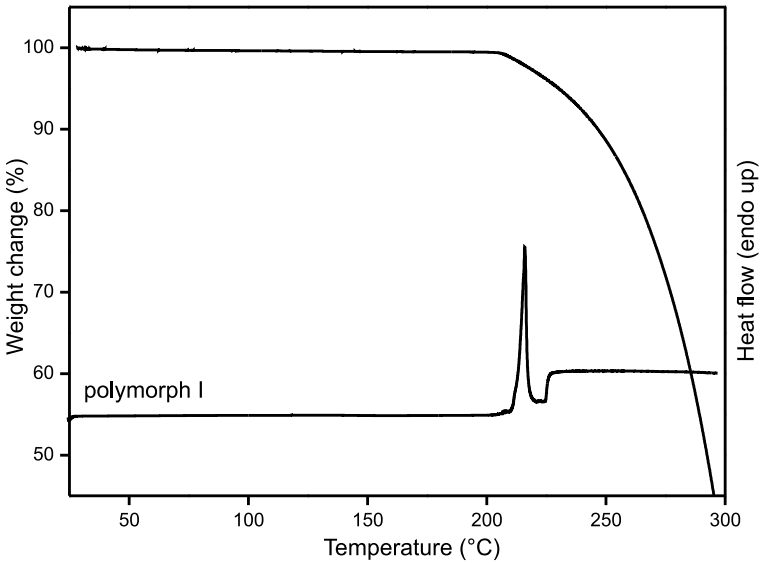


Figure 4.1. TGA (top) and corresponding DSC (bottom) thermograms of TRN polymorph I both recorded at 10 °C min^{-1}.

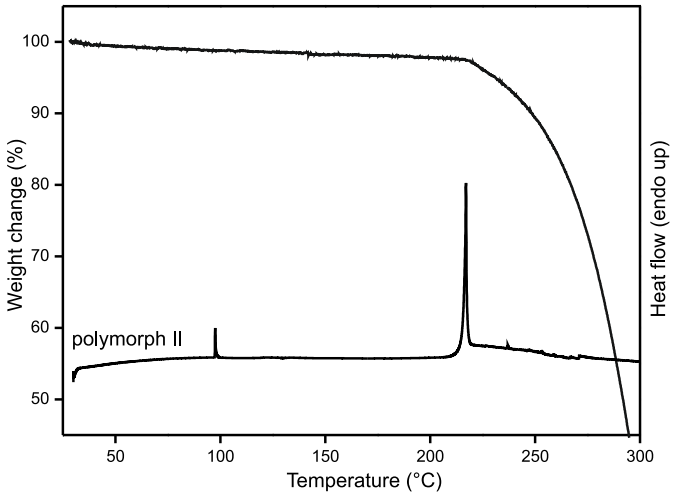


Figure 4.2. TG (top) and corresponding DSC (bottom) thermograms of TRN polymorph II both recorded at 10 °C min^{-1}.

4.4 Highlight on the TRN hydrate forms

Overall, 11 hydrates forms were obtained from our extensive screening process and subsequent DVS analysis. Five hydrate forms having close to one mole of water incorporated into the lattice. They are three polymorphic monohydrates, a 0.8 and 0.7-

0.8 hydrate respectively. One of the monohydrate has been reported before. As stated, the nomenclature used is based on the order of our finding, smaller roman numerals correspond to earlier, while larger number represent later discovery. The three polymorphic monohydrates are identified as Hydrate I, Hydrate VI, and Hydrate X, while the 0.8 hydrate is identified as Hydrate III, and the 0.7-0.8 hydrate is named Hydrate V. On top of that, we also found TRN to exist as three lower than one mole hydrates, and three larger than one mole hydrates. The lower hydrates are: a 0.6-0.7 hydrate (Hydrate VII), a hemihydrate (Hydrate XI) and a 0.4 hydrate (Hydrate VIII). Meanwhile the larger hydrates are: a trihydrate (Hydrate IX), a 2.3 hydrate (Hydrate II), and a 1.5-1.8 (transient) hydrate (Hydrate IV). To sum up, the sorting of the hydrate forms based on the order of discovery and water content are as follows:

Hydrate I = monohydrate I

Hydrate II = 2.3 hydrate

Hydrate III = 0.8 hydrate

Hydrate IV = 1.5-1.8 hydrate

Hydrate V = 0.7-0.8 hydrate

Hydrate VI = monohydrate II

Hydrate VII = 0.6-0.7 hydrate

Hydrate VIII = 0.4 hydrate

Hydrate IX = trihydrate

Hydrate X = monohydrate III

Hydrate XI = hemihydrate

4.5 Hydrate forms from direct re-crystallisation of TRN and pathways to forms derived from them

4.5.1 Hydrate I (monohydrate I)

Hydrate I (monohydrate I) was obtained by the evaporation of TRN from dioxane solution, with the PXRD pattern obtained was compared to the reported α[20] and Form I,[22] and confirmed to be similar to the trace reported by Kawashima. [20]

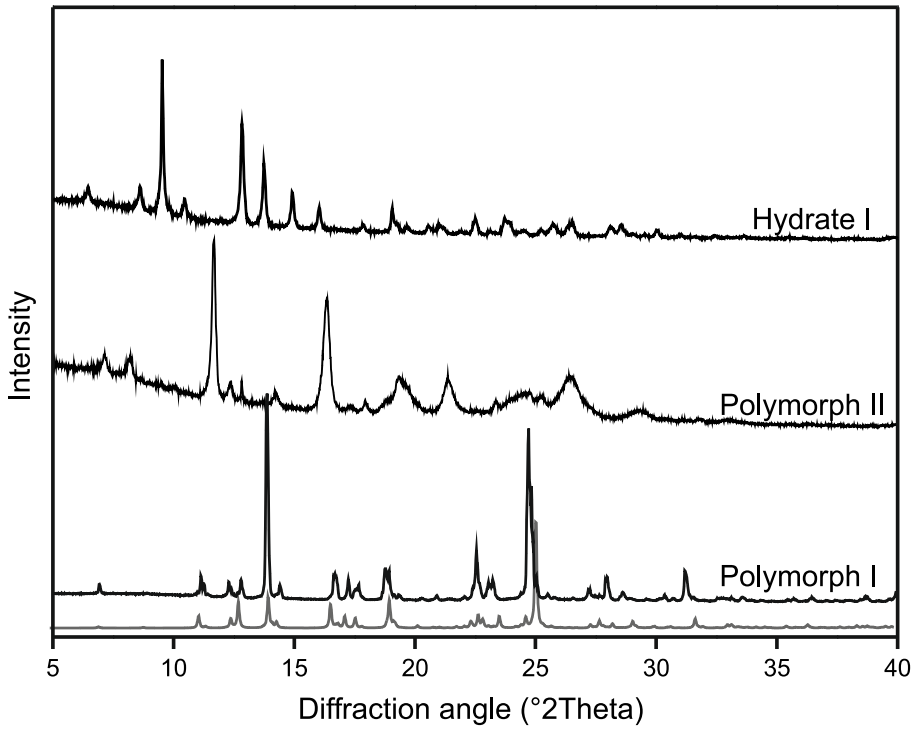


Figure 4.3. PXRD of TRN polymorph I, II and hydrate I. Grey coloured trace is the calculated powder pattern of polymorph I (α Form,[20] Form I[22])

TG trace of hydrate I (Figure 4.4) indicates that the onset for a typical dehydration curve was observed in the region of 65 °C and ends at around 95°C. The sample lost a total mass of 6.50% (corresponding to a calculated value of 1.2 moles of

water) up to this point and transforms into polymorph I, which is later confirmed via PXRD and FTIR. The calculated value for one (1) water molecule from the stoichiometry of TRN is 5.13%. The experimental value is slightly higher most likely due to the sample having some traces of crystallising solvent (dioxane) or water on its surface, evident from the immediate slope observed upon heating. The DVS isotherm of this form showed very little change across the different relative humidity (RH, Figure 4.5, (a)), varying only 0.80% (corresponding to 0.14 moles of water) between the two extreme RH. PXRD of hydrate I from before and after DVS analysis showed an identical pattern (Figure 4.5, (b)). The PXRD pattern and stable behaviour observed, even at lower RH is consistent with previous literature which state that this form could withstand drying as water is strongly bonded in the lattice.[20]

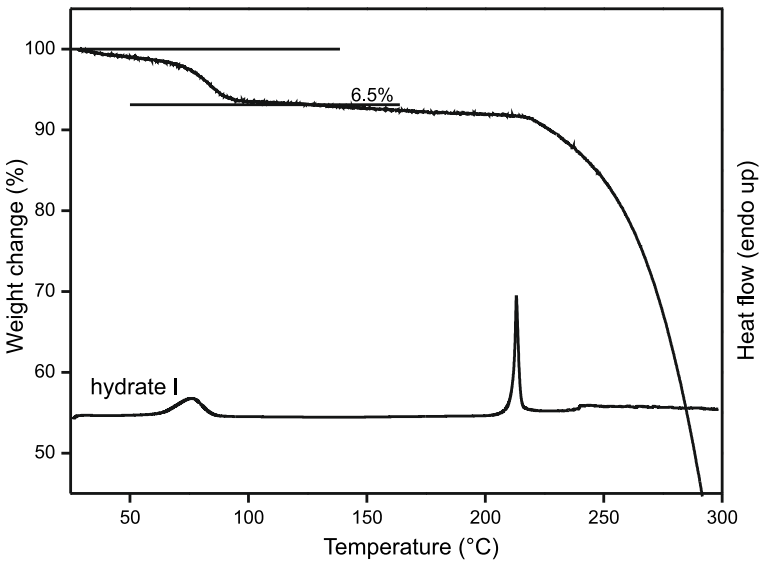


Figure 4.4. TG (top) and corresponding DSC (bottom) thermograms of TRN hydrate I both recorded at 10 °C min^{-1}

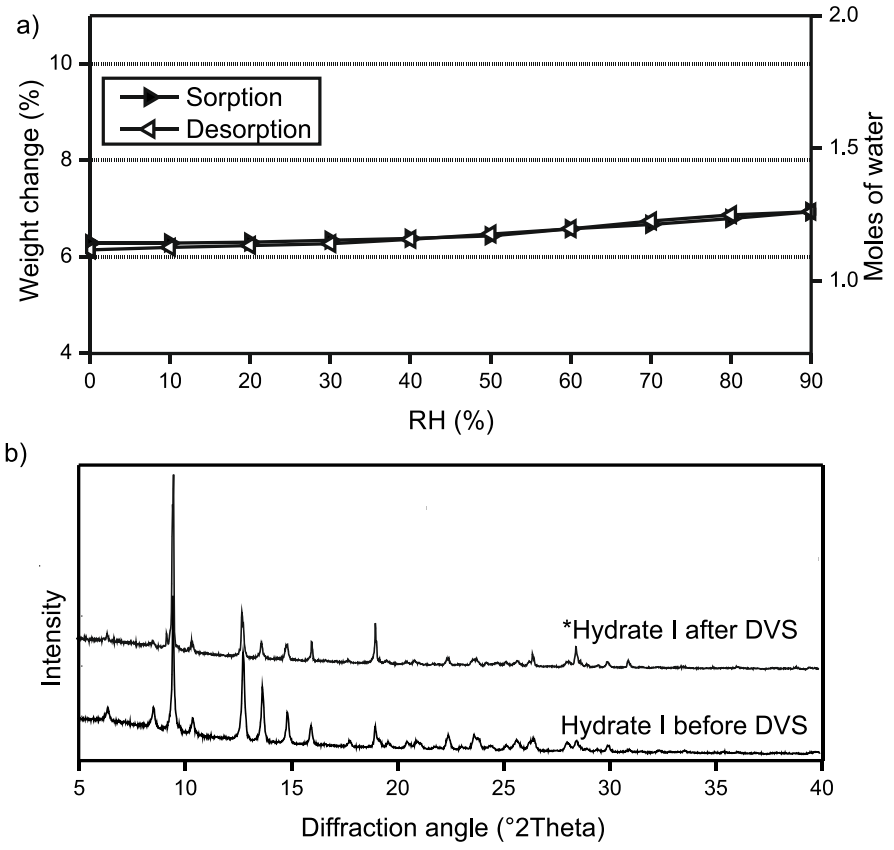


Figure 4.5. TRN hydrate I DVS cycle (a) with PXRD the sample from before and after DVS analysis (b)

4.5.2 Hydrate II (2.3 hydrate) polymorph III and hydrate III (0.8 hydrate)

Hydrate II was obtained by evaporation of TRN from methanol or ethyl-methyl-ketone solution under ambient condition. TG thermogram revealed 12.70% of weight change, corresponding to 2.64 moles of water (Figure 4.6). A single crystal of this form suitable for diffraction was grown by seeding and slowly cooling TRN from a hot acetone-water solution. This is the first time a crystal structure of a hydrate form for TRN is reported.

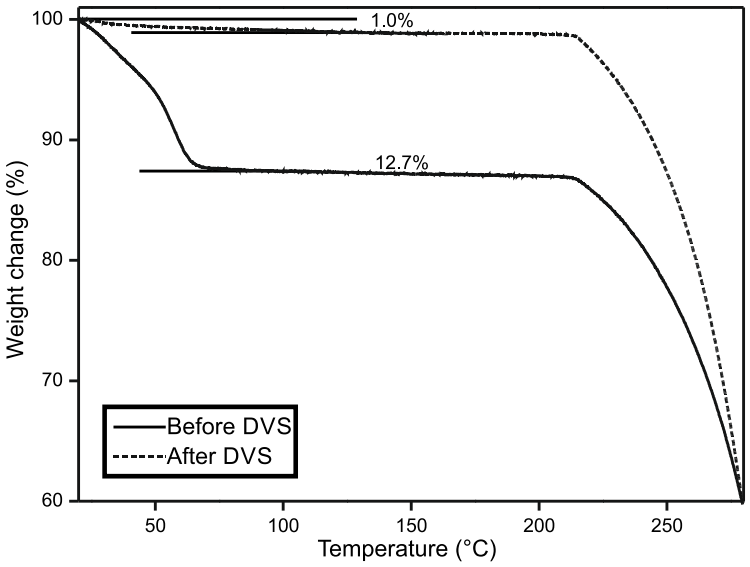


Figure 4.6. TGA of TRN hydrate II before and after DVS run (0% RH) both recorded at 10 °C min^{-1}

The structure crystallises in the triclinic space group *P*-1 with three molecular unit in the asymmetric unit (Figure 4.7). There is also intramolecular hydrogen bond between the amino and the acid group, with a distance of 1.963 Å between the donor and acceptor. The refined structure reveals 2.3 moles of water. One water molecule in the lattice acts as a proton acceptor (A) *via* the oxygen atom and coordinates to the acid. Following the water, two more hydrogen bonds were formed with two other TRN molecules by donating (D) the two protons to the acid and amide functional groups respectively (Figure 4.7 (a)). The two TRN molecules that are accepting the protons from water are in different planes, and oriented in a head-to-tail manner, hence accepting the protons at different functional group respectively. More importantly, there are two molecules of water in the channel, which formed from interlacing methoxy end of different TRN units (Figure 4.7 (b) and (c)).

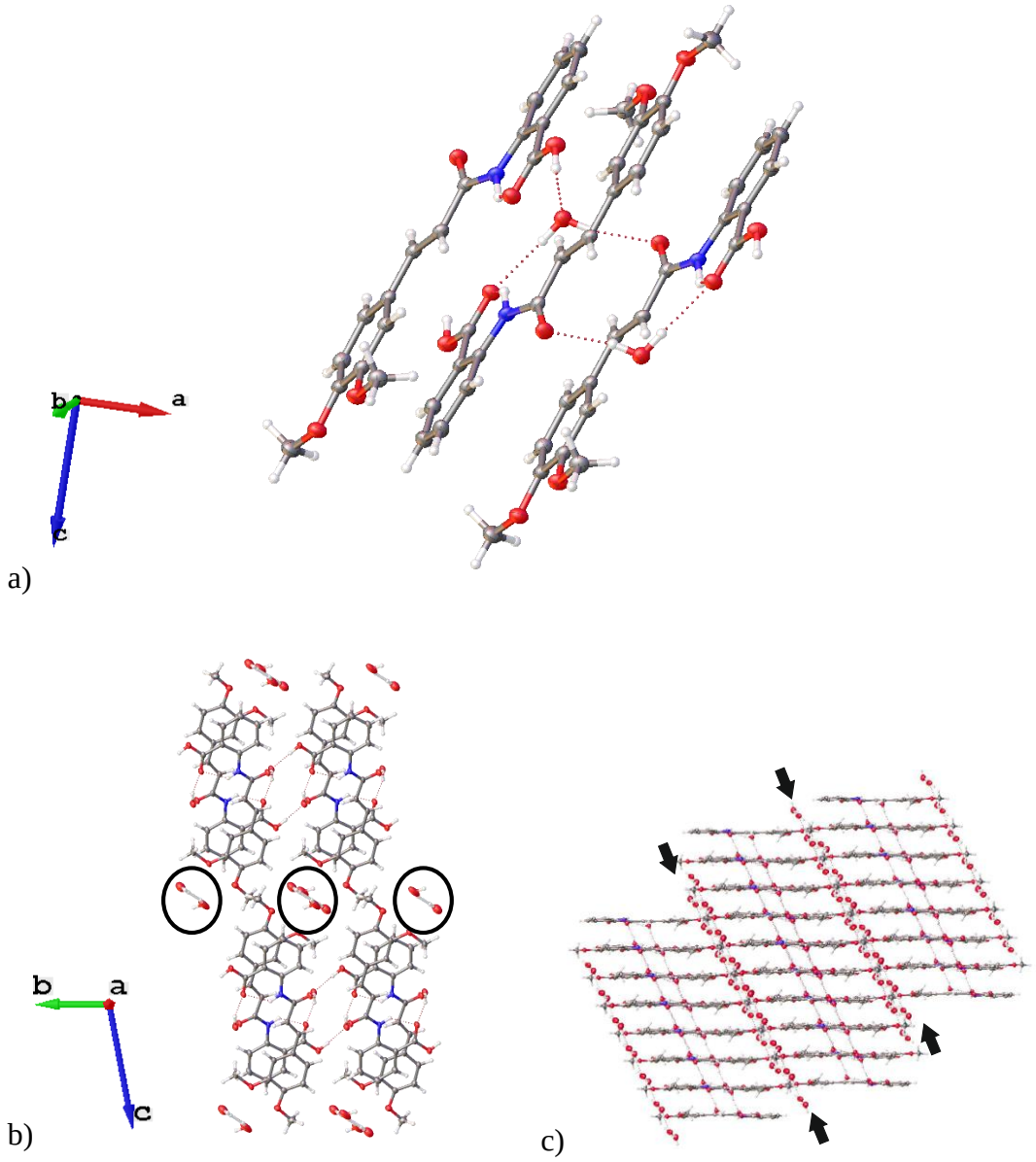


Figure 4.7. (a) Water molecules are acting as DDA, bridging three TRN molecule. (b) The two molecules of water which are in the channels are highlighted in by the black circle. (c) Black arrow is highlighting the channels. The colour code is carbon grey, oxygen red, and hydrogen light grey.

A follow up DVS isotherm of hydrate II showed comparable initial water content (to the TG) of 11.70%, corresponding to 2.41 moles of water at 40% RH, with little change in weight between 20-90% RH (Figure 4.8). Between these RH ranges, hydrate II shows a typical non-stoichiometric hydrate behaviour, where at the highest humidity range, hydrate II incorporates 12.93% (corresponding to 2.7 moles of water),

while at the lower end, the weight change recorded was 10.24% (corresponding to 2.1 moles of water). The non-stoichiometric behaviour is expected the feature is commonly associated with the presence of a channel, which can accommodate in and out around 0.6 moles of water. However, unlike the channel normally linked with non-stoichiometric hydrate, the channel structure here along with the water it occupies plays an integral role in stabilising the molecular structure, which role is further highlighted in the following DVS sorption-desorption curve, Figure 4.8.

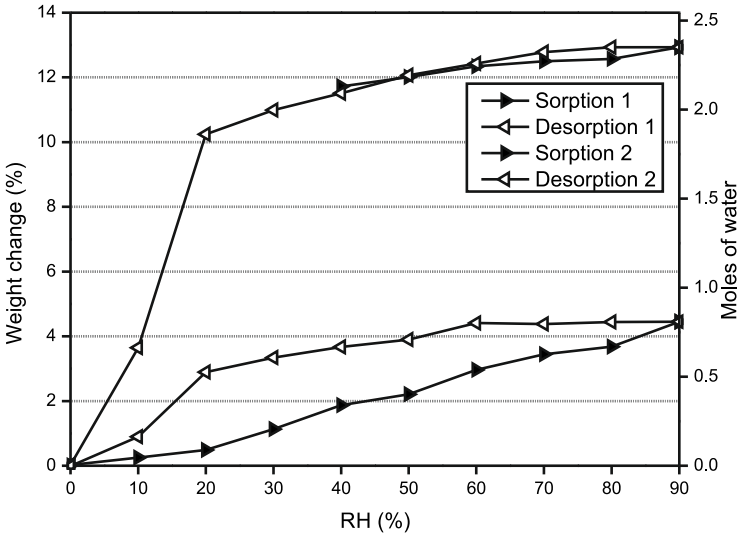


Figure 4.8. DVS isotherm of TRN hydrate II (2.3 hydrate)

DVS isotherm of hydrate II (Figure 4.8) shows, below 20% RH, the form lost most of the incorporated water. TG of the sample after the DVS run suggest that at most, 1.0% water is present at this point (Figure 4.6). The post-DVS TGA trace also does not show any typical dehydration step, but rather a continuous loss which again most likely due to presence of surface water which the sample acquired in between the analysis or decomposition due to small particle sizes of the anhydrous form. The follow up FTIR analysis showed comparable spectra between the heat dried and the sample dried at 0% RH. The majority of the peaks aligned well, however subtle

differences between the spectra were detected in the form of additional peaks, which is most likely due to the impurity of the heated sample from decomposition (Figure 4.9).

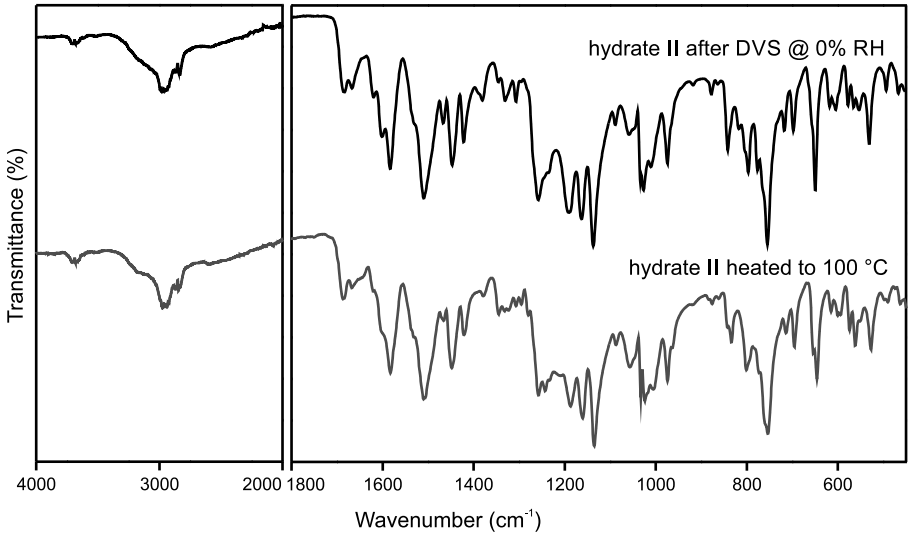


Figure 4.9. FTIR of dehydrated hydrate II, via heat and 0% RH

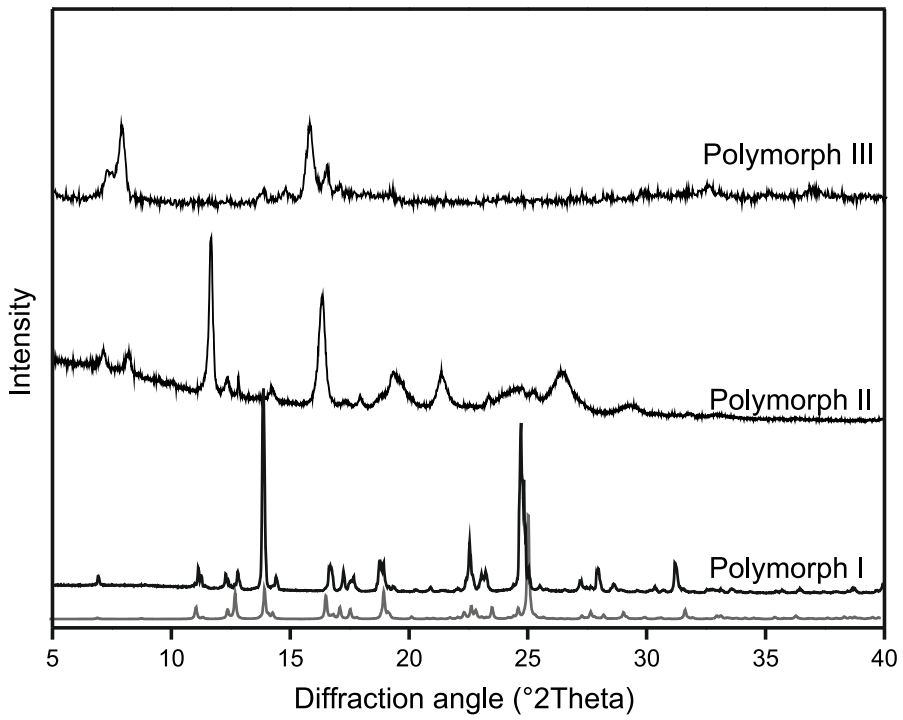


Figure 4.10. PXRD of TRN polymorph I, II and III. Grey coloured trace is the calculated powder pattern of polymorph I

PXRD of the anhydrous sample at 0% RH revealed a different pattern to the anhydrous polymorph I and II, hence named polymorph III (Figure 4.10). Comparison of polymorph III to the other reported anhydrous forms, *e.g.* Paneque *et al.*'s triclinic polymorph, and Kawashima's β and γ form) could not be made due to incomplete or ambiguous data.[20,21] Following the DVS up the second sorption cycle, polymorph III gained mass steadily, with a maximum gain of 4.45% (corresponding to 0.8 moles of water) at 90% RH. Further probe with longer isotherm (16 hours) revealed that the weight gained never reached the initial sum lost (Figure 4.11).

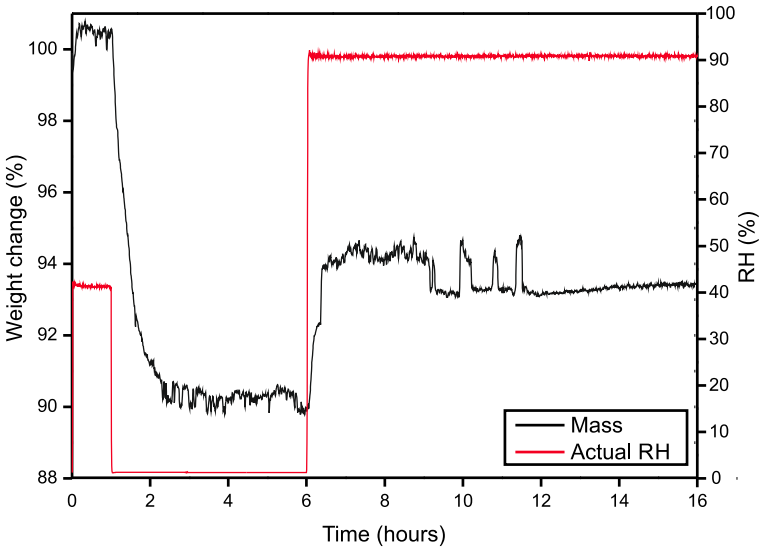


Figure 4.11. Hydrate II desorption to 0% RH followed by prolonged isotherm at 90% RH.

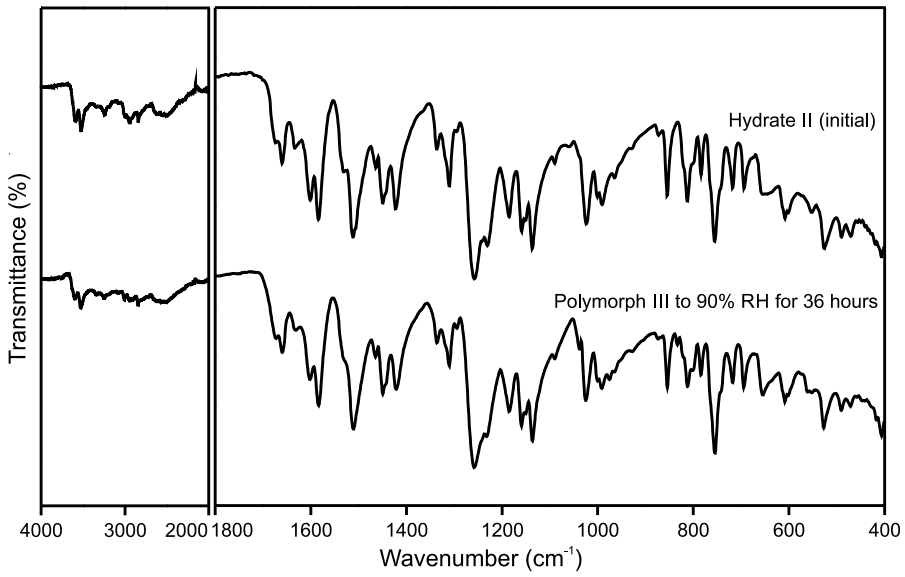


Figure 4.12. FTIR of polymorph III exposed to 98% RH for 36 hours showed similar spectra to hydrate II

FTIR of polymorph III exposed to 98% RH for 36 hours showed similar spectra to hydrate II (Figure 4.12). The reason for the comparable spectra is most likely due to similar vibrations and interactions present in both hydrate II and the re-hydrated polymorph III, potentially showing isostructural property between the two forms. Humidity-controlled PXRD confirms earlier assumption as the traces of hydrate II and the re-hydrated polymorph III, showed similar features as most of the major peaks aligned (grey dotted lines, Figure 4.13). Only subtle differences were observed and noted with * symbol (Figure 4.13). Complete dehydration or removal water from the crystal structure packing typically affect the structure in one three ways, first of which, the crystal lattice being broken and rearranged into a new anhydrous form as seen in here (hydrate II to polymorph III), as well as in aspartame hydrate.[31] Secondly, isostructural or isomorphic dehydrate could be form, where the crystal structure retains its crystalline property and unchanged, e.g. erythromycin A dihydrate[32,33] and cephalexin acetonitrile solvate[34]. The third and final effect of dehydration is a complete collapse of the crystalline framework, transforming into an amorphous phase, e.g. DTS

tetrahydrate (chapter 3), topotecan hydrochloride pentahydrate[35] and cromolyn sodium hydrates.[36] We proposed that, upon loss of all the water, hydrate II framework including the channel feature partially collapses and forms polymorph III (Figure 4.7 (b) and (c)). However, the channel feature irreversibly broken down, and due to the absent of this feature, the sample could never gain similar water content. Polymorph III's limited ability to accommodate water, lead to a new form upon exposure to high humidities. The new form bares similarities in the unit cells to its precursors, mainly hydrate II and part of polymorph III, which is come to known as 0.8 hydrate or hydrate III (Figure 4.13). Hydrate III and polymorph III interchanges in a nonstoichiometric manner, but along a different sorption-desorption pathway, attributed to the different sorption-desorption kinetics.

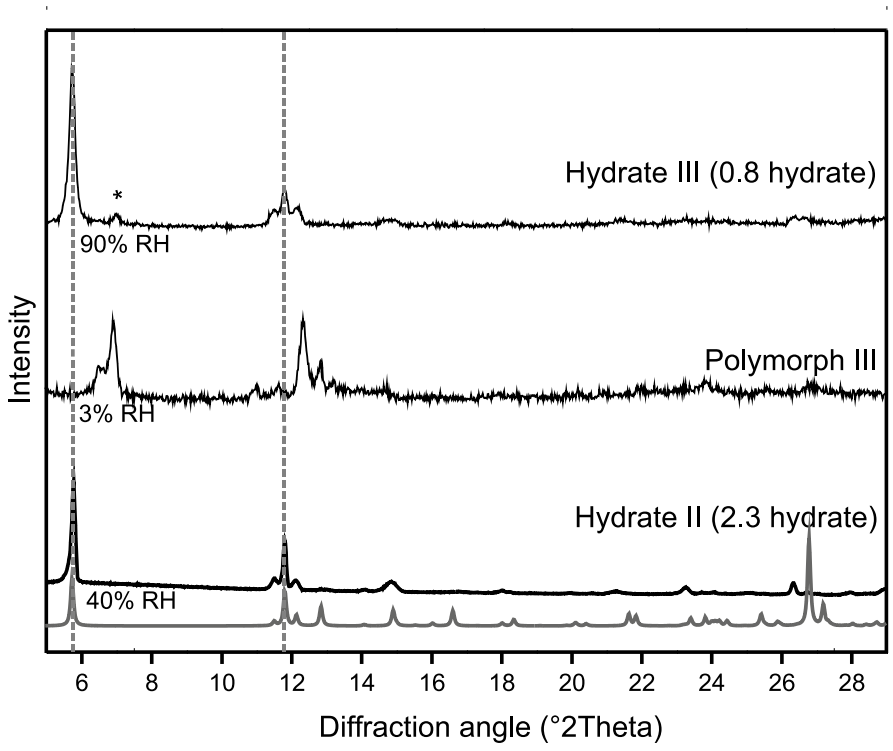
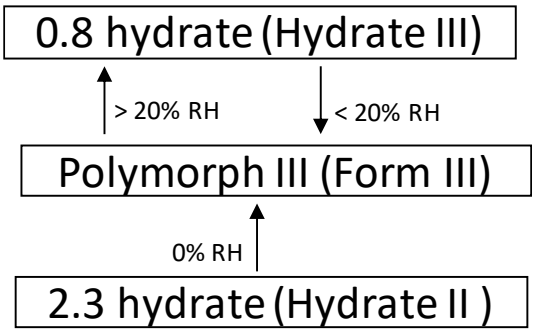


Figure 4.13. Predicted (GREY) and experimental PXRD (BLACK) of TRN hydrate II, polymorph III and hydrate III. Humidity controlled PXRD sample was taken at 40% RH before being exposed to 3% RH and subsequently exposed to 90% RH for four (4) hours at each step respectively.



Scheme 4.2. Pathway showing the relationship between hydrate II and its related forms

4.5.3 Hydrate IV (1.5-1.8 hydrate)

Precipitation of TRN from acetone solution with water as the anti-solvent yields a metastable form. FTIR confirms that the spectrum is novel when compared to all other spectra. KF and TG of this form yields a value of 9.0% (Figure 4.14) corresponds to 1.8 moles of water. However, as stated KF analysis for TRN was considered with caution as the anhydrous compound was found to react with KF reagent, generating 1.4% during analysis, and if the value is subtracted from the KF measurement of this form, the remaining 7.6% would correspond for 1.5 moles of water. In addition, the immediate mass loss recorded suggests that the incorporated solvent is very weakly bonded in the lattice. We are confident that the solvent is indeed incorporated and not just trapped on the surface as FTIR spectrum of a dried sample of this form showed a broad peak vibration at 3413 cm^{-1} (Figure 4.15), indicative of water OH vibration. Further analysis of this form proved to be challenging as the unstable nature limits our analytical method. Nevertheless, this form was identified as hydrate IV based on the currently available data.

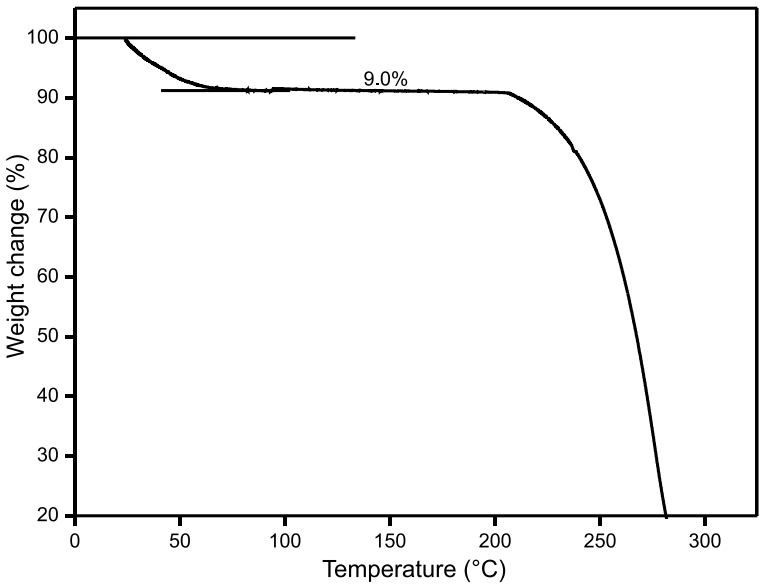


Figure 4.14. TGA of hydrate IV recorded at 10 °C $min^{-1.}$

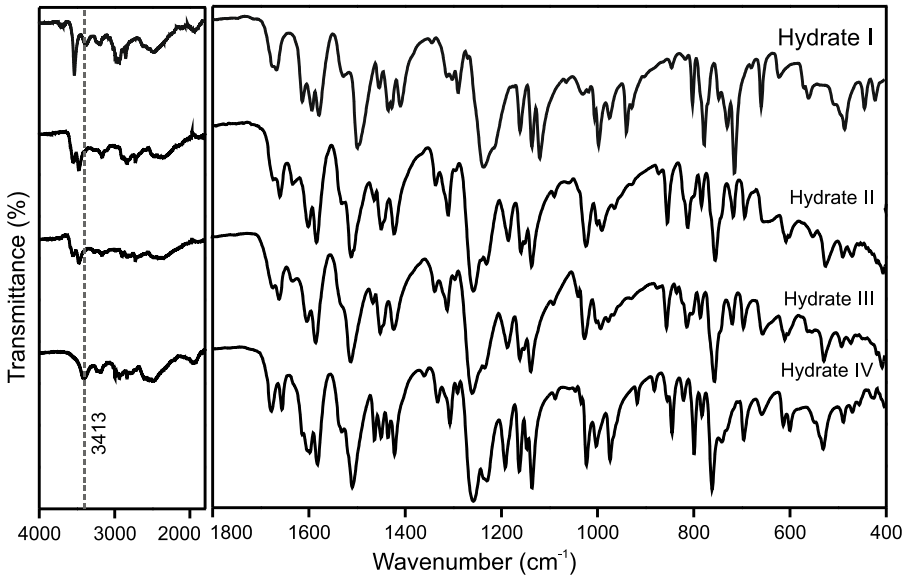


Figure 4.15. FTIR of hydrate I-IV, highlighting the vibration at 3413 cm^{-1} of hydrate IV

4.6 Methanol/water solvate (solvate I) and pathways to forms derived from solvate I

4.6.1 Solvate I (methanol/water solvate) and hydrate V (0.70-0.80 hydrate)

Solvate I is obtained by quench cooling of TRN from a hot methanol solution. The form was found to be metastable, transforming into polymorph I upon agitation in the presence of the mother liquor at ambient condition. NMR analysis of the fresh sample clearly showed the presence of methanol peak at 3.16 ppm, confirming that the crystal form indeed contains methanol.

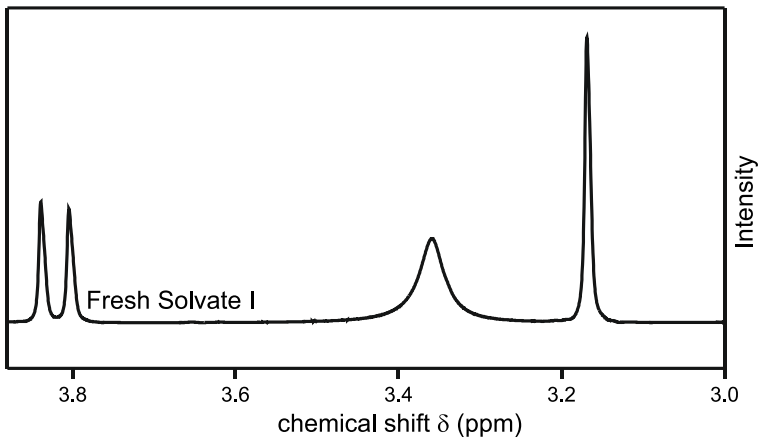


Figure 4.16. NMR spectra of the fresh solvate I sample

KF from the batch yielded 6% of water inclusion corresponding to 1.1 moles of water, suggesting that solvate I to be mixed with water. TG of the freshly prepared sample showed four different thermogram slopes with a total weight loss of 8.2% (Figure 4.17).

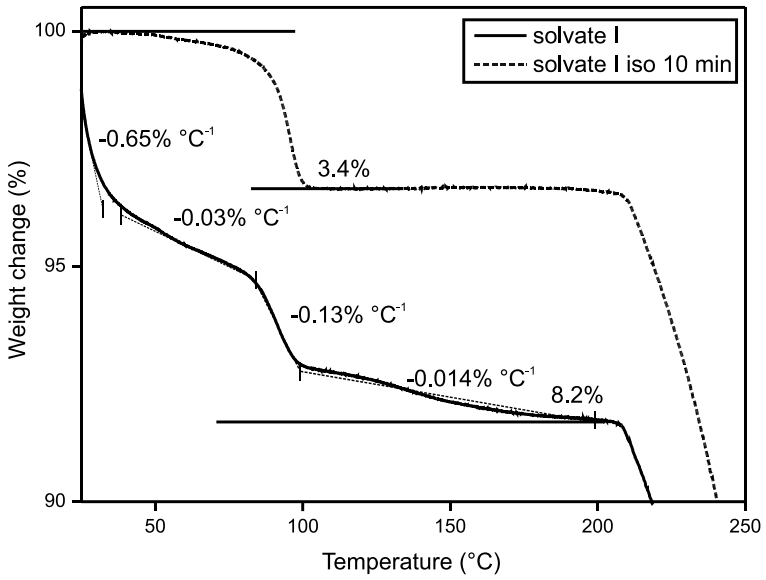


Figure 4.17. TGA of the freshly prepared TRN solvate I and solvate I isotherm for 10 minutes.

It is highly likely that the first steep slope (-0.65% $°C^{-1}$) corresponds to the release of a more volatile inclusion i.e. methanol, which suggests that in addition to its volatile nature, methanol is loosely bound, hence rapidly liberated with heat as low as 40 °C. The exact amount of methanol incorporated is a challenge to determine, with 0.40 moles calculated from the 3.8% loss at ambient up to 40 °C. However, having a nonstoichiometric value is not a common trait for a solvate, hence is highly likely that the solvent liberation occurs much earlier at ambient humidity and temperature.

To prove our hypothesis that the initial loss was from a weakly bounded volatile inclusion, the same sample is left at an isotherm, under dry nitrogen at 25 °C for 10 minutes. TG of the isotherm sample showed no initial steep slope, instead, a single typical dehydration curve is observed upon heating. The weight change recoded here 3.4% (corresponding to 0.64 moles of water). The following the TG slope at -0.03% $°C^{-1}$ of the fresh sample from 40-80 °C (Figure 4.17) a release of a less volatile inclusion, most likely water, with a loss of 1.4% (corresponding to 0.26 moles). Strong

indication that the inclusion liberated from this second slope is also weakly bound in the crystal lattice as this slope is also missing from the isotherm sample TGA curve. The third and fourth desolvation step from 80-200 °C, with a slope of -0.13% and -0.014% $°C^{-1}$ respectively records a weight sum loss of 2.9% (corresponding to 0.54 moles of water). The value corresponds well to the isotherm sample value upon heated up to the same temperature, highlighting a strongly bounded inclusion, containing the respective sum in the lattice. The total loss recorded from 40-200 °C is 4.3%, which is equivalent to 0.82 moles of water. As mentioned, KF of the fresh sample yielded 6% of water, which is higher than the total loss recorded between 40-200 °C, however, the higher KF value is expected as stated before, the anhydrous compound was found to react with KF reagent, generating 1.4% during analysis. Therefore, if the sum recorded from the anhydrous form is accounted for, then, the actual KF for the fresh solvate I is 4.6% (corresponding to 0.86 moles of water), which is comparable to the TG weight loss between 40-200 °C.

Interestingly, the DVS curves in Figure 4.18 (a) and (b) show comparable values upon losing the incorporated methanol, as the sample equilibrates in both DVS run at 40% RH. The methanol deprived sample appeared to be stable between 10-80% RH, containing somewhere between 0.70-0.80 moles of water, hence identified as hydrate V.

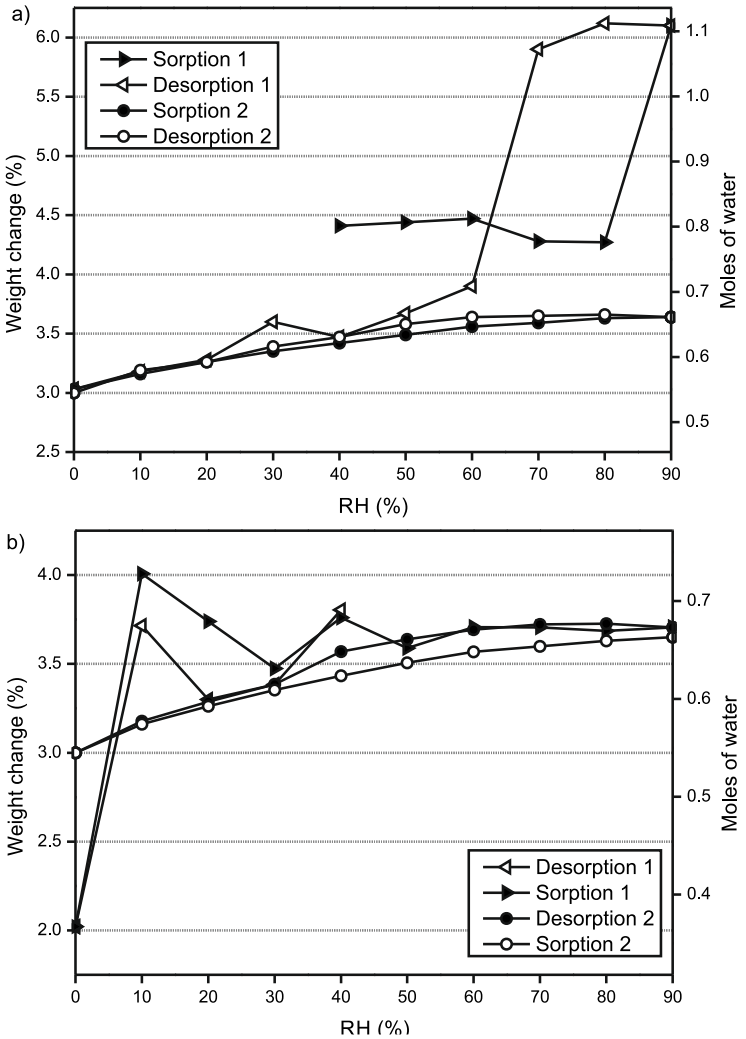


Figure 4.18. DVS isotherm (initially to higher humidities) of hydrate V (formed from methanol desolvation of solvate I) The sample contain between 0.84-0.81moles of water upon exposure to RH between 40-80% going up the humidity range. Meanwhile (b) DVS isotherm (initially to lower humidities) of hydrate V. The sample is shown to contain between 0.72-0.70 moles of water upon exposure to RH between 40-10% up the humidity range.

4.6.2 Hydrate VI (monohydrate), VII (0.60-0.70 hydrate) and VIII (0.40 hydrate)

Due to instability of solvate I, the PXRD obtained thus far is that of hydrate V. Following the DVS (Figure 4.18 (a)) up the RH range to 90% RH, hydrate V gained a further 0.34 moles of water, forming a monohydrate which is later identified as hydrate VI. The step feature observed form hydrate V to VI was indicative of a stoichiometric hydrate transformation. Following desorption cycle, hydrate VI loses the incorporated

water below 70% RH and transition into another stable form which contain somewhere between 0.60-0.70 moles of water, which showed non-stoichiometric sorption-desorption curve along 0-90% RH, Figure 4.18 (a). This stable 0.60-0.70 hydrate is identified as hydrate VII.

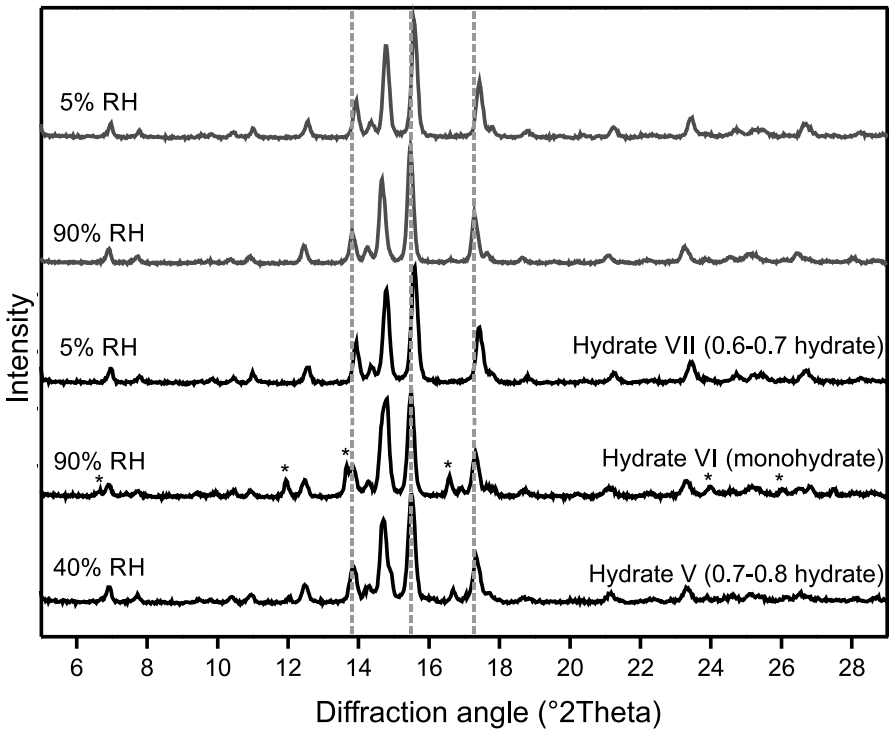


Figure 4.19. Humidity controlled PXRD of hydrate V (formed from methanol desolvation of solvate I) BLACK traces corresponds to the first sorption-desorption cycle, GREY traces corresponds to the second sorption-desorption cycle. Each step is left at isotherm for one hour before pattern is obtained

Humidity controlled PXRD trace of hydrate V from 40 to 90% RH, supports the finding, with the trace (second trace from bottom, black trace labelled 90% RH in Figure 4.19) showing several peak splitting and new peak emerging (indicated by (*) in Figure 4.19). The new peak along with peak splits confirms the presence of hydrate VI, mixed together with hydrate V. Their nearly similar PXRD trace suggest a rigid framework, accommodating between 0.2-0.3 moles of water without affecting the trace much. Humidity controlled PXRD trace of hydrate VII (Figure 4.19), shows very

similar trace to the starting hydrate V. It is also plausible that hydrate VII and hydrate V is the same form, only that the initial sample prepared for hydrate V potentially contain seed of this new form. Evidently, the second 90% RH trace is does not show the additional peak/changes observed at the previous 90% RH (that of hydrate VI). The following traces of the sample exposed to 90% RH, then followed by 5% RH (grey colour traces, fourth and fifth traces from bottom respectively in Figure 4.19) show similar peak features as well. The absence of peaks traces indicative of hydrate VI reiterate that the monohydrate hydrate VI is indeed a metastable state, only forming from initial sorption of hydrate V, which contain its seeds. Furthermore, slight shift to higher diffraction angle is noted (by the dotted line in Figure 4.19) to the traces of hydrate VII exposed to lower % RH. This general peak shift position to higher 2 Theta (°) angle (right-shift), according to Braggs law, is due to a decrease to reduced *d*-spacing, most likely due to the egress of water upon formation of hydrate VII at lower humidity. The high rigidity of the main structure persist through hydrate V and is drivative forms. The role of water in this hydrate set must have helped in maintaining the framework and stability, seen in the stable final form of hydrate VII.

Meanwhile, following down the RH range (Figure 4.18 (b)) to 0% RH, hydrate V sample lost 1.9% (at 0% RH) from the initial mass of 3.8% (at 40% RH after gravimetric equilibrium acheived), hence forming a 0.40 hydrate (named hydrate VIII). Like hydrate VI, hydrate VIII appeared to be metastable, gaining 1.7% in weight (0.30 moles of water) above 10% RH as it form a stable form afterwards. Following the second DVS sorption-desorption cycle, similar trend and water content indicative of hydrate VII is observed. The second sorption-desorption cycle in both run (Figure 4.18 A and B) saw 0.1 mole ingress and egress of water between the two RH extremes, typically observed in a non-stoichiometric hydrate. Comparison between the FTIR

spectra of the sample at the end of both DVS runs (initially going up *vs.* initially going down, Figure 4.20), shows very similar spectra, confirming that hydrate VIII also transition into hydrate VII following the second DVS sorption-desorption cycle.

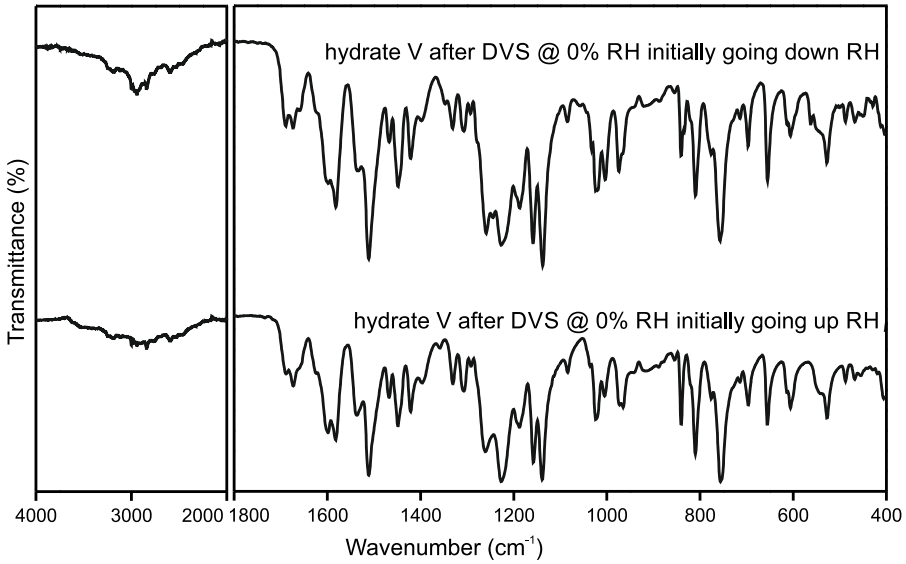
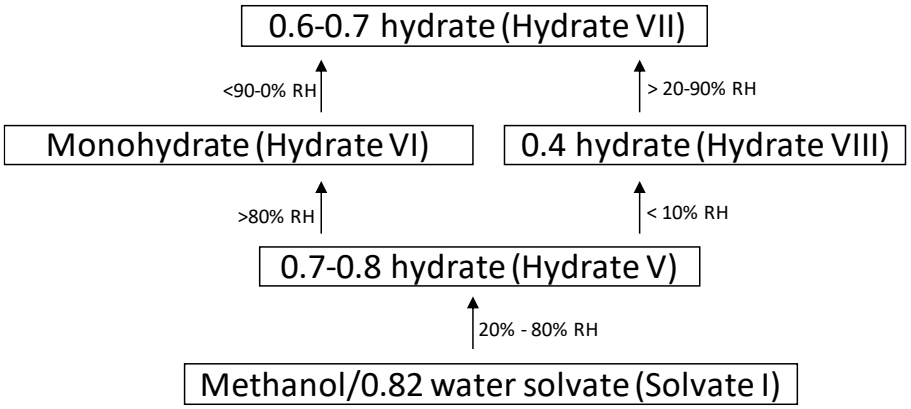


Figure 4.20. FTIR spectra of hydrate V at the end of DVS runs, initially going up vs. initially going down



Scheme 4.3. Pathway showing the relationship between solvate I and its related forms thus far

4.6.3 Hydrate IX (trihydrate)

In order to compare the PXRD of hydrate VI (a monohydrate) to the four other reported monohydrate polymorphs,[20] the freshly prepared methanol/water solvate was

placed in a 98% RH chamber to replicate the DVS environment. Surprisingly, the follow-up TGA recorded a higher than expected weight loss of 14.5%, corresponding to three moles of water, with an initial weight loss following the steep slope from ambient to 40 °C accounting for 9.90%, which corresponds to two moles of water. (Figure 4.21). Since the only possible interaction is with water, it is most likely that as the sample loses the methanol, water molecule fill up the created void, incorporating a total of three moles of water instead, compared to the one mole of water seen in the prior DVS (Figure 4.18 (a)). The high hydrate form was then identified as hydrate IX. The thermogram trace observed for the hydrate IX, do share similar feature with TG trace of solvate I (Figure 4.17) in the form if an initial steep desolvation slope, however the trihydrate trace only show three distinct slopes, with a clear curve indicating the completion of the dehydration process, at above 100 °C (Figure 4.21).

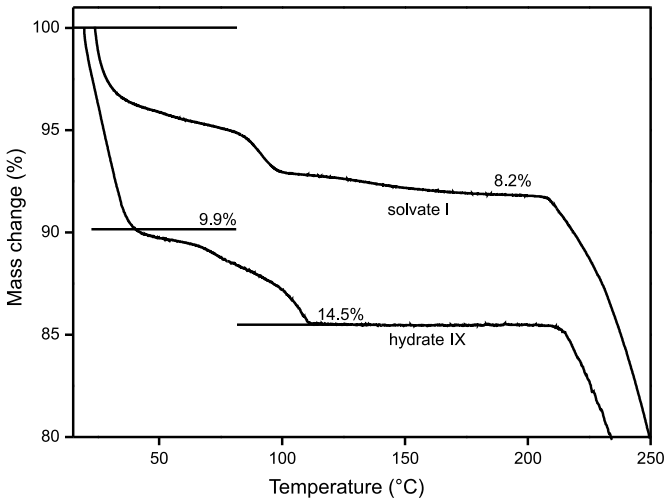


Figure 4.21. TGA of TRN solvate I *vs.* the same form exposed to 98% RH chamber forming the trihydrate (hydrate IX))

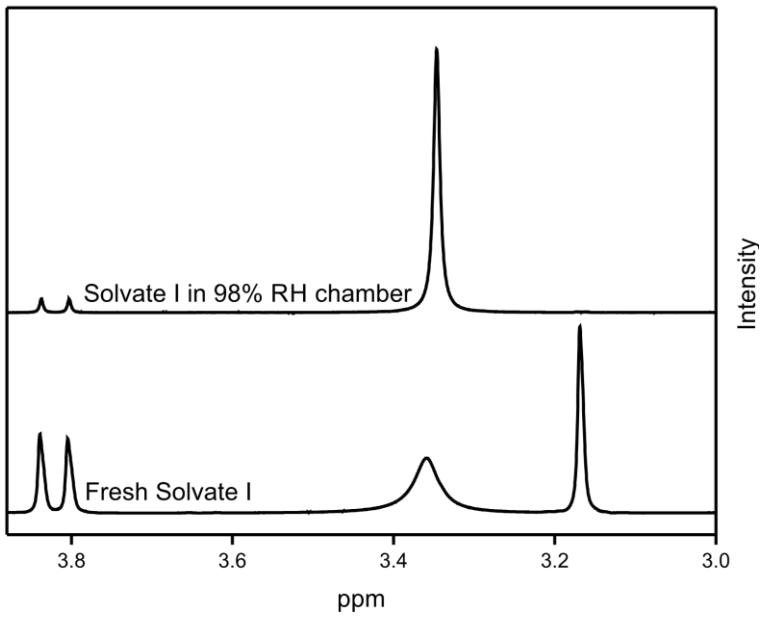


Figure 4.22. NMR of fresh TRN solvate I sample vs. sample exposed to 98% RH chamber or the trihydrate /hydrate IX)

NMR spectra of the fresh solvate I vs. the sample exposed to 98% RH, clearly shows the presence of methanol, and not the latter, confirming the exchange (Figure 4.22). It is most likely that as the two moles of water occupies the spaces that once occupied by methanol. Since similarly weak interactions are present in both, previously with methanol (solvate I), and now with water (hydrate IX), we suggest possible channel feature similar to hydrate II, and these exchanges occur within channels in the lattice. Similar solvent-water exchange feature was reported for cephalexin acetonitrile solvate, where reversible exchange between the solvent and water molecules can occur due to the a channel feature, without affecting crystalline structure much.[34,37]

A single crystal X-ray diffraction would be needed to ascertain the theory. Also, the solvent exchange bares little effect to the unit cell, such that PXRD of the trihydrate showed similarities to the other forms (hydrate V-VIII) derived from solvate I- without being entirely the same. We note some unique feature of hydrate IX in the

form of additional or missing peaks which are highlighted with (+) symbol in Figure 4.23.

The stability and the solid-state transition of hydrate IX is difficult to ascertain due to the metastable nature. The thermogram (Figure 4.21) does suggest that once the weakly bounded water is lost (two moles), and a more stable form containing at least one mole of water emerges. Due to PXRD similarities observed for the whole solvate I-derived 'family', it is not surprising if the stable monohydrate bares similarities to the hydrate V-VIII.

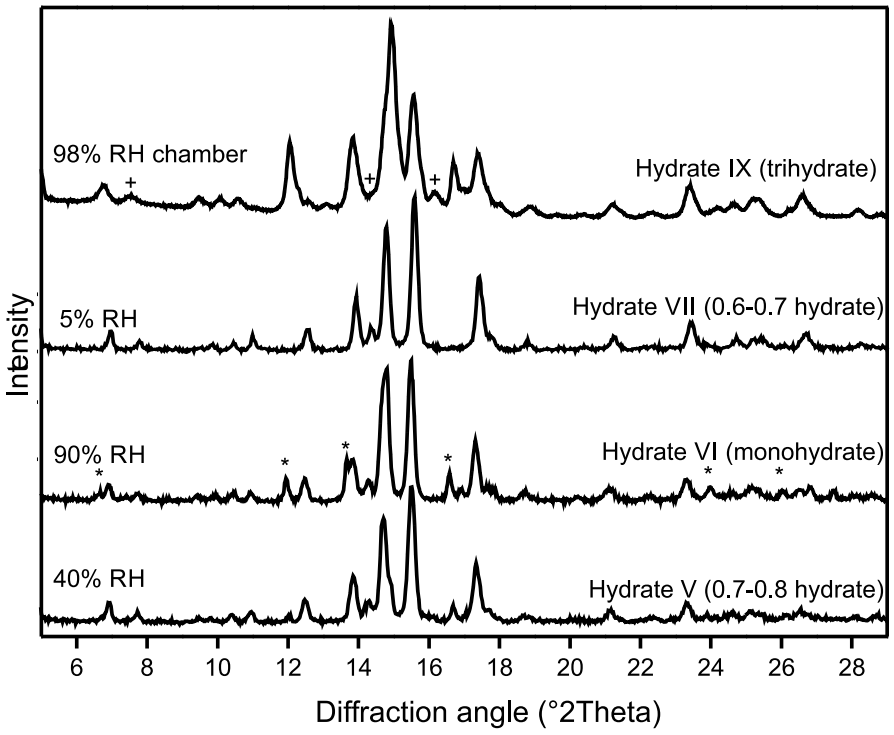
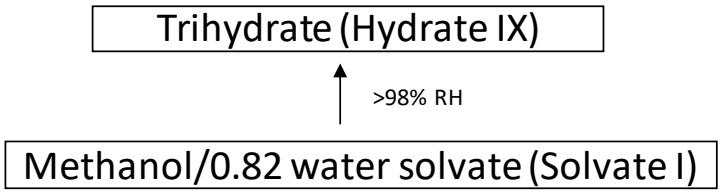


Figure 4.23. PXRD comparison of hydrate IX to other hydrate form derived from solvate I. Unique feature of this form is highlighted with (+) symbol.



Scheme 4.4. Pathway showing TRN solvate I relationship to TRN trihydrate

4.7 Other solvate forms from direct re-crystallisation of TRN and forms derived from them

The other solvates obtained by direct re-crystallisation of TRN from various solvent are pure solvate (not water mixed).

4.7.1 Solvate II (2-propanol monosolvate)

Quench cooling TRN from a hot 2-propanol yielded a novel solvate form which was confirmed *via* PXRD hence dubbed solvate II (Figure 4.24). TG analysis of this from indicated that 14.9% mass loss, calculated to 0.95 moles of 2-propanol incorporated into its crystal lattice (Figure 4.25). The high temperature for the onset of desolvation which is above 75 °C, suggests that the solvate from is stable.

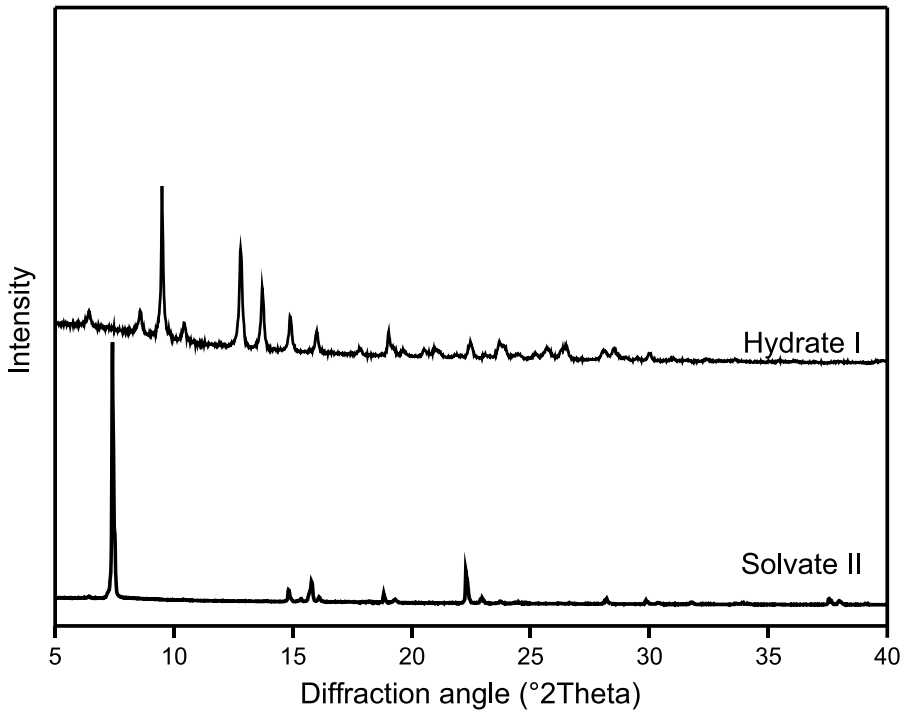


Figure 4.24. PXRD solvate II alongside the from which it transform to at higher RH, hydrate I.

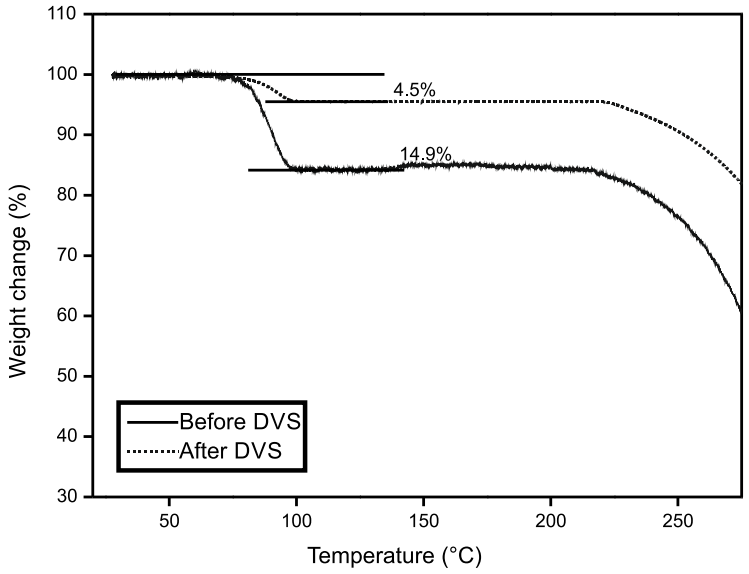


Figure 4.25. TGA of solvate II, showing the mass loss recorded before, and after DVS analysis (0% RH)

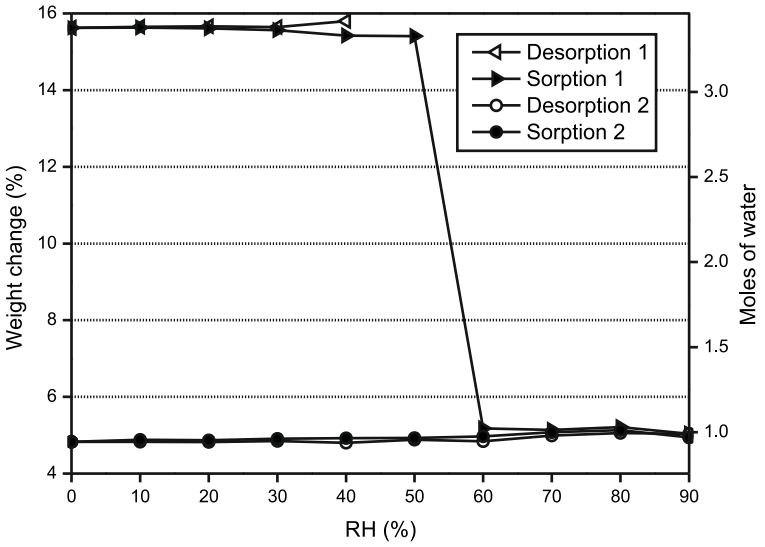


Figure 4.26. DVS isotherm of solvate II

This stability feature was also reflected in the DVS analysis, where upon exposure to lower humidities (40 down to 0% RH), solvate II showed no weight loss (Figure 4.26). However, a significant weight change is observed upon sorption to above 50% RH (coming up from 0% RH). A mass loss of 15.2 % is recorded, which is comparable to the sum for the incorporated 2-propanol. This lead to the suggestion that at higher humidities, water molecules displaces the 2-propanol in the solvate crystal lattice. The resultant form showed good stability along the humidity ranges (low and high), showing barely any changes. Subsequent TG of the DVS sample after completion of the run revealed that, upon displacing the solvent, 4.5% of water (calculated to 0.82 moles of water) gets incorporated into the form, possibly occupying the space vacated by the 2-propanol. FTIR analysis of the sample shows similar spectra to that of Hydrate I (Figure 4.27). The DVS behaviour is also in agreement, matching with hydrate I which does not change at any humidity variation. The solvate hydrate interchange behaviour was also reported for bisfinasteride monohydrate monotetrahydrofuran and bisfinasteride monohydratemono-1,4-dioxane, which are water-mixed solvates.[38]

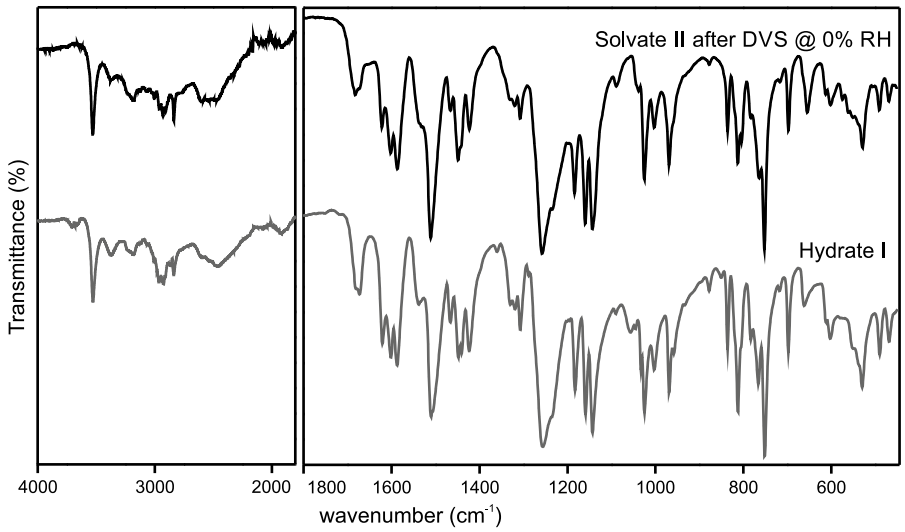
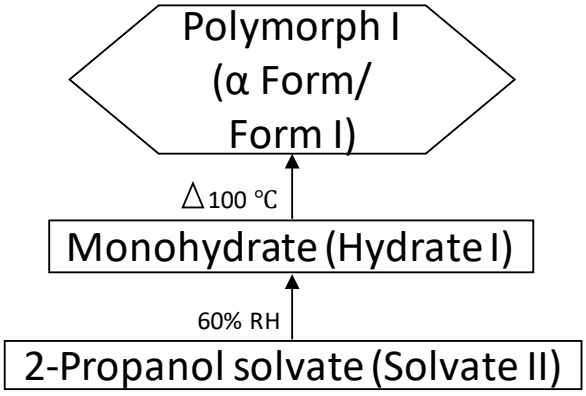


Figure 4.27. FTIR spectra of solvate II after DVS cycle, showing similarities to hydrate I spectra



Scheme 4.5. Pathway showing the relationship between TRN solvate II and its related forms

4.7.2 Solvate III (chloroform monosolvate), hydrate X (monohydrate) and hydrate XI (hemihydrate)

All thermodynamically and kinetically controlled crystallisation experiment from chloroform solution yielded identical form, which suggest that this form is thermodynamically stable. This solvate form has been reported before and identified as TRN chloroform monosolvate (solvate III).[22,23] TG of solvate III in Figure 4.28 shows a weight loss of 27.3% (corresponding to one mole of chloroform).

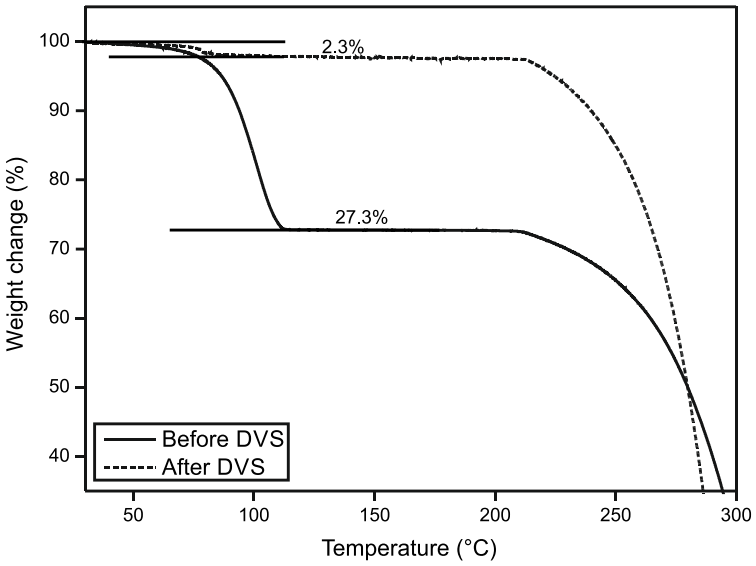


Figure 4.28. TGA of Solvate III before and after DVS analysis (weight loss as 0% RH)

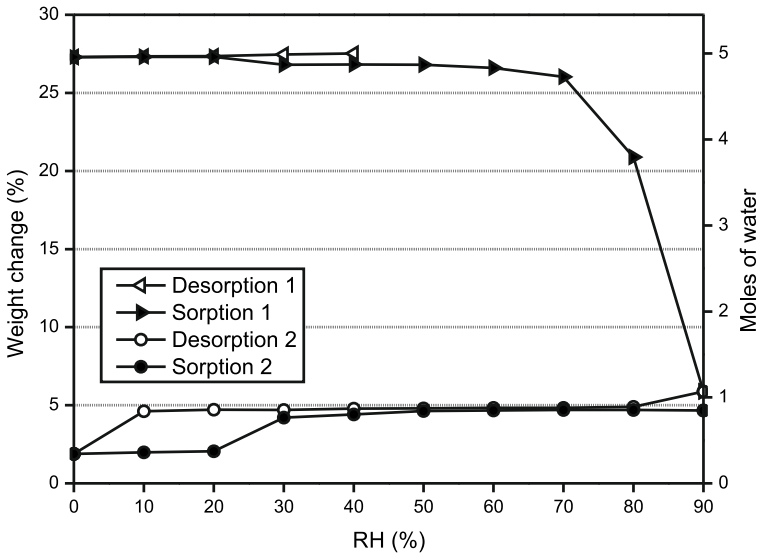


Figure 4.29. DVS isotherm of solvate III

Interestingly, following the DVS analysis curve in Figure 4.29, similar behaviour to that of solvate II is observed, showing no change in mass with reduced RH, whilst significant loss recorded at higher humidities (>70% RH). At 90% RH, the recorded loss is 27.5%, suggesting that all the incorporated chloroform is displaced. Interestingly, unlike solvate II, following subsequent desorption, a further mass loss

of 2.8% (calculated to 0.5 moles of water) is recorded below 10% RH. Following sorption to >20% RH, the form recovered back the lost water. The water lost and gain observed follow a step-like curve, indicative of a stoichiometric hydrate. A follow-up TGA (Figure 4.28) of the sample at 0% RH shows a comparable mass loss of 2.3% (corresponding to 0.4 moles of water). Calibrated to the TGA value, means that at 90% RH, the sample contain 0.9 (~1.0) moles of water and later identified as monohydrate hydrate X, while for the 0% RH form is identified as hemihydrate hydrate XI. According to Vogt et al., the chloroform molecules form channels in the solvate crystal lattice.[22] He suggest that due to this arrangement, there is a possibility for solvent removal without altering most of the packing interactions.

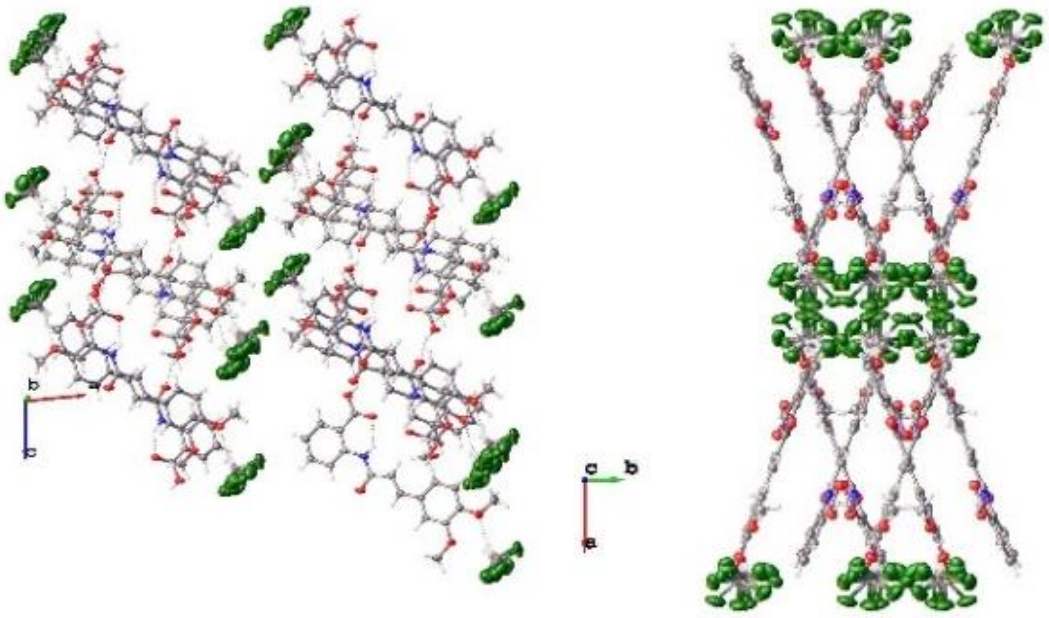


Figure 4.30. Crystal packing of solvate III, showing channel of chloroform molecule (GREEN)[8]

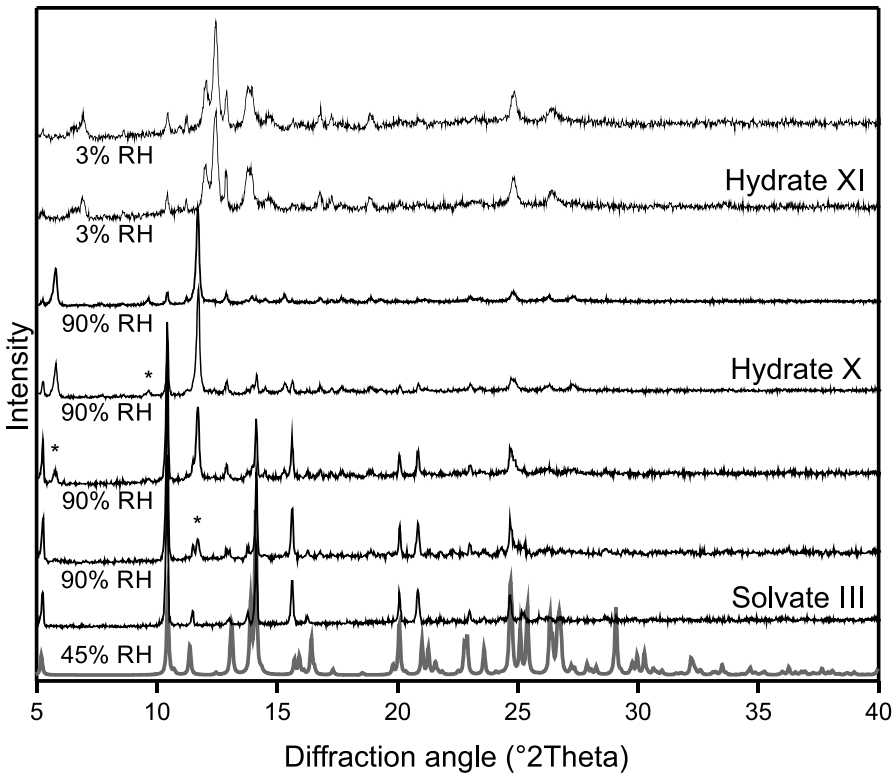
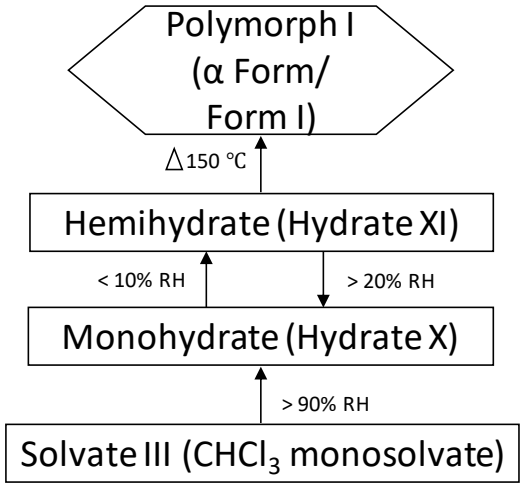


Figure 4.31. Humidity controlled PXRD of Solvate III (TRN chloroform monosolvate), matching to the calculated powder pattern (GREY). Each scan interval is two (2) hours.

However, the humidity controlled PXRD experiment done proved otherwise. As water displaces chloroform in the lattice, the pattern changes with new peak emerging after two hours, and after six hours, all peaks indicative of hydrate X appears (Figure 4.31). Eight hours of exposure shows no more changes. The following two-hour exposure to 3% humidity confirms hydrate XI formation, with no change observed after longer exposure.



Scheme 4.6. Pathway showing the relationship between solvate III and its related forms

4.7.3 Solvate IV (DCM ¾ solvate)

Quench cooling TRN from a hot dicholoromethane (DCM) solution yielded a solvate, which subsequent TG (Figure 4.32) revealed to contain 0.76 moles of DCM from 16.5% mass loss, whilst DVS of the same sample recorded a continuous loss, regardless of humidity, to a final value of 17.2% (calculated to 0.8 moles of DCM, Figure 4.33). TG data showed that the onset of mass loss occur early on, at 25 °C, which is supported by DVS isotherm (at 25 °C) recording similar, immediate mass loss.

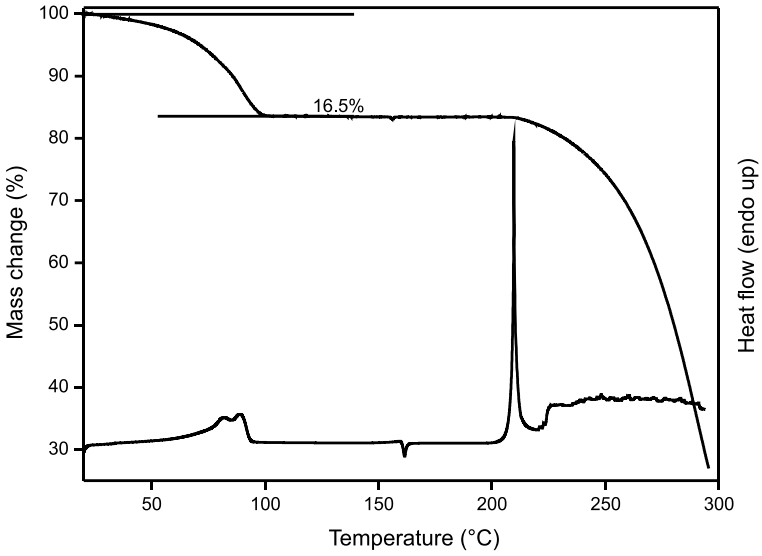


Figure 4.32. TGA and DSC analysis of Solvate IV

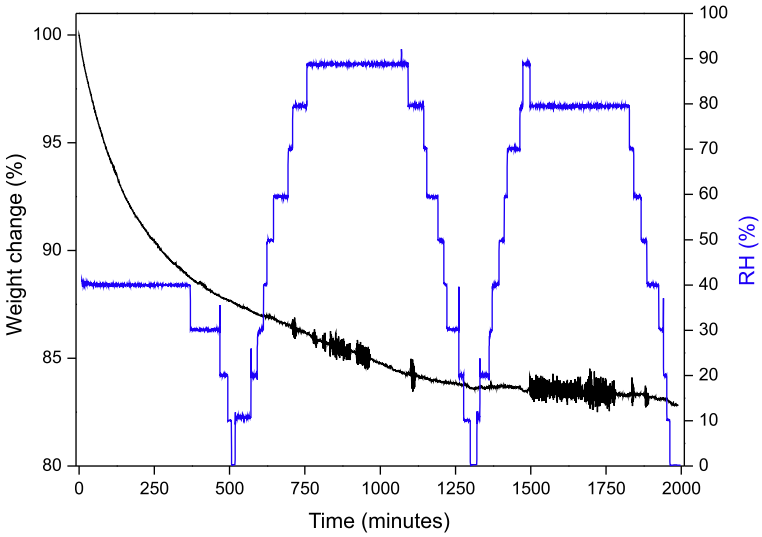


Figure 4.33. Desolvation of solvate IV (DCM ¾ solvate) at isotherm.

PXRD trace of the TRN DCM solvate (named solvate IV) obtained is distinctly different to the one reported (Figure 4.34).[22] The form obtained from this study is potentially different the reported form as the calculated weight loss of 16.5% corresponds to 0.76 moles of DCM which could be a ¾ DCM solvate. Our effort to obtain the reported form is unsuccessful. As mention, the immediate loss regardless of RH and temperature suggest the instability of this form. Interestingly, solvate IV

desolvates to a novel anhydrous polymorph. FTIR spectra suggest both desolvated form using heat and without heat(at 0% RH), TG and DVS samples respectively, produced identical form (Figure 4.35). PXRD trace also confirms the finding, even though the heated sample lost some crystallinity, distinctive feature is still observable (Figure 4.34). This polymorph is later named polymorph IV or form IV. DSC of solvate IV shows consistent desolvation trace, forming polymorph IV above 100°C (confirmed via FTIR). Further heating to 300 °C saw form IV transforms in an exothermic event (onset observed at 164 °C) into the anhydrous form I or α form which was confirmed via FTIR and PXRD (Figure 4.35 and Figure 4.36 respectively). The two crystal forms are most likely monotropically related as indicated by the exothermic transitions (Figure 4.32).[39,40]

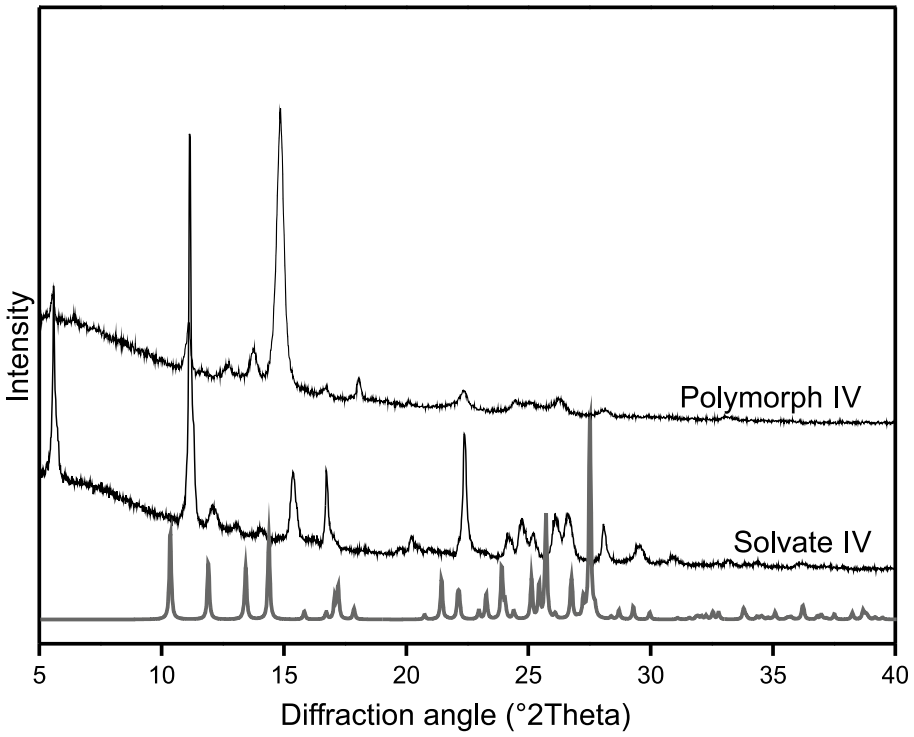


Figure 4.34. PXRD of Solvate IV (TRN DCM ¾ solvate), the pattern did not match to the calculated powder pattern (GREY)[22]

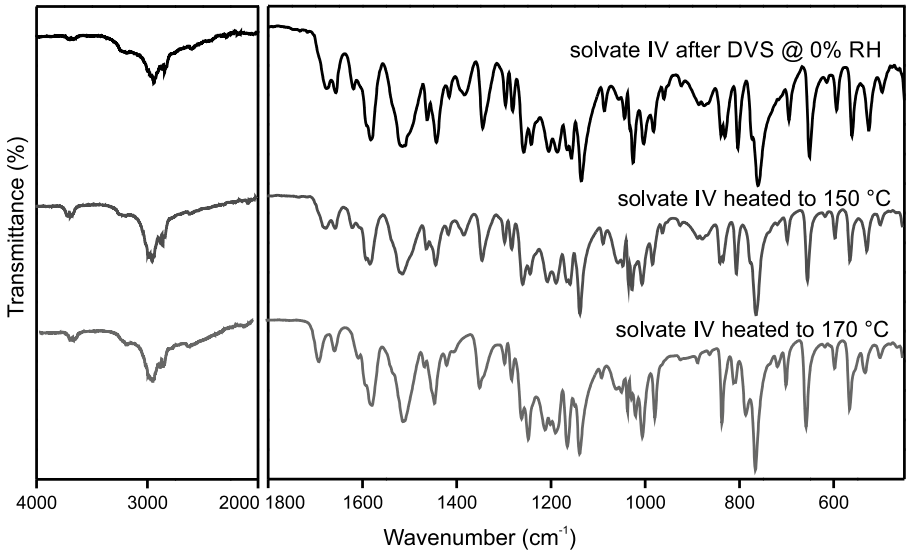


Figure 4.35. FTIR spectra of desolvated solvate IV without heat (0% RH) and at different heating interval. Heating to 150 °C yeilded polymorph IV while >170°C forms polymorph I.

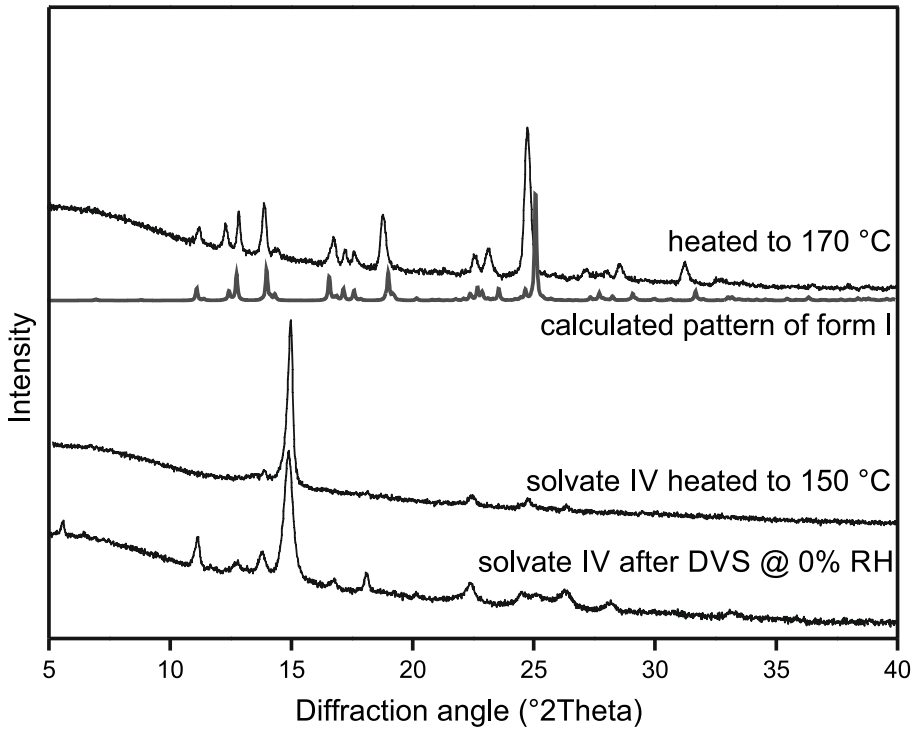
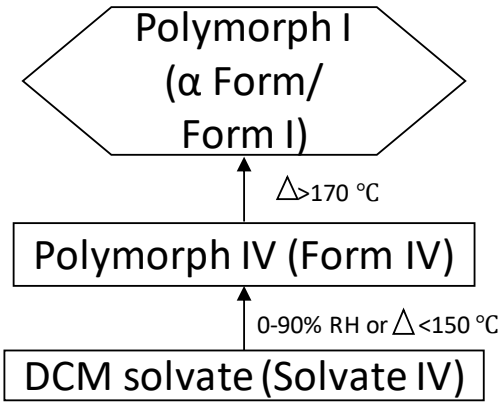


Figure 4.36. PXRD spectra of solvate IV ad different heating interval. Heating to 150 °C yeilded polymorph IV while >170°C forms polymorph I



Scheme 4.7. Pathway showing the relationship between solvate IV and its related forms

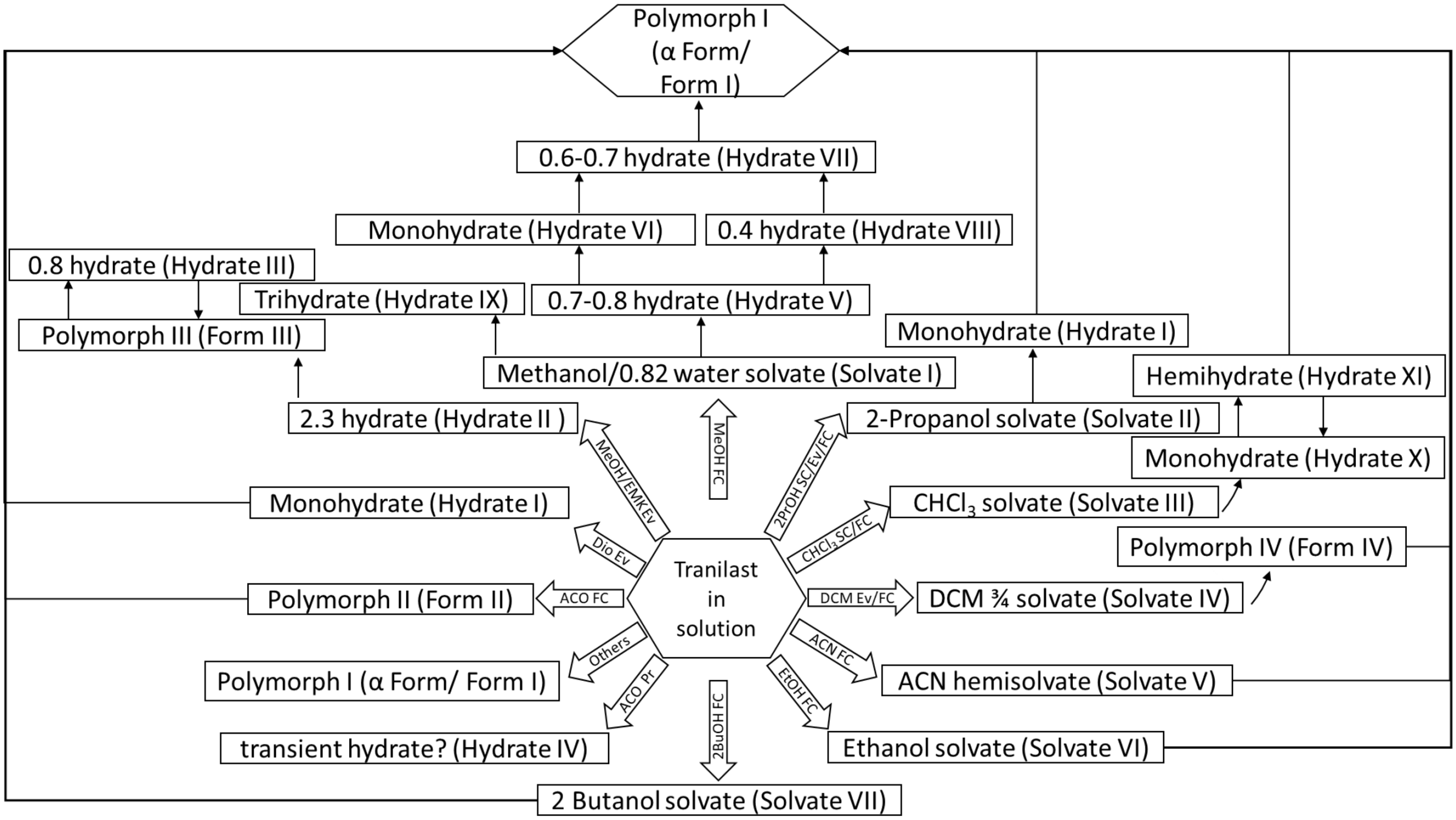
4.7.4 Solvate V, VI and VII

Finally, three more novel solvates identified as acetonitrile hemisolvate: solvate V, ethanol monosolvate: solvate VI and 2-butanol monosolvate: solvate VII, which were crystallised by quench cooling of TRN from hot acetonitrile, ethanol and 2-butanol respectively. All the novel three solvates desolvates to form I at ambient in similar manner to that solvate IV in Figure 4.33 or when heated to >150 °C.

4.8 Chapter summary and conclusion

The search aiming towards understanding hydrate formation has led to an astonishing discovery of a plethora of novel solid form of TRN. TRN shows an unusually complex hydration behaviour for an uncharged drug molecule. In total, 11 hydrate forms were discovered in this study. Kawashima reported five polymorphic monohydrate,[20] however comparison can only be made to one of the PXRD pattern provided as the rest is ambiguous. Five crystal forms having water content close to one mole was found, which are, three polymorphic monohydrates (one of which has been reported by Kawashima), and two 0.8 hydrates (exact water content are 0.8, 0.7-0.8).

In addition, three higher (a tri-, a 2.3 and a transient 1.5-1.8 hydrate) and three lower (a 0.6-0.7, a hemi, and a 0.4) hydrate forms were also found. a 0.4 hydrate. The 2.3 hydrate crystal structure provides first insight to TRN–water interaction. The solvate to hydrate conversion pathway presents a new outlook in hydrate formation. All-in-all, the study highlights the importance of thorough understanding of the solid-state landscape to ensure a safe and efficient manufacturing process. More importantly, the variety of role played by water, as a stabilising component and having crucial implication to the crystal structure e.g. the 2.3 hydrate to 0.8 hydrate transition. The multiple form observed here points to the dilemma of having multiple solid forms, acting as double-edged sword which can either hamper a drug true potential OR an opportunity for better or more process-able crystal form.



Scheme 4.8. Pathway showing the relationship between all screened TRN crystal forms

4.9 References

1. Griesser, U. J. & Burger, A. The effect of water vapor pressure on desolvation kinetics of caffeine 4/5-hydrate. *Int. J. Pharm.* **120,** 83–93 (1995).

2. Khankari, R. & Grant, D. J. W. Pharmaceutical hydrates. *Thermochim. Acta* **248,** 61–79 (1995).

3. Sastry, S. V., Nyshadham, J. R. & Fix, J. A. Recent technological advances in oral drug delivery – a review. *Pharm. Sci. Technolo. Today* **3,** 138–145 (2000).

4. Fasano, A. Novel Approaches for Oral Delivery of Macromolecules. *J. Pharm. Sci.* **87,** 1351–1356 (1998).

5. Hauss, D. J. Oral lipid-based formulations. *Adv. Drug Deliv. Rev.* **59,** 667–676 (2007).

6. Lipinski, C. Poor Aqueous Solubility – an Industry Wide Problem in Drug Discovery. *Am. Pharm. Rev.* **5,** 82–85 (2002).

7. Najib, M. N. M., Back, K. & Edkins, K. The Complex Solid-State Landscape of Sodium Diatrizoate Hydrates. *Chem. - A Eur. J.* **23,** 17339–17347 (2017).

8. Raijada, D. *et al.* Exploring the Solid-Form Landscape of Pharmaceutical Hydrates: Transformation Pathways of the Sodium Naproxen Anhydrate-Hydrate System. *Pharm. Res.* **30,** 280–289 (2013).

9. Tieger, E., Kiss, V., Pokol, G. & Finta, Z. Crystallisation of a salt hydrate with a complex solid form landscape. *CrystEngComm* **19,** 1912–1925 (2017).

10. Stahl, K., Treppendahl, S. P., Preikschat, H. & Fischer, E. Sodium 3-ammonio-1-hydroxypropylidene-1,1-bisphosphonate monohydrate. *Acta Crystallogr. Sect. E Struct. Reports Online* **61,** 132–134 (2004).

11. Vega, D., Fernández, D. & Ellena, J. A. Disodium pamidronate. *Acta Crystallogr. Sect. C Cryst. Struct. Commun.* **58,** m77–m80 (2002).

12. Zupančič, V., Ograjšek, N., Kotar-Jordan, B. & Vrečer, F. Physical characterization of pantoprazole sodium hydrates. *Int. J. Pharm.* **291,** 59–68 (2005).

13. Parkin, A., Parsons, S., Pulham, C. R. & IUCr. Paracetamol monohydrate at 150 K. *Acta Crystallogr. Sect. E Struct. Reports Online* **58,** 1345–1347 (2002).

14. McGregor, P. A., Allan, D. R., Parsons, S. & Pulham, C. R. Preparation and crystal structure of a trihydrate of paracetamol. *J. Pharm. Sci.* **91,** 1308–1311 (2002).

15. Fabbiani, F. P. A. *et al.* High-pressure recrystallisation—a route to new polymorphs and solvates. *CrystEngComm* **6,** 504–511 (2004).

16. Hegedüs, B. & Görög, S. The polymorphism of cimetidine. *J. Pharm. Biomed. Anal.* **3,** 303–313 (1985).

17. Ibers, J. A. & IUCr. Gabapentin and gabapentin monohydrate. *Acta Crystallogr. Sect. C Cryst. Struct. Commun.* **57,** 641–643 (2001).

18. Vasudev, P. G. *et al.* Crystal structures of a new polymorphic form of gabapentin monohydrate and the E and Z isomers of 4-tertiarybutylgabapentin. *Chem. Biol. Drug Des.* **73,** 83–96 (2009).

19. Fabbiani, F. P. A. *et al.* Searching for novel crystal forms by in situ high-pressure crystallisation: the example of gabapentin heptahydrate. *CrystEngComm* **12,** 2354 (2010).

20. Kawashima, Y. *et al.* Characterization of polymorphs of tranilast anhydrate and tranilast monohydrate when crystallized by two solvent change spherical crystallization techniques. *J. Pharm. Sci.* **80,** 472–478 (1991).

21. Paneque, A., Duque, J. & Pomés, R. *Caracterización cristalográfica y determinación precisa de los parámetros del Tranilast (C1sH17N05).*

22. Vogt, F. G. *et al.* Structural analysis of polymorphism and solvation in tranilast. *J. Pharm. Sci.* **94,** 651–665 (2005).

23. Villa, A. C., Manfredotti, A. G. & Guastini, C. . *Cryst. Struct. Commun.* **8,** 457 (1979).

24. Allen, P. V., Rahn, P. D., Sarapu, A. C. & Vanderwielens, A. J. Physical Characterization of Erythromycin: Anhydrate, Monohydrate, and Dihydrate Crystalline Solids. *J. Pharm. Sci.* **67,** 1087–1093 (1978).

25. Yuasa, R. *et al.* Pharmaceutical studies on hydrates of AM-715. Physical characteristics and intestinal absorption. *Yakugaku Zasshi* **102,** 469–76 (1982).

26. Koda, A., Nagai, H., Watanabe, S., Yanagihara, Y. & Sakamoto, K. Inhibition of hypersensitivity reactions by a new drug, N(3′,4′-dimethoxycinnamoyl) anthranilic acid (N-5′). *J. Allergy Clin. Immunol.* **57,** 396–407 (1976).

27. Azuma, H., Banno, K. & Yoshimura, T. Pharmacological Properties Of N-(3′,4′-Dimethoxycinnamoyl) Anthranilic Acid (N-5′), A New Anti-Atopic Agent. *Br. J. Pharmacol.* **58,** 483–488 (1976).

28. Isaji, M., Nakajoh, M. & Naito, J. Selective inhibition of collagen accumulation by N-(3, 4-dimethoxycinnamoyl)anthranilic acid (N-5') in granulation tissue. *Biochem. Pharmacol.* **36,** 469–474 (1987).

29. Darakhshan, S. & Pour, A. B. Tranilast: A review of its therapeutic applications. *Pharmacol. Res.* **91,** 15–28 (2015).

30. Burger, A. Interpretation of polymorphism studies. *Acta Pharm. Technol.* **28,** 1–20 (1982).

31. Leung, S. S., Padden, B. E., Munson, E. J. & Grant, D. J. W. Hydration and Dehydration Behavior of Aspartame Hemihydrate. *J. Pharm. Sci.* **87,** 508–513 (1998).

32. Miroshnyk, I. *et al.* Insight into thermally induced phase transformations of erythromycin A dihydrate. *Cryst. Growth Des.* **6,** 369–374 (2006).

33. Mirza, S. *et al.* Influence of solvents on the variety of crystalline forms of erythromycin. *AAPS PharmSci* **5,** E12 (2003).

34. Stephenson, G. A., Groleau, E. G., Kleemann, R. L., Xu, W. & Rigsbee, D. R. Formation of isomorphic desolvates: Creating a molecular vacuum. *J. Pharm. Sci.* **87,** 536–542 (1998).

35. Vogt, F. G. *et al.* A study of variable hydration states in topotecan hydrochloride. *J. Pharm. Biomed. Anal.* **40,** 1080–1088 (2006).

36. Chen, L. R., Young Jr., V. G., Lechuga-Ballesteros, D. & Grant, D. J. W. Solid-state behavior of cromolyn sodium hydrates. *J. Pharm. Sci.* **88,** 1191–1200 (1999).

37. Pfeiffer, R. R., Yang, K. S. & Tucker, M. A. Crystal Pseudopolymorphism of Cephaloglycin and Cephalexin. *J. Pharm. Sci.* **59,** 1809–1814 (1970).

38. Byard, S., Abraham, A., Paul, P. J., Harris, R. K. & Hodgkinson, P. A multi-technique approach to the study of structural stability and desolvation of two unusual channel hydrate solvates of finasteride. *J. Pharm. Sci.* **101,** 176–186 (2012).

39. Burger, A. & Ramberger, R. On the polymorphism of pharmaceuticals and other molecular crystals. II. *Mikrochim. Acta* **72,** 273–316 (1979).

40. Threlfall, T. L. Turning DSC Charts of Polymorphs into Phase Diagrams: A Tutorial Paper. *Org. Process Res. Dev.* **13,** 1224–1230 (2009).

CHAPTER 5

INFLUENCE OF WATER TOWARDS PRE-NUCLEATION AGGREGATES LEADING TO THE FORMATION OF STABLE CRYSTALLINE HYDRATES

5.1 Chapter overview

This chapter discusses the solid- and solution-state analysis of drugs with the ability to form a stable hydrate in the solid state, with emphasize on method development and refinement for later the solution-state. As discussed in chapter 1, 3 and 4, hydrates present constant challenges due to their low aqueous solubility. The poor aqueous solubility is due to the form's improved thermodynamic stability,[1] and having a lower free Gibbs energy than anhydrate form.[2] Although water is ubiquitous, hydrate emergence remains unpredictable and uncertain, even for the types of molecules which are prone to form hydrates.[3] The solution-state analysis thus presents a fast and early probe into hydrate formation, as the crystalline form does not need to be present or even known. Recent studies have reported that solution-state analysis has successfully shown intermolecular interaction reflective to the solid state,[4,5] hence the technique is used here to quantify the intermolecular interactions between water and hydrate-forming drug in solution through titration experiment. Four drugs, diatrizoic acid (DTA), cimetidine (CIM), tranilast (TRN), and piroxicam (PXM) were analysed using two methods, NMR and FTIR spectroscopy. The two methods worked in complementary, where FTIR analysis allowed qualitative observation of all the available and affected vibrations, on a faster time scale compared to the NMR. On the

other hand, NMR allowed quantitative measurement of the physical changes in the spectra which were monitored in the form of peak shifts as water is titrated into the respective solution. The general aim of both analytical methods was to observe early influence and interaction of water towards the respective compounds in solution and to probe whether the said interactions were measurable. The strength of the interactions between the components was realised in the form of association constant based on the changes to the NMR resonance peak shifts and subsequent fitting to the respective models, which were then used to determine a prediction value for hydrate formation.

5.2 Introduction

5.2.1 Background

The emergence of hydrate and the related problems in the pharmaceutical industry is an ongoing struggle. As discussed in chapter 1, 3 and 4, the fact is that while pharmaceutical solids are prone to hydrate formation,[6] resulting in hydrate form that modifies the physicochemical properties of the drug, more importantly reduces solubility,[7–10] which in effect will impact the drug efficacy[11,12] and jeopardise patients' safety, the phenomenon remains unpredictable and unclear,[3,13] costing pharmaceutical companies a tremendous amount of time, money, and efforts geared toward screening for all the potential hydrate form.[14] Active *in-silico* approach to computational solid form screening *via e.g.* crystal structure prediction using crystal energy landscapes and statistical models are slowly being extended to predict hydrate.[15–20] However, as stated in chapter 1 (1.2), the approach still demands time, money and efforts, which were the

initial reasons to use the approach, leaving hydrates formation largely unpredictable and remains a challenge in crystal engineering.[21]

5.2.2 The new approach towards understanding the role of water in hydrate-forming drug compounds

With that in mind, we propose a probe of the solution-state, by observing compound-water interaction at pre-nucleation state. As mentioned in chapter 1, we suggest that there is some degree of molecular recognition between a hydrate-forming compound and water which would lead to the formation of pre-nucleation complexes in solution. The said interaction would yield a significant structural binding value rather than a random interaction, especially for a compound that can form a stable hydrate. Through the early observation and probe, we aim to find a general pattern of solid-water interaction for hydrate forming compounds, with the aim to develop a faster, more efficient and more focused prediction approach. We hypothesise that (stable) hydrate forming compounds will have the ability to form a compound-water complex or at the very least show significant interaction with water, in solution. The importance and relevance of solution-state analysis have been discussed comprehensively in chapter 1 (1.3 and 1.5), with emphasis on the successful connection to the solid-state. One of the common solution-state technique is titration, which is normally used in supramolecular chemistry to quantify an interaction.

The principle behind FTIR analysis discussed in chapter 2 (2.2.5) and the method used in (2.3.2). FTIR analysis allowed observation on the effect of titration on all of the available and affected vibrations, especially on hydrogen bond sensitive vibrations, *e.g.* the carbonyl (C=O). The fast time scale of the method also made it

possible to monitor all of the formed species during the titration. On the other hand, NMR titration experiments were used primarily to determine the association constant between drug and water. The principle behind the method, along with the technique used was discussed in chapter 2 (2.3.3 and 2.3.7). The mentioned probes were initially done to drugs which have one common property, which is having the ability to form the stable hydrate. Stable hydrate was internally defined as water-incorporated crystals which have the ability to hold water in the crystal lattice at a low (less than 10%) relative humidity (RH) isotherm at 25°C and upon heating to at least 60 °C without being dehydrated and retaining the crystal form. Despite being seemingly simple, many criteria needed to be carefully considered to ensure that the final results were reliable. Among others are drug solubility, solvent selection, host and guest concentration, the physical changes detection method (*i.e.*, NMR, infrared), choice of stoichiometric binding model and *etc*. The continuous variation method, or Job's plot, was used in determining the stoichiometry of binding complexes, information later used to fit the binding models.

5.2.3 The model/the host: diatrizoic acid (DTA), cimetidine (CIM), tranilast (TRN), and piroxicam (PXM)

Four drugs were chosen for the initial probe due to their ability to exist as a stable hydrate based on earlier reports and in-house data. The probed drugs are, diatrizoic acid (DTA),[22] tranilast (TRN, chapter 4),[23] cimetidine (CIM)[24], and piroxicam (PXM)[25]

DTA is known to exist as two hydrated (dihydrate and tetartohydrate), three anhydrous and nine solvated solid forms.[22,26] The dihydrate form has been reported to

be extremely stable, and the crystal structure shows extensive hydrogen bond interactions with water *via* the amide and carboxylic acid groups.[22]

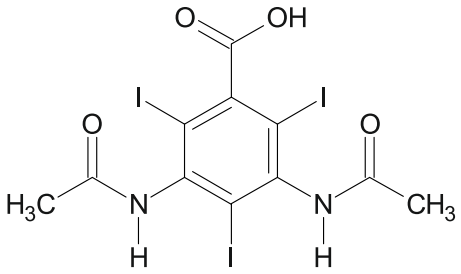


Figure 5.1. Chemical structure of DTA

The DTA molecule has two amide NH groups and one carboxylic acid OH functionality as hydrogen-bond donors, as well as two amide and one carboxylic acid carbonyl groups as hydrogen-bond acceptors (Figure 5.1). The balanced ratio of donors and acceptors in the DTA molecule promotes extensive hydrogen-bonded networks in the crystalline structure. Also, the three iodo substituents offer additional possibility of halogen-bonding interactions.[27]

The next pharmaceutical compound probed was cimetidine (CIM). CIM is made of three main functional units: a 4,5-disubstituted imidazole ring, a cysteine and an N-cyanoazamethine or guanidine derivative (Figure 5.2). The flexible guanidine chain and numerous hydrogen bonding sites (–NH groups and C≡N) can give rise to multiple crystal forms due to the ability of the molecule to adopt various conformations. CIM has been reported to exist as a polymorphic monohydrate (M1, M2 and M3) and four anhydrous polymorphs (Form A, B, C, and D).[24]

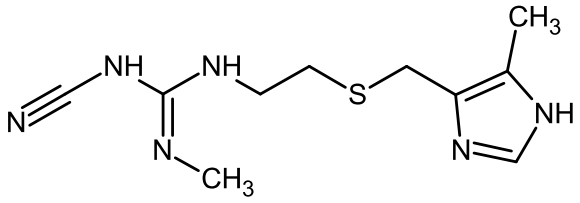


Figure 5.2. Chemical structure of CIM

Details on tranilast (TRN) was mentioned in chapter 4. We have reported that TRN exists as at least 11 hydrate forms: a trihydrate, a 2.3 hydrate, a 1.5-1.8 (transient) hydrate, three polymorphic monohydrates (one of which has been reported before), two 0.8 hydrates (exact water content are 0.8 and 0.7-0.8), a 0.6-0.7 hydrate, a hemihydrate and a 0.4 hydrate. We also reported four polymorphs and seven solvates, one of which found to be water mixed. The previous report on the anti-allergic agent reported that compound to exist as three anhydrous polymorphs (form I was also found in our analysis) and five polymorphic monohydrates (monohydrate I was similar), along with two solvates ($CHCl_3$ solvate was found as well).[23,28] However, the literature of solid-state forms are ambiguous, with CCDC database search accounts for two dissimilar crystal structure of the anhydrous polymorph, along with two different chloroform ($CHCl_3$) solvate structure. The other submitted solvate form is dichloromethane (DCM) solvate.[28] TRN structure consist of two proton donors and five acceptors site which are capable of forming hydrogen bond with water.

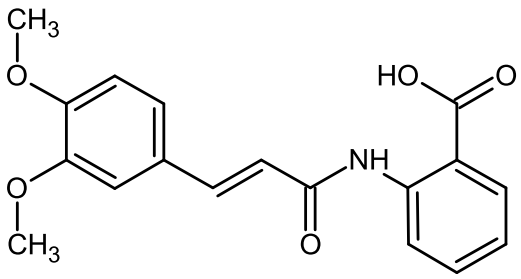


Figure 5.3. Chemical structure of TRN

Piroxicam (PXM) is a nonsteroidal anti-inflammatory drug (NSAID). The compound has two hydrogen bond donor, and six acceptor site. PXM also posseses acidic enolic OH (Figure 5.4, (a))[29] in its structure, a feature which gives PXM the ability to form inter- and intramolecular hydrogen bond allowing the structure to adopt different structures and various conformations depending on the surrounding condition, i.e. pH.[30] For example, at the lowest possible energy levels or ground state, the closed enol structure (Figure 5.4, (b)) transform into the keto-type form (Figure 5.4, (c)) upon electronic excitation in nonpolar solvents through an intramolecular proton transfer reaction.[31] The anionic structure (Figure 5.4, (d)) is favourable following neutral pH and biologically favourable conditions,[32] while in protic solvents, an open conformer or zwitterionic form (Figure 5.4, (e)) is formed, which consist of two intramolecular hydrogen bonds in the PXM molecule.[33–35]

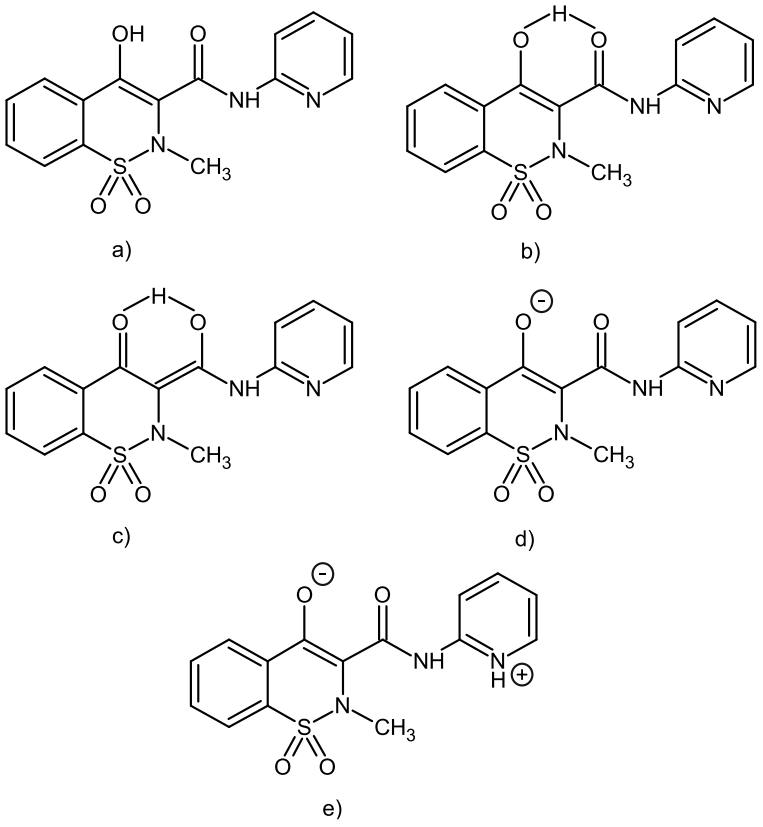


Figure 5.4. General chemical structure of PXM (a) and the different ionisation states modifications of PXM under various conditions (b)-(e).

5.3 Results and Discussion

5.3.1 DTA solid-state preliminary analysis

DTA starting compound was analysed to determine its state of form. PXRD in Figure 5.5 revealed that the trace is consistent with the dihydrate form. Dehydrating the sample (heating to above 100 °C) produced a different PXRD trace (Figure 5.5, bottom trace) to the starting compound.

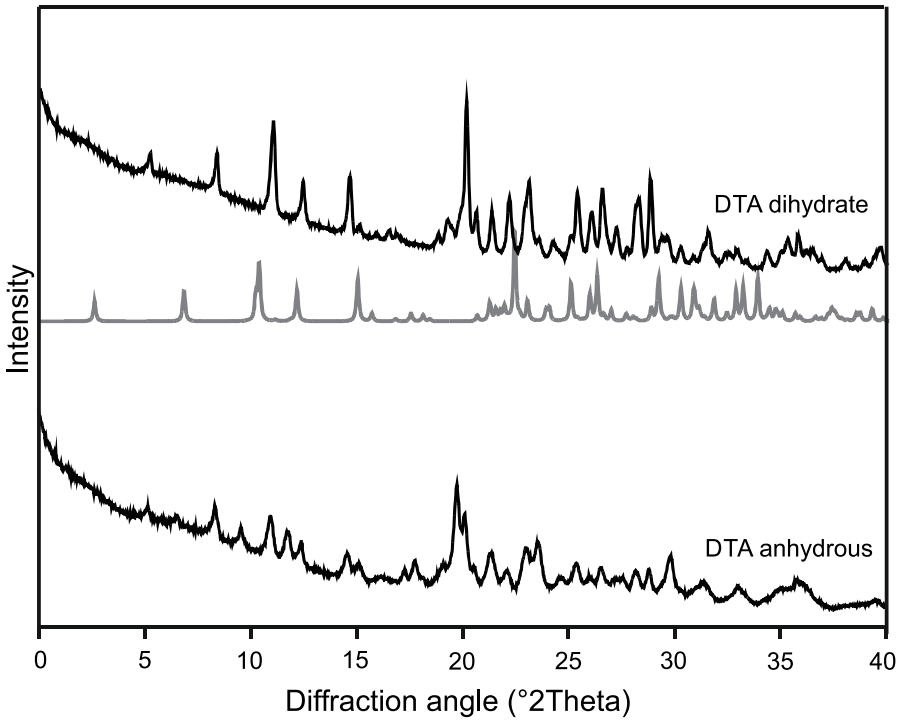


Figure 5.5. PXRD of DTA dihydrate and the anhydrous form II. The small differences between the measured and predicted DTA dihydrate patterns are due to the platy habit of this crystalline form, hence highly preferred oriented. Also, the two measurements were taken at two different temperatures, *i.e.* ambient and 120 K.[22]

TGA and DSC analysis in Figure 5.6 also revealed distinctly different traces between the two forms. The weight loss recorded from the TGA of the dihydrate was 5.525% (corresponding to 1.993 molar equivalent of water, two molar equivalents is

calculated to 5.543% mass change). DSC shows an endothermic event parallel to the dehydration curve observe in the TGA. In addition, an exothermic event typical of enantiotropic phase transition of form II to III, was also observed, which is similar to the previously reported literature.[22] A follow-up TGA of the anhydrous form exposed to the ambient environment for 30 minutes directly after dehydration highlights the compound's affinity towards water. Within that exposure time, almost all water loss (4.8%, corresponding to 1.7 moles of water) was recovered (Figure 5.6). Subsequent DVS analysis of the dihydrate form revealed a stable behaviour, with very little mass change throughout the humidity cycle (0.02% between the two extreme RH), indicative of surface water (Figure 5.7).

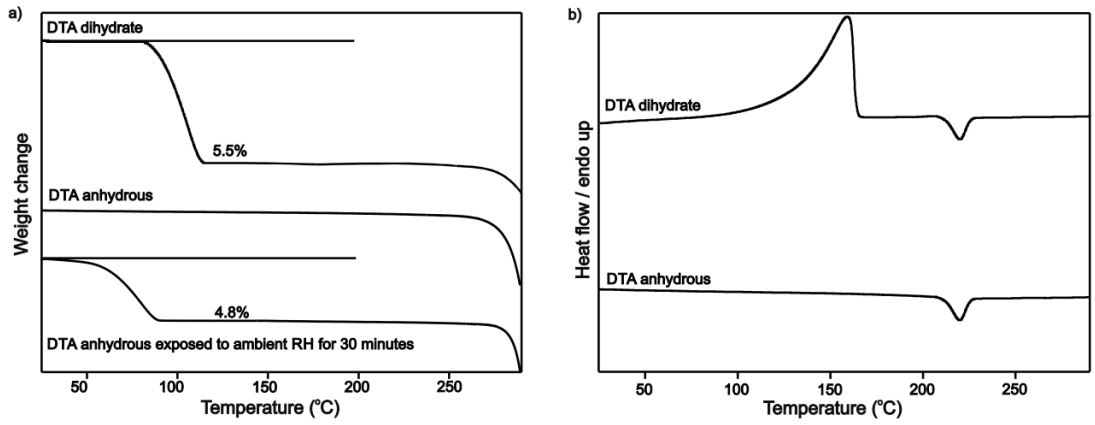


Figure 5.6. TGA (a) and DSC (b) of DTA dihydrate and anhydrous forms. Also, additional follow-up TGA of the anhydrous form, after ambient environment exposure for 30 minutes.

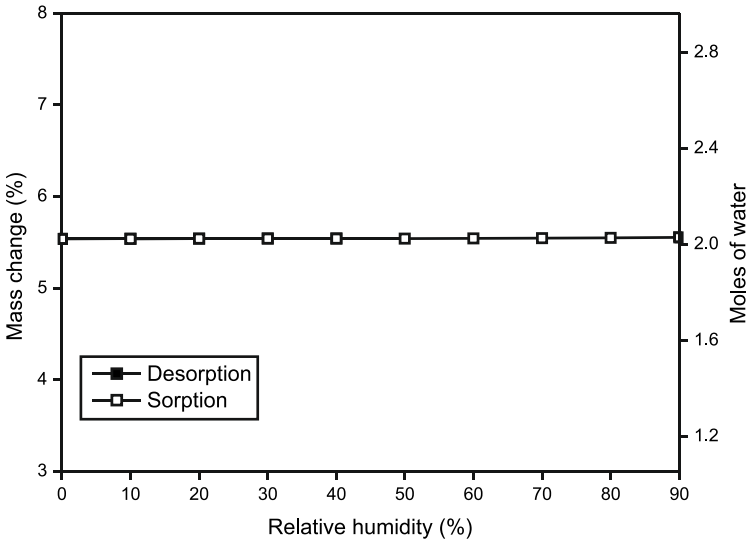


Figure 5.7. DVS isotherm of the DTA dihydrate.

Similar to the PXRD, TGA, and DSC trace, the FTIR spectra also shows clear differences between the dihydrate and anhydrous form. Interpretation of the subsequent FTIR spectra were based on vibrational frequency assignment for DTA from the report by Lerner, assigning the NH stretch to 2985 cm^{-1}, C=O of the acid to1700 cm^{-1} and amide to1661 cm^{-1}, and finally the secondary amide and aromatic C=C stretch to1551 cm^{-1} wavenumbers respectively.[36] In addition, the single-crystal neutron structure reported by Fucke *et al*. also guide our interpretation of the FTIR spectra.[22] Based on the single-crystal neutron structure, water coordinates to DTA *via* the carbonyl of the acid and amide exclusively.[22] Our in-house FTIR spectra of DTA showed comparable spectra to the reported data, with notable differences between the dihydrate and the anhydrous form especially on the respective carbonyl vibrations (Figure 5.8).[36,37]

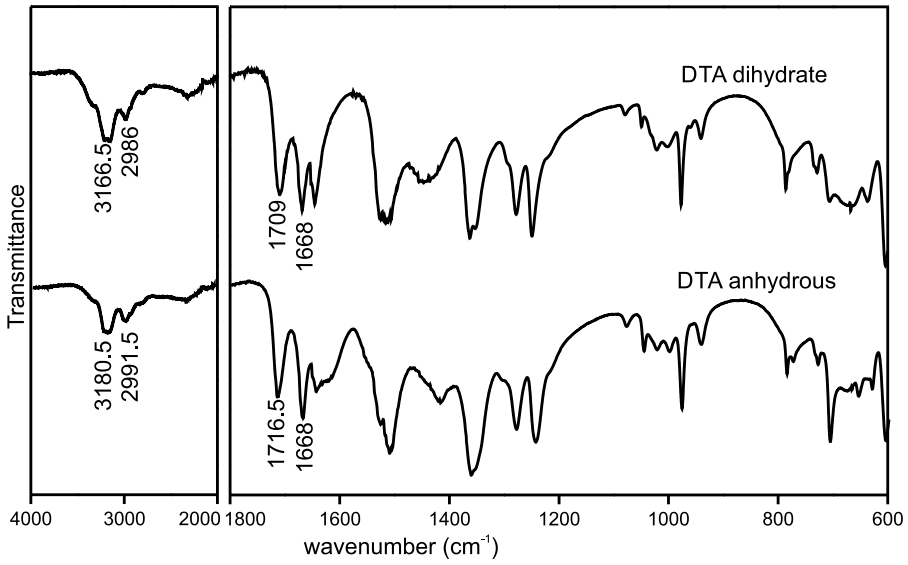


Figure 5.8. DTA dihydrate and anhydrous form FTIR spectra

At the higher wavenumber around 3000 cm^{-1}, both forms showed a broad double peak, followed by a weak shoulder. The double peaks are consistent with the stretching vibration of the two NH group, while the shoulder appearing just below 3000 cm^{-1} is consistent with the OH stretching vibration. Although the mentioned peak features are the same, the anhydrous peaks come at a much higher wavenumber, 3180.5 cm^{-1} compared to 3156.5 cm^{-1} of the dihydrate form. The shoulder in the anhydrous spectra also appeared at a higher position of 2991.5 cm^{-1} compared to 2986 cm^{-1} of the dihydrate.

More importantly in the fingerprint region, the vibration indicative of a carbonyl of the acid functionality, showed a significant difference between the forms, appearing at 1716.5 cm^{-1} (anhydrous), and 1709 cm^{-1} (dihydrate). Meanwhile, the carbonyl of the amide at 1668 cm^{-1}, did not change position. In principle, the dihydrate form would show more hydrogen bond due to the interactions with water and a direct effect of the formed hydrogen bond can often be observed on the acceptor side, DTA e.g. in X-H···O=C bonds, the carbonyl O=C bond is weakened leading to a lowering

of the stretching vibration frequency.[38] The presence of hydrogen bond (to water) affects the position of already existing peaks by transferring charges by withdrawing electron density, effectively 'pulling' the C=O away from one another and stretching the respective covalent bond Numerous solid-state IR studies have shown that the carbonyl region is a very sensitive region towards hydrogen bond, shifting to lower wavenumber as hydrogen bond forms, with a stronger hydrogen bond tends to shift the carbonyl frequency more (lower).[39–41] This observation follows the 'ball and spring theory', as discussed in chapter 2 where weakening or lengthening of the bond will decrease the vibrational frequency (and *vice versa*).[42,43] Therefore, it is as expected that the highlighted peaks of the anhydrous form would appear at higher wavenumbers (and lower in the dihydrate), reflecting the absence of hydrogen bond to water of the respective functionalities or bands after desolvation. As water is released from the lattice. and as the bond of the existing functional group becomes less affected or less stretched by hydrogen bonding to water, the affected vibrations/peaks, will shift (back) to higher wavenumber.

5.3.2 FTIR: DTA solution-state titration and kinetic study

The solid-state analysis guides the interpretation of the spectrum of 1.54 M DTA in DMSO. Figure 5.9 shows the complete spectral range from 4000 to 400 cm^{-1} with highlight on the regions of interest (inset) which are the NH and OH stretching region 3000-3600 cm^{-1} as well as the carbonyl region from 1750-1600 cm^{-1} of the acid and amide groups respectively.

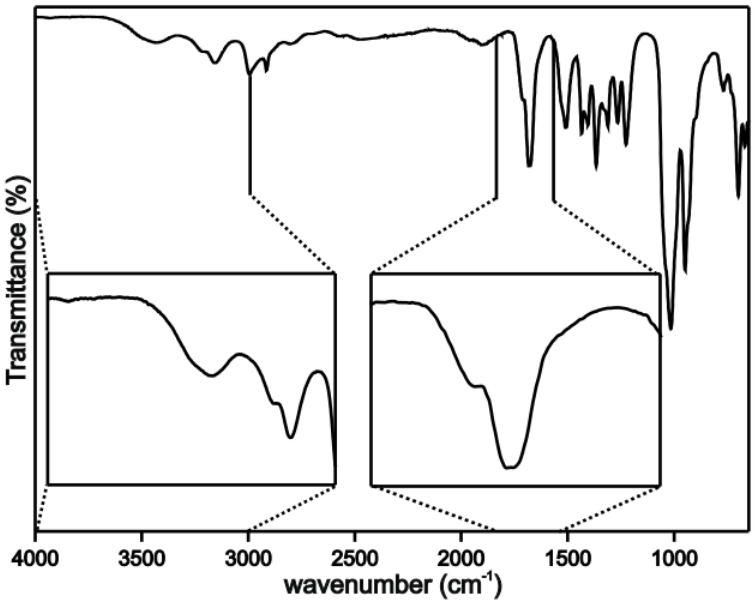


Figure 5.9. DTA 1.54 M in DMSO solution FTIR spectrum with vibration range of interest are highlighted in the inserts.

In solution, the DTA carbonyl region appears as a singular peak at 1683 cm^{-1}, with a shoulder at 1710 cm^{-1}. The distinction between the carbonyl of the acid and carbonyl of the amide group is difficult to ascertain. In the solid-state, carbonyl of the acid group appears at a higher wavenumber, followed by the amide.[36] It is highly like that similar scheme is replicated in solution, suggesting that the shoulder represent the carbonyl of the acid, while the main peak observed is the amide carbonyl moiety. The use of anhydrous DMSO allows for clear observation of OH and NH stretching vibrations at 3430 and 3155 cm^{-1} respectively.

Kinetics study to observe the ingress of water in the anhydrous DMSO-DTA solution mixture was done, in which the mixture is tested in an open setting where the system was left at ambient conditions (40% RH, 25 °C) and a time-dependent FTIR measurements were taken. The FTIR spectra were measured every six seconds for 150 minutes (Figure 5.10, (a)). The influence of DMSO was also probed as DMSO is reported to be hygroscopic.[44] Anhydrous DMSO-only preparation with a similar setup

was subjected to similar conditions for comparison (Figure 5.10, (b)). The experiment showed DTA propensity towards water in solution, based on the intensity of the OH vibrations (3400 cm^{-1}, 85 *vs.*75% transmittance), which clearly shows that more water ingresses in the DMSO-DTA solution mixture as higher DTA concentration used allows for faster and stronger water ingress from the environment compared to only DMSO at a similar timescale.

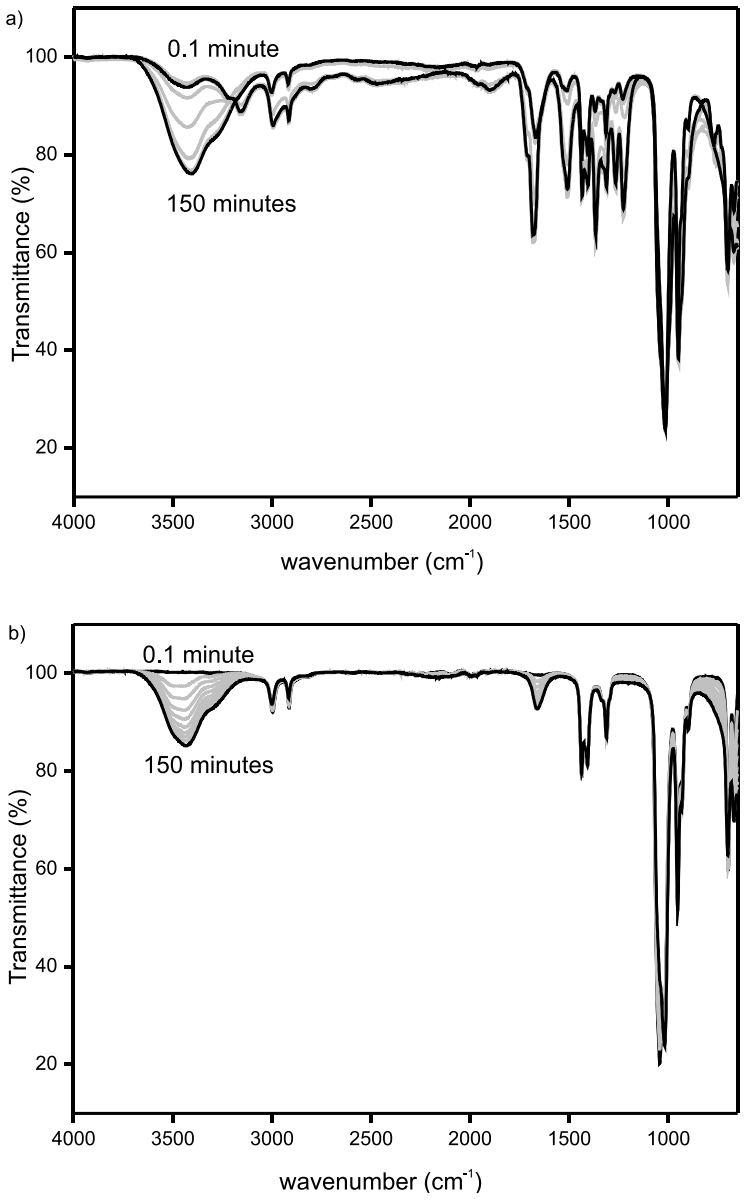


Figure 5.10. a) DMSO-DTA solution mix *vs* b): DMSO-only, exposed to ambient conditions for 150 minutes.

A water molecule has a broad symmetric (*v1*) and asymmetric OH stretching (*v3*) in the region of 3400 cm^{-1}, a very weak OH bending (*v2*) and libration vibration at 2128 cm^{-1}, as well as another *v2*, medium strength vibration in the region of 1644 cm^{-1}.[45] In DMSO-water mixture, the second bending, *v2* vibration can be observed at 1660 cm^{-1} which in Figure 5.10 (b) clearly shows that as pure DMSO was left exposed to the environment, water stretching and bending vibrations peaks grew with time as more water was absorbed. The *v2* vibration at 1644 cm^{-1} is weak, and in the DMSO-DTA mixture, it is obstructed by the strong and intense carbonyl vibration. Influence form this vibration towards the carbonyl peak shift is minimal, but cannot be ruled out or overlooked.

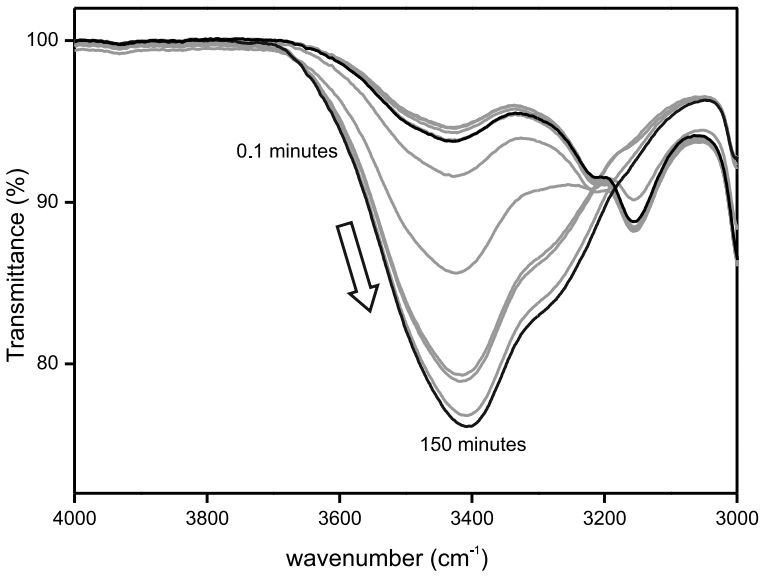


Figure 5.11. The FTIR spectra highlighting on the NH and OH stretching region of DTA in DMSO-DTA solution mixture following exposure to ambient conditions for 150 minutes.

Observation of DMSO-DTA mixture, focusing on the NH and OH stretching region from 3000-3600 cm^{-1} (Figure 5.11), showed an increase to the OH vibration relative to the exposure time. The increase in absorbance (or reduction in % transmittance) of the OH vibration is most likely due to the increase in concentration

(Beer's law, A = εlc, A, absorbance, ε, absorptivity, l, pathlength, c, concentration)[46], which is consistent with the ingress of water into the system as previously seen in DMSO-only experiment (Figure 5.10, (b)). Interestingly, the NH stretching does not change in shape or intensity, up to 40 minutes of exposure. After 55 minutes, the vibration is barely visible. The reason for this is most likely due to the overlapping of the OH vibration as more water is incorporated. As for the secondary amide and aromatic C=C at 1509 cm^{-1}, no change in peak position was observed throughout the experiment.

More importantly, observation of the carbonyl region in Figure 5.12, which is sensitive towards hydrogen bonding, [39–41] shows no immediate shift (from zero to five minutes), with the main carbonyl peak of the spectra remains constant at 1683 cm^{-1}. The first shift of a single wavenumber to the carbonyl of the amide group was observed after 10 minutes. The single shift to lower wavenumber suggests hydrogen bond formation to this region. Continuous hydrogen bond formation due to the ingress of water with time, withdraws electron density from the bridging hydrogen atom, resulting in the stretching of C=O double bond leading to right-shift in the wavenumbers as more bonds are formed. At 60 minutes, the shift of the amide carbonyl peak is complete totalling 13 cm^{-1}, from1683 to 1670 cm^{-1}.

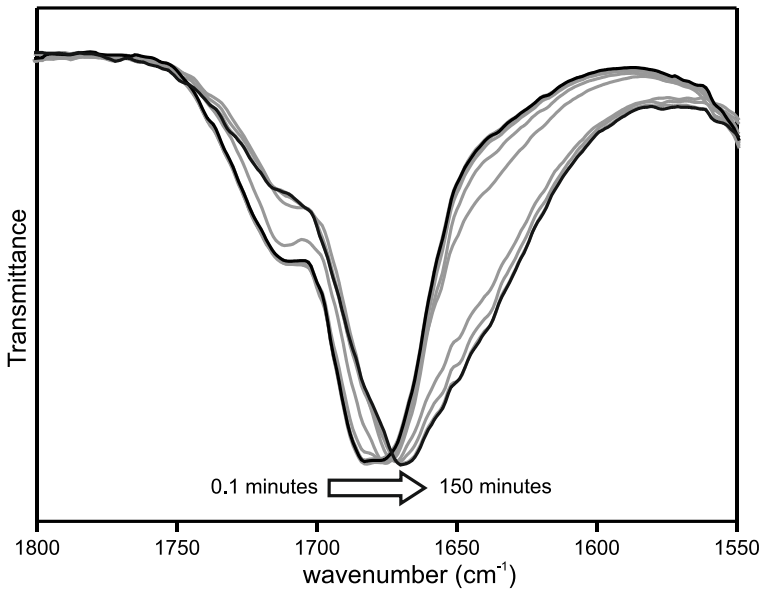


Figure 5.12. The FTIR spectra highlighting on the C=O stretching region of DTA in DMSO-DTA solution mixture following exposure to ambient conditions for 150 minutes.

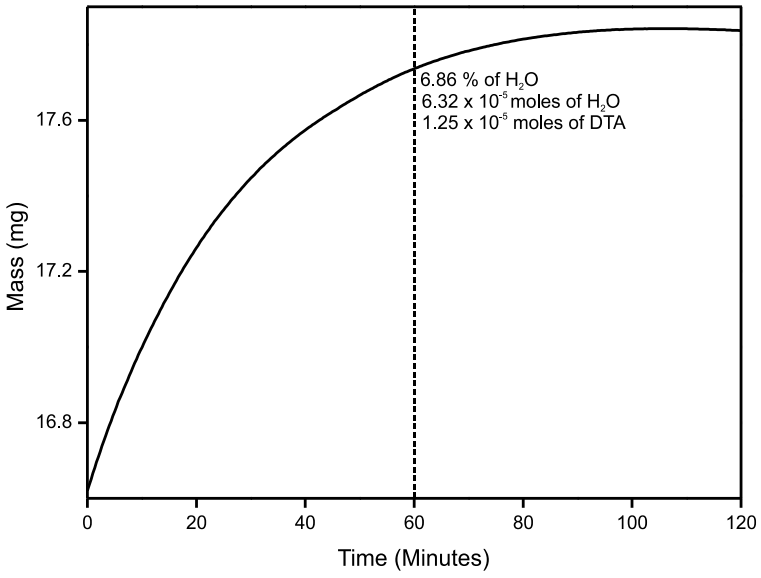


Figure 5.13. DMSO-DTA mixture vapour-sorption gravimetric experiment, where mixture sample was exposed to isotherm at 40% RH for 120 minutes

Estimation of the amount of water which has ingresses from the environment in the kinetics experiment would allow investigation into DTA-water interaction with controlled water content. A vapour-sorption gravimetric experiment chamber was set

up to similar conditions of 25 °C and 40% RH. Similar DTA solution with 1.54 M concentration was loaded and exposed to the above conditions for 120 minutes, and the mass change was recorded (Figure 5.13). At 40 minutes, the amount of water taken up by DMSO-DTA mixture is 5.89% (calculated to 5.42 x 10^{-5} moles of water) which is approximately 4.33 molar ratio. At this point, the mass change slope is steep, suggesting a high rate of water ingress. At 60 minutes, the amount of water taken up by DMSO-DTA mixture is 6.86% (calculated to 6.32 x 10^{-5} moles of water) which is 5.05 molar ratio. At this point, the slope is coming to a plateau (Figure 5.13).

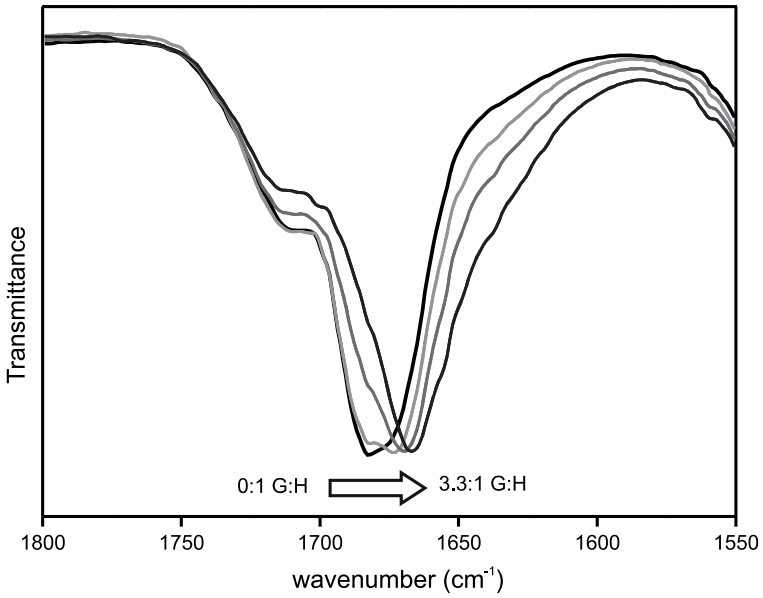


Figure 5.14. High concentration DTA-water FTIR spectra for the titration experiment with controlled water content in an open system

Based on the data from the vapour-sorption gravimetric experiment, DMSO-DTA solution titration with controlled amount of water was initially tested with four different water contents, namely 0, 0.825, 1.650, and 3.30 molar ratios. As expected, the observed shift occurs in the carbonyl region, shifting from 1683 to 1667 cm^{-1} (Figure 5.14). The shift is more evident as all the solution are well mixed, allowing all possible interaction with the carbonyl group as they are in equilibrium, unlike the time-

based the analysis where the surface area limits the interaction with water from the atmosphere.

Titration of a high concentration DTA in a closed system allows for more precise water content to be incorporated as small water quantities can be used, also eliminating the influence of water from the environment. However, high concentration DTA study in liquid cell chamber proved to be problematic as the high concentration causes signal overload, even with the smallest spacer, as the method is very sensitive. The high concentration of DTA also limits the water content DMSO-DTA mixture can accommodate before precipitating out. A lower DTA concentration allows for liquid cell study with more water amount which can be titrated into the system. The downside is that at a lower drug concentration, background or noise vibration becomes more apparent, and may 'interfere' in the observation of the peak of interest, especially the bending (*v2*) OH vibration at 1643.5 cm^{-1} as water is introduced. To minimise the interference, deuterated water (D_2O) and anhydrous DMSO, was used in the following titration.

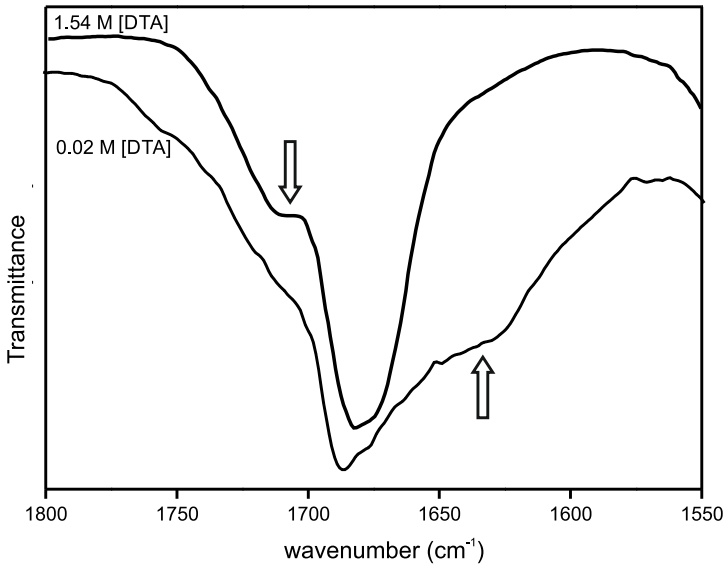


Figure 5.15. The FTIR spectra highlighting on the C=O stretching region of DTA in DMSO-DTA solution mixture with high *vs.* low DTA concentration

Figure 5.15 shows comparison between high (1.54 M) and lower (0.02 M) concentration DTA spectra, highlighting the carbonyl peak wavenumber range. The higher DTA concentration spectrum was from an open system, while the lower was from a closed system. Overall, the peak profile within the wavenumber range of interest shows that the main of the amide functionality still clear and consistent in both setup, with the peak observed in the lower DTA concentration appearing at four wavenumbers higher at 1687 cm^{-1} *vs.*1683 cm^{-1} in the high concentration DTA.

However, the spectra comparison also shows the presence of a shoulder at 1624 cm^{-1} at low DTA concentration (arrow pointing up, Figure 5.15). This shoulder is completely undetectable with the high concentration DTA analysis. Standard[47] and in-house FTIR spectrum of DMSO showed the mentioned shoulder as a very broad and weak peak with 96.5% transmittance. Closer examination revealed that this shoulder is coming off the OH *v2* vibration in a wet DMSO, as DMSO-only does not possess any vibration at this wavenumber.[48] Although the peak was marginal and weak, the

appearance of the water vibration was magnified with low concentration transmission cell analysis. The presence of water maybe to absorption from the environment during the transmission cell setup, or during transfer DMSO. The 1624 cm^{-1} shoulder does not shift but grows, comparable to the growth feature of the vibration at 1660 cm^{-1} comparable to the observation of the DMSO-only exposed to the environment experiment (Figure 5.10). This growth is most likely due to the increase in the concentration of water, giving rise to the increase in the intensity of the absorbance in accordance with Beer's law.[46] A slightly lower wavenumber vibration position observed in this experiment is most likely due to DTA presence in the solution mixture.

Another different feature in the spectra of the low concentration DTA analysis is the absence of the shoulder at 1710 cm^{-1} (arrow pointing down, Figure 5.15). As stated earlier, peak assignment based on the solid-state FTIR spectra of DTA suggests that this shoulder is most likely the carbonyl of the acid functionality. This shoulder was initially undetected at low D_2O content but becomes more apparent once D_2O was added to the system. As DTA concentration remained constant, the increase in the intensity of this carbonyl vibration (the C=O stretching) is generally due to the increase in dipole moment against distance. The said change could be caused by dimerisation involving carbonyl of the the acid group, giving rise to the shoulder. DTA dihydrate neutron diffraction study has reported DTA dimer formation through two hydrogen bonds from the amide (donor) to the carbonyl of the acid group in a centrosymmetric fashion.[22] Based on the observation of the low concentration DTA FTIR titration experiment, which showed the emergence of the carbonyl shoulder with the introduction of D_2O, it is possible that the dimerisation is induced or triggered by water. Also, in the high concentration DTA, this shoulder is present even at low water in the system. Since DTA molecule is abundant, it is very likely that the dimer is

present. Water could potentially induce the dimerisation here, as high DTA concentration generates a higher affinity towards water, in turn, facilitates water absorption from the environment, (inducing dimerisation) giving rise to the shoulder early on. Chemically inducing dimerisation is not a new concept as it has been in chemical sensor development[49] as well as a tool in cell biology for nearly 20 years.[50] One example of the use of chemical induced dimerisation the report by Jiao et al., where the authors used carbazole derivative sa fluorescence carrier, which formed carbazole dimer in the present of iodine.[49] In cell biology, the process is normally associated with the biological mechanism in which two proteins bind only in the presence of a certain small molecule, enzyme or other dimerising agent.[51]

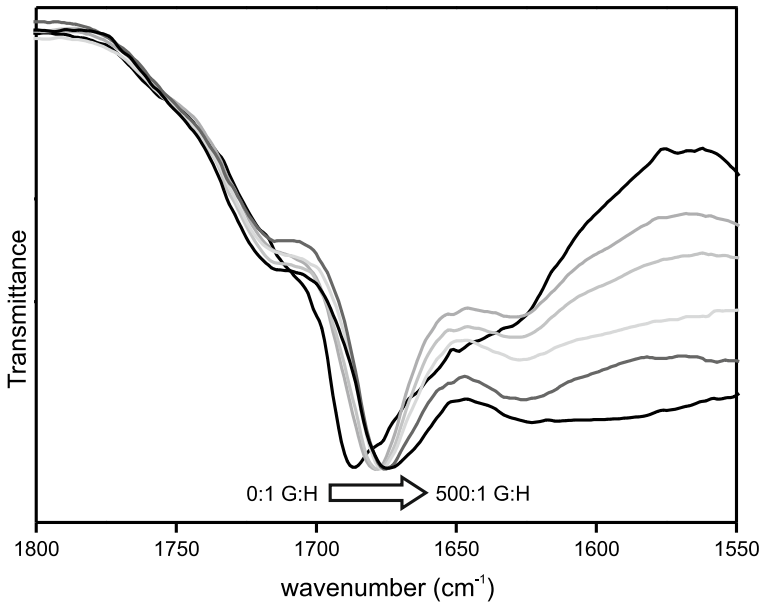


Figure 5.16. Low concentration DTA-water titration experiment with pre-determined water content in a closed system

In the low concentration DTA-water titration experiment with controlled water content in a closed system (Figure 5.16) an immediate shift to lower wavenumber was observed from 0-5:1 G:H molar ratio. At 5:1 G:H molar ratio, the peak appeared slightly broader. It is most likely that the broadening is due to the presence of the D_2O-

carbonyl hydrogen-bonded and non-hydrogen-bonded species, as the FTIR spectra account for all the vibrations of the overlapping species. At the highest D_2O content of 500:1 G:H molar ratio, the shift observed was 12 wavenumbers, to 1675 cm^{-1}. The value is comparable with values obtained from high DTA experiment, which shifts down 13 wavenumbers. DTA peaks observation above this range was challenging as D_2O has a broad and intense OD *v2* and libration vibration at 1555 cm^{-1}.[45]

5.3.3 ^{1}H NMR: DTA-water titration

Three chemical shift regions representing DTA protons were monitored in the initial ^{1}H NMR spectrum in DMSO-d_6 environment, with all peak aligned to TMS at 0 pm. The signal at 13.9 ppm corresponds to the carboxylic acid (OH) proton which was identified as proton 1. At around 10 ppm the NH protons of the amide functionalities were observed. Closer observation of the spectrum revealed that the NH amide protons appeared as two separate peaks, even though both amides are equivalent due to the mirror plane down the molecule. The reason for having different chemical shifts is due to the influence of the huge iodine molecules, which affected the electronic distribution of the respective NH differently. The two peak were later identified as proton 2 at 10.04 ppm and proton 3 at 9.95 ppm respectively. Lastly a singlet representing two methyl group (CH_3) was observed at around 2 ppm in the spectrum (Figure 5.17).

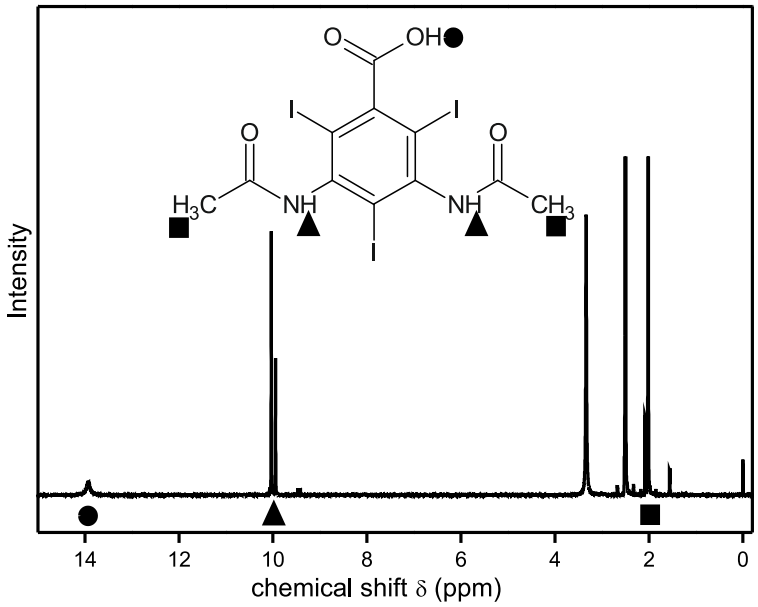


Figure 5.17. DTA ^{1}H NMR spectrum in DMSO-d_6 environment

Integration of the peaks which were calibrated to the six protons of the two methyl group, accounts correctly to the sum of protons associated with DTA. Other visible peaks are of the reference, TMS (0 ppm), DMSO-d_6 (2.5 ppm), water (3.3 ppm) and other impurities. The purity of DTA is calculated to 99.91% with 0.09% impurities, based on the initial NMR spectra. Potential decomposition was most likely the source of the impurity detected as the compound was purchased as a dihydrate, and require desolvation by heating the sample up to 150 ℃ prior to analysis.

Dilution experiment initially was done to ensure that the peak shifts observed, if any were to occur, were indeed due to interaction with water and not the effect of dilution. An adequate amount of anhydrous DMSO was titrated in small aliquots into 1.0 M DMSO-DTA mixture from 0-7:1 G:H molar ratios in 0.5 molar ratio gaps. The dilution experiment revealed that no significant peak shifts were observed to any of the protons, as highlighted in **Figure 5.18** which followed proton 2 and 3 dilution towards higher dilution factor.

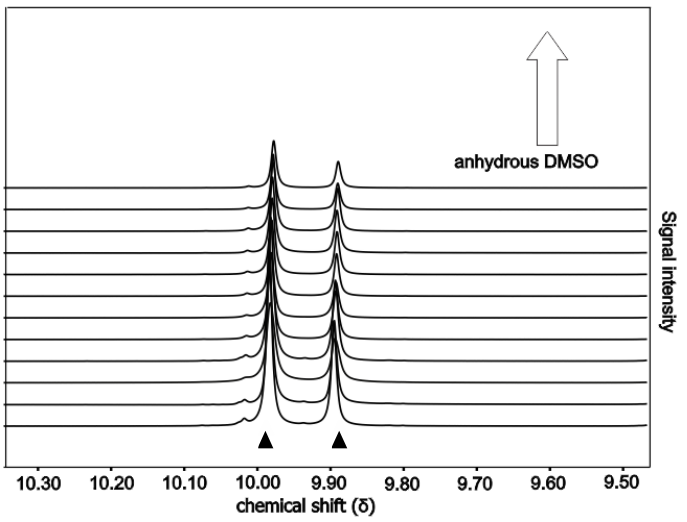


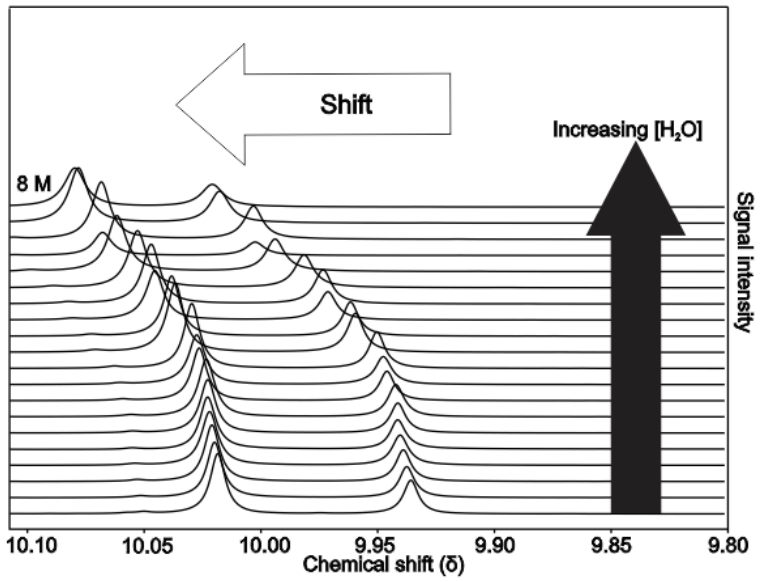
Figure 5.18. DMSO-DTA dilution experiment

A detailed explanation of the fundamental and importance of binding constant measurement has been discussed in Chapter 1 and 2. A stable complex between the reactants, *i.e.* DTA (host, H) and water (guest, G) would correlate to a large binding constant. The finding would prove, or disprove quantitatively our main hypothesis which states that a compound with the ability to form a stable hydrate will show significant interaction with water in solution. As mentioned in chapter 1 and 2, measurement of the binding constants *via* NMR spectroscopy was performed by monitoring the changes in the chemical shift *i.e.* peak shifts, of one or more proton signals in the ^{1}H NMR spectra of the receptor molecule at different guest concentrations.

Examination of the DTA ^{1}H-NMR spectrum revealed that the carboxylic acid OH proton peak appeared at 13.9 ppm as a single, broad peak. The broad shape is due to the peak being generated based on the average site of a fast exchanging proton on the NMR timescale. Monitoring of this peak was difficult as the peak became broader and barely visible above 5:1 G:H molar ratio mark. The methyl groups were also affected by water inclusion; however, the observed peak shift was not significant. The

strongest noticeable peak shift was to the NH of the amide groups. Monitoring of the NH chemical change is sensible since single-crystal neutron structure has also highlighted that the carbonyl of the amide functionality is one of the coordination point to water in the dihydrate structure,[22] therefore, the NH moiety is closest to the interaction point to water, hence experiencing the biggest effect form the compound-water complexation and the resultant electronic rearrangement. In addition, the NH moiety itself is capable of forming hydrogen bond to water by donating proton to the oxygen atom of the water molecule. Even though this motif is not observed in the solid-state, it is still highly possible in solution.

a)



b)

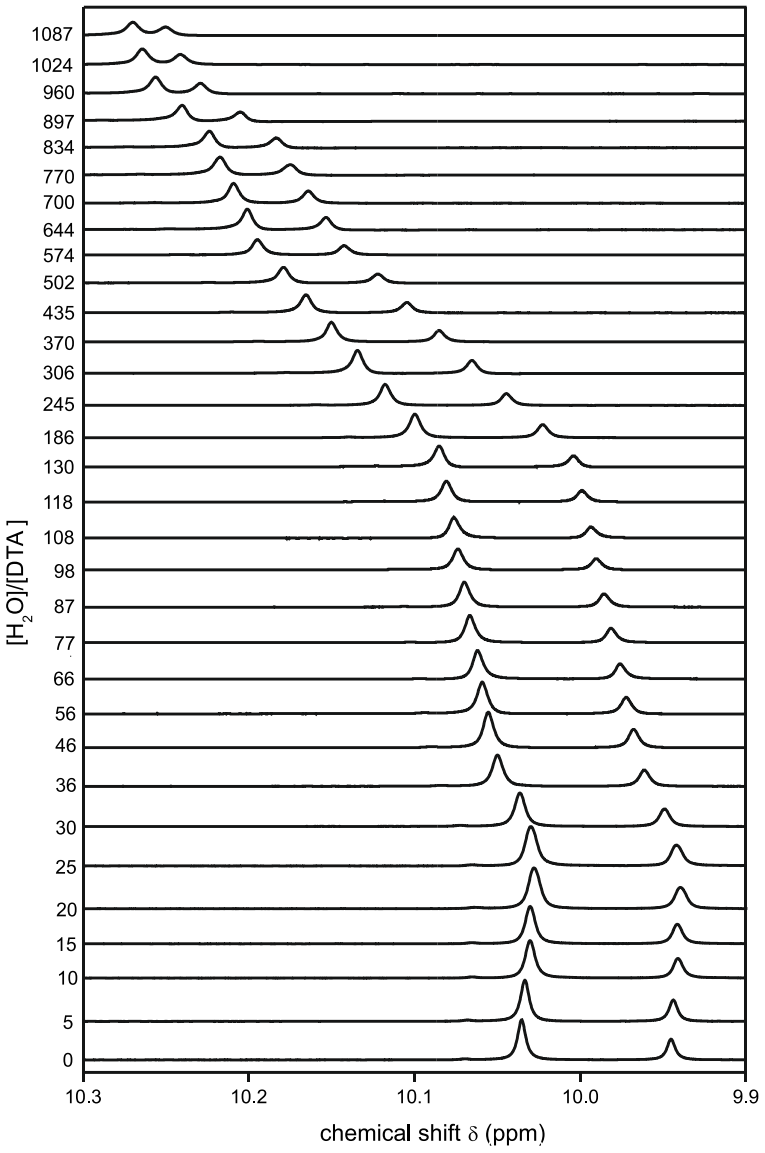


Figure 5.19. a) High *vs*. b) low DTA concentration of ^{1}HNMR DTA-water titration experiment

Similar to the FTIR probe, two constant DTA concentrations of high (1.0 M) and low (0.02 M) were used, titrated with varying concentrations of water as the guest. The method used was discussed in chapter 2, but basically closer guest (water) concentrations were introduced to the constant host (DTA) resulting in smaller G:H molar ratio gaps, which gradually followed by wider G:H molar ratio gaps with higher water concentration. The highest water content able to be titrated into the high concentration DTA experiment was eight molar ratios, with immediate precipitation

occurs above the value. Meanwhile, the low DTA concentration titration experiment was stable or remain in solution up to 1000 G:H molar ratio. From the observation of the amide NH protons at 10.04 and 9.95 ppm respectively in both runs, an immediate peak shift was observed, even at a very low molar ratio of water. High DTA concentration run (Figure 5.19 (a)) yielded a downfield shift (as a higher concentration of water is titrated in), while in the low DTA concentration experiment (Figure 5.19 (b)), an upfield shift was initially observed up to 25:1 G:H molar ratio. Above this value as a higher concentration of water was titrated in, the peak shifts change direction, moving downfield instead. Above 130:1 G:H molar ratio, the NH proton on the lower chemical shift showed a larger peak shift magnitude compared to the other NH on the higher chemical shift, resulting in the two peaks to almost converge to one another at 1087:1 G:H molar ratio. Even though the observed peak shift magnitude is small, the value is significant with close to 0.1 ppm recorded at the highest water content of 8 molar ratios in the high concentration DTA experiment, while for the low concentration DTA experiment, an overall peak shift of 0.24 ppm was recorded at 1087:1 G:H ratio.

The shift to higher ppm suggests deshielding of a proton.[52] In both DTA experiments the downfield shift observed were most likely due to one of these two explanations: 1) the NH acts as a proton donor and directly interact with water, resulting in loss of electron density (generated through-bond) around the bridging hydrogen atom as hydrogen bond is formed with water. Solid-state electron density redistribution study on α-oxalic acid and water of the dihydrate form showed similar electron density loss due to hydrogen bonding around the donor atom which was represented by topography contour change.[53,54] Recent simulation study between various compounds and water best highlight the event, clearly showing in contrasting

colours that the bridging hydrogen atom loses density during complexation (Figure 5.20).[55–58]

a) b)

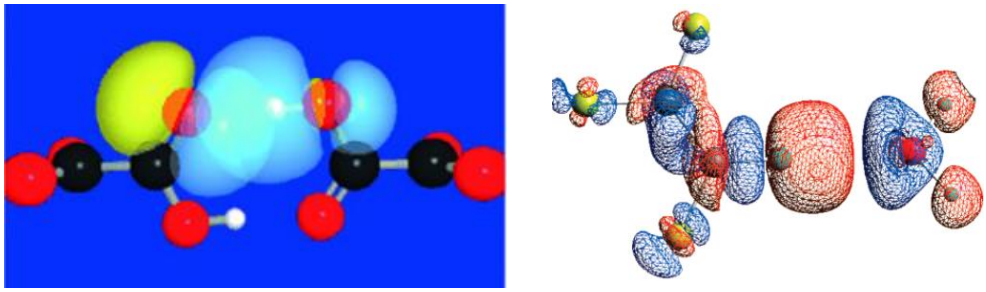


Figure 5.20. a) Shows HC_2O_4 dimer where yellow-coloured isosurface represents electron loss and the blue colour suggests electron increase.[57,58] b). Shows F_2CCFH-water complexation resulting in shifts or rearrangement of electron density throughout the compound. Blue regions corresponds to electron density gain, and red regions represent loss.[56]

In our titration experiments, following compound-water complexation in solution, the electron density shifted from H (of the NH) to O (in water) because of the higher electron affinity property of the oxygen atom. Therefore, the second explanation is more likely: 2) the shift observed is due to electron density reorganisations,[56,57] an indirect effect from the hydrogen bond formation between the carbonyl of the amide and water as observed in the FTIR titration study, and reported as one of the interaction point to water.[22] As the carbonyl of the amide and water form a complex, the DTA molecule underwent all-round electron density reorganisations, affecting bonds and electron density peripheral to the proton acceptor. The reorganisations of electron densities shown in the simulation of water dimer formation, and acetylene and the various fluorinated derivatives of acetylene complexation with water,[56] suggest that while proton acceptor (in this case O atom) which forms the hydrogen bond gains electron density from the hydrogen atom, a ‘see-saw’ or ‘ripple’

effect is seen, causing atoms to lose-and-gain electron density.[56] The 'ripple' or 'see-saw' effect is thus though to be a through-space effect- as reported by Wheeler, [59] which in our study was initiated by the polarisation of the C=O bond by hydrogen bonding to water and affecting bonds closer to the interaction site. The electrostatic nature carries through, resulting in a final partial positive charge on the observed N-H bond, hence deshielding H leading to the observed downfield shift.

In the low DTA concentration experiment, the monitored peak initially moved upfield which was observed form 1-25:1 G:H ratio. Even though the peak shift was marginal, the upfield peak shift movement, the consistent shape and magnitude was significant, indicative of 'real' interaction with a maximum shift of 0.005 ppm at 25:1 G:H molar ratio. The slight chemical shift recorded suggests shielding of the observed nuclei due to a small gain in electron density. We believe that this interaction is the early hydrogen bonding interaction involving the acid group, indicated by the small magnitude of the chemical shift due to the interaction point being 'further' bond distance away from the monitored proton 2 and 3. Williamson reported similar inductive effect to the observed proton relative to its neighbours. The author mentioned that a proton may protons experience considerable secondary chemical shift due to neighbouring atoms' interaction, either by pulling the electron density away, or pushing it towards the proton.[60] This observation is also in line with the statement on the regioselectivity for guest binding, where location of the nuclei most affected by the complex typically show the biggest peak shift.[61] This theory is also in line with the earlier observation of the low DTA concentration FTIR titration (Figure 5.16), which showed the initial absence of carbonyl acid shoulder, before becoming clearer with D_2O introduction leading to hydrogen bonding or dimerisation.

As explained in detail in Chapter 2, the common method to determine the stoichiometry of the binding event is through Job's plot measurement, which requires for the total number of moles of reactants to be kept constant for a series of measurements, done at different mole ratio or mole fraction of reactants.[62,63] The right-skewed (X_{max}=0.7) Job's plot in Figure 5.21 indicated that DTA and water interact in a 2:1 stoichiometry at equilibria.

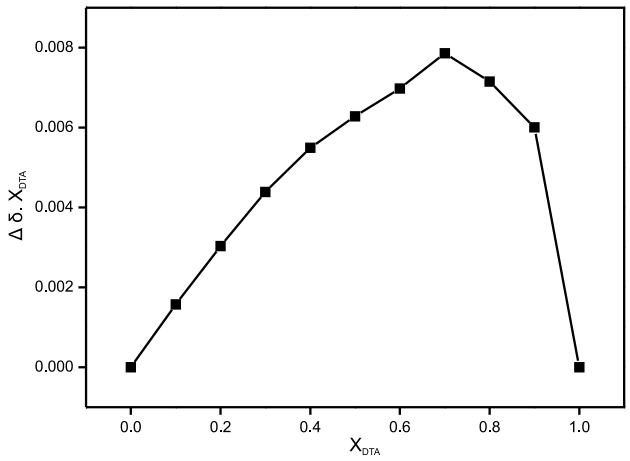


Figure 5.21. Job plot showing the 2:1 stoichiometry of the complexation between DTA and water in DMSO-d_6 using ^{1}H NMR. ([DTA] + [H2O] = 0.1 M)

The binding constant was determined by monitoring the changes in the chemical shift following DTA–water ^{1}H-NMR titration. Figure 5.22 shows a scatter plot corresponding to the amide proton peaks, proton 2 or NH-A =10 ppm, proton 3 or NH-B = 9.94 ppm, at 0:1 G:H molar ratio. The scatter plot shifts were created for both, high and low DTA concentration titration experiments, and fitted to the host-guest 2:1 binding model to obtain the K_{11} and K_{21} values. The fitting for the high DTA concentration titration experiments yielded a high K_{21} versus K_{11} value (**Figure 5.22 (a)**). The calculated K_{11} value is 1.95 x 10^{-5} M^{-1} (±4.4% error) while K_{21} value is 1128 M^{-1}(±10% error). The calculated errors are asymptotic error[64,65] calculated based on Levie approach.[66] Unlike standard error which is calculated at 95% confidence

interval, asymptotic error informs how far off a fitting to the 95% confidence interval level.[65] Based on the considerably smaller K_{11} compared to the K_{21}, and the speciation plot, two scenarios are likely, 1) the DTA-water complex is immediately transformed to DTA dimer-water complex or 2) DTA dimerisation is instantaneous in solution contributing to the low K_{11}.

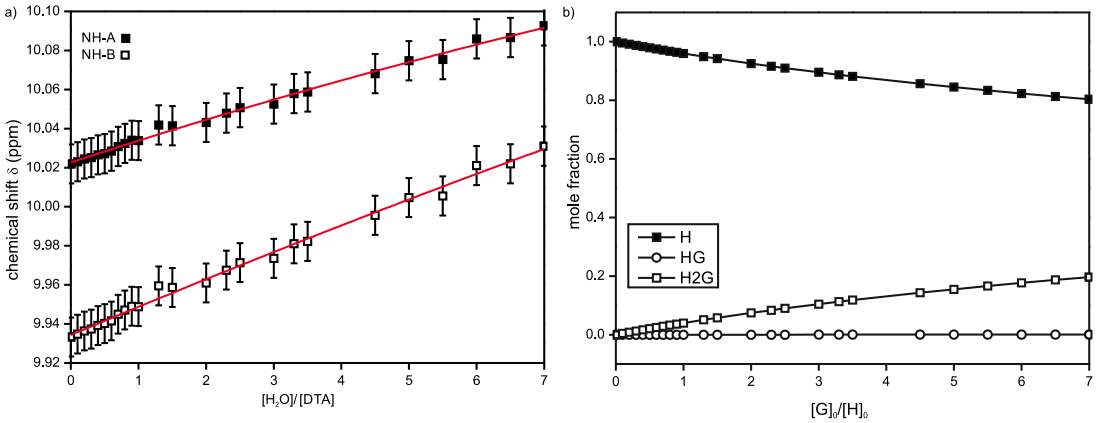


Figure 5.22. a) Scatter plot of the amide proton peaks, NH-A =10 ppm, NH-B = 9.9 ppm, from 0-7:1 G:H molar ratio of high DTA concentration ^{1}HNMR titration experiments, fitted to the 2:1 binding model, and b) shows the host, H guest G, speciation plot.

A similar trend of high K_{21} *vs.* K_{11} is also observed in the low DTA concentration titration experiments. From the fitting, the K_{11} is calculated to 2.94 x 10^{-4} M^{-1} (± 2.3%.error) while K_{21} value is 3005 M^{-1}(± 8.1%.error, Figure 5.23). The fitting, however, failed to consider the upfield shift from 0-25:1 G:H (Figure 5.23 (a)), with the fitted line missed the set of points below 25 molar ratios. However, since the up-field shift was small, the points were still within the error range of 0.2% of the fitted line.

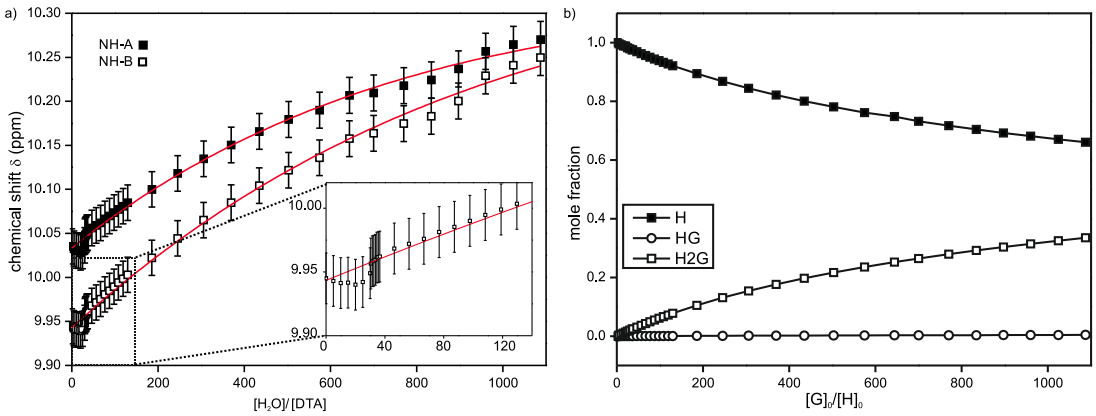


Figure 5.23. a) Scatter plot of the amide proton peaks, NH-A =10 ppm, NH-B = 9.9 ppm, from 0-1087:1 G:H molar ratio of low DTA concentration ^{1}HNMR titration experiments, fitted to the 2:1 binding model. The inset in a) shows the fitting overlooking the upfield points b) shows the host-guest, speciation plot.

If the peak shifts positions are broken into two sections, the initial up-field followed by the downfield shift, different *K* values are obtained. The best fitting for data from 0-25:1 G:H molar ratio generates a negative K_{11} value of -1.03 x 10^{-2} M^{-1}, with an error of ±12%. The high error is most likely due to a low number of data point as only six are available. Meanwhile, K_{21} value is calculated to be 875 M^{-1} (± 2.5%.error). Due to the negative cooperativity in K_{11}, the Gibbs free energy could not be calculated.

The fitting for DTA titration at low concentration which generated the lowest error was for the titration points from 25-1087:1 G:H molar ratio, which generated the following *K* values, K_{11} = 0.05 M^{-1} (± 7.4%.error), while K_{21} =619 M^{-1}(± 7.9%.error, Figure 5.24). Based on the speciation plot, it is suggested that the dimer-water complex is favourable upwards from 25 molar ratios of water, with H2G complex saturation at around 400 molar ratios (plateau observed in speciation plot). The DTA-water 1:1 complex is also seen increasing in concentration with more water titration, most likely due to an abundance of water molecules in the system.

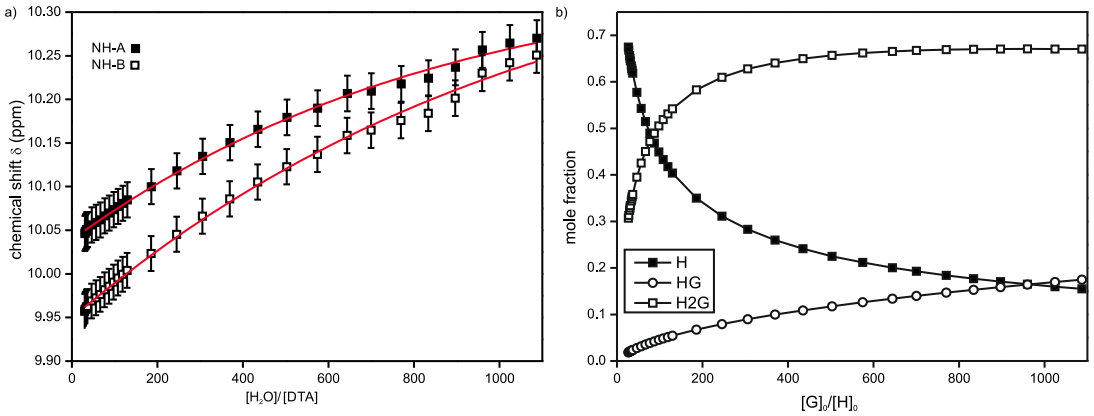


Figure 5.24 a) Scatter plot of the amide proton NH-A =10 ppm, NH-B = 9.9 ppm, at 25-1087:1 G:H molar ratio of low DTA concentration ^{1}HNMR titration experiments, fitted to the 2:1 binding model, and b) shows the host, H guest G, speciation plot.

Observation of the solution-state FTIR spectra, ^{1}HNMR chemical shift and the obtained K values suggest firstly, the carbonyl is the most likely water interaction point, corresponding well to interaction present in the solid-state i.e. the difference in spectra of the anhydrous and hydrate form, as well as the bonding reported in the crystal structure. The FTIR showed the carbonyl vibrations to shift to lower wavenumber consistently, regardless of DTA concentration following water introduction. In the ^{1}H-NMR, the amide functionalities shifted the most, suggesting that this region is most sensitive to water interaction. The sensitivity is most likely due to the close proximity of the group to the true interaction point, *i.e.* carbonyl of the amide, complementing FTIR data. Next, based on the K_{21} value, there is a strong interaction between DTA and water, following a 2:1 stoichiometry. Since the complexation processes are viewed in steps, the low K_{11} values suggest the initial 1:1 complex changes into DTA dimer-water complex very quickly, almost instantaneous with water introduction. Dimer species are present in both low and high concentrations.

However, the interpretation above is only valid if there are only two species, the DTA-water complex and the dimer-water complex, present in solution in equilibrium. In a dilute solution, DTA can form dimers *via* several possible configurations; an acid dimer (acid-OH···O- acid), an amide-acid dimer (amide -NH···O- acid), or an amide dimer (amide -NH···O- amide). Two of these interactions (amide-acid and amide-amide) can be observed in the crystal structure.[22]

The FTIR data suggests that dimerisation are indeed present in solution, however, it is unclear which dimer variation is present at which titration point. Also, it is highly likely that there are multiple dimer variations, giving rise to multiple dimer-water complexes or even a tetramer species. Furthermore, unlike the anion binding experiment which uses binding constant to measure the association strength, the magnitude of shift observed in this iteration (between an uncharged compound and water) is much smaller. From the first compound-water titration experiment, we learned that the dilute method is the way forward, as it allows for more water incorporation into the evaluated system, without precipitating out.

We believe that the *K* values obtained from fitting of the chemical shift is an apparent fit, instead of a true association. The main reason for this assumption is that thermodynamically, a dilute solution would have greater the entropy, and thus the smaller the free energy (Equation 1.1). The greater entropy would reflect on the increase randomness of a system, hence generating more activities and species possibilities for the components interactions in a dilute solution. Therefore, it is highly unlikely that in a dilute setup, only one species exists and predominates others. However, the used model does still represent the binding interaction, albeit an 'apparent' one as the peak shift data plotted do still 'fit' the mathematical model in

hand. The obtained binding constant, *K* is a thermodynamic parameter, hence it can be used to determine the free energy of association (in equilibrium, $\Delta G = 0$) based on the Gibbs equation, $\Delta G^0 = -RT \ln K$. (R is the universal gas constant, which has the value 8.31447 $J \cdot K^{-1} \cdot mol^{-1}$, T is temperature in Kelvin). The calculated K_{21} binding energies based on the different fitting scenario are listed below. Note that calculation on the magnitude of the overall binding process (β_{21}) is not calculated as the value of K_{11} is negligible ~0. We stress that since the process is considered as stepwise, it is unlikely that no HG (1:1) complexation occur in solution. However, this 'apparent' absence is due to the fitting of the model, as well as the very small magnitude of proton shift involving water titration. Hence, the ΔG calculated is specifically used as a guide and reference for water binding in solution.

Table 5.1. Calculated ΔG of DTA-water binding based on 2:1 binding model

[H]:[G] binding model	K_{11} (±% error)	K_{21} (±% error)	ΔG^0 for K_{21}
2DTA:H_2O (High [DTA])	1.95 x 10^{-5} M^{-1} (±4.4%.error)	1128 M^{-1} (±10%.error)	-17.41 kJ mol^{-1}
2DTA:H_2O (Low $[H_2O]_{0\text{-}1087}$/ $[DTA]_1$)	2.94 x 10^{-4} M^{-1} (±2.3%.error)	3005 M^{-1} (±8.1%.error)	-19.84 kJ mol^{-1}
2DTA:H_2O (Low $[H_2O]_{0\text{-}25}$/ $[DTA]_1$)	-1.03 x 10^{-2} M^{-1} (±12% error)	875 M^{-1} (±2.5%.error)	-16.78 kJ mol^{-1}
2DTA:H_2O (Low $[H_2O]_{25\text{-}1087}$/ $[DTA]_1$)	0.05 M^{-1} (±7.4%.error)	619 M^{-1} (±7.9%.error)	-15.93 kJ mol^{-1}

5.3.4 CIM solid-state preliminary analysis

The starting compound was analysed to determine its state of form, which PXRD and FTIR later revealed that it was the anhydrous Form A (Figure 5.25).[24,67] Following the method reported by Hegedüs and Görög, CIM monohydrate (M1) was obtained by quench cooling a hot 15% w/w CIM aqueous solution with (five times the volume) ice-cold water.[24] PXRD and FTIR spectra confirm the precipitated form to be the monohydrate M1 (Figure 5.25).[9]

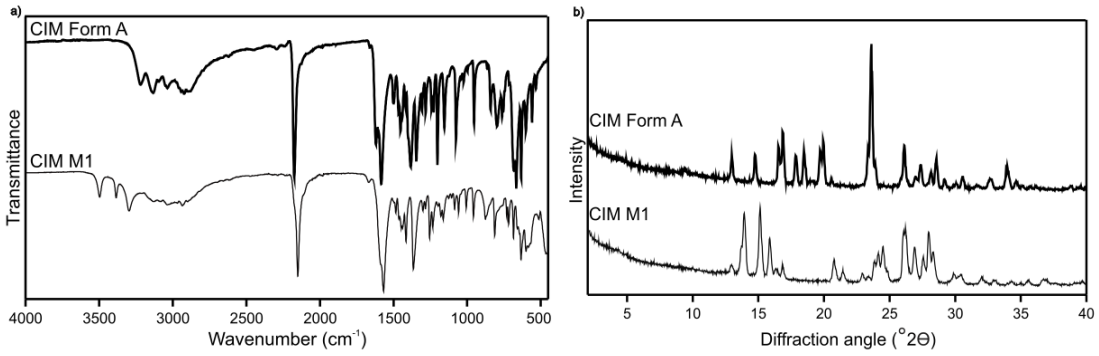


Figure 5.25. FTIR spectra (LEFT)and PXRD traces of CIM anhydrous Form A and monohydrate M1

TGA of the monohydrate M1 showed a mass loss of 6.32%, corresponding to 0.945 moles of water (the calculated value for a monohydrate is 6.67%, Figure 5.26). Meanwhile, the DSC trace (Figure 5.26 (a)) shows an endothermic event at 73 ℃, indicative of a dehydration process (comparable to the M1 TGA trace). Also, the melting event revealed to be at 140-142 ℃ (Figure 5.26), the slight variation between the two TG runs was most likely due to sample preparation. The obtained melting point was comparable to the earlier report of 143 ℃.[9] Following dehydration, the monohydrate M1 transforms spontaneously to Form A, as previously reported by Calvo *et.al*.[68]

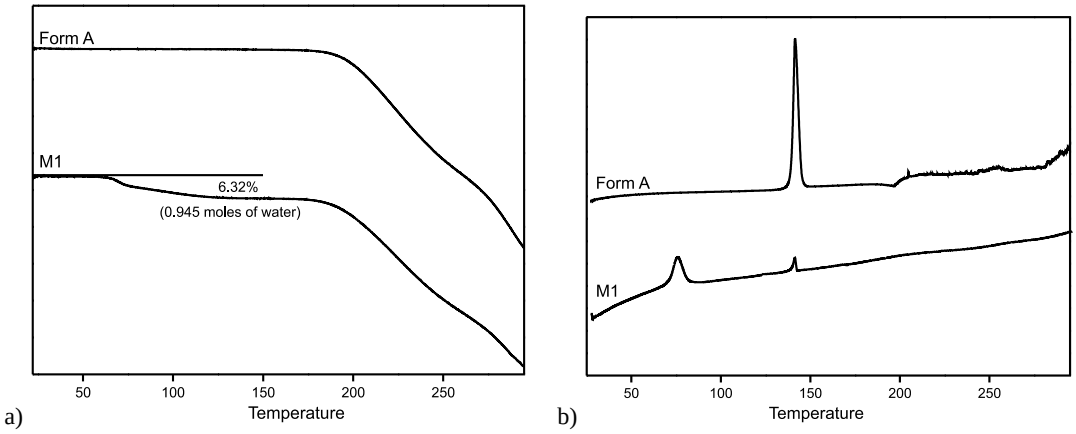


Figure 5.26. TGA (a) and DSC (b) traces of CIM Form A and monohydrate M1

DVS of the anhydrous Form A and the monohydrate M1 (Figure 5.27) indicates that both forms are stable, with very little mass change throughout the humidity cycle, 0.06% (Form A) and 0.12% (M1) difference between the two extreme RH, indicative of surface water.

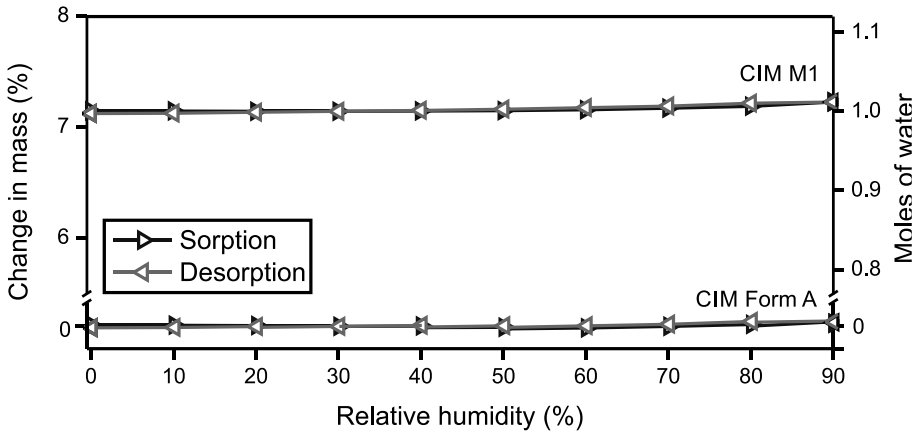


Figure 5.27. DVS of the anhydrous Form A and the monohydrate M1

The FTIR spectra show a clear difference between the anhydrous Form A and M1, especially in the nitrile vibration (C≡N, Figure 5.25). Kanumfre et al. reported the FTIR assignment for the C≡N stretch vibration to be at 2187 cm^{-1}, without stating the identity of the polymorph.[69] A more in-depth comparison by Hegedüs and Görög also provided FTIR peak assignment, with emphasis on difference to the C≡N peak position

for all four anhydrous forms A,B,C and D. Our in-house spectra are comparable to Hegedüs's assignment, with the C≡N stretch vibration emerging at 2174 $cm^{-1}$for the anhydrous Form A. A substantial shift of the C≡N is observed in the monohydrate M1 spectra as this band shifts 24 wavenumbers lower to 2150 cm^{-1}. It is evident from the shift to lower wavenumber that hydrogen bond to water takes place in the nitrile region as the C≡N is a strong hydrogen bond acceptor, comparable that of water.[70] Reasons relating a lower wavenumber shift to hydrogen bonding has been discussed in the DTA section above. This region will henceforth be a probe in the following FTIR solution-state titration experiments.

5.3.5 FTIR: CIM solution-state titration

Following the result from low DTA concentration analysis, solution-state FTIR titration for CIM was performed using a concentration of 0.05 M in DMSO solution, and titrated with different D_2O contents. Initial titration gap of five molar ratios was used up to 20:1 G:H molar ratios. Larger G:H molar ratios were later used namely 30:1, 40:1, 70:1, 100:1, 125:1, 150:1, 300:1, 400:1, 500:1 with the highest D_2O introduced was in 600:1 G:H molar ratios. The initial nitrile peak position at 0:1 G:H molar ratio was 2165 cm^{-1}. No shift was initially observed, up to 30:1 G:H molar ratios incorporated. At 40:1 G:H molar ratios, a single wavenumber shift was observed. Unexpectedly, the shift observed was to the higher wavenumber (Figure 5.28, (b)), suggesting hydrogen bond breaking, as more D_2O was introduced. The higher wavenumber shift trend continues, with the next two wavenumber shifts observed at 300:1 G:H molar ratios. The following 100 molar ratios gap onwards to 600 molar ratio saw the peak shift steadily, from 2168 to 2171cm^{-1}. The FTIR probe of the other

CIM vibrations was complicated as most CIM peaks in solution were covered either by the D_2O or the DMSO vibrations (Figure 5.28, (a)).

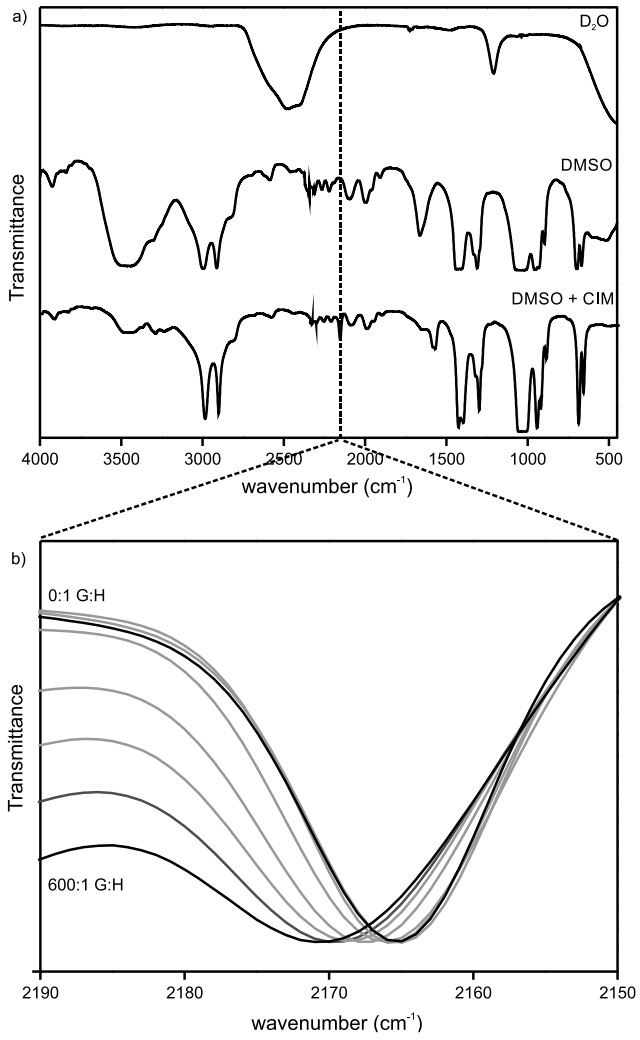


Figure 5.28. 0.05 M CIM in DMSO solution (a) showing unobstructed view of the vibration of interest. (b) shows the solution-state FTIR titration of CIM from 0-600 G:H ratios.

In the CIM Form A, the amino functionality on the guanidine part of the compound is involved in inter- and intramolecular hydrogen bonds.[71] The reported dimer motif in the structure of CIM Form A is between the $NH^{\delta+}\cdots{}^{\delta-}$:N≡C.[71] One of the slightly positive (δ+) hydrogen atom in the amide molecule is attracted to the lone pair on the nitrogen atom (δ-) in the nitrile, forming a hydrogen bond. It is unconfirmed whether the dimer motif persists in solution. However, the observed to shift to higher

wavenumber potentially due to the said motif being broken in the presence of large quantities of water in the system. Water OH is a stronger hydrogen bond donor compared to the guanidine,[70] therefore, as more D_2O titrated into the system, the dimer motif began to break as a strong acceptor *i.e.* C≡N is more likely to favour interaction with a strong donor *i.e.* OH. The effect of the intermolecular hydrogen bond breaking of the dimer offsets the change due to hydrogen bond formation between C≡N···DOD resulting in the delayed observed to shift to higher wavenumber.

5.3.6 ^{1}H NMR: CIM-water titration

Preliminary ^{1}H-NMR spectra of CIM in DMSO-d_6 and acetone-d_6 were obtained, integrated and assigned accordingly (Figure 5.29).[72] The proton were identified as proton 1-8 based on their position, from higher to lower ppm as they appear in the respective spectra (Figure 5.29). CIM peaks positions differ slightly between the two solvents, however, they do appear generally within the comparable region.

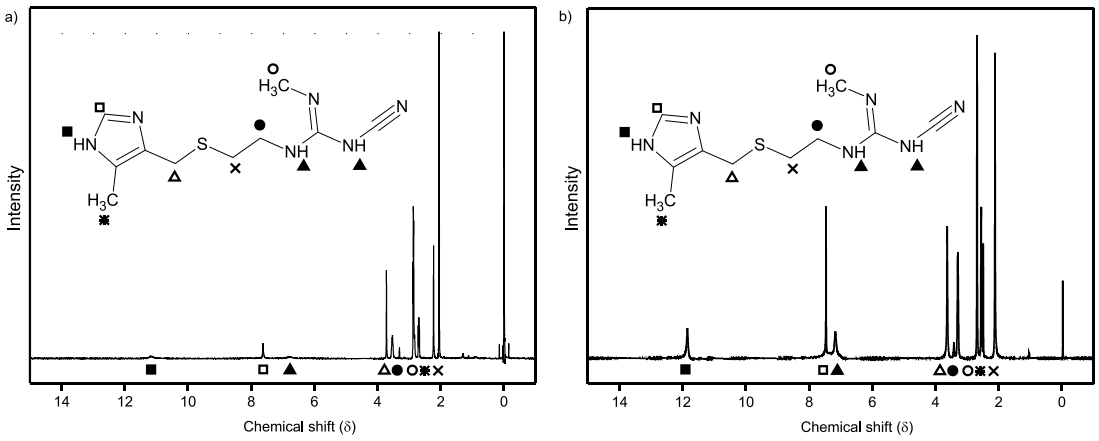


Figure 5.29. CIM proton 1-8 assignment form higher to lower ppm as they appear in the spectra along with their respective symbols. a) shows CIM spectrum in DMSO-d_6 environment, and b) in acetone-d_6 respectively.

^{1}H NMR dilution experiment with 40 molar ratios of DMSO, and 500 molar ratios of acetone respectively were done to ensure that the shifts, if any recorded were indeed due to interaction with water not the effect of dilution (Figure 5.30). As mentioned in chapter 2, ^{1}H NMR dilution experiments were carried out by preparing sufficient amount stock solutions of the CIM in DMSO-d_6 or acetone-d_6 at concentrations of 0.05 and 0.02 M, and diluting the main stock with sufficient molar ratio aliquots of the main solvent. In both experiments, no significant shifts were observed (Figure 5.30)

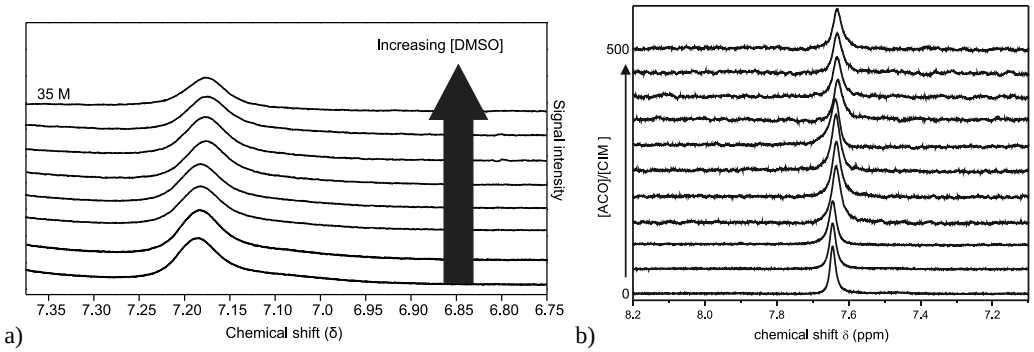


Figure 5.30. Peak shift in CIM dilution experiment. a) in DMSO-d_6 environment, while b) in acetone-d_6 environment

^{1}H NMR titration experiments were carried out at a constant concentration of CIM, 0.05 M in DMSO-d_6 and 0.02 M in acetone-d_6, titrated with varying concentrations of water. Similar to the DTA titration, a closer G:H concentration gaps were initially used, followed by wider G:H gaps containing higher water concentration introduced into the mixture. The amount of water titrated in was from 1-35: G:H molar ratio in DMSO-d_6 environment while in acetone-d_6, the guest introduced was from 1-450 G:H molar ratios.

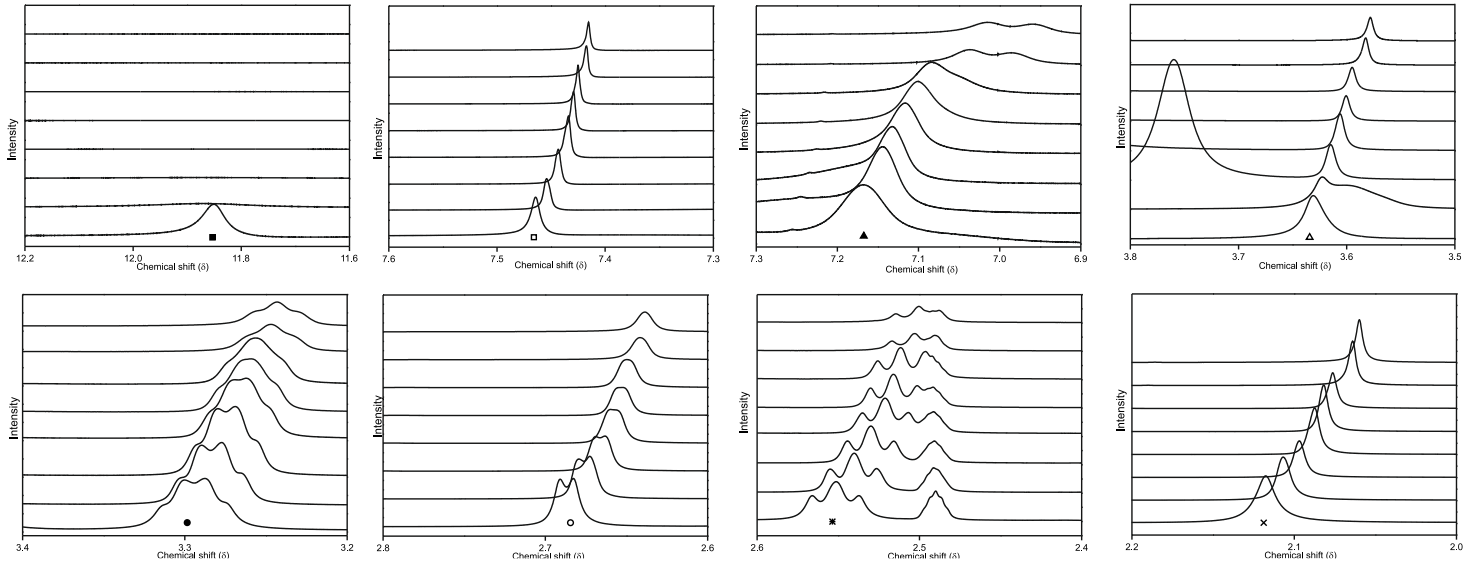


Figure 5.31. TOP form LEFT to RIGHT: Proton 1-4 peak shifts, while BOTTOM, from LEFT to RIGHT: Proton 5-8 peak shift in DMSO environment

Table 5.2. ^{1}H NMR chemical shift (ppm) of free cimetidine and complexed with water in deuterated DMSO at titration endpoint.

	Proton 1	Proton 2	Proton 3	Proton 4	Proton 5	Proton 6	Proton 7	Proton 8
Free CIM in DMSO	11.851	7.4643	7.1685	3.629	3.29	2.687	2.551	2.119
35:1 G:H in DMSO-d_6	11.87*	7.4154	6.9601	3.578	3.243	2.638	2.50	2.059
$\Delta\ \delta$	0.019	-0.0489	-0.2084	-0.051	-0.047	-0.049	-0.051	-0.06

In the titration in DMSO-d_6 environment (Figure 5.31), all protons showed upfield shift, except for the NH on the imidazole ring (proton 1). Proton 1 was clearly visible up to 4:1 G:H molar ratio. There was no significant shift observed to proton 1 from one to four molar ratios of water, before shifting by 0.02 ppm downfield at five molar ratios of water inclusion. However, the peak of proton 1 then broadens significantly above the mark due to the fast exchanging of the NH with the incorporated water, making it hardly visible, hence difficult to interpret further (Figure 5.31). Next is the proton CH of the imidazole ring (proton 2), which shifted to a lower ppm from five molar ratios of water upwards. Upon reaching 35 molar ratios, the peak shift recorded was almost 0.05 ppm (Figure 5.31). Next proton shift observed was in the NH peaks of the guanidine group (proton 3), with subsequent splitting at higher water concentration. The observed splitting started as a shoulder at 20:1 G:H molar ratios, before complete separation at 25:1 G:H molar ratios. At 35:1 G:H ratio, the peak which has separated out of the initial chemical shift has shifted by a total of 0.2 ppm (Figure 5.31). Since the observed peak and broad base was the actually representing two NH protons, the split observe was most likely due to the influence or effect of hydrogen bonding to the electronic environment of each of the NH protons. One of the protons is receiving more electron density from a neighbouring atom, due to CIM-water interaction, causing the proton to be more shielded than the other. Even though the nitrile CN region showed significant shift in wavenumber between the anhydrous and hydrate form in the solid-state, our solution-state FTIR titration experiment did not share similar feature. Significant shift was only observed at very high G:H molar ratio. Therefore, it is most likely that the NH proton 3 which was shifting the most is interacting directly to water through hydrogen bond between the NH···OH. The splitting could also be caused by the presence of a CIM-water complex,

having a slow exchange (between complex and reactant) on the NMR time scale at equilibria. A lower temperature ^{1}H-NMR run of the sample from 0-25:1 G:H ratio would slow-down the reaction even more, and cause the split peak to appear as a sharper more define peak, confirming the existence of the complex.

The upfield shifts trend continues with the protons of CH_2 connecting the imidazole ring and the thiol-S group (proton 4, Figure 5.31), which have shifted by 0.05 ppm. Interestingly, the peak profile of the following protons which were close to the secondary amine changes with water titration. The proton of the CH_2 linked to the secondary amine (proton 5) changes from a quartet to a triplet between 20-25: G:H molar ratios, while CH_3 linked to the secondary amine (proton 6) changes form a doublet to a singlet between 10-15:1 G:H molar ratios, again shifting upfield at higher water molar ratios. The signal splitting and convergence observed were most likely due to changes to electronic environments of the said protons, which were most likely attributed to the hydrogen bond formation from CIM-water complexation.

The final two protons, CH_2 connecting the guanidine and the thiol-S group (proton 7), and CH_3 on the imidazole ring (proton 8) shifted by 0.05 and 0.06 respectively (Figure 5.31). In fact, all the proton shifted by a similar value of around 0.05 ppm, apart from the NH group (Table 5.2). Therefore, a follow-up titration in acetone-d_6 was done as acetone allows for the observation of the labile protons e.g. the. NH group of. proton 1 and 3, at higher water molar ratios. Monitoring of the NH group were important because they are potentially the point of complexation themselves or they at close proximity to the true interaction point as the NH chemical shift were being affected the most.

In acetone-d_6 environment, significant chemical shifts were observed in all the protons of CIM following water titration up to 450:1 G:H molar ratio. All protons showed an upfield shift, apart from three protons showing downfield shifts which are, the proton of the NH on the imidazole ring structure (proton 1, ■), the proton of the CH_2, connecting the imidazole ring and the thiol-S group (proton 4, ▵), and the proton of the secondary amine –NH protons of the guanidine group (proton 3, ▲ Figure 5.33, Figure 5.32).

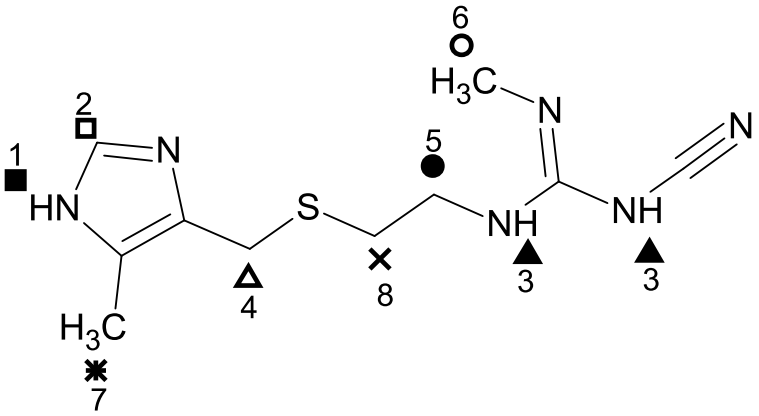


Figure 5.32. Point of reference, the structure of CIM, with their corresponding symbols and numbering scheme.

For most of the protons, their significant shifts were observed only after high water incorporation (> 50 molar ratios). Therefore, the focus of the titration analysis was more on the immediate shifting protons, even at lower water contents *i.e.* proton 1,2, and 3. The biggest shifts are observed in the protons of NH groups on the imidazole ring and the guanidine (proton 1 and 3). However, due to the fast exchanging nature NH proton with water in the acetone environment, which was also observed in DMSO-d_6 environment, the peak appeared very broad especially on the ring structure, and although visible, the exact peak position is difficult to ascertain and monitor (Figure 5.33). The proton 3 of the amide of the guanidine were visible at 450:1 G:H ratio while the NH on the imidazole ring is vaguely visible at 300:1 G:H ration. Proton

1 and 3 peaks has shifted downfield by 0.279 and 0.477 ppm at the respective water ratios, in relation to free CIM, the overall shift of all protons are listed in Table 5.3. Since the shifts of proton 4-8 are only apparent at higher water content, these small shifts are most likely electronic rearrangement effect from the main interaction points as more CIM-water aggregate are present in solution.

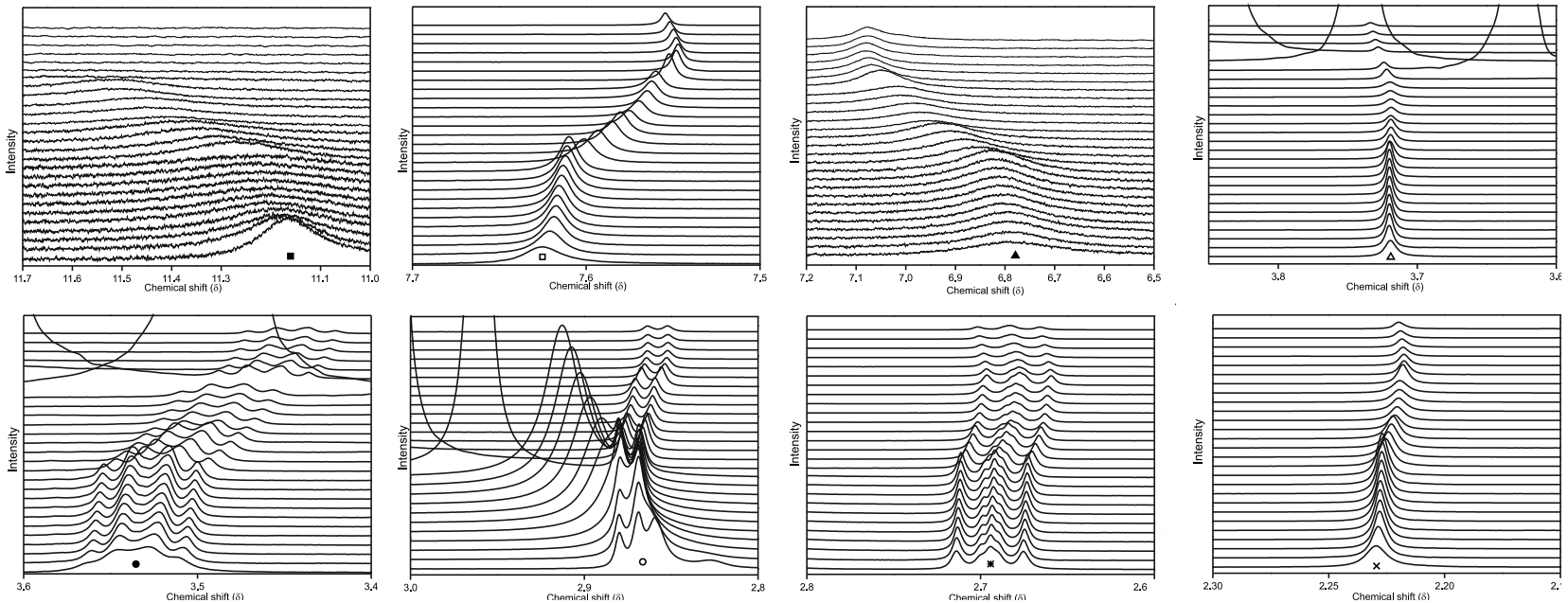


Figure 5.33. TOP form LEFT to RIGHT: Proton 1-4 peak shifts, while BOTTOM, from LEFT to RIGHT: Proton 5-8 peak shift in acetone-d_6 environment

Table 5.3. ^{1}H-NMR chemical shift (ppm) of free cimetidine and complexed with water in deuterated acetone.

	Proton 1	Proton 2	Proton 3	Proton 4	Proton 5	Proton 6	Proton 7	Proton 8
Free CIM in ACO	11.1685	7.6256	6.7968	3.7192	3.5285	2.8797	2.6753	2.2294
450:1 G:H in acetone-d_6	11.6457*	7.5542	7.0753	3.7336	3.4361	2.8634	2.6659	2.2197
$\Delta\ \delta$	0.4772	-0.0714	0.2785	0.0144	-0.0924	-0.0163	-0.0094	-0.0097

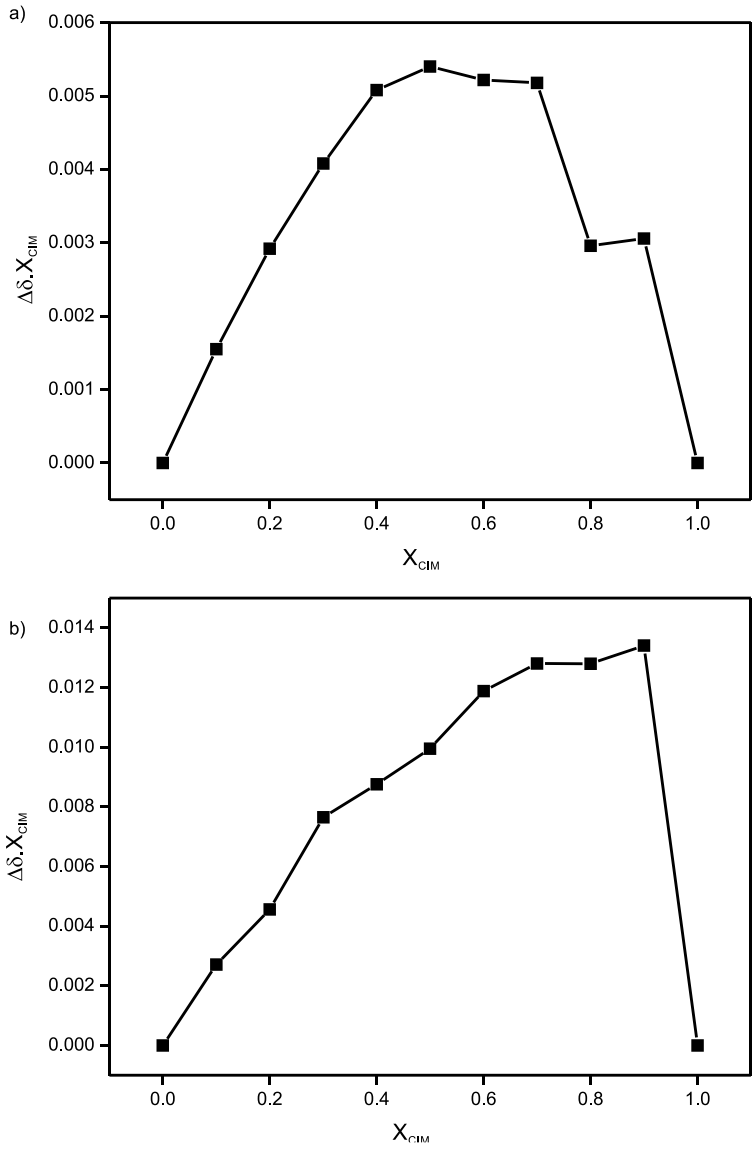


Figure 5.34. CIM Job plot experiment.in a) DMSO-d_6 environment, b) acetone-d_6 environment Job plot showing the 1:1 stoichiometry of the complexation between CIM and water in DMSO-d_6 while a 2:1 stoichiometry of the complexation in acetone using ^{1}H NMR. ([CIM] + [H_2O] = 0.1 M)

Job's plot indicated that CIM and water interact in a 1:1 stoichiometry at equilibria in DMSO, while in acetone a right-skewed plot (X_{max}=0.9) observed suggests a strong 2:1 stoichiometry (Figure 5.34). However, due to the shape and small value of the shift, similar assumption to DTA is taken here where we believe that more than one species exists in the dilute solution of each solvent. Therefore, the Job's plot does not necessarily show a true interaction stoichiometry. Nevertheless, the fittings

were done according to the respective stoichiometries indicated by the Job's plots. The stoichiometries, as well as the eventual fitting, are considered as apparent values which provide *K* information, and used as comparison to DTA *K* values.

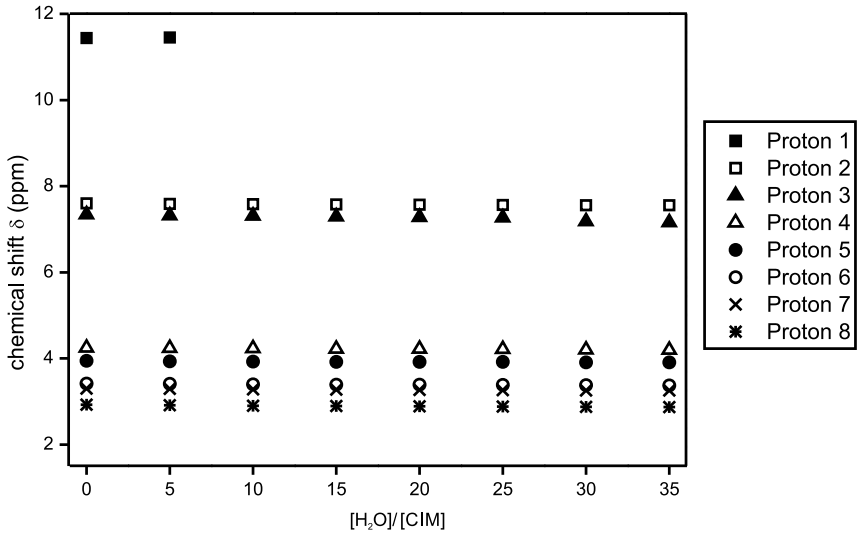


Figure 5.35. Proton 1-8 peak shift scatter plot form 0-35 G:H molar ratio $_{in}$ DMSO

The scatter plot of the protons shifts shows barely noticeable change (Figure 5.35). Binding constant fitting based on 1:1 stoichiometry for the titration experiment in DMSO environment yielded a very small *K* value of 1.5 x 10^{-5} M^{-1} (error ±1.3%) which translates into a positive Gibbs free energy of 27.5 kJ mol^{-1}, favouring dissociation event. The *K* and Gibbs free energy values suggest that 1:1 CIM-water complex simply does not form. The reason is most likely that the shift observed is small, in addition to the fact that the complexation reaction was still ongoing due to the lack of plateau curve observed in the scatter plot of the protons. Plus, the change in the peak profile, from a singlet to a doublet, a quartet to a triplet, and a doublet to a singlet, in consequence making the monitoring of the peak more challenging. Using acetone as the bulk solvent allows for more water inclusion, without changing the peak profiles. Plus, as mentioned earlier, the solvent change allows for the observation of proton 1 at higher water content. The modified experiment also showed an end to the

complexation reaction, with plateau observed on the scatter plot of proton 2 and proton 3 form 200 molar ratios upwards. (Figure 5.36 and Figure 5.37)

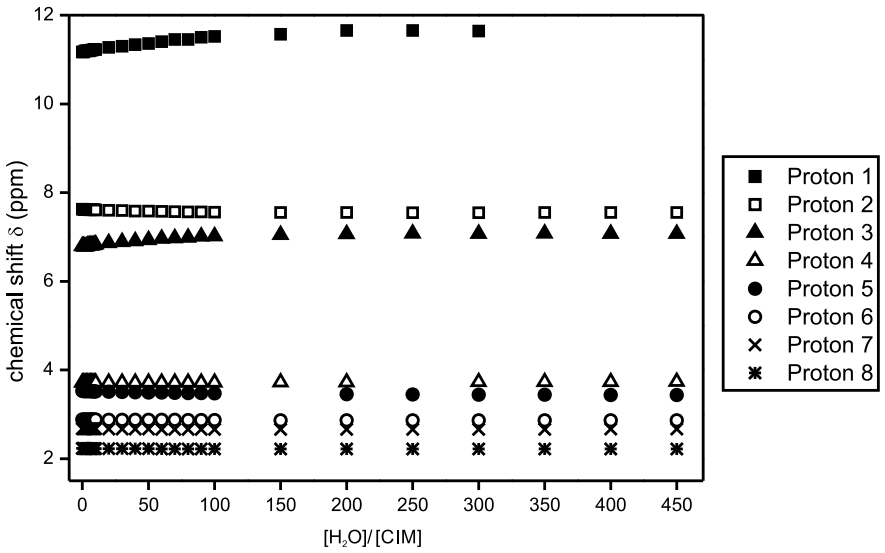


Figure 5.36. Proton 1-8 peak shift scatter plot form 0-450:1 G:H molar ratio in acetone environment

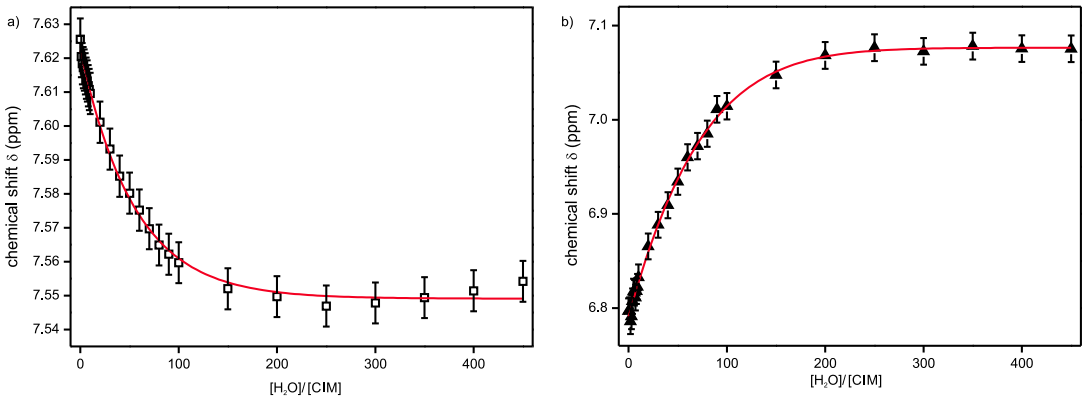


Figure 5.37. Example of fitting for binding constant determination to 2:1 model for proton 2 (a), and proton 3 (b).

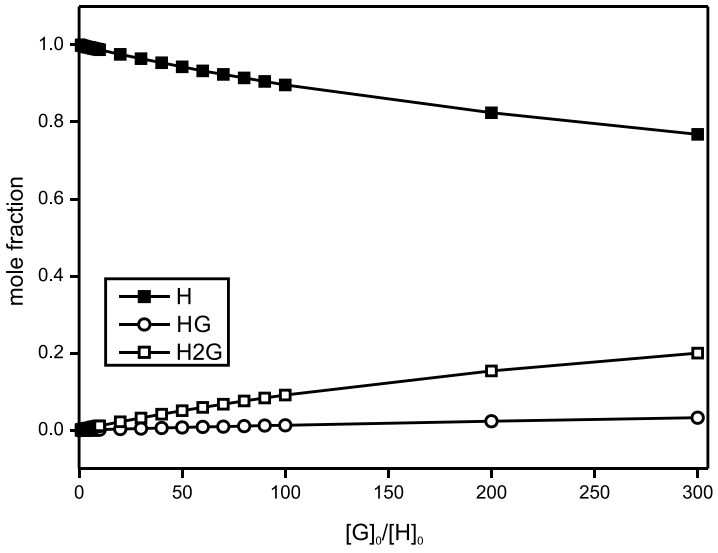


Figure 5.38. CIM speciation plot following 2:1 binding stoichiometry

The 2:1 fitting of all the protons up to 300 molar ratio as the final point where proton 1 is visible in the acetone environment yielded the following *K* values: K_{11} = 0.007 M^{-1} (error ±1.9%), and K_{21} =203 M^{-1} (error ±0.3%). Similar to DTA, the speciation plot which was based on the Job plot's 2:1 fitting (Figure 5.38) suggests an instantaneous H2G complexation from the very low K_{11} value obtained in both DMSO and acetone environment titration. However, since the Job's plot only consider a single species is present at a time in equilibria, the fitting and 2:1 stoichiometry relationship in the respective solvents is only an apparent on, as we assume that more than one species are present in equilibria. The calculated Gibbs free energy value of -13.16 kJ mol^{-1} is weaker compared to the DTA values, which was between -16 to 20 kJ mol^{-1}. Nevertheless, the value does reflect a significant CIM-water interaction, comparable to that of the DTA.

5.3.7 TRN-water preliminary data and FTIR titration

The solid-state forms of tranilast (TRN) have been extensively characterised in chapter 4. To recap, the anhydrous alpha form and monohydrate I are the predominant forms. A novel 2.3 hydrate was discovered, with the crystal structure of a hydrate form reported for the first time. One water molecule coordinates to three TRN molecules via the acid and amino functionalities (Figure 5.39). The remaining two water molecules are located in the channel at the methoxy end (not shown).

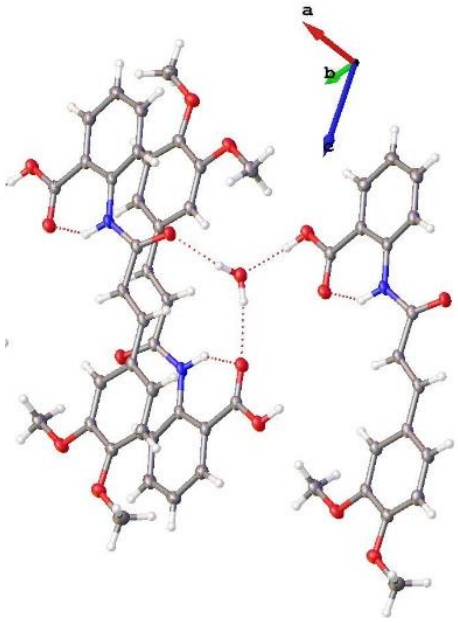


Figure 5.39. The solved structure of TRN 2.3 hydrate. Water molecules are acting as DDA, bridging three TRN molecule. The colour code is carbon grey, oxygen red, and hydrogen light grey.

In the following solution-state FTIR, the related vibrations are probed. The FTIR titration was done in anhydrous DMSO environment. Surprisingly, no changes to the peak position were observed. The second titration in acetonitrile environment was also done to check the whether DMSO hindered the compound-water interaction, however, no peak shift was observed as well. Both FTIR experiments suggest that TRN-water interaction was not ‘visible’ or ‘observable’ using FTIR spectroscopy.

5.3.8 [1]H NMR: TRN-water titration

Initial TRN proton [1]H-NMR spectrum was obtained in DMSO-d_6 environment. Overall, 13 proton regions could be observed, which integrates to the 18 protons of TRN. The obvious protons are the OH of the acid group, the NH, and the two methoxy functional groups which come at 13.61, 11.29, 3.84 and 3.81 ppm respectively (Figure 5.40, (a)). The protons were identified based on their chemical shift position, from higher to lower ppm on the spectra and labelled as proton 1-13 with their respective symbols to show their individual location on the spectra in (Figure 5.40).

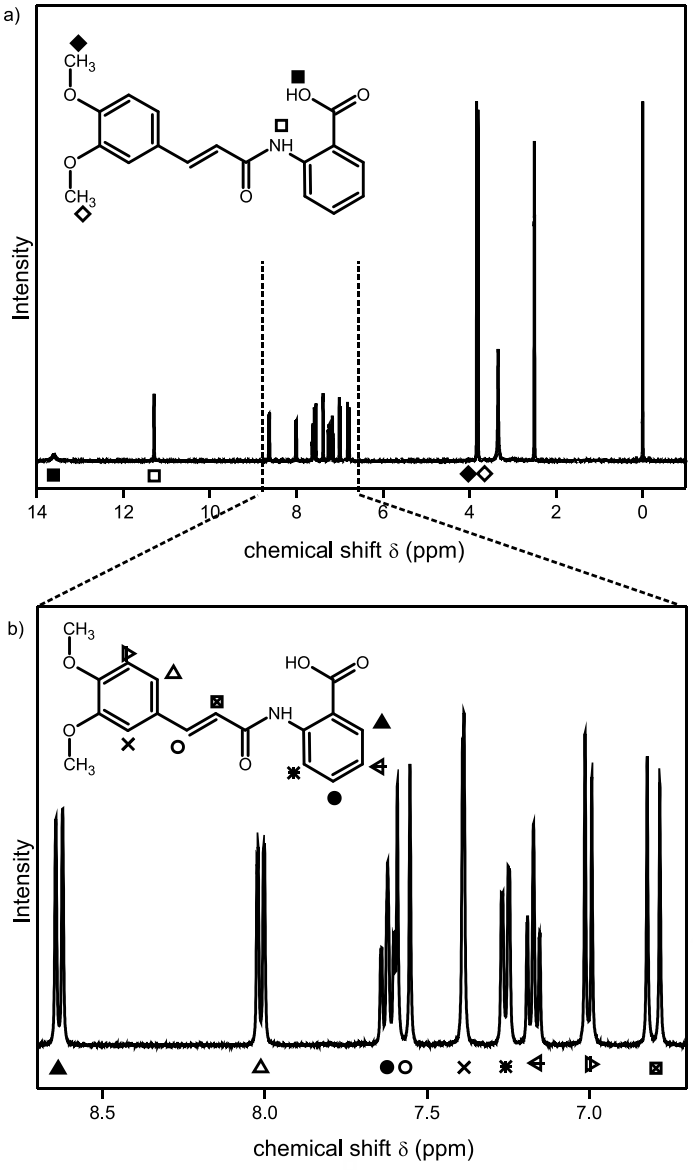


Figure 5.40. Peak assignment, a) the OH of the acid group, the NH, and the two methoxy groups identified as Proton 1, 2, 12 and 13, with their respective symbols. b) Proton 3-11 and their respective symbols.

Dilution with anhydrous DMSO up to 500 molar ratios did not show any significant shift, as indicated in Figure 5.41 which is the NH proton (proton 2) plotted at a similar scale as in Figure 5.43 (a) (from 11.4-11.2 ppm). Dilution experiment however did not show any significant peak shifts.

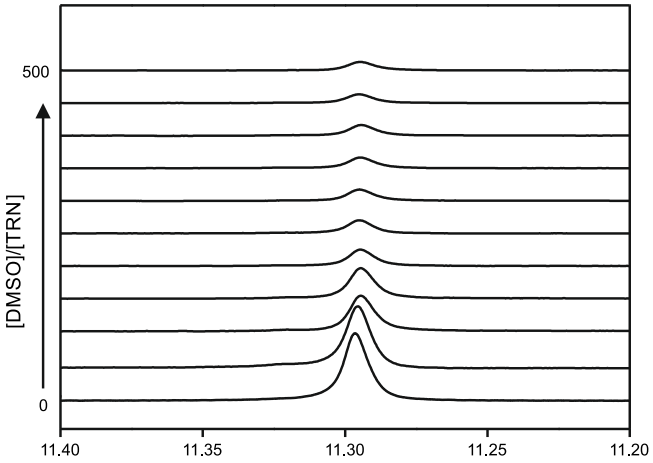


Figure 5.41. Proton 2 (NH) of TRN in a dilution experiment with anhydrous DMSO up to 500 molar ratios

Following the titration of water into the system, the OH (proton 1) was observed form 0-2:1 G:H molar ratio (Figure 5.41). Again, due to the fast exchanging OH proton with water, the peak was unobservable above 2:1 G:H molar ratio.

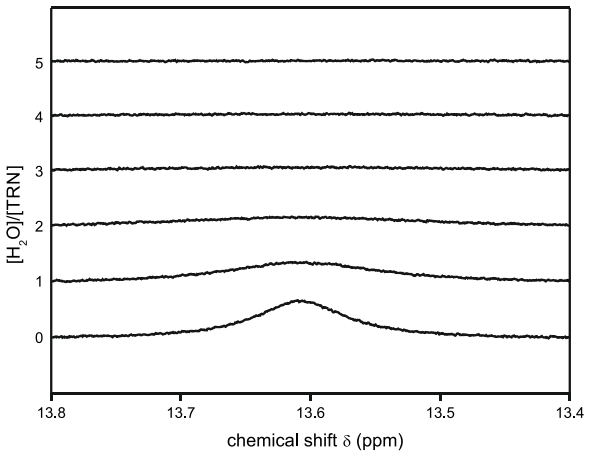


Figure 5.42. The spectra of proton 1 from zero to five molar ratios of water

The next proton observed was the NH proton (proton 2, ◘), which shifted downfield by 0.044 ppm at 400:1 G:H molar ratios. The downfield shift observed in Figure 5.43 (a) is consistent with the deshielding effect of bridging proton which involved in hydrogen bonding, losing electron density as hydrogen bond is formed. Interestingly, scatter plot of proton 2 showed a steep increase from 0-30: G:H molar ratio, followed by a plateau effect after the 30:1 molar ration mark (Figure 5.43, (b)). The magnitude of the peak shift at the plateau is significant with 0.02 ppm recorded. It is highly likely that from 0-30 G:H molar ratio, direct hydrogen bonding between the NH and water occurred, resulting in the initial plateau. This plateau curve persists to up to 70 molar ratio of water, then slightly shifting upfield from 80 to 150, before continuing to shift downfield above 150 molar ratios of water. It is possible that the slight upfield shift observed was instrument sensitivity limitation as the standard deviation for the peak position of the chemical shift observed for the NH from 30 to 150 mark is 0.0009 ppm which is not significant. If this is the case, then the plateau observed was actually from 30 to 150, instead of to 70 water molar ratios.

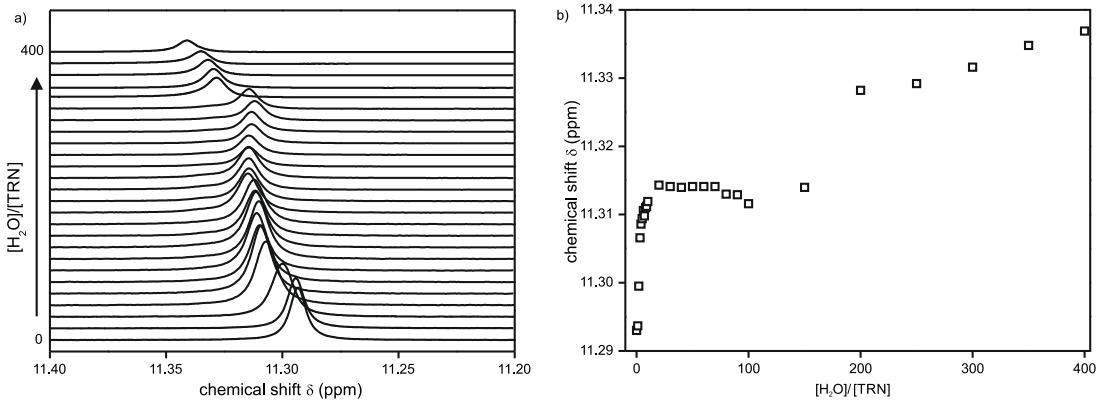


Figure 5.43. a) Shows the spectra of NH proton (proton 2) from 0-400 G:H molar ratios. b) shows the scatter plot of the peak position chemical shift.

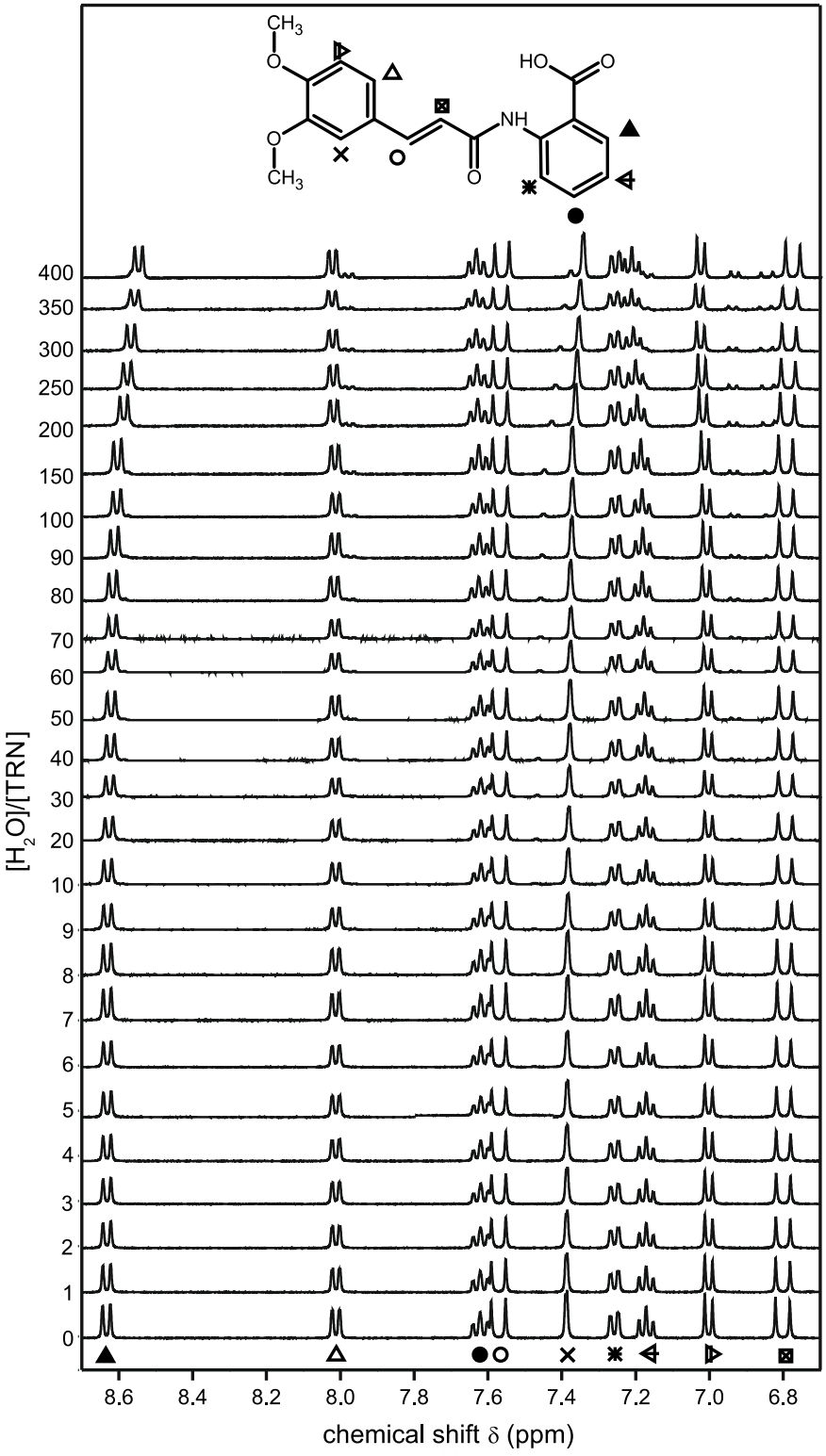


Figure 5.44. Spectra and chemical shift of TRN proton 3 to 11 from 0-400 G:H molar ratios.

Since they appear close to each other, observation on the chemical shift of the subsequent protons was based on Figure 5.44 above, which depicts the chemical shift

of proton 3 to 11, within chemical shift range of 8.7 to 6.7 ppm. The peaks were identified based on the assigned symbol indicated in Figure 5.40. The biggest shift in TRN-water titration came from proton 3 (▲, ortho position on the anthranilic acid ring), which has shifted upfield by 0.082 ppm. Proton 3 is the closest neighbouring proton to the carbonyl of the acid functionality. This large and significant shift suggests that this proton was most affected by the complexation interactions, confirming the involvement of the acid group in TRN-water interaction. Scatter plot of this proton revealed a linear shift upfield, with no plateau observed (Figure 5.45).

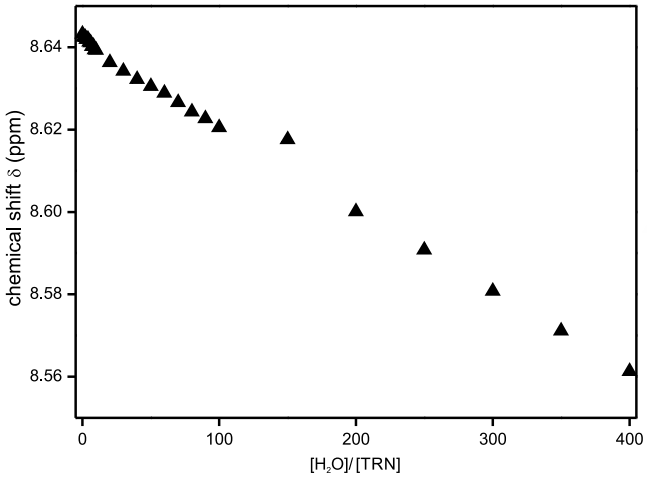


Figure 5.45. Scatter plot of proton 3 showing a linear upfield shift.

Proton 4 (△) and 5 (●) showed shift significant downfield by 0.013 and 0.014 ppm respectively. Though the magnitude of the shifts is comparable at 400 molar water incorporation, their scatter plot revealed distinctly different shift profile, and it is expected as both protons are located at different rings. Proton 4 is located at the ortho position on the methoxy attached benzene ring, while proton 5 is at the para position on the anthranilic acid ring. Proton 4 showed linear shift downfield (Figure 5.46, (a)), while proton 5 shifted upfield first (0-10:1 G:H), before shifting downfield above 10

molar ratios of water. After this value, proton 5 shifts downfield linearly as well (Figure 5.46, (b)).

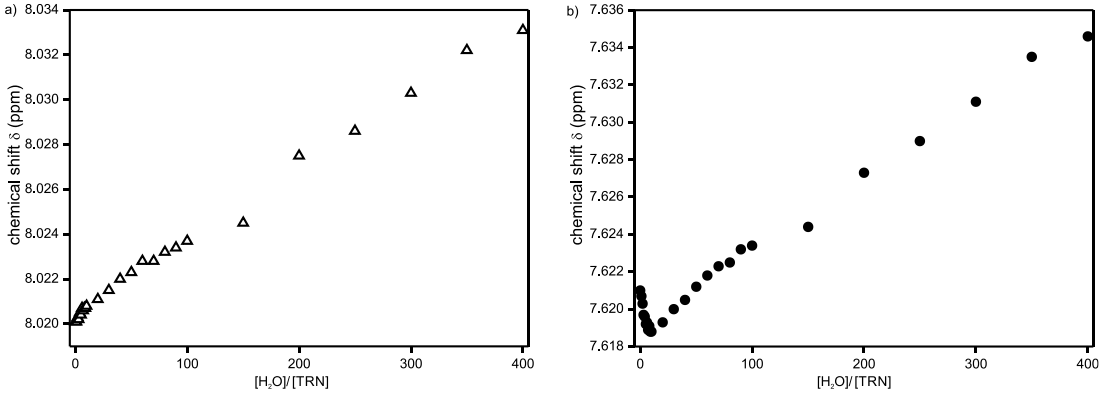


Figure 5.46. Scatter plot of proton 4 (a) showing a linear downfield shift and proton 5 (b) with the initial upfield, followed by a downfield shift.

Meanwhile, proton on the carbon which is connected to the 1' position the benzene ring (proton 6), shifted upfield by a mere 0.006 ppm after 400 molar ratios of water introduced. Significant shift (±0.002 ppm) was only observed after 20:1 G:H molar ratio. On the other hand, proton 7 which is the H on the ortho position on the benzene ring, neighbouring the methoxy group, shifted significantly early on at 5:1 G:H molar ratio, and has a total shift upfield by 0.04 ppm. Both scatter plots of proton 6 and 7 showed a similar linear trend upwards to 400 molar ratios of water as seen in Figure 5.47.

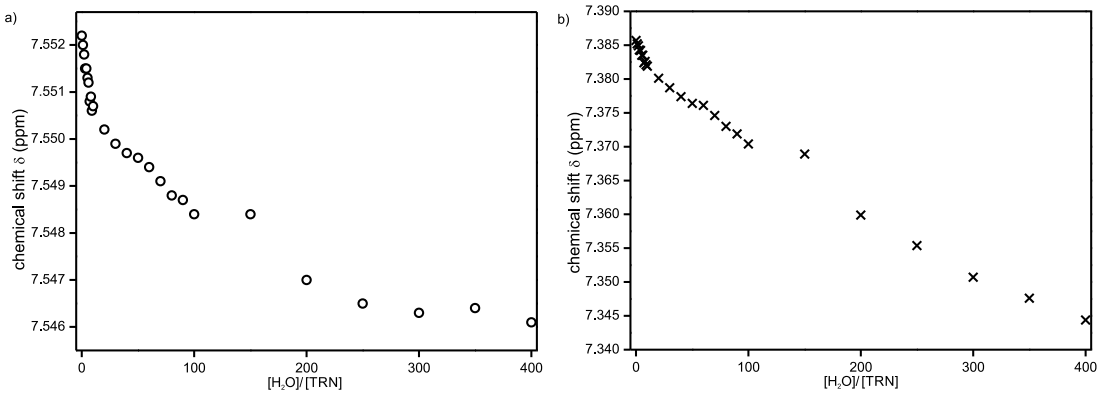


Figure 5.47. Scatter plot of proton 6 (a) and proton 7 (b), both showing upfield shifts.

The scatter plot for proton 8 (H on the meta position, next to the NH of the anthranilic acid ring) showed a plateau feature, observed from 30 to 70 water molar ratios (Figure 5.48). The only other proton which share similar plateau feature is proton 2, however, the plateau is a result of an upfield shift, the opposite direction to the one observed in NH of proton 2. The magnitude of the shift experienced by proton 8 at the plateau between 50-70:1 G:H ratio is 0.003 ppm, which is significantly smaller than the shift of the NH at the similar interval, 0.02 ppm. There is no doubt that the shift experienced by proton 8 is an indirect effect from the interaction of the NH. Interestingly, as more water is introduced, proton 8 shift changed direction, moving downfield from 200 water molar ratios upwards. At 400 molar ratios, the peak position is similar to the starting position. Misinterpretation of the peak shift might occur if just the two extreme ranges were to analysed in isolation.

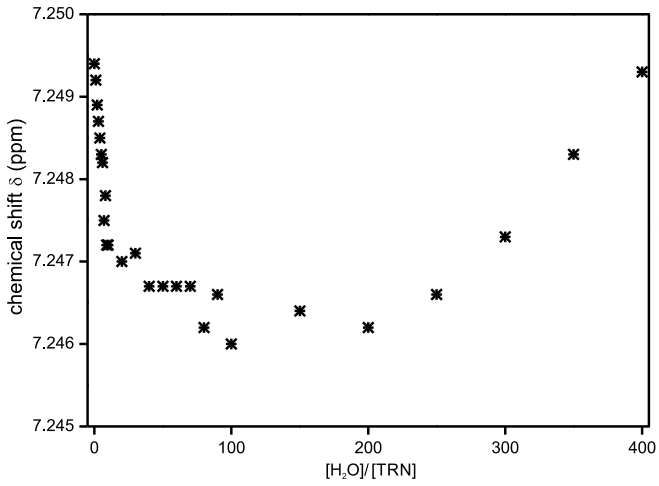


Figure 5.48. Scatter plot of proton 8 showing initial upfield, followed by a plateau curve, and subsequent downfield shift.

Proton 9 (◀), the H on the meta position of the anthranilic acid ring, shifted downfield by 0.042 ppm after 400 molar ratios of water in the system. Meanwhile, proton 10 (▶) which is the H on the meta position on the benzene ring, next to the

methoxy group, also shifted downfield, but only by 0.025 ppm at similar water ratios. Both proton 9 and 10 are located far apart from one another but do share similar linear trend from their respective scatter plot, shifting steadily as more water is titrated in (Figure 5.49).

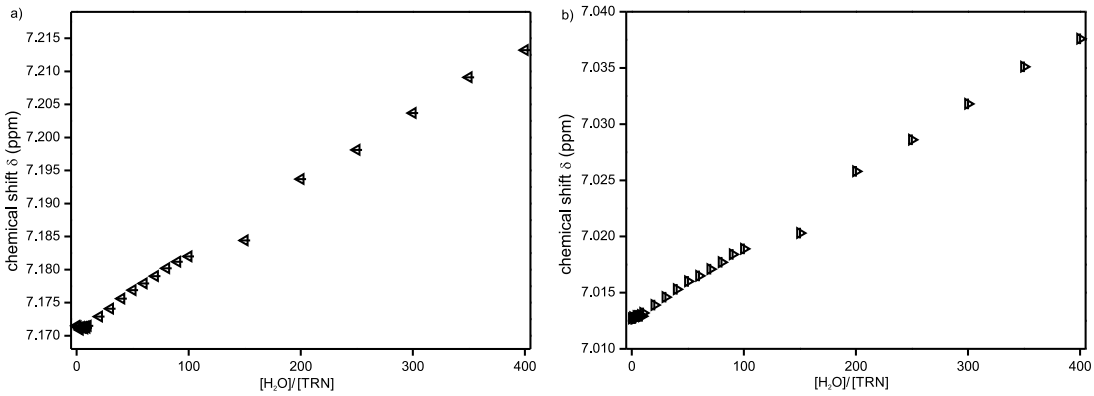


Figure 5.49. Scatter plot of proton 9 (a) and proton 10 (b), both showing downfield shifts

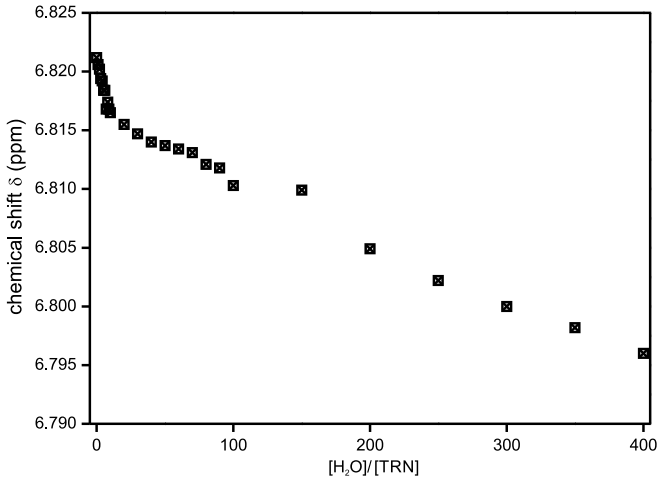


Figure 5.50. Scatter plot of proton 11 showing an upfield shift.

The proton on the carbon neighbouring the carbonyl (proton 11, ⊠) shifted upfield by 0.025 ppm. Similar to proton 9 and 10, an overall linear trend of the scatter plot can be observed. Meanwhile, the methoxy groups (proton 12 and 13) did not shift much throughout the titrations (Figure 5.51, (a)). The protons shift at the different magnitude, proton 12 did not show any significant shift from 0-100:1 G:H molar ratio

(+0.0004 ppm), while proton 13 shifted 0.002 ppm at similar water ratios. Scatter plot of both protons showed almost a straight line for proton 12 and a linear curve for proton 13 (Figure 5.51, (b)). At the end of the titration, the total shift downfield recorded were just 0.003 and 0.008 ppm for proton 12 and 13 respectively.

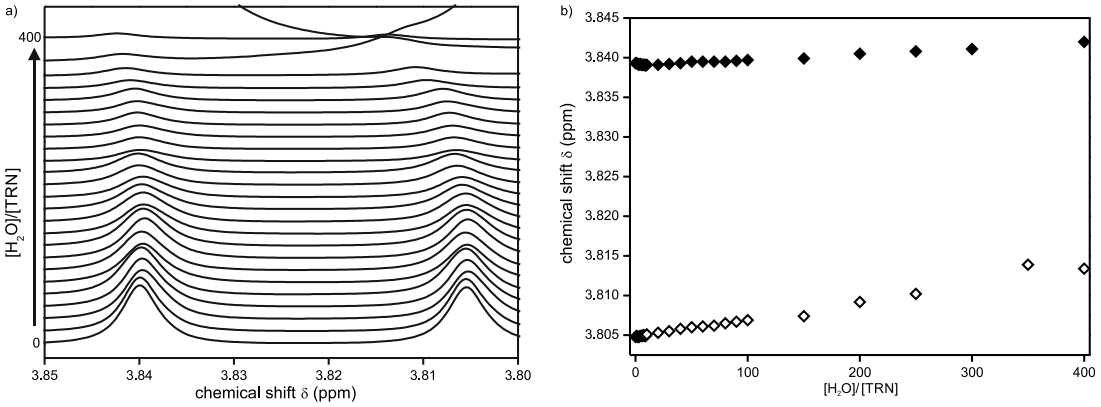


Figure 5.51. a) shows chemical shifts of proton 12 and 13, showing a non significant peak shift with water titration. b) shows the scatter plot of the peaks positions.

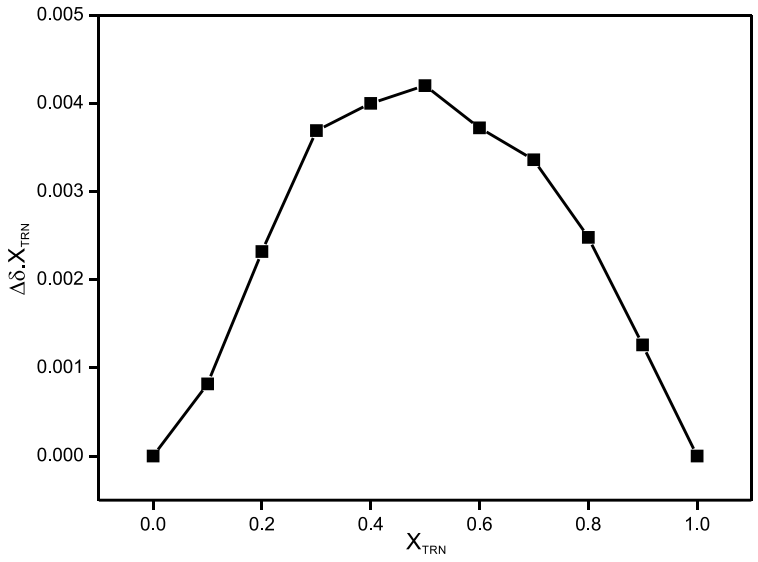


Figure 5.52. Job plot showing unclear complexation between TRN and water in DMSO-d_6 using ^{1}H-NMR. ([TRN] + [H_2O] = 0.1 M)

Job's plot indicated that TRN and water interact in a 1:1 stoichiometry at equilibria in DMSO (X_{max}=0.5). However, as mentioned before, there are potentially

more than one species present, and if that is the case, then the stoichiometry suggested is definitely off as Job plot is not capable of considering the two species in the same equilibrium. Therefore, a subsequent fitting is done to all available stoichiometry, 1:1, 1:2, and 2:1 (Table 5.4). The best fitting considered would be the ones with the least error when fitted to the mathematical model. Based on the fact that a plateau was observed form 30-70 molar ratios of water, the binding constant fitting is done up to this titration point. The following K values are obtained from the fitting of all TRN protons to the respective binding stoichiometry models.

Table 5.4. Calculated ΔG of TRN-water binding based on three (3) different binding models.

[H]:[G] binding model	K_1 (±% error)	K_{21} (±% error)	K_{12} (±% error)	ΔG for K_{21}
TRN:H_2O	10.6 M^{-1} (±14%)	N/A	N/A	-5.9 kJ mol^{-1}
2TRN:H_2O	2.01 M^{-1} (±3.2%)	60.22 M^{-1} (±2.3%)	N/A	-10.2 kJ mol^{-1}
TRN:2H_2O	13.86 M^{-1} (±5.3%)	N/A	0.51 M^{-1} (±3.9%)	-6.5 kJ mol^{-1}

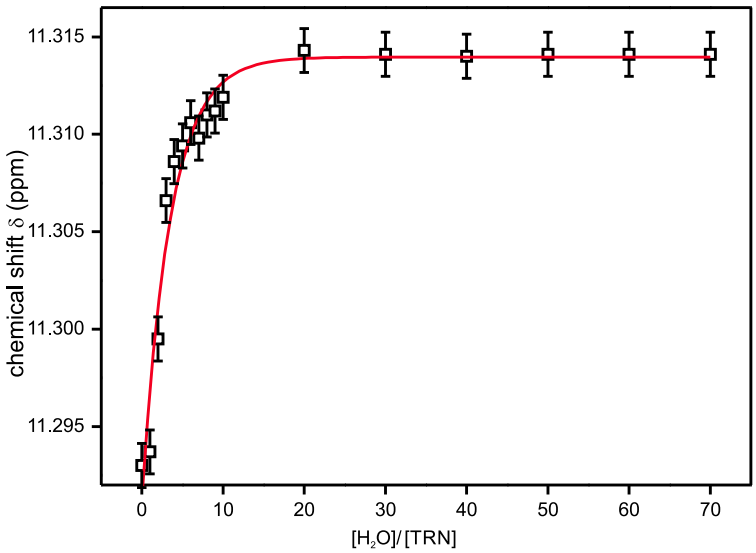


Figure 5.53. Example of fitting for binding constant determination for proton 2.

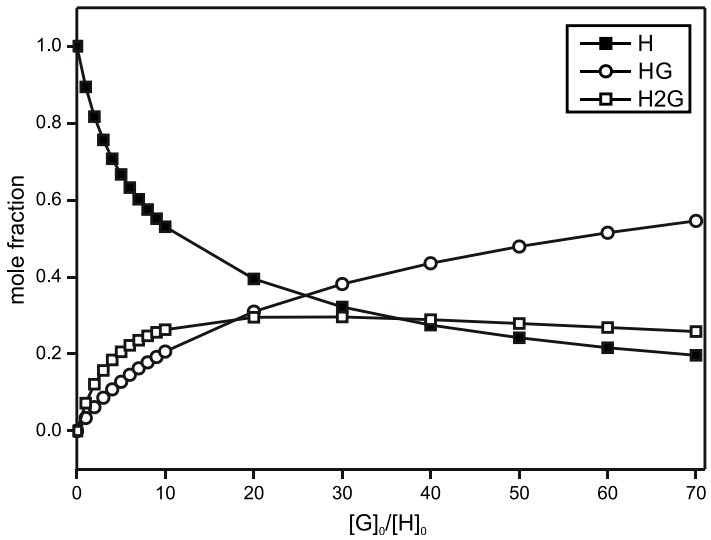


Figure 5.54. TRN speciation plot following 2:1 binding stoichiometry

Comparison based on the fitting errors clearly indicate that the best fitting of the three is the 2:1, with just 3% and 2% error in K_{11} and K_{21} values respectively. The speciation plot (Figure 5.54) indicated that the 2:1 complex reached a plateau at 10:1 G:H molar ratio, while 1:1 complexation continues to form with higher water titration. In fact, at 20:1 G:H molar ratio, the H2G complex reached its critical point and started

to reduce in number or mole fraction value gradually, and more HG formation afterwards.

The 2:1 stoichiometry fitting also allow for direct comparison to the two previous titration values of DTA and CIM. The K_{21} of 60 M^{-1} is considerably lower than DTA's K_{21} of 3005 M^{-1} (full titration point) or 615 M^{-1} (from 25-1087:1 G:H), and CIM's value of 203 M^{-1}. However, upon conversion to Gibb free energy (ΔG), the values are quite comparable. ΔG for K_{21} of TRN corresponds to -10.2 kJ mol^{-1}, while as mentioned in the section above, while the value for CIM corresponds to -13.16 kJ mol^{-1}, and DTA values was between -16 to -20 kJ mol^{-1}. Even though the obtained binding constant and the calculated ΔG only represent an 'apparent' binding, it is still useful as the values show some degree of molecular recognition, implying significant interaction between the tested compounds and water. Results from the solution-state analysis of the three compounds thus far, led us to believe that whilst FTIR probe is good initial approach as the method allows for qualitative observation of compound-water complexation, ^{1}H-NMR method is the best method to move forwards as from the experiment we are able to quantify the 'apparent' binding interaction to water. Moving forward, ^{1}H-NMR titration method with water as the guest will be the focus, with FTIR titration probe acting as a preliminary screen.

5.3.9 Preliminary FTIR solid and solution-state analysis of PXM

Observation of the FTIR for PXM anhydrous and monohydrate reveals two distinctly different spectra (Figure 5.55). The assignment for vibrations obtained from the FTIR of the anhydrous PXM (Form I) was based on the common vibrations of the available functional groups. The assignment to the functional groups (in descending

order) are as follows; N-H stretching intense single peak at 3392 cm^{-1}, amide C=O stretch at 1638 cm^{-1}, N-H bending 1528 cm^{-1}, S=O asymmetric stretch I and II at 1437 and 1353 cm^{-1} respectively, and finally the S=O symmetric stretch at 1179 cm^{-1}.

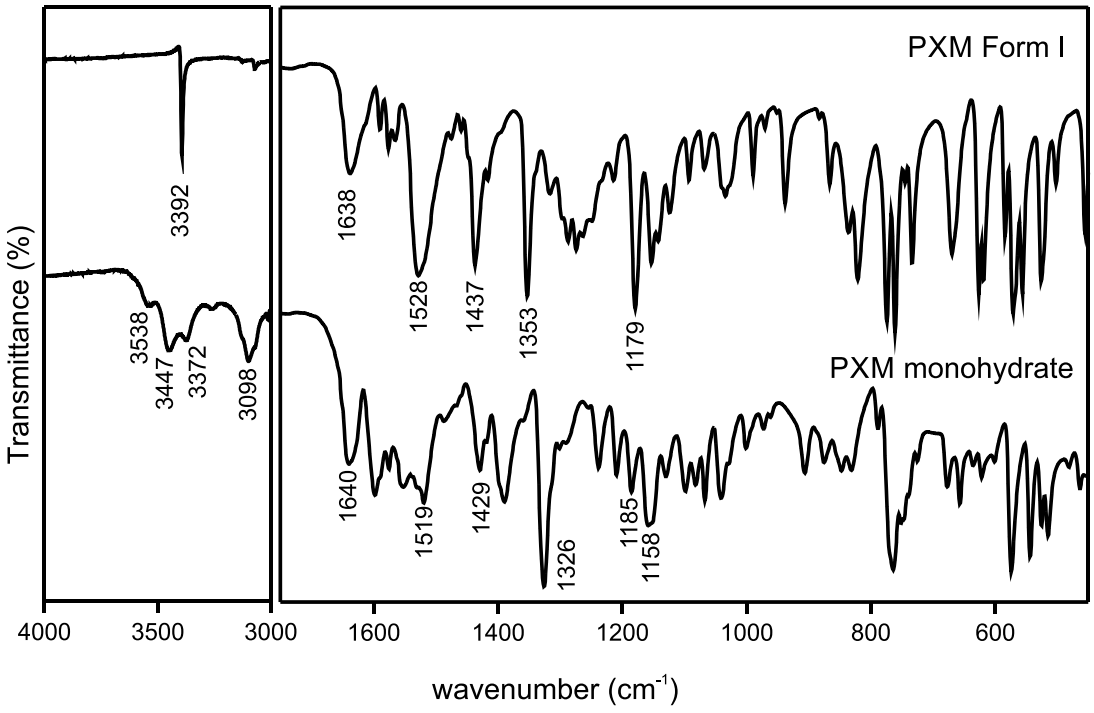


Figure 5.55. FTIR spectra of PXM anhydrous and monohydrate form with labelling of relevant peaks.

As for the monohydrate form, the mentioned peaks showed clear changes compared to the anhydrous form, for example in the N-H stretching region, the initially in the anhydrous form, a sharp and strong single peak was observed, however, in the hydrate form, this region is occupied by three broad peaks, at 3538, 3447 and 3372 cm^{-1}. The other two latter vibrations at 3447 and 3372 cm^{-1} are most likely from the N-H and N^{+}-H. The N^{+}-H vibration is present as the monohydrate structure is in the zwitterionic form (as shown in Figure 5.4 (d)).[34] The peak at 3538 and 3098 cm^{-1} is most likely the OH stretching vibration coming from the incorporated water. There is no significant change observed to the carbonyl vibration of the two forms with just two wavenumber difference, to higher wavenumber recorded in the monohydrate.

Next, the NH-bending vibration, which vibrates at 1528 cm^{-1} in the anhydrous form I, appeared shifted by nine wavenumbers lower to 1519 cm^{-1} in the monohydrate spectra. The only unclear vibration change was for the S=O symmetric stretch which appeared at 1179 cm^{-1} in the anhydrous form, as two closely related peak position present in close proximity of the peak in the monohydrate. Summary of the mention changes as well as other assigned peaks shifts are indicated in Table 5.5.

Table 5.5. Vibration assignments for PXM anhydrous Form I and the monohydrate

PXM functional group vibration	Anhydrous Form I	Monohydrate
N-H stretching	3392 cm^{-1}	broad peak at 3447 and 3470 cm^{-1}
amide C=O stretch	1638 cm^{-1}	1640 cm^{-1}
N-H bending	1528 cm^{-1}	1519 cm^{-1}
S=O asymmetric stretch	1437 and 1353 cm^{-1}	1429 and 1326 cm^{-1}
S=O symmetric stretch	1179 cm^{-1}	1185 or 1158 cm^{-1}

Based on these differences, it is safe to assume that the observed shifts are the result of both hydrogen bonding to water as well as different packing of the two forms. PXM monohydrate single crystal X-ray diffraction data revealed that the asymmetric unit of the monohydrate consists of two discrete PXM molecules, and two water molecules.[73] Two host molecules are bridged by one water molecule, hydrogen bonded to the deprotonated hydroxyl oxygen atom and the amide carbonyl. Plus, a second unbound water molecule is connected to the main motif, which hydrogen bonds to the first water molecule. This second, independent water molecule also act as bridge to a second core motif (two PXM and one water), and thus forms a water tetramer in between four PXM molecules.[34] Based on the reported hydrogen bond interactions in

the monohydrate, it is essential for the mentioned interaction points (carbonyl, sulfones and amide functionalities) to be observed in the following solution-state analysis.

Solution-state FTIR titration analysis of PXM was done in acetonitrile environment to avoid overlapping of the targeted interaction points as the compound consist of functional group of the two previously used solvents, *i.e.* the C=O in acetone and the S=O in DMSO. Although in PXM the functional group is sulfones (O=S=O), the asymmetric and symmetric S=O stretching still overlaps with the DMSO S=O vibration. A dilute solution containing 0.1 M PXM in acetonitrile was used in the initial titration, with one D_2O molar ratio gaps (up to three), followed by a larger gap to 50 molar ratios of D_2O. The observation of the relevant vibrations is as indicated in Figure 5.56.

In the higher wavenumber region, N-H stretching is observable at 0:1 G:H molar ratio, however as D_2O is introduced into the solution, the vibration became obstructed. Although D_2O do not possess any vibration above 3000 cm^{-1}, it is possible that the D_2O used has reacted with ambient water forming HOD species,[74] thus having vibration which covers the N-H stretch. From 1700 to 450 cm^{-1}, most of PXM vibrations can be observed. Surprisingly, the carbonyl vibration at 1636 cm^{-1} did not change nor shift, even at the highest D_2O content. The region between 1550 to 1350 cm^{-1}, which N-H bending S=O asymmetric stretch was observed in the solid-state is overlapped with the OD *v2* and combination of *v2*+ libration vibrations.[45] However the vibrations at 1305, 1183 and 1157 cm^{-1} have the distinct feature similar to that of the S=O asymmetric stretch which was observed at 1437 and 1353 cm^{-1}, and symmetric stretch at 1173 cm^{-1} in the anhydrous solid-state FTIR spectra. Similar to the carbonyl observation, no significant shift was detected as the difference between

the two D_2O molar ratio extremes with just one wavenumber higher for 1305 cm^{-1} vibration, and one wavenumber lower for 1157 cm^{-1} vibration. Also, the vibration at 1204 cm^{-1}, coming from the D_2O, overlaps with the monitoring of the vibration at 1183 cm^{-1}. Overall, the observation for PXM-D_2O titration also did not show any significant changes, similar to the earlier FTIR titration experiment for TRN-D_2O.

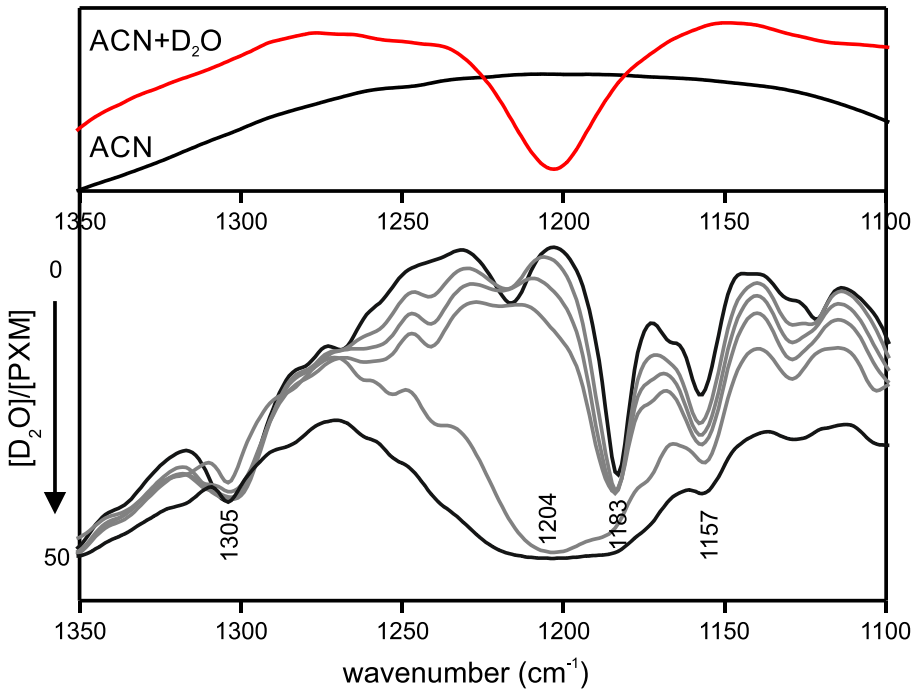


Figure 5.56. Solution-state FTIR titration analysis of PXM focusing on the region from 1350 to 1100 cm^{-1}.

5.3.10 ^{1}H NMR PXM-water titration

Initial ^{1}H-NMR spectrum a deuterated acetonitrile environment revealed 11 proton regions could be observed (Figure 5.57), which integrates well to the 13 protons of PXM. The obvious protons are the N^{+} Hat 13.52 ppm, the NH proton at 9.07 ppm, and the methyl groups 2.90 ppm (Figure 5.57, (a)).

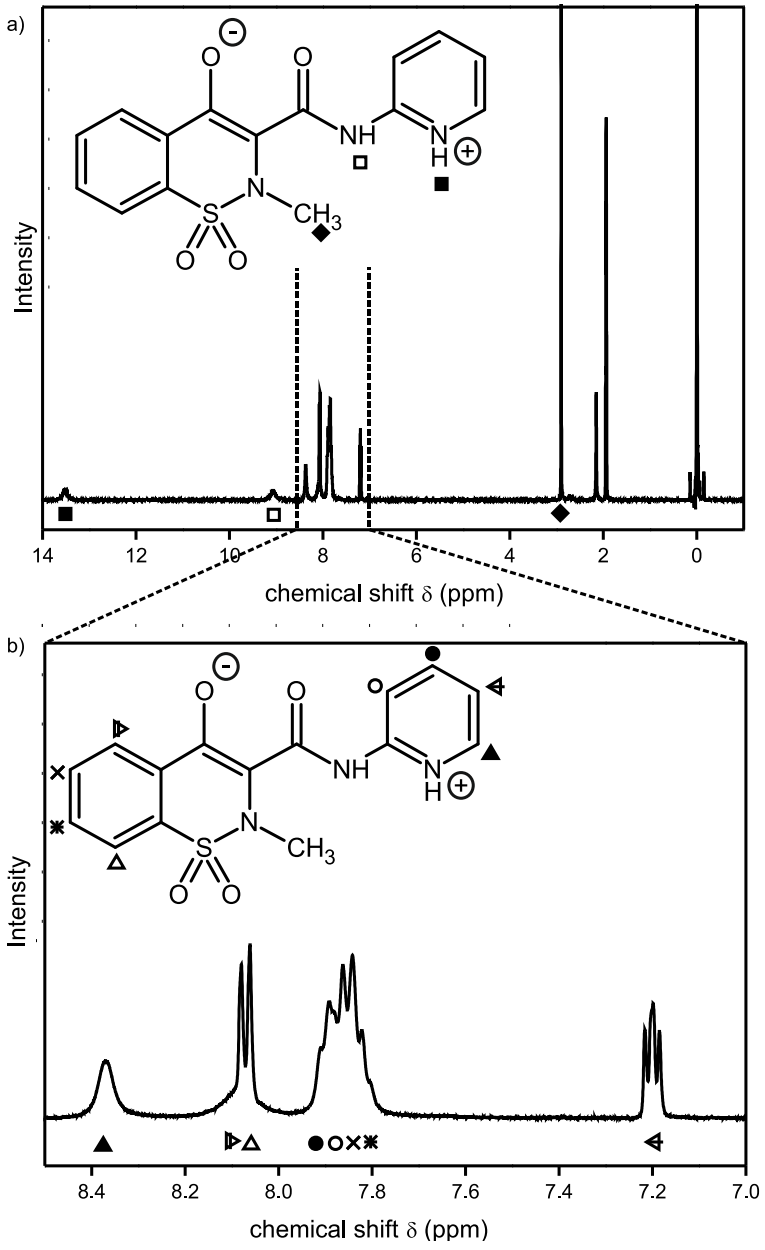


Figure 5.57. Peak assignment, a) the N^{+}H, the NH, and the methyl group identified as Proton 1, 2 and 11, with their respective symbols. b) shows proton 3-10 and their respective symbols.

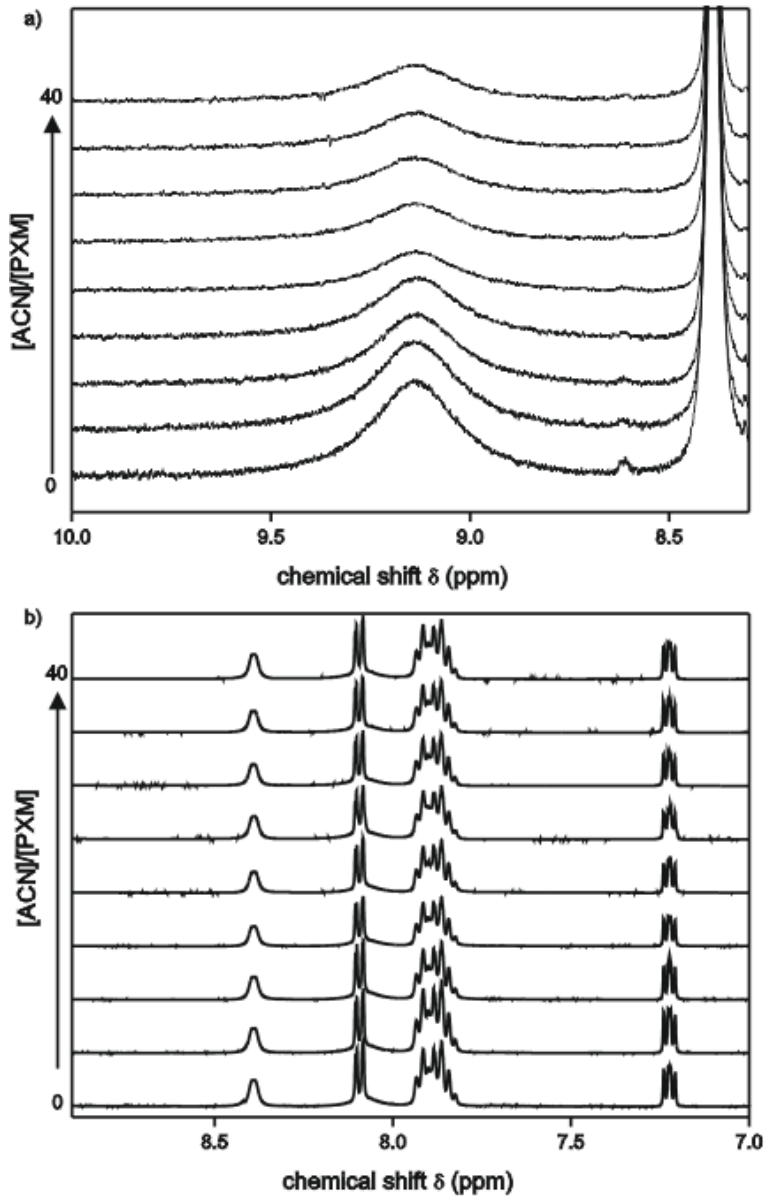


Figure 5.58. PXM dilution experiment with anhydrous acetonitrile from 0-40:1 G:H molar ratios with five molar ratios gap. a) highlight proton 2, while b) shows proton 3-10 chemical shift regions.

Dilution with anhydrous acetonitrile from 0-40:1 G:H molar ratios with five molar ratios gap did not show any significant shift, as shown in the NH proton (proton 2) plot (Figure 5.58 (a)) and the remaining proton 3-10 chemical shift regions, showing no observable peak change

The ^{1}H-NMR PXM-water titration was proceeded and observation of proton 1, the protonated $N^{+}H$ on the benzene ring, revealed that it can only be monitored up to

10:1 G:H molar ratios, with no observable chemical shift afterwards This feature is similar to previous observations of the fast exchange protons, which would make the peak appear too broad with water inclusion, hence difficult to monitor the peak shift (Figure 5.59).

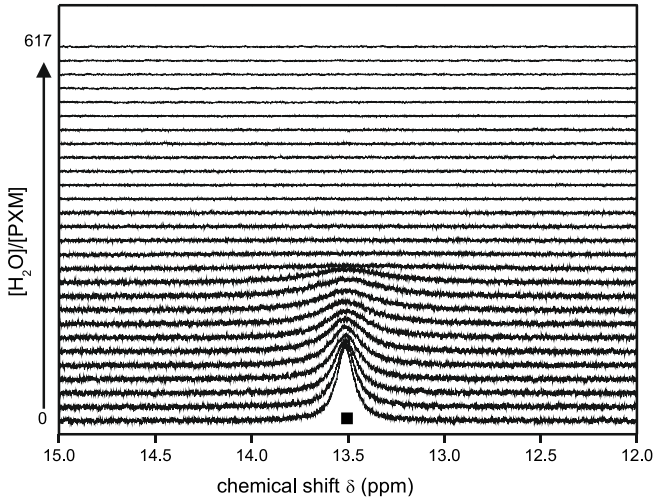


Figure 5.59. Spectra of proton 1 from zero to 617 molar ratios of water

Next observation was on proton 2, which is NH of the amide. This chemical shift was observable until the end of the titration, even though it is broad. The peak shifted downfield, indicative of hydrogen bond formation, with the NH acting as a donor. The proton which involve in hydrogen bonding or the bridging proton is associated with losing electron density, shifting downfield as a result of the deshielding.[56] Interestingly, the peak is quite clear from 1-10:1 G:H and 101-617:1 G:H molar ratios, however, between 15 to 90, the peak appeared broader (but still visible, Figure 5.60, (a)). The peak shifts linearly with more water titrated into the system, with a distinct slope change in the shift observed at above 90 molar ratios (Figure 5.60, (b)). This step is most likely a direct result of saturation of the NH binding site or interaction point in forming the PXM-water complex. Less active site results in a more gradual slope. Overall, the shift observed to proton 2 is the largest, with 2.2

ppm change recorded at the end of the titration. It is obvious that the NH is indeed one of the interaction point for water-PXM complexation in dilute solution. In the crystalline monohydrate, water coordinate to the deprotonated OH and the carbonyl, which is unobservable in this analysis.

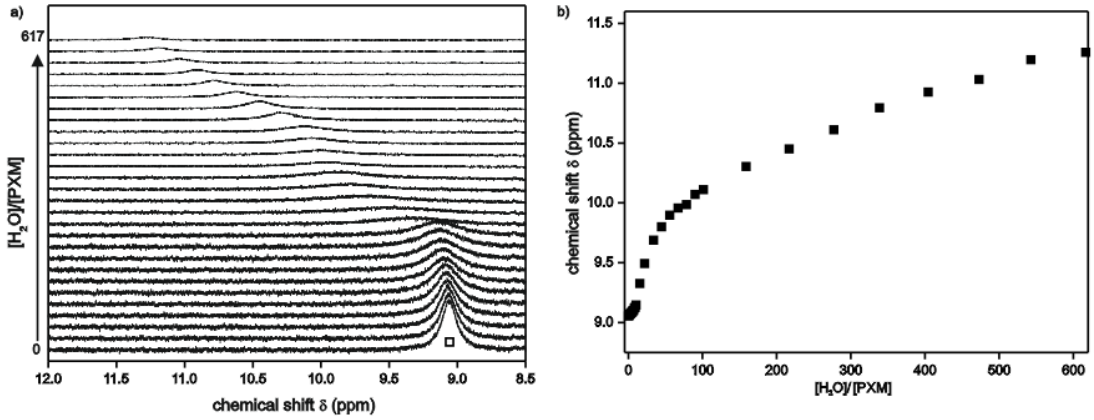


Figure 5.60.a) Spectra of proton 2 (NH), showing a downfield shift with water titration. b) scatter plot of the peaks positions.

The observation of proton 3, which is the proton at meta position on the protonated benzene ring, neighbouring the $N^{+}H$, revealed a broad single peak. (Figure 5.61). While the shift upfield observed is quite minimal, the change in peak profile is clear (Figure 5.61 (a)). The peak becomes broader as more water is introduced, and start to split at 4:1 G:H molar ratios, and completely split as 8 molar ratios of water is titrated into the system. The clear split peak can be distinctly observed from 15:1 G:H molar ratio onwards. The split observed suggest that there was significant interaction around proton 3, most likely by the $N^{+}H$ interaction with water, which caused significant electronic environment rearrangement and changes leading to the split.

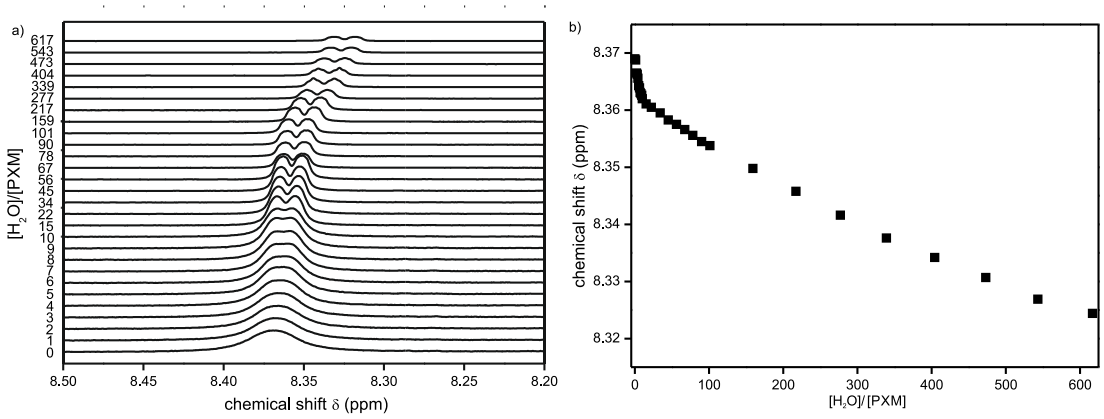


Figure 5.61. a) The spectra of proton 3, showing an upfield shift with water titration. b) shows scatter plot of the peaks positions.

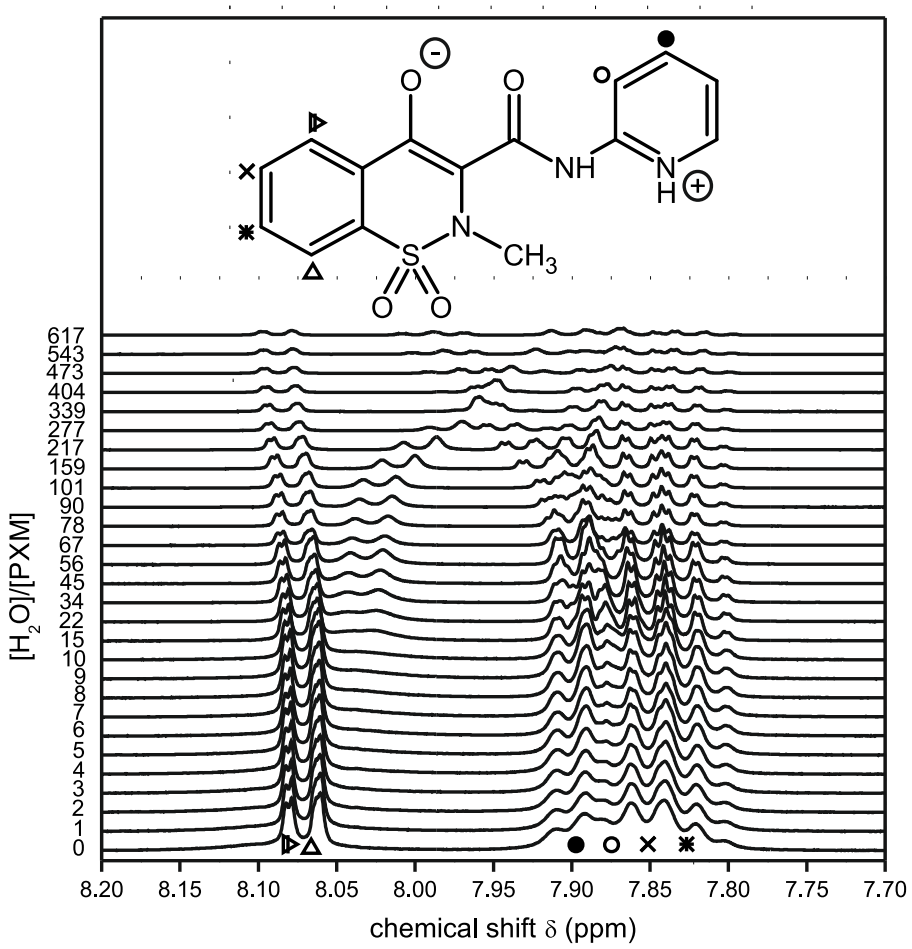


Figure 5.62. Spectra of proton 4-9, showing complex spectra shift and peak profile changes with water titration

A more complex observation of proton 4 (▶) and 5 (△), both located at around 8 ppm on the spectra, and on the structure are at an opposite position on the first

benzene ring, appearing as a shoulder (higher ppm) and a split peak. The two protons somewhat overlap, and it is hard to distinguish one from the other. Interestingly, as water is added into the system, the shoulder (initially on the left side of the split peak) at the higher ppm began to disappear, and at around 10-15 G:H molar ratio, the shoulder re-appeared, this time on the lower ppm, on the right-hand side of the split peak. At 22:1 G:H molar ratios, this shoulder began to grow, and at 34:1 G:H molar ratios, a clear split peak is observed. This new split peak grows and shifts upfield as more water is added. At 78:1 G:H molar ratios, the new split peak is completely separated from the original peak, continuing to shift upfield up to 217:1 G:H molar ratio. However, 277:1 G:H molar ratio, it overlaps with another peak, proton 6, which was shifting downfield. Between 250-404:1 G:H molar ratio an overlapping of the peaks occurred where proton 5 and 6 are seen 'jumbled' together and identification of the individual peak is difficult. Above 404 molar ratios of water, the combined peaks are separated as both peaks continue to shift in their respective directions. Even though the magnitude of the shift is small (0.045 ppm), clear water influence toward the chemical shift of the compound can be observed. Also, towards the end of the titration, the curve seems to level off, most likely achieving plateau > 617:1 G:H molar ratio.

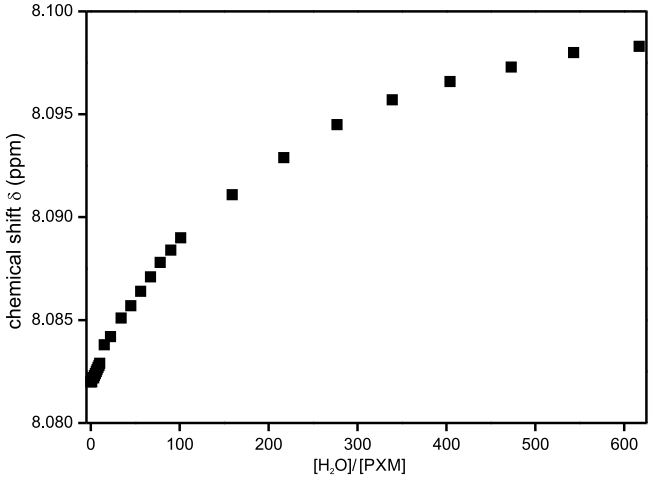


Figure 5.63. Scatter plot of the peaks positions of proton 4 or 5 (the initial split peak) showing a downfield shift.

Simulation spectra pattern for proton 6-9,[75–78] suggest that the peaks should appear as a triplet, a doublet, a triplet and a triplet, however these four protons peaks appeared overlapped together in the region of 7.8-7.9 ppm in the initial spectra at 0:1G:H molar ratio (Figure 5.62). Of the four protons, proton 6 shifts downfield, while the other three showed no significant shift. Due to the shift of proton 6, the overall peak profile changes from the initial spectra. At 617:1 G:H molar ration, when the peak has shifted furthest downfield from the original position, it is clear that proton 6 is a triplet, just as the prediction suggested. Note that monitoring of peak 5 to 9 is difficult due to the no profile change hence the peaks remained overlapped.

Proton 10, which is the proton at the para position on the protonated benzene ring, shifted downfield. Peak profile change was observed at 339:1 G:H molar ratio, before changing back to the original shape at 473:1 G:H molar ratio. The shift only becomes clear at higher water molar ratio with just 0.06 ppm difference between 0 and 617:1 G:H molar ratio (Figure 5.64).

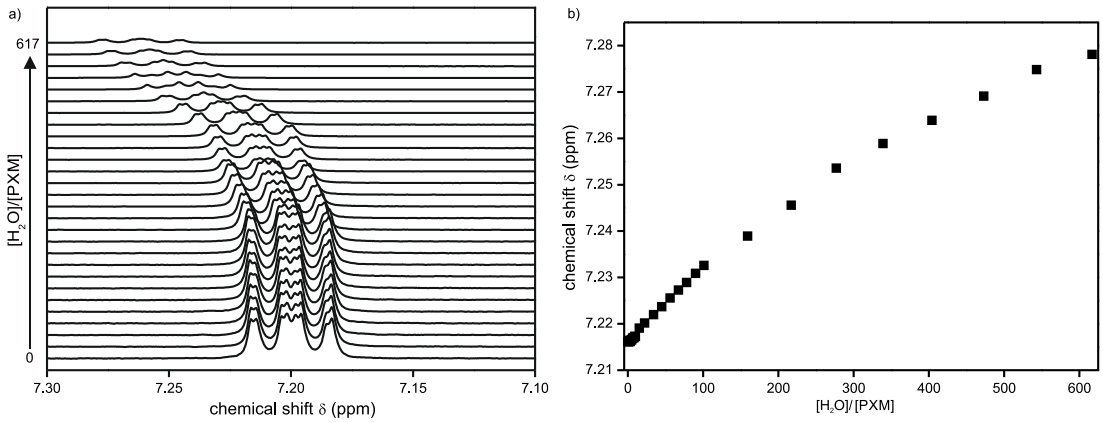


Figure 5.64.a) Spectra of proton 10, showing a downfield shift with water titration. b) shows the scatter plot of the peaks positions.

Likewise, proton 11which is the methyl functionality do not show any shift at lower water content (0-10:1 G:H molar ratios), then shifted downfield (15-159:1 G:H

molar ratios), followed by an upfield shift at higher water content 217-617:1 G:H molar ratios. The overall magnitude of the shift observed is 0.003 ppm, which means that the initial downfield shift was not significant (Figure 5.65).

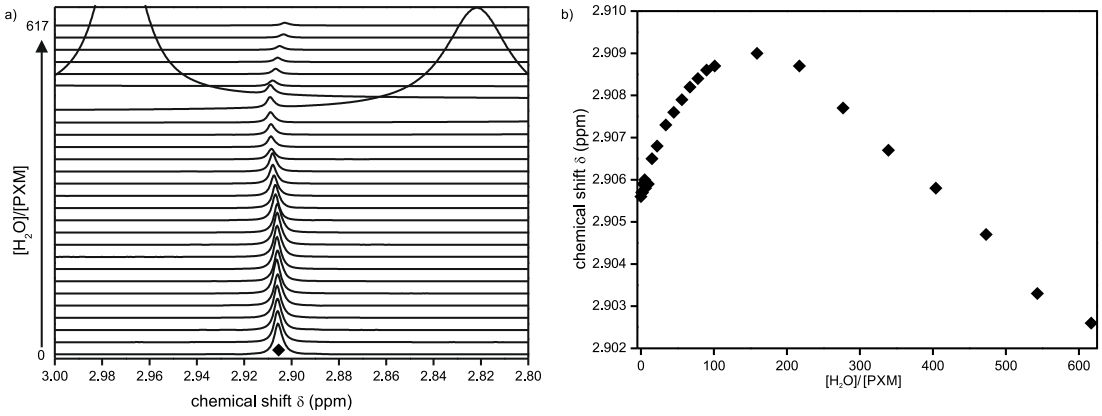


Figure 5.65. a) Spectra of proton 11, showing initial downfield followed by a subsequent upfield shift with water titration. b): scatter plot of the peaks positions.

The Job plot of PXM showed a 1:1 binding stoichiometry in solution, with X_{max}=0.5 (Figure 5.66). The curve obtained is not the typical of a Job plot, which is a result of the small Δδ. Plus, the broad nature of the observed NH peak did not help as the exact peak point is difficult to ascertain. All in all, the Job plot does reflect the stoichiometry of the crystalline state, consistent with neutron diffraction data which reported that the monohydrate stoichiometry to be a 2:2.[34]

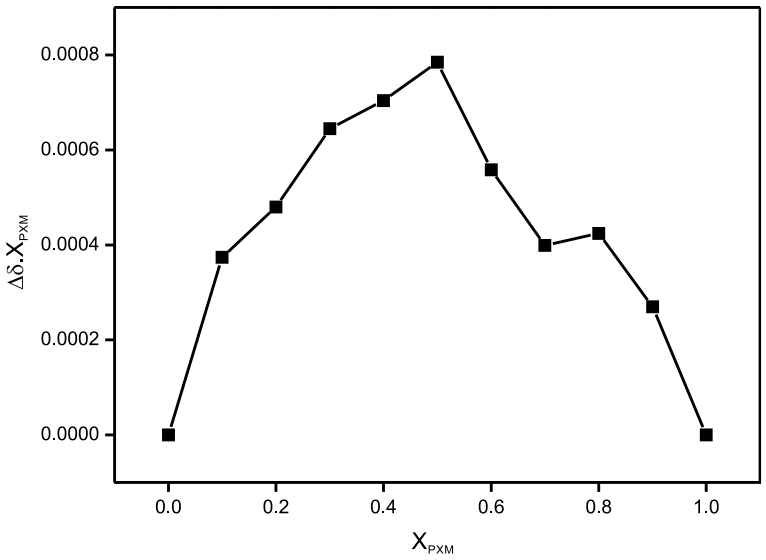


Figure 5.66. Job plot showing the 1:1 stoichiometry of the complexation between PXM and water in acetonitrile$_{d3}$ using ^{1}H NMR. ([PXM] + [H_2O] = 0.1 M)

Overall, the fitting to the available stoichiometry interaction models of 1:1, 2:1 and 1:2, for the chemical shift of all protons which are able to be monitored (proton 2, 3, 4, 10 and 11) is poor (Figure 5.67, (a)) as not all protons are being analysed. The best fitting, with the least error when the line fitted to the mathematical model, is 1:1 with a *K* value of 0.3 M^{-1}. This K value translates into ΔG of 2.98 kJ mol^{-1}, which directly indicate that the complexation to water does not occur. However, we do believe that the complexation does take place, evident from the various changes to the chemical shift observed *e.g.* the peaks shifts and the peak profile changes. If direct comparison were to be made to the three previous compounds, DTA, CIM, and TRN, then the 2:1 binding need to be calculated. From the 2:1 binding model, the generated K_{11} value is 1.7 M^{-1} while K_{21} obtained is 336 M^{-1}. The calculated ΔG for K_{21} is -14.4 kJ mol^{-1}. Summary of all PXM fitting to all available binding models are listed in Table 5.6.

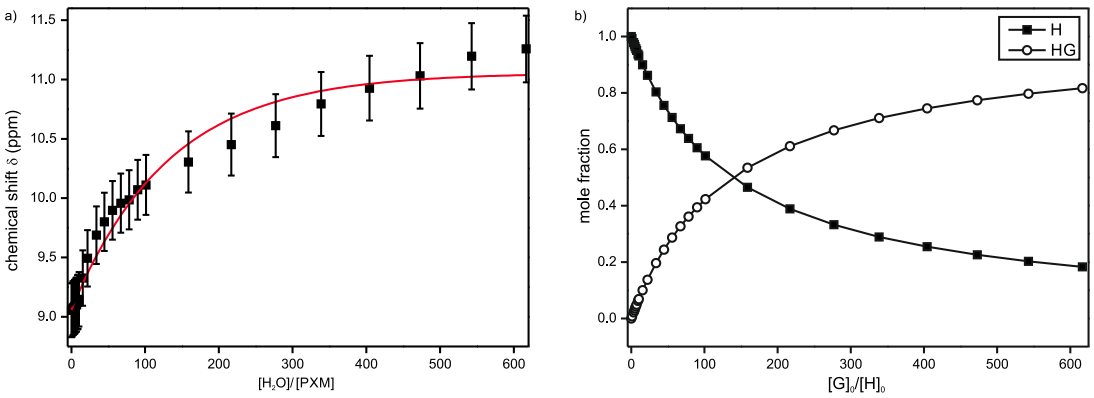


Figure 5.67.a) Example of fitting of proton 2 for binding constant determination fitted to 1:1 binding model. b) PXM speciation plot following 1:1 binding stoichiometry

Table 5.6. Calculated ΔG of PXM-water binding based on three (3) different binding models

[H]:[G] binding model	K_1 (±% error)	K_{21} (±% error)	K_{12} (±% error)	ΔG for K_{21}
PXM:H_2O	0.3 M-1 (±2.5%)	N/A	N/A	2.98 kJ mol^{-1}
2PXM:H_2O	1.7 M^{-1} (±16.7%)	336 M^{-1} (±18%)	N/A	-14.4 kJ mol^{-1}
PXM:2H_2O	0.37 M^{-1} (±1.7%)	N/A	-0.08 M^{-1} (± -7.8%)	NA-kJ mol^{-1}

5.4 Conclusion

Results from the analysis thus far reveals that titration using FTIR allows for qualitative observation of potential interaction points. The method's fast timescale compared to ^{1}H-NMR would also allow observation of multiple species at play Gaussian fits to spectra were to be used.[79] Hydrogen bond sensitive vibrations *i.e.* carbonyl is a good region to focus on as shown in the case of DTA. Limited sensitivity of the method saw small changes to the remaining three model compounds FTIR spectra. However, shifts or changes are not guaranteed upon water introduction as seen in the solution-state FTIR water titration of TRN and PXM. Other drawbacks to this method include 1) tested compounds and selected solvent having overlapping vibrations, 2) for a solvent which do not share the same vibration, the solubility of the compound limits their selection, 3) problem with water/D_2O vibrations, where the broad OH/OD vibrations potentially overlaps with the vibration of interest *i.e.* NH stretch. Even though the probe using FTIR are only limited to qualitative analysis, it was still useful to narrow down a specific region in the follow-up analysis. The best example for a successful FTIR titration is the DTA-water titration where a shift totalling 13 wavenumbers was observed to the carbonyl region, and the shift started even at low water incorporation, highlighting the compound's high affinity towards water. Also, the FTIR method allows for observation of the interactions between drug and water through a carbonyl, which is not possible through ^{1}H-NMR method.

We found that ^{1}H-NMR was able to detect and monitor the changes to the electronic environment of the monitored nuclei in the form of peak shifts, represented by $\Delta\delta$ which resulted from the compound-water titration. The location of the nuclei most affected by water inclusion also gives qualitative information about the

regioselectivity for guest binding.[61] Unlike anion/cation binding or other host-guest titration (enzyme-substrate) experiments where a large shift is commonly observed, and the active/binding site is charged and known, our water titration experiment involved neutral compound (except for PXM, which is zwitterionic) which all result in a small shift even at very high water content (>400 molar ratios). For example, the Δδ observed form anion binding experiment between 1,4-dimethoxypillar[5]arene (DMP5) and the guest molecule *n*-octylpyrazinium hexafuorophosphate (G) showing clear shift of around 3 ppm form the addition of 4.3 molar ratios of G,[80] while titration on various indolocarbazole- and urea-based synthetic receptors (33 in total) toward acetate ion showed Δδ of the NH protons of the free receptor and the receptor−anion complex somewhere between 3.26 to 3.69 ppm, obtained from the various compounds.[81]

On the other hand, the shift observed in our analysis normally is less than one ppm even at the highest water content of >400 molar ratios, apart from one peak, proton 2 (NH) in PXM titration which has yielded 2.2 ppm at 617:1 G:H molar ratio. The value is reasonable since PXM is zwitterionic in solution, having both negative and positive charge, hence more attracting force to the polar guest. Due the small shifts, chemical shift plot to obtain the binding constant is done against all protons which can be monitored, and help minimises the fitting error. However, for peaks that undergone profile changes and showed complex peak transformation *i.e.* in PXM proton 4-9, Δδ monitoring was hindered.

The direction of the resonance peak shift usually gives an indication whether a proton is forming or breaking hydrogen bond, however, since the overall proton peak shifts and their respective electronic rearrangement were observed in determining the

binding constant (*K*), the shift direction is irrelevant as any shift, upfield or downfield would still reflect the water-compound complex (Figure 5.20). The difficulty to determine the strength of the observed shift or interaction is underlined with the fact that in a dilute water-solvent binary system, most likely more than one species form, hence the Job's plot along with the traditional binding stoichiometry model has to be used with caution. All the *K* values obtained from the experiments thus only represent an 'apparent' binding constant, fitted against their respective binding models.

Table 5.7. Calculated ΔG of all compound-water binding based on 2:1 binding model.

[H]:[G] binding model	K_1 (±% error)	K_{21} (±% error)	K_{12} (±% error)	ΔG for K_{21}
2DTA:H_2O	2.94 x 10^{-4} M^{-1} (±2.3%)	3005 M^{-1} (±8.1%)	N/A	-19.8 kJ mol^{-1}
2CIM:H_2O	7 x $10^{-3}M^{-1}$ (±1.9%)	203 M^{-1} (±0.3%)	N/A	-16.1 kJ mol^{-1}
2TRN:H_2O	2.01 M^{-1} (±3.2%)	60.22 M^{-1} (±2.3%)	N/A	-10.2 kJ mol^{-1}
2PXM:H_2O	1.7 M^{-1} (±16.7%)	336 M^{-1} (±18%)	N/A	-14.4 kJ mol^{-1}

Interestingly, all K_{21} fitting values suggest a significant binding constant (>60 M^{-1}), which still support previous notion stating that the 'apparent' binding values do represent some degree of molecular recognition by suggesting a significant interaction between the tested compounds and water. A large K lead to a large ΔG, and the smaller or more negative ΔG generally result in the formation of stronger complexes.[61] The ΔG values of < -10.2 kJ mol^{-1} are comparable to the cation binding, K^+ to 18-Crown-6 (or 1,4,7,10,13,16-hexaoxacyclooctadecane), which were reported to be between -

11.4 to -12.1 kJ mol^{-1}.[61,82] To conclude, in this investigation on stable hydrate, the 'apparent' significant values of K_{21} and ΔG, could potentially be a reflection of their superior hydrate forming ability.

5.5 References

1. Khankari, R. & Grant, D. J. W. Pharmaceutical hydrates. *Thermochim. Acta* **248,** 61–79 (1995).

2. Tian, F. *et al.* Factors affecting crystallization of hydrates. *Journal of Pharmacy and Pharmacology* **62,** 1534–1546 (2010).

3. Braun, D. E., Karamertzanis, P. G. & Price, S. L. Which, if any, hydrates will crystallise? Predicting hydrate formation of two dihydroxybenzoic acids. *Chem. Commun. (Camb).* **47,** 5443–5445 (2011).

4. Parveen, S., Davey, R. J., Dent, G. & Pritchard, R. G. Linking solution chemistry to crystal nucleation: The case of tetrolic acid. *Chem. Commun.* **0,** 1531–1533 (2005).

5. Edkins, R. M., Hayden, E., Steed, J. W. & Fucke, K. Conserved hydrogen bonding in tetrahydrocarbazolone derivatives: influence of solution-state assembly on crystal form nucleation. *Chem. Commun.* **51,** 5314–5317 (2015).

6. Griesser, U. J. & Burger, A. The effect of water vapor pressure on desolvation kinetics of caffeine 4/5-hydrate. *Int. J. Pharm.* **120,** 83–93 (1995).

7. Khankari, R., Chen, L. & Grant, D. J. W. Physical characterization of nedocromil sodium hydrates. *J. Pharm. Sci.* **87,** 1052–1061 (1998).

8. Bartolomei, M., Bertocchi, P., Antoniella, E. & Rodomonte, A. Physico-chemical characterisation and intrinsic dissolution studies of a new hydrate form of diclofenac sodium: Comparison with anhydrous form. *J. Pharm. Biomed. Anal.* **40,** 1105–1113 (2006).

9. Otsuka, M., Kato, F. & Matsuda, Y. Physicochemical stability of cimetidine amorphous forms estimated by isothermal microcalorimetry. *AAPS PharmSciTech* **3,** E30 (2002).

10. Kawabata, Y., Wada, K., Nakatani, M., Yamada, S. & Onoue, S. Formulation design for poorly water-soluble drugs based on biopharmaceutics classification system: Basic approaches and practical applications. *Int. J. Pharm.* **420,** 1–10 (2011).

11. Vrecˇer, F., Srcˇicˇ, S. & Sˇmid-Korbar, J. Investigation of piroxicam polymorphism. *Int. J. Pharm.* **68,** 35–41 (1991).

12. Feth, M. P. *et al.* Challenges in the development of hydrate phases as active pharmaceutical ingredients - An example. *Eur. J. Pharm. Sci.* **42,** 116–129 (2011).

13. Cabri, W., Ghetti, P., Pozzi, G. & Alpegiani, M. Polymorphisms and patent, market, and legal battles: Cefdinir case study. *Org. Process Res. Dev.* **11,** 64–72 (2007).

14. Miller, J. M., Collman, B. M., Greene, L. R., Grant, D. J. W. & Blackburn, A. C. Identifying the Stable Polymorph Early in the Drug Discovery–Development Process. *Pharm. Dev. Technol.* **10,** 291–297 (2005).

15. Braun, D. E., Gelbrich, T., Kahlenberg, V. & Griesser, U. J. Insights into hydrate formation and stability of morphinanes from a combination of experimental and computational approaches. *Mol. Pharm.* **11,** 3145–3163 (2014).

16. Braun, D. E., Kahlenberg, V. & Griesser, U. J. Experimental and Computational Hydrate Screening: Cytosine, 5-Flucytosine, and Their Solid Solution. *Cryst. Growth Des.* **17,** 4347–4364 (2017).

17. Braun, D. E., Karamertzanis, P. G. & Price, S. L. Which, if any, hydrates will crystallise? Predicting hydrate formation of two dihydroxybenzoic acids. *Chem. Commun. (Camb).* **47,** 5443–5 (2011).

18. Price, S. L., Braun, D. E. & Reutzel-Edens, S. M. Can computed crystal energy landscapes help understand pharmaceutical solids? *Chem. Commun.* **52,** 7065–7077 (2016).

19. Takieddin, K., Khimyak, Y. Z. & Fábián, L. Prediction of Hydrate and Solvate Formation Using Statistical Models. *Cryst. Growth Des.* **16,** 70–81 (2016).

20. Hulme, A. T. & Price, S. L. Toward the Prediction of Organic Hydrate Crystal Structures. *J. Chem. Theory Comput.* **3,** 1597–1608 (2007).

21. Clarke, H. D. *et al.* Structure-stability relationships in cocrystal hydrates: Does the promiscuity of water make crystalline hydrates the nemesis of crystal engineering? *Cryst. Growth Des.* **10,** 2152–2167 (2010).

22. Fucke, K. *et al.* Insights into the Crystallisation Process from Anhydrous, Hydrated and Solvated Crystal Forms of Diatrizoic Acid. *Chem. - A Eur. J.* **21,** 1036–1047 (2015).

23. Kawashima, Y. *et al.* Characterization of polymorphs of tranilast anhydrate and tranilast monohydrate when crystallized by two solvent change spherical crystallization techniques. *J. Pharm. Sci.* **80,** 472–478 (1991).

24. Hegedüs, B. & Görög, S. The polymorphism of cimetidine. *J. Pharm. Biomed. Anal.* **3,** 303–313 (1985).

25. Vrečer, F., Vrbinc, M. & Meden, A. Characterization of piroxicam crystal modifications. *Int. J. Pharm.* **256,** 3–15 (2003).

26. Tønnesen, L. E., Pedersen, B. F. & Klaveness, J. Acta Chem. Scand. 603–608 (1996). doi:10.3891/acta.chem.scand.50-0603

27. Folen, V. A., G. Schwartzman, Maienthal, M. & W. L. Brannon. Identification of different crystalline forms of diatrizoic acid. *J Assoc Off Anal Chem* **61,** 72–75 (1968).

28. Vogt, F. G. *et al.* Structural analysis of polymorphism and solvation in tranilast. *J. Pharm. Sci.* **94,** 651–665 (2005).

29. Jayaselli, J., Cheemala, J. M. S., Geetha Rani, D. P. & Sarbani Pal. Derivatization of enolic OH of piroxicam: a comparative study on esters and sulfonates. *J. Braz. Chem. Soc.* **19,** 509–515 (2008).

30. Burch, R. M., Wise, W. C. & Halushka, P. V. Prostaglandin-independent inhibition of calcium transport by nonsteroidal anti-inflammatory drugs: differential effects of carboxylic acids and piroxicam. *J. Pharmacol. Exp. Ther.* **227,** 84–91 (1983).

31. Kim, Y. H., Cho, D. W., Kang, S. G., Yoon, M. & Kim, D. Excited-state intramolecular proton transfer emission of piroxicam in aqueous β-cyclodextrin solutions. *J. Lumin.* **59,** 209–217 (1994).

32. Andrade, S. M. & Costa, S. M. B. Fluorescence studies of the drug Piroxicam in reverse micelles of AOT and microemulsions of Triton X-IO0. *Prog. Colloid Polym. Sci.* **100,** 195–200 (1996).

33. Andrade, S. M. & Costa, S. M. B. Hydrogen bonding effects in the photophysics of a drug, Piroxicam, in homogeneous media and dioxane–water mixtures. *Phys. Chem. Chem. Phys.* **1,** 4213–4218 (1999).

34. Fucke, K. *et al.* Unexpected low-temperature behaviour of piroxicam monohydrate. *Chemphyschem* **14,** 675–9 (2013).

35. Bordner, J. Piroxicam Monohydrate: a Zwitterionic Form, C15H13N3O4S.H20. *Acta Cryst* **C40,** 989–990 (1984).

36. Lerner, H. H. Diatrizoic Acid. *Anal. Profiles Drug Subst.* **4,** 137–167 (1975).

37. Fucke, K. *et al.* Supporting Information Insights into the Crystallisation Process from Anhydrous, Hydrated and Solvated Crystal Forms of Diatrizoic Acid. doi:10.5291/ILL-DATA.5-12-274

38. Steiner, T. The hydrogen bond in the solid state. *Angew. Chem. Int. Ed.* **41,** 49–76 (2002).

39. Mattia, J. & Painter, P. A comparison of hydrogen bonding and order in a polyurethane and poly(urethane-urea) and their blends with poly(ethylene

glycol). *Macromolecules* **40,** 1546–1554 (2007).

40. Nie, B., Stutzman, J. & Xie, A. A Vibrational Spectral Maker for Probing the Hydrogen-Bonding Status of Protonated Asp and Glu Residues. *Biophys. J.* **88,** 2833–2847 (2005).

41. Ryu, I. S., Liu, X., Jin, Y., Sun, J. & Lee, Y. J. Stoichiometric analysis of competing intermolecular hydrogen bonds using infrared spectroscopy. *RSC Adv.* **8,** 23481–23488 (2018).

42. Colthup, N. B., Daly, L. H. & Wiberley, S. E. *Introduction to infrared and Raman spectroscopy*. (Academic Press, 1975).

43. Socrates, G. *Infrared and raman characteristic group frequencies : tables and charts.* (John Wiley & Sons, 2007).

44. Brayton, C. F. Dimethyl sulfoxide (DMSO): a review. *Cornell Vet.* **76,** 61–90 (1986).

45. Max, J.-J. & Chapados, C. Isotope effects in liquid water by infrared spectroscopy. III. H2O and D2O spectra from 6000to0cm−1. *J. Chem. Phys.* **131,** 184505 (2009).

46. Swinehart, D. F. The Beer-Lambert Law. *J. Chem. Educ.* **39,** 333 (1962).

47. NIST Chemistry WebBook. Available at: https://webbook.nist.gov/chemistry/. (Accessed: 28th November 2018)

48. Cotton, F. A., Francis, R. & Horrocks, W. D. Sulfoxides as ligands. II. The infrared spectra of some dimethyl sulfoxide complexes. *J. Phys. Chem.* **64,** 1534–1536 (1960).

49. Jiao, C.-X., Shen, Q., Huan, S.-Y., Shen, G.-L. & Yu, R.-Q. Conjugated carbazole dimer as fluorescence carrier for preparation of iodine-sensitive chemical sensor. *Anal. Chim. Acta* **528,** 229–234 (2005).

50. DeRose, R., Miyamoto, T. & Inoue, T. Manipulating signaling at will: chemically-inducible dimerization (CID) techniques resolve problems in cell

biology. *Pflugers Arch.* **465,** 409–17 (2013).

51. Kopytek, S. J., Standaert, R. F., Dyer, J. C. & Hu, J. C. Chemically induced dimerization of dihydrofolate reductase by a homobifunctional dimer of methotrexate. *Chem. Biol.* **7,** 313–321 (2000).

52. Mohrig, J. R., Hammond, C. N. & Schatz, P. F. *Laboratory Techniques in Organic Chemistry*. (W. H. Freeman, 2006).

53. Krijn, M. P. C. M. & Feil, D. Electron density distributions in hydrogen bonds: A local density-functional study of α-oxalic acid dihydrate and comparison with experiment. *The Journal of Chemical Physics* **89,** 4199–4208 (1988).

54. Feil, D. The electron density distribution in the hydrogen bond. A quantum chemical and crystallographic study. *J. Mol. Struct.* **237,** 33–46 (1990).

55. Joseph, J. & Jemmis, E. D. Red-, blue-, or no-shift in hydrogen bonds: A unified explanation. *J. Am. Chem. Soc.* **129,** 4620–4632 (2007).

56. Scheiner, S. & Kar, T. Red- versus blue-shifting hydrogen bonds: Are there fundamental distinctions? *J. Phys. Chem. A* **106,** 1784–1789 (2002).

57. Zhang, Z., Li, D., Jiang, W. & Wang, Z. The electron density delocalization of hydrogen bond systems. *Adv. Phys. X* **3,** 1428915 (2018).

58. Weinhold, F. & Klein, R. A. Anti-Electrostatic Hydrogen Bonds. *Angew. Chemie* **126,** 11396–11399 (2014).

59. Wheeler, S. E. & Houk, K. N. Through-Space Effects of Substituents Dominate Molecular Electrostatic Potentials of Substituted Arenes. *J. Chem. Theory Comput.* **5,** 2301–2312 (2009).

60. Williamson, M. P. Using chemical shift perturbation to characterise ligand binding. *Prog. Nucl. Magn. Reson. Spectrosc.* **73,** 1–16 (2013).

61. Steed, J. W. & Atwood, J. L. *Supramolecular Chemistry*. (Wiley, 2009).

62. Olson, E. J. & Bühlmann, P. Getting More out of a Job Plot: Determination of Reactant to Product Stoichiometry in Cases of Displacement Reactions and *n* :

n Complex Formation. *J. Org. Chem.* **76,** 8406–8412 (2011).

63. Ulatowski, F., Dąbrowa, K., Bałakier, T. & Jurczak, J. Recognizing the Limited Applicability of Job Plots in Studying Host–Guest Interactions in Supramolecular Chemistry. *J. Org. Chem.* **81,** 1746–1756 (2016).

64. Thordarson, P. Determining association constants from titration experiments in supramolecular chemistry. *Chem. Soc. Rev.* **40,** 1305–1323 (2011).

65. Motulsky, H. & Christopoulos, A. Fitting curves with GraphPad Prism. in *Fitting Models to Biological Data Using Linear and Nonlinear Regression* 296–297 (2003). doi:10.1002/pst.167

66. de Levie, R. Estimating Parameter Precision in Nonlinear Least Squares with Excel's Solver. *J. Chem. Educ.* **76,** 1594 (1999).

67. Feng, Y. *et al.* Qualitative and simultaneous quantitative analysis of cimetidine polymorphs by ultraviolet-visible and shortwave near-infrared diffuse reflectance spectroscopy and multivariate calibration models. *J. Pharm. Biomed. Anal.* **104,** 112–121 (2015).

68. Calvo, N. L., Maggio, R. M. & Kaufman, T. S. A dynamic thermal ATR-FTIR / chemometric approach to the analysis of polymorphic interconversions . Cimetidine as a model drug. *J. Pharm. Biomed. Anal.* **92,** 90–97 (2014).

69. Kanumfre, F., Lima, E. M. De, Scheidt, G., Carneiro, P. I. B. & Rosso, N. D. Potentiometric and Spectrophotometric Studies of Mn and Ni Cimetidine Complexes. *J. Braz. Chem. Soc* **21,** 800–805 (2010).

70. Zheng, S. *et al.* Proposed Hydrogen-Bonding Index of Donor or Acceptor Reflecting Its Intrinsic Contribution to Hydrogen-Bonding Strength. *J. Chem. Inf. Model.* **57,** 1535–1547 (2017).

71. Bueno, W. A. & Sobrinho, E. G. Hydrogen bonds in the cimetidine molecule. *Spectrochim. Acta Part A Mol. Biomol. Spectrosc.* **51,** 287–292 (1995).

72. SDBSWeb. *National Institute of Advanced Industrial Science and Technology (AIST)* (1999). Available at: https://sdbs.db.aist.go.jp/sdbs/cgi-

bin/direct_frame_disp.cgi?sdbsno=18959.

73. Lai, F. *et al.* A comparison of the experimental and theoretical charge density distributions in two polymorphic modifications of piroxicam. *Phys. Chem. Chem. Phys.* **18,** 28802–28818 (2016).

74. Walrafen, G. E. Raman and Infrared Spectral Investigations of Water Structure. in *The Physics and Physical Chemistry of Water* 151–214 (Springer New York, 1972). doi:10.1007/978-1-4684-8334-5_5

75. Binev, Y. & Aires-de-Sousa, J. Structure-based predictions of1H NMR chemical shifts using feed-forward neural networks. *J. Chem. Inf. Comput. Sci.* **44,** 940–945 (2004).

76. Aires-de-Sousa, J., Hemmer, M. C. & Gasteiger, J. Prediction of ^{1} H NMR Chemical Shifts Using Neural Networks. *Anal. Chem.* **74,** 80–90 (2002).

77. Castillo, A. M., Patiny, L. & Wist, J. Fast and accurate algorithm for the simulation of NMR spectra of large spin systems. *J. Magn. Reson.* **209,** 123–130 (2011).

78. Banfi, D. & Patiny, L. www.nmrdb.org: Resurrecting and Processing NMR Spectra On-line. *Chim. Int. J. Chem.* **62,** 280–281 (2008).

79. Bargar, J. R., Kubicki, J. D., Reitmeyer, R. & Davis, J. A. ATR-FTIR spectroscopic characterization of coexisting carbonate surface complexes on hematite. *Geochim. Cosmochim. Acta* **69,** 1527–1542 (2005).

80. Sun, S. *et al.* Pillar[5]arene-based side-chain polypseudorotaxanes as an anion-responsive fluorescent sensor. *Polym. Chem.* **4,** 2224 (2013).

81. Kadam, S. A., Haav, K., Toom, L., Haljasorg, T. & Leito, I. NMR method for simultaneous host-guest binding constant measurement. *J. Org. Chem.* **79,** 2501–2513 (2014).

82. Dang, L. X. & Kollman, P. A. *Free Energy of Association of the 18-Crown-6:K+ Complex in Water: A Molecular Dynamics Simulation*. *J. Am. Chem. Soc* **112,** (1990).

CHAPTER 6

THE AFFINITY AND SELECTIVITY OF METASTABLE, ELUSIVE, AND NON-HYDRATE FORMING COMPOUNDS TOWARDS WATER AND PRE-NUCLEATION AGGREGATE FORMATION

6.1 Introduction

In chapter 5, a potential commonality is discovered in the form of the apparent significant values of K_{21} and ΔG obtained from the ^{1}H-NMR water titration, which could aid in crystalline hydrate prediction as the values reflect on the tested compound's superior hydrate forming ability. In short, the *K* values obtained from the titration experiment of the compounds which are able to form stable hydrate are between 60-3000 M^{-1} which corresponds to ΔG values of -20 to -10 kJ mol^{-1}. In this chapter we are applying the new methodology in systems where no strong hydrated crystal forms known. This chapter highlights the ^{1}H-NMR water titration analysis on naproxen, a compound which has yet to be reported to exists as crystalline hydrate or exist as an elusive hydrate form. In addition, analysis is also done on paracetamol, a compound which is known to exist as metastable or weak crystalline hydrate. The results from these two compounds would guide interpretation of the two mentioned categories of hydrate. ΔG values obtained from the two model compound will serve as a gauge and determine the grey areas for weak hydrates prediction as well as provide cut offs for non-hydrate-forming compounds. To further scrutinise the method, a 'blind test' on five other compounds is performed, during which information on the existence of crystalline hydrates is blocked. This validation will determine whether the

procedure is robust enough to predict the hydrate, as well as sensitive enough to distinguish between the different hydrate forming abilities of selected the compounds. This is the final proof whether the observed changes are true or only serendipity at play.

6.2 The tested compounds and results

6.2.1 The elusive or non-hydrate forming drug: Naproxen

Naproxen (NAP, Figure 6.1) or (2S)-2-(6-Methoxy-2-naphthyl) propanoic acid is a non-steroidal anti-inflammatory drug (NSAID), commonly used to treat mild to moderate pain, which includes relieve for arthritic pain,[1] dysmenorrhoea,[2] as well as prophylactic treatment and acute attack of migraine.[3]

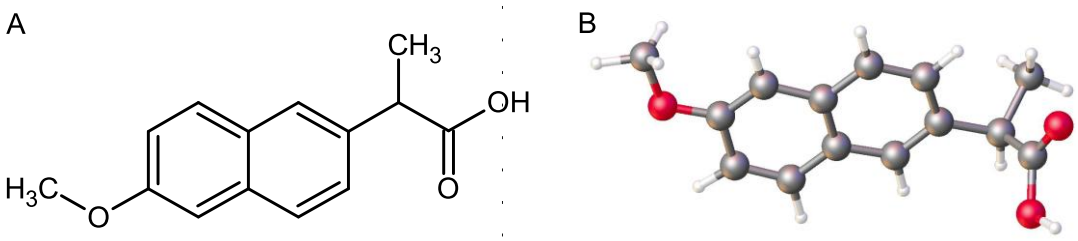


Figure 6.1. Two-dimensional chemical structure (**A**) and three-dimensional arrangement (**B**) of Naproxen. The colour code is carbon grey, oxygen red, and hydrogen light grey.

NAP has been reported to exists four polymorphs,[4] with a patent suggesting the existence of a hydrate form. However, no hydrate form has yet been reported for NAP in a scientific literature. The patent which is aimed for the Chinese market, claims the existence of a NAP 1.5 hydrate form by providing PXRD pattern along with TGA of the crystalline hydrate as means of identification.[5] Based on the TGA curve provided by the patent, water appeared to be weakly bound as heating from 50 to just

below 100 ℃ effectively dehydrates the sample completely. The hydrate form appears to be elusive as all our effort to obtain the hydrate form, or any hydrate form for that matter have yet to be successful. Among the methods used were, thorough polymorph screening with 20 different solvents, recrystallisation using mixed water-solvent system, as well as using aqueous slurry with temperature cycling. Our efforts replicating the reported method in the patent was also unsuccessful in reproducing the hydrate form, suggesting that the hydrate either doesn't exist or is very elusive.

6.2.1.1 Preliminary ^{1}H-NMR spectrum of NAP

Ten chemical shift peaks regions representing the 14 protons of NAP were monitored in the ^{1}H-NMR spectrum in acetonitrile-d_3 environment, highlighted in Figure 6.2A and B. Integration of the peaks which were calibrated to the three protons of the methyl group, accounts correctly to the sum of the protons associated with NAP. The peaks are identified as proton 1-10 based on the position, in descending order, on the spectra. The first easily recognisable chemical shift region is the signal at 9 ppm, which corresponds to the carboxylic acid (OH) proton, named proton 1 (Figure 6.2A). Proton 2-7 are located on the two aromatic benzene rings, which is highlighted in Figure 6.2B. Next is the signal at 3.9 ppm which correspond to the one of the two methyl groups (CH_3), and named proton 8. The signal at 3.84 ppm in the spectra corresponds to the protons of CH_2, connecting the methyl and the carbonyl and named proton 9. Finally, the signal at 1.5 ppm corresponds to the final methyl group named proton 10. Other visible peaks are of the reference, TMS (0 ppm), acetonitrile-d_3 (1.9 ppm) and water (2.15ppm).

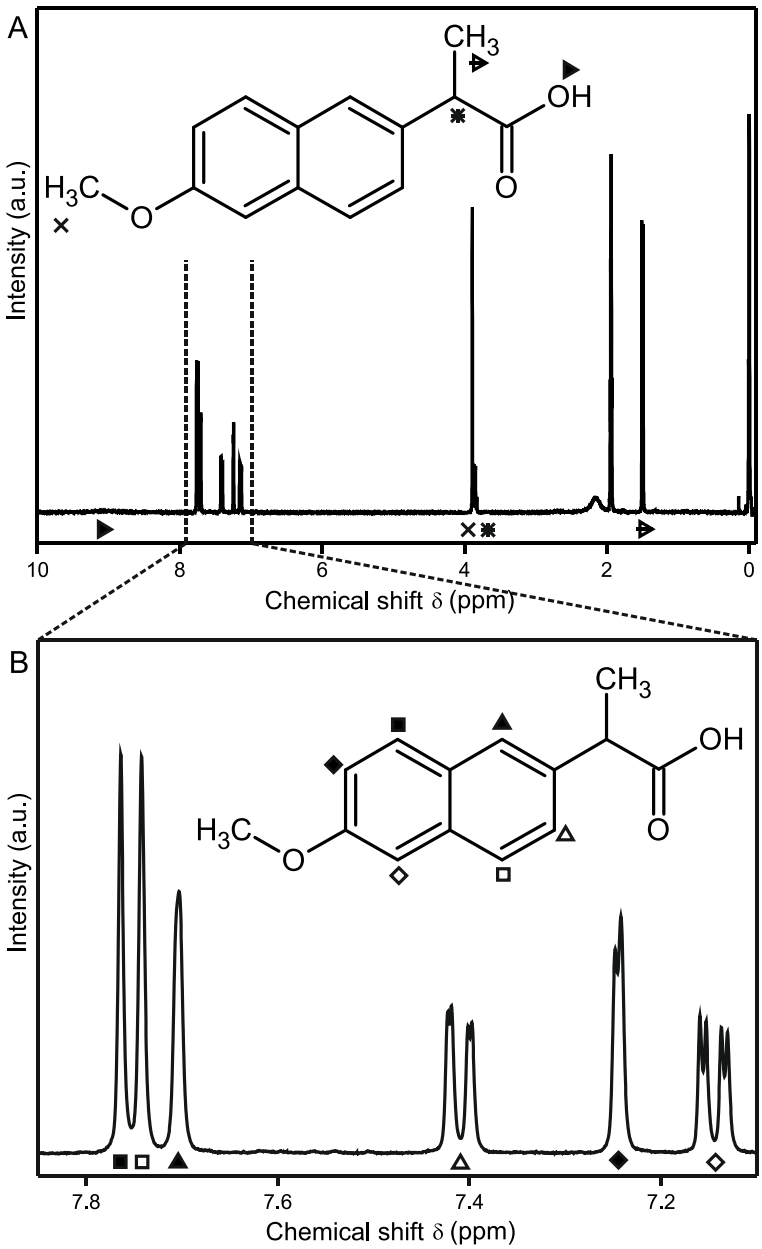


Figure 6.2. ^{1}H-NMR spectrum of NAP in acetonitrile-d_3 environment. Specific chemical shift regions on the spectra which are identified as proton 1-10 are highlighted with the respective symbols and correspond to inset chemical structure. Figure 3 **A** highlights proton 1, 8-10 and **B** highlights proton 2-7.

6.2.1.2 ^{1}H-NMR dilution experiment of NAP

^{1}H-NMR dilution of 0.02 M NAP in acetonitrile-d_3 environment with non-deuterated acetonitrile saw all the peaks shifted downfield, with the biggest shift recorded was +0.0009 ppm, experienced by the proton at the chemical shift position of 7.4 ppm (Figure 6.3). Since all shift occurred at fourth decimal place, it is confirmed

that no significant effect from dilution is observable for NAP upon dilution to up to 450:1 G:H ratio, ensuring that any shift observed during the titrations is due to the addition of water as guest.

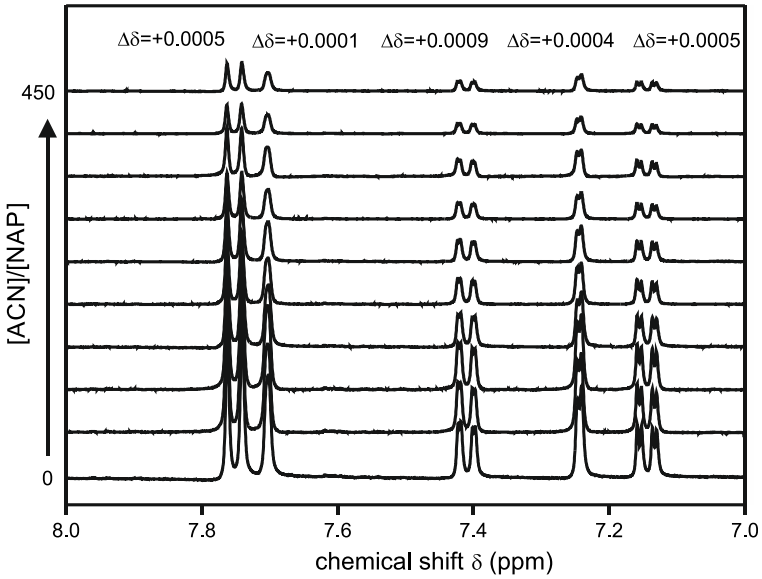


Figure 6.3. Dilution of 0.02 M NAP with non-deuterated acetonitrile. Dilution is done in a single tube, with the highest dilution factor used is 450 molar ratios.

6.2.1.3 ^{1}H-NMR titration experiment of NAP

^{1}H-NMR titration experiment of 0.02 M NAP in acetonitrile-d_3 solvent environment saw most of the observed protons to have small shifts. The overall peak shift peak shifts for all the protons, bar proton 1, at the end of the titration at 450:1 G:H is summarised in Table 6.1. Similar to previous measurements in chapter 5, we only consider any peak shift as significant when the value exceeds ±0.002 ppm of the measurement error mark, for reasons mentioned in chapter 2. With respect to ^{1}H-NMR titration of NAP with water, a consistent shift trend is observed for all protons of NAP, however, the magnitude is small and significant shift is only observed above 30-40:1 G:H ratio mark.

Table 6.1. Peak shift difference between the start, and the last titration point of 450:1 G:H molar ratio.

	Proton 2	Proton 3	Proton 4	Proton 5	Proton 6	Proton 7	Proton 8	Proton 9	Proton 10
$\Delta\delta$	0.02	0.02	0.017	0.022	0.021	0.015	0.008	0.009	0.006

Proton 1 (Figure 6.4) appearing as a single, broad peak, due to the peak being generated based on the average site of a fast exchanging OH proton on NMR timescale. Monitoring of this peak is difficult as the peak becomes too broad to observe as soon as water is introduced into the system.

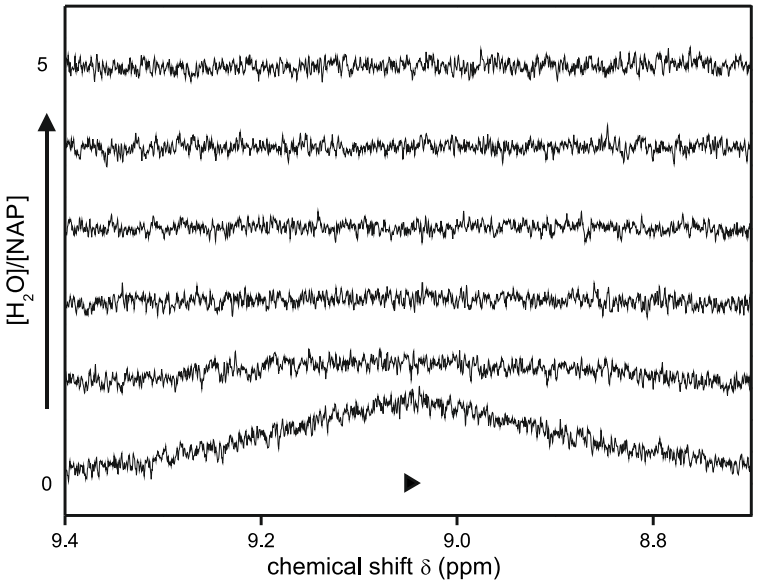


Figure 6.4. ^{1}H-NMR chemical shift region for proton 1, showing the broad nature of the peak, and its disappearance once water is introduced into the system

Meanwhile, observation of all the other protons (Figure 6.5, 6.6, and 6.7), saw downfield shifts, apart from proton 9 (Figure 6.6, * symbol, CH connecting the methyl and the carbonyl), which saw an initial upfield shift from 0-50:1 G:H ratio. The scatter plot also show that the curve is almost at plateau between 50-70:1 G:H ratio (Figure 6.6). From 80:1 G:H ratio onwards, proton 9 shifted downfield. Since proton 9 is the closest visible proton on ^{1}H-NMR to the acid, the effect observed would reflect the

interaction involving the acid group. However, all the mentioned shift to proton 9 is small, with a total shift magnitude of just 0.009 ppm at 450:1 G:H ratio. The peak shift only become apparent when proton 9 is plotted independently, hence the mentioned interaction is very weak, even for a secondary effect. Overall, the biggest peak shift observed for NAP-water titration is recorded for proton 5, with just 0.022 ppm difference from 0-450:1 G:H ratio.

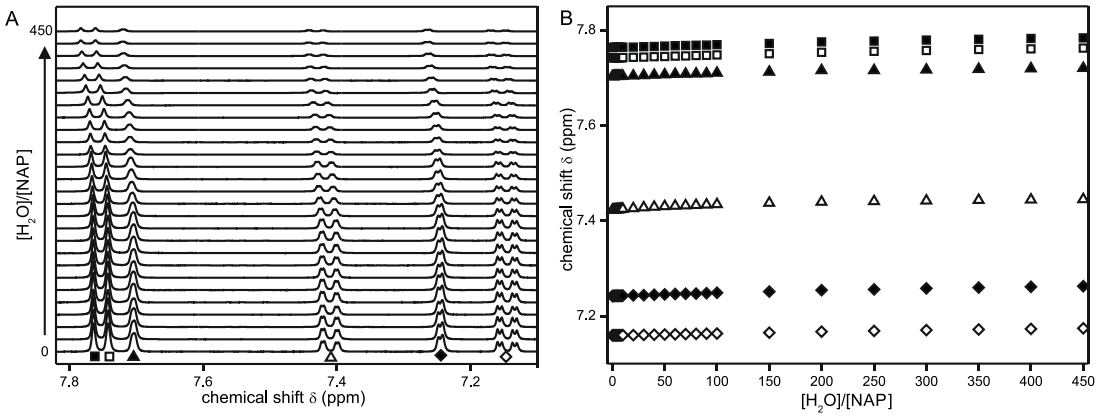


Figure 6.5. **A** showing ^{1}H-NMR chemical shift region for Proton 2-7 and their respective peak shifts. **B** shows the scatter plot to the respective peaks.

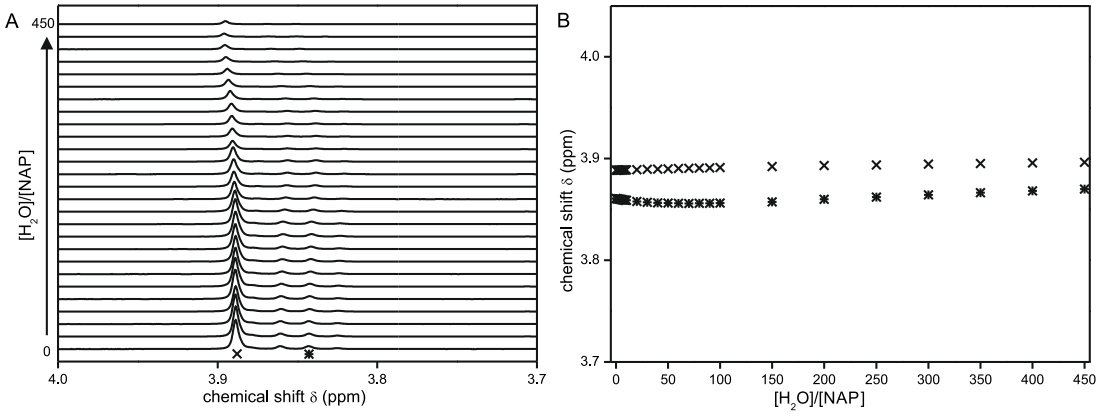


Figure 6.6. **A** shows ^{1}H-NMR chemical shift region for proton 8 and 9, with their respective peak shifts. **B** shows the scatter plot to the respective peaks.

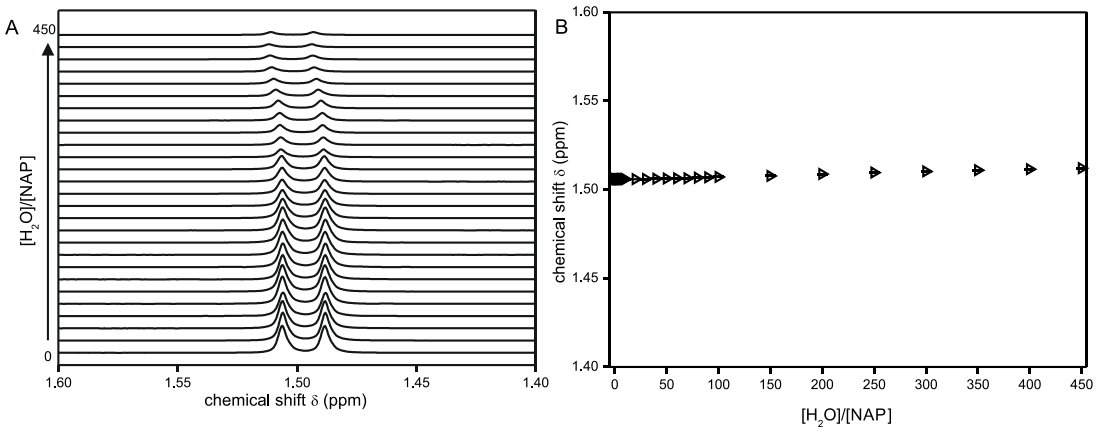


Figure 6.7. **A** showing ^{1}H-NMR chemical shift region for Proton 10 and their respective peak shifts. **B** shows the scatter plot to the respective peaks

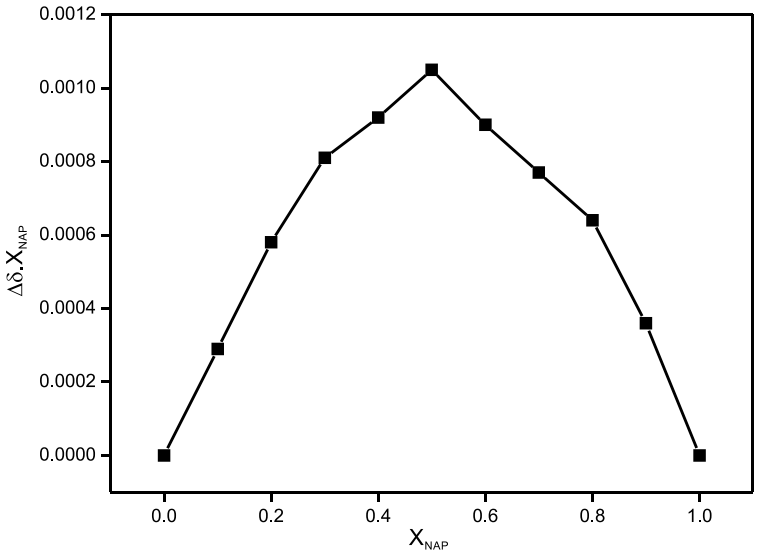


Figure 6.8. Job plot of NAP showing the stoichiometry of interaction as 1:1, with X_{max}= 0.5.

The Job plot of NAP reveals that the stoichiometry of interaction is 1:1, with X_{max}= 0.5 (Figure 6.8). Fitting of all the proton to 1:1 binding model yielded a *K* value of 0.1 M^{-1}. *K* values for fitting to other available binding models, 2:1 and 1:2 stoichiometries are listed in Table 6.2.

Table 6.2. *K* values based on the fitting to all available binding model, the 1:1, 2:1 and 1:2, H:G ratios

H:G binding model	K_1 (±% error)	K_{21} (±% error)	K_{12} (±% error)

NAP:H_2O	0.10 M^{-1} (±0.5%)	N/A	N/A
2NAP:H_2O	0.20 M^{-1} (±0.5%)	9.88 M^{-1} (±0.5%)	N/A
NAP:$2H_2O$	0.53 M^{-1} (±1.2%)	N/A	0.10 M^{-1} (±0.6%)

However, all the obtained *K* values suggested a non-significant interaction between water and NAP molecules. The highest *K* value was form the K_{21} (2:1), with 9.88 M^{-1}, which is calculated to -5.7 kJ mol^{-1}, which accounts for about half of the sum obtained for the lowest ΔG for stable hydrate probe. We believe that any compound showing ΔG > -6 kJ mol^{-1} following our titration method will not exist as a crystalline hydrate form or that the hydrate form is very elusive. As it stands, the proposed ΔG values for the hydrate prediction gauge is as illustrated in Figure 6.9.

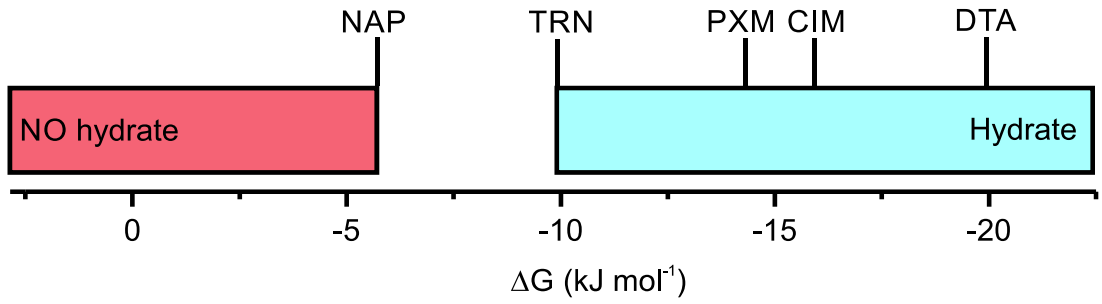


Figure 6.9. Proposed ΔG values for the hydrate prediction gauge

6.2.2 The metastable or weak hydrate forming drugs: Paracetamol

Paracetamol (PCM, Figure 6.10) is the most common over-the-counter (OTC) drug and used as a mild analgesic and antipyretic. The structure contains a balanced number of proton donor and acceptor, with two of each.[6] However, PCM structure can

change due to resonance of the free electron pair of the nitrogen atom. These resonance structures of PCM causes the nitrogen role to change from proton acceptor to donor. [7]

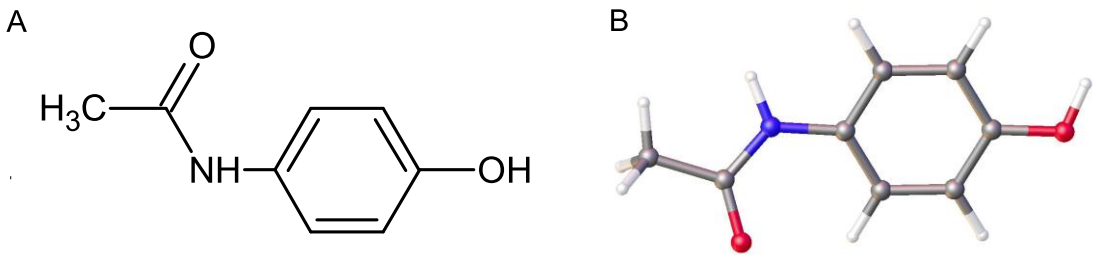


Figure 6.10. Two-dimensional chemical structure (**A**) and three-dimensional arrangement (**B**) of Paracetamol. The colour code is carbon grey, oxygen red, nitrogen blue, and hydrogen light grey.

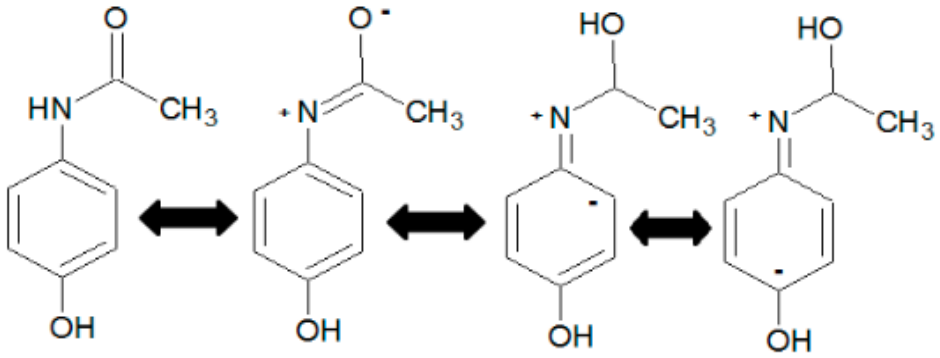


Table 6.3. Resonance structures of a paracetamol molecule. Figure was adapted from Bernal et al.[7]

PCM has been reported to exists as five polymorphs, three of which have been structurally characterised as the monoclinic Form I,[8] orthorhombic Form II,[9] and the unstable orthorhombic Form III.[9–11] New evidence of additional forms IV and V at high pressure has been reported.[12] In 2002, Pulham's group from Edinburgh reported two metastable PCM hydrate forms, identified as the monohydrate and trihydrate.[13,14] The monohydrate was obtained by quench cooling (60 to -0.15°C) a mixture of PCM and disodium terephthalate,[14] while trihydrate was obtained by slow cooling a hot PCM aqueous solution (4 g dm^{-3}) for 12 hours to 0 °C.[13] Peterson et al. later reported

that the trihydrate crystal is stable in temperature up to 5 °C at ambient pressure.[15] Both forms dehydrates at ambient temperature into Form I. Two years later, Pulham's group reported a third hydrate form, a dihydrate, which was recrystallise from water at a pressure of 1.1 GPa.[16] All reports suggest that the hydrate forms are indeed metastable under ambient condition.

6.2.2.1 Preliminary ^{1}H-NMR spectrum of PCM

^{1}H-NMR spectrum of PCM in the acetonitrile-d_3 saw five chemical shift regions on the spectra (Figure 6.11), first of which is observed at 8.08 ppm, which corresponds to the OH and named proton 1. Proton 2 the peak at 7.34 ppm corresponding to the two protons on the benzene ring, facing the NH group. Proton 3 at 6.758 ppm corresponds to the NH and next to the peak, at 6.746 ppm proton 4 is present as a split peak which corresponds to the two protons on the benzene ring, facing the OH group. Finally, proton 5 is the methyl group, which appear at 2.0 ppm on the spectrum.

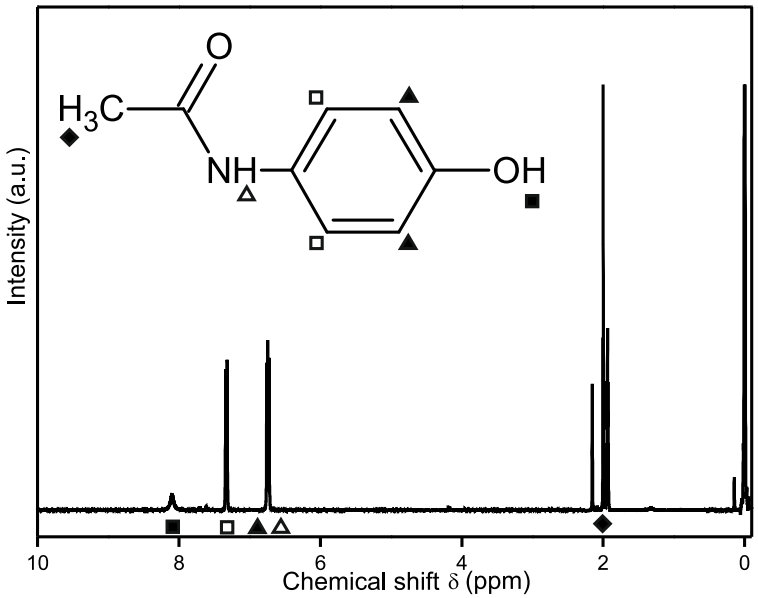


Figure 6.11. ^{1}H-NMR spectra of PCM in acetonitrile-d_3 environment. Specific chemical shift regions on the spectra which are identified as proton 1-5 are highlighted with the respective symbols and corresponds to inset chemical structure.

6.2.2.2 ^{1}H-NMR dilution experiment of PCM

Dilution of 0.02 M PCM was done to just 10:1 G:H ratio of acetonitrile (Figure 6.12). At the end of the dilution, proton 1 (■) saw +0.0017 ppm shift downfield, while the proton 2 (▫) has also shifted downfield by +0.0004 ppm. The biggest shift recorded in the dilution experiment is to the proton 3 (▲), which shows a downfield shift of +0.0095 ppm. Proton 4 (△) and 5 (◆, not shown in Figure 6.12) did not shift at all (0.0000 ppm) throughout the dilution experiment. As the peak shifts observed here are not significant, any peak shifts observed following PCM-water titration, if any does occur, will be due to interaction with water, and not the effect of dilution.

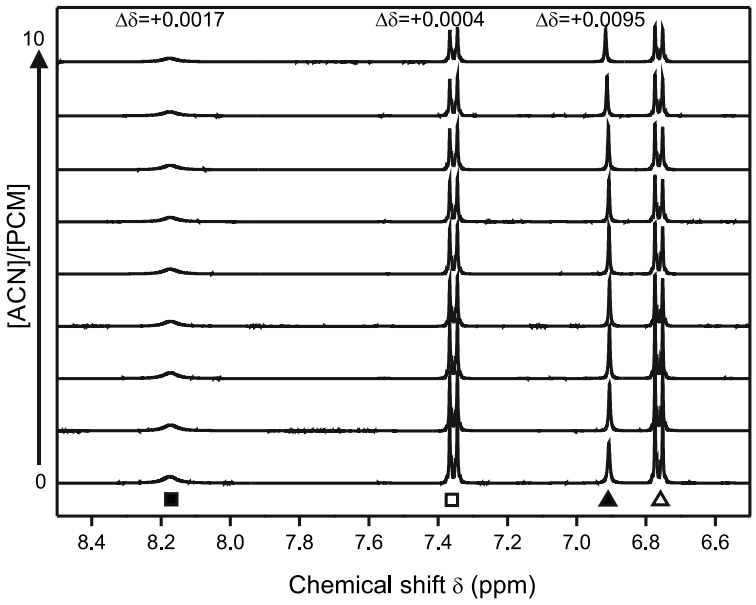


Figure 6.12. ^{1}H-NMR spectra of the dilution experiment of 0.02 M PCM with non-deuterated acetonitrile up to 10:1 G:H ratio.

6.2.2.3 ^{1}H-NMR titration experiment of PCM

Following titration of water into PCM-acetonitrile-d_3 solution, it is quite surprising to be able to observe the phenol -OH peak throughout the titration experiment. Normally, the OH undergo fast exchange with water, and would appear as a broad and eventually unobservable peak following water incorporation. Typically, ^{1}H-NMR resonance peak for phenol -OH group is broad at room temperature, and susceptible to fast exchange with protons of the protic solvents or with protons of the residual water in aprotic solvents.[17] Further broadening of the peak is also contributed exchange between various –OH and –COOH groups which may be present in a particular molecule, especially in low polarity and dielectric constant organic solvents environments.[17] Charisiadis *et al.* reported three factors which influence the exchange rates for phenol -OH peak and in turn the peak broadness, which are pH, temperature and solvent environment effect.[17] As the former two reasons are kept constant in our experiment, it is highly likely that the reason for the proton 1 (OH) peak preservation

is due the slowing down of the intermolecular proton exchanges contributed by non-protic nature of acetonitrile environment. In addition, Charisiadis *et al.* also reported that the use of dry non-protic solvents with strong hydrogen bonding ability *e.g.* DMSO, significantly reduces the –OH exchange rate in majority of their polyphenol model compounds.

The biggest peak shift is observed on the NH (proton 3, ▲) at 6.75 ppm, which shifted significantly as soon as water is introduced (Figure 6.13). The peak becomes broader as more water is added, and completely unobservable above 390 molar ratios of water. The scatter plot also highlights the peak shift for the NH proton (▲), showing unexpectedly strong shift compared to other protons, and reaching plateau at around 390:1 G:H ratio. The overall shift from zero to 390:1 G:H ratio is 1.78 ppm, which is very big in terms of water-compound interaction. Direction of the shift downfield signals direct hydrogen bond to water.[18] It is surprising to see such strong interaction, for compound only reported to exist as three metastable hydrate forms.[13,14,16]

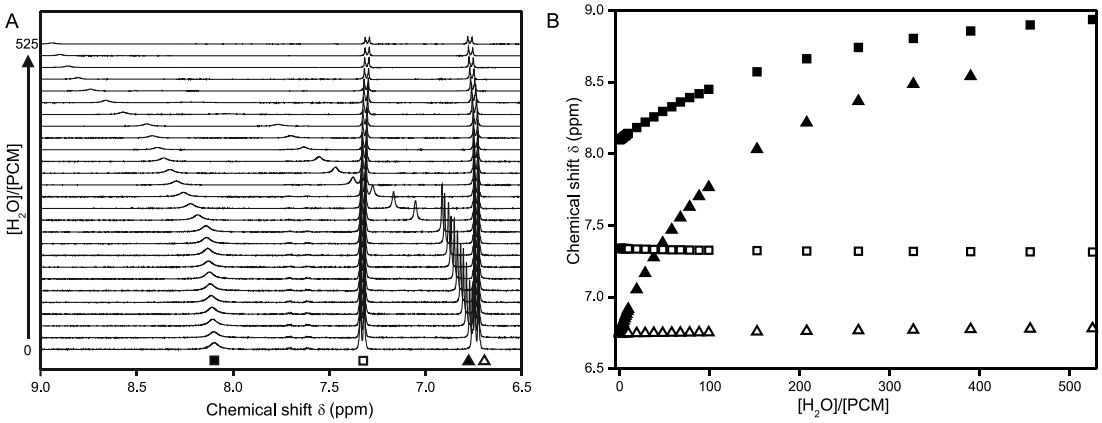


Figure 6.13. **A** ^{1}H-NMR chemical shift for PCM proton 1-4 showing peak shift, while **B** shows the scatter plot of the peak shift for respective protons.

Meanwhile peaks of proton 2 (▫) has shifted upfield by 0.024 ppm while proton 4 (▵) has downfield shifted by 0.029 ppm. Finally, proton 5 (◆) at 2.0 ppm has recorded a total shift of 0.038 ppm at the end of the titration (Figure 6.14)

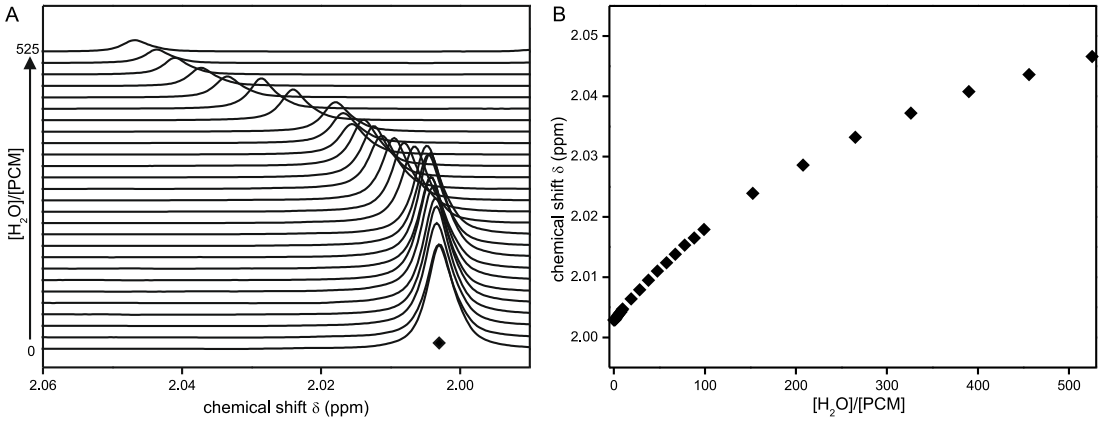


Figure 6.14. **A** showing the final ^{1}H-NMR peak shift for PCM, which is proton 5- corresponding to the CH_3, with **B** showing the scatter plot of the peak shift.

The Job's plot measurement showed that the interaction favours the 2:1 H:G binding based on the right-skewed plot with X_{max}=0.6 (Figure 6.15).

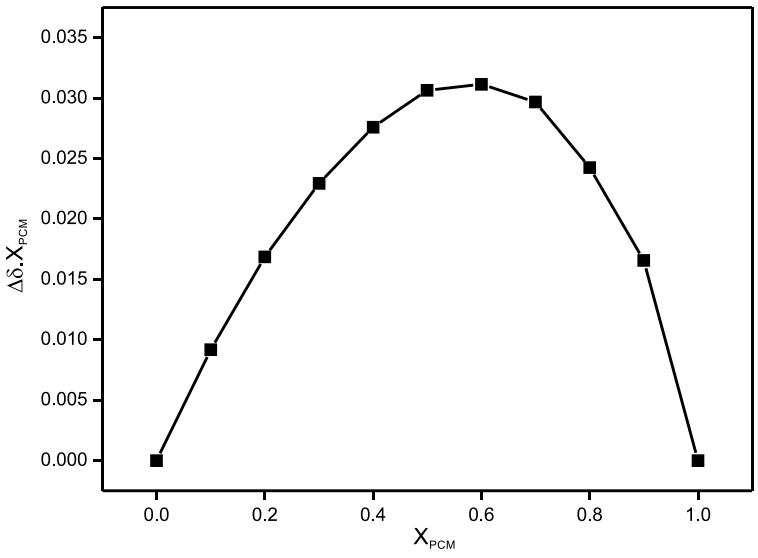


Figure 6.15. The job plot of PCM revealed that the stoichiometry of interaction is favouring the 2:1 binding with Xmax=0.6.

Since we are confident that the NH is the coordination site for PCM-water complexation, the binding constant fit is initially based on just the NH peak shifts values, which generated a K_{21} value of 157.4 M^{-1} (Table 6.4), calculated to ΔG of -12.5 kJ mol^{-1}. In order to make a more comparable comparison to the previous data where we do not normally see such a strong interaction, fitting to the binding model is done on all protons bar the labile OH and NH (* values in Table 6.4). Interestingly, the fitting of the said protons which only generally show secondary effect form the PCM-water complexation has resulted in a K_{21} value of 80 M^{-1}, calculated to ΔG of -10.9 kJ mol^{-1}. This placed PCM on the hydrate side of our hydrate gauge, again confirming the method's ability to predict hydrate formation (Figure 6.16). However, the result also suggest that the method used is not sensitive enough to differentiate metastable and strong hydrate-forming compound, or PCM do possess a strong undiscovered hydrate form, though the latter assumption is unlikely.

Table 6.4. *K* values based on the fitting of NH proton (Proton 3) to all available binding model, the 1:1, 2:1 and 1:2 H:G ratios. * Generated *K* values based on the fitting of non-labile protons (Proton 2, 4, and 5)

H:G binding model	K_1 (±% error)	K_{21} (±% error)	K_{12} (±% error)
PCM:H_2O	0.36 M^{-1} (±0.7%)	N/A	N/A
2PCM:H_2O	0.024M^{-1} (±2.2%)	157.4 M^{-1} (±1.3%)	N/A
PCM:2H_2O	0.23M^{-1} (±0.17%)	N/A	-0.17M^{-1} (±-0.17%)
PCM:H_2O*	0.13 M^{-1} (±5%)	N/A	N/A
2PCM:H_2O*	0.11M^{-1} (±0.7%)	80 M^{-1} (±0.9%)	N/A
PCM:2H_2O*	0.83M^{-1} (±1.8%)	N/A	0.07M^{-1} (±-0.8%)

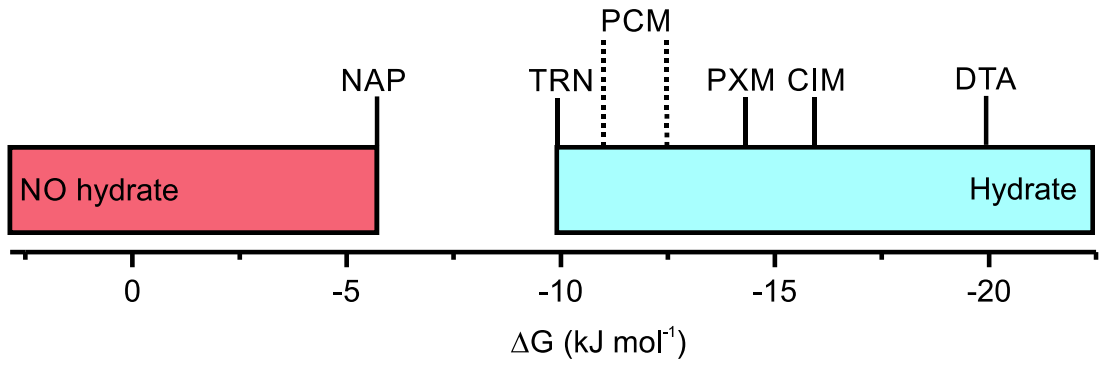


Figure 6.16. PCM ΔG position on the hydrate prediction gauge favouring hydrate formation

6.2.3 The blind test

A blind test was done to further scrutinise the procedure and ensure that the resultant *K* and ΔG distinguishing hydrate and non-hydrate obtained thus far is not just serendipity at play. By keeping the information on the hydrate state of the compounds away throughout the duration of the experiment and *K* determination, avoids any bias in the subsequent *K* determination. Five compounds were analysed in the blind test, namely pyrazine, acetozalamide, dapsone and flurbiprofen. Prediction is done after ΔG has been calculated. Correct match between the predictions and actual state of hydration will indicate the % reliability of the predictive tool. The only information given is the chemical structure of the respective compounds.

6.2.3.1 Pyrazine

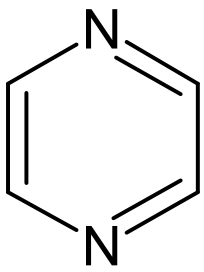


Figure 6.17. Chemical structure of Pyrazine

Pyrazine (PYZ, Figure 6.17) is a heterocyclic aromatic organic compound with the chemical formula $C_4H_4N_2$. The compound contains two hydrogen-bond acceptors but are devoid of any strong hydrogen-bond donors. PYZ is the simplest compound tested thus far. The preliminary ^{1}H-NMR spectrum shows a single peak at 8.579 ppm, which is integrated to its four protons (Figure 6.18). Other observed peaks are the marker (TMS), acetonitrile-d_3 and water, of which positions have been mentioned before.

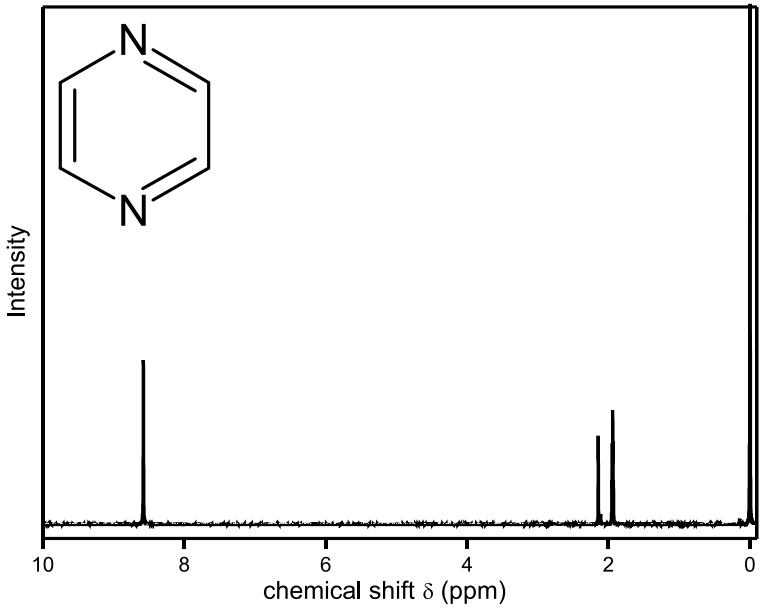


Figure 6.18. ^{1}H-NMR spectrum of PYZ in acetonitrile-d_3 environment. Specific chemical shift region on the spectra appears as a single peak corresponding to the four protons in the inset chemical structure.

6.2.3.2 ^{1}H-NMR dilution experiment of PYZ

PYZ 0.02 M dilution experiment saw the singular peak which corresponds to all four of PYZ protons, shifts downfield by 0.0002 ppm upon dilution to up to 500:1 G:H molar ratios of acetonitrile (Figure 6.19). The shift is very small and confirms that dilution of the compound bares little to non-significant shift and effect. In addition, any peak shift observed following titration will be due to interaction with water.

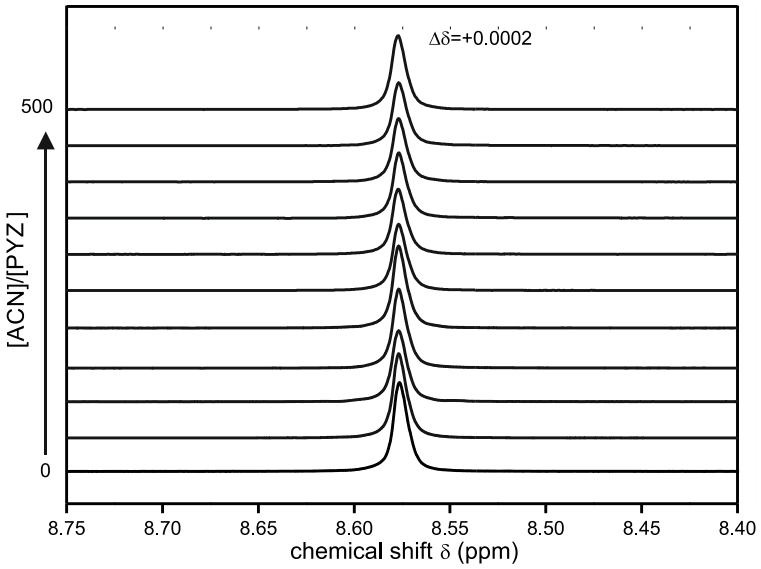


Figure 6.19. Dilution of 0.02 M PYZ with non-deuterated acetonitrile. Dilution is done in a single tube, with the highest dilution factor used is 500:1 G:H molar ratios.

6.2.3.3 ^{1}H-NMR titration experiment of PYZ

Titration from 0-10:1 G:H ratio saw no shift, however above the 10 molar ratio mark, a downfield shift trend emerges with significant shift (±0.002 ppm) detected after 20:1 G:H ratio. At the end of the titration of 593:1 G:H ratio, a total peak shift of 0.04 ppm was observed, which is much larger than the shift observed in the dilution experiment (+0.0002 ppm at 500:1 acetonitrile:H ratio). Looking at the compound structure without the influence from water, the N atoms would have an effect to the electron circulation of the ring as the N atom is more electronegative than carbon. We know that the compound contains two hydrogen-bond acceptors but are devoid of strong hydrogen-bond donors. Therefore, the only possible interaction with water, if any is indeed present, will be *via* the N atom, accepting the proton from water in order to form hydrogen bond. As water is introduced, the weak affinity to water is clear as delayed interaction is observed (Figure 6.20A). Significant interaction only occurs at

higher water content, >20:1 G:H ratios, where PYZ and water starts to form hydrogen bond *via* the N atoms (O-H···N). The N atoms gain electron density from the bridging protons of water,[18] the additional electron density obtained would cause the N atoms to become less δ-, having a lesser affinity and influence towards the electron circulation of the benzene ring at both ends.

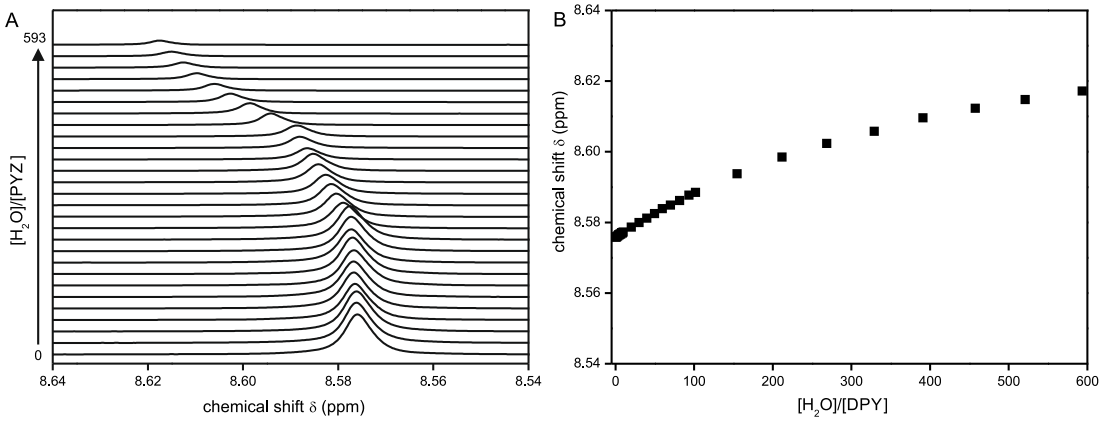


Figure 6.20. **A** shows the ^{1}H-NMR peak shift for PYZ, showing the initial delayed shift from 0-10, G:H ratio, while **B**. shows the scatter plot, with a larger shift is observed once more water is introduced into the system.

The job plot revealed that the stoichiometry of interaction is 1:1, with X_{max}=0.5 (Figure 6.21). We consider the result from the job plot of PYZ with caution as the peak shift occurred on the fourth decimal place. Factoring against the host fraction accentuates the peak shift at a particular host fraction, however, as the magnitude is non-significant, it is still difficult to ascertain whether the shift is truly due to water interaction. Plus, since PYZ only showed as a single peak, no other peak can be used as reference or comparison.

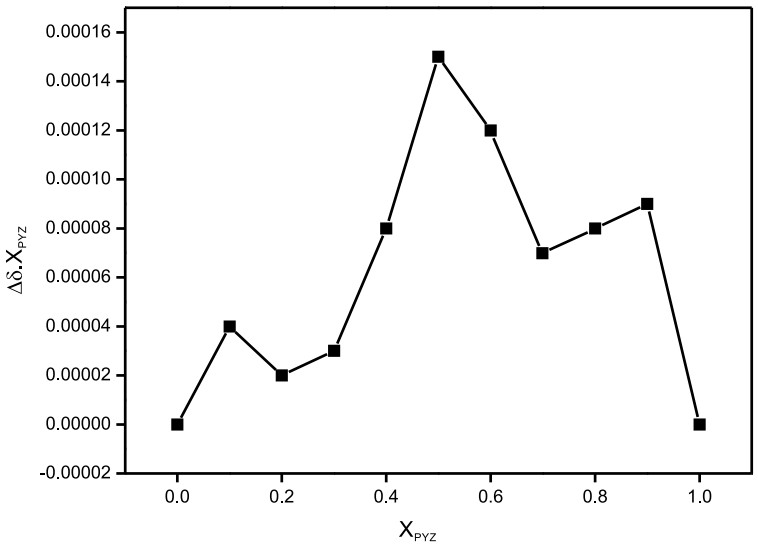


Figure 6.21. Job plot of PYZ showing the stoichiometry of interaction as 1:1, with X_{max}= 0.5.

Fitting of the peak shift data for PYZ protons to 1:1 binding model yielded a *K* value of 0.1 M^{-1}. The 1:1 fitting also yielded the least error (0.5%) to the fitted model compared to other available binding models, with the K values for fitting to other available binding models, 2:1 and 1:2 stoichiometries are listed in Table 6.5. For comparison purposes, the K_{21} obtained would translate into ΔG of -7.1 kJ mol^{-1}.

Table 6.5. *K* values based on the fitting to all available binding model, the 1:1, 2:1 and 1:2, H:G ratios

H:G binding model	K_1 (±% error)	K_{21} (±% error)	K_{12} (±% error)
PYZ:H_2O	0.1 M^{-1} (±0.5%)	N/A	N/A
2PYZ:H_2O	0.03 M^{-1} (±2.9%)	18 M^{-1} (±2.3%)	N/A
PYZ:2H_2O	0.05 M-1 (±0.7%)	N/A	-0.1 M^{-1} (±1.7%)

Based on the calculated ΔG from the K_{21} value, which places PYZ on the grey zone, closer to NAP by +1.4 kJ mol^{-1} and thus closer to the NO hydrate region on the hydrate gauge (Figure 6.22). In contrast, PYZ is -3.1 kJ mol^{-1} away from the hydrate-forming zone. Therefore, based on the placement on our gauge, and comparison to

other ΔG values obtained thus far, we predict that PYZ do not exist as a crystalline hydrate form or that if the hydrate form does exist, it is very elusive.

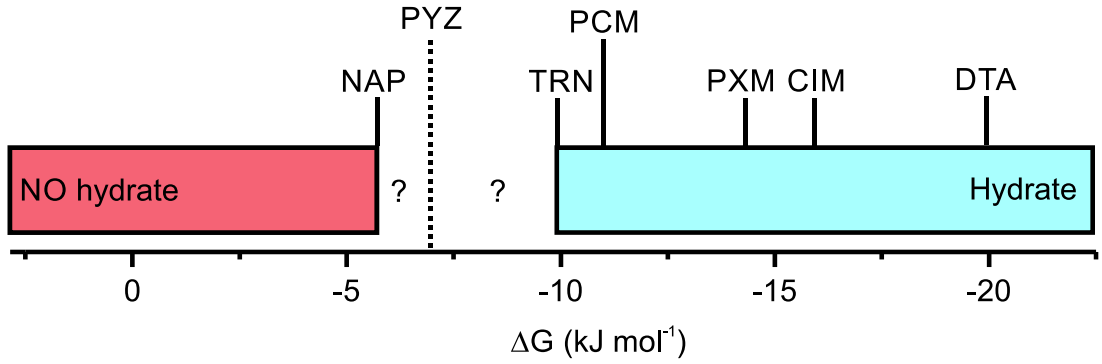


Figure 6.22. ΔG position of PYZ on the hydrate prediction gauge does not favour hydrate formation

After our prediction is done, the hydrate-forming capability of PYZ was revealed. Screening effort by Bajpai et al. using water slurry at ambient temperature; subjecting PYZ humid conditions (75% RH), and solvent drop grinding, all yielded the anhydrous form.[19] To date, no hydrate form for this compound has been reported which correspond well to our titration data, which suggest weak binding to water from the K_{21}. The high ΔG, with just 1.4 kJ mol^{-1} different from NAP value reflect on the low stability of the PYZ-water aggregate in solution.

6.2.3.4 Acetazolamide

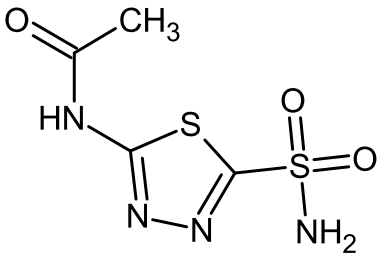


Figure 6.23. Chemical structure of Acetazolamide

Acetazolamide (ACT, Figure 6.23), is a monographed,[20] potent carbonic anhydrase inhibitor, which is mainly use in the therapy of glaucoma and epilepsy.[21] Based on the chemical structure, ACT possesses several sites of hydrogen bond donors, *i.e.* the NH, NH_2 and acceptors, *i.e.* the carbonyl, the sulfonyl, all of which could potentially hydrogen bond with water. The preliminary 1-H NMR of ACT is done in DMSO-d_6 environment since ACT is sparingly soluble in acetonitrile.

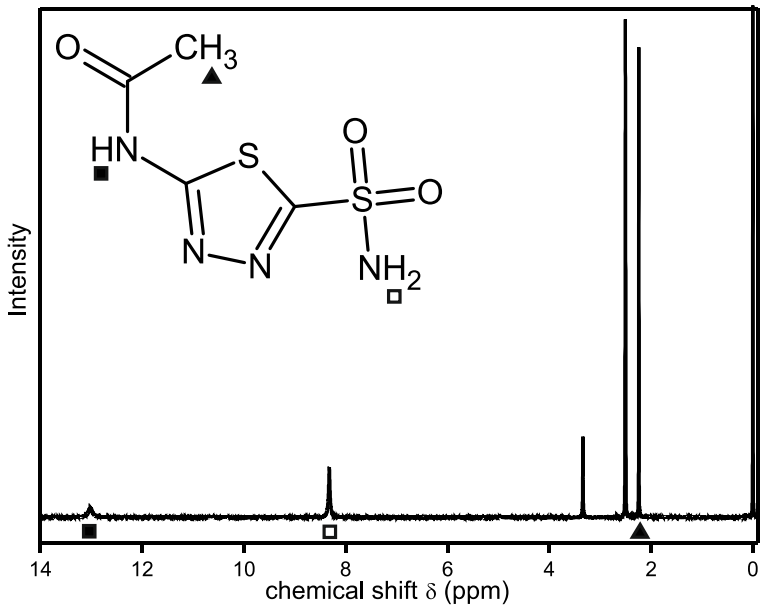


Figure 6.24. ^{1}H-NMR spectrum of ACT in DMSO-d_6 environment. Specific chemical shift regions on the spectra which are identified as proton 1 (■), 2 (▫) and 3 (▲) are highlighted with the respective symbols and corresponds to inset chemical structure.

The three observable regions for ^{1}H-NMR spectra of ACT are the NH, NH_2, CH_3, all of which appear as single peak, at 13.0, 8.3, and 2.2 ppm, which are then identified as proton 1 (■), 2 (□) and 3 (▲) respectively (Figure 6.24). The peak which appear at chemical shift 13.0 ppm, corresponds to the NH proton while the peak at chemical shift 8.3 ppm, corresponding to the NH_2. Finally, at 2.2 ppm, we observe the peak corresponding to the methyl group. Other visible peaks are of the reference, TMS (0 ppm), DMSO-d_6 (2.5 ppm) and water (3.3 ppm).

6.2.3.5 ^{1}H-NMR dilution experiment of ACT

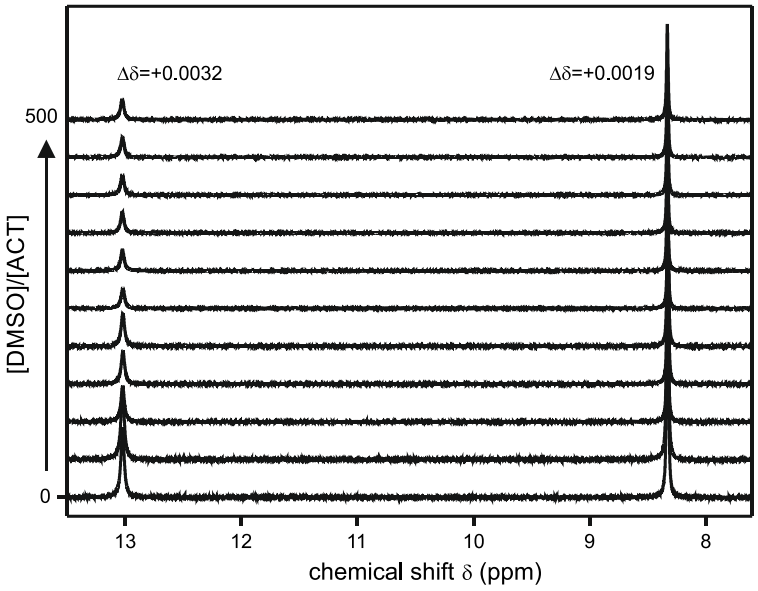


Figure 6.25. Dilution of 0.02 M ACT with non-deuterated anhydrous DMSO. Dilution is done in a single tube, with the highest dilution factor used is 500:1 G:H molar ratios.

Dilution of 0.02 M ACT with non-deuterated anhydrous DMSO up to 500:1 G:H in DMSO-d_6 environment (Figure 6.25) saw an overall downfield shift to proton 1 and 2 peaks. The magnitude of the downfield shifts is 0.0032 and 0.0019 ppm respectively. The methyl peak at 2.2 ppm did not shift at all following dilution. We note that the DMSO is hygroscopic,[22] even though anhydrous DMSO was used, there

is possibility for water to be absorbed by DMSO and influence the dilution. However, we do take the shifted peak values as part of the error for ACT titration measurement.

6.2.3.6 ^{1}H-NMR titration experiment of ACT

Firstly, proton 1 NH peak is very broad, which is typical for a labile proton, hence the peak is vaguely visible from 0-10:1 G:H molar ratio (Figure 6.26). The NH is connected to the 1,3,4-thiadiazole group, which is an unsaturated heterocyclic compounds, which leads to a faster proton exchange between the NH and water molecule. The nature of proton 1 makes the monitoring of this proton difficult.

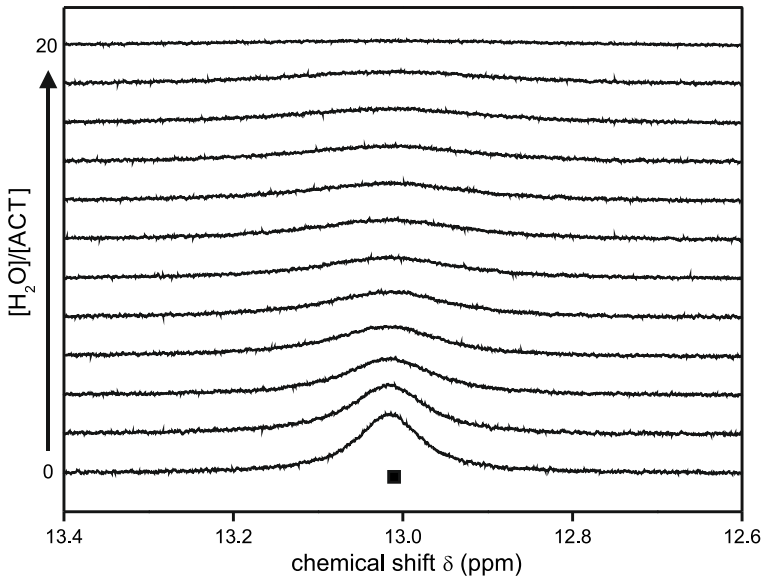


Figure 6.26. ^{1}H-NMR chemical shift region for proton 1, showing the broad nature of the peak, and its broadening and eventual disappearance once 20 molar ratios of water are introduced into the system

The remaining two protons are easier to be monitored as both showed downfield shift, which becomes more apparent as more water is titrated into the system (Figure 6.27 and 28). Overall, at 500:1 G:H molar ratio, the NH_2 peak (proton 2, Figure 6.27) has shifted by 0.065 ppm while the CH_3 (proton 3, Figure 6.28) has shifted by only 0.018 ppm. Compared to the dilution data, proton 2 shifted by 0.0019 ppm while

proton 3 saw no detectable shift, which suggest that following water titration there is some interaction with water - only that they are weak. Even though both of the monitored protons are at close proximity to functional groups which are most likely to form hydrogen bond to water i.e. the C=O (O-H···O=C) and O=S (O-H···O=S), delayed interaction with water is observed. Significant peak shifts were only detected after 30:1 G:H ratio for the NH_2 and after 70:1 G:H ratio for CH_3 peak respectively. This delayed shifts are similar to the events observed in PYZ.

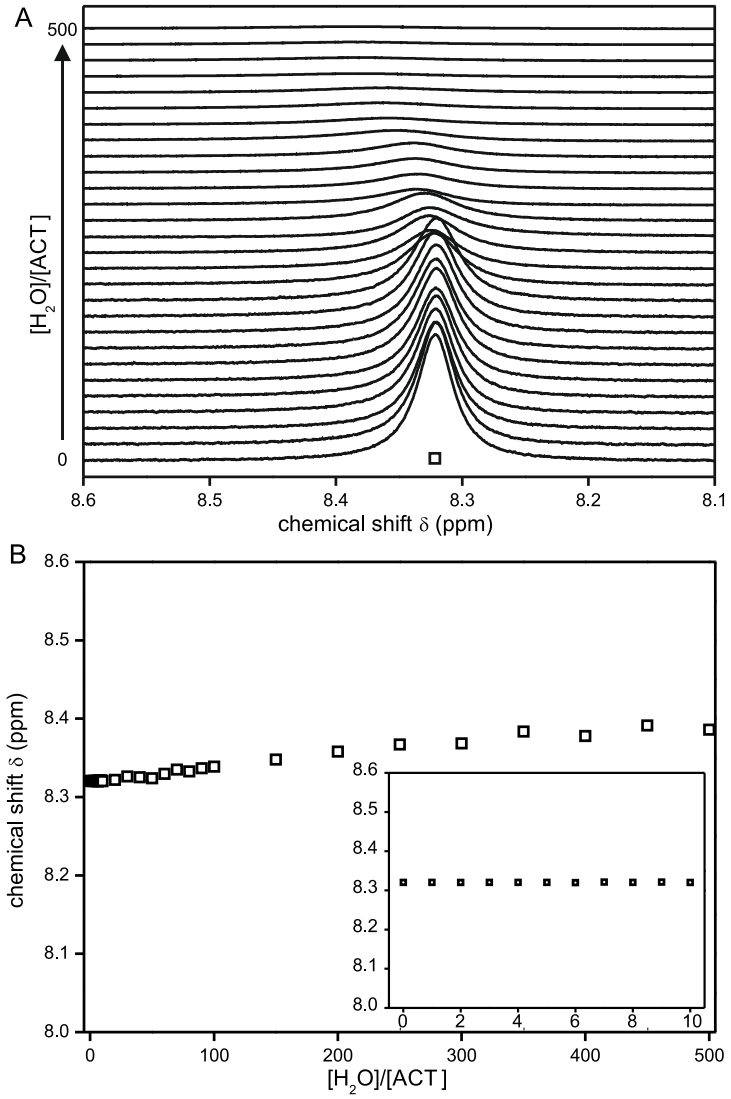


Figure 6.27. **A** depicts the ^{1}H-NMR peak shift for ACT **proton 2**, showing the initial delayed shift from 0-10, G:H ratio. **B** shows the scatter plot showing a larger shift observed once more water is introduced into the system as compared to data points at the lower water content (inset, 0-10 G:H ratio).

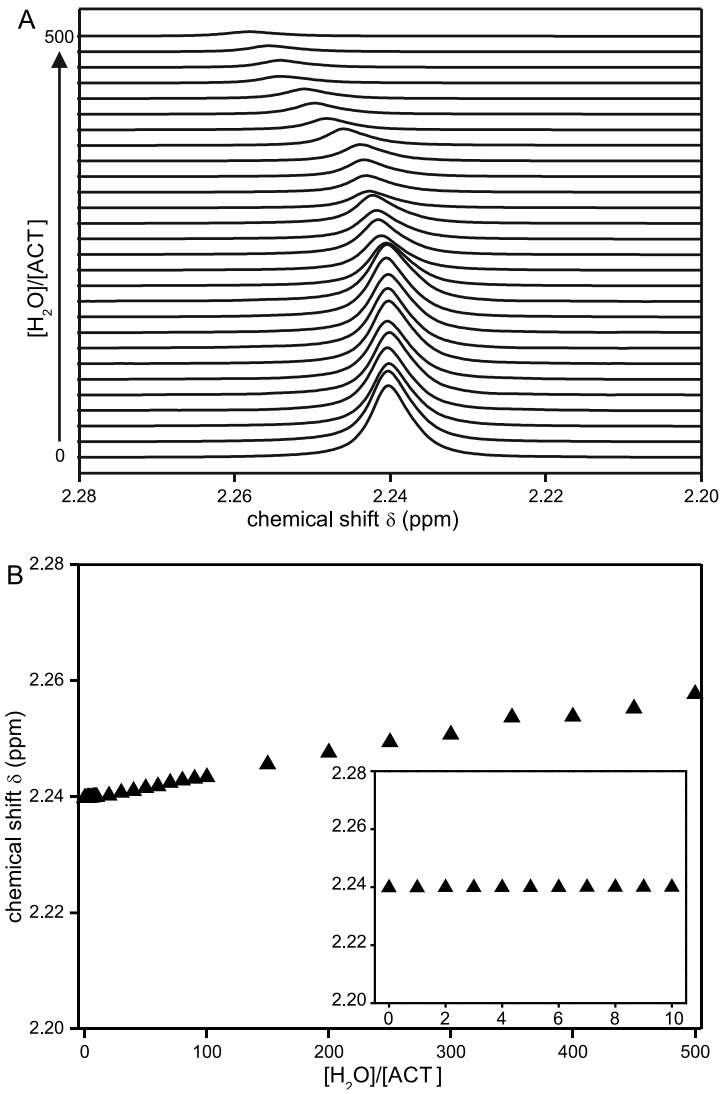


Figure 6.28. **A** shows ^{1}H-NMR peak shift for ACT **proton 3**, showing the initial delayed shift from 0-10, G:H ratio. Scatter plot showed a larger shift is observed once more water is introduced into the system as compared to data points at the lower water content (inset, 0-10 G:H ratio).

The Job plot of ACT revealed that the stoichiometry of interaction is 1:1, with X_{max}=0.5 (Figure 6.29). Similar to PYZ, we consider the result from the job plot of ACT with caution as the peak shift occurred on the fourth decimal place, hence it is difficult to ascertain whether the shift is truly due to water interaction.

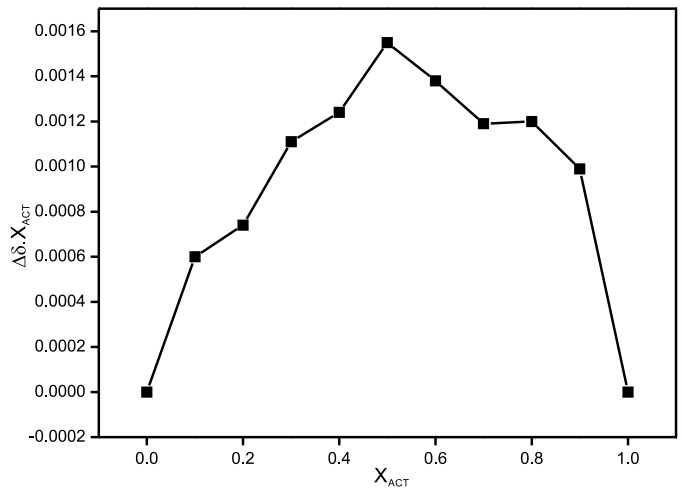


Figure 6.29. Job plot of ACT showing the stoichiometry of interaction as 1:1, with Xmax= 0.5

Subsequent binding constant fitting to all available binding model yielded non-significant K values. Whichever the model is fitted against the data, all the obtained K value is small, which the summary of the fitting is listed in Table 6.6. The best fitting with the least error to the fitted line is the 1:1 model - as suggested by the Job's plot. The 2:1 binding stoichiometry yielded 8% in fitting error while the 1:2 model fits the worst with >10% error. Conversion to ΔG based ok K_{21} for comparison purposes is not possible as negative ln value would generate error (not mathematically possible). Therefore, the lowest ΔG is used for comparison, which is calculated based on the largest *K* that we obtained, 0.32 M^{-1}. The calculated ΔG is 3.2 kJ mol^{-1}.

Table 6.6. *K* values based on the fitting to all available binding model, the 1:1, 2:1 and 1:2, H:G ratios

H:G binding model	K_1 (±% error)	K_{21} (±% error)	K_{12} (±% error)
ACT:H_2O	0.04 M^{-1} (±3.7%)	N/A	N/A
2ACT:H_2O	0.32 M^{-1} (± 8%)	-6.4 M^{-1} (±8%)	N/A
ACT:2H_2O	0.3 M^{-1} (±30%)	N/A	0.2 M^{-1} (±13%)

Based on the calculated ΔG, ACT is placed in the far end of our NO hydrate zone on our hydrate gauge. Therefore, based on the placement on our gauge, and comparison to other ΔG values obtained thus far, we predict that ACT do not exist as a crystalline hydrate form.

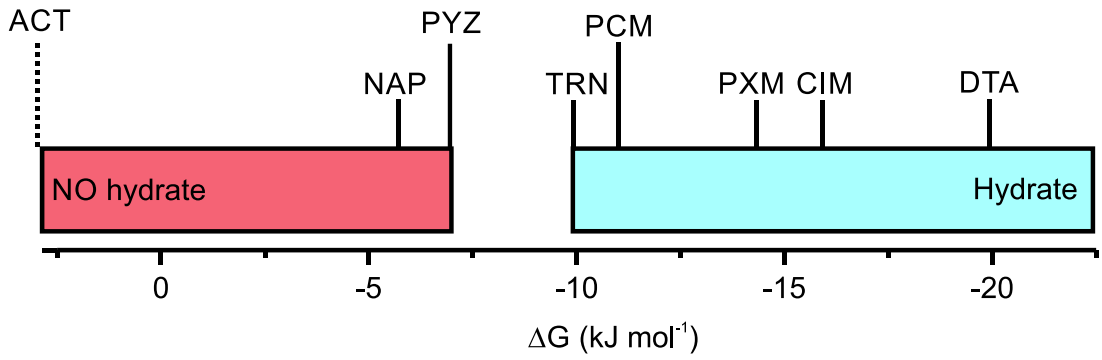


Figure 6.30. ΔG position of ACT on the hydrate prediction gauge which is in the NO hydrate zone.

Literature search afterwards revealed that ACT exists as two polymorphic forms, which were identified and characterised as Mod. I and Mod. II,[23] with no reported hydrate form. The lack of hydrate form does correspond well to our titration data, highlighting the method's ability to discriminate non-hydrate forming compounds. We can state with high certainty a compound which show positive ΔG from our titration will definitely do not exist as a hydrate form.

6.2.3.7 Dapsone

Dapsone (DAP, Figure 6.31) or 4,4′-diaminodiphenyl sulfone is a monographed drug,[20] which belongs to a class of drugs known as sulfones. DAP is primarily used to treat skin disorder *i.e.* dermatitis herpetiformis (in combination with trimethoprim).[24] It is also used in combination with rifampicin and clofazimine for the treatment of leprosy.[24] Based on the chemical structure, DAP have a balanced proton donors and acceptors, and could potentially hydrogen bond to water.

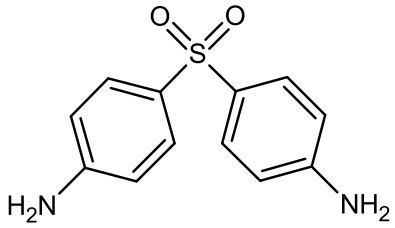


Figure 6.31. Chemical structure of Dapsone

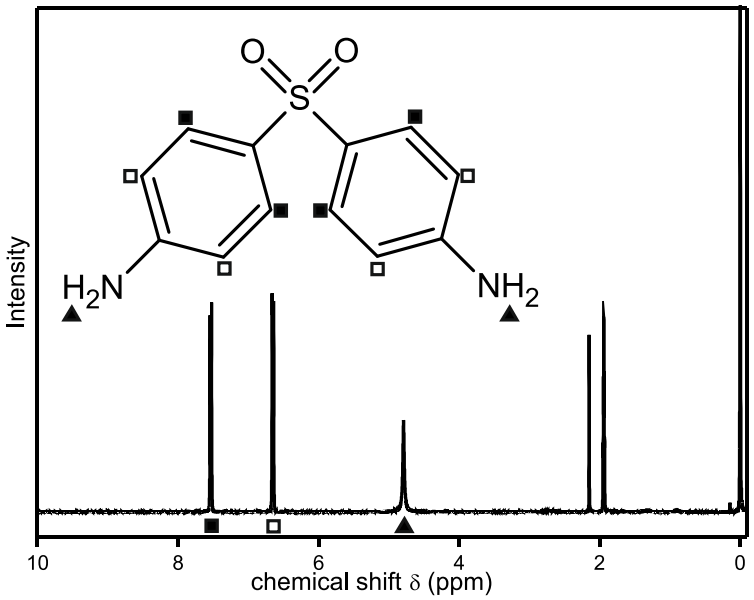


Figure 6.32. ^{1}H-NMR spectrum of DAP in acetonitrile-d_3 environment. Specific chemical shift regions on the spectra which are identified as proton 1 (■), 2 (▫) and 3 (▲) are highlighted with the respective symbols and corresponds to inset chemical structure.

The three observable chemical shift regions for preliinary ^{1}H-NMR spectrum of DAP are the peaks at 7.5, 6.6 and 4.8 ppm, which integrates to the 12 protons of DAP (Figure 6.32). The chemical shift at 7.5 ppm corresponds to the four protons on the benzene rings on the meta position, close to the sulfone (proton 1), while the peak at 6.6 ppm corresponds to the four protons on the ortho position of the benzene rings which are facing the amino groups (proton 2), and finally the peak at 4.8 ppm, which corresponds to the two NH_2 on the para position on both benzene rings (proton 3).

6.2.3.8 ^{1}H-NMR dilution experiment of DAP

DAP 0.02 M dilution experiment with non-deuterated acetonitrile saw all peaks shifted upfield, with the largest peak shift observed between 0-500 G:H ratio is 0.0015 ppm, which is to the peak of proton 3 or the NH_2 protons of DAP (Figure 6.33). Even though the recorded upfield peak shift is still non-significant, the obtained value and the direction of the shift is noted and is useful in the discussion and comparison in the titration experiment section for DAP.

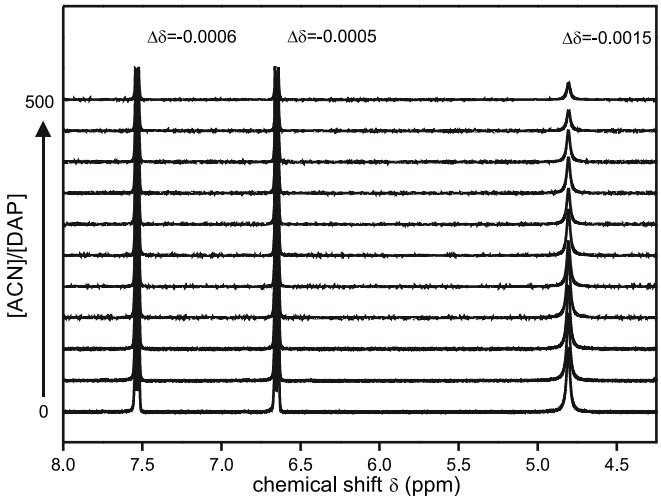


Figure 6.33. Dilution of 0.02 M DAP with non-deuterated acetonitrile. Dilution is done in a single tube, with the highest dilution factor used is 500:1 G:H molar ratios.

6.2.3.9 ^{1}H-NMR titration experiment of DAP

Following water titration, all protons showed downfield shifts (Figure 6.34-35), with the largest peak shift observed in proton 3 with 0.35 ppm (Figure 6.36), followed by proton 2 with 0.048 ppm (Figure 6.35), while proton 1 has only shifted by 0.016 ppm (Figure 6.34). Based on the magnitude of the peaks shift of the protons, proton 1 is least affected by the hydrogen bond to water, suggesting that the interaction point to water is furthest away from proton 1. In addition, proton 2 has shifted more

than proton 1, hence indicating the closer vicinity to the true site of interaction. Both peak shifts data complement each other, pointing towards NH_2 as the DAP-water interaction point.

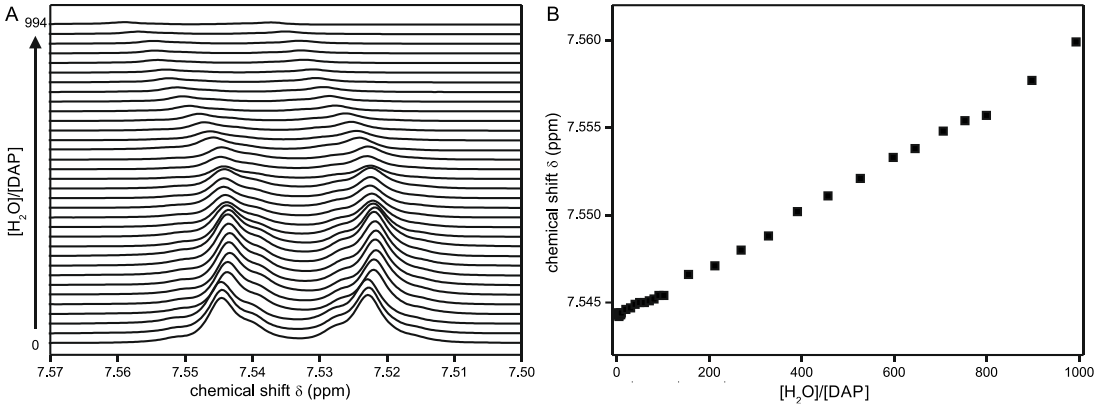


Figure 6.34. **A** ^{1}H-NMR peak shift for DAP **proton 1**, showing shift from 0-994, G:H ratio. While **B** shows scatter plot, with a linear shaped shift observed for the peak of proton 1 as more water is introduced into the system.

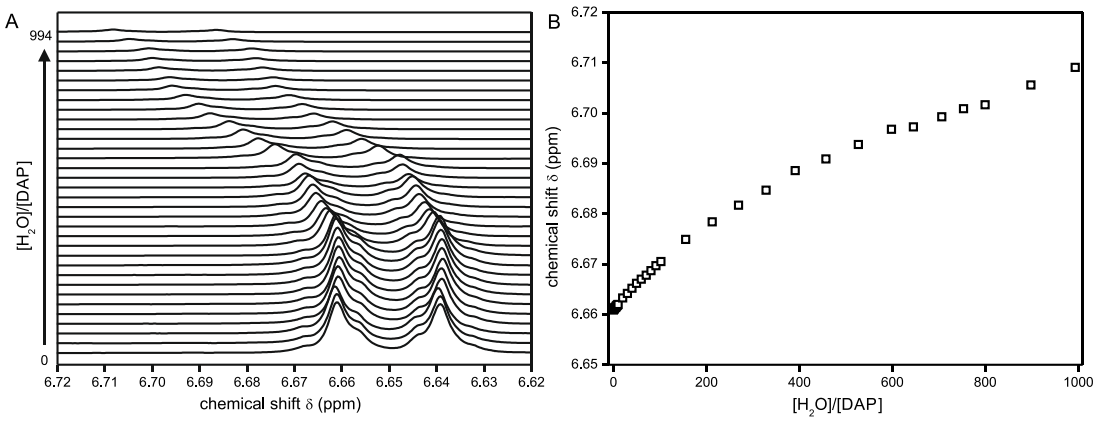


Figure 6.35. **A** ^{1}H-NMR peak shift for DAP proton 2, showing shift from 0-994, G:H ratio. While **B** shows scatter plot, with a linear shaped shift observed for the peak of proton 2 as more water is introduced into the system.

NH_2 or proton 3 peak shift shows the strongest shift, reaching significance early on in the titration, at 4:1 G:H ratio. This observation corroborates earlier assumption, confirming that proton 3 is indeed the interaction point to water. Scatter plot showed a non-linear shape shift (Figure 6.36B) with a plateau feature observed around 400:1 G:H ratio. Observation above the 400 molar ratio mark saw that the

magnitude of the shift is small compared to the sum of water in the system, suggesting that site of interaction (proton 3), is potentially saturated after the particular threshold.

The continuous peak shift observed in proton 3 even after the plateau was achieved could well be due the fact that larger amount of water in this case changes the solvent characteristics, and with that the magnetic environment of the compound.

Based on the direction of the peak shifts observed, the water is directly interacting with the DAP by accepting a hydrogen bond through proton 3,causing the H atom of the NH_2 to lose electron density from the interaction,[18] becomes deshielded and resulting in the observed downfield shift (Figure 6.36 A).

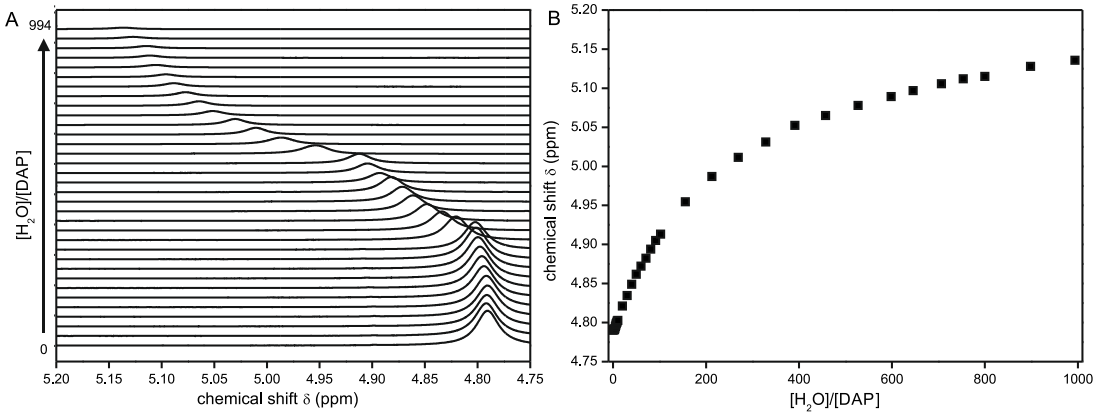


Figure 6.36. **A** shows the ^{1}H-NMR peak shift for DAP **proton 3**, showing an immediate shift from 0-4, G:H ratio. Meanwhile **B** depicts the scatter plot shows a non-linear shape shift observed as more water is introduced into the system.

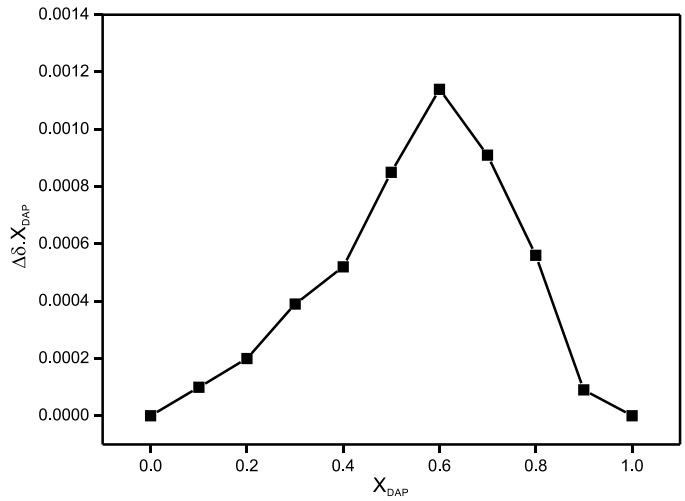


Figure 6.37. The Job plot of DAP revealed that the stoichiometry of interaction is favouring the 2:1 binding with X_{max}=0.6.

The Job plot of DAP revealed that the stoichiometry of interaction is favouring the 2:1 binding with X_{max}=0.6 (Figure 6.37). Though peak shift from the job plot is small, there is a clear evidence from the X_{max} value that there is a host fraction value which is favoured which yielded the biggest peak shift, and further accentuated upon factoring the host fraction value. Subsequent binding constant fitting to the 2:1 binding model yielded a K_1 value of 0.5 M^{-1} and a K_{21} value of 32.6 M^{-1} (Table 6.7). The calculated ΔG for K_{21} is -8.6 kJ mol^{-1}.

Table 6.7. K values based on the fitting to all available binding model, the 1:1, 2:1 and 1:2, H:G ratios

H:G binding model	K_1 (±% error)	K_{21} (±% error)	K_{12} (±% error)
DAP:H_2O	0.2 M^{-1} (±1.2 %)	N/A	N/A
2DAP:H_2O	0.5 M^{-1} (±0.8%)	32.6 M^{-1} (±7%)	N/A
DAP:2H_2O	0.2 M^{-1} (±5.6%)	N/A	0.009 M^{-1} (±4.2%)

Based on the calculated ΔG, DAP is placed in the grey zone, almost on the midpoint between the NO hydrate, and hydrate-forming zone. The relative distance to the neighboring compound in their respective group is +1.5 kJ mol^{-1} to PYZ and -1.6 kJ mol^{-1} to TRN.

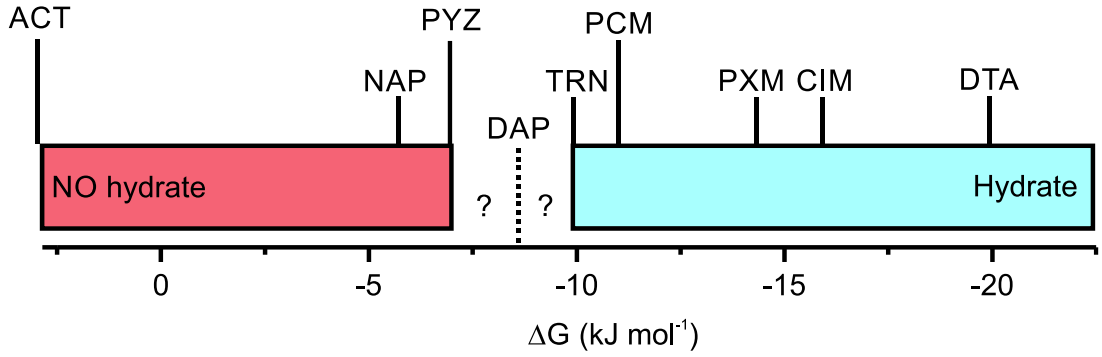


Figure 6.38. Placement of DAP on the hydrate prediction gauge in the grey zone between the respective areas.

Since DAP hydrate prediction is not clear-cut based on the ΔG alone, we turn to the observed peak shift. We noticed that all DAP protons showed clear shifts. DAP showed high water affinity following water titration, showing immediate shift even at lower water content and achieving significance peak shift at 4:1 G:H ratio. In addition, the shift magnitude of NH_2 (0.35 ppm) was large compared to the proton shifts that we have observed thus far, which showed hydrate-forming capability. Even though the placement on our gauge is unclear, based on overall observation of the titration experiment and comparison to other ΔG values obtained thus far, we predict that DAP can exist as a crystalline hydrate form.

Subsequent literature search revealed that DAP has been reported to exist as four polymorphic anhydrous form (Mod. I-IV)[25] and a single hydrate form with DAP:water stoichiometry of 3:1 (0.33-hydrate),[26–28] having a typical non-stoichiometric hydration and dehydration behaviour.[29] CCDC search revealed three

submitted single crystal structure for DAP 0.33 hydrate, with the latest submitted by Yathirajan et al.[26–28] Based on the latest crystal structure data, the water molecules are not located in structural channels but in isolated-sites of the host framework, which is contradicting the hydration and dehydration non-stoichiometric behaviour.[29] The submitted structure indicated that water hydrogen bonds to DAP molecule through the amino and sulfonyl group. Solid-state DAP-water coordination *via* the amino group revealed the role of water molecule as a proton acceptor ($NH_2\cdots OH$), which is similar and complements our earlier ^{1}H-NMR solution observation. TGA from the Braun et al.[29] also reveals that dehydration of the crystalline hydrate form occur between 40 to 90 °C which reflects on how weakly water is bonded to DAP.[29] The presence of the weak hydrate form does reflect our titration data.

6.2.3.10 4,4'-Dipyridyl

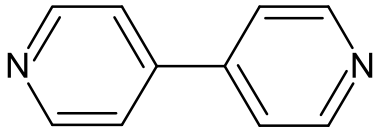


Figure 6.39. Chemical structure of 4,4'-Dipyridyl

4,4'-Dipyridyl (DPY, Figure 6.39) is not a monograph drug, but it is used in transition-metal complex catalyst chemistry for uniform polymerisation,[30] in luminescence chemistry,[31,32] and in spectrophotometric analysis.[33] DPY is made of two pyridine moieties which are linked by a bond between positions C-4 and C-4'. Similar to PYZ, the compound lacks any hydrogen bond donor, and has two acceptors on each side of the rings.

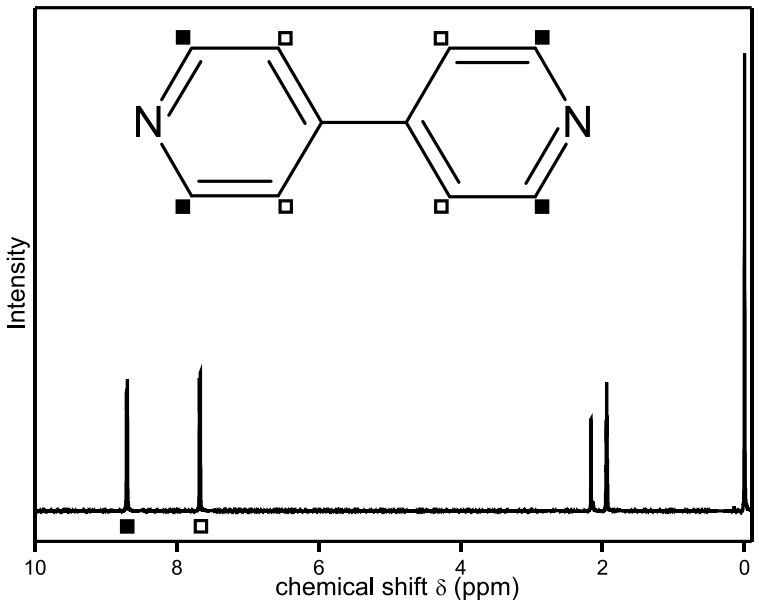


Figure 6.40. ^{1}H-NMR spectrum of DPY in acetonitrile-d_3 environment. Specific chemical shift regions on the spectra which are identified as proton 1 and 2 are highlighted with the respective symbols and corresponds to inset chemical structure.

Preliminary ^{1}H NMR spectrum of DPY in acetonitrile-d_3 environment revealed two split peaks, appearing at 8.7 and 7.7 ppm. The peaks are identified as proton 1 and 2 and integrated equally to its eight protons (Figure 6.40).

6.2.3.11 ^{1}H-NMR dilution experiment of DPY

DPY 0.02 M dilution experiment with protiated acetonitrile also saw the two split peaks shifted upfield (Figure 6.41). Since all shift occurred at fourth decimal place, shifting by 0.0004 and 0.0002 ppm respectively, confirms that no significant effect from dilution is observable for DPY dilution when diluted to up to 500:1 G:H ratio. Details on the peak position and as to which proton they correspond to is discussed in the titration section.

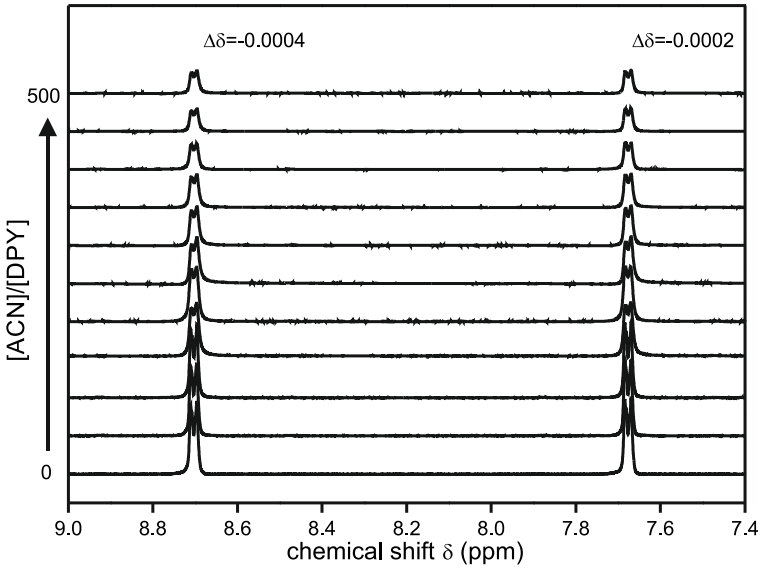


Figure 6.41. Dilution of 0.02 M DPY with non-deuterated acetonitrile. Dilution was performed in a single tube, with the highest dilution factor used was 500:1 G:H molar ratios.

6.2.3.12 ^{1}H-NMR titration experiment of DPY

Unlike the dilution experiment where both peaks have shifted (or the lack of it) upfield, following water titration, each peak has shifted in the opposite directions, upfield for the protons close to the nitrogen atom (N, proton 1,_Figure 6.42), and downfield for the protons away from the N (proton 2, Figure 6.42). Without the influence of water, the N atoms would have an effect to the electron circulation of the ring as N is more electronegative than carbon, which is similar to the observation of PYZ. As water is introduced and starts to form hydrogen bond with the N atoms (O-H···N), the N atoms gain electron density from the bridging protons of water. The additional electron density obtained would cause the N atoms to become less δ-, having lower affinity and influence towards the electron circulation of the benzene ring, observed from the shielding and deshielding effect to the monitored hydrogen atoms environment. The different direction in peak shift is most likely due to the nature of benzene ring, having ortho, para directing groups which are electron-donating groups; and meta directing groups which are electron-withdrawing groups. Therefore, as the

complexation to water affects these protons' electronic rearrangement, the observed effect and shift direction difference is expected.

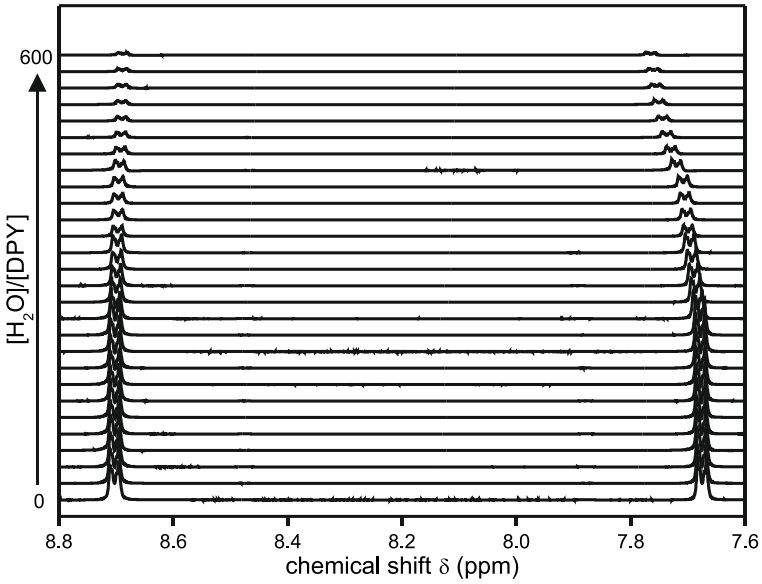


Figure 6.42. ^{1}H-NMR peak shift for DPY proton 1 and 2 showing peak shift in opposite direction, upfield for proton 1 and downfield for proton 2.

Interestingly, proton 2 experience a larger deshielding effect, hence having bigger shift downfield by 0.09 ppm. Compared to proton 1, which underwent a shielding effect, with only 0.01 ppm shift is observed. Even though the effect is small, it can still be clearly seen from the scatter plot curves of both peak points (Figure 6.43), where a steeper slope is observed for the plot of proton 1(Figure 6.43A), while a more gradual one for the proton 2 (Figure 6.43B).

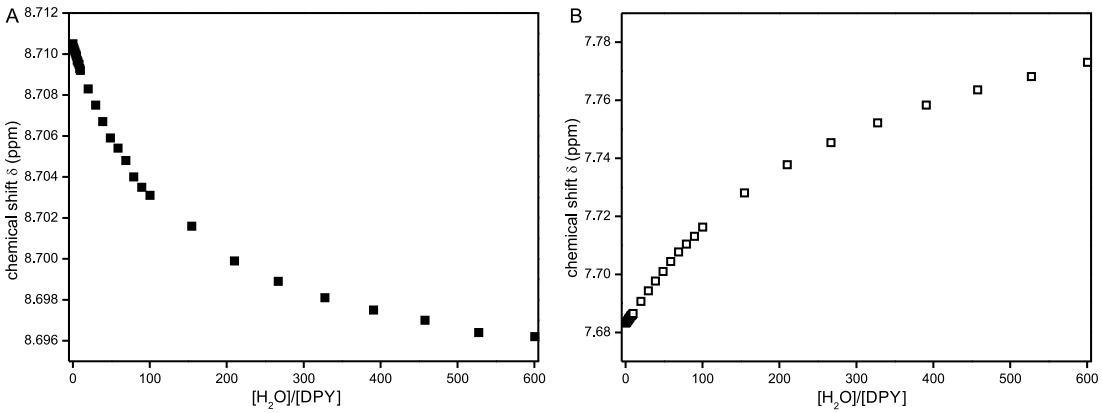


Figure 6.43. Scatter plot of proton 1 and proton 2. **A** showed proton 1 upfield shift to lower ppm with increasing water:DPY ratio. **B** showed proton 2 downfield shift to higher ppm with increasing water:DPY ratio.

The Job's plot of DPY revealed that the stoichiometry of interaction favours the 2:1 binding with X_{max}=0.6 (Figure 6.44). The K_{21} value of 35.3 M^{-1} obtained is almost comparable with the value obtained for DAP, with the K_{21} translates into ΔG^0 of -8.8 kJ mol^{-1}. Values for fitting to other binding model is listed Table 6.8.

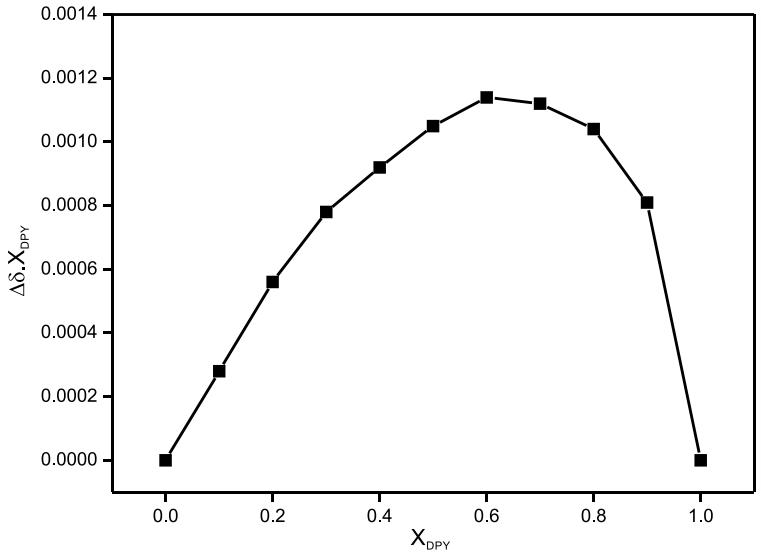


Figure 6.44. The Job's plot of DPY revealed that the stoichiometry of interaction is favouring the 2:1 binding with X_{max}=0.6.

Table 6.8. K values based on the fitting to all available binding model, the 1:1, 2:1 and 1:2, H:G ratios

H:G binding model	K_1 (±% error)	K_{21} (±% error)	K_{12} (±% error)
DPY:H_2O	0.16 M^{-1} (±1.4%)	N/A	N/A
2DPY:H_2O	0.37 M^{-1} (±2.1%)	35.3 M^{-1} (±3 %)	N/A
DPY:2H_2O	1.0 M^{-1} (±2.6%)	N/A	0.15 M^{-1} (±0.9%)

Based on the calculated ΔG for DPY which is slightly lower than DAP, places DPY just inside the hydrate-forming zone on our hydrate gauge. Therefore, based on the placement on our gauge, and comparison to other □G values obtained thus far, we predict that DPY can exist as a crystalline hydrate form.

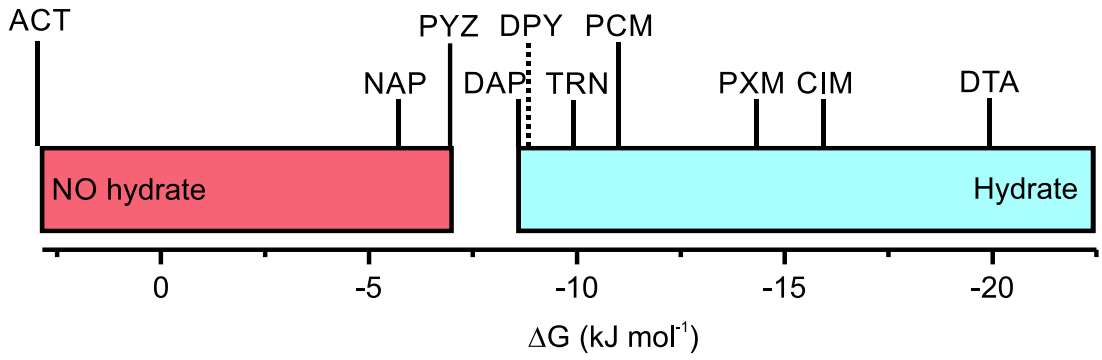


Figure 6.45. DPY placement on the hydrate-forming area on the gauge.

Literature search following the end of our in-house titration experiment revealed that DPY exists as an anhydrous and a dihydrate form,[34,35] and based on the submitted structure of the crystalline hydrate, the interactions between the water and the DPY molecule lead to the DPY···H_2O···H_2O···DPY motif. DPY and water are connected through the O-H···N, while water dimers are formed from the O-H···O bonding. Chains of O-H···O hydrogen-bonded water molecules are located between the bipyridine stacks. Altogether, four crystallographically independent water

molecules and two crystallographically independent bipyridine molecules are involved.[34] Although the dihydrate is reported to be stable at ambient temperature and humidity, TGA curve revealed that the loss of water occur almost immediately after heating around 50 °C, with most of the water released below 100 °C.[36] The reported hydrate form hence reflects well to our prediction.

6.2.3.13 Flurbiprofen

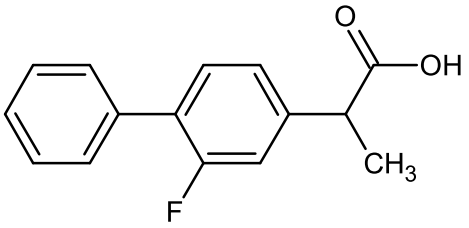


Figure 6.46. Chemical structure of Flurbiprofen

Flurbiprofen (FBN, Figure 6.46) is a nonsteroidal anti-inflammatory drug (NSAID), used to treat mild to moderate pain, including pain and inflammation caused by osteoarthritis or rheumatoid arthritis.[37] The structure offers interaction sites for hydrogen bonding through the acid group, donating proton *via* the OH, and accepting *via* the carbonyl.

Similar to ACT, FBN is sparingly soluble in acetonitrile, hence DMSO-d_6 is used. Preliminary ^{1}H-NMR revealed that the monitored chemical shift region for FBN is highlighted in Figure 6.47. FBN spectra is complex to follow, especially for the protons of the two benzene rings. Nine peaks on the spectra can be observed, with the obvious peaks are the OH of the acid (proton 1) at 12.5 ppm, the CH connecting the acid, the methyl and the benzene ring (proton 8) appearing at 3.8 ppm, and finally the methyl at 1.4 ppm (proton 9). Proton 2-7 corresponds to the eight protons on the two benzene rings, appearing as overlapping peaks between 7.6-7.2 ppm (Figure 6.47B).

Careful observation on peak profile e.g. single, doublet, triplet etc. and the respective number of neighbouring protons was done to ascertain the peak identity. Other visible peaks are of the reference, TMS (0 ppm), DMSO-d_6 (2.5 ppm) and water (3.3 ppm).

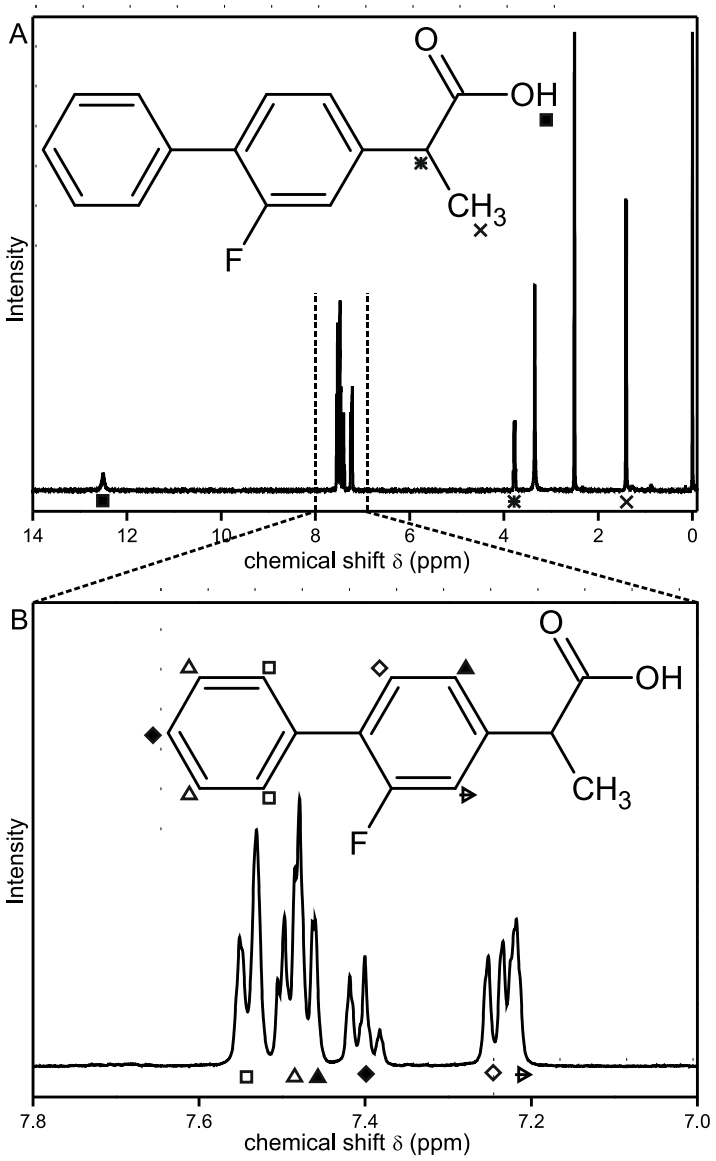


Figure 6.47.^{1}H-NMR spectra of FBN in acetonitrile-d_3 environment. Specific chemical shift regions on the spectra which are identified as proton 1-9 are highlighted with the respective symbols and corresponds to inset chemical structure. **A** highlights proton 1, 8 and 9, while **B** highlights proton 2-7.

6.2.3.14 ^{1}H-NMR dilution experiment of FBN

Dilution experiment 0.02 M FBN with non-deuterated anhydrous DMSO up to 500:1 G:H ratio (Figure 6.48) saw no significant shift to any the protons. Similar to previous dilution experiments, peak shifts occurred on the fourth decimal place confirms the absent of influence or effect from dilution experiment towards the peak shift. Details on the peak position and as to which proton they correspond to is discussed in the titration section.

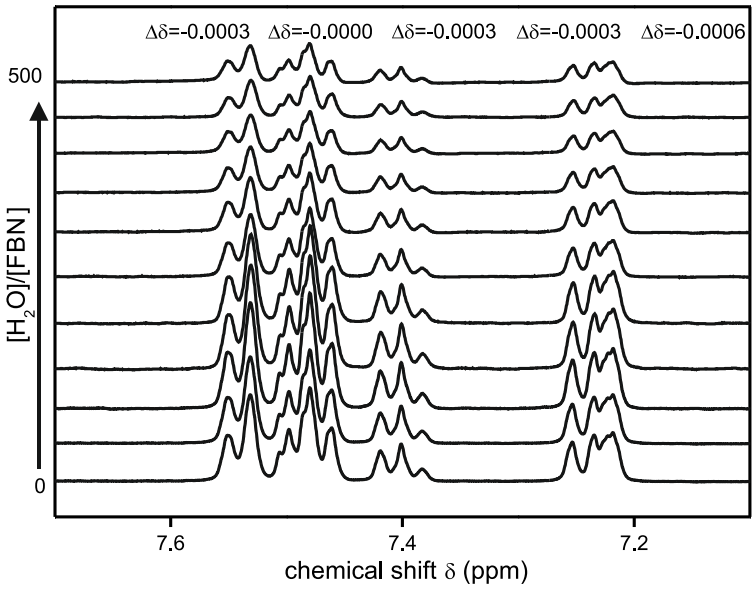


Figure 6.48. Dilution of 0.02 M FBN with non-deuterated anhydrous DMSO. Dilution is done in a single tube, with the highest dilution factor used is 500:1 G:H molar ratios.

6.2.3.15 ^{1}H-NMR titration experiment of FBN

Similar to the previous observations, the (OH) proton 1 peak is broad and visible at zero water (Figure 6.49), however as soon as water is introduced the peak becomes even broader, due to fast exchanging nature of the proton on NMR timescale.

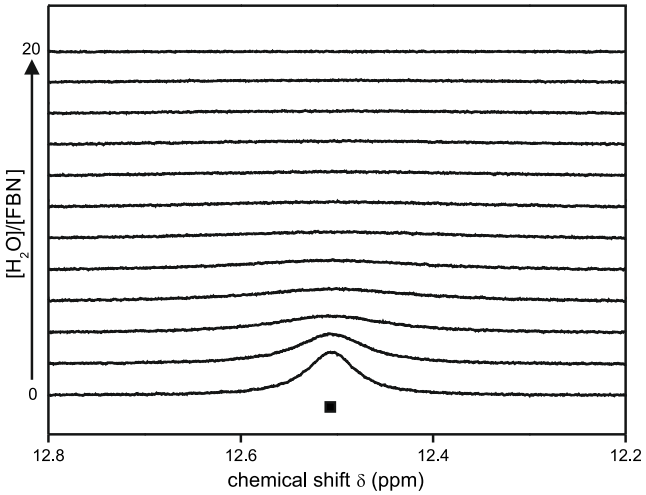


Figure 6.49. ^{1}H-NMR chemical shift region for proton 1 of FBN, showing the broad nature of the peak, and its broadening and eventual disappearance once 20 molar ratios of water are introduced into the system

Proton 2, 3 and 5 did not show a significant shift at lower water content, before shifting downfield when more water is introduced into the system (Figure 6.50). Dilution experiment saw these protons saw non-significant upfield shifts with 0.0003 ppm peak shift recorded at 500:1 DMSO:H ratio. Meanwhile, following titration, the downfield shift recorded is between 0.004 to 0.017 ppm at 456:1 G:H ratio.

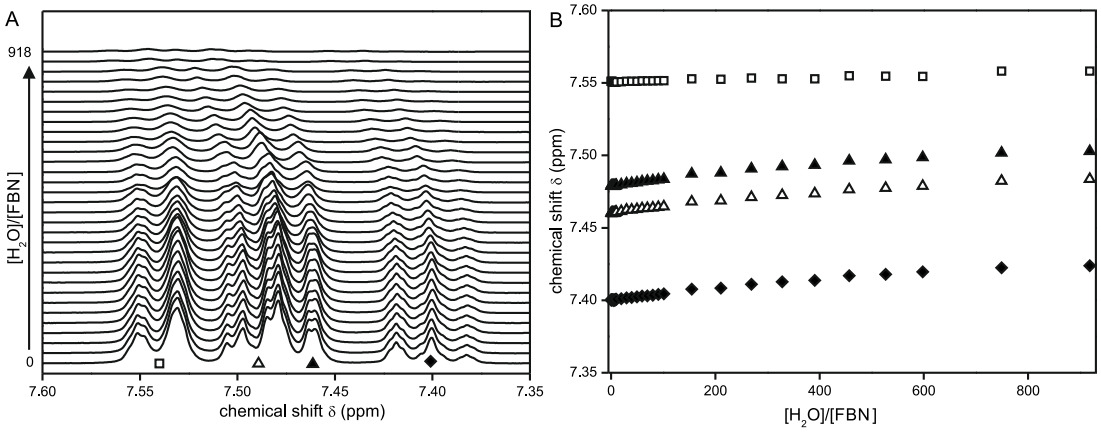


Figure 6.50. **A** ^{1}H-NMR peak shift for FBN proton 2-5 showing peak shift, while **B** shows the scatter plot of the peak shift for respective protons.

Proton 4, 6 and 7 changed profile at higher water concentration in the system (Figure 6.50, Figure 6.51). Proton 4 initially appeared as a broad-split peak, changed into a single peak with no splitting at higher water concentration in the system (Figure 6.50). Meanwhile, proton 6 which initially appeared as double peaks (♦ ,◇ symbols representing the double peaks), began to change into a broad single peak, at 210:1 G:H molar ratios of water in the system (Figure 6.51). This change is most likely due to the change in solvent environment, and with that the magnetic resonance of the protons. The convergence of the two peaks is clearly shown in Figure 6.51B. As for proton 7 (Figure 6.51A), the initially single peak splits into two broad peaks at 328:1 G:H ratio. These peak profile changes are observed to the protons of the ring attached with the fluorine and propanoic acid group.

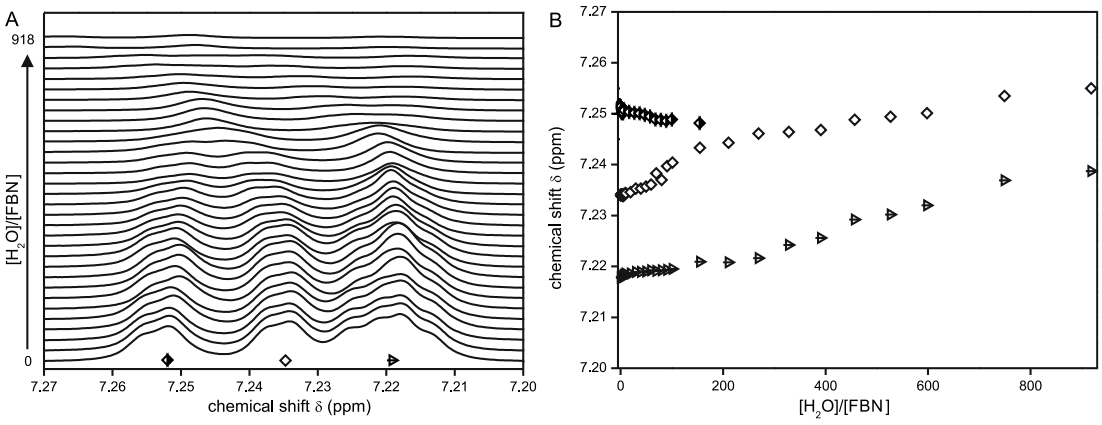


Figure 6.51. **A** ^{1}H-NMR peak shift for FBN proton 6 (♦ , ◇ representing the slip peaks) and 7 showing peak shift, while **B** shows the scatter plot of the peak shift for respective protons.

Dilution experiment did not show any peak profile change, even at high diluent concentration. This lead us to believe there is a weak interaction present, which is influenced by the presence of large amount of water. Overall, only small peak shifts are observed to all protons of FBN following the titration experiment. The peaks seem

to shift linearly downfield as more water is introduced, with no plateau feature observed even at 918:1 G:H ratios (Figure 6.50B and Figure 6.51B).

Proton 8 and 9 did not show much shift with 0.009 and 0.013 ppm respectively following water titration up to 918:1 G:H molar ratio (Figure 6.52 Figure 6.53). The lack of peak shift to these protons are not unexpected as these protons correspond to the CH and CH_3 respectively, hence are least likely to be affected by any electron rearrangement, or the effect of these rearrangements if they are indeed present, which are then visible on the spectra.

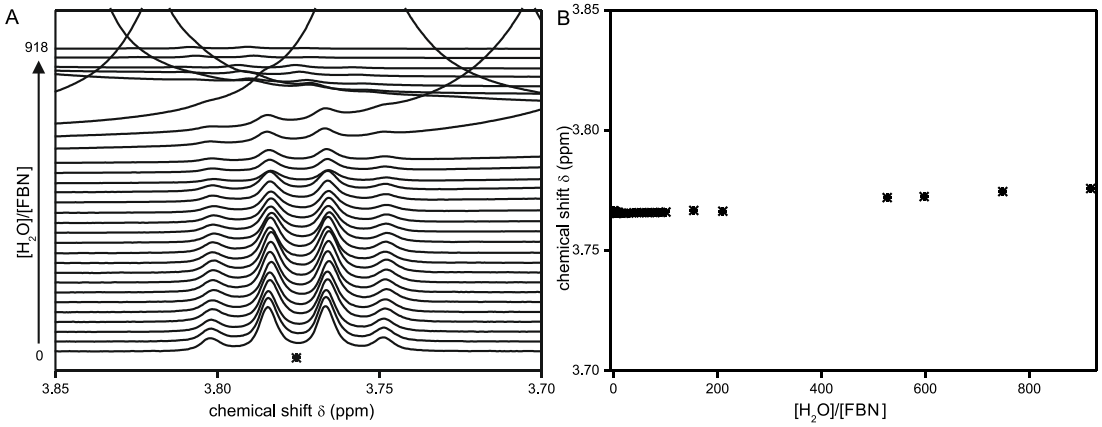


Figure 6.52. **A** ^{1}H-NMR peak shift for FBN proton 8 showing peak shift, while **B** shows the scatter plot of the peak shift for respective protons. Massive peaks at higher G:H ratios corresponds to the water peaks which is moving across the chemical region at its concentration increases.

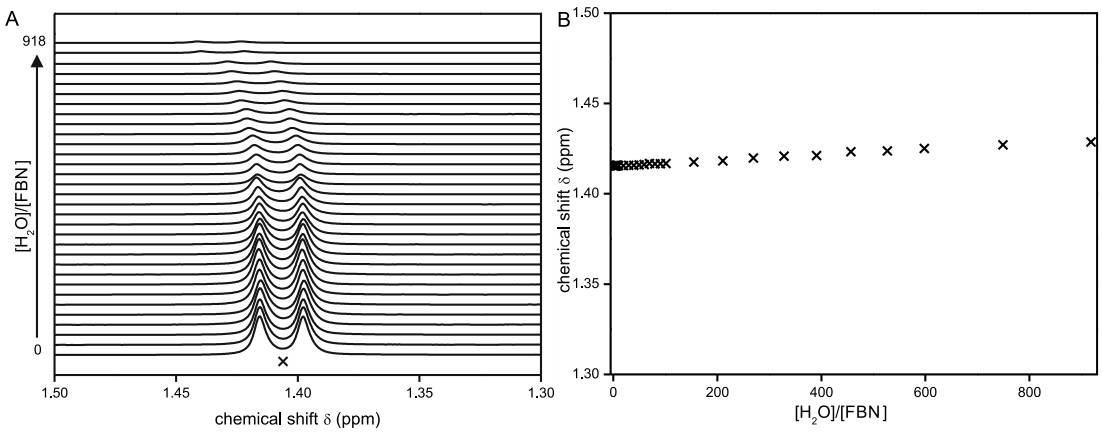


Figure 6.53. **A** ^{1}H-NMR peak shift for FBN proton 9 showing peak shift, while **B** shows the scatter plot of the peak shift for respective protons.

The Job plot of FBN revealed that the stoichiometry of interaction is favouring the 1:2 binding with X_{max}=0.4 (Figure 6.54). The fitting to 1:2 binding model yielded a K_{12} of 25 M^{-1}. All K_1 values from all the fitting are non-significant, while K_{21} suggest a negative cooperativity between the reactant and product, which is highly unlikely (Table 6.9). Hence, the K value FBN could not be directly to the other compounds, as all of them fits the K_{21} model. K_{12} translates into ΔG of -8.0 kJ mol^{-1}.

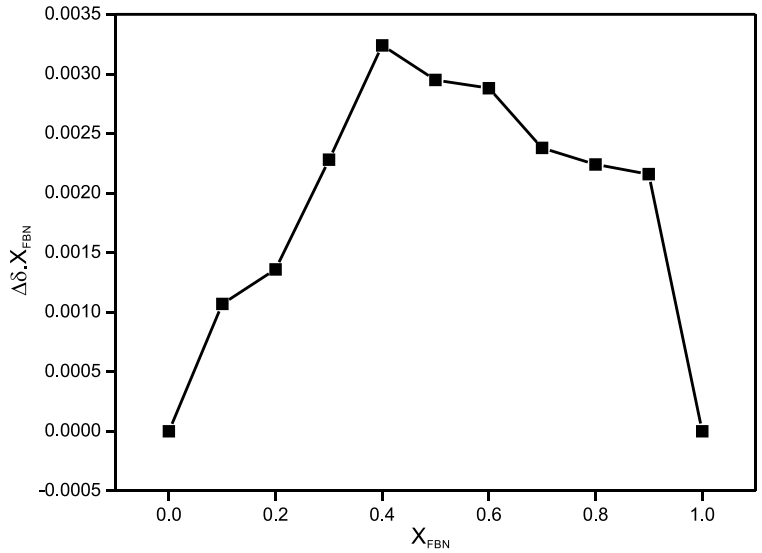


Figure 6.54. The Job's plot of FBN revealed that the stoichiometry of interaction is favouring the 1:2 binding with X_{max}=0.4.

Table 6.9. K values based on the fitting to all available binding model, the 1:1, 2:1 and 1:2, H:G ratios

H:G binding model	K_1 (±% error)	K_{21} (±% error)	K_{12} (±% error)
FBN:H_2O	0.06 M^{-1} (±2.7%)	N/A	N/A
2FBN:H_2O	0.12 M^{-1} (±1.7%)	-21.9 M^{-1} (±3.1%)	N/A
FBN:2H_2O	8 x10^{-5} M^{-1} (±1.8%)	N/A	25 M^{-1} (±4.5%)

The calculated ΔG palaces FBN in the grey zone. The placement of FBN is puzzling as the peak shift magnitude were not the largest or the clearest *e.g.* DAP, however, the values from the global fitting of the protons revealed comparable value to that of DAP. However, it is noted that the ΔG calculated is not based on the K_{21} but, K_{12} which means it is not a one-to-one comparison. We are predicting hydrate presence in FBN solely due its placement on our gauge favouring the hydrate-forming zone.

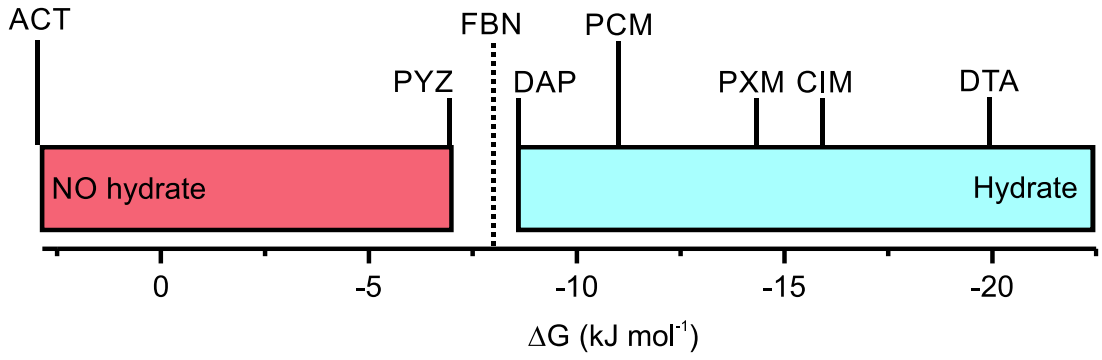


Figure 6.55. ΔG placement of FBN on our hydrate gauge. TRN and DPY marker on the gauge are opted out for clarity.

Follow up literature search found that FBN has been reported to exists as three polymorphs, Form I, II, and III, as well as a 3FBN:2H_2O phase (3/2 hydrate), which nucleates selectively from only a few polymers.[38] The crystalline hydrate was grown from the evaporation of methanol solution in the presence of polymers such as poly

(n-butyl methacrylate), polycaprolactone, chlorinated polyethylene, and styrene butadiene ABA block copolymer. In addition, the 3/2 hydrate was also reported to crystallise from evaporation of ethanol solutions, mixed with sodium salt of alginic acid and poly (vinyl alcohol).[38] Crystallisation from methanol evaporation only yielded the hydrate form in the presence of the mentioned polymers, and without the polymers, the hydrate form did not form- even in the presence of additional water in the methanol solution.[38]

Closer examination of the hydrate form revealed that the water molecules are disordered in the structure model, and is located in the channels formed by six FBN molecules (Figure 6.56).

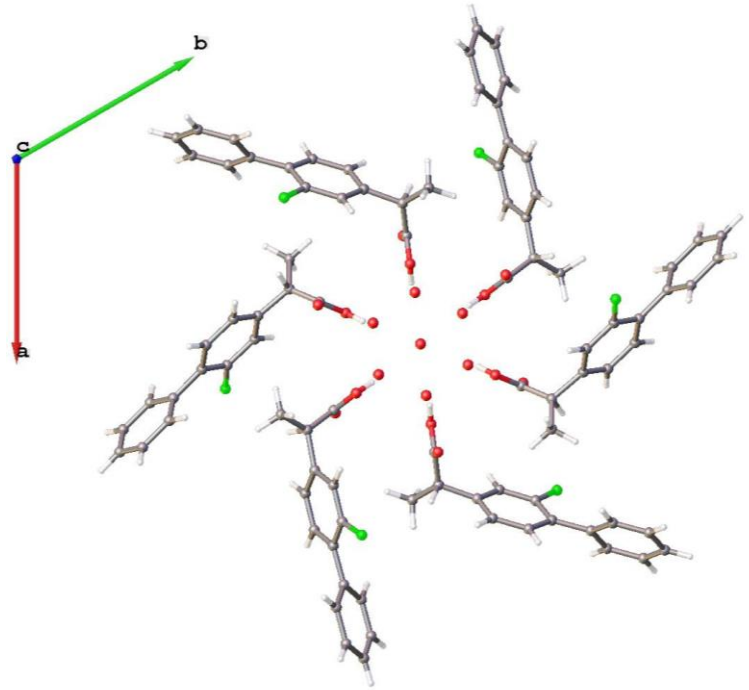


Figure 6.56. FBN 3/2 hydrate structure showing the channel formed by six FBN molecules, where water molecules are located.[38] The colour code is carbon grey, oxygen red, fluorine green and hydrogen light grey

Water is reported to hydrogen bond as a donor and acceptor following interaction with FBN.[38] As an acceptor, water hydrogen bonds *via* the oxygen atom,

to the carboxylic acid (OH) of FBN.[38] Two additional hydrogen bonds is also reported involving water as a donor, hydrogen bonding to the carbonyl and the oxygen of the acid respectively, which is indicated by the close proximity of the O⋯ O distances.[38]

Since the hydrogen bonding between FBN and water is reported to be through the OH group, [38] it is actually in-line with our ^{1}H-NMR observation. Following our titration method, the OH was unobservable *via* ^{1}H-NMR method due to the fast exchanging OH proton. Furthermore, the closest proton to the interaction point (OH) is the final two protons, proton 8 and 9 which correspond to the CH and CH_3 and did not shift much. However, from the global fitting of all protons which have undergone electronic rearrangements showing peak shifts following FBN-water interaction, a modest was obtained, and calculated to ΔG of -8.0 kJ mol^{-1}. The obtained values reflect on the compound's weak affinity to water. The fact that the 3/2 hydrate only form in the presence of a specific polymer which could influence or increase affinity towards water, which also points to the weak interaction observed in our titration. We suggest the value obtained here as the limit to our titration method, as lower value would obscure the distinction between weak hydrate and non-hydrate forming compound which is at this point ΔG >-7 kJ mol^{-1}.

6.3 Conclusion

Titration data from the first two model compound showing no strong hydrate form provided initial cut-off of used to define our prediction tool. Titration of the first model compound NAP yielded a K_{21} of 9.88 M^{-1} when all protons' peak shifts were plotted and fitted against the respective binding model. The *K* was translated to ΔG of -5.7 kJ mol^{-1}. Similarly, when PCM was analysed, the resultant *K* and ΔG form the fitting of all non-labile protons were 80 M^{-1} and -10.9 kJ mol^{-1}. Based on these values and the previously recorded data for stable hydrate-forming compounds (DTA, CIM, TRN, and PXM), a hydrate prediction gauge was constructed, having hydrate and non-hydrate-forming zone (Figure 6.9).

A blind test on five compound were also done, and we have correctly predicted the hydrate-forming capabilities of the five compounds. Most of the ΔG for the blind test compounds fell in the grey zone, between <-6 kJ mol^{-1} and >-10 kJ mol^{-1} of our initial zones limits. These limits are the adjusted based new data from our blind tests. We are confident that the adjusted limits based on, 1) the significant shift (>0.002 ppm) at low water incorporation-showing strong affinity towards water, 2) the overall shape of the generated curve from the chemical shifts, -reflective of a real host-guest reaction rather than random interactions. The energy values appeared close between the hydrate and non-hydrate region as they are calculated, however the actual *K* value obtained vastly differ between the zones. In principle a difference of ±1 kJ mol^{-1} would actually represent a significant difference in *K* and not a fixed value. For example, the *K* values of 25,.16.7 and 11.2 M^{-1}, will correspond to the calculated ΔG values of -8, -7 and -6 kJ mol^{-1} respectively. Meaning a difference of 1 kJ mol^{-1} between -8 and -7 kJ mol^{-1} corresponds to a difference of *K* by 8.3 M^{-1}, while between -7 and -6 kJ mol^{-1}, 5.5 M^{-}

[1]. Following the first blind test result, PYZ data provided a new cut-off for non-hydrate forming zone of -7.1 kJ mol^{-1}. Initial prediction for PYZ hydrate state was done based on its placement on our gauge, which was in close proximity to non-hydrate zone, +1.4 kJ mol^{-1}, compared to -3.1 kJ mol^{-1} away from the hydrate zone. Subsequent literature search confirmed our prediction, and effectively expand our non-hydrate zone to be ΔG of >-7.1 kJ mol^{-1}. ACT hydrate state was the easiest to determine as the titration did not show significant shift at lower water contents, and the fitting yielded a small *K* of 0.32 M^{-1}, which translated into positive ΔG value. This places ACT on the non-hydrate zone on our gauge, which subsequent literature search confirmed to be correct.

DAP present the biggest challenge to our prediction method as the ΔG not only placed the compound in the grey zone, but right in the middle of the two-defined zones with +1.5 kJ mol^{-1} to the non-hydrate zone and -1.6 kJ mol^{-1} to the hydrate zone. Observation of the peak shift behaviour helped our prediction as all of DAP's protons showed clear shifts, and DAP showed high water affinity following water titration, with immediate shift even at lower water content. Plus, the shift magnitude of NH_2 (0.35 ppm) is very significant compared to the proton shifts that we have observed thus far, which showed hydrate-forming capability.

Analysis of the final two compounds, DPY and FBN yielded comparable ΔG values to that of DAP. Based on the calculated ΔG DPY is placed on the hydrate-forming zone of our gauge. Our prediction matches the literature search with a dihydrate form reported.[34,35] Meanwhile FBN is place on the narrower grey zone, however, with the value is so close to DAP (which we now know has a hydrate form) with just +0.6 kJ mol^{-1} difference, we hence predicted that the compound to be able to

exist as a hydrate form. Again, our prediction was in-line with previous report of a 3/2 hydrate.[38]

By the end of the blind test, the grey zone has shrunk form the initial area defined at the beginning of the probe. We suggest the value obtained for FBN as the limit to our titration method, as lower value would obscure the distinction between hydrate and non-hydrate forming compound. As mentioned earlier, all of the ΔG obtained from our blind tests, fell in the initial grey zone between <-6 kJ mol^{-1} and >-10 kJ mol^{-1} of our initial zones limits. Interestingly, all of the blind test compounds which are now placed in the hydrate-forming zone share a common property, which is all of them forms weak hydrates. Whilst we cannot definitively discriminate between strong and weak hydrate forming compounds, we can see an emerging trend of comparable *K* and ΔG values, with placement on the higher end on our hydrate gauge. The only compound which showed unusually strong affinity to water is PCM considering the fact that PCM hydrate forms are metastable. However, the values obtain for PCM still fit in hydrate forming compound zone (Figure 6.57).

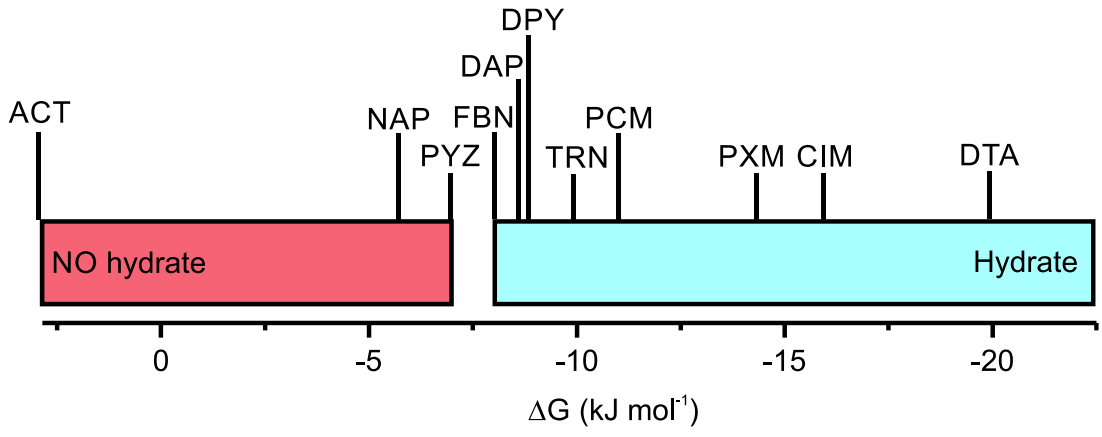


Figure 6.57. Overall placement of all analysed compounds which is based on the respective ΔG, on our generated hydrate gauge.

Overall, results from chapter 5 and 6 suggest that the procedure used is able to show and measure the apparent binding interaction, and energies between the uncharged host and guest. In each of the experiments, accompanying dilution control experiment was done to ensure that any shift observed was based on water interaction rather than dilution effect. Overall, dilution experiment of all tested compounds yielded non-significant shifts, and bares little effect to the peak shifts of the compound. Dilution experiments also did not result in the change of peak profile in any of the spectra.

We acknowledge that the resultant peak shifts are small, and the fitting is only apparent to the available model and unlike a typical host-guest titration, our binding curve does not reflect the true stoichiometry of the interacting components, as the amount of guest needed to observe the changes are massive. However, we have noticed an immediate shift at 1:1 G:H ratio especially for compound showing good hydrate forming ability, compared to the delayed shift for the poor or non-hydrate forming compound. Moreover, there is clear evidence that there is a degree of molecular recognition between the interacting components leading to the formation of pre-nucleation aggregates. We stipulate that since the interaction is weak, the amount of guest added need to be overwhelmingly large, so that the chemical shift changes is observable on ^{1}H-NMR.

We have successfully showed that different compounds with different hydrate forming ability would show different affinity and selectivity to the tested guest (water) reflected by a different *K* values and the respective ΔG (Figure 6.57), and listed in Table 6.10. Based on method and our ΔG hydrate gauge, we are able to distinguish between hydrate and non-hydrate forming compound (Figure 6.57). In addition, we

can see an emerging trend of comparable *K* and ΔG values in weak hydrates compared to stable hydrates, however definitive distinction between the two hydrate types required a larger library of compounds analysed using our method (Figure 6.57). The lowest *K* and ΔG value was acquired from metastable hydrate forming compound, FBN. We propose that the value from FBN-water titration to be the minimum cut-off for the apparent binding which indicate hydrate formation. We also suggest that any *K* value lower than the FBN-water titration value of 25 M^{-1} or ΔG bigger than -8.0 kJ mol^{-1}, would indicate that hydrate formation is not possible (Figure 6.57).

Table 6.10. All K_{21} and ΔG for all the probed compounds.

[H]:[G] binding model	K_{21}	ΔG
2DTA:H_2O	3005 M^{-1}	-19.8 kJ mol^{-1}
2CIM:H_2O	203 M^{-1}	-16.1 kJ mol^{-1}
2TRN:H_2O	60.22 M^{-1}	-10.2 kJ mol^{-1}
2PXM:H_2O	519.4 M^{-1}	-15.5 kJ mol^{-1}
2NAP:H_2O	9.88 M^{-1}	-5.7 kJ mol^{-1}
2PYZ:H_2O	18.0 M^{-1}	-7.1 kJ mol^{-1}
ACT:H_2O*	0.32 M^{-1}	3.2 kJ mol^{-1}
2DAP:H_2O	32.6 M^{-1}	-8.6 kJ mol^{-1}
2DPY:H_2O	35.3 M^{-1}	-8.8 kJ mol^{-1}
FBN:2H_2O**	25 M^{-1}	-8.0 kJ mol^{-1}
2PCM:H_2O***	157.4 M^{-1}	-12.5 kJ mol^{-1}

2PCMH_2O****:	80.0 M^{-1}	-10.9 kJ mol^{-1}

*ACT K_1, **FBN K_{12}, ***PCM K_{21}(NH only), ****PCM K_{21} (non-labile proton only)

6.4 References

1. Brogden, R. N., Pinder, R. M., Sawyer, P. R., Speight, T. M. & Avery, G. S. Naproxen. *Drugs* **9,** 326–363 (1975).

2. Chan, W. Y. Prostaglandins and Nonsteroidal Antiinflammatory Drugs in Dysmenorrhea. *Annu. Rev. Pharmacol. Toxicol.* **23,** 131–149 (1983).

3. Dahl, H. 8: Naproxen (Naprosyn®). Pharmacokinetics: therapeutical relevance and tolerance profile. *Cephalalgia* **6,** 68–75 (1986).

4. Song, J. S. & Sohn, Y. T. Crystal forms of naproxen. *Arch. Pharm. Res.* **34,** 87–90 (2011).

5. Yingjun, M. & Xiaoshu, W. Patent no: CN102276447B Naproxen hydrate crystal, preparation method thereof and medicinal composition containing naproxen hydrate crystal and sumatriptan. (2013).

6. Bernal, V., Erto, A., Giraldo, L. & Moreno-Piraján, J. C. Effect of solution pH on the adsorption of paracetamol on chemically modified activated carbons. *Molecules* **22,** 1–14 (2017).

7. Bernal, V., Erto, A., Giraldo, L. & Moreno-Piraján, J. Effect of Solution pH on the Adsorption of Paracetamol on Chemically Modified Activated Carbons. *Molecules* **22,** 1032 (2017).

8. Nichols, G. & Frampton, C. S. Physicochemical Characterization of the

Orthorhombic Polymorph of Paracetamol Crystallized from Solution. *J. Pharm. Sci.* **87,** 684–693 (1998).

9. Di Martino, P., Conflant, P., Drache, M., Huvenne, J.-P. & Guyot-Hermann, A.-M. Preparation and physical characterization of forms II and III of paracetamol. *J. Therm. Anal.* **48,** 447–458 (1997).

10. Perrin, M.-A., Neumann, M. A., Elmaleh, H. & Zaske, L. Crystal structure determination of the elusive paracetamol Form III. *Chem. Commun.* **0,** 3181 (2009).

11. Burger, A. Interpretation of polymorphism studies. *Acta Pharm. Technol.* **28,** 1–20 (1982).

12. Smith, S. J., Bishop, M. M., Montgomery, J. M., Hamilton, T. P. & Vohra, Y. K. Polymorphism in paracetamol: Evidence of additional forms IV and v at high pressure. *J. Phys. Chem. A* **118,** 6068–6077 (2014).

13. McGregor, P. A., Allan, D. R., Parsons, S. & Pulham, C. R. Preparation and crystal structure of a trihydrate of paracetamol. *J. Pharm. Sci.* **91,** 1308–1311 (2002).

14. Parkin, A., Parsons, S., Pulham, C. R. & IUCr. Paracetamol monohydrate at 150 K. *Acta Crystallogr. Sect. E Struct. Reports Online* **58,** 1345–1347 (2002).

15. Peterson, M. L. *et al.* Crystallization and transformation of acetaminophen trihydrate. *Cryst. Growth Des.* **3,** 761–765 (2003).

16. Fabbiani, F. P. A. *et al.* High-pressure recrystallisation—a route to new polymorphs and solvates. *CrystEngComm* **6,** 504–511 (2004).

17. Charisiadis, P. *et al.* 1H-NMR as a Structural and Analytical Tool of Intra- and Intermolecular Hydrogen Bonds of Phenol-Containing Natural Products and Model Compounds. *Molecules* **19,** 13643–13682 (2014).

18. Scheiner, S. & Kar, T. Red- versus blue-shifting hydrogen bonds: Are there fundamental distinctions? *J. Phys. Chem. A* **106,** 1784–1789 (2002).

19. Bajpai, A. *et al.* Towards an understanding of the propensity for crystalline hydrate formation by molecular compounds. *IUCrJ* **3,** 430–439 (2016).

20. *Pharmacopoeia Europaea 9.0*. (Deutscher Apotheker Verlag, 2016).

21. BNF: British National Formulary - NICE (Acetozalamide). *BNF* (2018). Available at: https://bnf.nice.org.uk/drug/acetazolamide.html. (Accessed: 9th January 2019)

22. Brayton, C. F. Dimethyl sulfoxide (DMSO): a review. *Cornell Vet.* **76,** 61–90 (1986).

23. Griesser, U. J., Burger, A. & Mereiter, K. The Polymorphic Drug Substances of the European Pharmacopoeia. Part 9. Physicochemical Properties and Crystal Structure of Acetazolamide Crystal Forms. *J. Pharm. Sci.* **86,** 352–358 (1997).

24. BNF: British National Formulary - NICE (Dapsone). *BNF* (2018). Available at: https://bnf.nice.org.uk/drug/dapsone.html. (Accessed: 11th January 2019)

25. Kuhnert-Brandstätter, M. & Moser, I. Zur Polymorphie von Dapson und Ethambutoldihydrochlorid. *Mikrochim. Acta* **71,** 125–136 (1979).

26. Yathirajan, H. S., Nagaraja, P., Nagaraj, B., Bhaskar, B. L. & Lynch, D. E. *CCDC 255853: Experimental Crystal Structure Determination*. *Cambridge Crystallographic Data Centre* (2007).

27. Bel'skii, V. K., Chernikova, N. Y., Rotaru, V. K. & Kruchinin, M. M. (. *Kristallografiya* 690 (1983).

28. Kuz'mina, L. G., Struchkov, Y. T., Novozhilova, N. V. & Tudorovskaya, G. L. (. *Kristallografiya* 695 (1981).

29. Braun, D. E. & Griesser, U. J. Supramolecular Organization of Nonstoichiometric Drug Hydrates: Dapsone. *Front. Chem.* **6,** 31 (2018).

30. Ouchi, M., Terashima, T. & Sawamoto, M. Transition Metal-Catalyzed Living Radical Polymerization: Toward Perfection in Catalysis and Precision Polymer Synthesis. *Chem. Rev.* **109,** 4963–5050 (2009).

31. Liu, G.-Z., Li, S.-H., Li, X.-L., Xin, L.-Y. & Wang, L.-Y. Three series of MOFs featuring various metal(ii)-carboxylate chains cross-linked by dipyridyl-typed coligands: synthesis, structure, and solvent-dependent luminescence. *CrystEngComm* **15,** 4571 (2013).

32. Slone, R. V., Hupp, J. T., Stern, C. L. & Albrecht-Schmitt, T. E. Self-Assembly of Luminescent Molecular Squares Featuring Octahedral Rhenium Corners. *Inorg. Chem.* **35,** 4096–4097 (1996).

33. Da Silva, P. A. B., De Souza, G. C. S., Paim, A. P. S. & Lavorante, A. F. Spectrophotometric determination of reducing sugar in wines employing in-line dialysis and a multicommuted flow analysis approach. *J. Chil. Chem. Soc.* **63,** 3994–4000 (2018).

34. Näther, C., Riedel, J. & Jeß, I. 4,4′-Bipyridine dihydrate at 130 K. *Acta Crystallogr. Sect. C Cryst. Struct. Commun.* **57,** 111–112 (2001).

35. Boag, N. M., Coward, K. M., Jones, A. C., Pemble, M. E. & Thompson, J. R. 4,4'-Bipyridyl at 203K. *Acta Crystallogr. Sect. C Cryst. Struct. Commun.* **55,** 672–674 (1999).

36. Bajpai, A. *et al.* Towards an understanding of the propensity for crystalline hydrate formation by molecular compounds. *IUCrJ* **3,** 430–439 (2016).

37. BNF: British National Formulary - NICE (Flurbiprofen). *BNF* (2018). Available at: https://bnf.nice.org.uk/drug/flurbiprofen.html. (Accessed: 4th February 2019)

38. Grzesiak, A. L. & Matzger, A. J. New form discovery for the analgesics flurbiprofen and sulindac facilitated by polymer-induced heteronucleation. *J. Pharm. Sci.* **96,** 2978–2986 (2007).

CHAPTER 7

EXTENDED USE OF THE TITRATION TECHNOLOGY: PROBING DIMETHYLFORMAMIDE SOLVATE FORMATION AND PROSPECTIVE SCREENING TOOL FOR PROTEIN BINDING FRAGMENTS

7.1 Introduction

The titration procedure used in chapter 5 and 6 is explored further by probing into its potential use to measure the interactions and binding strength between other uncharged host-guest molecules. Throughout this chapter, dimethylformamide (DMF, Figure 7.1) is used as the main guest instead of water, and observation is focused on the binding constant determination and pre-nucleation aggregates formation between the model compound and DMF. DMF is a polar aprotic, clear liquid that has been widely used in industries as a solvent, an additive, or an intermediate because of its extensive miscibility with water and most common organic solvents.[1] The density of DMF is 0.95 g cm^{-3} at 20 °C, which is similar to that of water.[1]

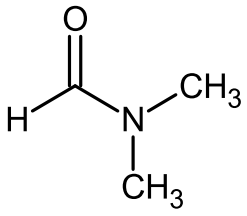


Figure 7.1. Chemical structure of DMF

Our initial interest in the pre-nucleation aggregates involving DMF is driven by the ability of our first model compound, a derivative of the tetrazole cycle, to form an extremely stable DMF solvate. The DMF solvate is claimed to persist even after passing through a silica gel column for purification after synthesis. A successful

connection between the extremely stable crystalline DMF solvate and ^{1}H-NMR titration would allow for the expansion of the used procedure to aid in the prediction of a stable solvate.

7.2 Results for the model compound: 4-(1H-Tetrazol-5-yl) phenol

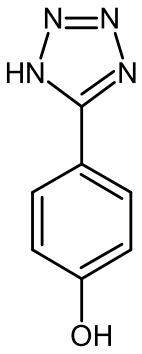


Figure 7.2. Chemical structure of 4-(1H-Tetrazol-5-yl) phenol

The 4-(1H-tetrazol-5-yl) phenol (TTZ, Figure *7.2*), which was used in our experiments was synthesised by Dr. Clinton Veale's group at the University of KwaZulu Natal in South Africa. The TTZ used is a derivative of the tetrazole cycle, which is a promising pharmacophore fragment frequently used in the development of physiologically active compound as well as novel drugs.[2–4]

Initial ^{1}H-NMR in DMSO-d_6 environment shows three chemical shift peaks corresponding to the OH of the phenol at 10.18 ppm (proton 1, ▲), the phenol protons at the ortho position, 7.85 ppm (doublet, proton 2, ■), and finally the phenol protons at the meta position, 6.95 ppm (doublet, proton 3, ∘), all of which are highlighted in Figure 7.3.

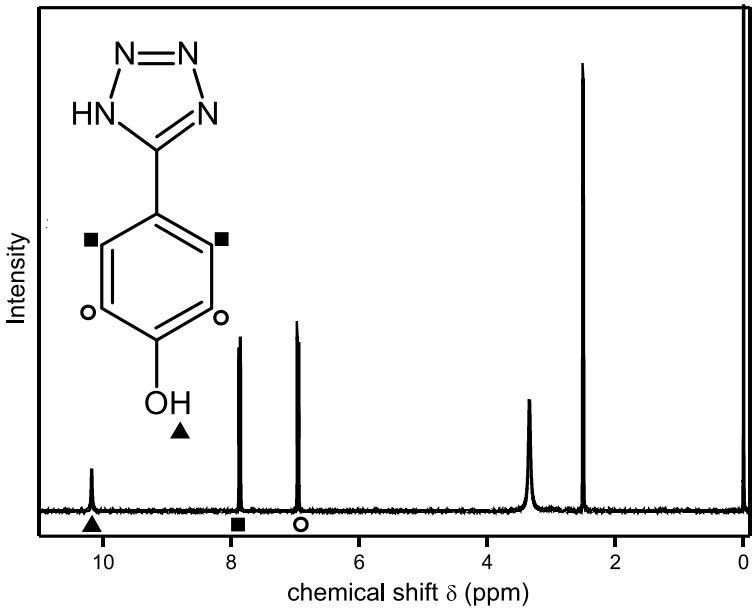


Figure 7.3. ^{1}H-NMR spectrum of TTZ in DMSO-d_6 environment. Specific chemical shift regions on the spectrum which are identified as proton 1 (▲), 2 (■) and 3 (○) are highlighted with the respective symbols and corresponding inset of the chemical structure.

7.2.1 TTZ ^{1}H-NMR dilution experiment

Similar to the previous approach (chapter 5 and 6), TTZ-water ^{1}H-NMR titration was done to investigate the binding affinity towards water as the compound has been reported to exist as a 1.5 hydrate.[5] Before the titration was performed, a quick dilution experiment was done to ensure that the subsequent peak shift observed, if any does occur, is a result from the titration experiment, and not the effect of dilution. For the dilution experiment, the three mentioned protons of TTZ in DMSO-d_6 are monitored, with only two points checked - one with no guest, and the other with 450:1, G:H ratio of the main solvent. Three separate tubes with the same stock were used to account for measurement error. Dilution with anhydrous, non-deuterated DMSO showed an overall upfield shift to the three observable protons, with the biggest shift close to -0.01 ppm observed to proton 1. The remaining protons showed a similar peak shift magnitude of -0.0016 ppm which is not significant based on our cut-off of ±0.002

ppm. The shift magnitude and direction of proton 1 in the dilution experiment is considered during the analysis of the subsequent titration experiment.

Table 7.1. Dilution effect of TTZ with 450 molar equivalents of anhydrous DMSO

Tube number (G ratio)	Proton 1	Proton 2	Proton 3,
Average Δδ at 0:1 DMSO: TTZ ratio	10.1755	7.8747	6.9665
Average Δδ at 0:450 DMSO: TTZ ratio	10.1656	7.8731	6.9649
Average shift difference	**-0.0099**	**-0.0016**	**-0.0016**

7.2.2 TTZ-water ^{1}H-NMR titration in DMSO-d_6

The subsequent TTZ-water titration from 0-450:1 G:H molar ratio reveals that all the observed peaks underwent a downfield shift, with the biggest shift occurring to proton 1 (▲), which has shifted by +0.335 ppm (Figure 7.4). Compared to the dilution data, the peak shift recorded for the same proton was just -0.01 ppm and the shift was towards the opposite direction. Therefore, the large, significant peak shift observed in the titration experiment represent true interaction with water and suggest that OH of the phenol is the most likely interaction point to water in the DMSO-d_6 solution. In addition, significant shifts are also observed to proton 2 (■) and 3 (∘) which has shifted by +0.0127 and +0.0316 ppm, respectively (Figure 7.4). The larger shift to proton 3 is consistent with the close proximity of this proton to the mentioned interaction point, proton 1 as seen in our previous titration. Scatter plot of the three protons peak shifts revealed an almost linear curve with the increasing water molar ratios (Figure 7.5 and Figure 7.6).

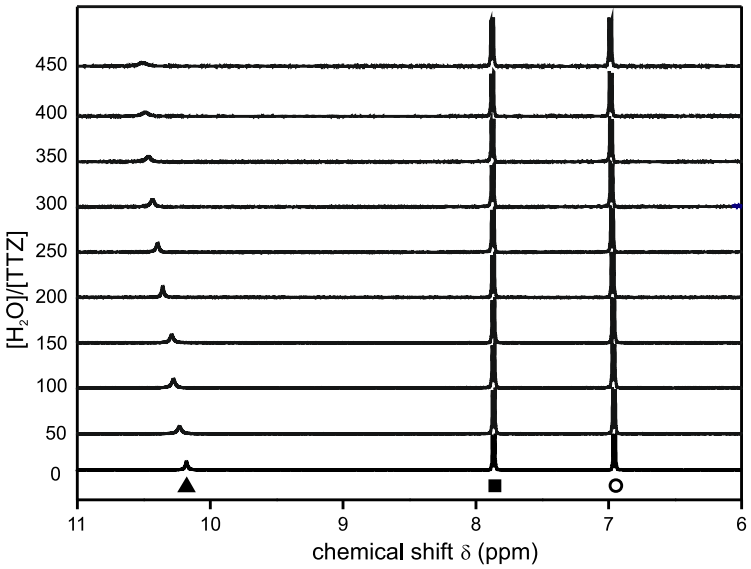


Figure 7.4. ^{1}H-NMR chemical shift region for proton 1, 2 and 3 and their respective peak shifts following water titration at 50 molar ratio gaps.

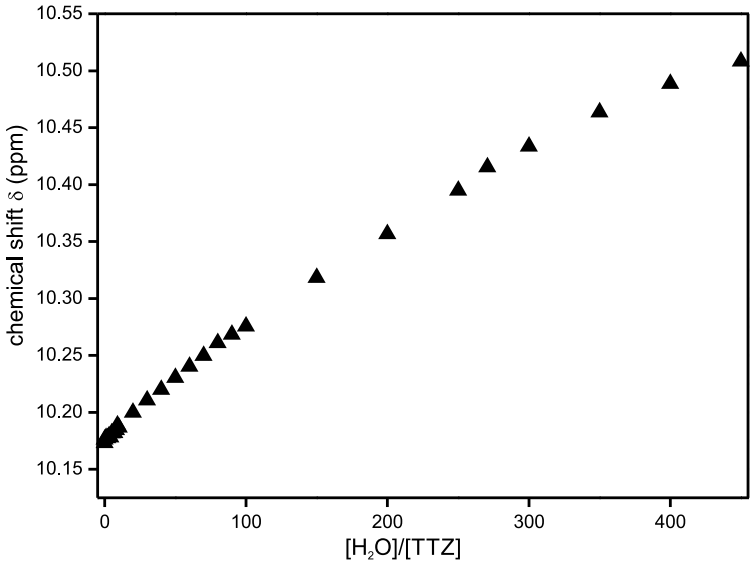


Figure 7.5. The scatter plot corresponding to the peak shift of proton 1 following water titration up to 450 molar ratios.

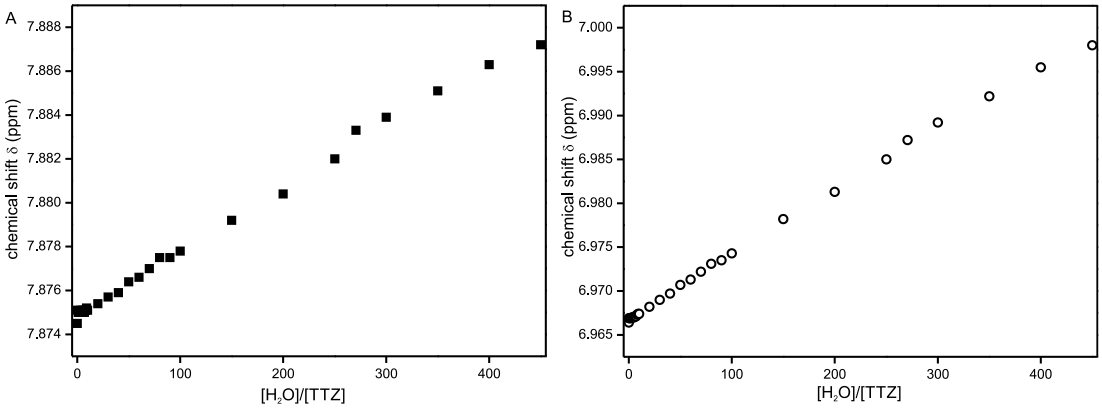


Figure 7.6. The scatter plot corresponding to the peak shift of proton 2 (A) and 3 (B) following water titration up to 450 molar ratios.

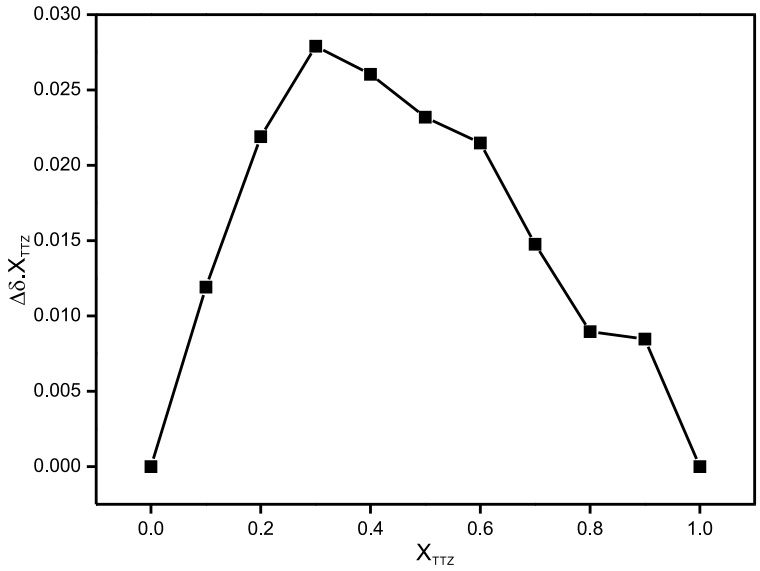


Figure 7.7. Job plot of TTZ-water interaction suggesting the stoichiometry of interaction as 1:2, with X_{max}= 0.3

Job plot for TTZ-water interaction reveals that the stoichiometry of interaction is 1:2, with a left-skewed plot and X_{max}= 0.3. The Job plot here acts only as a guide as mentioned previously, the outcome is not reflective of the real interactions in our study. The best fit, which generates the least error between our data points and the modelled curve, is to the 1:1 model, with a *K* value of 0.06 M^{-1}. However, this value is too low for a significant interaction, as we have seen from the actual chemical peak shift, especially of proton 1 (▲). Since we are confident that the interaction is not random, follow up interpretation is based on the next best fit, which is to the 2:1

stoichiometry model (Table 7.2), which yielded the largest *K* value obtained in the form of the K_{21}, with 2155 M^{-1} calculated from the fitted data. The K_{21} value translates into ΔG of -19 kJ mol^{-1}. The obtained K_{21} and ΔG values are consistent with the values for stable hydrate obtained in chapter 5, and when placed on our hydrate gauge, it is indeed in the hydrate-form. Based on our predicted data, TTZ can exists as a stable hydrate form, which may or may not be the reported 1.5 hydrate as the stability of the reported hydrate remains unknown. The other *K* and ΔG values from the fitting to the different models are listed in Table 7.2.

Table 7.2. Calculated ΔG of TTZ-water binding in DMSO-d_6 environment based on three (3) different binding models.

[H]:[G] binding model	K_1 (±% error)	K_{21} (±% error)	K_{12} (±% error)	ΔG for K_{21}
TTZ:H_2O	0.06 M^{-1} (±0.7%)	N/A	N/A	+7.8 kJ mol^{-1}
2TTZ:H_2O	3.5 x 10^{-4} M^{-1} (±4.5%)	**2155 M^{-1}** (±3.5%)	N/A	**-19 kJ mol^{-1}**
TTZ:2H_2O	14 M^{-1} (±29%)	N/A	0.05 M^{-1} (±0.8%)	-7.3 kJ mol^{-1}

7.2.3 TTZ-DMF ^{1}H-NMR titration in DMSO-d_6

It has come to our knowledge that TTZ can form an extremely stable DMF solvate. Hence TTZ is the ideal model compound to apply our titration method and probe whether the same technique can be extended for stable solvate prediction. Similar to the TTZ-water titration (Figure 7.5 and Figure 7.6), proton 1 (▲), proton 2 (▪) and 3 (∘) all showed downfield shifts, with scatter plot showing almost linear

curve. However, the magnitude of the peak shifts between the two titration are different, showing significantly lower shift in proton 1, while higher shifts in proton 2 and 3 (Table 7.3).

Table 7.3. Comparison between the peak shift magnitude in water and DMF titration in DMSO environment

Titration range	Proton 1 (ppm)	Proton 2 (ppm)	Proton 3(ppm)
0-450:1 H_2O:TTZ titration	+0.335	+0.0127	+0.0316
0-450:1 DMF:TTZ titration	+0.0771	+0.0743	+0.0564

As a consequence, global fitting of the three protons' peaks shift from the titration of DMF in DMSO-d_6 has resulted in low *K* and high ΔG. The smallest ΔG obtained was from the best fitting of all monitored protons to a 1:2 model, with -8.8 kJ mol^{-1}. The value is considerably high compared to the -19 kJ mol^{-1} obtained from water titration. The unclear result suggests that TTZ-DMF interaction in DMSO environment is present, but limited. It is unclear to what could be the reason. To date no TTZ-DMSO solvate has been reported, and the existence of such solvate form could be one of the limiting factor.

[H]:[G] binding model	K_1 (±% error)	K_{21} (±% error)	K_{12} (±% error)	ΔG for K_{21}
TTZ:DMF	9 x 10^{-3} M^{-1} (±2%)	N/A	N/A	+11.7 kJ mol^{-1}

2TTZ:DMF	$-4.5 \times 10^{-2}\ M^{-1}$ (±2.3%)	$2.7\ M^{-1}$ (±1.3%)	N/A	$-2.5\ kJ\ mol^{-1}$
TTZ:2DMF	$1.8 \times 10^{-4}\ M^{-1}$ (±3.2%)	N/A	$34.9\ M^{-1}$ (±21.5%)	$-8.8\ kJ\ mol^{-1}$

Since we observed good TTZ-water interaction before (7.2.2), a repeat in DMF-d_7 environment will confirm the complex's stability in solution. While properties of water have been discussed in detail in chapter 1, the binary solution mixture of DMF and water is yet to be mentioned. DMF-water mixing process is exothermic for all concentrations, which is a result of hydrogen bond formation reported to occur *via* the carbonilic oxygen of the amide and the molecules of water,[6] later confirmed by Raman spectroscopy.[7] Hydrogen bonds between water and the carbonyl oxygen of DMF molecule are stronger than those between water molecules, and this effect is strengthened by the nitrogen atom due to the resonance structure of DMF.[8] Water is well known to be highly structured in its pure liquid state. The introduction of DMF into a pure aqueous solution therefore causes disruption to the specific structure effects of pure water and leading to the absence of these structures.[9]

7.2.4 TTZ ^{1}H-NMR cross-titration with water and DMF: Part I

^{1}H-NMR TTZ-water titration has shown that TTZ has a strong affinity to water, which is reflective to the compound's ability to exist as a hydrate form. Therefore, it is most likely that in a D_2O solution environment, TTZ-water aggregates would be the main species present in solution. A TTZ cross-titration with water and DMF in the respective opposite solvent environment was done in order to compare the affinity of TTZ to the respective guests. TTZ-water titration in DMF-d_7 environment would ascertain whether TTZ's affinity towards water is preserved, while the cross-titration

in D_2O environment would establish whether a stronger affinity towards DMF is present-again due to the claimed existence of the extremely stable DMF solvate. A greater affinity towards DMF would mean the DMF could displace TTZ-water aggregates in solution and form TTZ-DMF complex and *vice versa*.

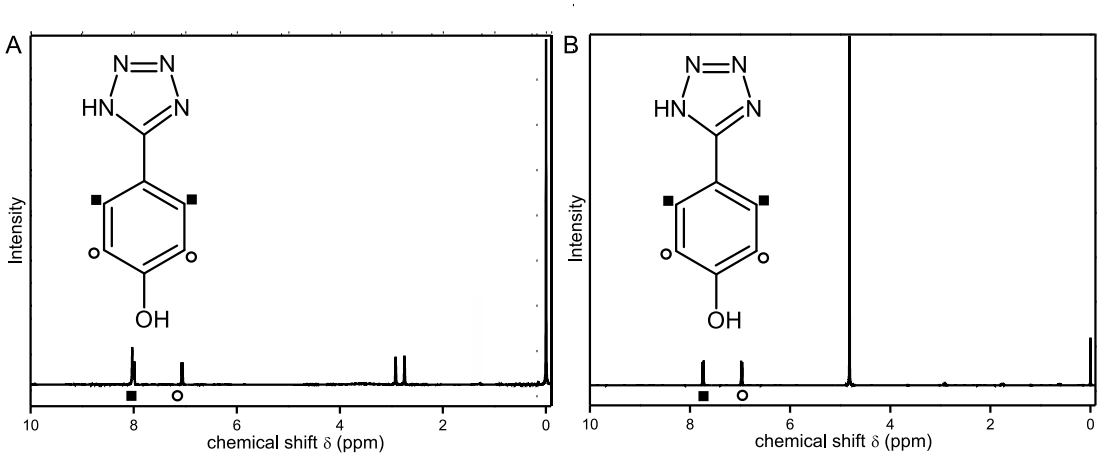


Figure 7.8. The peaks of TTZ in DMF environment for water titration (**A**). The peaks of TTZ in D_2O environment for DMF titration (**B**). The calibration standard used in **A** is TMS while in **B** DSS, both showing peak at 0.00 ppm.

The monitored protons of TTZ in DMF-d_7 and D_2O environments are highlighted in Figure 7.8, with two chemical shift regions representing the 4 protons of TTZ. The protons at the ortho position (proton 1, ■) appear at 7.99 ppm while the protons at the meta (proton 2, ∘) at 7.05 ppm in DMF-d_7 environment. Meanwhile, in D_2O solution, the mentioned peaks appear at 7.74 and 6.97 ppm respectively. DMF-d_7 peaks appear at three chemical shift regions, 8.02 (singlet), 2.92 (quintet) and 2.75 ppm (quintet), while D_2O appears as a single peak at 4.8 ppm. Note that the calibration standard used for TTZ-DMF titration in the D_2O environment is 4,4-dimethyl-4-silapentane-1-sulfonic acid (DSS), which is similar to tetramethylsilane (TMS, used in DMF-d_7), but with much higher water solubility. The proton spectrum of DSS also exhibits minor peaks at 2.91 ppm (triplet), 1.75 ppm (nonet), and 0.63 ppm (triplet) at

an intensity of 22% of the reference peak at 0 ppm which do not shift and the peak does not interfere with our observation as well.

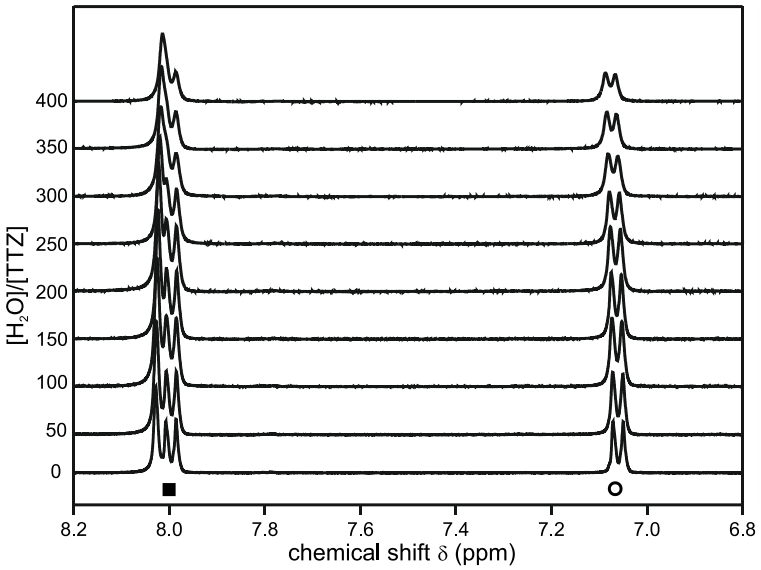


Figure 7.9. 0.02 M TTZ-H_2O titration in a deuterated DMF-d_7 environment up to 400:1 G:H ratio.

TTZ-water titration in DMF-d_7 environment also saw two split peaks corresponding to the two protons on the ortho (proton 1) and meta (proton 2) position respectively (Figure 7.9). In addition, DMF-d_7 single peak appeared in close proximity to proton 1, and eventually overlaps at higher DMF:H molar ratio. The OH and NH are not detectable due to the fast exchange nature of the proton in a water environment. The scatter plot following 50 molar ratio gaps of water titration from 0-400:1 G:H ratio shows an erratic and inconsistently peak shifts of proton 1 (■), with an overall non-significant change observed (±0.001 ppm), while proton 2 (○) at the meta position shows significantly larger change, shifting in almost a linear manner by +0.0165 ppm at the end of the titration (Figure 7.10). The irregular plot observed in proton 1 is due to the very small peak shift, which indicates that the proton's electronic environment is least affected of the two by water inclusion. The different shift magnitude of proton 1 and 2, suggest that proton 2 is at a closer proximity to the actual interaction site,

hence experiencing a larger electron re-arrangement and deshielding effect. TTZ-water complexation is, therefore, most likely to take place *via* the OH functionality, which corresponds well the previous TTZ-water titration data in DMSO-d_6 environment where a larger peak shift is also observed for the meta positioned proton 3 (+0.0316 ppm), compared to the ortho positioned proton 2 (+0.0127 ppm). The overall weaker peak shift magnitude correlates with a lower TTZ affinity towards the water in a DMF-d_7 environment.

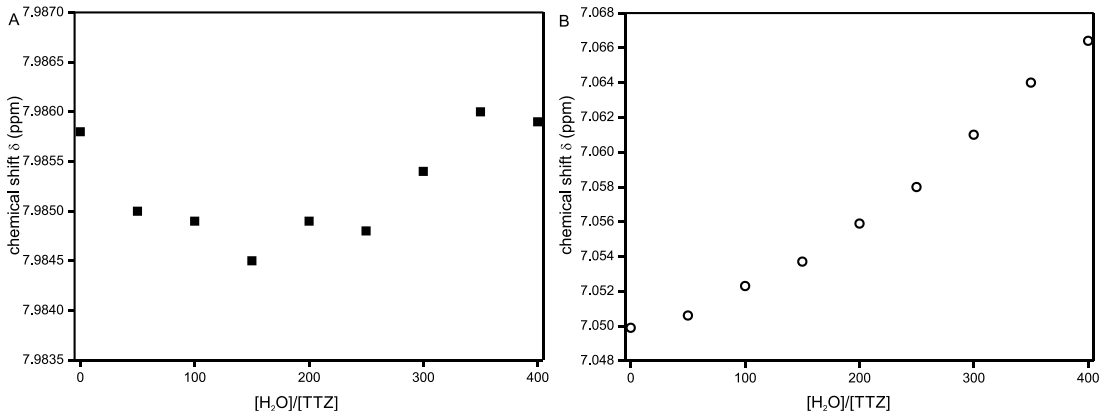


Figure 7.10. **A** shows the scatter plot for peak shift of proton at the ortho position, while **B** shows the scatter plot for peak shift of proton at meta position on TTZ benzene ring for TTZ-water titration in DMF-d_7 environment.

As stated, the peak shift magnitude of proton 2 (∘) is just +0.0165 at 400:1 G:H. Such shift would translate into very small peak shift in Job plot analysis, hence the Job plot is deemed unnecessary in this iteration of the procedure. In addition, the Job plot data thus far failed to reflect and represent the true interaction stoichiometry of our titration experiment data. The best fitting of our data to the available mathematical model guides the interpretation, ignoring the speciation of the host, guest and their complexes as again, the figures obtained are only an apparent representation of the true interaction. The weak peak shifts following TTZ-water titration in DMF-d_7 solvent translate into weak and non-significant *K* values based on the 1:1, 2:1 and 1:2

fitting (Table 7.4). The largest *K* value obtained from the fitting of all the monitored protons' peaks shift of TTZ in DMF-d_7 environment is the K_{21}, with just 4.7 M^{-1}, and a calculated ΔG of -3.8 kJ mol^{-1}. Based on the *K* and ΔG values, it is safe to say that TTZ-water complexation is blocked, inhibited or simply does not take place in the presence large quantities of DMF, which also hints towards a strong TTZ-DMF association.

Table 7.4. Calculated ΔG of TTZ-water binding in the DMF-d_7 environment based on three (3) different binding models.

[H]:[G] binding model	K_1 (±% error)	K_{21} (±% error)	K_{12} (±% error)	ΔG for K_{21}
TTZ:H_2O	7.7 x $10^{-7}M^{-1}$ (±0.02%)	N/A	N/A	+39 kJ mol^{-1}
2TTZ:H_2O	3.3 x 10^{-2} M^{-1} (±4.2%)	4.7 M^{-1} (±1.7%)	N/A	-3.8 kJ mol^{-1}
TTZ:2H_2O	0.15 M^{-1} (±11.7%)	N/A	-7.6 x 10^{-3} M^{-1} (±-6.5%)	N/A kJ mol^{-1}

7.2.5 TTZ ^{1}H-NMR cross-titration with water and DMF: Part II

Subsequent TTZ-DMF-d_7 titration in D_2O environment also saw an overall downfield shift, but in contrast, a significant peak shifts are observed to both the ortho (▪, proton 1) and meta (∘, proton 2) protons of TTZ between 0-400:1 G:H ratio (Figure 7.11). Unlike the water titration, a larger peak shift is observed to the ortho positioned proton 1, with a downfield peak shift recorded of +0.215 ppm from 0-400:1 G:H ratio. Meanwhile, for proton 2, the peak shift recorded is +0.128 ppm, which is also significant and strong shift. The different peak shift magnitude between proton 1 and 2, suggest that the interaction point between TTZ and DMF is much closer to proton

1, which points towards the NH on the 5-member ring of four nitrogen atoms (the tetrazole group). The overall larger shift observed in TTZ-DMF titration compared to TTZ-water titration in the respective opposite solvent environments, suggests a higher affinity to DMF-d_7. Moreover, the overwhelmingly higher affinity to DMF is clear, and is able to displace TTZ-water species in water environment, considering the strong interaction observed earlier between TTZ and water. The scatter plot of the two monitored peaks reveals a curved plot and a plateau feature, with increasing G:H ratio (Figure 7.12).

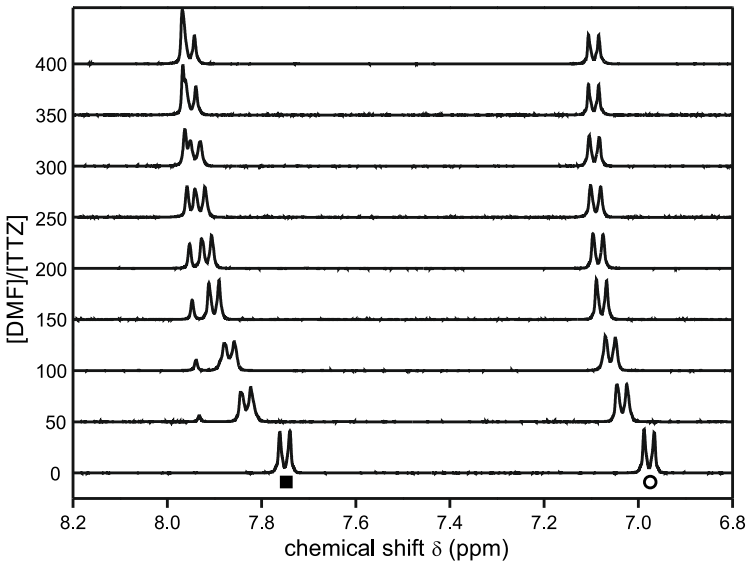


Figure 7.11. 0.02 M TTZ-DMF-d_7 titration in a deuterated water environment up to 400:1 G:H ratio. Note that the chemical shift scale is similar to that of Figure 9.

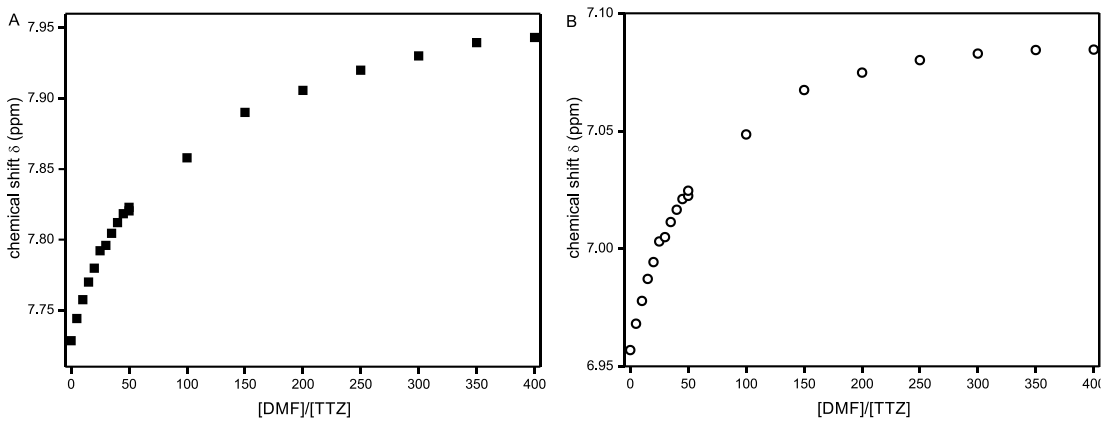


Figure 7.12. **A** shows the scatter plot for peak shift of proton at the ortho position, while **B** shows the scatter plot for peak shift of proton at meta position on TTZ benzene ring for TTZ-DMF titration in D_2O environment.

Job's plot for TTZ-DMF interaction in D_2O solution revealed similar stoichiometry to the TTZ-water interaction in DMSO-d_6 environment where 1:2 interaction stoichiometry is favoured (X_{max}=0.4). However, the best fitting of the three available binding models is the 2:1 stoichiometry, again, similar to TTZ-water titration earlier.

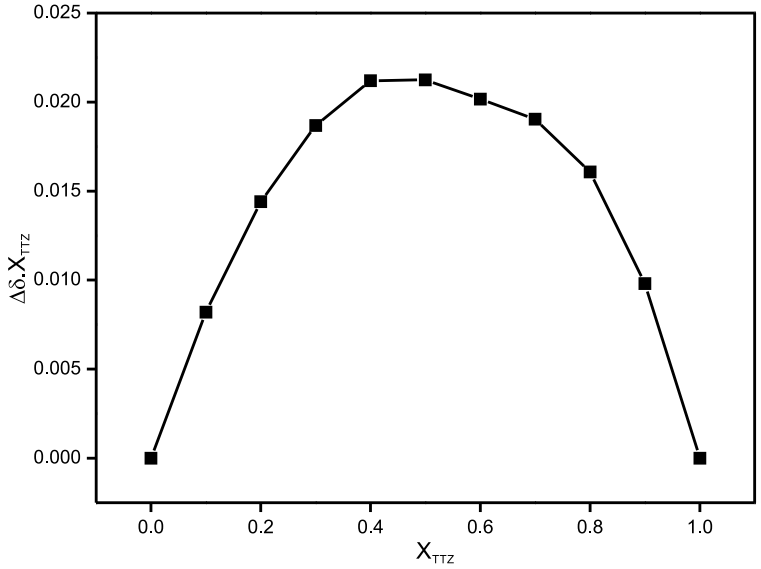


Figure 7.13. Job plot of TTZ-DMF-d_7 interaction suggesting the stoichiometry of interaction as 1:2, with X_{max}= 0.4

Table 7.5. Calculated ΔG of TTZ-DMF-d_7 binding in D_2O environment based on three (3) different binding models.

[H]:[G] binding model	K_1 (±% error)	K_{21} (±% error)	K_{12} (±% error)	ΔG for K_{21}
TTZ:DMF	0.65 M^{-1} (±3.4%)	N/A	N/A	+1.2 kJ mol^{-1}
2TTZ:DMF	5.2 x 10^{-3} M^{-1} (±4.2%)	**2229 M^{-1}** (±3.1%)	N/A	**-19.1 kJ mol^{-1}**
TTZ:2DMF	0.84 M^{-1} (±2.3%)	N/A	4.1 x 10^{-2} M^{-1} (±6.5%)	+8.9 kJ mol^{-1}

The K_{21} value generated is impressive considering TTZ and water did show high affinity towards one another following titration in DMSO. The corresponding ΔG value of -19.1 kJ mol^{-1} obtained for TTZ-DMF is significant and is comparable to the ΔG calculated for TTZ-water titration in DMSO-d_6, which is -19.0 kJ mol^{-1}. The large *K* and ΔG acquired in D_2O environment suggests a much stronger affinity to DMF *vs.* water displacing TTZ-water aggregates and forming TTZ-DMF pre-nucleation complexes, which supports the existence of the reported extremely stable DMF solvate. In addition, the shift, or the lack of it, in TTZ-water cross-titration experiment in DMF-d_7 environment provide further evidence which reiterate the earlier notion of a stronger TTZ-DMF pre-nucleation aggregates formation.

7.2.6 ^{1}H-NMR TTZ-DMF titration in an acetone-d_6 environment

A third TTZ-DMF titration was repeated in acetone-d_6 to confirm that the *K* and ΔG values obtained from the titration in D_2O environment was reproducible. In the acetone-d_6 environment, deuterated and protiated anhydrous DMF were used as guests in two separate titrations. The two setup were done to compare whether the

deuteration status of the guests bares any impact on the peak shift and subsequent *K* and ΔG values. In the protiated DMF setup (Figure 7.14A), a single massive DMF peak overlaps with the proton peak at the ortho position (■, proton 1), while the same peak is covered by TTZ peak due to its lower intensity in DMF-d_7 setup. Therefore, monitoring of the peak shift of the obstructed proton 1 in protiated DMF titration (Figure 7.14A) was possible following titration using DMF-d7 (Figure 7.14B). Proton 1 did not show significant peak shift following titration with just +0.0009 ppm recorded at 100:1 G:H ratio. Meanwhile. similar effect was observed to the proton at the meta position (∘, proton 2)in both protiated and deuterated solvents. DMF titration causes proton 2 peak to shift upfield, suggesting that the proton gain electron density, and undergo shielding effect.

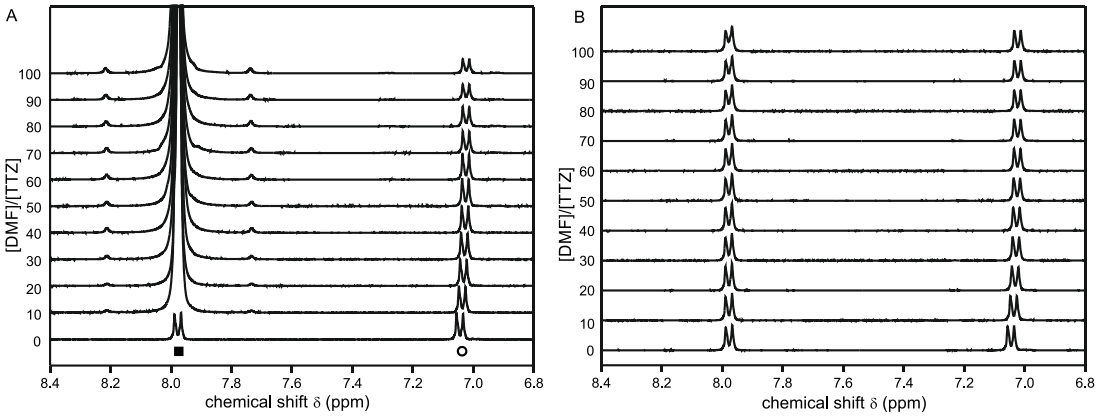


Figure 7.14. 0.02 M TTZ-DMF titration (A) protiated DMF and (B) DMF-d_7 in acetone-d_6 environment, up to 100:1 G:H ratio.

In acetone environment, TTZ-DMF complexation occurs directly *via* the carbonyl of the DMF as it acts as a proton acceptor by forming a hydrogen bond with TTZ through the functional group (OH), as more influence from the complexation is observed in the peak shift of the proton at the meta position (∘, proton 2) which shows

a significantly large upfield shift of -0.021ppm in protiated setup, and -0.022 ppm in deuterated setup at 100:1 G:H ratio (Figure 7.15).

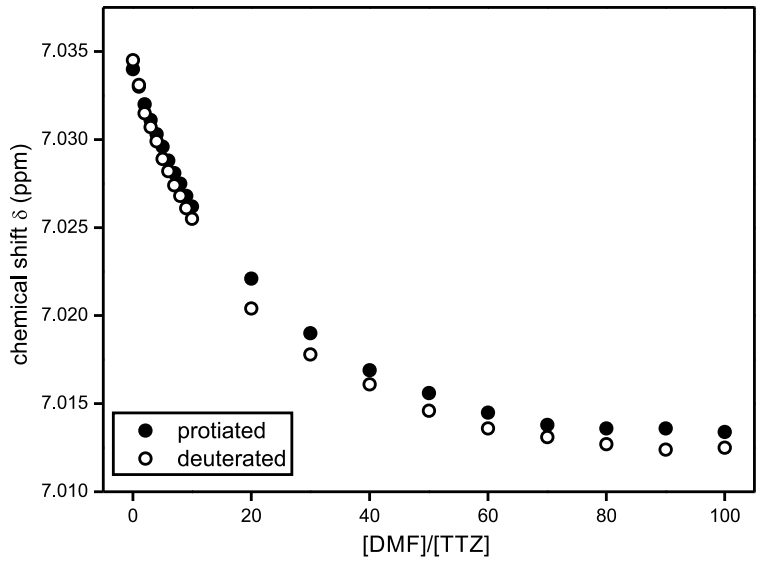


Figure 7.15. The scatter plot for peak shift of proton at meta position (proton 2) on TTZ benzene ring for TTZ-DMF titration (protiated and deuterated) in the acetone-d_6 environment.

As mentioned in earlier chapters, the direction of the shift is not much of a concern in determining the binding association between the components, as either upfield or downfield peak shift would correspond to the complexation to the titrated guest. Following DMF titration, proton 2 peak shift reaches significance (-0.002 ppm) early on at 2:1 G:H ratio (Figure 7.15), signalling a strong affinity to DMF.

Table 7.6. Calculated ΔG of TTZ- protiated* and DMF-d_7 binding in an acetone-d_6 environment based on proton 2 fitting to three (3) different binding models.

[H]:[G] binding model	K_1 (±% error)	K_{21} (±% error)	K_{12} (±% error)	ΔG for K_{21}
TTZ:DMF*	2.2 M^{-1} (±3.5%)	N/A	N/A	-2.2 kJ mol^{-1}
2TTZ:DMF*	0.02 M^{-1} (±2.2%)	**1057 M^{-1}** (±0.7%)	N/A	**-17.25 kJ mol^{-1}**

TTZ:2DMF*	1.5 M^{-1} (±1.4%)	N/A	-0.36 M^{-1} (±-2.0%)	N/A kJ mol^{-1}
TTZ:DMF-d_7	2.8 M^{-1} (±3.5%)	N/A	N/A	-2.2 kJ mol^{-1}
2TTZ:DMF-d_7	0.025 M^{-1} (±3.1%)	**1145 M^{-1}** (±0.99%)	N/A	**-17.45 kJ mol^{-1}**
TTZ:2DMF-d_7	2.16 M^{-1} (±2%)	N/A	-0.36 M^{-1} (±-2.9%)	N/A kJ mol^{-1}

The best fitting for TTZ-DMF interaction in acetone-d_6 is to the 2:1 model, generating a significant K_{21} value of 1057 M^{-1}, which translates into -17.25 kJ mol^{-1} in ΔG. Meanwhile, the fitting of 2 in the titration with DMF-d_7, yielded a K_{21} value of M^{-1}, which translates into -17.45 kJ mol^{-1}. Interestingly, both titration yielded comparable *K* values, and more importantly, the calculated ΔG values, which are still significantly large and reflect well to the presence of the stable DMF-TTZ pre-aggregation complex in solution.

7.2.7 TTZ-DMF ^{1}H-NMR titration in water environment MD simulation

Since Job's plot was not able to show us the speciation of the interacting components for most of our titration analysis, MD simulation is done to highlight the interacting species in solution.

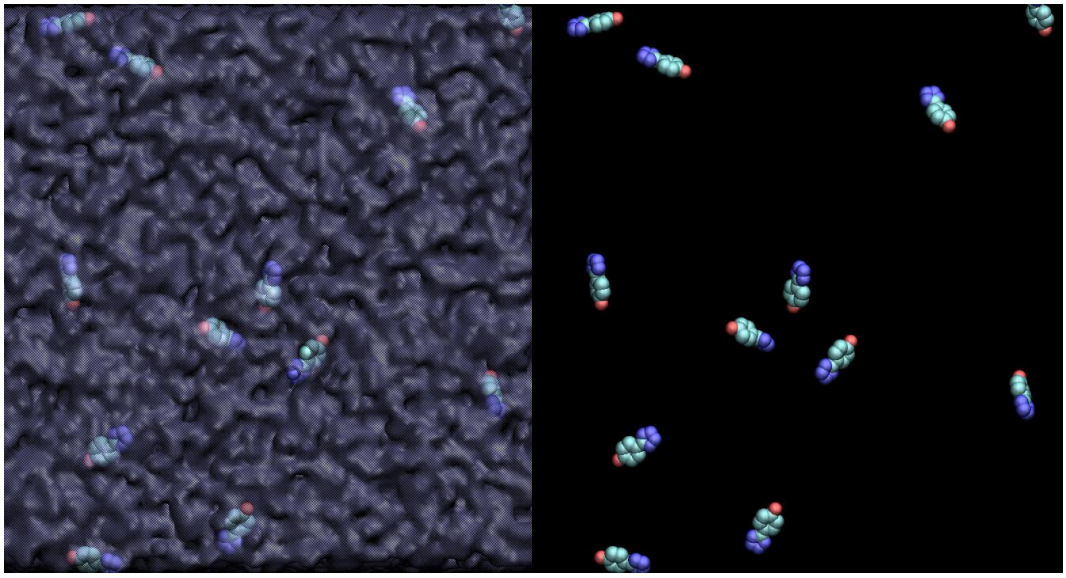


Figure 7.16. TTZ in aqueous solution TTZ in vdW representation (cyan carbon atoms). Water on the left displayed as a blue continuous surface. Right: detail of TTZ molecule placement in the periodic cell (water molecules are not displayed).

The 5:1 DMF:TTZ molar ratio system was chosen as the starting point for DMF introduction in the MD simulation as we have seen significant shift of +0.016 ppm from our NMR titration at this G:H ratio. Comparison between the first two MD figures (Figure 7.16 and Figure 7.17) clearly show the affinity of TTZ towards DMF, as from the 12 TTZ molecules in the simulated box (Figure 7.16), ½ of them have bonded to DMF in Figure 7.17. The observed interaction however is not limited to 1:1 interaction as not only 1:1 (red circle, Figure 7.17) was observed, but 1:2 (light blue circle, Figure 7.17), 2:2 (green circle), 1:3 (yellow circle, Figure 7.17) and TTZ dimer (orange circle, Figure 7.17) complexations were also observed.

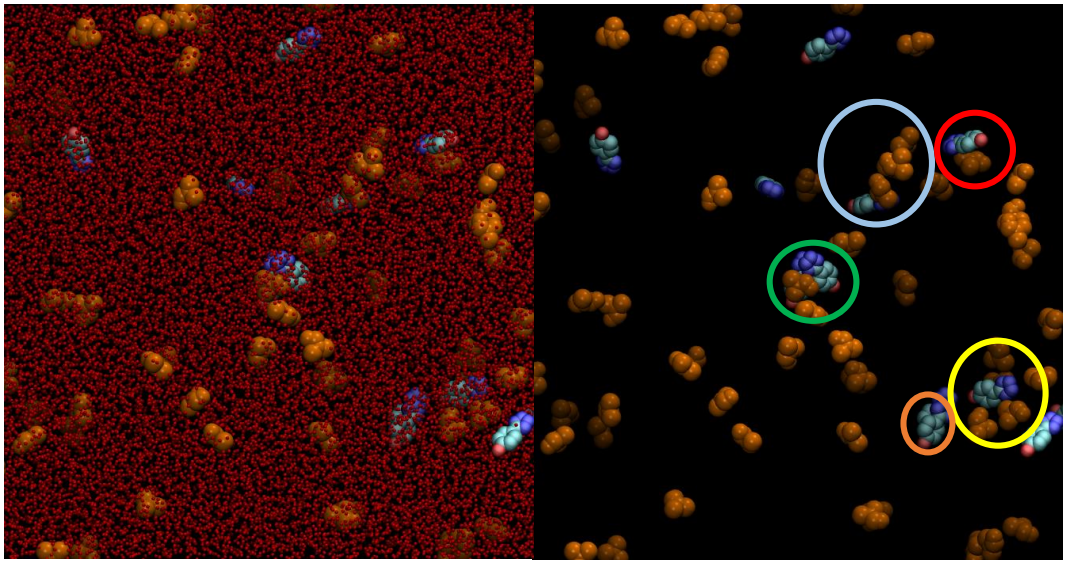


Figure 7.17. TTZ/DMF (5 eq.) system in water. TTZ (cyan carbon atoms) and DMF (all atom in orange) in vdW representation. Water in CPK representation (oxygen atoms only, in red). Right: TTZ/DMF molecules placement in the periodic cell (water molecules are not displayed).

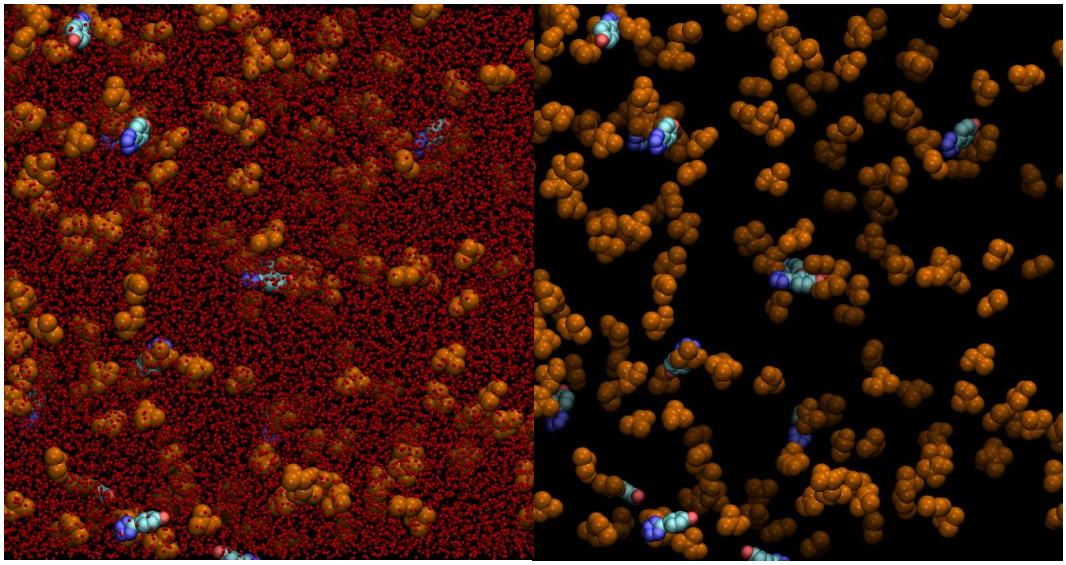


Figure 7.18. TTZ/DMF (15 eq.) system in water. TTZ (cyan carbon atoms) and DMF (all atom in orange) in vdW representation. Water in CPK representation (oxygen atoms only, in red). Right: TTZ/DMF molecules placement in the periodic cell (water molecules are not displayed).

In the 15:1 DMF:TTZ molar ratio system (Figure 7.18), no free TTZ molecule was observed. This trend continues in the subsequent 25-50:1 DMF:TTZ molar ratio system (Figure 7.19 to Figure 7.20).

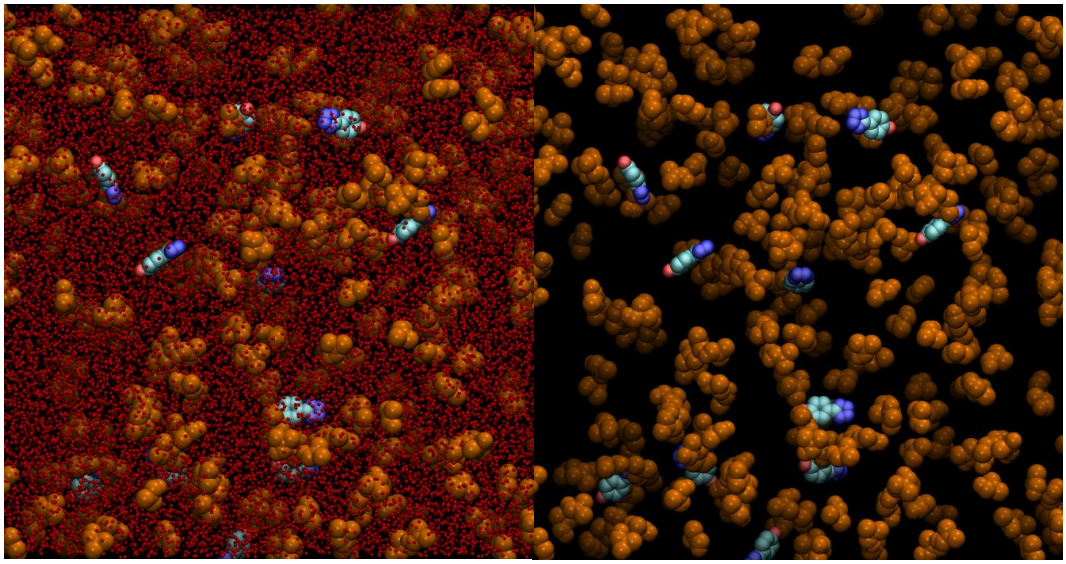


Figure 7.19. TTZ/DMF (25 eq.) system in water. TTZ (cyan carbon atoms) and DMF (all atom in orange) in vdW representation. Water in CPK representation (oxygen atoms only, in red). Right: TTZ/DMF molecules placement in the periodic cell (water molecules are not displayed).

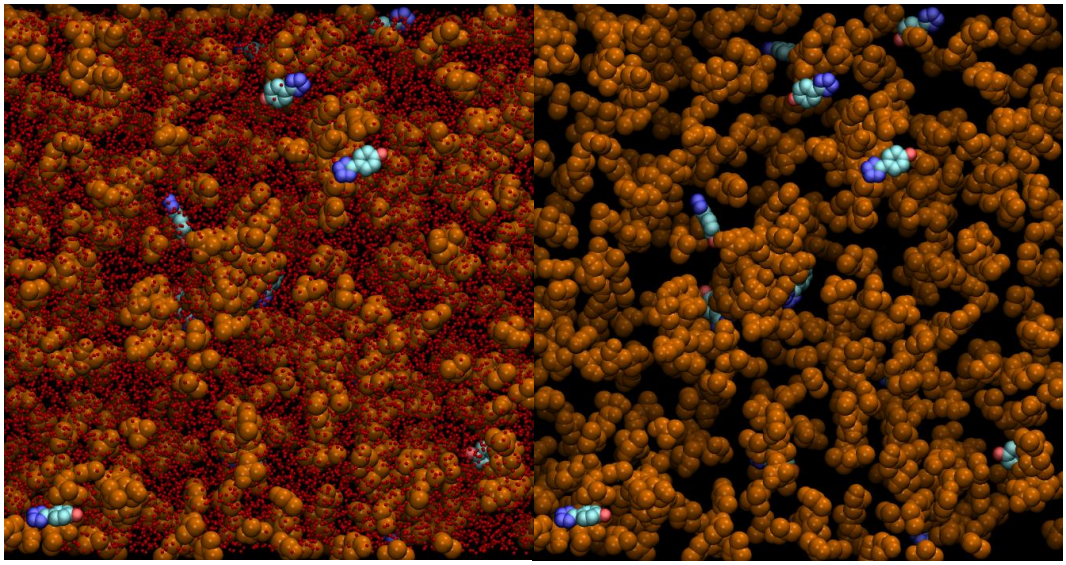


Figure 7.20. TTZ/DMF (50 eq.) system in water. TTZ (cyan carbon atoms) and DMF (all atom in orange) in vdW representation. Water in CPK representation (oxygen atoms only, in red). Right: TTZ/DMF molecules placement in the periodic cell (water molecules are not displayed).

MD simulation (Figure 7.17-Figure 7.20) corresponds well to our assumption that in a dilute aqueous solution, there is no single species of TTZ-DMF complex would dominate the interaction space, but rather clusters of mixed 1:1, 1:2, 2:1 and

etc. are present simultaneously. The simulation also re-affirms our earlier statement that the binding measured thus far is an apparent value, based on the apparent stoichiometry.

7.3 DMF as a prospective proteomimetic agent

Since our method was able to measure the apparent binding for a stable DMF solvate, the potential to further expand the method's usage to quantify protein-binding preferency through DMF titration is probed. DMF has been reported to have protein-like property. The proteomimetic property of DMF has been first suggested by Nozaki and Tanford, which stated that the DMF solvent could be used as a reasonable model for the interior of globular proteins. They reported that the polypeptide backbone CONH groups and apolar hydrocarbon side-chain groups create an amide-like surrounding,[10] which view is later supported by the statistical investigation by Roberts and Bohacek on side chain-side chain contacts between amino acid residues in proteins.[11] It has been mentioned later that amides can serve as model compounds for the investigations of the properties of peptides in aqueous solution.[12,13] Due to its amide-like and to an extent, proteomimetic properties, it is highly plausible to explore the use of DMF to predict strong protein-binding compound or fragments by using our titration method. Therefore, in addition to the mentioned primary aim, a follow-up probe is designed to assess the potential use of DMF as a proteomimetic agent though a series of tests with several compounds having different protein binding ability. Though protein binding is highly specific, our titration goal is only as a preliminary screen between a drug fragment to a generic protein. A successful connection will speed up the fragment screening and selection significantly. A series of DMF titration experiments, similar to that of the blind test in chapter 6 was designed to investigate

whether DMF titration can be used to reflect the four selected test compounds' protein binding ability. Information on the respective compounds' protein affinity is blocked and prediction is done based on the significant *K* and ΔG values, which is set based on the initial TTZ-DMF titration. The significance *K* value is set to be in the range of 1000- 2000 M^{-1} for DMF titration in D_2O or acetone-d_6 environment, which translate into a ΔG of -17 to 19 kJ mol^{-1}. Job's plot is not done for any of the protein/DMF binding test compounds and the best fitting to the available mathematical model guides our data analysis and interpretation. Successful implementation of the procedure with DMF as the guest could potentially serve as a screening tool for promising pharmacophore fragments in the development of physiologically active compound and novel drugs.

7.3.1 2-Chloro-4-hydroxybenzoic acid (2C4HBA)

The first compound probed in the test series is 2-chloro-4-hydroxybenzoic acid or 2C4HBA in short. Observation of the structure reveals two hydrogen bond donors and three hydrogen bond acceptors. The compound is sparingly soluble in water and soluble in acetone. Therefore, 0.02 M 2C4HBA-DMF titration was done in D_2O and acetone-d_6 environment from 0-400 G:H molar ratio. Initial 2C4HBA ^{1}H-HNMR spectra in D_2O and acetone-d_6 reveals similar chemical shift for the three highlighted protons as illustrated in Figure 7.21. In addition, in acetone-d_6 environment a fourth peak is visible, which is the broad peak at 9.8 ppm (Figure 7.21B), corresponding to a labile OH proton. The peak becomes too broad to be observed following the titration, hence focus will be on the clear peaks of the three other protons.

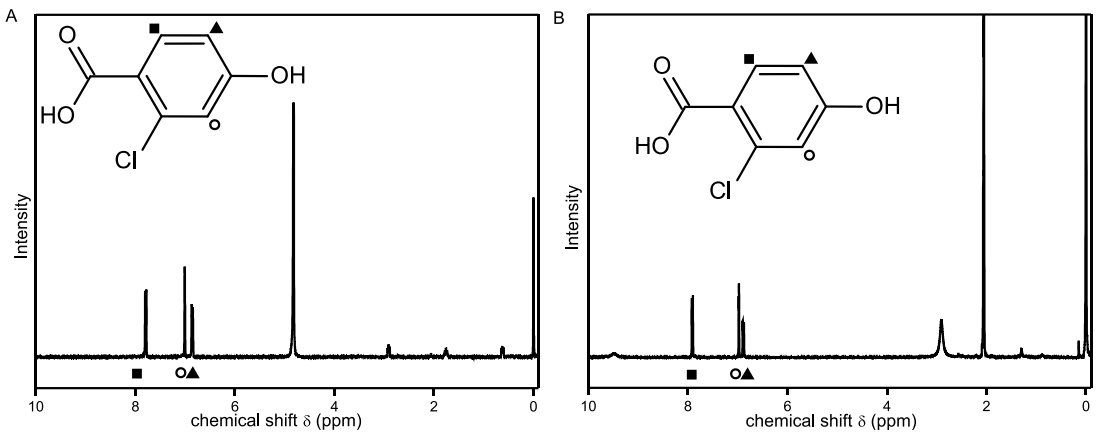


Figure 7.21. ^{1}H-NMR spectrum of 2C4HBA in D_2O (A) and acetone-d_6 (B) environments. Specific chemical shift regions on the spectrum which are identified as proton 1 (■), 2 (○) and 3 (▲) are highlighted with the respective symbols and corresponding inset of the chemical structure.

In D_2O environment, the first monitored peak is the peak at 7.8 ppm corresponding to the proton ortho position on the ring (doublet, proton 1, ▪). Next, the proton on the meta position, next to the chlorine substitute, appearing as a single peak due to lack of other neighbouring H, at the chemical shift 7.0 ppm (proton 2, ∘). The final monitored proton is located on the meta position, next to proton 1, which appears on the spectrum at 6.8 ppm (doublet, proton 3, ▲). Following the titration from 0-150 G:H molar ratio, all the observed peaks undergo downfield shift, with the biggest shift of +0.052 ppm occurring to proton 1, which is the closest proton to the acid group which can be monitored. Proton 2 and 3 also showed significant shift, but at a lower magnitude, shifting by +0.006 and +0.03 ppm respectively.

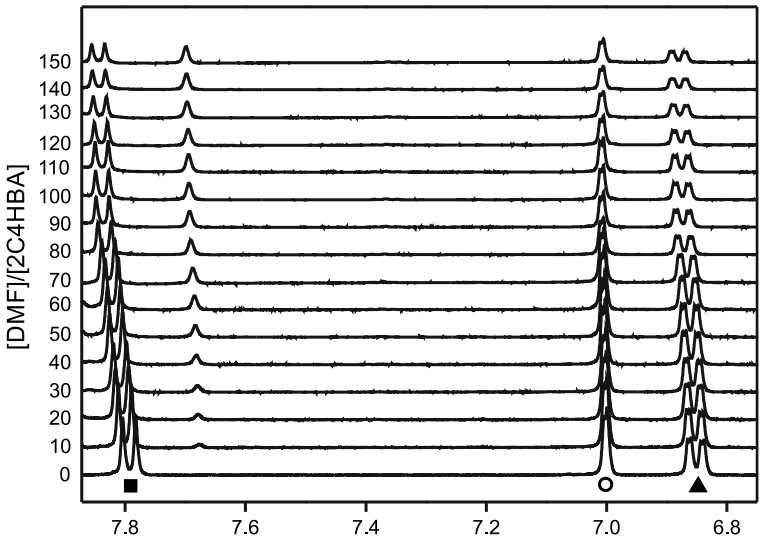


Figure 7.22. 0.02 M 2C4HBA-DMF titration in D_2O environment, up to 150:1 G:H ratio. Note that the growing small peak at 7.7 ppm is one of the satellite peaks of the guest, DMF.

Scatter plot of proton 1 (▪) reveals an almost a linear curve with increasing guest ratio, with a step feature observed in the generated scatter plot at 80 and 90:1 G:H ratio (Figure 7.23). Interestingly, scatter plot of proton 2 initially showed similar linear trend, however at 80:1 G:H ratio a plateau feature is observed (Figure 7.24). As for proton 3, the scatter plot profile is very similar to that of proton 1 (Figure 7.25).

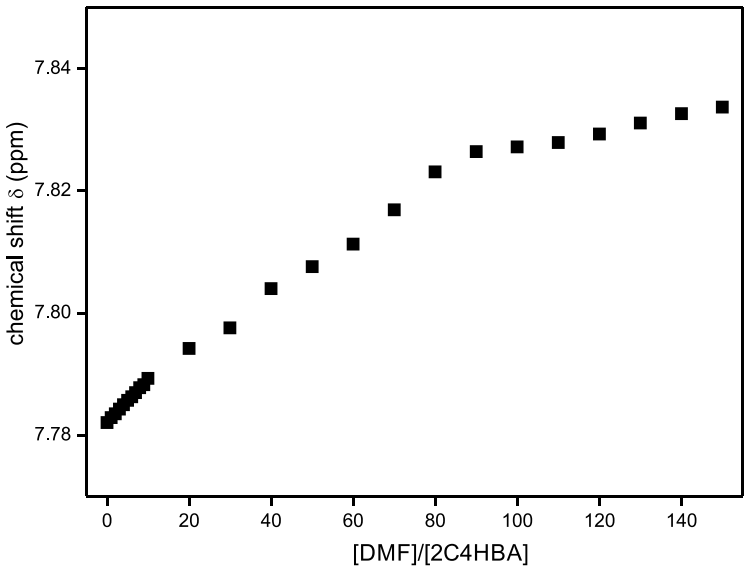


Figure 7.23. The scatter plot for peak shift of proton 1 in 2C4BHA-DMF titration in D_2O environment.

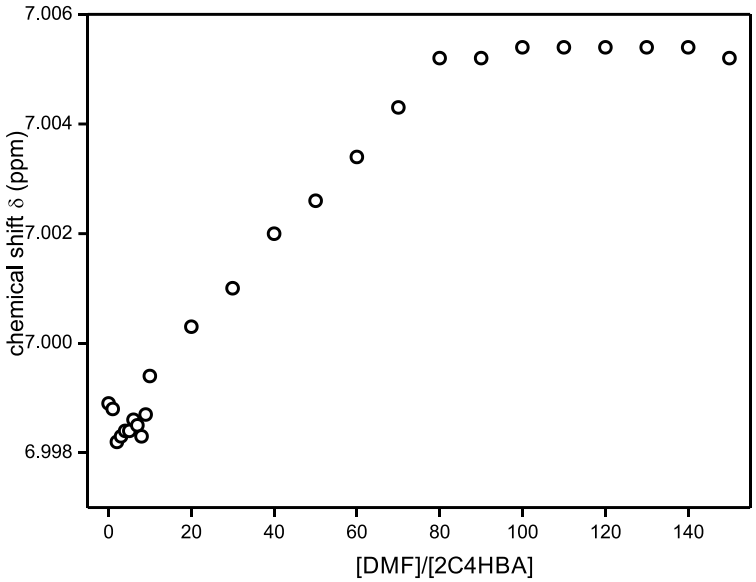


Figure 7.24. The scatter plot for peak shift of proton 2 in 2C4BHA-DMF titration in D_2O environment.

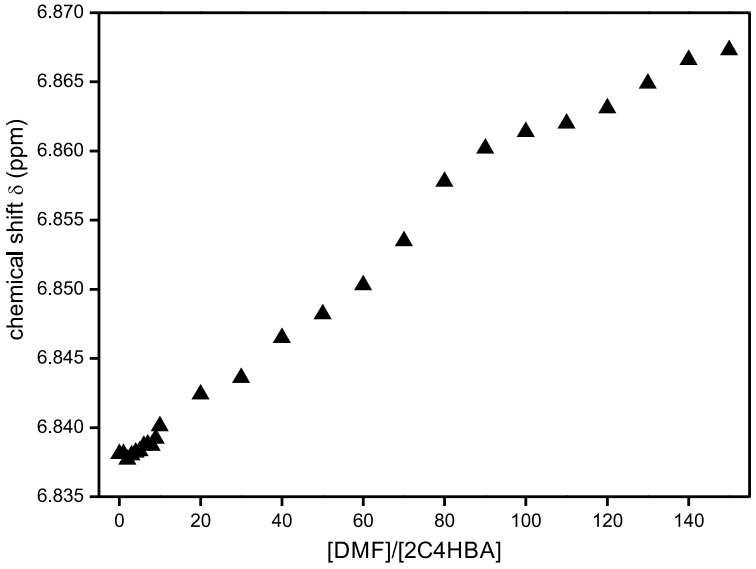


Figure 7.25.The scatter plot for peak shift of proton 3 in 2C4BHA-DMF titration in D_2O environment.

The fitting to the 1:1 model generated the least error following 2C4BHA-DMF titration in D_2O environment, generating a *K* value of 0.27 M^{-1}. However, the largest *K* value obtained from the fitting to the three available models, is when the data is fitted to the 1:2 stoichiometry, resulting in a K_{12} value of 168 M^{-1}. Even though the K_{12} obtained here shows a significant value, it is not a direct comparison to the K_{21} values obtained earlier for TTZ. In addition, 2C4HBA is commercially available as a hydrate

form,[14] hence the complex with water in solution may hinder DMF interaction. Therefore, a second 2C4HBA-DMF titration in acetone-d_6 environment is done as 2C4HBA is very soluble in acetone.

Table 7.7. Calculated ΔG of 2C4HBA-DMF binding in D_2O environment based on three (3) different binding models.

[H]:[G] binding model	K_1 (±% error)	K_{21} (±% error)	K_{12} (±% error)	ΔG for K_{21}
2C4HBA:DMF	0.27 M^{-1} (±2.8%)	N/A	N/A	+3.6 kJ mol^{-1}
2(2C4HBA):DMF	0.84 M^{-1} (±0.3%)	-25 M^{-1} (±-5 x 10^{-6}%)	N/A	N/A kJ mol^{-1}
2C4HBA:2DMF	8.9 x 10^{-4} M^{-1} (±1.9%)	N/A	**168 M^{-1}** (±6.9%)	**-12.7 kJ mol^{-1}**

Interestingly, an overall upfield shift is observed for three protons in 2C4HBA-DMF titration in acetone-d_6 environment, which is similar to the effects observed in TTZ-DMF titration in the same environment. All three plots show a linear increase followed by a plateau feature. Proton 1 curve reaches plateau at 150:1 G:H ratios, while proton 2 and 3 reach plateau at 100:1 G:H ratios. Above 110:1 G:H ratios, proton 2 and 3 started to shift in the opposite direction, which suggest a secondary phase towards DMF interaction. Therefore, to probe early 2C4HBA-DMF interactions, the binding constant determination is calculated based on the fit of data points up to 110:1 G:H ratio.

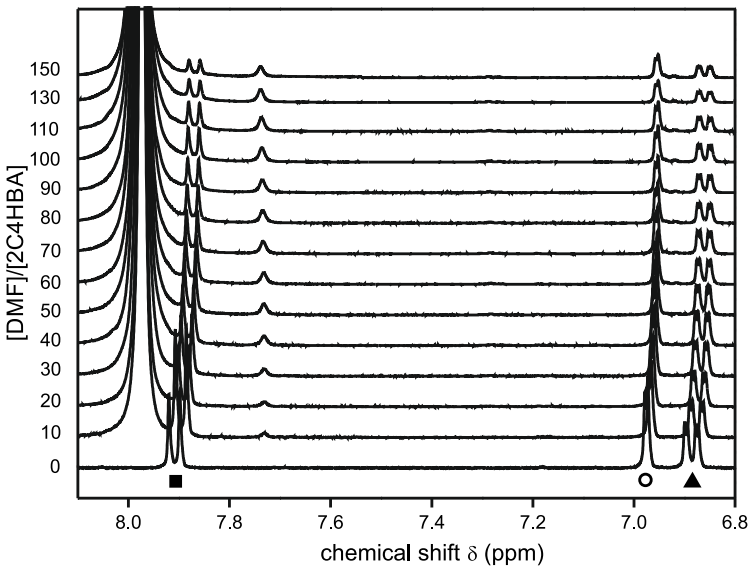


Figure 7.26. 0.02 M 2C4HBA-DMF titration in acetone-d_6 environment, up to 150:1 G:H ratio

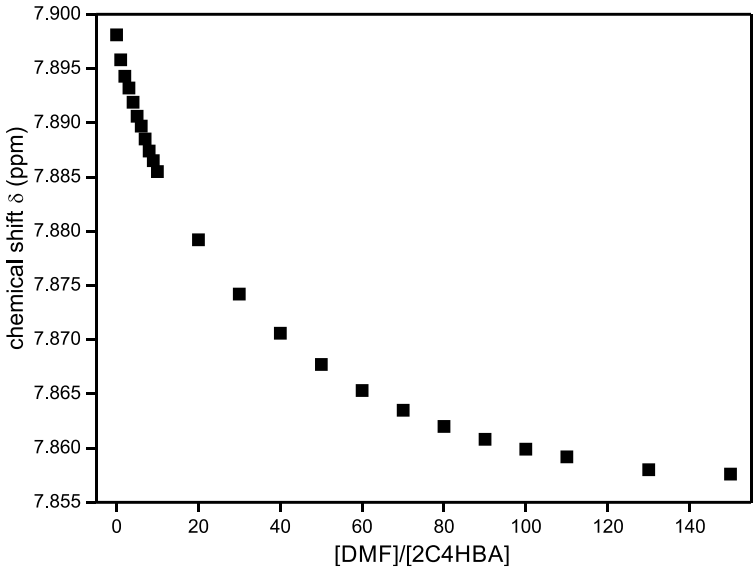


Figure 7.27. The scatter plot for peak shift of proton 1 (■) in 2C4BHA-DMF titration in acetone-d_6 environment.

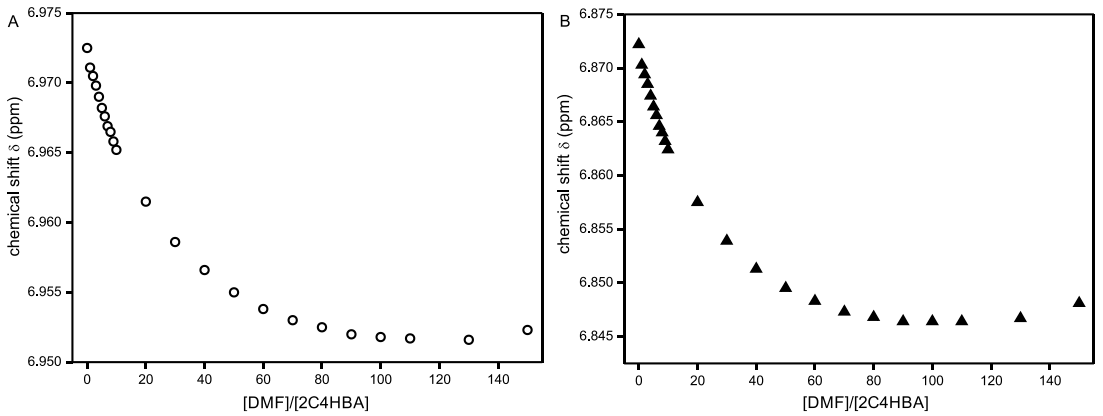


Figure 7.28. The scatter plot for peak shift of proton 2 (○) and 3(▲) in 2C4BHA-DMF titration in acetone-d_6 environment.

Fitting to the three available models revealed that the best fitting is to the 2:1 stoichiometry with a caculated K_{21} value of 1508 M^{-1}, and translates into ΔG of -18.1 kJ mol^{-1} which are higher than the values obtained for TTZ-DMF titration in the same environment, hence falls within the specified significance range. We are confident that 2C4HBA and DMF does interact, and form pre-nucleation aggregate in solution. Note that TTZ-DMF in acetone fitting is only to one proton, but still give a significant K and ΔG values, comparable to the values obtained here. All the data obtained here suggests that the compound binds well to DMF and possibly protein.

Table 7.8. Calculated ΔG of 2C4HBA-DMF binding in an acetone-d_6 environment based on three (3) different binding models.

[H]:[G] binding model	K_1 (±% error)	K_{21} (±% error)	K_{12} (±% error)	ΔG for K_{21}
2C4HBA:DMF	1.9 M^{-1} (±2.1%)	N/A	N/A	kJ mol^{-1}
2(2C4HBA):DMF	0.017 M^{-1} (±2.6%)	**1508 M^{-1}** (±1.4%)	N/A	**-18.1 kJ mol^{-1}**

2C4HBA:2 DMF	1.8 M^{-1} (±1.3%)	N/A	-0.16 M^{-1} (±-5.6%)	kJ mol^{-1}

7.3.2 4-Hydroxybenzoic acid (PHBA)

The second compound in our test is para-hydroxybenzoic acid (PHBA). PHBA is very soluble in acetone, and sparingly soluble in water. However, with 0.02 M PHBA concentration used, no precipitation was detected during PHBA-DMF titration. In both deuterated solvent environment, PHBA appears as two split peaks, with proton close the acid (proton 1, ▪) appearing at 7.9 ppm and the proton close to OH (proton 2, ∘) appearing at 6.9 ppm (Figure 7.30).

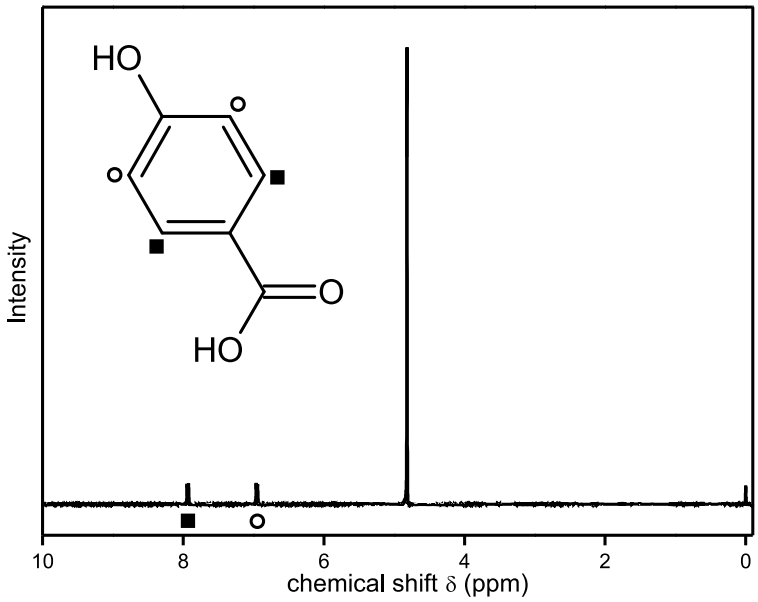


Figure 7.29. ^{1}H-NMR spctrum of PHBA in D_2O environment. Specific chemical shift regions on the spectrum which are identified as proton 1 (▪) and 2 (∘) are highlighted with the respective symbols and corresponding inset of the chemical structure.

PHBA-DMF titration in D_2O environment only allows for the observation of proton 2, as proton 1 peak overlaps with the titrated anhydrous non-deuterated DMF peak (Figure 7.30). Scatter plot of proton 2 reveals an upfield peak shifts from 0-50

G:H ratio, before reaching to a plateau between 50-70 G:H ratio and finally shifting downfield after the 70 molar ratio mark (Figure 7.31). Proton 2 shift reaches significant value (>0.002 ppm shift) at 30:1 G:H ratio. Since proton 1 is unobservable, which is the closer proton to the acid functional group, it is difficult to conclude the role of the acid and the influence on the overall binding. We speculate that early interaction to DMF occurs between 0-70 guest ratio, and above the mark, a secondary, forced-interaction to DMF occurs mainly due to the large amount of DMF present. Therefore, to measure the early PHBA-DMF interaction and complexation, the binding constant determination fitting is only to the data point up to 70 molar ratios.

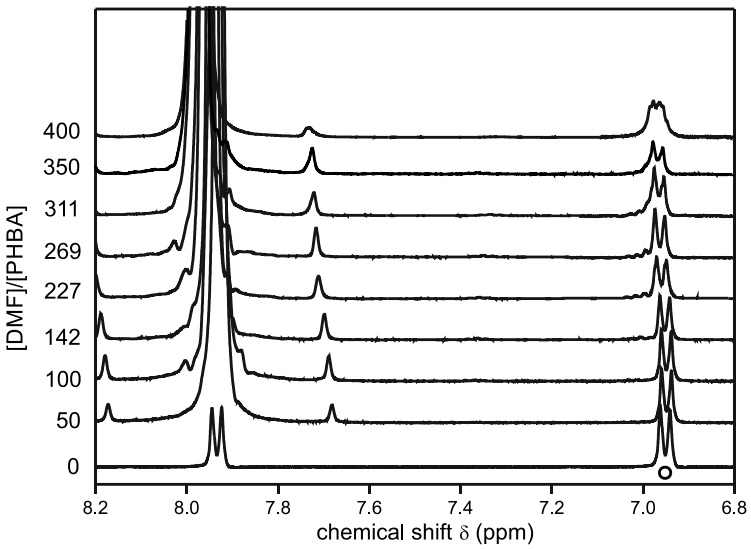


Figure 7.30. 0.02 M PHBA-DMF titration in D_2O environment, up to 400:1 G:H ratio

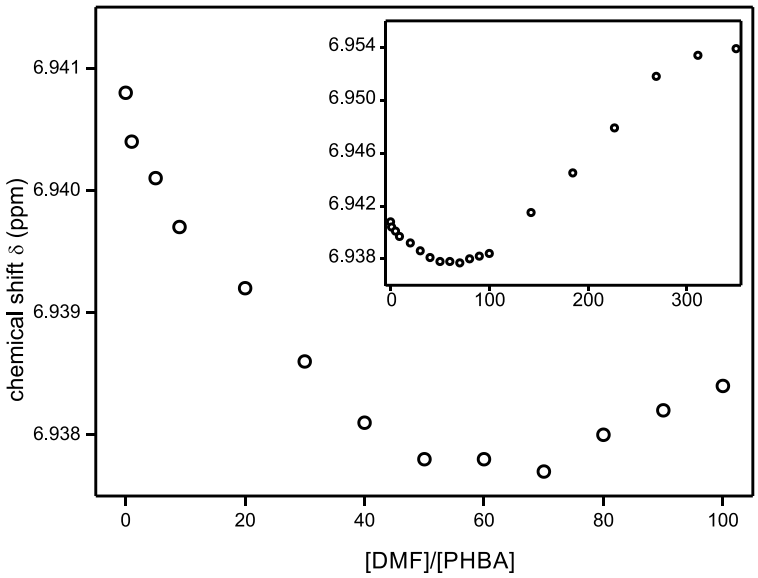


Figure 7.31. The scatter plot for peak shift of proton 2 (○) in PBHA-DMF titration up to 100, and up to 400:1 G:H ratio (inset) in D_2O environment.

The data points for proton 2 peak shift fits poorly to all available stoichiometry models, resulting in K values with high errors of > 10%. The largest K calculated is for the 2:1 fit with 56.5 M^{-1}, however the validity of this fitting is questionable as the error to the fit is >100%. The fitting error is most likely contributed to small dataset as only one proton is monitored, to a small number of data points between 0 and 70 G:H ratio, with a shift magnitude of just -0.0031 ppm, which is just above the significance cut-off.

Table 7.9. Calculated ΔG of PHBA-DMF binding in D_2O environment based on three (3) different binding models.

[H]:[G] binding model	K_1 (±% error)	K_{21} (±% error)	K_{12} (±% error)	ΔG for K_{21}
PHBA:DMF	1.7 M^{-1} (±12.9%)	N/A	N/A	-1.5 kJ mol^{-1}
2PHBA:DMF	2.1 M^{-1} (±137.8%)	56.5 M^{-1} (±252.5%)	N/A	N/A kJ mol^{-1}

PHBA:2DMF	0.85 M^{-1} (±12.5%)	N/A	-0.95 M^{-1} (±-10.7%)	N/A kJ mol^{-1}

A follow-up PHBA-DMF titration is done in acetone-d_6 environment due to its improved solubility in the mentioned solvent environment. Also, the acetone-d_6 environment allows for the observation of proton 1 at 7.9 ppm, as DMF peak appears at 7.97 ppm instead, while proton 2 appears at 6.91 ppm. Interestingly, following DMF titration, a downfield shift to higher ppm is observed for both protons, (Figure 7.32) which is similar to the two previous observations of TTZ-DMF and 2C4HBA-DMF titration in the same solvent. Scatter plot of both protons showed almost a linear curve with a plateau feature, with proton 1 achieving plateau at 200:1 G:H ratio while proton 2 curve reaches plateau at 100:1 G:H ratio (Figure 7.33). Above 150:1 G:H ratio, proton 2 peak starts to shift in the opposite direction, similar to the directional change observed to the same peak in D_2O environment at 70:1 G:H ratio, which suggest a second phase of the interaction involving DMF. The binding constant determination in acetone environment hence is fitted to data up to 150 molar ratios of both proton peak shifts, as the cut off would represent the initial phase of PHBA-DMF interaction.

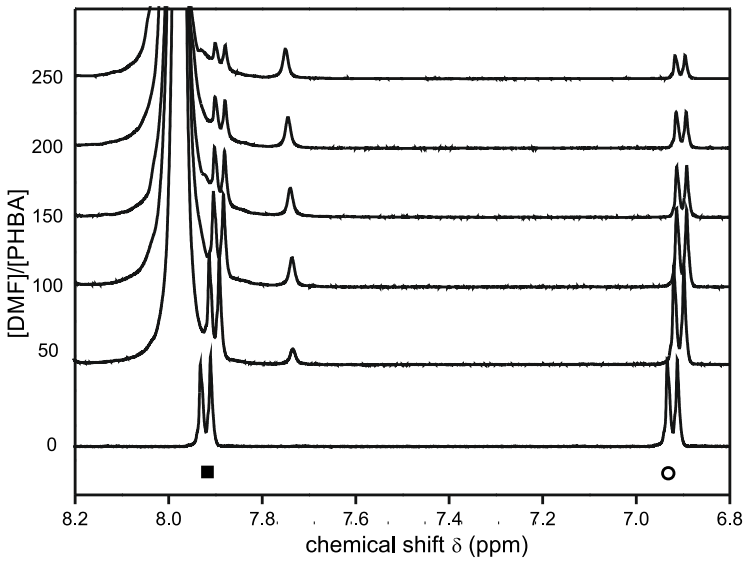


Figure 7.32. 0.02 M PHBA-DMF titration in acetone-d_6 environment, up to 250:1 G:H ratio

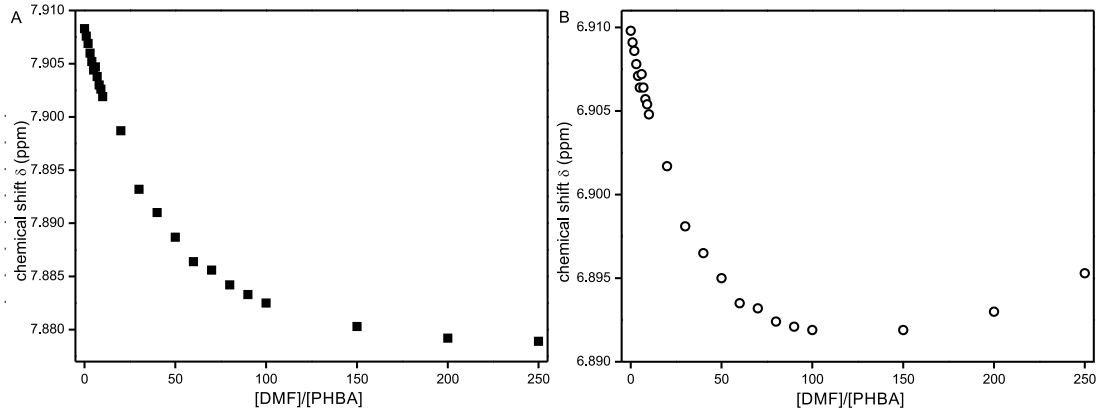


Figure 7.33. The scatter plot for peak shift of proton 1 (A, ■) and 2 (B, ○) PBHA-DMF titration up to 250:1 G:H ratio in acetone-d_6 environment.

Table 7.10. Calculated ΔG of PHBA-DMF binding in acetone-d_6 environment based on three (3) different binding models.

[H]:[G] binding model	K_1 (±% error)	K_{21} (±% error)	K_{12} (±% error)	ΔG for K_{21}
PHBA:DMF	1.2 M^{-1} (±3.9%)	N/A	N/A	-0.5 kJ mol^{-1}
2PHBA:DMF	0.25 M^{-1} (±3.8%)	13.5 M^{-1} (±1.5%)	N/A	-6.4 kJ mol^{-1}

PHBA:2DMF	0.79 M^{-1} (±2.4%)	N/A	0.11 M^{-1} (±8.2%)	+5.5 kJ mol^{-1}

The fitting to all the models from DMF titration in both water and acetone solvent environments generated the highest *K* value of just 13.5 M^{-1}, in the form of K_{21} in acetone environment, which corresponds to a ΔG of -6.4 kJ mol^{-1}. The values are not in the range of the set significance values (1000-2000 M^{-1} and 17-19 kJ mol^{-1}), as well as the values obtained for TTZ-DMF titration in the same environments. The result points to the obvious fact that PHBA shows a low affinity towards DMF hence does not form pre-nucleation aggregate in any of the tested solution, and ultimately suggesting that the compound is not a good DMF or protein binder.

7.3.3 5-Phenyl-1H-tetrazole (5PHT)

The third compound has poor solubility in water, hence DMF titration is done in acetone environment. Three chemical shift regions representing the five observable proton is monitored. Protons on the ortho position on the phenyl appeared as split double peaks and identified as proton 1 (■). Proton 2 (○) and 3 (▲) resonance peaks overlaps in the acetone environment, nevertheless the peaks are still distinguishable.

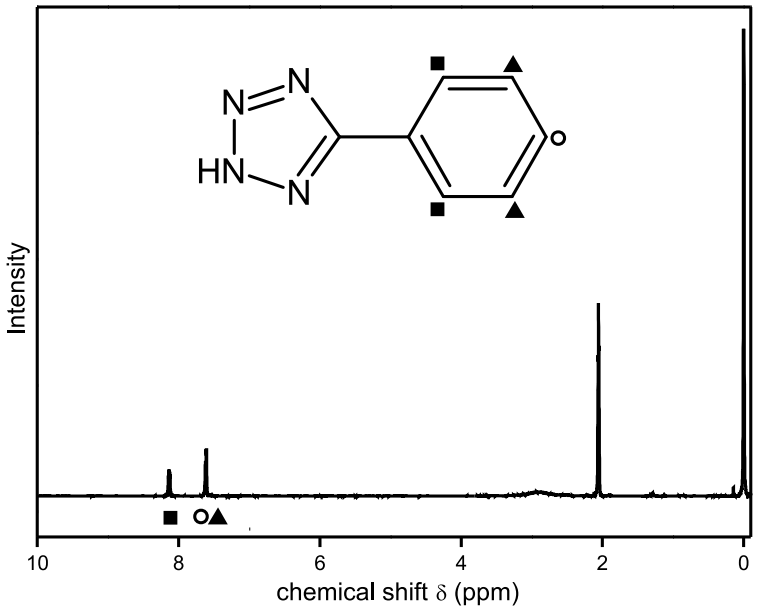


Figure 7.34. ^{1}H-NMR spectrum of 5PHT in acetone-d_6 environment. Specific chemical shift regions on the spectrum which are identified as proton 1 (■), 2 (○) and 3 (▲) are highlighted with the respective symbols and corresponding inset of the chemical structure.

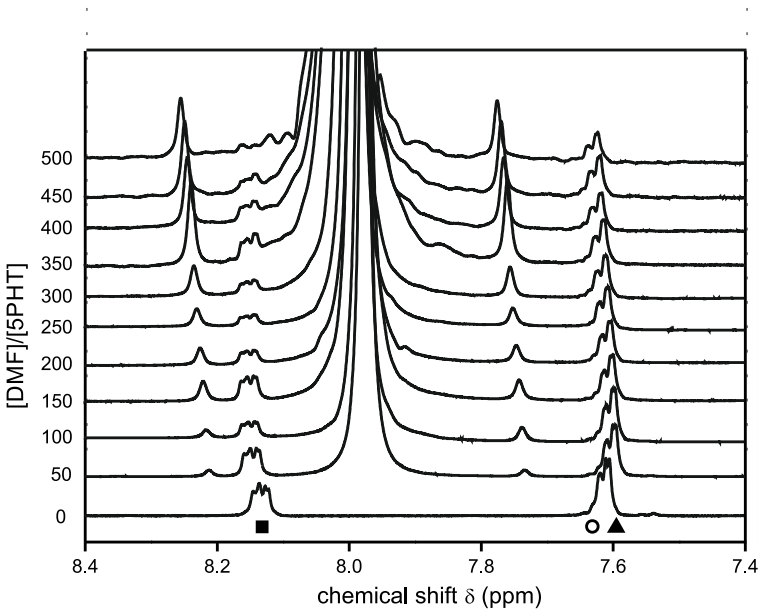


Figure 7.35. 0.02 M 5PHT-DMF titration in acetone-d_6 environment, up to 500:1 G:H ratio

Proton 1 (▪) peak shifts downfield, with the scatter plot of the peak shift showing an increase in shift with the increase of molar ratio of guest added. The scatter plot for peak shift of proton 1 shows a steep linear curve, which come to a plateau above 100:1 G:H ratio (Figure 7.36). Proton 2 (○) and 3 (▲) show similar peak shift

profile to one-another and different to proton 1. At lower DMF concentration, proton 2 and 3 peaks shift upfield and level off at around 70:1 G:H ratio. Both peaks started to shift in the opposite direction above 70:1 G:H ratio (Figure 7.37). Proton 1 shows significant shift up to 100:1 G:H ratio with +0.0165 ppm downfield shift recorded, while proton 2 and 3 shift upfield by -0.01 and -0.009 ppm at the same range. Based on the shift magnitude, we suggest that DMF interact with 5PHT *via* the NH tetrazole ring, hence the effect is observed more to proton 1 (▪). The plateau curve from the scatter plot of proton 1 suggests that the interaction point is saturated at around 100 molar ratio, which is then followed by a second phase of interaction to DMF above 100. Similar change in peak shift direction was also observed during 2C4HBA and PHBA titration in both D_2O and acetone-d_6 environment at higher DMF concentration, The interaction at higher DMF concentration seems to influence proton 2 (∘) and 3 (▲) more, 'forcing' interaction to DMF at higher guest ratio of >100. Therefore, to measure the early 5PHT-DMF interaction and complexation, the binding constant determination is only fitted to the three protons' peaks shift data points up to 100 molar ratios.

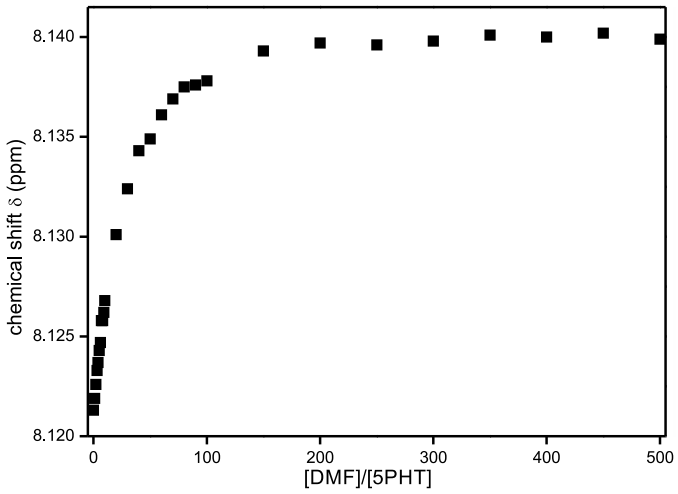


Figure 7.36. The scatter plot for peak shift of proton 1 up to 500 guest molar ratio in D_2O environment.

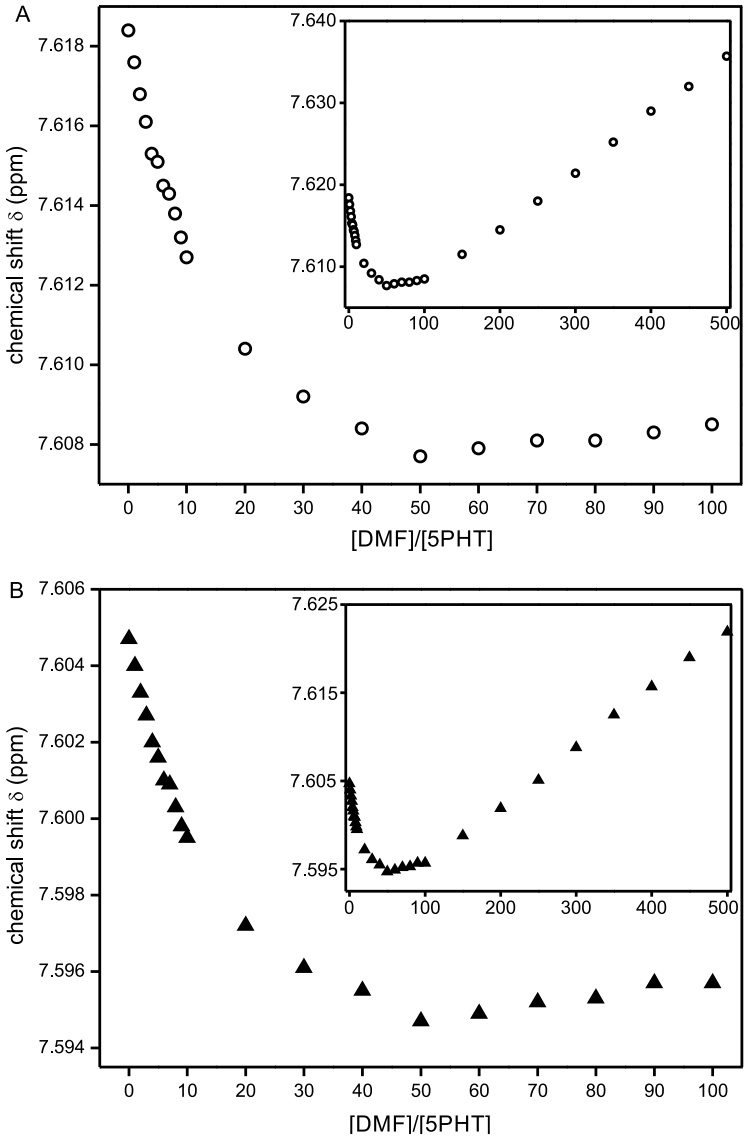


Figure 7.37. The scatter plot for peak shift of proton 2 (A) and 3 (B) up to 100 guest molar ratio, and 500 (inset) guest molar ratio in D_2O environment.

Table 7.11. Calculated ΔG of 5PHT-DMF binding in acetone-d_6 environment based on three (3) different binding models.

[H]:[G] binding model	K_1 (±% error)	K_{21} (±% error)	K_{12} (±% error)	ΔG for K_{21}
5PHT:DMF	2.9 M^{-1} (±7.8%)	N/A	N/A	-2.6 kJ mol^{-1}
2(5PHT):DMF	0.95 M^{-1} (±1.8%)	3.8 M^{-1} (±1.0%)	N/A	-3.3 kJ mol^{-1}

5PHT:2DMF	2.2 M^{-1} (±1.8%)	N/A	0.59 M^{-1} (±3.7%)	+1.3 kJ mol^{-1}

The best fitting for the three protons' peaks shift is to the 2:1 model, which gives a K_{21} value of 3.8 M^{-1}, corresponding to ΔG of -3.3 kJ mol^{-1}. The low *K* and ΔG obtained from 5PHT-TTZ titration in acetone environment are lower than the value obtained for PHBA-DMF titration, and even much lower than the set significance cut-off as well as the TTZ-DMF titration values in the same environment. Therefore, we are confident that 5PHT have a low affinity towards DMF hence does not form pre-nucleation aggregate in solution, ultimately suggesting that the compound is not a good DMF and most certainly protein binder.

7.3.4 5-(4-Pyridyl)-1H-Tetrazole (54PYT)

The final compound in the blind test is 5-(4-pyridyl)-1H-tetrazole (54PYT). Initial ^{1}H-NMR spectrum in D_2O environment shows two chemical peaks shift corresponding to the pyridyl proton at the meta position (doublet, proton 1, ▪ at 8.8 ppm), and the pyridyl protons at the ortho positions (doublet, proton 2, ∘ at 8.4 ppm), all of which are highlighted in Figure 7.38.

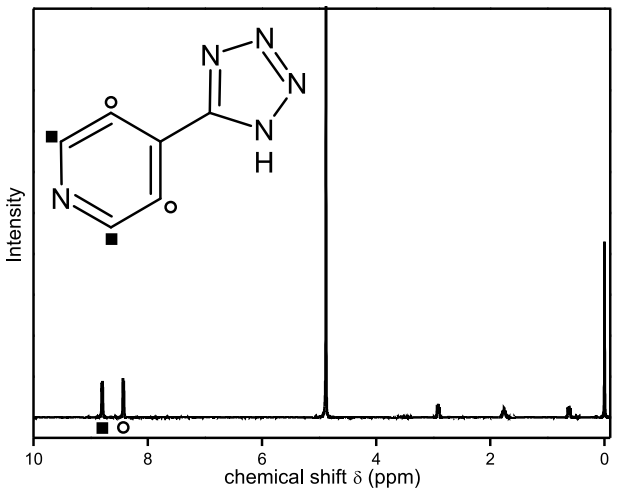


Figure 7.38. ^{1}H-NMR spectrum of 54PYT in D_2O environment. Specific chemical shift regions on the spectrum which are identified as proton 1 (■) and 2 (°) are highlighted with the respective symbols and corresponding inset of the chemical structure.

Following DMF titration, a clear, immediate and significant peak shift is observed early on, at 1:1 G:H ratio. Overall, both peaks shift downfield (Figure 7.39), with the scatter plot showing similar linear trend, before reaching plateau at 100:1 G:H ratio (Figure 7.40). Between 0-200 G:H ratio, proton 1 has shifted by 0.08 ppm while proton 2 by 0.094 ppm. A larger peak shift magnitude observed in proton 2 (°), is most likely due to the closer proximity to the interaction point, the NH on the tetrazole ring.

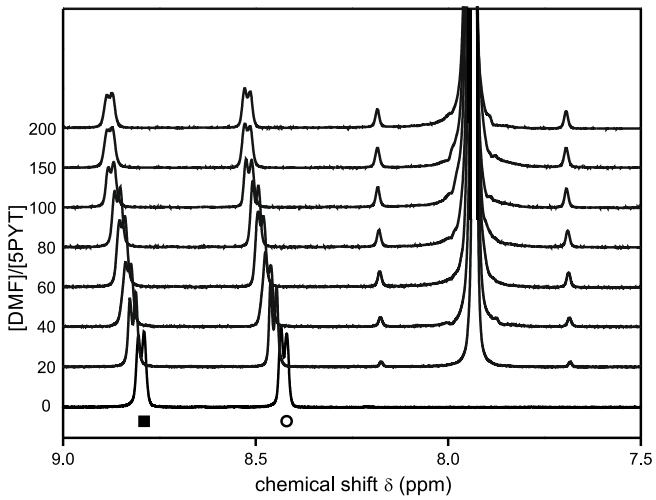


Figure 7.39. 0.02 M 54PYT-DMF titration in D_2O environment, up to 200:1 G:H ratio

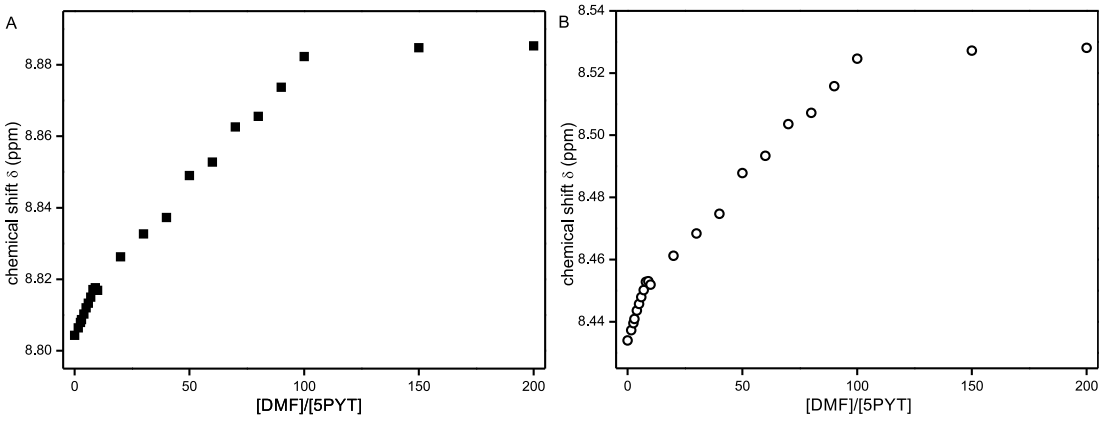


Figure 7.40.The scatter plot for peak shift of proton 1 (A) and 2 (B) up to 200 guest molar ratio in D2O environment.

The best fitting for the three protons' peaks shift is to the 2:1 model, which gives a K_{21} value of 1469 M^{-1}, corresponding to ΔG of -18.1 kJ mol^{-1}. The *K* and ΔG value fall within the set significance cut-off and is also comparable to the values of the model compound, TTZ-DMF titration in D_2O, which suggests significant interaction between 54PYT and DMF in solution, and points to a good DMF and potentially protein binder.

Table 7.12. Calculated ΔG of 54PYT-DMF binding in D_2O environment based on three (3) different binding models.

[H]:[G] binding model	K_1 (±% error)	K_{21} (±% error)	K_{12} (±% error)	ΔG for K_{21}
5P4YT:DMF	0.66 M^{-1} (±5.9%)	N/A	N/A	+1.2 kJ mol^{-1}
2(54PYT):DMF	1.0 x 10^{-3} M^{-1} (±6.0%)	**1469 M^{-1}** (±0.6%)	N/A	**-18.1 kJ mol^{-1}**
54PYT:2DMF	0.2 M^{-1} (±4.3%)	N/A	-0.29 M^{-1} (±-5.0%)	N/A kJ mol^{-1}

7.4 Chapter conclusion

We have investigated TTZ-DMF titration aimed towards stable solvate formation by utilising our method. We have found TTZ to show a strong binding constant and the corresponding ΔG, confirming the existence of TTZ respective crystalline hydrate and solvate forms. The *K* value of 2155 M^{-1} (calculated to ΔG of 19 kJ mol^{-1}) obtained for TTZ-water titration in DMSO is comparable to the values obtained in chapter 5, during the probe of compounds having the ability to form stable hydrates. The obtained *K* value hence hints towards the existence of a stable TTZ crystalline hydrate form, which may or may not be the reported 1.5 hydrate as its stability is unknown. TTZ-water titration reiterates our method's ability to screen hydrate and the data obtained is added to our hydrate-gauge library (Figure 7.41).

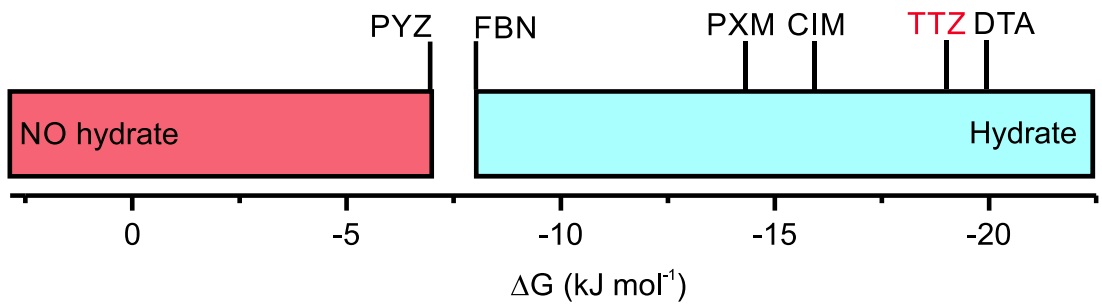


Figure 7.41. ΔG of TTZ and its placement on our hydrate gauge with respect to previously analysed compound using our titration method

The TTZ-DMF titration also revealed that the procedure used is flexible and can be applied to guests other than water. The high *K* value obtained in TTZ-DMF-d_7 titration of 2229 M^{-1} (calculated to ΔG of 19.1 kJ mol^{-1}) in water environment and 1057 (protiated) and 1145 M^{-1} (deuterated, calculated to ΔG of 17.25 and 17.45 kJ mol^{-1} respectively) in acetone environments reflects well the claimed existence of an extremely stable DMF solvate. What is more impressive, the *K* value from DMF

titration in D_2O is even larger than the *K* value for TTZ-water titration in DMSO-d_6, which is already quite significant.

Further use of our procedure is probed, as strong and weak interaction between the amide solvent (DMF), and four different compounds with different protein binding ability was successfully distinguished, in aqueous and acetone solution. The consistently high values obtained for DMF titration of > 1000 M^{-1} which corresponds to ΔG of <-17 kJ mol^{-1} for compound showing good protein binding ability (TTZ, 2C4HBA and 54PYT), sets the lower limit for significance of DMF binding, regardless of the used solvent, D_2O or acetone-d_6. We also consistently saw higher peak shift magnitude to proton which is closer to the interaction point *vs* proton further away, which helps in identifying the functional group at play with the respective guest. In the TTZ-water titrations regardless of the environment, DMSO or DMF, the protons on the ring which is closer to the OH consistently have higher peak shift magnitude. While for compound having the NH 5-membered ring, in DMF titration, protons which are at closer proximity to this ring would experience bigger peak shift magnitude.

Overall, the method used is able to reflect on the existence of the stable TTZ-DMF solvate formation. Though we have shown positive correlation between the solution and the solid state with respect to solvate prediction, a larger scope and variety of solvate-forming compound analysed by our method would confirm, and expand the use of our method predict solvate formation. Using DMF as the guest, we were able to probe the binding of four compounds to DMF, and the result obtained thus far reflect on the protein-binding ability of those compound. This means that DMF can be used as a proteomimetic agent and be used an early screening tool for other relevant compounds or pharmacophore fragments. On the grand scheme of things, the result

opens up door for other uncharged guest to be used, allowing probe into pre-nucleation aggregates and subsequent prediction of the solid phase. For hydrate prediction, the grey area between hydrate-forming and non-hydrate forming is becoming clearer with every compound analysed using our method and updated into our library. With enough database, distinction between weak and strong hydrate can also be made.

Table 7.13. All K_{21} or K_{12} and ΔG for all the probed compounds.

[H]:[G] binding model	K, K_{21} or K_{12}	ΔG	Our prediction and conclusion	Hydrate/Actual protein binding ability
2TTZ:H_2O in DMSO-d_6	2155 M^{-1}	-19 kJ mol^{-1}	YES for hydrate	1.5 hydrate
2TTZ:H_2O in DMF-d_7	4.7 M^{-1}	-3.8 kJ mol^{-1}	N/A	N/A
TTZ:2DMF-d_7 in DMSO	34.9 M^{-1}	-8.8 kJ mol^{-1}	Unclear	DMF solvate
2TTZ:DMF-d_7 in D_2O	2229 M^{-1}	-19.1 kJ mol^{-1}	Stable solvate	DMF solvate
			Good DMF binder	Good protein binder
2TTZ:DMF in ACO-d_6	1057 M^{-1}	-17.25 kJ mol^{-1}	Good DMF binder	Good protein binder
2TTZ:DMF-d_7 in ACO-d_6	1145 M^{-1}	-17.45 kJ mol^{-1}	Good DMF binder	Good protein binder
2C4HBA:2DMF in D_2O*	168 M^{-1}	-12.7 kJ mol^{-1}	Unclear	Hydrate present Good protein binder
2(2C4HBA):DMF in ACO-d_6	1508 M^{-1}	-18.1 kJ mol^{-1}	Good DMF binder	Good protein binder
PHBA: DMF in D_2O	1.7 M^{-1}	-1.3 kJ mol^{-1}	High error fit	Unclear

2PHBA:DMF in ACO-d_6	13.5 M^{-1}	-6.4 kJ mol^{-1}	Not a good DMF binder	Unclear
2(5PHT):DMF in ACO-d_6	3.8 M^{-1}	-3.3 kJ mol^{-1}	Not a good DMF binder	Not a good protein binder
2(54PYT):DMF in D_2O	1469 M^{-1}	-18 kJ mol^{-1}	Good DMF binder	Good protein binder

*2C4HBA K_{12}, ** PHBA K_{11}

7.5 References

1. Bipp, H. & Kieczka, H. Formamides. in *Ullmann's Encyclopedia of Industrial Chemistry* (Wiley-VCH Verlag GmbH & Co. KGaA, 2011).

2. Malik, M. A., Wani, M. Y., Al-Thabaiti, S. A. & Shiekh, R. A. Tetrazoles as carboxylic acid isosteres: chemistry and biology. *J. Incl. Phenom. Macrocycl. Chem.* **78,** 15–37 (2014).

3. Wei, C.-X., Bian, M. & Gong, G.-H. Tetrazolium Compounds: Synthesis and Applications in Medicine. *Molecules* **20,** 5528–5553 (2015).

4. Popova, E. A., Protas, A. V & Trifonov, R. E. Tetrazole Derivatives as Promising Anticancer Agents. *Anticancer. Agents Med. Chem.* **17,** (2017).

5. Gallardo, H., Begnini, I. M., Vencato, I. & IUCr. 5-(4-Hydroxyphenyl)tetrazole–Water (2/3). *Acta Crystallogr. Sect. C Cryst. Struct. Commun.* **53,** 143–144 (1997).

6. Cilense, M., Benedetti, A. V. & Vollet, D. R. Thermodynamic properties of liquid mixtures. II. Dimethylformamide-water. *Thermochim. Acta* **63,** 151–156 (1983).

7. Rodgers, G. E. & Plane, R. A. A Raman spectrophotometric study of the effect of N , N -dimethylformamide and the electrolytes NaClO 4 , Zn(ClO 4) 2 ,

NaNO 3 , and Zn(NO 3) 2 on the structure of liquid water. *J. Chem. Phys.* **63,** 818–829 (1975).

8. Petersen, R. C. Interactions in the binary liquid system N,N-dimethylacetamide-water: Viscosity and density. *Journal of Physical Chemistry* **64,** 184–185 (1960).

9. Lin, R., Hu, X. & Ren, X. Homogeneous enthalpic interaction of amino acids in DMF–H2O mixed solvents. *Thermochim. Acta* **352–353,** 31–37 (2000).

10. Nozaki, Y. & Tanford, C. The solubility of amino acids and two glycine peptides in aqueous ethanol and dioxane solutions. *J. Biol. Chem.* **246,** 2211–2217 (1971).

11. Roberts, D. C. & Bohacek, R. S. Estimation of peptide hormone noncovalent binding site functionality from frequencies of interaction of amino acid side chains in proteins. *Int. J. Pept. Protein Res.* **21,** 491–512 (1983).

12. Sijpkes, A. H., Staneke, P. O. & Somsen, G. Enthalpies of interaction of some N-acetyl amides of l-serine, l-threonine and l-hydroxyproline dissolved in N,N-dimethylformamide at 298.15 k. *Thermochim. Acta* **167,** 65–72 (1990).

13. Sijpkes, A. H. & Somsen, G. Enthalpic interaction coefficients of some dipeptides dissolved in N,N-dimethylformamide. *J. Chem. Soc. Faraday Trans. 1 Phys. Chem. Condens. Phases* **85,** 2563 (1989).

14. Sigma-Aldrich. *CDS021563: 2-Chloro-4-hydroxybenzoic acid hydrate SDS*. (2016).